26$^{\text{th}}$ International Conference on Plastic Optical Fibres
PROCEEDINGS

26th$^{\text{th}}$ International Conference on Plastic Optical Fibres, POF 2017
September 13 to 15, 2017
Aveiro, Portugal

ICPOF

instituto de
telecomunicações

Preface

Welcome to POF2017 !

Welcome to Aveiro and to the 26th International Conference on Plastic Optical Fibres, POF2017. This is a leading event in POF research, application and industrial activities, where scientists and engineers from both academia and industry will have an opportunity to exchange ideas, share new achievements and discuss the latest R&D results.

In an open friendly environment, this forum is an excellent opportunity to foster the establishment of the widest range of cooperation projects and relationships with colleagues and institutions from all around the world while promoting Optics and Photonics and its impact in the development of our societies.

The organizing committee are grateful for the support and active participation of the sponsors and endorsers of the conference and the contributions of hundreds of authors and co-authors from around the globe.

Because POF2017 is also about networking, we have prepared an intense social program, which we hope you will enjoy !

Aveiro, September 13, 2017

The conference Chairs,
Rogério Nunes Nogueira
Ana Maria Rocha
Lúcia Bilro

Sponsorship

Silver Sponsor

pcl Photonic Communications Lab

▲ Hochschule Harz
Harz University of Applied Sciences

Endorsements & Sponsors

OSA® Student Chapter

universidade de aveiro

SPOF

innova scientific

INFORMATION GATEKEEPERS INC.

POF Plastic Optical Fiber Trade Organization

Committees

Chair of International Program Committee

Yasuhiro Koike, Keio University, Japan

Conference Chair

Rogério Nogueira, Instituto de Telecomunicações, Aveiro, Portugal

Local Organizing Committee Co-Chairs

Ana Maria Rocha, Instituto de Telecomunicações, Aveiro, Portugal
Lúcia Bilro, Instituto de Telecomunicações, Aveiro, Portugal Portugal

Local Organizing Committee

Álvaro Almeida, Instituto de Telecomunicações, Aveiro, Portugal
Daniel Duarte, Instituto de Telecomunicações, Aveiro, Portugal
Filipa Sequeira, Instituto de Telecomunicações, Aveiro, Portugal
Ricardo Oliveira, Instituto de Telecomunicações, Aveiro, Portugal
Telmo Almeida, Instituto de Telecomunicações, Aveiro, Portugal
Vanessa Cunha Duarte, Instituto de Telecomunicações, Aveiro, Portugal

International Program Committee

Yasuhiro Koike (Chair), Keio University, Japan
Lee L. Blyler Jr., Chromis Fiberoptics, US
Werner Daum, Federal Institute for Materials Research and Testing (BAM), Germany
Roberto Gaudino, Politecnico di Torino, Italy
Jacques Goudeau, Nexans Research Center, France
Yoichi Ikemoto, Sekisui Chemical, Japan
Demetri Kalymnios, London Metropolitan University, UK
A.M.J. (Ton) Koonen, Eindhoven University of Technology, Netherlands
Katerina Krebber, Federal Institute for Materials Research and Testing (BAM), Germany
John D. Lambkin, Firecomms, Ireland
Maryanne C.J. Large, University of Sydney, Australia
Jung Wook Lee, Korea Information and Communication Supervision Association, South Korea
Ann Mescher, University of Washington, US
Kazuki Nakamura, Mitsubishi Rayon, Japan
Hans Poisel, POF AC, University of Applied Sciences Nuernberg, Germany

Paul Polishuk, IGI Group, US
Stephen Ralph, Georgia Institute of Technology, US
Patricia Scully, Manchester University, UK
Tetsuya Toma, Keio University, Japan
Yuji Watanabe, Asahi Glass, Japan
Marcelo Martins Werneck, Universidade Federal do Rio de Janeiro, Brazil
Whitney White, Chromis Fiberoptics, US
Olaf Ziemann, POF AC, University of Applied Sciences Nuernberg, Germany
Joseba Zubia, University of the Basque Country, Spain
David Webb, Aston Institute of Photonic Technologies, UK

Table of Contents

7 Data Communications

Tutorial

8 Sensors III

9 Light Transmission

Poster Session

Fabrication of Bragg gratings in polymer optical fibers using 248 nm UV radiation

R. Oliveira[1*,] L. Bilro[1], R. Nogueira[1]

1 Instituto de Telecomunicações, Campus Santiago, 3810-193 Aveiro, Portugal
*Corresponding author: oliveiraricas@av.it.pt

Abstract: In this paper it is shown that a 248 nm UV laser commonly used for the inscription of silica FBGs can be successfully used for the production of PFBGs in POFs composed of different structures and materials. The success of the result is due to the modification of the refractive index under the incubation phenomenon, for which the ablation of the polymer material is not observed. Additionally, the time needed to inscribe a single PFBG is just a few seconds, a record time that has never been reached with any other UV radiation.

1.   Introduction

Nowadays, applications related with polymer optical fibers (POFs) have increased their number. The reason is essentially due to the opportunities that POFs can offer when compared with silica fibers. Among them are: the negative and much larger thermo-optic coefficient [1]; the smaller Young modulus [2], allowing to withstand at high elongation regimes [3]; flexibility in bending; non-brittle nature, biological compatibility [4], ability to detect humidity [5], among others.

Fiber Bragg Gratings (FBGs) are very attractive due to the easy integration in optical components. When recorded in POFs, two important technologies are combined. The inscription of FBGs in POFs is being essentially performed by long UV and short visible wavelengths, where the material attenuation as well as photosensitivity is lower. The drawback associated with such wavelength range is essentially the long inscription time, which also depends on the polymer material, fiber diameter, doping and fiber structure. Additionally, constrains related with the stability of the mechanical apparatus during the long inscription process, may be problematic due the size of the structures being created. Nevertheless, volume fabrication of these structures may be challenging for the future of this technology.

All around the world, there are a vast number of inscription setups that are being used for the production of silica FBGs. Examples of those systems are the ones employing a 248 nm UV lasers. Regarding the polymers employed on the fabrication of POFs, it is known that the photosensitivity increases for deeper UV wavelengths. Therefore, the use of 248 nm inscription systems for polymer fiber Bragg grating (PFBG) fabrication, can be benefit.

Despite the high characteristics offered by PFBGs, there are several issues when working with POFs. Those are found at the very beginning of the production of any POF based device. Examples of that are the cleaving and splicing processes required to have the fiber ready to work. The problem becomes even worst when considering POFs of small diameter or the presence of air holes in case of microstructured fibers. For the cleaving, it has been reported the formation of several defects such as cracks, surface roughness, core shift among others, which inevitably lead to have high coupling losses.

The interrogation of PFBGs has its main problems on the coupling process between the silica to POF fibers. One of the reasons is related with the poor quality end face of the POFs. For that reason we will briefly describe the preparation of the POF tip by a cleaving/polishing process. The description of the PFBG inscription through the use of a KrF UV radiation will then be followed. Results concerning the inscription time, and final spectra, will be show for fibers of different structures/materials. Finally, a conclusion on the type of the grating as well as on the type of refractive index modification will be given.

2.   Fiber preparation

The POFs used in this work were acquired from different manufactures and they are based on different fiber materials and structures. The different POF parameters can be found in Table 1:

Table 1

POF Fiber	Source	Type	Material	Hole Layers	Clad D (µm)	Core D_c (µm)
SM-125	Kiriama Pty Ltd.	mPOF	PMMA	6	125	4
FM-Zeonex	UNICAMP	SI-POF	PMMA cladd; Zeonex core	-	300	13
FM w/ Rh6G	Kiriama Pty Ltd.	mPOF	PMMA doped w/ RH6G	4	180	11
FM-250	Kiriama Pty Ltd.	mPOF	PMMA	6	250	18
HiBi1	InPhoTech	mPOF	PMMA	3	250	5x8
HiBi2	UNICAMP	mPOF	PMMA	6	270	6.5x8.6
G3-250	Kiriama Pty Ltd.	mPOF	PMMA	3	250	34
MM-150	Kiriama Pty Ltd.	mPOF	PMMA	3	150	40
MM-Zeonex	UNICAMP	uncladd	Zeonex	-	-	73.5

To begin the POFs end face preparation, a hot blade was used to first cleave the fiber, avoiding crack formation in the transversal and longitudinal directions, and allowing at the same time the formation of a flat surface. The cutting process was handmade with the fibers laid onto a piece of glass and cleaved transversally. The base was left at room temperature, while the blade temperature was set to cleave the fibers without melt or create cracks. That temperature was set to be below the melting point of the plastic materials (around 70 or 80 ºC). After the cleaving process, the POFs were analysed with an optical fiber scope (OFS300-200C) to check if any visible crack was formed. If so, the process is repeated with higher temperatures. After the cleaving process, the fibers were subjected to a polishing procedure [6]. For that, ceramic ferrules with bores selected to cover different POF diameters were employed. After selecting the specific ferrule, that closely matches the POF being used, the cleaved POF is inserted in the ferrule bore and pulled down against the polishing machine film. The polishing process that is composed of two cycles of 15 seconds each, is then initialized. The first cycle is made with a 3 µm grain size polishing film (PF03.0S-P-2) and the second one with 0.3 µm (PF00.XW-P-2). The grain sizes of the polishing films were chosen to first roughly scratch the POFs end face, removing imperfections from the hot blade process and the second one to give a smooth termination. To avoid small dust particles at the end face of the fiber, specifically for the mPOFs, water spray was spread onto the second polishing film prior to the polishing step. The final result may be seen in Figure 1.
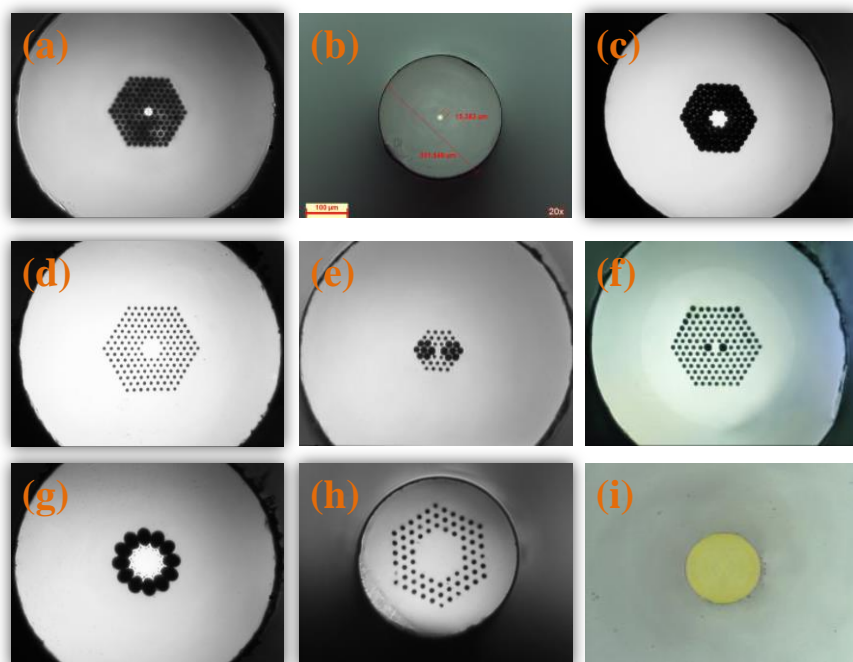
Figure 1 Microscope images of the tips of different POFs. (a) SM-125; (b) FM-Zeonex; (c) FM w/RH6G; (d) FM250; (e) HiBi1; (f) HiBi2; (g) G3-250 MM; (h) MM-150; (i) unclad ZEONEX 480R.

2.   *POFBG fabrication*

For the Bragg grating inscription, it was used a Bragg Star Industrial-LN excimer laser operating at 248 nm. The laser beam has a spot size of 6 mm in width and 1.5 mm in height, with pulse duration of 15 ns. The laser parameters were adjusted to low frequency and low energy, allowing the refractive index modification under the incubation phenomenon. The setup used for the PFBG fabrication is based on the phase mask method and it is shown on Figure 2.
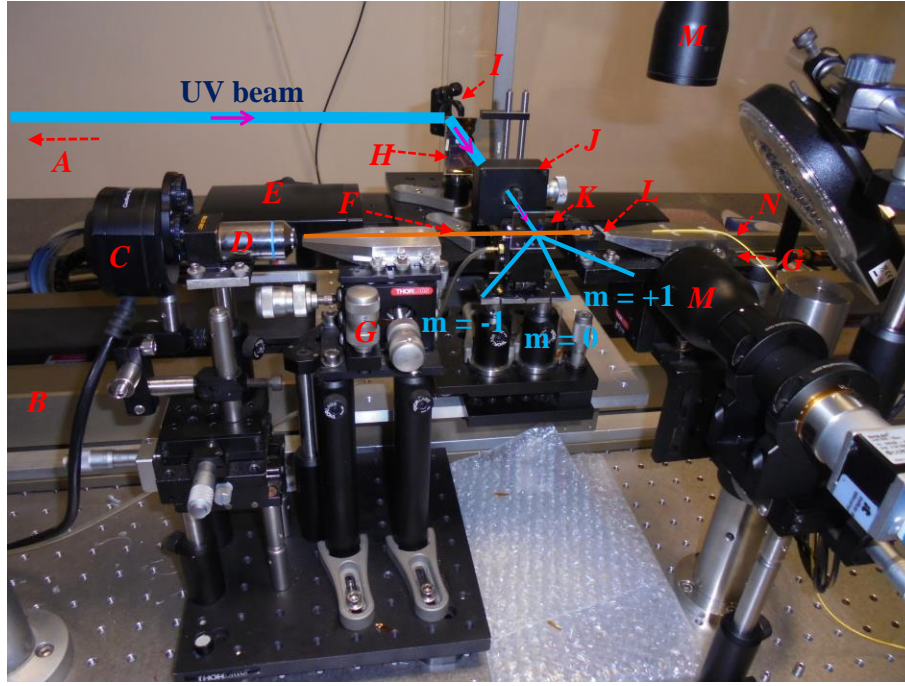
Figure 2 Picture of the inscription setup employing the phase mask technique. Legend: "*A*" → KrF laser (not shown); "*B*" → Linear stage (ABL20100); "*C*" → Beam profiler; "*D*" → 40 X objective; "*E*" → Motorised linear stage (M-ILS150CC); "*F*" → POF; "*G*" → 3D mechanical stages; "*H*" → Lens; "*I*" → Mirror; "*J*" → Slit; "*K*" → Phase Mask; "*L*" → Butt coupling; "*M*" → Telescopic cameras; "*N*" → Silica pigtail fiber.

As can be seen from Figure 2, the laser beam is reflected at the mirror ("I"), and shaped at the POF ("F"), after passing through a cylindrical lens ("H"), slit ("J"), and phase mask ("k"). The POF is secured by clamps that are on top of the micrometer stages ("G"), used to align the fiber against the laser beam and also to make a temporary free space coupling ("L"), between the SM pigtail silica fiber, cleaved with an FC/APC contact, and one end of the polished POF. Between the coupling, index matching gel is used to reduce the background noise and also to avoid Fresnel reflections. At the other POF terminal, a beam profiler ("C") together with a 40 X magnification lens ("D"), is used to easily align the core of the silica fiber against the POF. This is easily performed by looking at the POFs near field pattern and also to the real time images provided by the telescopic cameras("M"), around the joint splice.

3.   **Results and discussion**

Preliminary tests in a FM-250 mPOF, revealed that for 60 seconds exposure with a frequency of 1 Hz and 3 mJ/cm^2, there were no evidences of surface ablation at the polymer surface [7].

The inscription of the PFBG was tested at the 1550 nm region due the availability of devices. The Bragg grating inscription was monitored in real time and it was revealed the capability to write PFBGs in few seconds, as reported in [7]. Results concerning the PFBG peak power evolution may be seen in Figure 3 for some of the PFBGs described in Table 1.
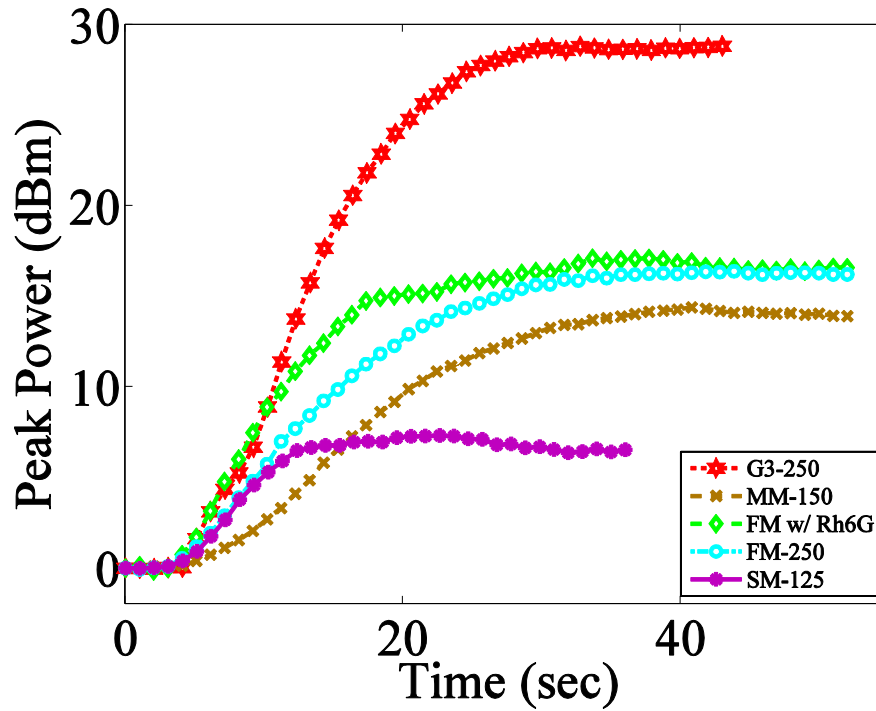
Figure 3 Peak power evolution for four different POFBGs.

As shown in Figure 3, the POFBGs reach the saturation level in few seconds. Results concerning the PFBG spectra for the POFs described in Table 1, can be visualised on Figure 4.
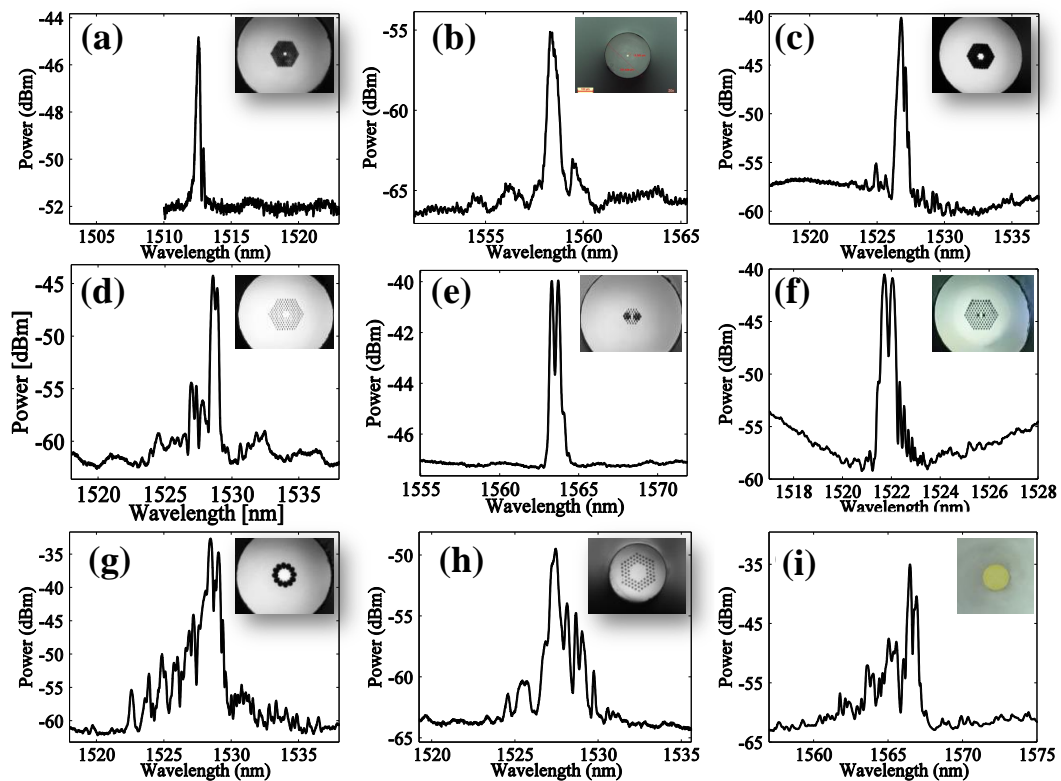
Figure 4. POFBGs in (a) SM-125; (b) FM-Zeonex; (c) FM w/RH6G; (d) FM250; (e) HiBi1; (f) HiBi2; (g) G3-250 MM; (h) MM-150; (i) unclad ZEONEX 480R.

As can be seen, the reflection spectra shown in Figure 4(a-e), present single and few peaks, contrary to the observed for the spectra shown in Figure 4(g-i). The result is already expected due the single mode nature presented in (a, e and (f)), few mode in (b-d) and multimode in (g-i). Yet, it is worth to mention that the Bragg reflection spectra are highly dependent on the coupling coefficient between the silica fundamental core mode with the different modes allowed to propagate in the POFs.

We believed that the produced gratings are of type I. Evidences to that may be found on the resonance Bragg peak shown for the single mode fibers (i.e. Figure 4(a, e and (f)), which does not show losses at the short wavelength side of the spectrum. Additionally, analysis of microscope images of the POF regions exposed to the UV interference beam, reveals no damages at the fiber surface which is in accordance with a type I Bragg grating. The results prompt thus to a refractive index modulation in the core POF done during the incubation phenomenon and below the PMMA ablation threshold. The capability to modulate the refractive index of the polymer material was only achieved due to the combination of three key factors, which were: the low fluence; the low repetition rate; and low number of pulses.

Another important feature observed during the inscription of these gratings is that the Bragg wavelength peak suffered a permanent blue shift. This result is an indication of a negative refractive index change. The phenomenon can then be explained as a consequence of the photodegradation process. In a first instance, the polymer main chain suffers a side chain split, generating new unsaturated species. The complete separation of the side chain of PMMA causes the formation of a radical electron at the α-C-atom, which leads to a destabilization of the polymer main chain causing its scission and forming short length molecules, promoting to a high degree of freedom, *i.e.* decreased refractive index.

3.   Conclusions

In this paper it was shown that UV radiation, commonly employed for the inscription of silica FBGs can be worthily if applied for the production of PFBGs in several POFs, such as single-mode, few mode, multimode, HiBi, unclad, etc.. The success of the result is due to the modification of the refractive index under the incubation phenomenon, for which the ablation of the polymer material is not observed. In addition to the possibility of the use of the already developed inscription systems, the time needed to inscribe a single PFBG is just a few seconds. These attractive features can lead this fiber optic technology for a more intense use in a near future. In the overall, the 248 nm UV radiation showed that common Bragg grating systems designed for silica fibers can be used to inscribe FBGs is POFs, paving the way for a more intense use of these structures in both telecommunications and sensors industries.

Acknowledgements

References

[1]   K. Minami, *Handbook of Plastic Optics*, 2nd ed. Weinheim, Germany: Wiley-VCH Verlag GmbH & Co. KGaA, 2010.

[2]   A. Cusano, A. Cutolo, and J. Albert, *Fiber Bragg grating sensors: Recent advancements, industrial applications and market exploitation*, 1st ed. Sharjah : Bentham Science Publishers, 2011.

[3]   Z. Xiong, G. D. Peng, B. Wu, and P. L. Chu, "Highly tunable Bragg gratings in single-mode polymer optical fibers," *IEEE Photonics Technol. Lett.*, vol. 11, no. 3, pp. 352–354, 1999.

[4]   G. Emiliyanov, J. B. Jensen, O. Bang, P. E. Hoiby, L. H. Pedersen, E. M. Kjær, and L. Lindvold, "Localized biosensing with Topas microstructured polymer optical fiber," *Opt. Lett.*, vol. 32, no. 5, pp. 460–462, 2007.

[5]   W. Zhang, D. J. Webb, and G.-D. Peng, "Investigation Into Time Response of Polymer Fiber Bragg Grating Based Humidity Sensors," *J. Light. Technol.*, vol. 30, no. 8, pp. 1090–1096, 2012.

[6]   R. Oliveira, L. Bilro, and R. Nogueira, "Smooth end face termination of microstructured, graded-index, and step-index polymer optical fibers," *Appl. Opt.*, vol. 54, no. 18, pp. 5629–5633, Jun. 2015.

[7]   R. Oliveira, L. Bilro, and R. Nogueira, "Bragg gratings in a few mode microstructured polymer optical fiber in less than 30 seconds," *Opt. Express*, vol. 23, no. 8, pp. 10181–10187, 2015.

Selective POF sensors based on surface plasmon resonance exploiting aptamers, MIPs and antibodies as receptors

N. Cennamo[1*], S. D'Auria[2], A. Varriale[2], M. Pesavento[3], L. Pasquardini[4], L. De Maria[5], L. Zeni[1]

1 Department of Industrial and Information Engineering, University of Campania Luigi Vanvitelli, Via Roma 29, 81031 Aversa, Italy
2 Institute of Food Science, Via Roma 52, 83100 Avellino, Italy
3 Department of Chemistry, University of Pavia, Via Taramelli 12, 27100 Pavia, Italy
4 Department of Industrial Engineering, University of Trento, Via Sommarive 9, 38123 Povo, Italy
5 RSE Research on Energetic System S.p.A, Via Rubattino 54, 20134 Milano, Italy

*Corresponding author: nunzio.cennamo@unicampania.it

Abstract: A simple approach to low-cost plasmonic sensing has been obtained with a specific multilayer deposited on a D-shaped Plastic Optical Fiber (POF). When receptors are used for Bio/Chemicals detection, this low cost sensing platform can be exploited in different fields: industrial applications, medical diagnostics, environmental monitoring, food safety and security. The experimental setup, used in these applications, is low-cost and very easy to use. In the last years, we have explored very important applications, with fine experimental results, different kinds of receptors combined with the same POF platform, as Molecularly Imprinted Polymers (MIPs) and Bio-receptors.

1. Introduction

Surface plasmon resonance (SPR) is widely used as a detection principle for many sensors operating in different application fields, such as bio and chemical sensing. When artificial receptors are used for Bio/chemicals detection, the film on the metal surface selectively recognizes and captures the analyte present in a liquid sample so producing a local change in the refractive index at the metal surface. The value of the refractive index change depends on the structure of the analyte molecules [1]. SPR biosensors based on Kretschmann and Otto configurations are usually bulky and require expensive optical equipment, it is not easy to miniaturize them and, in addition, their remote interrogation may be difficult to develop. Jorgenson et al. replaced the prism by a multimode optical fiber [2]. The metal was deposited on the bare core of the fiber. The use of an optical fiber allows for remote sensing and may reduce the cost and the dimensions of the device. Due to the propagation of the light in the fiber, the angle of incidence on the metallic layer exceeds the critical angle, which depends on the refractive indices of both core and cladding components. Therefore SPR only exists for surrounding dielectrics whose refractive index lies in a narrow range. To overcome this drawback, Jorgenson et al. used a polychromatic light source and a spectrograph. This device is low cost, easy to implement and can offer some attractive advantages such as the possibility to be used in the presence of flammable substances and human hazardous environments because of its electricity-free and remote sensing capabilities. Furthermore, because of the small size and non-invasive features, it can be used for medical (self-) diagnosis with the possibility to integrate SPR sensor platforms with optoelectronic devices, eventually leading to "lab on a chip". In the scientific literature, many different configurations based on SPR in silica optical fibers, have been described [3-5]. In this work, a geometry of sensors based on SPR in silica optical fiber is adapted and borrowed for Plastic Optical Fibers (POFs), so representing a simple approach to low cost plasmonic sensing [6]. Several low-cost bio/chemical sensors based on different kinds of receptors, deposited on an SPR D-shaped POF platform, are reported [7-11]. For SPR sensor platforms, POFs are especially advantageous due to their excellent flexibility, easy manipulation, great numerical aperture, large diameter, and the fact that plastic is able to withstand smaller bend radii than glass. Furthermore, the advantage of the POF sensors is that they are simpler to manufacture than those based on silica optical fibers.

2. SPR-POF sensor platform

The optical sensor platform is based on surface plasmon resonance (SPR) in a D–shaped POF, with a buffer layer between the exposed POF core and the thin gold film. This optical platform is realized by removing the

cladding of POF (along half circumference), spin coating a buffer layer on the exposed core and finally sputtering a thin gold film. The planar gold surface can be employed for depositing a receptor layer, as we will explain in the next sections (in this case the selective detection of the analyte is possible). The sensing region is about 10 mm in length. The buffer layer is made of photoresist Microposit S1813, with a refractive index greater than that of the POF core. This buffer layer improves the performances of the SPR sensor and the adhesion of the gold film on the platform [6]. In the visible range of interest, the refractive indices of the optical materials are about 1.49 RIU for POF core (PMMA), 1.41 RIU for cladding (fluorinated polymer) and 1.61 RIU for buffer layer (Microposit S1813). The size of the POF is 980 µm of core (1 mm in diameter), whereas the multilayer on D-shaped POF presents a thickness of the buffer layer of about 1.5 µm and a thin gold film of 60 nm. The experimental configuration based on simple and low-cost components, as shown in Figure 1, is composed by a halogen lamp (HL–2000–LL, manufactured by Ocean Optics, Dunedin, FL, USA) exhibiting a wavelength emission range from 360 nm to 1700 nm, as the light source, the SPR-POF platform and a spectrometer (FLAME-S-VIS-NIR-ES, manufactured by Ocean Optics, Dunedin, FL, USA), with a detection range from 350 nm to 1023 nm, connected to a PC [6].
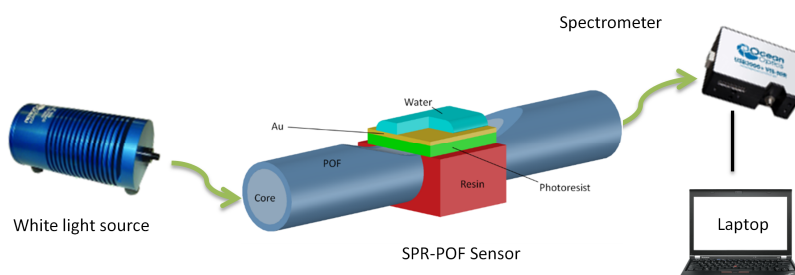
Figure 1. Experimental setup of the SPR-POF sensor system.

3. SPR-POF Biosensors

In this section we want to present two examples of bio-receptors, deposited on the SPR-POF platform, used in two medical diagnostic applications.

3.1 Aptamer receptor for VEGF detection

In the first case, we want to show a DNA aptamer receptor used for the detection of Vascular endothelial growth factor (VEGF), selected as a circulating protein potentially associated with cancer. The detection of VEGF is investigated, as a proof of concept, for the protein biomarkers detection by SPR on POF with aptamers as receptors. DNA aptamers are short oligonucleotide sequences that bind to non-nucleic acid targets with high affinity and specificity. In this case, two different kinds of aptasensor can been realized, one derivatized with aptamer only and one with aptamer and passivating agent (mercaptoethanol) (Apt–MPET) [7]. In this work we present only the second one (Apt–MPET), because the passivation process improves the performances of the aptasensor. The gold film was firstly cleaned with an argon plasma, applying 6.8W of power to the RF coil for one minute to remove organic contaminants. Before the functionalization process, aptamers were subjected to thermal shock (95 °C for 1min, ice for 10min) in order to unfold the sequence strands and make the dithiol groups available for the immobilization reaction. The functionalization procedure was then accomplished by immersion into a 1 µM aptamer solution in 1 M potassium phosphate buffer pH 7 for one hour. To obtain Apt–MPET, a passivation step in 1mM mercaptoethanol solution in the same buffer for 30 min was performed after the functionalization with the aptamer. After washing in buffer and finally in ultrapure MilliQ water, the aptasensor was ready to use. The VEGF detection and BSA control was done in 20mM Tris-HCl buffer pH 7.4. All sensing measurements were performed in a laboratory room with a temperature control set at 23°C. Figure 2 shows the SPR transmission spectra (normalized to the reference spectrum) when the same buffer solution is present, before and after the functionalization with Apt–MPET. The shift of resonance wavelength indicates that the refractive index in contact with the gold surface is increased, indicating that the Apt–MPET were immobilized on the gold surface [7]. In the same Figure the transmission spectra of the SPR biosensor obtained by contacting solutions at increasing concentrations of VEGF in buffer solution in the range 0-100 nM are shown.
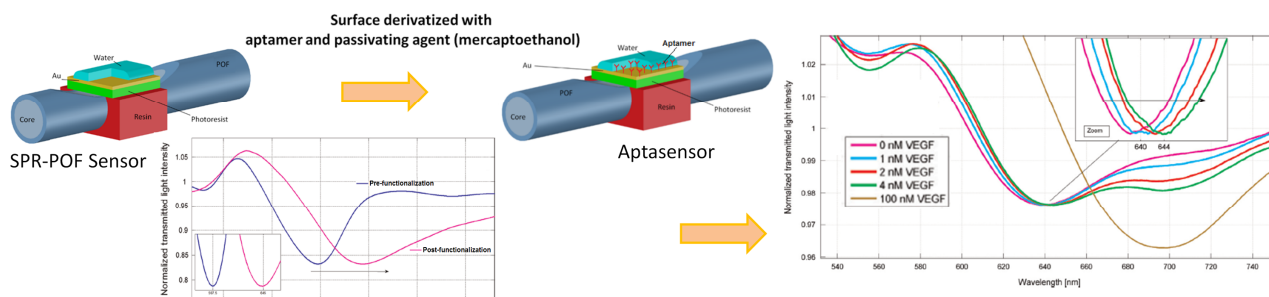
Figure 2. Apt–MPET: SPR normalized transmission spectra obtained with the same buffer solution before and after the functionalization process and incubating different amount of VEGF (0–100nM) [7].

3.2 Antibody receptor for transglutaminase detection

In this section a bio-receptor for the diagnosis and/or follow-up of celiac disease is reported. In particular, the POF-based sensor was used to monitor the formation of the transglutaminase/anti-transglutaminase antibodies, a new hallmark for the diagnosis of celiac disease [8]. On the gold surface of the SPR-POF sensor, the guinea pig transglutaminase was immobilized by a simple approach. Before the functionalization, the gold surface of the chip was cleaned with ultrapure water and the deposition of droplets of a protein solution of 1 mg/ml (25µl) on the surface was performed. Then it was exposed to UV illumination (254 nm) for 10 min and incubated for 4 h at room temperature. When the surface was dried, a second deposition of protein was carried out (25µl of protein solution 1 mg/ml with UV illumination step of 10 min) and the chips were incubated over night at room temperature. The ability of the POF-sensor to detect the binding of anti-transglutaminase antibodies to the immobilized transglutaminase was studied [8]. The obtained results showed that the POF-SPR biosensor is able to sense the transglutaminase/antitransglutaminase complex in the range of concentrations between 30 nM and 3000 nM, as shown in Figure 3.
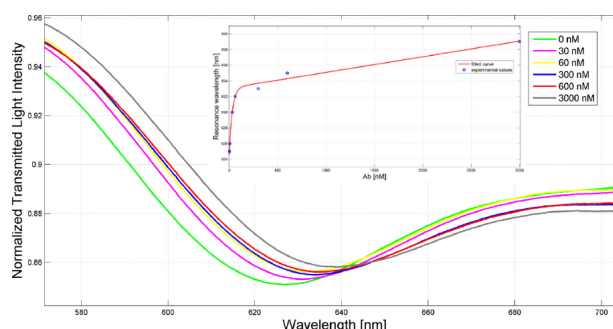
Figure 3. Transglutaminase/anti-transglutaminase antibody: SPR normalized transmission spectra obtained incubating different amount of analyte (0–3000nM). Inset: Resonance wavelength versus concentration of analyte [8].

4. SPR-POF Chemical Sensor

The combination of a D-shaped plastic optical fiber and a molecularly imprinted polymer (MIP) receptor is an effective way to obtain a highly selective and sensitive SPR optical sensor platform. Several examples of applications of this optical chemical sensor platform have been reported, as for example the selective detection of trinitrotoluene (TNT), for security applications [9], of furfural (furan-2-carbaldehyde) and dibenzyl disulfide (DBDS) in power transformer insulating oil (industrial applications) [10], and of L-nicotine [11] in clinical applications. MIPs are synthetical receptors obtained by the molecular imprinting methods, presenting a number of favorable aspects for sensing in comparison with bioreceptors, including a better stability out of the native environment, reproducibility and low cost. They are porous solids containing specific sites interacting with the molecule of interest, according to a "key and lock" model.

For example, in this work we have reported an MIP receptor for furfural detection in power transformer insulating oil. The gold planar surface over the D-shaped POF (SPR active surface) was washed with ethanol

and then dried in a thermostatic oven at 60 °C prior to depositing the sensing layer, a specific molecularly imprinted polymer (MIP) layer. The prepolymeric mixture for MIP was prepared according to the classical procedure reported in [10] with only slight modifications. Divinylbenzene (DVB), the cross-linker, was also the solvent in which the functional monomer (that is, methacrylic acid, MAA), and the template, furfural (2-FAL) are dissolved [10]. Fifty µL of the prepolymeric mixture were dropped over the sensing region of the optical fiber and spun for 45 s at 700 rpm. Thermal polymerization was then carried out for 16 h at 70°C. The template was extracted by repeated washings with 96% ethanol. Figure 4 shows the spectra of the SPR-POF-MIP sensor for 2-FAL detection (at about 860 nm a red-shift is present for increasing concentration of analyte) [10]. The dependence of the minimum wavelength on the 2-FAL concentration is evident.
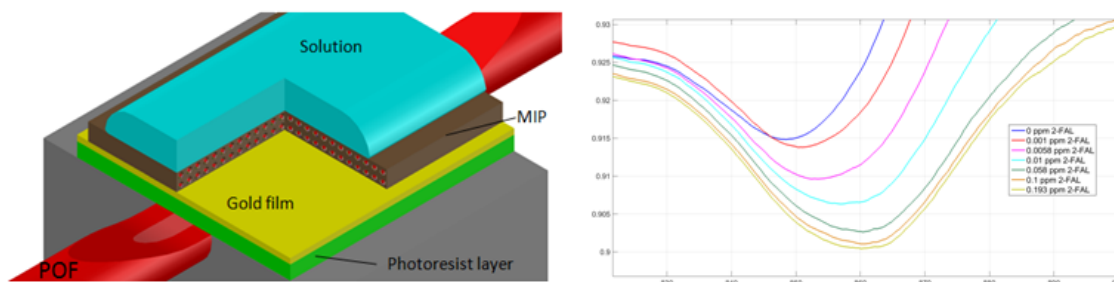
Figure 4. MIP receptor layer and SPR normalized transmission spectra for different concentrations of 2-FAL in oil [10].

5. Conclusions

We have reported on the ability of a low-cost SPR-POF sensor platform to be exploited in some bio-chemical applications. The SPR-POF sensor system is easy to use, small size, low-cost and it can be used to monitor different kinds of receptors, as MIPs, Antibodies and DNA Aptamers.

6. References

[1] Homola, J. Present and future of surface plasmon resonance biosensors. Anal. Bioanal. Ch. 2003, 377, 528–539

[2] Jorgenson, R.C.; Yee, S.S. A fiber-optic chemical sensor based on surface plasmon resonance. Sens. Actuators B: Chem. 1993, 12, 213–220

[3] Wang, X.D.; Wolfbeis, O.S. Fiber-Optic Chemical Sensors and Biosensors (2013–2015). Anal. Chem. 2016, 88, 203–227

[4] Leung, A.; Shankar, P.M.; Mutharasan, R. A review of fiber-optic biosensors. Sens. Actuators B Chem. 2007, 125, 688–703

[5] Monk, D.J.; Walt, D.R. Optical fiber-based biosensors. Anal. Bioanal. Chem. 2004, 379, 931–945.

[6] Cennamo, N.; Massarotti, D.; Conte, L.; Zeni, L. Low cost sensors based on SPR in a plastic optical fiber for biosensor implementation. Sensors 2011, 11, 11752–11760

[7] Cennamo, N.; Pesavento, M.; Lunelli, L.; Vanzetti, L.; Pederzolli, C.; Zeni, L.; Pasquardini, L. An easy way to realize SPR aptasensor: A multimode plastic optical fiber platform for cancer biomarkers detection. Talanta 2015, 140, 88–95

[8] Cennamo, N.; Varriale, A.; Pennacchio, A.; Staiano, M.; Massarotti, D.; Zeni, L.; D'Auria, S. An innovative plastic optical fiber based biosensor for new bio/applications. The case of celiac disease. Sens. Actuators B Chem. 2013, 176, 1008–1014

[9] Cennamo, N.; D'Agostino, G.; Galatus, R.; Bibbò, L.; Pesavento, M.; Zeni, L. Sensors based on surface plasmon resonance in a plastic optical fiber for the detection of trinitrotoluene. Sens. Actuators B Chem. 2013, 118, 221–226

[10] Cennamo, N.; De Maria, L.; Chemelli, C.; Profumo, A.; Zeni, L.; Pesavento, M. Markers Detection in Transformer Oil by Plasmonic Chemical Sensor System Based on POF and MIPs, IEEE SENSORS JOURNAL 2016, 16, 7663- 7670

[11] Cennamo, N.; D'Agostino, G.; Pesavento, M.; Zeni, L. High selectivity and sensitivity sensor based on MIP and SPR in tapered plastic optical fibers for the detection of L-nicotine. Sens. Actuators B Chem. 2014, 191, 529–536

Plastic Optical Fiber Fuse: Observation, Characterization, and Applications

Y. Mizuno[1*], H. Lee[1], N. Hayashi[2], and K. Nakamura[1]

[1]Institute of Innovative Research, Tokyo Institute of Technology,
4259, Nagatsuta-cho, Midori-ku, Yokohama 226-8503, Japan
[2]Research Center for Advanced Science and Technology, The University of Tokyo,
4-6-1, Komaba, Meguro-ku, Tokyo 153-8904, Japan
*Corresponding author: ymizuno@sonic.pi.titech.ac.jp

Abstract: In this invited paper, we review the unique properties of what is called an optical fiber fuse phenomenon in plastic optical fibers (POFs), including its slow propagation velocity (1–2 orders of magnitude slower than that in silica fibers) and low threshold power density (1/180 of the value for silica fibers). We also show that an oscillatory continuous curve instead of periodic voids is formed after the passage of the fuse, and that the bright spot is not a plasma but an optical discharge, the temperature of which is ~3600 K. In addition, we present possible device applications of the POF fuse.

1. Introduction

Brillouin scattering in polymer optical fibers (POFs) was first observed in 2010 [1]; since then its properties have been widely studied for sensing applications [2–8] due to its various merits over conventional glass fibers, such as high flexibility, high safety, and the capabilities of high-precision temperature sensing [2] as well as large-strain sensing [6]. Distributed strain and temperature measurement based on Brillouin scattering in POFs has also been demonstrated by two different spatially resolving techniques: one using Brillouin optical frequency-domain analysis (BOFDA) [9] by Minardo et al [10], and the other using Brillouin optical correlation-domain reflectometry (BOCDR) [11,12] by our group [13]. Very recently, high-speed configurations of BOCDR (phase-detected [14] and slope-assisted [15,16]) have been developed and currently applied to POF sensing. Although these achievements are important technological steps, their signal-to-noise ratio is not sufficiently high because of the low Stokes power that originates from the large core diameter and multimode nature of POFs [1,4]. One method for tackling this problem is to employ higher-power incident light, but too high power is reported to induce damage or burning at the butt-coupled interfaces [7] and potentially what is called an optical fiber fuse phenomenon.

Fiber fuse is the continuous self-destruction of a fiber by propagating light [17,18]. High-power light propagating through the fiber results in local heating and the creation of an optical discharge that is then captured in the fiber core and travels back along the fiber toward the light source, consuming the light energy and leaving a train of voids [19]. While fiber fuse propagation is stunningly beautiful [20], the fiber cannot be used after the passage of the fuse. This effect is now regarded as one of the critical factors limiting the maximal optical power that can be delivered [21,22]. The fuse properties must be well characterized so that all possible measures are taken to avoid the creation of a fiber fuse.

The fuse properties in various glass fibers including standard silica-based single-mode fibers (SMFs) [17–20,23–25], microstructured fibers [26], fluoride fibers [27], chalcogenide fibers [27], erbium-doped fibers [28], photonic crystal fibers [29], and hole-assisted fibers [29] are well documented. The fiber fuse is reported to be typically induced at an input optical power of one to several watts (one to several megawatts per square centimeter) and to have a propagation velocity of one to several meters per second. These properties differ according to the type of glass fiber; the threshold power, for instance, is reported to be much higher in photonic crystal and hole-assisted fibers than in silica SMFs [29], and nonlinear saturation of the fuse velocity has been observed in erbium-doped fibers [28]. To date, however, reports detailing similar properties of POFs have not been published despite their pressing need.

In this invited paper, we review the unique properties of the POF fuse, which have been well described in Refs. [30–32]. The propagation velocity of the bright spot is one to two orders of magnitude slower than that in standard silica SMFs. The threshold power density is 1/180 of the reported value for silica SMFs. We find that, after the passage of the fuse, an oscillatory continuous curve is formed in the POF. We also show that the POF fuse can be easily terminated by local elastic deformation of the waveguide structure, and that the bright spot is not a plasma but an optical discharge, the temperature of which is ~3600 K.

2. Fundamental characterization

The perfluorinated graded-index POF [33] employed in this experiment consists of a core (50 μm diameter), cladding (100 μm diameter), and overcladding (750 μm diameter) encased in polyvinyl chloride. The core and cladding layers are composed of doped and undoped polyperfluoro-butenylvinyl ether, respectively. The refractive index at the core center is 1.356, whereas that of the cladding layer is 1.342 [34]; these values are almost independent of the optical wavelength [35]. The propagation loss is relatively low (~250 dB/km) even at 1.55 μm, and inexpensive optical amplifiers (EDFAs) can be used to boost the optical power.

Figure 1(a) depicts the experimental setup, in which 7-dBm (5-mW) output light from a 1546-nm distributed-feedback laser diode (~1-MHz linewidth) was amplified by an EDFA to up to 23 dBm (200 mW) and injected into a 15-m-long POF. Two optical isolators were inserted to protect the laser and EDFA from reflected light. We confirmed that the fiber fuse can be initiated in the same way as in glass fibers [17–20,23–29] by external stimuli. For the demonstration discussed here, we used a POF end surface polished roughly with 0.5-μm alumina powder. From observations of the propagation of the fuse along the POF (Fig. 1(b)), the propagation velocity was calculated to be approximately 24 mm/s, which is extremely slow in comparison to Todoroki's [20] result for a silica SMF. The optical power of the propagating light was calculated using the measured power of the injected light, the coupling loss at the SMF/POF interface, and the propagation loss in the POF to be approximately 75 mW, corresponding to a maximal power density of 7.6 kW/cm^2 (See Ref. [30] for the calculation method). A magnified view of the fuse propagation along a straight portion of the POF is shown in Fig. 1(c) (70.5 mW, 22.8 mm/s).

We found that the fuse propagation velocity in the POF, measured at 1.55 μm, had an almost linear dependence on the maximal power density with a slope of 1590 mm·s^{-1}·MW^{-1}·cm^2 (Fig. 2(a)). The power density at which the fuse ceased, i.e. the threshold power density, was 6.6 kW/cm^2 at a propagation velocity of 21.9 mm/s. Comparing these results with those of silica SMFs (Fig. 2(b); results [23] at 1.48 μm and the theoretical line [24] at 1.55 μm) revealed that at 1.55 μm the slope in the POF data (corresponding to the efficiency of the velocity control) was 170 times as steep as that in the silica SMF (9.41 mm·s^{-1}·MW^{-1}·cm^2), and the threshold power density of the POF was 180 times lower than that of the silica SMF (~1.2 MW/cm^2). The minimal propagation velocity achieved at 1.55 μm was 11 times as low as that experimentally obtained in a silica SMF at 1.48 μm (250 mm/s) [25].
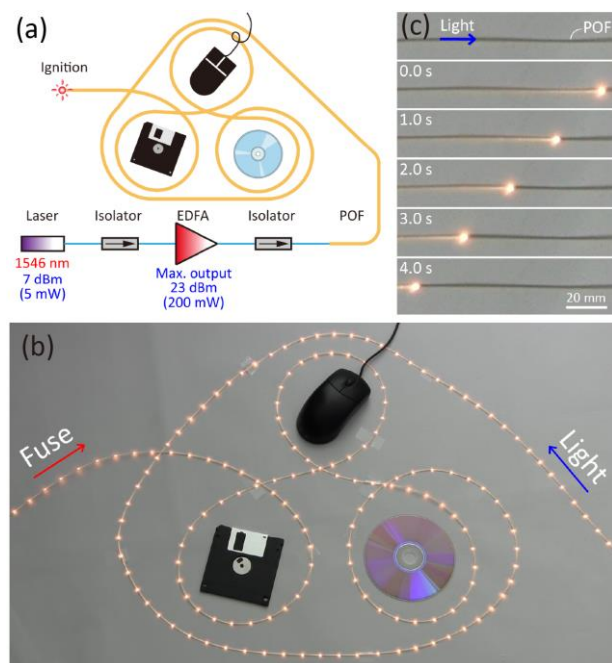
Fig. 1. (a) Experimental setup [30]. (b) Composite photograph of the fiber fuse propagating along the POF [30]; photographs were taken at 1-second intervals. The fiber arrangement was that of Todoroki [20] to allow a direct comparison between the POF and silica SMF. (c) Magnified view of the propagating fuse [30]. A movie of (b) is available online at: http://www.youtube.com/watch?v=t0k_B6EOQhg.
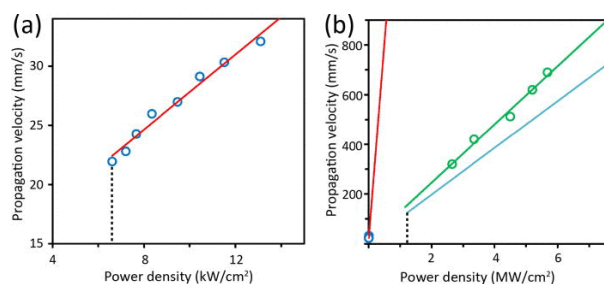
Fig. 2. (a) Propagation velocity of the fiber fuse in a POF measured at 1.55 μm as a function of the maximum power density in the core [30]. Measured data are shown as blue circles, and the red line is a linear fit. (b) Propagation velocities of the fiber fuse as a function of the power density [30]. The measured data for the silica SMF at 1.48 μm (data extracted from the literature [23]) are shown as green circles, and the green line is a linear fit. The blue line is a theoretical prediction [24] for the silica SMF at 1.55 μm. The data in (a) is also reproduced for comparison.

3. Microscopic observation and spectral analysis

Digital micrographs taken after the passage of the fuse disclose the extent of the damage to the fiber. The fuse was initially triggered by exploiting the rough surface at the end of the POF (Fig. 3(a)) and was verified to be induced at the center of the core, which supports the assumption in our calculation that the maximal power density in the fiber cross section affects the fuse induction and can be used to determine the threshold power density. The passage of the fuse (Fig. 3(b)) appeared as a continuous black carbonized curve that oscillated periodically along the length of the POF, which is considerably different from the bullet-shaped voids observed in glass SMFs. The oscillation period was approximately 1300 μm, which is in general agreement with the theoretical oscillation period of the ray [37]. Figure 3(c) shows the position where the fuse ceased after the incident optical power was reduced to that below the threshold; since the fuse remained at this point for several seconds, it melted a relatively large area of the POF, which resulted in the observed bending.

Optical propagation loss in the POF after the passage of the fuse was measured for incremental cutbacks from 30 cm to 20 cm (Fig. 3(d)) and a fixed input power of 10 dBm (10 mW) at 1.55 μm.

Fig. 3. (a) Micrograph of the POF end at which the fuse was initiated. (b) The path of the fuse in the POF. (c) The point at which the fuse was terminated by decreasing the input power. (d) The dependence of the output power on the cut-back length. The open circles are measured points, and the solid line is a linear fit. The slope of the line is 1.4 dB/cm. (e) Image of the fuse termination in the POF at the position of a ring. All the figures are cited from Ref. [30].

A loss of 1.4 dB/cm indicates that, unlike silica SMFs [17–20,23–25], light can propagate through the POF for several tens of centimeters after the passage of the fuse. We believe this is because undamaged regions remain in the core and cladding layers as these diameters are relatively large, which is a unique characteristic of POFs. Yet this propagation loss is somewhat significant for communication applications, and so once the fuse is induced, it is crucial to stop the propagation as soon as possible.

Several methods for terminating fiber fuses have been developed for glass fibers [29,38–40], which are in principle also applicable to POFs. One method is to thin the outer diameter of the fiber at a certain position while maintaining the core diameter [39]; this can reduce the internal pressure and arrest the propagating fuse via deformation. In silica SMFs, this structure is fabricated using hydrofluoric acid as an etchant [39], but in a POF, chloroform could be used to etch the overcladding layer [41]. An even easier method, which we present here, is to pressure-bond a small metal ring around the fiber; this method is only applicable to POFs with an extremely high flexibility [6]. The optical power of the particular propagating mode that provides the bright spot with energy is decreased below the threshold by deformation, and the propagating fuse is thus terminated. The resulting induced optical loss is negligibly low, and an image of the fuse termination at the position of the ring (Fig. 3(e)) shows that bending did not occur. Once the ring is detached, the polymer material will return to the original configuration (elastic deformation).

Finally, we performed spectral analysis. Figure 4 shows the measured emission spectrum of the bright spot propagating along the POF (~300 mW incident power). Its comparison with the blackbody-like spectra of an incandescent light bulb and background shows that, although the POF fuse spectrum has some characteristic peaks, all three spectra are similar. This would indicate that the bright spot of the POF fuse originates not so much from plasma emission as from thermal radiation, because if the bright spot mainly consists of plasma, the emission spectrum will generally contain some line-shaped components [42,43]. This result may raise doubts as to whether the fast-propagating fuse in glass fibers should be referred to as plasma, as this conclusion has been reached without convincing evidence (the emission spectra so far reported [44–46] do not

provide completely clear evidence of the fuse being composed mainly of plasma). Spectra theoretically calculated using Planck's law indicate that the temperature of the bright spot is ~3600 K, which can also be verified using Wien's displacement law.

4. Conclusion

We reviewed the properties of the POF fuse. A propagation velocity of 21.9 mm/s, which is 1–2 orders of magnitude slower than that in standard silica fibers, was demonstrated. The achieved threshold power density was 1/180 of the value for silica fibers. We also showed that a unique oscillatory continuous carbonized curve is formed after the passage of the fuse, which can be terminated easily. We believe that these results serve as a significant guideline for the development of distributed strain and temperature sensing systems based on Brillouin scattering in POFs in the future.

Fig. 4. Emission spectra of the bright spot of the POF fuse, an incandescent light bulb, and background (sunlight) [31]. The red circles indicate some characteristic peaks of the POF fuse spectrum.

Although the POF fuse is basically nothing but an enemy for POF-based Brillouin sensing, the optical fiber fuse in glass fibers has been exploited to develop sensing devices for strain [53], temperature [54], refractive index [55], and humidity [56]. If similar devices are implemented using fused POFs, novel functions can be expected; extensive research in this direction is currently going on.

5. References

[1] Y. Mizuno et al, Appl. Phys. Lett. **97**, 021103 (2010).
[2] Y. Mizuno et al, Opt. Lett. **35**, 3985 (2010).
[3] Y. Mizuno et al, Opt. Lett. **36**, 2378 (2011).
[4] Y. Mizuno et al, IEEE Photon. Tech. Lett. **23**, 1863 (2011).
[5] Y. Mizuno et al, IEEE Photon. Tech. Lett. **24**, 1496 (2012).
[6] N. Hayashi et al, Opt. Express **20**, 21101 (2012).
[7] Y. Mizuno et al, Opt. Lett. **38**, 1467 (2013).
[8] N. Hayashi et al, J. Lightw. Tech. **31**, 3162 (2013).
[9] D. Garus et al, Opt. Lett. **21**, 1402 (1996).
[10] A. Minardo et al, IEEE Photon. Tech. Lett. **26**, 387 (2014).
[11] Y. Mizuno et al, Opt. Express **16**, 12148 (2008).
[12] Y. Mizuno et al, J. Lightw. Tech. **28**, 3300 (2010).
[13] N. Hayashi et al, J. Lightw. Tech. **32**, 3999 (2014).
[14] Y. Mizuno et al, Light: Sci. Appl. **5**, e16184 (2016).
[15] H. Lee et al, IEEE Photon. J. **8**, 6802807 (2016).
[16] H. Lee et al, Opt. Express **24**, 29190 (2016).
[17] R. Kashyap and K. J. Blow, Electron. Lett. **24**, 47 (1988).
[18] R. Kashyap, Opt. Express **21**, 6422 (2013).
[19] S. Todoroki, *Fiber Fuse – Light-Induced Continuous Breakdown of Silica Glass Optical Fiber* (Springer, Japan, 2014).
[20] S. Todoroki, Opt. Express **13**, 6381 (2005).
[21] T. Morioka, et al., IEEE Commun. Mag. **50**, s31 (2012).
[22] M. Jinno et al, Nat Photonics **1**, 157 (2007).
[23] R. M. Atkins et al, Opt. Lett. **28**, 974 (2003).
[24] Y. Shuto et al, IEEE J. Quantum. Electron. **40**, 1113 (2004).
[25] S. Todoroki, Proc. OFC/NFOEC 2013, JW2A.11.
[26] E. M. Dianov et al., IEEE Photon. Tech. Lett. **16**, 180 (2004).
[27] E. M. Dianov et al., Electron. Lett. **38**, 783 (2002).
[28] F. Domingues et al., Electron. Lett. **48**, 1295 (2012).
[29] N. Hanzawa et al., J. Lightw. Tech. **28**, 2115 (2010).
[30] Y. Mizuno et al, Appl. Phys. Lett. **104**, 043302 (2014)
[31] Y. Mizuno et al, Sci. Rep. **4**, 4800 (2014).
[32] Y. Mizuno et al, IEEE Photon. J. **6**, 6600307 (2014).
[33] Y. Koike and M. Asai, NPG Asia Mater. **1**, 22 (2009).
[34] M. Naritomi et al, Bull. Chem. Soc. Jpn. **77**, 2121 (2004).
[35] T. Ishigure et al, J. Lightw. Tech. **18**, 178 (2000).
[36] D. Gloge et al, Bell Syst. Tech. J. **52**, 1563 (1973).
[37] G. P. Agrawal, *Fiber-Optic Communication Systems* (Wiley-VCH, Hoboken, 2010).
[38] D. P. Hand and T. A. Birks, Electron. Lett. **25**, 33 (1989).
[39] E. M. Dianov et al., Opt. Lett. **29**, 1852 (2004).
[40] K. S. Abedin et al, Opt. Express **17**, 6525 (2009).
[41] R. Gravina et al, Sensors **9**, 10423 (2009).
[42] C. Tendero et al, Spectrochim. Acta, Part B **61**, 2 (2006).
[43] K. Tachibana, IEEJ Trans. Elec. Elec. Eng. **1**, 145 (2006).
[44] E. M. Dianov et al, IEEE Photon. Tech. Lett. **18**, 752 (2006).
[45] D. P. Hand and P. St. J. Russell, Opt. Lett. **13**, 767 (1988).
[46] S. Todoroki, Jpn. J. Appl. Phys. **44**, 4022 (2005).
[47] K. S. Abedin et al, Opt. Express **18**, 21315 (2010).
[48] K. S. Abedin et al, Opt. Express **17**, 6525 (2009).
[49] G. P. Agrawal, *Nonlinear Fiber Optics* (Academic Press, California, 1995).
[50] D. D. Davis et al, Proc. SPIE **2714**, 202 (1995).
[51] I. A. Bufetov et al, Quantum Electron. **38**, 441 (2008).
[52] H. Hidai et al, Opt. Express **18**, 20313 (2010).
[53] P. F. C. Antunes et al, IEEE Photon. Tech. Lett. **26**, 78 (2014).
[54] M. F. Domingues et al, Microw. Opt. Tech. Lett. **57**, 972 (2015).
[55] M. F. Domingues et al, Measurement **77**, 265 (2016).
[56] N. Alberto et al, Opt. Quant. Electron. **48**, 216 (2016).
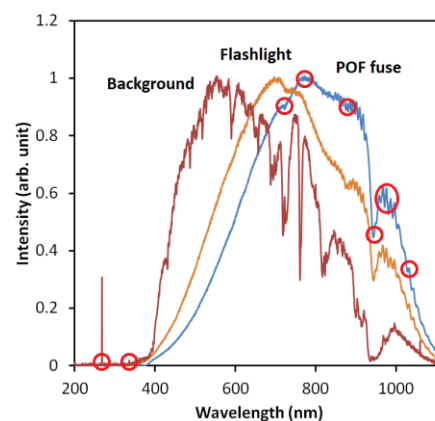
Polymer Optical Fibers as Radiation Sensors?

P. Stajanca[*], K. Krebber

Bundesanstalt für Materialforschung und –prüfung (BAM), Unter den Eichen 87, 12205 Berlin, Germany

*Corresponding author: pavol.stajanca@bam.de

Abstract: Application importance of ionizing radiation has been growing steadily over the last decades. Extensive utilization of ionizing radiation generates demand for development of suitable monitoring techniques. Radiation monitoring systems based on optical fibers offer several key advantages such as small footprint, possibility of remote and real-time measurement as well as electromagnetic immunity. In this contribution, we investigate radiation-induced attenuation (RIA)-based sensing with perfluorinated polymer optical fibers (PF-POFs). The RIA response of two commercial PF-POFs is assessed in a low dose region and performance and limitations of the system are discussed. The concept represents a potential high-sensitivity, low-cost and easy-to-use on-line radiation monitoring system with distributed detection capability.

1. Introduction

Considerable attention has been devoted to the development of polymer optical fibers (POFs) over the last decades [1, 2]. In certain cases, POFs may represent more suitable or cost effective alternative to their silica-based counterparts. Thanks to some of their advantageous characteristics, POFs have found applications in the area of data transmission, optical sensing or lighting. Compared to the silica fibers, POFs are cheaper, more robust and flexible, thus potentially yielding more cost effective and user-friendlier sensing systems. In addition, they have better biocompatibility and are generally more acceptable for medical applications as well.

Nowadays, ionizing radiation is finding new applications in many areas including nuclear industry, material processing, medicine or food industry [3]. As a result, novel systems for monitoring and control of irradiation processes are being researched and developed. Optical fiber-based dosimetry (OFD) techniques offer numerous advantages such as electromagnetic immunity, small dimensions and possibility of remote and real time monitoring [4, 5]. These make them interesting especially for monitoring in hazardous and difficult to access locations. Among available OFD solutions, monitoring of radiation-induced attenuation (RIA) of the fiber is the most straightforward technique. Radiation-induced attenuation is caused by absorption on various structural defects generated by high-energy radiation and is typically strongly wavelength and material dependent [6].

Even though most of the research up to now has been focused on glass optical fibers (GOFs) [6], cheaper and user-friendlier POFs can be an attractive alternative especially in less demanding applications. O'Keeffe et al. investigated RIA in commercial polymethyl methacrylate (PMMA) POFs for monitoring of radiation processes in sterilization and medical applications [7-9]. In our previous works we demonstrated that perfluorinated POFs (PF-POFs) exhibit considerably higher RIA sensitivity than PMMA fibers and could be useful for radiation monitoring up to kGy-level doses [10, 11]. Here we focus further on the low dose region and investigate fiber's ability to detect doses on a single Gy level, which could be interesting for early-stage radiation leak detection or medical applications. Performance of two different types of commercial PF-POFs under ^{60}Co gamma irradiation is evaluated and compared.

2. Experimental methodology

Two different types of commercial PF-POFs were tested; GigaPOF-50SR produced by co-extrusion by Chromis Fiberoptics [12], and Fontex fiber drawn from preform by Asahi Glass Company [13]. As the particular manufacturing conditions may influence fiber's RIA response, both fiber types were tested and compared. Roughly 1.5 m long samples were cut from the investigated fibers. Central part of the sample with length of 1 m was coiled (7 cm diameter) and attached to a thin acrylic plate. Both ends of the sample were put into F-ST clamp connectors and polished to facilitate easy connection with auxiliary multimode GOF bringing light to and from the sample. Fiber-coupled Halogen lamp (AQ4305, Yokogawa) and CCD spectrometer (HR4000, Ocean Optics) were used to monitor fiber transmission during irradiation. The employed optoelectronics allow measurement in 450-900 nm wavelength region. Schematic illustration of the utilized irradiation setup can be viewed in Figure 1.

Fiber irradiation was performed at ^{60}Co irradiation facility of Helmholtz Zentrum Berlin (HZB). Prepared samples were irradiated under different conditions and fiber spectral transmission is periodically measured with the spectrometer and logged on the utilized computer. The dose rate can be adjusted by varying the distance of the sample from the radiation source while the total dose level is controlled by overall irradiation time. The fiber RIA (in dB/m) is evaluated from the spectral transmission measurement as

$$RIA(\lambda, D) = -\frac{10}{L_0}\log\left(\frac{I(\lambda,D)}{I(\lambda,0)}\right), \tag{1}$$

where $I(\lambda, D)$ is the recorded transmitted spectral intensity at dose $D(t)$ and L_0 is the length of irradiated sample (1 m). The dose values $D(t)$ were calculated based on irradiation time and used irradiation dose rate.
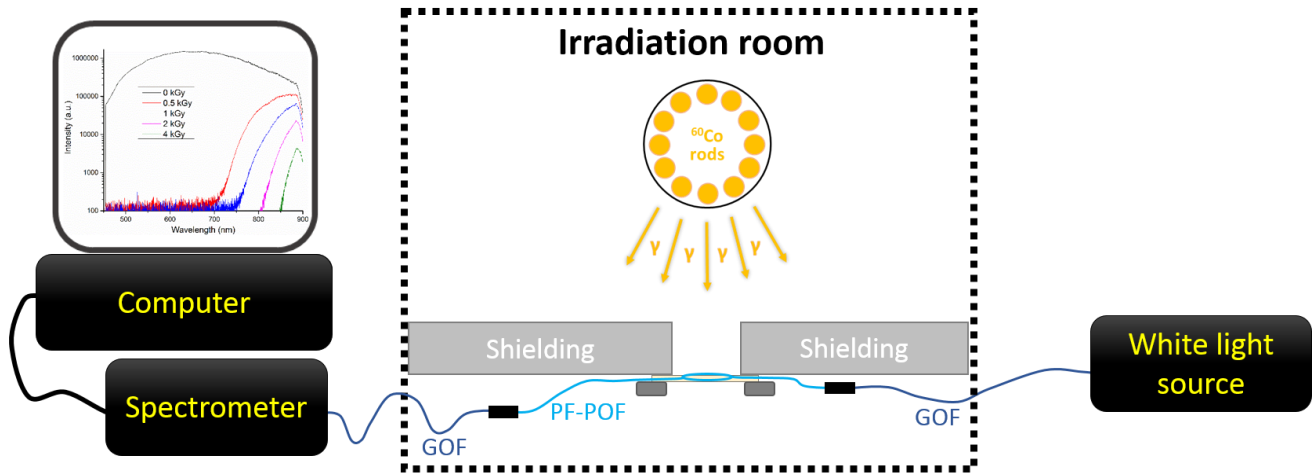
Figure 1. Schematic illustration of the utilized irradiation setup.

3. Results

For quantitative dosimetry applications, dose rate dependence of RIA measurement is an important question. To assess the RIA dose rate dependence for the two tested fibers, fiber RIA response was investigated at two different dose rates, namely 150 Gy/h and 15 Gy/h. Figure 2 compares the spectral dependence of the fiber RIA measured after irradiation to 50 Gy at the two different dose rates. One can see that for relatively high dose rate of 150 Gy/h (Figure 2a), RIA of both fibers has very similar spectral character and magnitude. The highest RIA sensitivity is achieved at the blue end of the monitored spectra, while the sensitivity starts to drop rapidly for wavelengths longer than 650 nm. For the lower dose rate of 15 Gy/h (Figure 2b), the same spectral character of RIA is maintained. However, while magnitude of RIA for GigaPOF-50SR remains comparable to irradiation at 150 Gy/h, significant decrease of induced RIA is observed for Fontex PF-POF. This indicates a drop of Fontex RIA sensitivity at lower dose rates. The strong dose rate dependence of RIA growth in this fiber is undesirable with regard to dosimetry applications. Therefore, Fontes fiber could be deemed rather unsuitable for radiation monitoring and we further focus only on GigaPOF-50SR.

The magnitude of observed RIA change at the two different dose rates for GigaPOF-50SR is less significant, i.e. the fiber's radiation response is less dose rate dependent. This is especially true for lower wavelengths at the blue end of the monitored spectrum. For example, while RIA drop between irradiation at 150 Gy/h and 15 Gy/h is below 6% at 460 nm, it reaches 12% at 650 nm. Considering lower dose rate dependence and higher sensitivity, operation at wavelengths on the blue edge of the monitored spectra is clearly superior for low dose radiation monitoring.

Figure 3a shows the GigaPOF-50SR's RIA evolution at increasing total dose for the two irradiations at different dose rates. 460 nm is chosen as an interrogation wavelength with the highest radiation sensitivity and lower dose dependence available with our experimental configuration. Since we target low dose detection and monitoring, only data for dose below 10 Gy is displayed. Good agreement between the measurement at 150 Gy/h and 15 Gy/h is visible. The green curve is a linear fit for the compound data set combining two individual measurements at different dose rates. The slope of the fitted curve, representing RIA sensitivity at given wavelength, is

138.9 ± 0.3 dBm^{-1}/kGy. This is more than 200x higher than the maximal demonstrated sensitivity of PMMA POF (0.6 dBm^{-1}/kGy at 525 nm) [7]. Thanks to the much higher sensitivity, a sub-gray resolution required for medical applications could be reached, which was not possible with PMMA fiber [9].
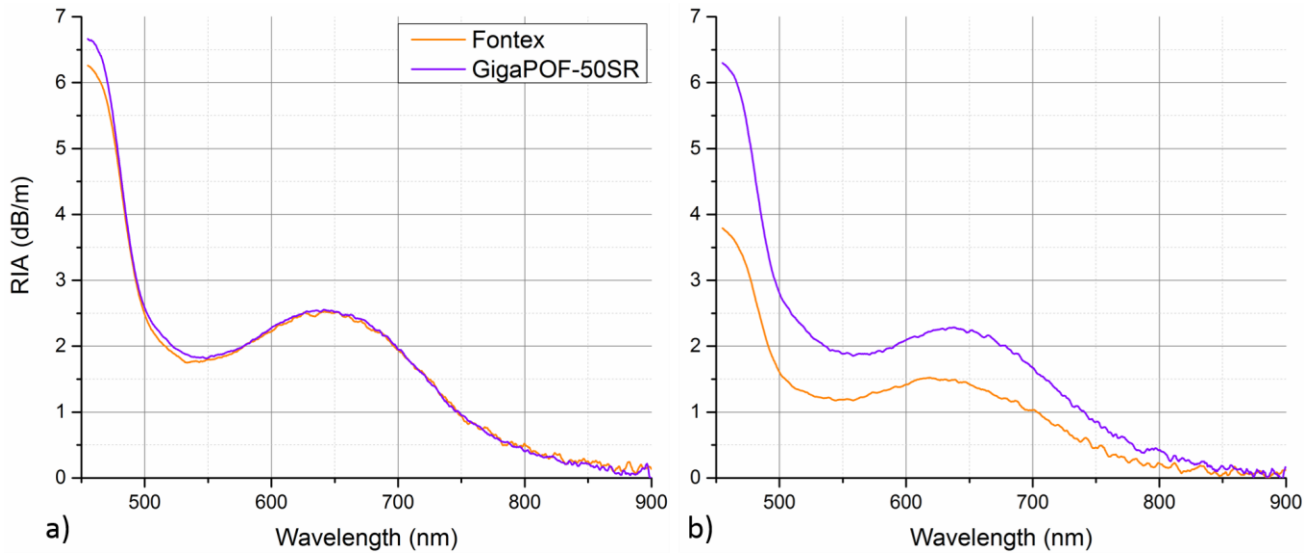
Figure 2. Spectral RIA of the two investigated PF-POFs for irradiation to 50 Gy at a dose rate of 150 Gy/h (a) and 15 Gy/h (b).

Comparing measured data points and linear fit in Figure 3a, one can notice the actual RIA response is slightly sub-linear, especially for irradiation at 15 Gy/h. To evaluate the accuracy of the linear approximation in the RIA-based dose measurement, error between the actual dose and the dose calculated from the RIA measurement using determined linear sensitivity was evaluated. Figure 3b depicts the determined dose error of RIA measurement against actual radiation dose level. Due to sub-linearity of RIA response at 15 Gy/h, measurement error increases with rising dose level. Nevertheless, for the monitored dose region (0-10 Gy), measurement error stays within ± 0.3 Gy. Therefore, under employed conditions, the presented RIA-based dose measurement with co-extruded PF-POF can provide sub-gray resolution and accuracy. Considering the results from spectral RIA investigation, potentially higher sensitivity and accuracy could be achieved at lower wavelengths that lie beyond the monitoring limit of our present setup.
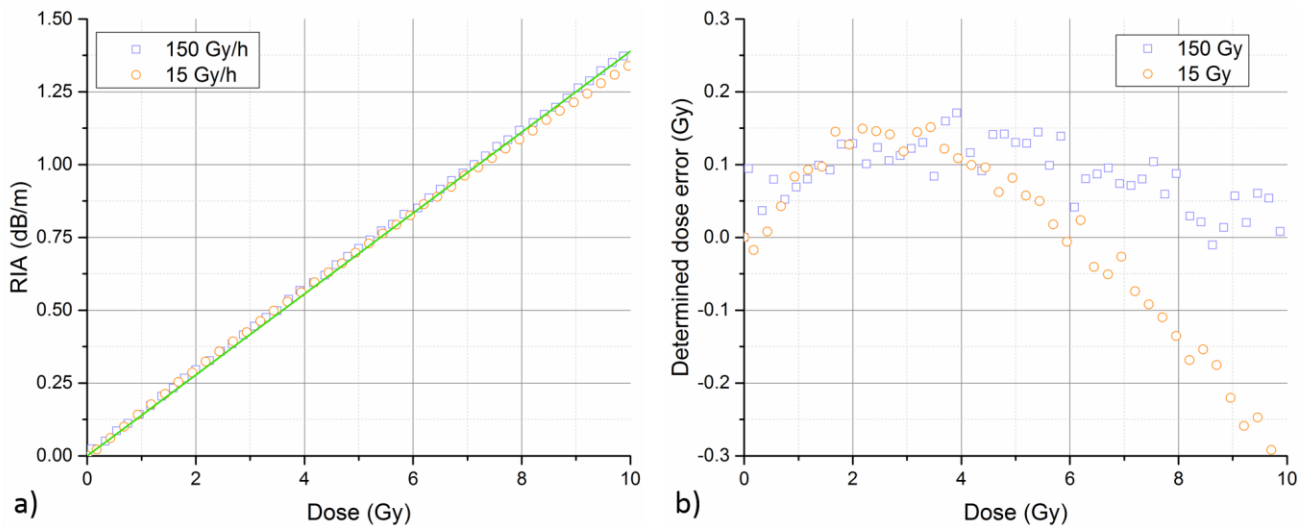
Figure 3. a) RIA of GigaPOF-50SR as a function of total dose for irradiation at two different dose rates. Green line is a common linear fit for combination of both data sets measured at different dose rates. b) Error between actual dose values and dose levels determined using RIA measurement and determined linear sensitivity (slope of green curve in figure 3a).

4. Conclusions

The presented paper evaluates gamma radiation response of two types of commercial PF-POFs in a low dose region. The performance of the fibers is compared with regard to dose rate dependence of their RIA response. Significant change of measured RIA for irradiation at different dose rates in case of PF-POF drawn from preform (Fontex, Asahi Glass Company) indicates strong dose rate dependence. Due to that, utilization of this fiber for radiation monitoring applications is rather unfavorable. Much lower dose rate dependence was observed for co-extruded PF-POF (GigaPOF-50SR, Chromis Fiberoptics), especially at low wavelengths from the blue end of the monitored spectral range. Operating at these wavelengths, RIA monitoring with GigaPOF-50SR could yield high-sensitivity dose measurement with sub-gray resolution and accuracy. For operation at 460 nm, the measurement offers high radiation sensitivity of 138.9 ± 0.3 dBm^{-1}/kGy and accuracy of 0.3 Gy under employed experimental conditions. Considering that the tested fiber is relatively affordable, user-friendly, commercial off-the-shelf POF, we believe it could be an interesting candidate in various radiation related areas.

5. Acknowledgements

4. References

1. O. Ziemann, J. Krauser, P. E. Zamzow, and W. Daum, *POF Handbook: Optical Short Range Transmission Systems (2nd edition)* (Springer, Berlin, 2008).
2. Y. Koike, *Fundamentals of Plastic Optical Fibers* (Wiley, Weinheim, 2015).
3. I. Bikit, *Gamma Rays: Technology, Applications, and Health Implications* (Nova Science Publishers, Incorporated, 2014).
4. S. O'Keeffe, C. Fitzpatrick, E. Lewis, and A. I. Al-Shamma'a, "A review of optical fibre radiation dosimeters," Sensor Review **28**, 136-142 (2008).
5. A. L. Huston, B. L. Justus, P. L. Falkstein, R. W. Miller, H. Ning, and R. Altemus, "Remote optical fiber dosimetry," Nuclear Instruments and Methods in Physics B **184**, 55-67 (2001).
6. S. Girard, J. Kuhnhenn, A. Gusarov, B. Brichard, M. Van Uffelen, Y. Querdane, A. Boukenter, and C. Marcendella, "Radiation Effects on Silica-Based Optical Fibers: Recent Advances and Future Challenges," IEEE Trans. Nucl. Sci. **60**, 2015-2036 (2013).
7. S. O'Keeffe and E. Lewis, "Polymer optical fibre for in situ monitoring of gamma radiation processes," International Journal on Smart Sensing and Intelligent Systems **2**, 490-502 (2009).
8. S. O'Keeffe, A. Fernandez-Fernandez, C. Fitzpatrick, B. Brichard, and E. Lewis, "Real-rime gamma dosimetry using PMMA optical fibres for applications in the sterilization industry," Meas. Sci. Technol. **18**, 3171-3176 (2007).
9. S. O'Keeffe, E. Lewis, A. Santhanam, A. Winningham, and J. P. Rolland, "Low dose plastic optical fibre radiation dosimeter for clinical dosimetry applications," in *IEEE Sensors 2009 Conference,* (Christchurch, New Zealand 2009), pp. 1689-1692.
10. P. Stajanca and K. Krebber, "Towards on-line radiation monitoring with perfluorinated polymer optical fibers," Proc. of SPIE **10323**, 103231O (2017).
11. P. Stajanca, L. Mihai, D. Sporea, D. Negut, H. Sturm, M. Schukar, and K. Krebber, "Effects of gamma radiation on perfluorinated polymer optical fibers," Opt. Mater. **58**, 226-233 (2016).
12. Chromis Fiberoptics, "GigaPOF-50SR", retrieved July 2017, http://www.chromisfiber.com/pdf/GigaPOF50SR.pdf.
13. Asahi Glass Company, "Fontex™", retrieved July 2017, http://www.lucina.jp/eg_fontex/.

Plastic Optical Fiber Biosensors

Marcelo Werneck[1*], Rafaela Lopes[1], Domingos Rodrigues[1], Natália Costa[1], Larissa Soares[1], Ariadny Arcas[1], Fabio Dutra[2], Greice Costa[3], Louise Landi[4], Arthur Werneck[5] and Regina Allil[1]

1 Photonics and Instrumentation Laboratory, Electrical Engineering Program and Nanotechnology Engineering Program, Universidade Federal do Rio de Janeiro, Rio de Janeiro, Brazil
2 PETROBRAS Research and Development Center, Rio de Janeiro, Brazil
3 Department of Physics, Universidade Federal Rural do Rio de Janeiro, Seropédica, Rio de Janeiro, Brazil
4 Photonics and Instrumentation Laboratory – Department of Electronic and Computing, School of Engineering, Universidade Federal do Rio de Janeiro, Rio de Janeiro, Brazil
5 Photonics and Instrumentation Laboratory, Software Engineering, Instituto Infinet, Rio de Janeiro, Brazil
*werneck@lif.coppe.ufrj.br

Keywords—plastic optical fiber, biosensor, sulfate-reducing bacteria, immunocapture

Abstract: The need for robust, rapid, disposable and low-cost detection of viruses and bacteria has become paramount for medical diagnosis, environment control or food industry. Refractive index (RI) sensing functionalized with specific antibodies offers a promising detection mechanism. With this technique in mind we developed sensors based either in surface plasmon resonance or in evanescent wave, driven by a LED-photodiode pair or smartphone technology. Good results were obtained for measuring refractive index and bacteria such as *Desulfovibrio alaskensis* and *Escherichia coli*. The use of a simple U-bent sensor allows a viable alternative for mass production, leading to a highly robust and machinable sensor and ease probe fabrication allowing low cost and good repeatability.

1. Introduction

The need for robust, rapid, disposable and low-cost detection of viruses and bacteria has become paramount for medical diagnosis, environment control or food industry. Refractive index (RI) sensing offers a promising detection mechanism to address this need. Typically, specific antibodies are functionalized onto the surface of optical waveguide through several techniques and coating surfaces. When a virus or bacteria binds to the antibody, the local dielectric surrounding the fiber surface or coating is altered, causing either a change in the critical angle for total internal reflection (TIR) of by shifting the plasmon frequency resonance in a phenomenon known as surface plasmon resonance (SPR). The optical fiber biosensor detects the presence of the cells around the fiber by refractive index (RI) variation such as in our previous works found in Ferreira et al. (1999), Beres et al. (2011) and Wandemur et al. (2014). Some other studies detect the fluorescence emitted by the cells (Fixe et al., 2004; Emiliyanov et al., 2013), or by enzymatic reaction (Chai et al., 2011).

2. Sensing principles

2.1. Total Internal Reflection

The use of RI as a sensing parameter is based on the fact that bacteria present a RI of approximately 1.39, slightly higher than that of pure water (n=1.334) (Beres et al., 2011). Due to this small difference, it is not possible to detect bacteria simply by measuring the RI of a water containing a reasonable concentration of bacteria, say 10^5 or 10^4 colony forming units (CFU), since the average RI of the mixture is not different to that of pure water, except at the fifth or sixth decimal position. Therefore, in order to detect bacteria one has to concentrate them around the fiber by covalently capturing the cells by a specific antibody bound around the sensitive region of the fiber. In this way, all bacteria of that specific species will be captured and fixed around the sensor producing an increase of the RI that will be detected by the sensor in a technique known as immunocapture. The principle of RI sensing is based on the evanescent wave (EW). When light propagates through a waveguide, the modes are bounded inside the core by the phenomenon known as total internal reflection (TIR). In this way, the solution's RI will dominate the output power of light that is guided by the fiber.

2.2. Surface Plasmon Resonance

SPR is the excitation by light of surface plasmon (electrons) of thin films in planar surfaces. In this interaction the evanescent field generated when there is a TIR excites the electrons with power losses by absorption in specific wavelengths. Localized Surface Plasmon Resonance (LSPR) is the excitation of conduction band electrons for nanometer-sized metallic particles. Light incident on the nanoparticles induces the conduction electrons to oscillate collectively with a resonant frequency that depends on the nanoparticles' size, shape and composition. Therefore, RI variations on the thin film displaces the resonance wavelength. This technique

demands for a white light source and an optical spectrum analyzer to detect the shifted spectrum of the return light.

3. Technologies and Results

Optical Fiber Biosensor were developed based in four different setups, all using 1 mm PMMA POF: U-Shape sensor, BioMobil as a smartphone application, AuNRs tip and Nanofilm coated.

3.1. U-shape sensor

The system set-up consists of an LED connected to one end of the U-shape sensor and a photodetector at the other end. The light received by the photodiode is a function of the RI of the surrounding medium. The software performs a division of one output signal by the other in order to produce a stable referenced signal. Fig. 1 (left) shows a picture of the system and Fig. 2 (right) the block diagram.
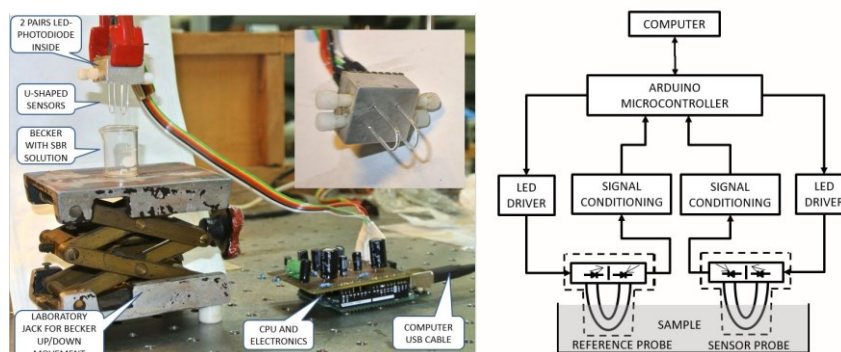
Fig. 1. Left: Picture of the system in operation. Right: Block diagram. The laboratory jack is used to move the becker with bacteria solution up and down in order to immerse the sensors into the solution. Inset: Sensor head showing the two sensors, the reference and the sensitive.

The U-Shape sensor was used for detection of bacteria of two kinds. The first one is the *Escherichia coli* which is an indicator of water contamination and is of interest of medical diagnosis, environment control or food industry. Fig 2 (Left) shows the results for *E. coli* for concentrations of 10^8, 10^6 and 10^4 CFU/mL (colony form units per milliliter). In oil and gas exploration and production (E&P) industry, sulfate-reducing bacteria (SRB) can cause corrosions as they can produce biofilms at the internal surface of oil pipes and tanks. The metal structures exposed to sulfate-containing water allows the SRB to produce hydrogen sulfite which, in presence of water, reacts producing sulfuric acid (H_2SO_4) which corrodes steel. In this study, we developed a biosensor for in situ and fast detection of SRB. The biosensor is based on immunocapture by direct immobilization of an antibody to the optical fiber surface so that only the bacteria of interest concentrates at the fiber surface. For the tests we used the *Desulfovibrio alaskensis,* a species of SRB group, recovered from a soured oil well in Campos Oil Basin, in Brazil. The results for a 10^6 concentration is shown in Fig. 2 (Right).
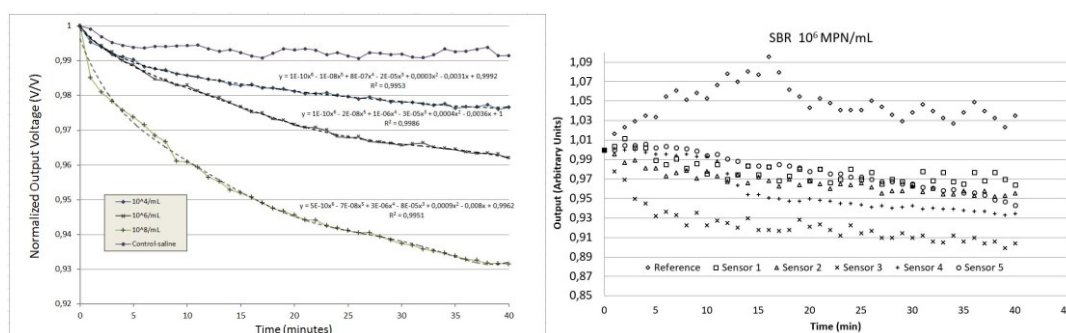
Fig. 2. Left: Detection of *E. coli* for concentrations of 10^8, 10^6 and 10^4 CFU/mL. Right: Detection of SRB by the biosensor for a concentration of *D. alaskensis* at 10^6 MPN/mL.

3.2. BioMobil

The BioMobil is a form of biosensor standalone system based on a smartphone. Applying the technology described above and using the smartphone LED flash/lantern instead of the LED and the camera substituting the photodiode. The idea is to use a sensor support for fixing the U-Shape probe in front of the camera/flash section at the back of the smartphone, as shown in Fig 3. An Android application does all the work.
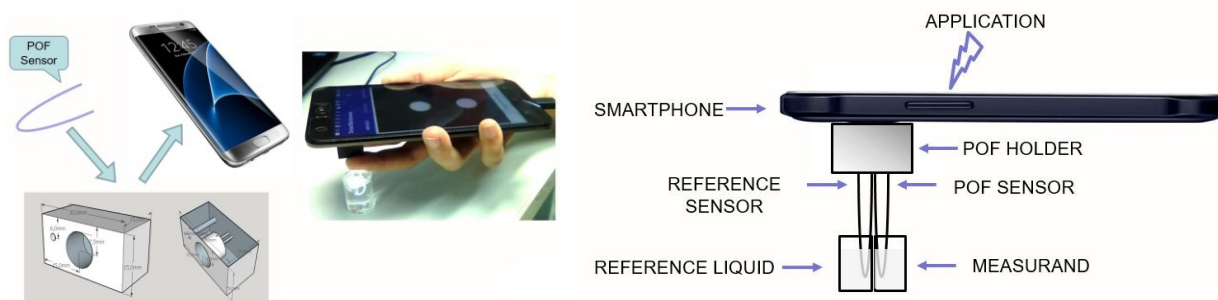
Fig. 3. The BioMobil structure.

Two fibers were used using the same scheme as the one used for the U-Shape, shown in the last section. Fig 4 (Left) shows the application screen, with a picture taken from the two fiber ends. The software calculates the total light collected on the picture by a compilation of all pixels. Fig 4 (Right) shows the results of the measurements for calibrated RI liquids.
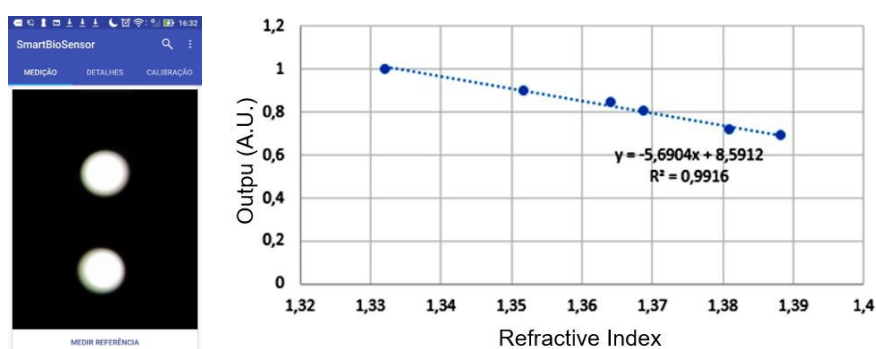
Fig. 4. Software and results of BioMobil in RI measurements.

3.3. AuNR Based Sensor

A POF-AuNR (gold nano-rods) sensor was produced with a 1 mm POF (SK-40 ESKA, Japan) with core and cladding materials of PMMA and fluorinated polymer, respectively. To fabricate the sensor, the fiber was cut into 12 cm long segments and the cladding was removed using acetone. Then the tapering the POF tip was performed by dipping its tip in cyclopentanone solution for 6 hours to expose the core of the POF. By tapering the POF tip increases its sensitivity, by decreasing the number of propagating modes. Then, the AuNRs were attached onto the tip of the tapered POF by immersing the tip in a solution of octanethiol and tetrahydrofuran for 30 min following by a drop of the AuNRs suspension placed onto the tip of the POF.

The optical setup shown in Fig. 5 (Left) was designed to measure the reflectance from the AuNRs attached to the tip of the POF as the RI of the surrounding medium is varied. By changing the surrounding RI, the SPR resonance and subsequent reflectance peak and amplitude is shifted. A 3 dB coupler merges the halogen white light source (Ocean Optics HL-2000) and the spectrometer (Ocean Optics USB4000) to the POF sensor. The change of the LSPR absorption wavelengths was investigated, varying the surrounding refractive index. For this, the sensing element was immersed in various refractive index liquids with known values (n = 1.26, 1.30, 1.40 and 1.70). Fig. 5 (Center) shows the reflected signals from the tip of the sensor for various RI. A shift and an attenuation of the LSPR was observed as the refractive index of the external medium varies. In Fig. 5 (Right) it is shown the wavelength shift of the LSPR of the AuNRs for different RI, presenting a linear behavior and blue shift.

3.4. Thin Film Coating

1-mm diameter PMMA (Mitsubishi Rayon Eska GH 4001) POF was cut into 10-cm-long sections and both end surfaces were cleaved and polished for better light coupling. The sections were bent around a mold and heated at about 70 °C for 15 s to produce U-bent probes with 25 mm length and 8 mm waist diameter. A sputtering system (Aja International, USA) with RF magnetron was used for gold depositon over the U-bent probe producing coating of 30, 50, 70 and 100 nanometer of gold thickness. Polyclonal anti-*E. coli* antibody from rabbit (Bio-Rad Labs, Brazil) was used to co-valently bind at the gold surface. The optical setup was the same used for the U-Shape Sensor described above. The sensor was then tested with *Escherichia coli* in concentrations od 10^8 CFU/mL. The sensor showed an increase in output voltage due to the increase in the

surrounding RI caused by immunocapture effect as the antibody keeps capturing the bacteria present in the water. In order to verify the probes for SPR occurrence, tests were carried out with a spectrophotometer (Model HR-400, Ocean Optics) and a white light source at wavelength of 845 nm. Fig. 6 shows the result. At left the results of the 70-nm gold coated U-bent sensor in bacteria concentrations of 1.5×10^8 CFU/mL and at right results with the spectrophotometer for a bacteria concentration of 10^3 CFU/mL.
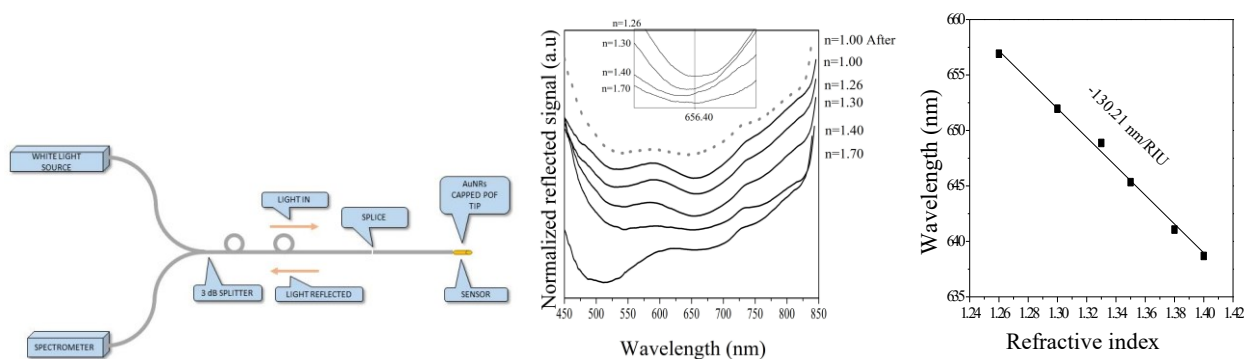
Fig. 5. Left: LSPR setup for refractive index sensing. Center: Reflected signal of the LSPR of the AuNRs with the change of the surrounding RI. Right: Wavelength shift as a function of RI.

4. Discussion and Conclusions

The use of a simple U-bent sensor allows a viable alternative for mass production since the 1-mm diameter PMMA fiber is less fragile than silica fibers, leading to a highly robust and machinable sensor and ease probe fabrication allowing low cost and good repeatability. The capturing mechanism under which the bacteria are fixed to the fiber surface is still unknown, making it difficult at this early stage of the research to quantify the bacteria concentration in a sample just by observing the drop of the sensor output signal. As a future work it is important to improve the sensitivity of this system in order to be possible to detect and quantify smaller concentrations of bacteria at the order of 10^3 CFU/mL and 10^2 CFU/mL so as to be possible to use it as a field tool for offshore analysis.
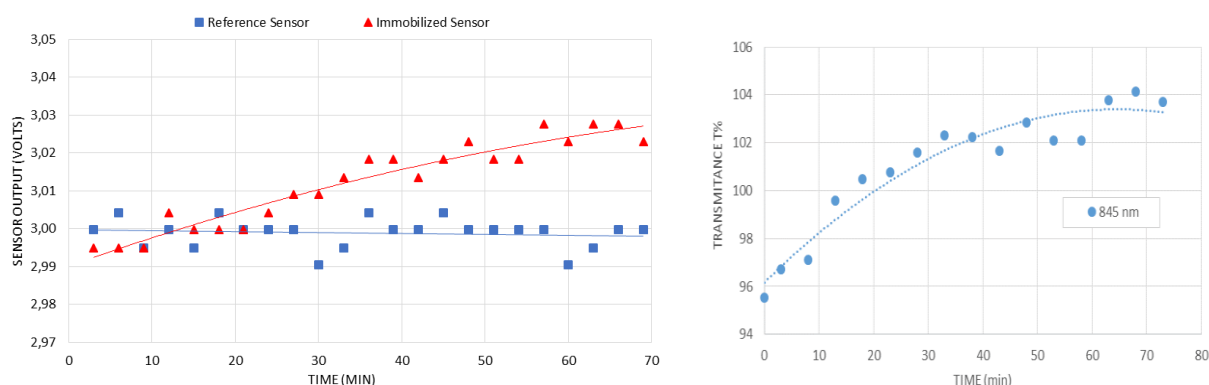
Fig. 6. Results of the 70-nm gold coated U-bent sensor in bacteria concentrations. Left: 1.5×10^8 CFU/mL. Right: 1.5×10^3 CFU/mL, obtained with the spectrophotometer at 845 nm.

5. References

Beres, C., de Nazaré, F. V. B, de Souza, N. C. C., Miguel, M. A. L. and Werneck, M. M. "Tapered Plastic Optical Fiber-Based Biosensor - Tests and Application", DOI: 10.1016/j.bios.2011.09.024, Biosensors and Bioelectronics, Vol. 30, pp. 328-332, September 2011.

Chai, C., Liu, G., Yao, B., "A portable optical sensor based on a one-off test strip for fast evaluation of bacterial contamination in raw tofu", Sens. Actuators B 152, 1–7, 2011.

Emiliyanov, G, Hoiby, P. E., Pedersen, L. H., Bang, O., "Selective Serial Multi-Antibody Biosensing with TOPAS Microstructured Polymer Optical Fibers", Sensors 13, 3242-3251, 2013.

Ferreira, A.P., Werneck, M.M. and Ribeiro, R.M., "Aerobiological pathogen detection by evanescent wave fibre optic sensor" Biotechnology Techniques, 13: (7) 447-452 July 1999, Kluwer Academic Publ., ISSN: 0951-208X.

Fixe, F., Dufva, M., Telleman, P., & Christensen, C. B. V. (2004). Functionalization of poly(methyl methacrylate) (PMMA) as a substrate for DNA microarrays. Nucleic Acids Research, 32(1), DOI: 10.1093/nar/gng157, 2004.

Wandemur, G., Rodrigues D., Allil, R., Queiroz, V, Peixoto, R., Werneck, M., Miguel, M., "Plastic Optical Fiber-Based Biosensor Platform for Rapid Cell Detection", DOI: 10.1016/j.bios.2013.11.030, Biosensors & Bioelectronics, ISSN: 0956-5663, Vol. 54, pp 661-666, April 15, 2014.

Application of a Compact F-SAS Sensor System Using POF for Pediatric Sleep Apnea Syndrome

S. Mitachi[1], M. Hayashi[1], Ryo Saito[1], and T. Sugiyama[2*]

1 Tokyo University of Technology, 1404-1 Katakura, Nachioji, Tokyo 192-0982 Japan
2 Dep. of Pediatrics, University of Yamanashi, 1110 Schimokato Chuo, Yamanashi 409-3898 Japan
*Corresponding author: mitachi@stf.teu.ac.jp

Abstract: We have developed an optical-fiber sleep apnea syndrome (F-SAS) sensor using plastic optical fiber (POF), which captures changes in side pressure of the body caused by breathing as signal light changes by using the micro-bending loss of optical fiber. In this study, we applied the compact F-SAS sensor to examining SAS diagnosis in a child patient and report on improved pediatric analysis. The analysis results revealed the correlation value to be R = 0.87 was a significant improvement over the correlation value of R = 0.697 between the apnea/hypopnea index (AHI) obtained by a sleep apnea syndrome examination apparatus (SAS 2100) and respiratory disturbance index (RDI) obtained by the conventional F-SAS sensor. As a result of comparing sleep event results between the F-SAS sensor and polysomnography (PSG), agreement was found in all sleep apnea events.

1. Introduction

Obstructive sleep apnea syndrome (OSAS) in children is a disease in which respiratory arrest during sleep is frequently observed due to narrowing of the upper airways, such as due to tonsil hypertrophy, growth disorders, and a lowered quality of life (QOL) such as from having a decreased ability to learn. We developed a compact F-SAS sensor with high density mounting on its control part with the help of grants from the Fukushima Prefecture Medical and Welfare Equipment Development Project. We reviewed the improvement made to pediatric analysis software by using this sensor and report it [1-5]. Further, we report on a comparison of sleep events with the conventional F-SAS sensor and polysomnography (PSG) in children [3].

2. Experiment

The compact F-SAS sensor is made portable by it having only 15.3% of the volume of a conventional F-SAS sensor, as is shown in Fig. 1. Under the approval of the Ethics Committee at the Dept. of Pediatrics at the University of Yamanashi, the subject wore a portable sleep apnea syndrome examination apparatus (SAS 2100) while a plastic optical fiber sheet was placed under the subject's bed. The subject's apnea/hypopnea index (AHI) was measured by the SAS 2100 and the respiratory disturbance index (RDI) was measured with new analysis software developed for the compact F-SAS sensor.

Compact type Conventional type SAS 2100
175×100×45mm 330×240×65 mm
Figure 1. Comparison of compact F-SAS sensor and conventional one (left) and SAS 2100 (right)

Further, this type of F-SAS sensor and Alice PDX of Philips-Respironics GK, a PSG device used to inspect sleep for OSAS diagnosis, were used for measurement. Figure 2 below shows a diagram of the F-SAS sensor and PSG (Alice PDX).

F-SAS sensor control unit

Optical fiber sheet

Internal structure of fiber sheet
(400-mm long × 800-mm wide)

Bending loss due to fluctuation of side pressure applied to optical fiber due to respiratory motion is measured in form of output light.

Optical signal (attenuation)

Core

Clad

Optical signal

Optical signal (attenuation)
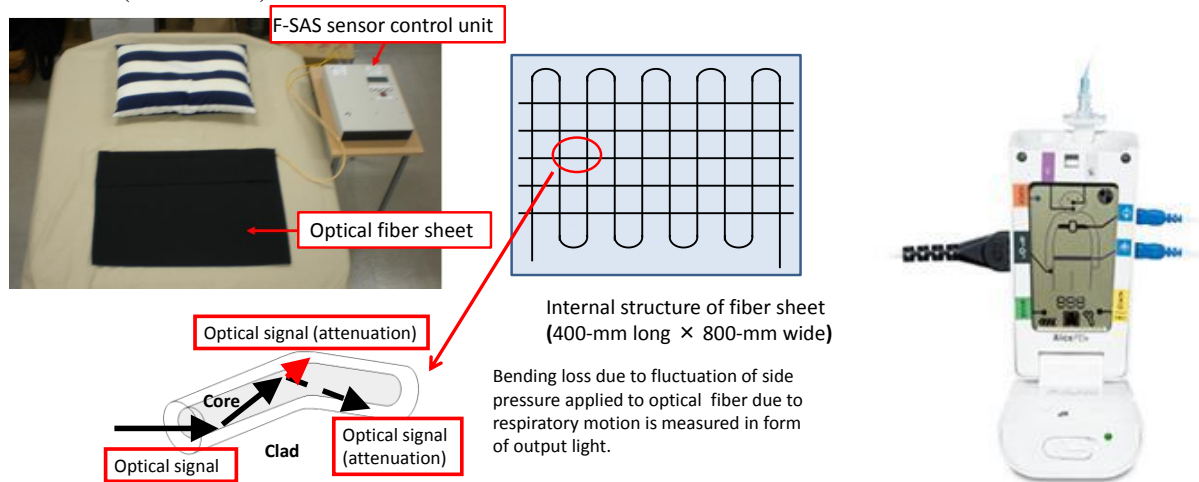
Figure 2. F - SAS sensor (left) and PSG (right)

3. Results

Their correlation value was then obtained. The new analysis software was made up of a new algorithm that is difficult to use when the number of body movements per hour exceeds a certain number, and it analyzes the RDI by checking both the gasping judgment and weakness judgment against the data from a seriously ill patient. In this study, we improved the algorithm for severe markers in children and aimed to expand the application area to the compact F-SAS sensor. We compared severe markers obtained with the compact F-SAS sensor and existing simple polysomnography (PSG) (SAS 2100 manufactured by Nihon Kohden).

In this study, 27 data collected by the compact F-SAS sensor were analyzed by using the new analysis software, which were a severe marker caused by RDI, severe markers with periodic distribution, severe markers due to gasping respiratory frequency, severe markers due to hypopnea, and severe marker due to body movement frequency. The results are shown below. Before introducing the markers, the correlation value of R was 0.697 as shown in Fig. 3. After introducing the severe markers obtained by RDI, R = 0.58 as shown in Fig. 4. After introducing the severe markers with periodic distribution, R = 0.67, and it was R = 0.52 after introducing the severe markers due to gasping respiratory frequency, R = 0.76 after introducing the severe markers due to hypopnea, and R = 0.87 after introducing the severe markers due to body movement frequency, as shown in Fig. 5.
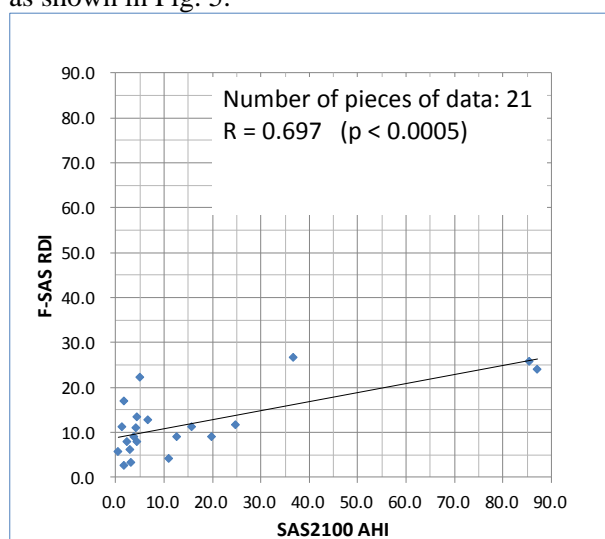
Figure 3. Scatter diagram of F-SAS RDI and SAS 2100 AHI before introduction of severe marker
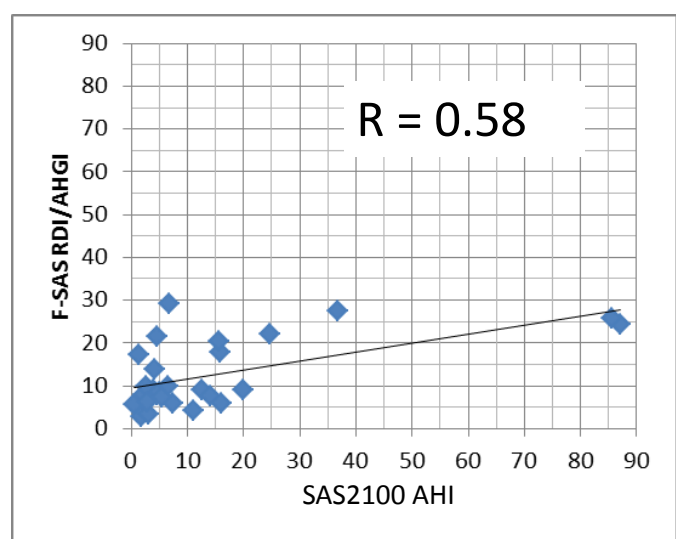
Figure 4. Scatter diagram of F-SAS RDI/AHGI and SAS 2100 AHI of severe marker algorithm by RDI

A scatter diagram of the correlation between the AHI obtained by SAS 2100 and RDI obtained by the compact F-SAS sensor is shown in Fig. 5.
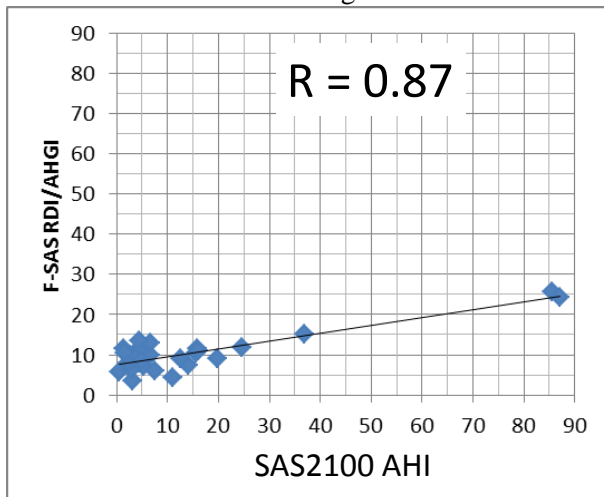
Figure 5. Scatter diagram of F-SAS RDI / AHGI and SAS 2100 AHI of severe marker algorithm based on body movement frequency

Table 1 Correlation value in each severe marker

Severe marker	Correlation value
RDI	0.58
Periodic distribution	0.67
Candle breathing frequency	0.52
Low breathing frequency	0.76
Number of body movements	0.87

The analysis results revealed the correlation value to be R=0.87, which is a significant improvement over the correlation value of R=0.697 between AHI obtained by SAS 2100 and RDI obtained by the conventional F-SAS sensor. From this, the software using the new algorithm effectively analyzes the RDI. In the future, to further improve the sensitivity of the compact F-SAS sensor, the remaining gap between the AHI and RDI in seriously ill patients must be bridged. To do this, algorithms will need to be developed that allow the analysis software of F-SAS sensors to capture highly disturbed respiration in seriously ill patients.

We improve the accuracy of the software used for analysis with the F-SAS sensor for child development. This was done for the development of PSG equipment of Philips Respirnics GK used in a pediatric clinical trial at Yamanashi University School of Medicine for the purpose of comparing apneic events between the pediatric F-SAS sensor and PSG. That is, the respiratory events were judged and compared from the waveform data at bedtime, which is the analysis result of the F-SAS sensor and PSG. On the basis of the definition of the scoring rule of children for sleeping respiratory events, proposed by the American Academy of Sleep Medicine (AASM) in 2007, apnea events were judged from the waveforms of PSG.
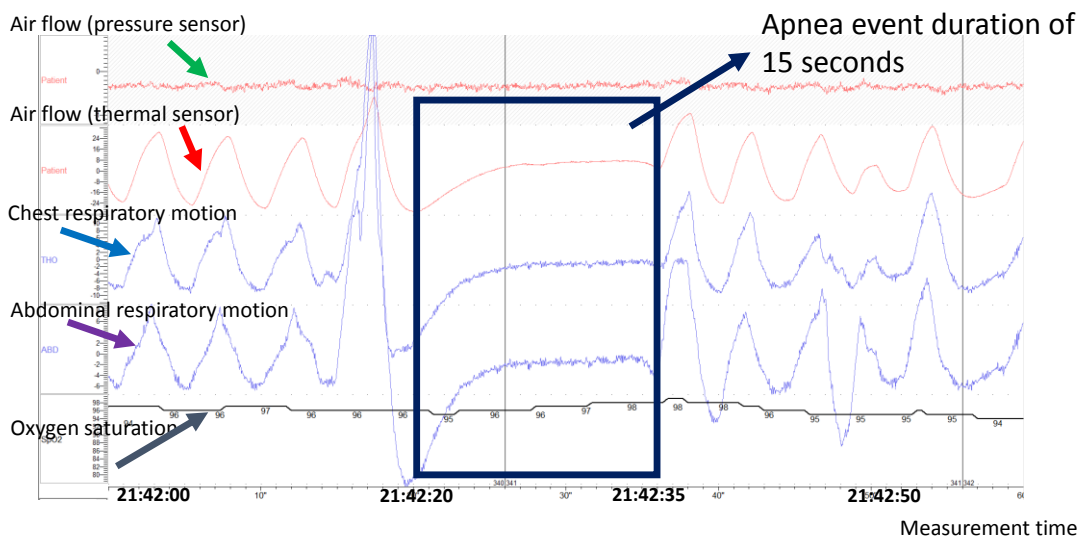
Figure 6 Measurement analysis result of PSG (apnea waveform)

The analysis results are as follows. The subject was a boy, aged 4 years and 0 months. The measurement comparison time was 21:18:39 to 23:36:24. His height was 99.1 cm, and his weight was 16.6 kg. The

respiration cycle was 6 seconds/turn. Concerning the maximum amplitude of the thermal sensor, which was 24 (unit unknown), a drop of 90% or more can be seen for 15 seconds. Table 2 shows that all five apnea event durations of F-SAS and PSG were consistent. As a result of comparing apneic events between F-SAS sensor and PSG, five apneic events in five out of five matched. In this subject, all apnea events could be detected by the F - SAS sensor.

Figure 7 Measurement analysis result of F-SAS sensor (apnea waveform)

This result suggests that the application to diagnosing sleep apnea syndrome in children with the compact F-SAS sensor may be effective. In the future, in order to improve the accuracy more, it is important to further analyze the data.

Table 2 Results of apnea events comparison between F-SAS sensor and PSG

Apnea event start time (F-SAS)	Apnea event duration (F-SAS) [sec]	Apnea event start time (PSG)	Apnea event duration (PSG) [sec]
21:30:12	18	21:23:20	18
21:49:12	15	21:42:20	15
22:02:12	13	21:55:20	13
22:52:50	12	22:45:58	12
22:56:54	12	22:50:02	12

4. Conclusion

In summary, a good correlation value of 0.87 was obtained between the RDI calculated by a new compact F-SAS sensor analysis system using an algorithm for severely ill children and AHI calculated by using the SAS 2100. Also, by comparing the sleep-event results of the F-SAS sensor with those of the PSG, it was observed that apnea sleep events matched. This suggests that it might be valid applied to diagnosing sleep apnea with the pediatric F-SAS sensor. We further analyze the subject data for further improvement.

5. References

[1] Masaki Hayashi, Seiko Mitachi, and Takeshi Sugiyama, "The software improvement of pediatric analysis for portable F-SAS sensor", The Institute of Electronics, Information and Communication Engineers, C-3-13, Electronics Presentation paper I, p137, 10-13rd March, 2015 in Kusatu.

[2] Nao Hasegawa, Seiko Mitachi, and Takeshi Sugiyama, "Application of a Portable F-SAS Sensor System to Pediatric Sleep Apnea Syndrome", C-3-6, Electronics Presentation paper I, p.161, 18-21st March, 2014 in Niigata.

[3] Ryo Saito, Seiko Mitachi, and Takeshi Sugiyama, "Comparison of Apnea Event by Pediatric F-SAS Sensor and Polysomnography", The Institute of Electronics, Information and Communication Engineers, C-3-26, Electronics Presentation paper I, p.164, 15-18th March, 2016 in Fukuoka.

[4] Seiko Mitachi, Tomohiro Kameyama, Yohei Kamiyama, Kumiko Shimoyama, and Makoto Satoh, "Comparison between automated analysis by F-SAS sensor system and diagnosis by Polysomnography", The Institute of Electronics, Information and Communication Engineers, C-3-70, Electronics Presentation paper I, p.230, 19-22nd March, 2013 in Gifu.

[5] Seiko Mitach, Hiroshi Ikarashi, Takeshi Sugiyama, "Application of diagnosis with pediatric sleep apnea syndrome of F-SAS sensor", Proceedings of the 58th JASAP Spring Meeting, 2011, p.05-156, 25a-KB-11(2011).

POF over WDM - beyond the dispersion limit

U.H.P. Fischer[1], S. Höll[2], M. Haupt[1], M. Joncic[1]
[1]Harz University of Applied Sciences, Friedrichstr. 57-59, 38855 Wernigerode, Germany
[2] Sicoya GmbH

*Corresponding author: ufischerhirchert@hs-harz.de

Abstract: Data communication over Polymer Optical Fibers (POF) is limited to only one channel for data transmission. Therefore the bandwidth is strongly restricted. By using more than one channel, it is possible to break through the limit. This technique is called Wavelength Division Multiplexing (WDM). It uses different wavelengths in the visible spectrum to transmit data parallel over one fiber. Two components are essential for this technology: A multiplexer (MUX) and a demultiplexer (DEMUX). The multiplexer collects the light of the different sources to one fiber and the demultiplexer separates the light at the end of the fiber into the different fiber output ports. In this paper, we propose spectral grids in the visible spectrum, which are compatible with existing standards like ITU recommendations for WDM networks. Additionally, results of a demonstrator of an integrated polymeric demultiplexer produced with injection moulding are presented. The paper discusses the results of the different development steps, the measurements done with the first demonstrator and the challenges related to the injection moulding process.

1. Introduction

Polymer Optical Fibers (POF) are used in various fields of applications. The core material consists of PMMA (Polymethylmethacrylate), while the cover is made of fluorinated PMMA. The whole fiber has a diameter of 1 mm. POFs are used for optical data transmission based on the same principle as glass fiber. As a communication medium they offer a couple of advantages related to other data communication systems such as copper cables, glass fibers and wireless systems, and have great potential to replace them in different applications.

Namely, in comparison with glass fibres (GOF), POFs have the advantage of easy and economical processing and are more flexible for optical connections [1]. However, one advantage of using glass fibres is their low attenuation, which is below 0.2 dB/km in the infrared range. The larger core diameter of POFs leads to higher mode dispersion and thus to higher attenuation across the electromagnetic spectrum. This increased attenuation leaves only one remaining transmission window, namely the visible spectrum of light (400 – 700 nm). Hence, POFs are best suited for the use in short distance data communication. Here, POFs can outperform the current standard of copper cable as communication medium. On the one hand, they feature lower weight and space. On the other hand, POFs are not susceptible to electromagnetic interference. [2-3]. For these reasons, POFs are already used in various application domains, for example in the automotive sector and for in-house communication [4, 5, 6, 7]. At present, the great potential of the POF is not available as the alternative techniques offer transmission rates up to 10 Gb over copper and up to 40 Gb over glass fibers in the network area. The WDM technique offers an approach to achieve these high data rates also in the POF range.
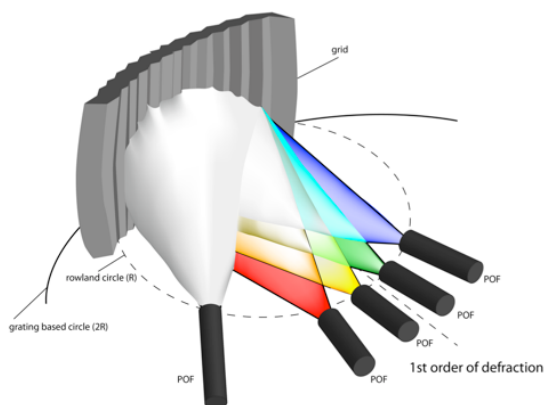
Figure 1.: Rowland set-up of demultiplexer
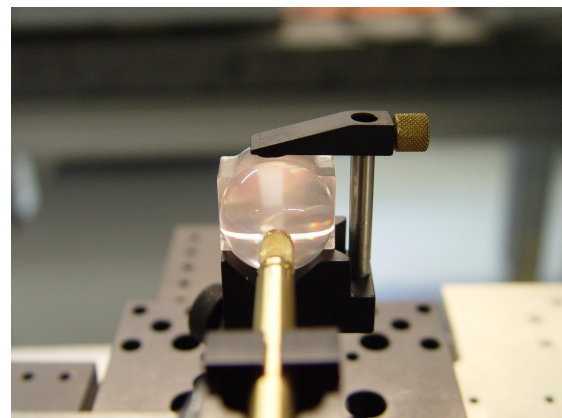
Fig. 2: integrated demultiplexer prototype

For WDM two essential components are needed: a multiplexer and a demultiplexer. To create a functional demultiplexer for POF, several preconditions must be fulfilled. Firstly, a mirror must focus the divergent light beam coming form the POF. The shape of this mirror cannot be spherical because of the appearing spherical aberration. Instead, a toric shape of the mirror prevents spherical aberration [8, 9, 10].

The second function is the separation of the different transmitted wavelengths, which can be achieved by a diffraction grating. This principle is illustrated in figure 1. The light is split into different orders of diffraction. The first order is the important one to regain all information. There, the outgoing POFs can be placed.

To separate the channels at the output ports, one interesting option for high multimode transmission systems is to use an optical grating. Here, the optical grating is placed on an aspheric mirror, which focuses the monochromatic parts of light into the outgoing fibers. In order to keep the advantage of cost-effective POFs it is necessary to mass-produce the MUX and DEMUX component at reasonable prices. For polymers, injection molding is the only technology, which offers high potential to achieves this goal. Before starting the production of the mold insert, a demonstrator of the DEMUX is fabricated by directly machining it in the PMMA material by means of diamond turning technique (see figure 2). Thus, the same diamond-turning technology is used for the manufacture of the mold insert. This step is done due to validate the simulation results with the produced component.

2. Manufacturing of the Demonstrator

By using the injection molding process, the manufacturing of the mold insert is the most important factor. Due to the three-dimensional toric structure of the grating planar manufacturing methods like lithography, especially LIGA (German acronym for Lithographie, Galvanoformung, Abformung - Lithography, Electroplating, and Molding) cannot be used. LIGA is used to manufacture planar spectrometers based on the glass fiber technology [11, 12, 13, 14]. But in our case, the three-dimensional grating needs another machining method. Especially the microstructure of the grating and the exact curve shape of the toric surface require high precision. The microstructure has the shape of a saw tooth with a pitch between the teeth of 2.5 µm. Figure 3 shows an enlarged 3D-Model of the grating. After investigate several machining methods only the diamond turning meets the high demands of the micro structured grating.
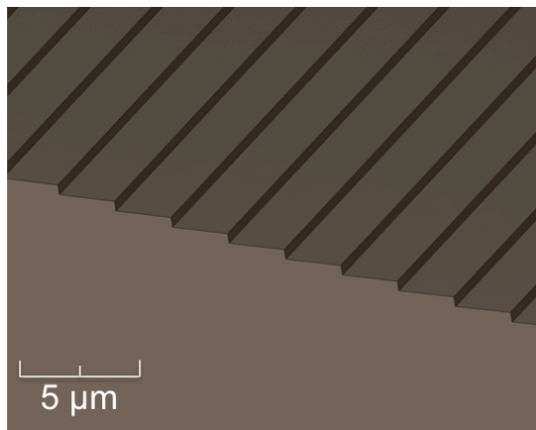
Fig. 3: Grating of the demultiplexer
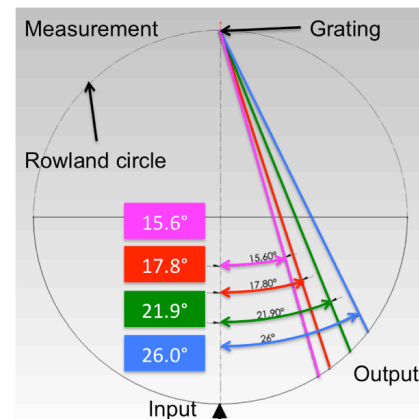
Figure 4. Measurement results of the focal points for different wavelengths (405 nm violet ray; 450 nm blue ray; 520 nm green ray; 650 nm red ray

3. Optical measurements

In order to measure the position of the focal points of the different separated wavelength a special measurement setup was build. It uses a parallel-kinematics precision alignment system to align a fiber at the surface of the hemisphere. A fixed input-fiber is used to couple white light into the DEMUX as shown in figure 4. In this figure can be seen that the separated wavelength are focused at a ring on the hemisphere. This ring is scanned by the fiber on the alignment system. The light of the scanning fiber is analyzed by a spectrometer. The positions of the wavelengths measured by the setup are depicted in figure 4. In comparison to the simulation a shift of the positions can be recognized. Nevertheless, the separation of the wavelengths was measured and confirms the functionality of the demultiplexer.

4. Spectral grids in the visible spectrum for POF WDM applications

Besides developing low-IL cost-effective POF WDM components and fast POF WDM transmission systems, it is also important to allocate a unique set of WDM transmission channels in the visible spectrum to support WDM applications over SI-POF. To evaluate the applicability of a spectral grid to support visible spectrum WDM applications over SI-POF, the appropriate criteria were first established. Those criteria refer to:

- Channel distribution with respect to the spectral attenuation of SI-POF;

- Performances of different demultiplexing techniques;

- Availability of laser diodes in the visible spectrum.

4.1. Extension of ITU-T G.694.2 CWDM grid into the visible spectrum

If ITU-T G.694.2 CWDM wavelength grid would be extended into the visible spectrum, 15 equidistant channels between 400 nm and 700 nm would be obtained, as shown in Fig. 5. The parameters of the grid including the nominal central wavelengths. The channel spacing of 20 nm makes good utilization of the available spectral range. In the red window the extension has a channel at 651 nm, which is very close to the attenuation minimum at 650 nm. The channel distribution also corresponds well to three other attenuation windows. The channels experiencing the highest attenuation are those at 611 nm, 631 nm, 671 nm and 691 nm. Those channels could be used for distances up to 20 m since they would experience approximately the same attenuation as 651 nm channel over 50 m, but lower intermodal dispersion. Good channel allocation, sufficient channel spacing, high channel count and good availability of the transmitters make the extension of CWDM grid very suitable to support WDM applications over SI-POF.
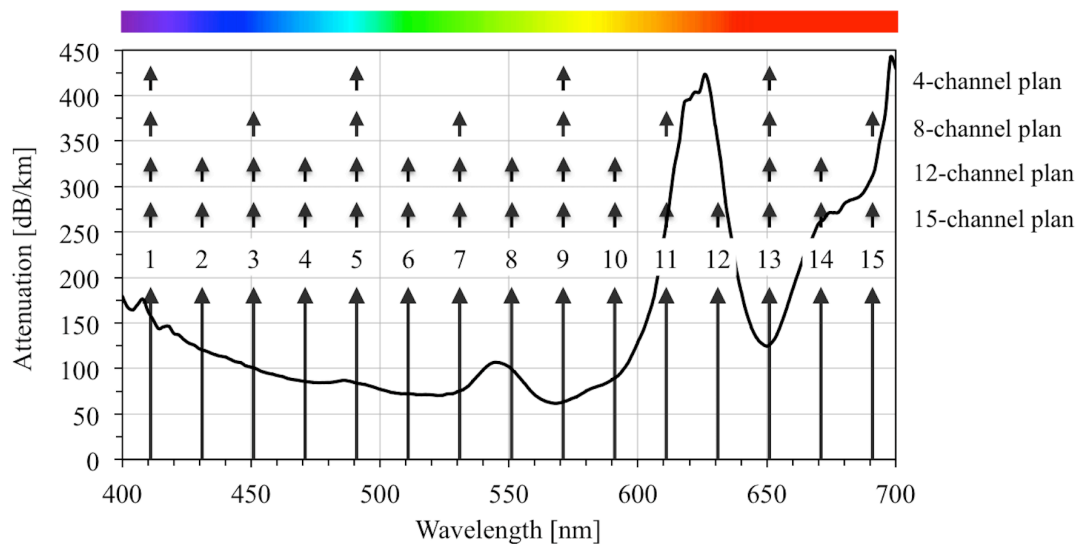
Fig. 5: Extension of CWDM wavelength grid into the visible spectrum and channel plans for 4-,   8-, 12- and 15-channel applications.

5. Conclusions

In summary, injection moulding the DEMUX element for POFs poses several challenges, especially the microstructure of the grating on a three-dimensional surface. It is shown that the current manufacturing process is able to produce the structure size and the exact radius needed for the DEMUX. The optical measurements to prove the principle were done. These confirm the separation of the wavelength in the visible spectrum.

WDM applications over SI-POF with 40 Gbit/s transmission are a realistic aim for the next future developments in POF systems. It seems to be possible to transmit 40 Gbit/s via 15 channels and a channel rate of 2,7 Gbit/s as a overall data rate with WDM. This opens the range of POF applications to existing cloud ccnters and future in-house networks with extensions to 100m-link length.

6. Acknowledgements

7. References

1. W. Daum, J. Krauser, P. E. Zamzow, O. Ziemann, POF Handbook: Optical Short Range Transmission Systems, Springer-Verlag, 2008

2. H. S. Nalwa (Ed.), Polymer Optical Fibres, American Scientific Publishers, California 2004

3. Club des Fibres Optiques Plastiques (CFOP) France, Plastic Optical Fibres – Practical Applications, J. Marcou, John Wiley & Sons, Masson, 1997

4. J. Brandrup, E. H. Immergut, E. A. Grulke, Polymer Handbook, 4th Edition, Wiley-Interscience, 1999

5. R. T. Chen and G. F. Lipscomb, Eds, "WDM and Photonic Switching Devices for Network Applications", in Proceedings of SPIE, vol. 3949, 2000

6. Colachino, J., "Mux/DeMux Optical Specifications and Measurements", Lightchip Inc. white paper, Lightreading, 2001

7. A. H. Gnauck, A. R. Chraplyvy, R. W. Tkach, J. L. Zyskind, J. W. Sulhoff, A.J. Lucero, et. al., "One terabit/s transmission experiment", Proceedings OFC'96, 1996

8. Fischer-Hirchert, U.H.P.: Photonic packaging sourcebook: Fiber-chip coupling for optical components, basic calculations, modules. 2015.

9. U. H. P. Fischer, M. Haupt, "WDM over POF: the inexpensive way to breakthrough the limitation of bandwidth of standard POF communication", SPIE Symposium on Integrated Optoelectronic Devices, Photonics West San Jose, 2007

10. U. H. P. Fischer, M.Haupt, "Integrated WDM System for POF Communication with Low Cost Injection Moulded Key Components", Access Networks and In-house Communications, 2010

11. M. Stricker, G. Pillwein, J. Giessauf, "Focus on Precision - Injection Molding Optical Components" in Kunststoffe international, vol. 4, pp. 15-19, 2009

12. J. P. Ferguson, S. Schoenfelder, "Micromoulded spectrometers produced by the Liga Process," Searching for Information: Artificial Intelligence and Information Retrieval Approaches, IEE Two-day Seminar (Ref. No. 1999/199), pp.11/1-11/4, 1999

13. M. A. Davies ; C. J. Evans ; R. R. Vohra ; B. C. Bergner and S. R. Patterson, "Application of precision diamond machining to the manufacture of microphotonics components", Proc. SPIE 5183, Lithographic and Micromachining Techniques for Optical Component Fabrication II, 94, November 2003

14. D. Dornfeld, S. Min, Y. Takeuchi,"Recent Advances in Mechanical Micromachining", CIRP Annals - Manufacturing Technology, vol. 55, Issue 2, 2006, p. 7

Materials for Fluorescent Fibers - Molecular Weight Inconsistence in Perylene/Lumogen doped PMMA

Daniel Zaremba[1], Jana Kielhorn[1], Robert Evert[1], Florian Jakobs[1], Itxaso Parola[2], Reinhard Caspary[1], Wolfgang Kowalsky[1], and Hans-Hermann Johannes[1]*

1 Technische Universität Braunschweig, Institut für Hochfrequenztechnik, Labor für Elektrooptik, Bienroder Weg 94, D-38106 Braunschweig, Germany.

2 University of the Basque Country (UPV/EHU), Faculty of Engineering of Bilbao (EIB), Plaza Ingeniero Torres Quevedo 1, E-48013 Bilbao, Spain.

*Corresponding author: h2.johannes@ihf.tu-bs.de

Abstract: Producing fluorescent polymer optical fibers is a key step towards new applications like fluorescent fiber solar collectors (FFSCs), sensors, contactless coupling devices, or polymer fiber integrated light sources and lasers. Therefore, an integration of fluorescent dyes into the polymer matrix is necessary. A dye concentration depend deviation from the targeted molecular weight of the polymers is shown.

1. Introduction

The need for dye doped polymers or polymer optical fibers (POFs) increases with its growing number of potential applications. Especially fluorescent polymers gaining interest in integrated optical applications like luminescent solar collectors (LSCs) or fluorescent fiber solar collectors (FFSCs) [1, 2], fluorescent sensors [3], polymer lasers [4, 5], or contactless coupling devices [6]. Therefore, an integration of fluorescent dyes into a polymer matrix is necessary and becomes accessible via suspension or copolymerization. In this work, the four perylene based fluorescent dyes Sigma Aldrich Perylene, BASF Lumogen F Yellow 083, TCI Perylene Orange, and BASF Lumogen Red F300 were suspended into a monomer solution of MMA and polymerized in bulk. Controlling reagents were added to form bulk polymer samples and preforms. The latter necessitate a controlled molecular weight distribution to enable fiber production. The molecular weight should therefore be in the range of around 100000 g/mol (PDI < 2). The chain length is adjusted by the chain transfer agent and initiator ratio and controlled by sizes exclusion chromatography (SEC). It is shown that the targeted molecular weight cannot be reached for the targeted perylen/lumogen doped materials while using the PMMA tested parameter sets. Instead a dye concentration dependence of the polymer chainlength is shown. Test samples using similar produced rhodamine B, *tri*-cyanine, or metal organic (Eu^{3+}, Tb^{3+} or Ir^{3+} dyes) doped PMMA do not show any deviation from the targeted molecular weight distribution

2. Results and Discussion

2.1 Polymer preparation and analysis

Polymer fabrication: Various dye concentrations (0.005, 0.01, 0.02, 0.03 and 0.04 mol%) of Sigma Aldrich Perylene, BASF Lumogen F Yellow 083, TCI Perylene Orange, and BASF Lumogen Red F300, mixed with lauroylperoxide (0.03 mol%) and *n*-butyl-mercaptan (0.1 mol%) are solved in a nitrogen saturated MMA solution at room temperature and polymerized in sealed glass containers for five days undergoing a temperature ramp from 20 to 100 °C. This temperature is maintained constant for 1 day before cooling to 20 °C over 24 hours.

Size exclusion chromatography: Molecular weight analysis is performed on an Agilent Technologies SECcurity GPC 1260 Infinity system with RI-detector, PSS WinGPC UniChrom software V8.00, and PSS GRAM 30 Å and GRAM 1000 Å columns. The measurements are performed at 40 °C with a sample concentration of 1 mg/mL in dimethylformamide (DMF). The System is calibrated with PSS ReadyCal-Kit for *poly*(methyl-methacrylate) (PMMA) M_p 800 to 1820000 Da.

2.2 Polymerization and Dyes

Preparing bulk PMMA for a preform based fiber drawing process as it is used at our institute is challenging because of several reasons. First an extreme high purity is necessary, second homogeneous and bubble free

preforms are needed, and third a precise molecular mass distribution is required. In our process the latter is determined to a number average molar mass (Mn) of 100000 g/mol and a PDI < 2. These parameters can be achieved for pure PMMA preforms using 0.03 mol% lauroylperoxide as initiator and 0.1 mol% *n*-butyl-mercaptan as chain transfer agent (see figure 1).
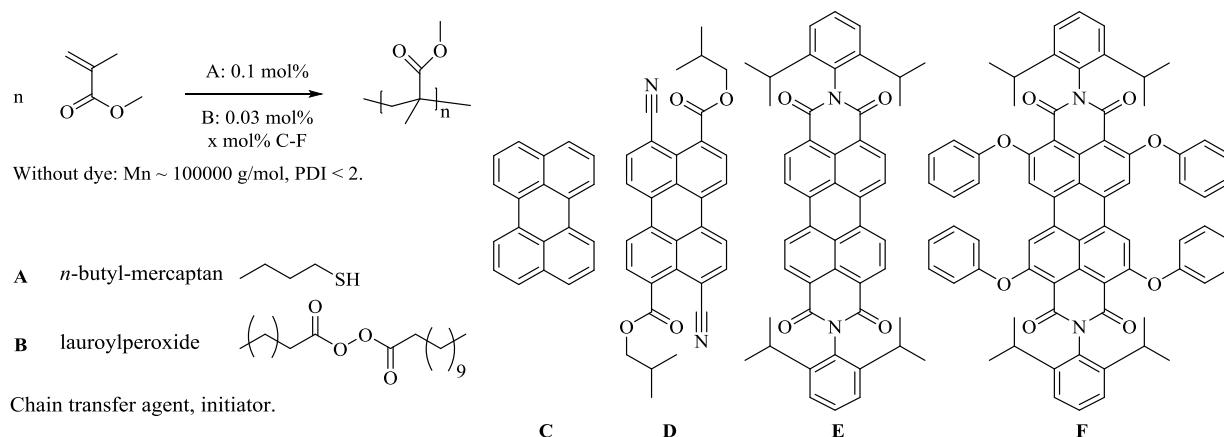
Figure 1. General reaction scheme for the preparation of PMMA with chain transfer agent (**A**) and initiator (**B**). Used dye in this study Sigma Aldrich Perylene (**C**), BASF Lumogen F Yellow 083 (**D**), TCI Perylene Orange (**E**), and BASF Lumogen Red F300 (**F**).

Figure 1 also shows the fluorescent perylene or lumogen dyes that were used in this study. All those dyes have a characteristically perylene substructure in common. It is responsible for their high stability (e.g. polymerizeability in a free radical process and resistance against temperature load during polymerization and fiberdrawing). They further show good optical properties like high quantum efficiencies and less photo bleaching. Side groups enable a tuning of the spectral absorption and emission spectra. Lumogens can therefor widely cover all areas of the visible spectra [7]. Fluorescent fiber integration is therefore very attractive. Normalized spectra for doped PMMA samples with Sigma Aldrich Perylene, BASF Lumogen F Yellow 083, TCI Perylene Orange, and BASF Lumogen Red F300 are shown in figure 2. Doped preforms with dopant concentrations of 0.005, 0.01, 0.02, 0.03 and 0.04 mol% were made.
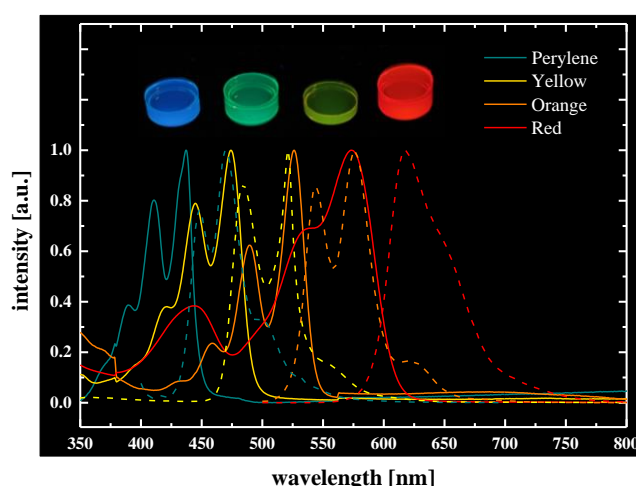
Figure 2. Fluorescent dye doped PMMA samples (0.0001 mol%) and corresponding normalized spectra. Absorption (lines) and emission (dotted lines) for Sigma Aldrich Perylene (blue), BASF Lumogen F Yellow 083 (yellow), TCI Perylene Orange (orange), and BASF Lumogen Red F300 (red).

2.3 Sizes exclusion chromatography

The molecular mass distribution of the preforms was determined by size exclusion chromatography. While pure PMMA preforms with the needed parameters were made the dye doped preforms showed characteristically deviations from the targeted molecular weight. The results are shown in figure 3. TCI Perylene Orange is not soluble in a concentration of 0.04 mol% in MMA.

As can be seen from the data the molecular weight is higher than the expected value of 100000 g/mol. It further increases with an increasing dopant concentration. Comparative experiments with fluorescence dyes of a different type (e.g. rhodamine B, *tri*-cyanine, or metal organic dyes (Eu^{3+}, Tb^{3+} or Ir^{3+}) have not shown a similar effect. This can be taken as a hint to the perylene substructure causing the oberved molecular weight inconsistences. The effect is the same for all four tested dyes but it strongly varies in strength. The bare perylene structure without any substituents shows the strongest Mn increase. Therefore, a polymer analogous test reaction with perylene, initiator, and chain transfer agent in toluene instead of MMA was performed. An additional absorption between 450 and 580 nm occurs over time. This observation can further be supported by online monitoring of the polymerization process. From this, a possible reaction between the polymerization agents and the dye can be assumed. A less active concentration of lauroylperoxide or *n*-butyl-mercaptan would explain an increase in the chain length.
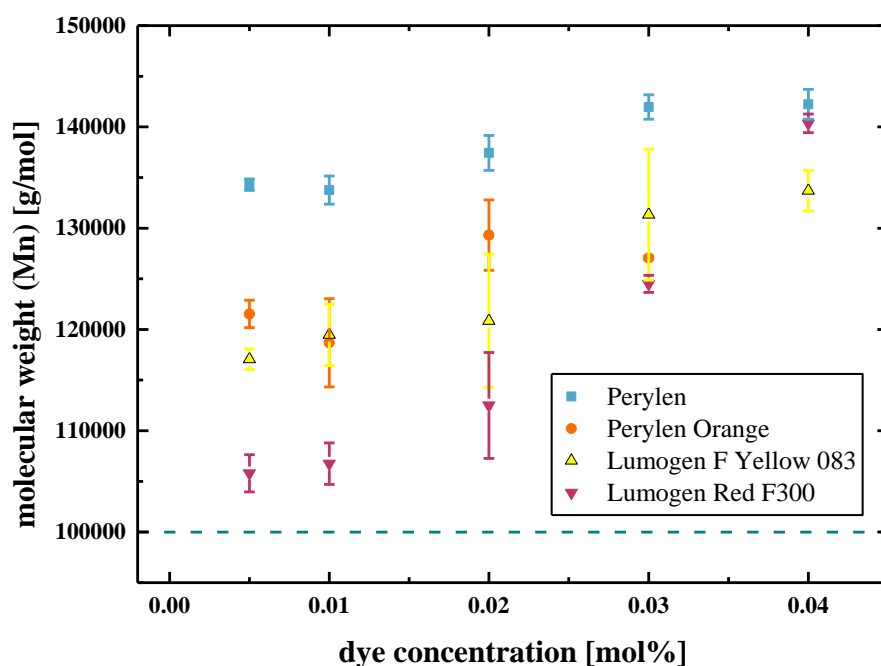
Figure 3. Measured number average molar mass (Mn) for PMMA samples doped with various dyes in different concentration and reference line for undoped PMMA at 100000 g/mol.

3. Conclusion

In the production of preforms for fluorescent polymer optical fibers made of PMMA characteristic displacements in the targeted molecular weight distributions are determined by size exclusion chromatography. With increasing dopant concentration of the fluorescent dyes Sigma Aldrich Perylene, BASF Lumogen F Yellow 083, TCI Perylene Orange, and BASF Lumogen Red F300 the molecular weight also raises. A possible explanation traces this effect back to the perylene substructure, reducing the active concentration of either the initiator or the chain transfer agent. To overcome these problems a slightly increased chain transfer agent concentration can be used to decrease the molecular weight to the targeted value.

4. Acknowledgements

5. References

[1]   Sark, Wilfried G.J.H.M. van, Barnham KW, Slooff LH, Chatten AJ, Büchtemann A, Meyer A et al. Luminescent Solar Concentrators - A review of recent results. Opt. Express 2008; 16 (26):21773, DOI: 10.1364/OE.16.021773.

[2]   Correia SF, Lima PP, André PS, Ferreira, Maria Rute Sá, Carlos, Luís António Dias. High-efficiency luminescent solar concentrators for flexible waveguiding photovoltaics. Solar Energy Materials and Solar Cells 2015; 138:51–7, DOI: 10.1016/j.solmat.2015.02.032.

[3]   Zubia J, Arrue J. Plastic Optical Fibers: An Introduction to Their Technological Processes and Applications. Optical Fiber Technology 2001; 7(2):101–40, DOI: 10.1006/ofte.2000.0355.

[4]   Kuriki K, Kobayashi T, Imai N, Tamura T, Nishihara S, Nishizawa Y et al. High-efficiency organic dye-doped polymer optical fiber lasers. Appl. Phys. Lett. 2000; 77(3):331, DOI: 10.1063/1.126967.

[5]   Gang Ding Peng, Chu PK, Zhengjun Xiong, Whitbread TW, Chaplin RP. Dye-doped step-index polymer optical fiber for broadband optical amplification. J. Lightwave Technol. 1996; 14(10):2215–23, DOI: 10.1109/50.541210.

[6]   Poisel H, Ziemann O, Bachmann A, Brechtel M, Winkler F, Mohrberg T, Dengler P, Doerjes P, Langhals H, Schluecker T, Schoppel G. Fiberoptic rotary joints reach a new dimension in transmission capacity. 23rd International Conference on Plastic Optical Fibers, POF 2014; Keio University Hiyoshi CampusHiyoshi, Yokohama; Japan; 8 October 2014 through 10 October 2014.

[7]   Langhals H, Kirner S. Novel Fluorescent Dyes by the Extension of the Core of Perylenetetracarboxylic Bisimides. Eur. J. Org. Chem. 2000; 2000(2):365–80, DOI: 10.1002/(SICI)1099-0690(200001)2000:2<365::AID-EJOC365>3.0.CO;2-R.

Post-Fabrication Cladding Doping of Commercial PMMA Polymer Optical Fiber

P. Stajanca[*], K. Krebber

Bundesanstalt für Materialforschung und –prüfung (BAM), Unter den Eichen 87, 12205 Berlin, Germany

*Corresponding author: pavol.stajanca@bam.de

Abstract: Possibility of post-fabrication doping of commercial PMMA fibers using well-known solution doping technique is presented. The cladding of 1 mm PMMA fiber is doped with Rhodamine B with the help of methanol-mediated diffusion of the dye molecules into the fiber material. Doping of the fiber core was not possible even at extended doping times. The proposed method represents rather simple and cheap way for preparing custom cladding-doped POFs with high flexibility of dopant choice and fiber length. Produced cladding-doped fibers have potential for various sensing or lighting applications.

1. Introduction

Compared to glass-based fibers, large core polymer optical fibers (POFs) can be very robustness but still flexible, thus offering easier handling, light in-coupling and connectorization [1]. Thanks to lower processing temperatures of polymer materials, various organic dyes can be introduced into polymer optical fibers. Over the last decades, dye-doped fluorescent POFs have been explored for use in illumination [2], lasing and amplification [3], as well as sensing applications [4]. In general, both fiber core and cladding can be doped. In practice, core doped variant is prevailing for most applications. Nevertheless, cladding-doped fibers could be of interest as well, especially in sensing applications where dye interaction with surrounding environment is necessary. Numerous fluorescence-based sensing schemes have been suggested with optical fibers over the recent years. These include sensors for gamma or UV radiation [5, 6], pH factor [7], humidity [8], oxygen [9], and others.

A limited selection of core-doped POFs is available commercially. Specialized custom sensing solutions usually rely on attaching sensitive dye either to the tip or side of the fiber. The former option is relatively straightforward. The dye can be excited directly by the light guided in the fiber and fluorescence is coupled back to the core. On the other hand, only single point sensor can be achieved with this geometry. In the latter case, dye can be excited either by light propagation in the fiber or by side illumination and multi-point sensing can be achieved. However, local modification of the fiber, such as tapering or etching [10], is typically required in order to excite and collect the fluorescence. This kind of modification usually increases the loss in the fiber, deteriorates its mechanical integrity and offers only limited interaction range. Cladding doping is in principle feasible [2], but is typically done in the pre-drawing stage representing additional technical difficulty.

Here we show that cladding of a low-cost commercial polymethyl methacrylate (PMMA) fiber can be doped post-fabrication, using a well-known solution doping technique [11]. This method represents rather simple and cheap way for preparing custom cladding-doped POFs with high flexibility of dopant choice and doped fiber length. Since the cladding material is permeable for many liquids, utilizing right choice of dopant, fiber cladding could be sensitized to a number of compounds.

2. Methodology and materials

All the experiments in this work were performed with 1 mm multimode PMMA POF (Eska CK-40, Mitsubishi Rayon Co., LTD.). For simplicity, we focus here only on Rhodamine B as a dopant dye. However, we successfully doped the fiber also with several other organic dyes. Methanol was used as a suitable solvent known to be used for solution doping of PMMA [11]. All the doping experiments were performed at room temperatures (18-24 ˚C).

At ambient temperatures, ingress of methanol into PMMA exhibits Case II diffusion behaviour [12, 13], which is characterized by a sharp boundary between the intact inner PMMA region and swollen outer layer. Due to solvent-induced swelling, even larger molecules such as organic dyes can penetrate into the PMMA molecular structure. To study penetration of methanol and Rhodamine B into the investigated PMMA fiber, 500 mg of Rhodamine B was dissolved in 200 ml of methanol. This relatively high-concentration solution was used in

order to facilitate better visibility of the dopant ingress into the fiber. The pristine PMMA fiber was cut into short 4 cm pieces that were fit into small laboratory glass bottles. The bottles were then filled with the prepared dye-solvent solution. Different fiber samples were left in the solution for different times spanning from 10 h to 1 week. After taking each sample out, it was thoroughly washed and left to dry for over a week at ambient temperature. After drying, one end of the fiber sample was cut approximately 2 mm away from the original end face and polished. The fiber cross-section was then investigated with an optical microscope to monitor the progress of lateral penetration of methanol and dye into the fiber.

3. Results

As illustrated in Figure 1a for doping time of 24 hours, a clear boundary between intact inner PMMA region and outer layer that was penetrated by methanol can be seen in microscope images of the fibers cross-section. To evaluate progress of methanol front, diameter of the whole fiber D and inner undoped region d was measured from the microscope image for all the samples with different doping times. Relative methanol penetration P was then calculated as $P = (D - d)/D$. Figure 2 depicts the measured relative methanol penetration into the PMMA fiber as a function of doping time. A gradual progress of methanol intake into the fiber is obvious and full methanol penetration is observed for the sample that was left in the doping solution for 92 hours (Figure 1b). Fitting the measured data points with linear regression indicates that the full penetration should be achieved already for the doping times between 60 and 70 hours.
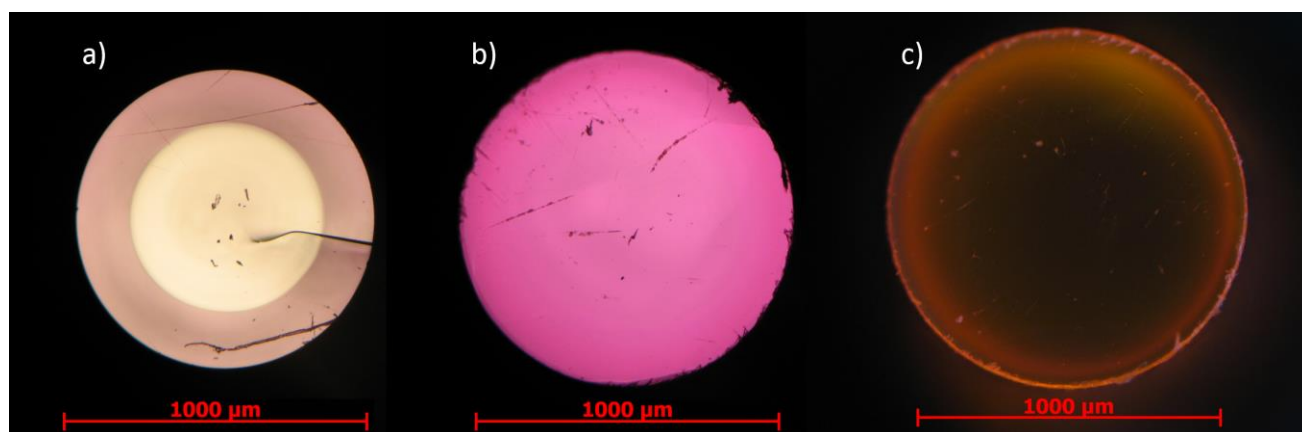
Figure 1. a) Microscope images of the fiber cross-section: a) image taken in a transmission mode for the fiber doped for 24 hours. b) Image taken in a transmission mode for the fiber doped for 92 hours. c) Image taken under lateral UV excitation for the fiber doped for a one week.

Similarly as in reference [11], we notice that ingress of the dopant into the fiber lags behind the methanol front. This is the consequence of a relatively large size of the organic dye molecules. On the other hand, while methanol solution doping has been used to transport the dopant into the PMMA fiber [11], in our experiment we noticed that the dye molecule penetrates only the outer cladding of the fiber made of perfluoropolymer. Even for doping times considerably longer than required for full methanol penetration into the fiber, no further ingress of dopant into PMMA core of the fiber was observed. This is illustrated in Figure 1c showing the cross-section of the fiber that was in the doping solution for a one week. The image was recoded with the optical microscope while the monitored fiber end face was illuminated laterally by a UV light. The image shows that the UV-excited fluorescence of Rhodamine B is confined to the cladding region. Thus only cladding doping of the fiber is possible and longer doping times do not bring any progress regarding dopant penetration into the fiber core. Contrary, extended doping times lead to notable annealing of the fiber. Analogically to high temperatures, ingress of solvents into the drawn polymer fiber may mediate the fiber annealing [14]. The annealing is typically associated with fiber shrinkage and respective diameter increase. The diameter increase can be noticed by comparing the Figures 1a and 1c for the fibers that were in the doping solution for 24 h and one week, respectively. Diameter increase of more than 150 µm is measured between these two fibers. In our case, fiber annealing generates visible imperfections at the core-cladding interface, which is detrimental for fiber transmission properties. Doping times considerably longer than required for full methanol penetration are therefore undesirable. On the other hand, two separate region in the fiber core are crated for shorter doping

times; pure PMMA center and outer region that was penetrated by methanol. Most probably due to methanol-induced annealing, these two regions exist in the fiber even after the drying of the fiber following the doping process. This inter-core structure is undesirable as it influences the light guiding along the fiber. Therefore, shortest doping time yielding full methanol penetration is considered as optimal.
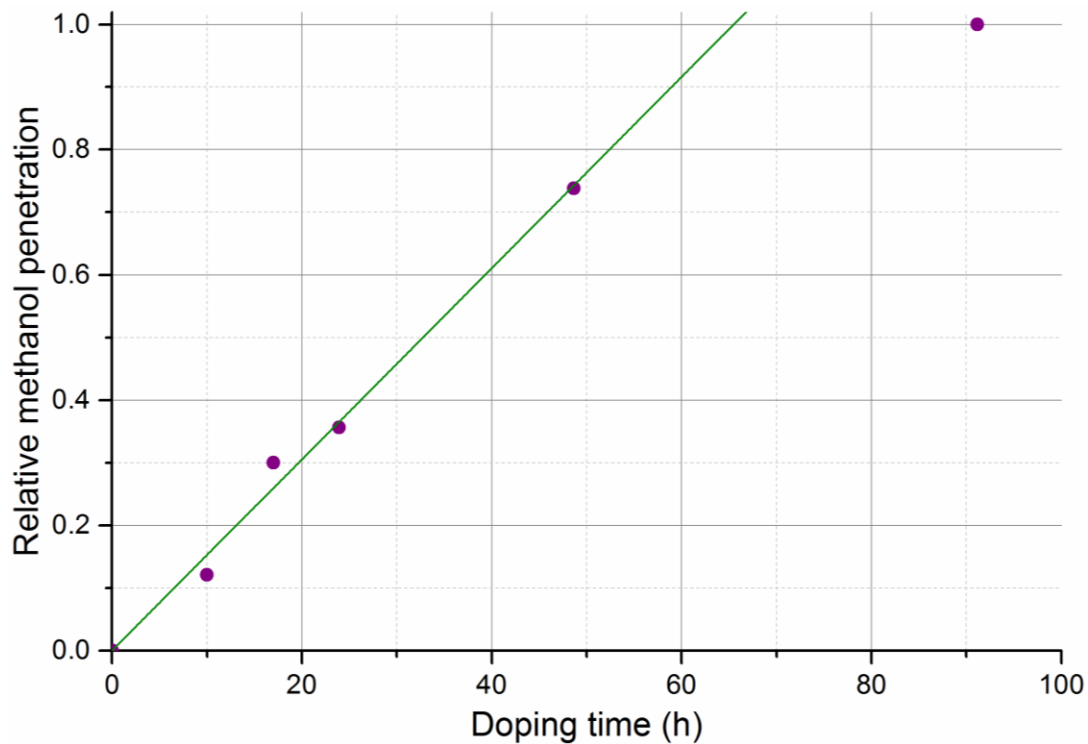
Figure 2. Relative methanol penetration into the 1mm PMMA POF as a function of doping time. Purple dots are measured data points while the green line is a linear fit of the data with intercept fixed to 0.

The proposed doping process is scalable by using large amount of doping solutions and glass containers. Figure 3a shows a picture of a 10 m long section of the fiber that was doped by the same technique. The fiber was wound into a coil with approximately 20 cm diameter so it can fit on the bottom of a glass dish with lid and inner diameter of 23 cm. The dish was then filled with the rest of the doping solution that was not used in the previous study with short fiber pieces. The doping time of the fiber was 60 hours. The prepared fiber can be easily connectorized with a suitable SMA clamp connectors.
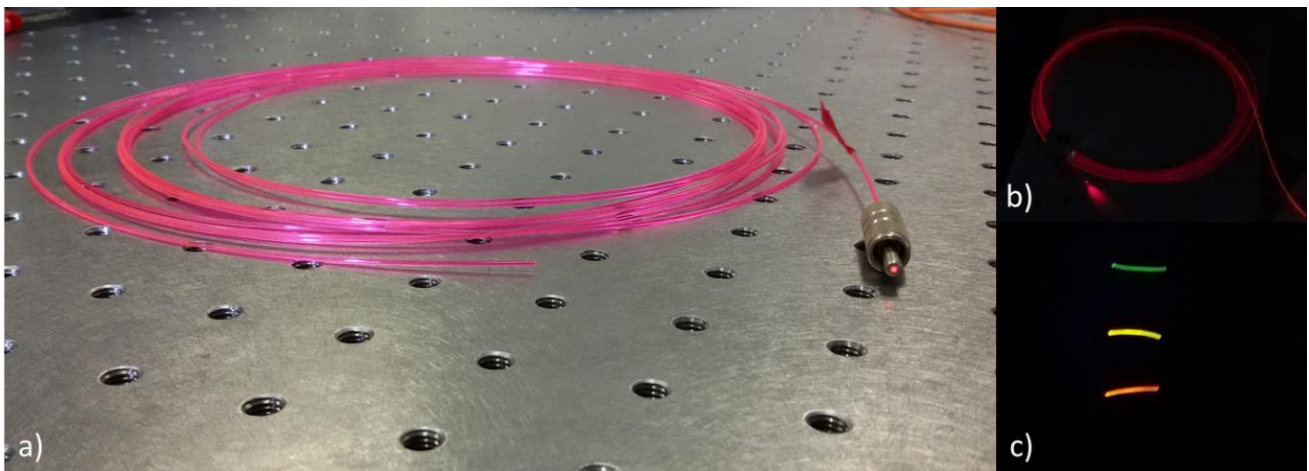
Figure 3. 10 long section of 1 mm PMMA POF with cladding doped with Rhodamine B under: a) side and b) in-core excitation by a white light. c) Short segments of the POF doped with Fluorescein, Rhodamine 6G and Rhodamine B (top to bottom) under side excitation by UV light.

When excited by external source, fluorescence of Rhodamine B dye immobilized in the cladding is partly collected and guided by the core along the fiber (Figure 3a). This can be used for sensing applications such as detection of UV radiation [6]. Even though the core of the fiber is not doped directly, the light guided in the core can interact with the dye at the core-cladding boundary and excite the dye fluorescence (Figure 3b). Therefore, the fiber could have potential for lighting applications as well [2]. Lastly, even though we focused on doping with Rhodamine B in this work, we successfully used the introduced approach also with other organic dyes such as Fluorescein or Rhodamine 6G (Figure 3c).

4. Conclusions

In this work we investigated the feasibility of using well-known solution doping technique for post-fabrication doping of commercial PMMA POFs. Using methanol-Rhodamine B doping solution, we showed that this technique can be used to dope the cladding of 1 mm PMMA fiber (Eska CK-40, Mitsubishi Rayon Co., LTD.). The doping of the fiber core was not possible. We studied the dynamics of the diffusion of the solvent-dye solution into the fiber and identified the optimal doping time. We demonstrated that the presented approach can be scaled to produce doped fibers of extended lengths. The procedure can be adopted also for use with other dopants. The resultant fibers could be used for various task within sensing or lighting applications.

5. Acknowledgements

6. References

1. O. Ziemann, J. Krauser, P. E. Zamzow, and W. Daum, *POF Handbook: Optical Short Range Transmission Systems (2nd edition)* (Springer, Berlin, 2008).
2. R. Narro-Garcia, R. Quintero-Torres, J. L. Dominguez-Juarez, and M. A. Ocampo, "Polymeroptical fiber with Rhodamine doped cladding for fiber light systems," J. Lumin. **169**, 295-300 (2016).
3. J. Arrue, F. Jimenez, I. Ayesta, M. A. Illarramendi, and J. Zubia, "Polymer-Optical-Fiber Lasers and Amplifiers Doped with Organic Dyes," Polymers **3**, 1162-1180 (2011).
4. R. J. Barlett, R. Philip-Chandy, P. Eldridge, D. F. Merchant, R. Morgan, and P. Scully, "Plastic optical fibre sensors and devices," Trans. Inst. Measurement Control **22**, 431-457 (2000).
5. W. B. Lyons, C. Fitzpatrick, C. Flanagan, and E. Lewis, "A novel multipoint luminescent coated ultra violet fibre sensor utilising artificial neural network pattern recognition techniques," Sensor Actuat. A-Phys. **115**, 267-272 (2004).
6. C. Fitzpatrick, C. O'Donoghue, and E. Lewis, "A novel multi-point ultraviolet optical fibre sensor based on cladding luminescence," Meas. Sci. Technol. **14**, 1477-1483 (2003).
7. X. H. Yang and L. L. Wang, "Fluorescence pH probe based on microstructured polymer optical fiber," Opt. Express **15**, 16478-16483 (2007).
8. S. Muto, H. Sato, and T. Hosaka, "Optical Humidity Sensor Using Fluorescent Plastic Fiber and Its Application to Breathing-Condition Monitor," Jpn. J. Appl. Phys. **33**, 6060-6064 (1994).
9. M. Morisawa and S. Muto, "POF sensors for detecting oxygen in air and water," in *7th International Plastic Optical Fibres Conference '98,* (Berlin, Germany, 1998), pp. 243-244.
10. C. Pulido and O. Esteban, "Improved fluorescence signal with tapered polymer optical fibers under side-illumination," Sensor Actuat. B-Chem. **146**, 190-194 (2010).
11. M. C. J. Large, S. Ponrathnam, A. Argyros, N. S. Pujari, and F. Cox, "Solution doping of microstructured polymer optical fibres," Opt. Express **12**, 1966-1971 (2004).
12. N. L. Thomas and A. H. Windle, "Transport of Methanol in Poly(methyl methacrylate)," Polymer **19**, 255-265 (1978).
13. N. L. Thomas and A. H. Windle, "A deformation model for case II diffusion," Polymer **21**, 613-619 (1980).
14. A. Fasano, G. Woyessa, J. Janting, H. K. Rasmussen, and O. Bang, "Solution-Mediated Annealing of Polymer Optical Fiber Bragg Gratings at Room Temperature," IEEE Phot. Technol. Lett. **29**, 687-690 (2017).

First Demonstration of POF Taper Fabrication Using Hot Water

Y. Mizuno[1*], H. Lee[1], H. Ujihara[1], N. Hayashi[2], and K. Nakamura[1]

[1]Institute of Innovative Research, Tokyo Institute of Technology,
4259, Nagatsuta-cho, Midori-ku, Yokohama 226-8503, Japan
[2]Research Center for Advanced Science and Technology, The University of Tokyo,
4-6-1, Komaba, Meguro-ku, Tokyo 153-8904, Japan

*Corresponding author: ymizuno@sonic.pi.titech.ac.jp

Abstract: We perform a pilot trial of highly convenient taper fabrication for polymer optical fibers (POFs) using hot water. A ~380-mm-long POF taper is successfully fabricated, and its ~150-mm-long waist has a uniform outer diameter of ~230 μm. The shape is in good agreement with the theoretical prediction. The optical loss dependence on the strain applied to the waist shows an interesting behavior containing three regimes, the origins of which are inferred by microscopic observations. We then discuss the controllability of the taper length.

1. Introduction

Brillouin scattering in optical fibers [1] has been exploited to develop various devices such as strain and temperature sensors [2–5]. To improve their performance, the Brillouin scattering properties in some special glass fibers have been investigated [6,7]. However, as glass fibers are fragile and break at relatively small strains (~3% for silica single-mode fibers (SMFs)), they cannot be directly used to measure larger strains. One method for tackling this problem is to use polymer optical fibers (POFs), which are so flexible that they can withstand even over 100% strain [8].

Several types of POFs are currently commercially available. The most widely used type is poly(methyl methacrylate)-based (PMMA-) step-index POFs [9], which mainly transmit visible light. However, Brillouin scattering in PMMA-POFs has not yet been experimentally observed, because some of the optical devices necessary for Brillouin measurement are not commercially available at visible wavelengths. Another type widely used in laboratories is perfluorinated graded-index (PFGI-) POFs [10] composed of cyclic transparent optical polymer (CYTOP), which transmit not only visible light but also telecom wavelength light. As many kinds of optical devices can be used at telecom wavelengths, Brillouin scattering in PFGI-POFs has already been experimentally observed [11]. To date, we have investigated its physical properties at 1.55 μm, including the gain coefficient [11], threshold power [11], Brillouin frequency shift (BFS) [11], and the BFS dependences on strain [12,13] and temperature [12], proving its applicability to high-sensitivity temperature sensing [12] and large-strain sensing [13]. Meanwhile, one serious demerit of PFGI-POFs in Brillouin sensing applications is that the Brillouin Stokes power is relatively low because of their large core diameters (50–120 μm) [11]. The Stokes power in PFGI-POFs should be enhanced to implement the sensors with a high signal-to-noise ratio [14].

One simple method for enhancing the Stokes power in PFGI-POFs is to increase the incident light power, the maximal limit of which is, however, much lower than that of silica SMFs. This is because the threshold power of optical fiber fuse in PFGI-POFs is relatively low [15]. Another method is to induce stimulated Brillouin scattering using a pump-probe technique [16], which is suitable for two-end-access sensing systems [2,3,17] but cannot be directly employed in single-end-access systems [4,5,18]. Combined use of pulsed pump light and a low-power optical amplifier is also known to be an effective method for enhancing the Stokes power [19], but it is not compatible with continuous wave (CW)-based sensing systems [3–5,18]. Thus, to enhance the Stokes power in CW-based one-end-access sensing systems, such as Brillouin optical correlation-domain reflectometry [4,5,18], yet another method is desirable. For this purpose, here we focus on the use of long tapered PFGI-POFs, which can enhance the Stokes power (generated at the tapered section), because the optical power density at the core center grows higher [20].

To date, many kinds of tapering techniques have been demonstrated [21–28]. Among them, what we call a heat-and-pull technique has been most widely used to taper optical fibers, including glass fibers [21–23], PMMA-POFs [24,25], and PFGI-POFs [20,26,27]. Many kinds of heat sources have been used for heating

fibers, including flame [20,21], a CO2 laser,30) a compact furnace [24–26], a fusion splicer [23], and a solder gun [27], but these are sometimes not easy to handle, prepare, or control. To overcome this inconvenience in tapering POFs, hot water appears to be a good candidate as a heat source, because the glass-transition temperature of POFs is relatively low (~100°C) [29]. Besides, as the heat is applied to the POFs almost uniformly (both radially and longitudinally) in hot water, its higher controllability might facilitate the fabrication of long tapered POFs. However, no papers regarding the tapering POFs using hot water have been published yet.

In this paper, as a pilot trial, we demonstrate the heat-and-pull fabrication of PFGI-POF tapers using hot water as a heat source. In experiment, a ~380-mm-long PFGI-POF taper with ~150-mm-long

Fig. 1. Schematic of the POF tapering setup using hot water.

waist is successfully fabricated. The waist has an almost uniform outer diameter of ~230 μm, and this geometry agrees well with the theoretical prediction. During fabrication, the optical propagation loss is measured as a function of strain applied to the waist. It exhibits an interesting behavior containing three regimes, the origins of which are experimentally investigated.

2. Experimental setup

The PFGI-POFs (Fontex, Asahi Glass) tapered in this experiment have a three-layered structure: core (diameter: 50 μm; refractive index: ~1.36), cladding (diameter: 70 μm), and overcladding (diameter: 490 μm). The core and cladding consist of doped and undoped CYTOP, respectively, the water absorption of which is negligibly small [30], and the overcladding is composed of polycarbonate. The optical propagation loss is relatively low (~0.25 dB/m) even at 1.55 μm. The length of the PFGI-POF samples was 800 mm.

The experimental setup is depicted in Fig. 1. The output of a semiconductor laser at 1550 nm (power: 10 dBm) was injected into one end of a PFGI-POF via a silica SMF (butt-coupled) [11], and the transmitted light was directly guided to an optical power meter. The room temperature was 18°C. First, a 150-mm-long section around the midpoint of the PFGI-POF was immersed into hot water (maintained at 97°C) in a round vessel (diameter: 300 mm), and the temporal variation in the transmitted power was monitored until the power became almost constant. Subsequently, the PFGI-POF was pulled (or in other words, strained) in both directions via pulleys (diameter: 95 mm) at a rate of 0.50 mm/s (0.25 mm/s for each direction) until the PFGI-POF was completely cut. The transmitted power was also monitored during the pulling process. The same experiments were performed using other PFGI-POF samples with different pulling periods (pulling stopped before the samples were cut), and the tapered sections were observed using an optical microscope.

3. Experimental results

Figure 2 shows the temporal variation in the total optical loss after the 150-mm-long section of the PFGI-POF was immersed into hot water. The loss increased with time (probably caused by thermal shrinkage) [31], and approximately 80 min later, it became almost constant at ~3.6 dB.

Figure 3 shows the optical loss plotted as a function of the strain applied to the taper waist ε, which can be calculated as follows. Under the assumption that the volume of a fiber is maintained before and after the tapering process, it follows by simple calculation that the strain at the taper waist ε is given by

$$\varepsilon = e^{D/L_w} - 1, \qquad (1)$$

where D is the total pulled length in both directions, and L_w is the length of the fiber section immersed into hot water (150 mm in this experiment). As seen in Fig. 3, the loss remained unchanged for strains of less than ~100%. For larger strains of up to ~400%, the loss
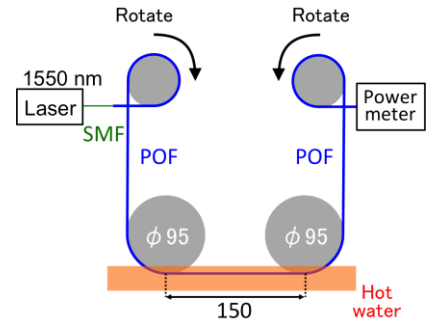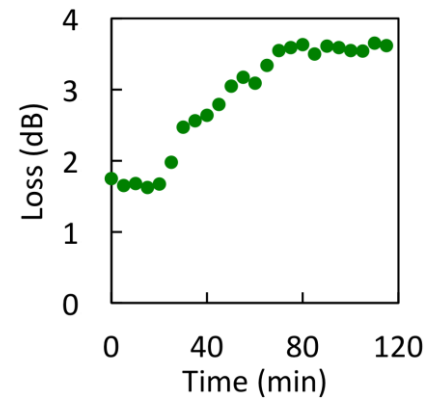
Fig. 2. Temporal variation in the propagation loss after the POF was partially immersed into hot water.

increased with a coefficient of ~0.010 dB/%. For even larger strains, the loss increased drastically with a coefficient of ~0.048 dB/%, and the PFGI-POF was completely cut at its midpoint when the strain reached ~560%. Thus, the loss dependence on the strain exhibited three regimes, the origin of which is discussed in the following paragraph.

Another PFGI-POF sample was tapered in the same manner, and when the strain was 360%, it was removed from the hot water. The loss was 7.2 dB. Figures 4(a) and 4(b) show the micrographs of the untapered section and the taper waist, respectively. In Fig. 4(a), the core and cladding (their boundary is not visible) as well as the overcladding were transparent, whereas in Fig. 4(b), the core and cladding showed white turbidity caused by a phenomenon called crazing (i.e., stress concentration forms nanoscale voids in the polymer, by which light is scattered, resulting in whitening) [32]. The distribution of the outer diameter along the length measured with a microscope is shown in Fig. 5. A ~380-mm-long section was tapered, and the outer diameter of the ~150-mm-long waist around its midpoint was approximately 230 μm, which was relatively uniform with a standard deviation of ~4 μm. This shape is in good agreement with the theoretical trend indicated by a solid curve (calculated using Eq. (1); theoretical outer diameter of the waist: 233 μm). The sections that were not immersed into hot water at all should be non-tapered, but actually, they were slightly tapered, because the vapor from the hot water served as a heat source. This could be mitigated by thermally shielding part of the PFGI-POF. Subsequently, yet another PFGI-POF sample was also tapered at 500% strain. The micrograph of the midpoint of the waist is shown in Fig. 4(c). The turbid core and cladding were cut, and only the overcladding maintained the fiber shape. Based on the aforementioned experimental observations, we can infer the origins of the three regimes of the loss dependence on strain. Namely, the change at ~100% strain corresponds to the start of white turbidity of the core and cladding, that at ~400% strain to the breakage of the turbid core and cladding, and that at ~560% strain to the breakage of the overcladding.

Fig. 3. Propagation loss of the tapered POF plotted as a function of the strain applied to the waist.
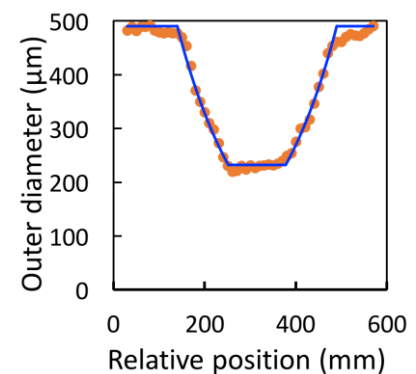
Fig. 5. Outer diameter distribution of the tapered POF (strain: 360%). The solid curve is a theoretical trend.

Finally, we discuss the length of the PFGI-POF tapers fabricated by this technique. As mentioned above, longer PFGI-POF tapers are desirable for Brillouin sensing applications. If the PFGI-POFs are pulled equally in both directions, the resultant tapered length is determined by the initial length of the PFGI-POF section immersed into hot water. Therefore, if a larger (or longer) vessel is used, longer PFGI-POF tapers can be easily fabricated. Even when the size of the vessel is fixed, we expect that much longer PFGI-POF tapers can be obtained if we give a new twist to the pulling structure. For instance, if one end of the PFGI-POF is pulled

| (a) | (b) | (c) |

Fig. 4. Micrographs of the tapered POFs; (a) untapered section, (b) waist (strain: 360%), and (c) waist (strain: 500%).

at 0.75 mm/s and the other end is pushed at 0.25 mm/s, the PFGI-POF is actually pulled at a rate of 0.50 mm/s while the pulled section is scanned along the PFGI-POF. This scheme may result in an extremely long PFGI-POF taper with high uniformity, on which point further study is required.

4. Conclusion

We performed a pilot trial of taper fabrication for PFGI-POFs using hot water. We experimentally fabricated a ~380-mm-long PFGI-POF taper with a ~150-mm-long waist, the outer diameter of which was uniform (~230 μm). The geometry was in good agreement with the theory. The optical loss had an interesting dependence on the strain applied to the waist, containing three regimes, the mechanism of which was elucidated by microscopic observations. Besides, we discussed the method of elongating the PFGI-POF tapers. Compared with other tapering techniques, our technique using hot water potentially has the advantages of ease of handling, cost efficiency, safety (no chemicals used), and high controllability of the length; thus, we believe long PFGI-POF tapers fabricated using our technique will be a powerful tool for enhancing the signal-to-noise ratio of POF-based distributed Brillouin sensors in future.

5. References

[1]   G. P. Agrawal, *Nonlinear Fiber Optics* (Academic Press, California, 1995).
[2]   T. Horiguchi and M. Tateda, J. Lightwave Technol. **7**, 1170 (1989).
[3]   D. Garus, K. Krebber, F. Schliep, and T. Gogolla, Opt. Lett. **21**, 1402 (1996).
[4]   Y. Mizuno, W. Zou, Z. He, and K. Hotate, Opt. Express **16**, 12148 (2008).
[5]   Y. Mizuno, W. Zou, Z. He, and K. Hotate, J. Lightwave Technol. **28**, 3300 (2010).
[6]   K. S. Abedin, Opt. Express **13**, 10266 (2005).
[7]   Y. Mizuno, N. Hayashi, and K. Nakamura, J. Appl. Phys. **112**, 043109 (2012).
[8]   H. Ujihara, N. Hayashi, M. Tabaru, Y. Mizuno, and K. Nakamura, IEICE Electron. Express **11**, 20140707 (2014).
[9]   M. G. Kuzyk, *Polymer Fiber Optics: Materials, Physics, and Applications* (CRC Press, Boca Raton, 2006).
[10]   Y. Koike and M. Asai, NPG Asia Mater. **1**, 22 (2009).
[11]   Y. Mizuno and K. Nakamura, Appl. Phys. Lett. **97**, 021103 (2010).
[12]   Y. Mizuno and K. Nakamura, Opt. Lett. **35**, 3985 (2010).
[13]   N. Hayashi, Y. Mizuno, and K. Nakamura, Opt. Express **20**, 21101 (2012).
[14]   N. Hayashi, Y. Mizuno, and K. Nakamura, J. Lightwave Technol. **32**, 3397 (2014).
[15]   Y. Mizuno, N. Hayashi, H. Tanaka, K. Nakamura, and S. Todoroki, Sci. Rep. **4**, 4800 (2014).
[16]   Y. Mizuno, M. Kishi, K. Hotate, T. Ishigure, and K. Nakamura, Opt. Lett. **36**, 2378 (2011).
[17]   D. Zhou, Y. Dong, B. Wang, T. Jiang, D. Ba, P. Xu, H. Zhang, Z. Lu, and H. Li, Opt. Express **25**, 1889 (2017).
[18]   Y. Mizuno, N. Hayashi, H. Fukuda, K. Y. Song, and K. Nakamura, Light: Sci. Appl. **5**, e16184 (2016).
[19]   Y. Mizuno and K. Nakamura, Appl. Phys. Express **5**, 032501 (2012).
[20]   N. Hayashi, H. Fukuda, Y. Mizuno, and K. Nakamura, J. Appl. Phys. **115**, 173108 (2014).
[21]   J. C. Knight, G. Cheung, F. Jacques, and T. A. Birks, Opt. Lett. **22**, 1129 (1997).
[22]   T. E. Dimmick, G. Kakarantzas, T. A. Birks, and P. St. J. Russell, Appl. Opt. **38**, 6845 (1999).
[23]   F. Lissillour, D. Messager, G. Stéphan, and P. Féron, Opt. Lett. **26**, 1051 (2001).
[24]   Y. Jeong, S. Bae, and K. Oh, Curr. Appl. Phys. **9**, e273 (2009).
[25]   D. J. Feng, G. X. Liu, X. L. Liu, M. S. Jiang, and Q. M. Mei, Appl. Opt. **53**, 2007 (2014).
[26]   R. Gravina, G. Testa, and R. Bernini, Sensors **9**, 10423 (2009).
[27]   A. A. Jasim, N. Hayashi, S. W. Harun, H. Ahmad, R. Penny, Y. Mizuno and K. Nakamura, Sens. Actuat. A, Phys. **219**, 94 (2014).
[28]   H. Ujihara, N. Hayashi, K. Minakawa, Y. Mizuno, and K. Nakamura, Appl. Phys. Express **8**, 072501 (2015).
[29]   K. Koike, H. Teng, Y. Koike, and Y. Okamoto, Polym. Adv. Technol. **25**, 204 (2014).
[30]   S. Ando, T. Matsuura, and S. Sasaki, Chemtech **24**, 20 (1994).
[31]   V. A. Beloshenko, Y. E. Beygelzimer, and V. N. Varyukhin Polymer **41**, 3837 (2000).
[32]   Z. M. Xiao, M. K. Lim, and K. M. Liew, J. Mater. Process. Technol. **48**, 437 (1995).

Self-healing silicone rubber for fluorescent partial discharge POF sensors in high-voltage cable accessories

L. Barnefske[1]*, V. Wachtendorf[1]

[1]Bundesanstalt für Materialforschung und -prüfung (BAM), Unter den Eichen 87, 12205 Berlin
*Corresponding author: lena.barnefske@bam.de

Abstract: To avoid a catastrophic failure of insulation in high-voltage (HV) applications, a monitoring of partial discharges (PDs) is necessary. Fluorescently labelled polymer optical fibers (F-POF) offer an electrically passive method for PD detection in HV facilities. F-POFs could be embedded in HV cable accessories, which are usually made of silicone rubber. Herein they detect the light emitted by the PD and convert it into an electrical signal that can be monitored. Due to the difficult accessibility of HV cable accessories, a self-healing silicone rubber with prolonged service life after PD detection represents an attractive material design for HV accessories. With this contribution, we would like to present and discuss the possibilities of combining self-healing materials with POF-based sensors for PD detection in HV applications.

Key words: Fluorescent polymer optical fibres, partial discharge detection, high voltage cable accessories, self-healing, silicone rubber

1. Introduction

In 1976 silicone rubber was introduced as an electrical insulator used in high-voltage (HV) applications [1]. Today, silicone rubber is mainly used as weather shielding in composite insulators and in cables for cable joints or terminations. It offers a lot of advantages compared to previously used insulators like ceramic or glass. For example, the light weight of the material gave the opportunity for changes in construction and installation. Other advantageous aspects are the resistance against vandalism and of course the outstanding hydrophobicity of silicone rubber [2,3]. Nevertheless, these materials suffer from electrical discharges caused either by voids inside the material or by a loss of hydrophobicity on the surface of the insulation due to environmental contamination. Electrical treeing or dry band arcing could further damage the insulator until breakdown. Here the damage is mainly driven by thermally induced decomposition of the silicone rubber [4].

Fluorescently labelled polymer optical fibres (F-POF) were investigated as sensors for detection of partial discharges (PD) [5]. PD are initially small sparks causing an electrical charge generation and emission of an acoustic and light wave [6]. F-POF are able to detect the light transmitted from PD independent of the incident angle. The fluorophore in the outer part of the fibre absorbs this light and emits a spectrally-shifted fluorescent signal that is guided through the fibre core to a remote detector. This approach offers a lot of advantages compared to electromagnetic detection methods. Among others, the most outstanding one is that POF sensors are based on a non-electrical functional principle which does not require electrical power supply and they are immune to electromagnetic interference. The first utilization of F-POF for detection of PD in silicone rubber in HV was proposed in 2011 [7]. The authors state the requirements for the material design according to POF and polymeric matrix. Firstly, the fluorescent fibre should be made out of silicone rubber in order to fit the electrical and mechanical properties of the insulation material and avoid heterogeneities. The development of such silicone fibres was presented in 2015 [8]. Further research in the field of F-POF sensors for PD detection gave promising results for adoption of the sensors in the field of HV accessories [9,10]. Secondly, for a highly efficient transmission of PD optical signal to the detection fibre, the silicone matrix of the insulation material should be optically transparent. Usually however, in silicone rubber, high amounts of fillers such as silica or aluminium trihydrate are used to achieve the required mechanical and electrical properties. Therefore, the material is often optically opaque [3].

Since HV cable accessories are often not easily accessible, it would be cost and time consuming to exchange the insulator after PD detection with a F-POF sensor. Self-healing materials aim to heal a crack automatically after a damage had occurred usually with the aim to prolong the service life of the materials by maintaining a

specific performance above the level of reliability. During the last decades, a lot of research has been performed on self-healing composite materials based on incorporation of capsules with an extrinsic healing agent. However, the materials are typically thermoset polymers, whose elastic moduli differ strongly from rubber materials such as silicone rubber [11], and are often inappropriate for HV outdoor applications. In 2014 the group of Glomm introduced the first results on the concept of self-healing electrical insulation material [12]. The presented system consisted of a thermoset epoxy matrix with integrated capsules made of a dicyclopentadiene (DCPD) core and an urea-formaldehyde shell. The size of these capsules was of about 250 µm in diameter. This research showed that the damage caused by electrical discharge shows parallels to mechanical damage. Capsules were ruptured by the electrical tree path ways herein. Nevertheless, this system exhibited a lot of inhomogeneities due to the composition of the composite material and the size of the capsules.

Our idea is to develop a smart material that would allow using F-POF as a PD sensor, and at the same time is able to trigger a self-healing reaction as an answer to the degradation caused by PD.

2. Material design

The material design is shown in figure 1 and consist of a silicone rubber matrix into which poly(dimethylsiloxane)-poly(organosiloxane) (PDMS-POS) core-shell system as a filler component is integrated. The silicone rubber matrix (SIR) is a two-component system consisting of a high molecular weight vinyl-functionalized PDMS and a cross linking hydrido-functionalized PDMS-copolymer as well as a platinum catalyst. The vinyl- and hydrido-functionalized PDMS components cure by a hydrosilanization reaction which starts already at room temperature, but can be accelerated at higher temperatures. Capsules consist of a liquid functionalized PDMS core, either vinyl- or hydrido-functionalized PDMS, and a solid shell made of poly(organosiloxane) (POS).
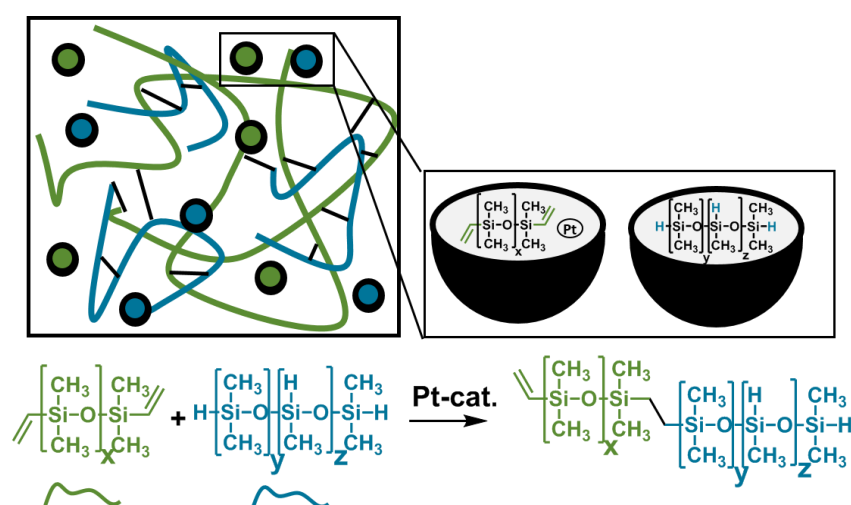
Fig. 1: Material design of the self-healing silicone rubber. Two-component silicone rubber matrix filled with two kinds of PDMS-POS capsules. In case the capsules are ruptured, platinum catalysed reaction takes place to heal the material.

Capsules were synthesized in a micro-emulsion polymerization based on the sol-gel procedure of methyl-trimethoxysilane, with sodium dodecylbenzesulfonic acid as surfactant and acidic catalyst. The size of capsules was determined by scanning electron microscopy and is around 1.2-1.5 µm. Core content of the capsules was determined by thermogravimetric analysis to be in the range of 15 to 30 wt-%, depending on the core material. Fluorescent optical dyes were used for verification of core-shell structure [13]. Hydrido-group content of cross linking PDMS was analysed before and after acidic treatment and showed a small decrease of around 25%, which ensures that enough hydrido-groups were still available [14].

Capsules were integrated into silicone rubber matrix by mixing with a high-speed disperser as well as by ultrasonic treatment to ensure a homogeneous dispersion of filler in the matrix. Uncured silicone rubber composite was poured into a glass mould. After removing the air bubbles under vacuum it was cured at a temperature of 100 °C for one hour. Further curing at room temperature took place overnight.

3. Results and discussion

To verify the influence of capsules on mechanical properties of our silicone rubber composite, we utilized tear testing on our samples with the same strain rate after initial notching. Figure 2 left shows an exemplary function of force over displacement. The slope of increasing force over displacement is higher for capsule-filled silicone rubber (SIR + 2 wt-% capsules) compared to unfilled (SIR) one, revealing the stiffness of the material. A view on the crack surface of the tear with an optical microscope reveals different crack profiles for materials without (SIR, fig. 2 middle) and with capsules (SIR + 2 wt-%, fig. 2 right). The capsules appear to hinder crack propagation, wherefore shorter cracks could be observed. These results are promising for further investigations of the self-healing ability with a higher capsule content and on the study of the rupture of the capsules by mechanical or electrical damage.
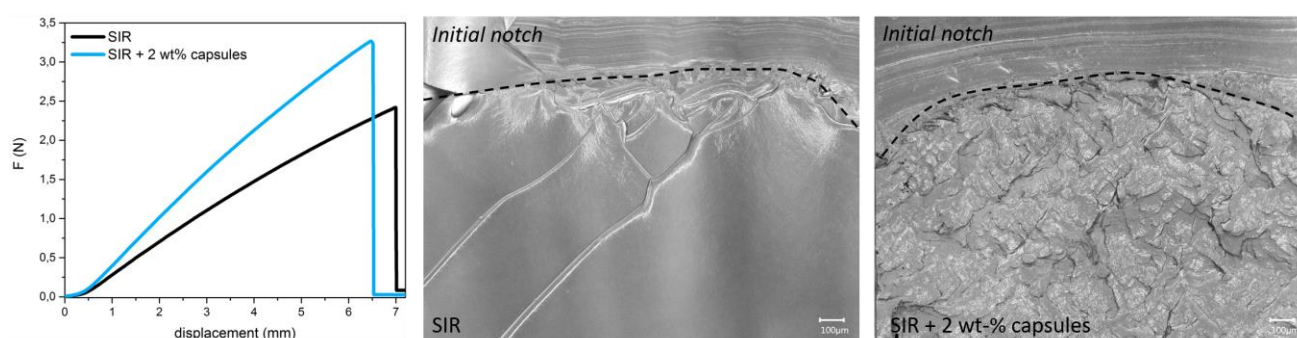
Fig. 2: Left: Force-displacement diagram form tear testing and images from an optical microscope. Middle and right: View on tear surfaces of the silicone rubber samples after tearing with the same strain rate are shown. On the top of the microscopic picture the initial notch (marked with dashed line) is indicated. Middle picture: sample without fillers (SIR) and right picture: sample with 2 wt-% of PDMS-POS capsules (SIR + 2 wt-% capsules).

For the implementation of F-POF as sensors of PD in HV insulation material, one critical aspect is the optical transparency of the material in the visible wave length range. As the composition of the matrix and capsules are based on the same chemical elements, the refractive index difference ought to be small, therefore minimizing scattering losses. Another aspect for optical transparency is the size of the filler. Usually capsule-based self-healing materials contain capsules in the size range of greater micrometre. We decided to synthesize smaller capsules of about 1-2 µm to keep a balance between self-healing ability, reinforcement and light scattering. We examined the optical transparency of our composite material over a wave length range from 200 nm to 850 nm with two different techniques. The results are shown in figure 3. The solid lines represent the measurements in a usual transmission holder and the dotted ones the data from the measurement with an integrating sphere. The integrating sphere collects all radiation transmitted by the sample independently of the angle (both scattered and directed radiation). On the opposite, a usual holder only collects a certain angle of radiation transmitted, which means that with increasing amount of scattered radiation the detector will be reached by less radiation. Results from the usual sample holder show a decrease of transparency down to 40% with decreasing wave length for filled silicone rubber (SIR + 2 wt-% capsules), a translucent material is obtained consequently. Unfilled silicone rubber (SIR) keeps high transparency above 80% up to 300 nm wave length. The data from integrating sphere show that loss of transparency of filled silicone rubber sample is mainly caused by the scattering of light by the filler. Increased scattering in the insulation material might decrease the efficiency of F-POF fluorescence generation, but should not disable the PD detection. Further

modification of the material is intended to decrease the size of the capsules and therefore decrease the amount of light scattering.
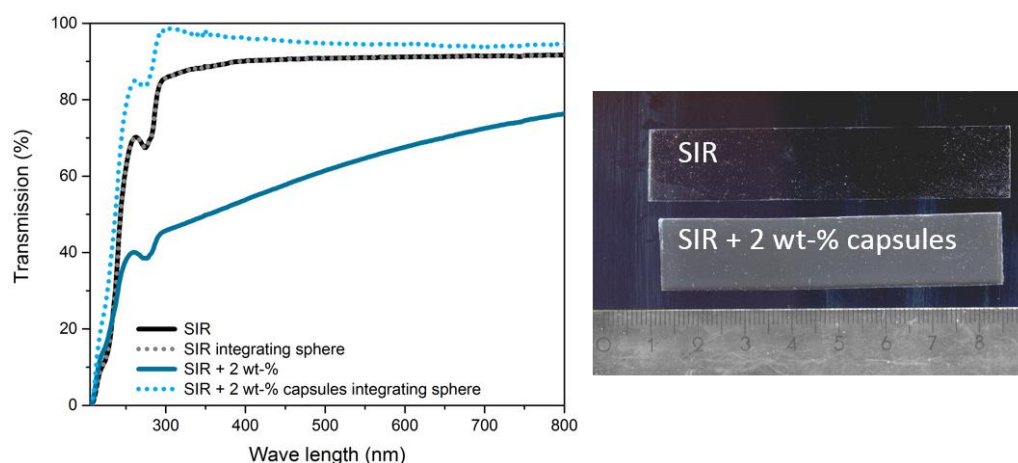
Fig. 3: Left: Optical characterization of pure and capsule-filled silicone rubber measured with and without integrating sphere. Right: Scanner photograph of the two tested silicone rubber samples in transmission.

4. Conclusion

With our contribution we introduced the fabrication of a silicone rubber composite with capsules for reinforcement and self-healing ability for potential application in high-voltage accessories. In this field F-POF sensors can be applied for PD detection. We discussed the material design for the use of F-POF sensors for PD detection with additional self-healing ability on damage. The material design aim to avoid heterogeneities and is therefore based on the same chemical elements. Our material showed mechanical improvement due to integration of capsules into the silicone rubber and prevent large crack sizes at tearing. Unfortunately, loss of optical transparency was observed. By measuring the optical transparency with two different techniques we showed that loss of transparency is caused by light scattering and not by light adsorption. Further investigations are necessary to accomplish requirements of F-POF sensors and to evaluate the reduction of the PD detection probability by our translucent material.

Acknowledgement

References

[1] H. Kärner, Konstruktiver Aufbau, Eigenschaften und Betriebsverhalten eines Kunststoff-Langstabisolators, ETZ-A 1970, 91 (7), 392-396

[2] J. F. Hall, History and bibliography of polymeric insulators for outdoor applications, IEEE Transactions on Power Delivery, 1993, 8 (1), 376-385

[3] R. Hackam, Outdoor HV composite polymeric insulators, IEEE Transactions on Dielectrics and Electrical Insulation, 6 (5) 1999, 557-585

[4] S.-H. Kim, E. A. Cherney, R. Hackam, K. G. Rutherford, Chemical changes at the surface of RTV silicone rubber coatings on insulators during dry-band arcing, IEEE Transactions on Dielectrics and Electrical Insulation, 1994, 1 (1), 106-123

[5] R. Mangeret, J. Farenc, Bui Ai, P. Destruel, D. Puertolas, Optical detection of partial discharges using fluorescent fiber, IEEE Transactions on Electrical Insulation, 1991, 26 (4), 783-789

[6] D. Siebler, C. Lothongkam, P. Rohwetter, W. Habel, G. Heidmann, Fluorescent fiber optical partial discharge sensors in high-voltage cable facilities, Proceedings 22nd International Conference on Plastic Optical Fibers, 11.-13.09.2013, Rio do Janeiro, Brazil, 322-327

[7] W. R. Habel, U. Buchholz, G. Heidmann, M. Hoehse, C. Lothongkam, Fibre-optic sensors for early damage detection in plastic insulations of high-voltage facilities, Proceedings XVII International Symposium on High Voltage Engineering, 22.-26.08.2011, Hannover, Germany

[8] M. Hohberg, D. Siebler, P. Rohwetter, Production process and characterization of sensitized all elastomeric POF, Proceedings 24th International Conference on Plastic Optical Fibers, 22-24.09.2015, Nuremberg, Germany, 91-94

[9] D. Siebler, P. Rohwetter, R. Brusenbach, C. Lothongkam, G. Heidmann, A. Leistner, R. Plath, Sensitivity-enhanced detection of partial discharge in cable accessories using fluorescent polymer optical fibre-sensor, Proceedings 23rd International Conference on Plastic Optical Fibers, 8.-10.10.2014, Hiyoshi, Yokohama

[10] D. Siebler, P. Rohwetter, G. Heidmann, A. Leistner, R. Plath, Proceedings VDE-Hochspannungstechnik, 14.-16.11.2016 in Berlin, Germany, 608-613

[11] V. K. Thakur, M. R. Kessler, Self-healing polymer nanocomposite materials: A review, Polymer 2015, 69, 369-383

[12] C. Lesaint, V. Risinggård, J. Hølto, H. H. Sæternes, Ø. Hestad, S. Hvidsten, W. R. Glomm, Self-healing high voltage electrical insulation materials, Proceedings Electrical Insulation Conference, 8.-11.06.2014 Philadelphia, Pennsylvania, USA

[13] L. Barnefske, S. Benemann, D. Siebler, H. Sturm, PDMS-POS-capsules for prospective self-healing silicone rubber, Proceedings 6th International Conference on self-healing materials, 25.-28.06.2017, Friedrichshafen, Germany

[14] L. Barnefske, D. Siebler, S. Benemann, H. Sturm, PDMS-POS capsules for prospective self-healing materials, Proceedings 5th International Conference on Multifunctional, Hybrid and Nanomaterials, 6.-10.03.2017 Lisbon, Portugal

Real-Time Two-Dimensional Pressure Sensing for Patient Monitoring based on Optical Coupling between Crossing Polymer Optical Fibres

Henrie van den Boom[1*], Sebastiaan Overeem[2,3], Federico Forni[1], Ton Koonen[1]

[1] Institute for Photonic Integration, IPI, Eindhoven University of Technology, The Netherlands
[2] Sleep Medicine Centre Kempenhaeghe, Heeze, The Netherlands
[3] Dept. of Electrical Engineering, Eindhoven University of Technology, The Netherlands

*Corresponding author: h.p.a.v.d.boom@tue.nl

Abstract: Position detection is a key function needed for monitoring patients with sleep-related movement disorders. Tools are urgently needed to obtain a detailed patient-friendly long-term assessment of sleep-related movements in the home situation. We present an optical two-dimensional pressure sensing system for real-time patient monitoring that is based on optical coupling between crossing polymer or plastic optical fibres (POFs) and can easily be placed under a mattress in a home environment. Because the system deploys a grid of standard 1 mm diameter Step Index PMMA POF, it is low-cost, robust, flexible, compact, waterproof, scalable, not affected by external electrical fields, nor does it generate any electrical fields. Moreover, an alternative simple pressure sensitive POF crossing construction, based on local fibre bending is presented, which is more sensitive and more robust than crossing fibres left intact.

1. Introduction

Sleep-related movement disorders form a spectrum of invalidating diseases, characterized by abnormal motor function during sleep. Tools are needed to obtain a detailed long-term assessment of sleep related movements in the home situation, in order to reach a precise clinical diagnosis, make an estimation of severity and to enable treatment follow-up. In our POF conference 2016 invited paper "Robust Two-Dimensional Pressure Sensing Mattress based on Optical Coupling between Crossing Polymer Optical Fibres", we proposed a position-sensing method based on sensing local pressures exerted on a surface, equipped with a two-dimensional (2D) structure of polymer or plastic optical fibres, and experimental results of a single crosspoint using PMMA Graded Index Plastic Optical Fibre (GI-POF) in combination with a semiconductor laser were reported [1].

In this paper, novel experimental results using standard PMMA Step Index Plastic Optical Fibre (SI-POF) [2-3] in combination with low-cost LEDs devised for lighting are presented. Because the SI-POF yields less cross-fibre signal coupling in the crosspoints, a modified construction at the crossings of the fibres has been applied. Moreover, using LEDs instead of lasers, makes the system more robust and lower-cost.

First a description of the system, followed by experimental results of a single crosspoint are given. As a proof-of-concept, a setup and a measured 2D pressure profile of a person lying on a mattress are presented. Moreover, a real-time system has been realized and described. Finally, a modified simple pressure-sensitive POF crossing construction is presented using rigid rings, which results in local fibre bending at the crossings when pressure is applied. The advantage of this solution is that the fibres can be left intact, so a 2D POF structure can be produced more easily.

2. System description

Figure 1, shows the principle of operation of the real-time 2D pressure sensing system based on monitoring the local pressure exerted per crosspoint on a 2D structure embedded in a 2D surface, such as a mattress. The system consists of a 2D sensing module, an Optoelectronics module and a Data Acquisition and Control module. The 2D sensing module is composed of a grid of SI-POFs which form a matrix of crosspoints. The so-called transmitting fibres of the POF grid are connected to LEDs and the receiving fibres to photodiodes of the Optoelectronics module. The Data Acquisition and Control module controls the LEDs and processes the measured data from the Optoelectronics module. The optical coupling between the POFs at the crosspoints is a function of the local pressure, so by detecting the optical power received by the photodiodes, the pressure on a crosspoint can be measured. Because the optical coupling effect between transmitting and receiving SI-POF fibres is very small, high-sensitivity optical receivers are needed, using transimpedance amplifiers (TIAs) with high gain and a high input impedance. Sensitivity is increased further by modulating each optical source with a

low frequency carrier and applying highly-selective synchronous or lock-in detection, executed by multiplying the received amplified signal with the same carrier signal driving the LEDs and low-pass filtering the output.
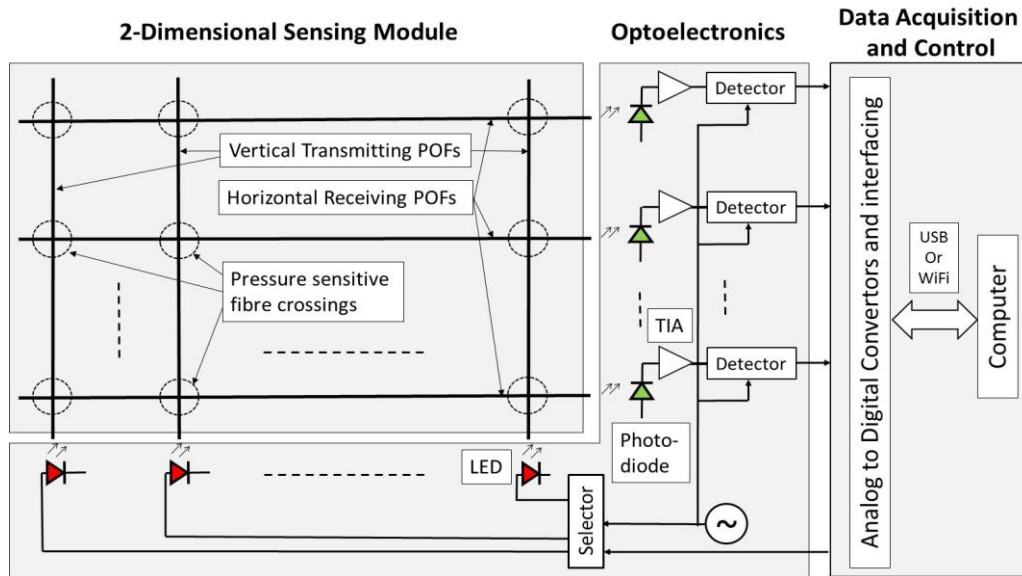
Figure 1. 2D position sensing system deploying a matrix of step index plastic optical fibre (SI-POF) crosspoints.

To achieve a simple and scalable system, a crosspoint scanning method is implemented. The Data Acquisition and Control module in figure 1 controls the Selector, which selects only one LED at a time, and the crossings are scanned column by column. Reading simultaneously the detector outputs line-by-line enables the Data Acquisition and Control module to do the 2D pressure detection. This solution is readily scalable because N photo detectors plus M LED sources can detect $N \times M$ sensor points.

3. Experiments with locally removed cladding crossings

A typical standard Step Index POF (SI-POF) consists of a core with a diameter of 0.98mm surrounded by a cladding with a diameter of 1mm and is made of a polymer, typically PMMA (poly-methyl metacrylate) which is transparent for light in the visible spectrum (400-700nm) [2-3]. The light is guided through the POF in its core, in which the light is confined by reflection at the core-cladding boundary. The refractive index of the core of a SI-POF is uniform across the whole core. A jacket or protective coating surrounds the cladding and protects the core-cladding structure against external influences.

A possible practical implementation of a single pressure sensitive SI-POF crosspoint is shown in figure 2. It is composed by two fibres crossing each other at an angle of 90 degrees. Light is injected in the transmitting fibre and guided within the core of the fibre. The jacket or protective coating of the transmitting fibre is removed locally at the crossing, see figure 2a. Moreover, a small area of the cladding

Figure 2. Pressure sensitive SI-POF crosspoint.

of the transmitting fibre is also removed so a small percentage (< 0.1%) of the light in the core can escape. Because of this small percentage, the optical power in the transmitting fibre is nearly constant over the whole length of the fibre (which is less than a few meters). At the crossing, the jacket or protective coating of the receiving fibre is removed over a few centimetres and replaced by an elastic scattering non-absorbing primary

coating, see figure 2b, and is positioned such that the elastic scattering primary coating of the receiving fibre can make physical contact to the core/cladding of the transmitting fibre at a fixed position, see figure 2c. By applying pressure at the crossing some light of the transmitting fibre, which is coupled in the elastic scattering primary coating of the receiving fibre, may then be transmitted via the cladding into the core of that receiving fibre. In order to further enhance the coupling of light which has escaped from the transmission fibre into the receiving fibre, a reflective structure (such as a reflective aluminium foil) is added locally at the crosspoint, as shown in figure 2b and 2c. Thus in a single crosspoint which is only about 3mm thick, some light gets from the transmitting fibre into the receiving fibre. The amount of this transitioning light depends upon the force exerted onto the crosspoint.

The characteristics of a single crosspoint have been measured by loading the crosspoint with an external weight. A simple visible white light LED with an output power coupled into the SI-POF of about 3 mW is modulated with a square wave signal with a frequency of 1 kHz. At the receiver side, the current of a silicon photodiode is amplified with a transimpedance amplifier with a feedback resistor of 50 Mohm. The combination of an analog switch and a differential amplifier performs the synchronous detection operation. After low-pass filtering, the DC detector output voltage is measured with a multimeter. Figure 3 shows the measured output voltage as a function of the applied weight, without and with reflective aluminium foil. A weight of 100g can already be detected. This measured signal shows a clear and nearly linear relation to the weight pressure on the crosspoint. No significant influence of weight pressure of neighbouring crosspoints is observed.

A proof-of-principle setup has been realized to measure a 2D pressure profile of a person lying on a mattress, see figure 4, in which scanning (i.e. the switching of the receiving fibres to a single photodiode) is done by hand. The sensor grid consists of 8 transmitting and 8 receiving SI-POFs, so the grid consists of 64 crossings. The pressure profile from shoulder to hip of the person in figure 4 is clearly visible.

Next, a real-time 2D profile measurement set-up has been realised using a National Instruments MyRIO controller device [4] as the interface between optical receiver outputs and selector of the optoelectronics, see figure 1, and computer. With this MyRIO controller, 8 profiles per second can be real-time visualised on an external computer or stored on a USB stick directly connected to the MyRIO for analysis afterwards. Because of the small amount of data needed for one profile, very long time periods can be stored efficiently on a USB stick with limited capacity.
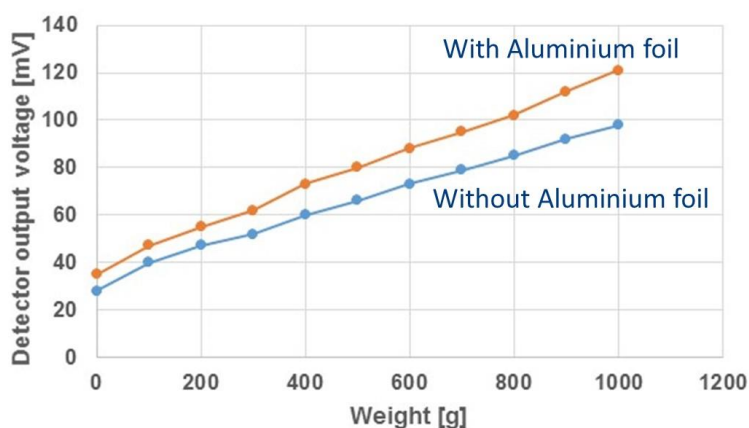
Figure 3. Detector output voltage, versus exerted pressure on the crosspoint.

Figure 4. Pressure profile of a person lying on a mattress with an 8 x 8 POF grid underneath.

4. Experiments with bending based crossing

Bending optical fibres can introduce losses because of light that escapes [2]. Bending a waveguide with a sufficiently small bend radius, will slightly disrupt the confinement of the light in the core of a transmitting fibre so a small fraction of the light will leak through the cladding. The light that escapes can be captured in a crossing fibre. Bending enhances both light emitted from a transmitting waveguide and the ability of a receiving waveguide to couple incident light into its core. So locally bending of crossing optical fibres when pressure or force is exerted, can result in optical coupling between the two crossing fibres, which is proportional to this exerted pressure or force.

Figure 5. Crossing fibres having two rigid rings to enhance bending under pressure.
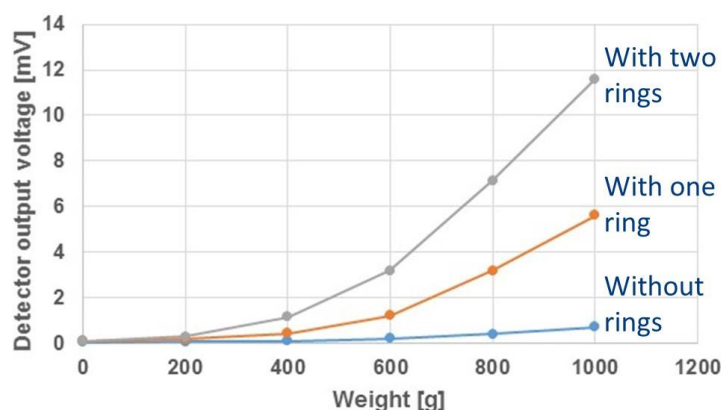
Figure 6. Detector output voltage, versus exerted pressure on the crosspoint without and with one or two rings.

Here, the application of simple rigid rings at a crossing is proposed, which realizes bending of the fibres when pressure is exerted. Figure 5 shows a top- and side-view of a POF crossing sensor having rigid rings to enhance waveguide bending under pressure. Inside the hole of the rings, the fibres will bend when pressure is applied on the rings, and optical cross coupling is mainly due to bending of the transmitting and/or receiving waveguides in this case. This construction is easy to produce, because when bare fibres are used, the fibres can be left intact and alignment is not critical. The crossing is still very robust. In figure 6 measurement results are shown, of a SI-POF fibre crossing without and with one or two rigid rings using the measurement setup described in section 3. The rings have an inside hole diameter of 8.5mm and an outside diameter of 50mm. These measurement results clearly show the enhancement of the optical coupling of the crossing POFs. Moreover, the linearity of these transfer characteristics can be improved by some signal processing done in software.

Conclusion

An optical method to perform two-dimensional location sensing, based on the pressure-sensing function realized by measuring the changes in optical characteristics of a two-dimensional structure composed of slightly deformable crosspoints made of step index plastic optical fibre has been described and experimentally verified. Because of the use of plastic optical fibre, this sensing method is robust, flexible, scalable, waterproof, is not affected by external electrical fields, nor does it generate any electrical fields itself, and is only a few mm thick so can e.g. easily be put under (or integrated inside) a mattress. The method is also low-cost because readily available optical and electrical components can be used like LEDs for lighting and silicon photodiodes, and only low-frequency components are needed. Measurements of a single crosspoint show a sensitive and nearly linear pressure detection characteristic. Two-dimensional pressure profile measurement results of a person lying on a mattress clearly show his position. Using a National Instruments MyRIO controller device, a real-time two-dimensional profile measurement setup has been realised, visualising and storing 8 pressure profiles per second. An alternative simple, robust and easy to produce POF crosspoint principle based on fibre bending is described and experimental results with rigid rings are given.

The two-dimensional pressure sensing principle based on optical coupling between crossing fibres, can be used for many other applications; for instance it can be used under (or woven into) a carpet or under a PVC floor to detect walking and falling of (elderly) persons, which is much more privacy-friendly than using video cameras.

References

[1] Henrie van den Boom et al., "Robust Two-Dimensional Pressure Sensing Mattress based on Optical Coupling between Crossing Polymer Optical Fibres", Proc. 25th International Conference on Plastic Optical Fibres (POF2016), Sep. 13-15, 2016, Birmingham, United Kingdom.
[2] Olaf Ziemann et al, POF Handbook, Springer, 2008.
[3] http://www.fiberfin.com/index.php/products/security.html
[4] http://www.ni.com/nl-nl/shop/select/myrio-student-embedded-device

Effects of Localized Pressure in POFs

J. Learte[1], M.A. Losada[1*], A. Lopez[1], J. Mateo[1], J. Zubia[2]

1 GTF, Aragón Institute of Engineering Research (i3A), Department of Electronic Engineering, University of Zaragoza, María de Luna 1, E-50018 Zaragoza, Spain.
2 Departamento de Ingeniería de Comunicaciones, ETSI/Universidad del País Vasco, Euskal-Herriko Unibertsitatea, Alameda de Urquijo S/N, Bilbao 48013, Spain.

*Corresponding author: alosada@unizar.es

Abstract: In this work, we tested the impact of localized pressure over plastic optical fibers of 1-mm core diameter and high numerical aperture. We designed a set-up to apply a localized force over the fiber mimicking the effects of a staple or a similar fastening system while monitoring the exerted pressure using a force sensor. Thus, we measured power loss versus pressure for fibers of two different index profiles. In addition, we calculated a matrix to characterize the effects of pressure on the fiber optical power distribution.

1. Introduction

One of the advantages of POFs is their ease of installation that makes them a suitable candidate for a do-it-yourself domestic network where the user decides the particular layout adapted to his/her needs. In this environment, it is necessary to bend the fiber around nooks and corners and to hold it against the wall or inside a preexistent conduit using hooks, pegs or staples that can exert a strong continuous pressure over small sections of the fiber at different positions of the link. Although most POFs are provided with flexible jackets with good mechanical resistance that can sustain tensile forces, torsion and impacts with relative low loss compliant with international standards [1,2], these tests are defined under conditions that do not resemble those occurring when installing the fibers inside a house with realistic configurations and by untrained agents.

Thus, our aim is to characterize the effects of pressure over POFs using a set-up designed to apply a controlled force over a small fiber section reproducing the effects of a staple or another fastening system. We have tested Polymethyl-methacrylate (PMMA) fibers with 1-mm diameter core, 0.5 numerical aperture and two different index profiles: step-index (SI-POF) and graded index (GI-POF). Apart from power loss, it is reasonable to expect that pressure will induce substantial power transfer among modes that will change the fiber power distribution. These changes have been quantified by comparing the fiber output Far Field Pattern (FFP) with and without pressure that were measured changing the input angle. In addition, these FFP scans were used to obtain the pressure characteristic matrix using an empirical method previously developed and applied to other localized disturbances such as a scrambler, different types of connectors, and small radius curvatures [3-5]. These matrices can be integrated into simulation frameworks to provide the impact of the disturbances on network performance, independently on their position in the link [6].

2. Optical power loss versus pressure

We have designed a device to apply an intense force over a small section of the fiber (15 mm^2) that resembles the pressure exerted over the fiber when fixing it onto a plane surface such as a wall. The amount of pressure is monitored using a 400 Series Force Sensing Resistor from Interlink Electronics that was previously calibrated to obtain the correspondence between the applied force and the measured resistance. This sensor is placed onto a flat metallic platform (a) below a void cylinder (b) as shows the left picture in Figure 1. A metallic piece (c) is designed to fit this hole and to transmit the force to the sensor while presenting an upper circular base where the fiber is placed. The fiber is held using a rectangular plaque (d) that is fixed to the circular surface using two screws. The position of these screws serves to control the applied force as shows the picture on the right. When the screws are turned, the pressure exerted over the fiber is transmitted through the system and the induced resistance is measured.

Using this device, optical power loss versus pressure has been measured for two 1-mm core PMMA fibers with 0.5 NA: a step-index fiber GH4001 from Mitsubishi (GH) and a graded-index fiber OM-GIGA from Optimedia (GI). For this purpose, a 660-nm LED source and a power-meter from FOTEC both with VersaLink

connectors were used. The measurement protocol was the following: first, the power transmitted by a 1.25-meter segment of the fiber was measured to serve as a reference. Then, a variable force was applied at 20 cm from the fiber output end while measuring power loss. This experiment was repeated for three different segments of each of the tested fibers.
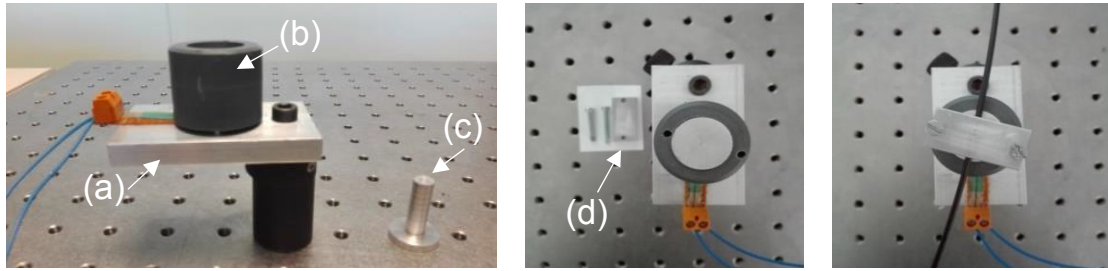
Figure 1. Sensor onto a flat metallic platform (a) below a void cylinder (b). Metallic piece (c) designed to fit this hole and to transmit the force to the sensor. The fiber is held using a rectangular plaque (d) fixed using two screws.

Figure 2 shows the results of power loss versus pressure for the GH fiber on the left and for the GI-POF on the right. Circles in different colors show measurements using different specimens of the fibers. The black line is a polynomial fit to the average of these data. The graphs reveal that the SI-POF is more resistant to pressure as it has hardly any power loss for pressure values below 3.5 N/mm^2. Above this threshold, however, loss raises very steeply. Pressure losses for the GI-POF start at lower values, over 2.75 N/mm^2, than for the SI-POF but, although the rise is shallower, losses are higher above 4 N/mm2. The higher variability observed in the GI-POF measurements can be justified by the fact that the fiber segments used were taken from different reels. Our data suggest that index profile is an important factor to determine the behavior of the fiber under pressure.
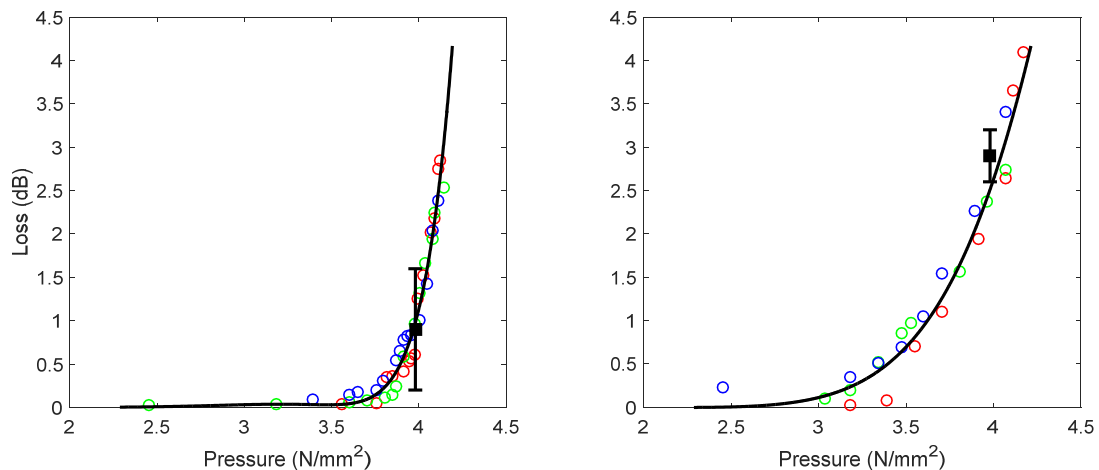
Figure 2. Power loss versus applied pressure for step-index (left) and graded-index (right) POFs.

In addition, the error bar shown at 4 N/mm^2 in the plots represents the loss mean and standard deviation as obtained when modeling the effect of this pressure value over the optical power distribution for both fiber types, as will be explained in Section 4.

3. Comparison of FFPs with and without pressure

To analyze the causes underlying the dependence of attenuation with pressure for different index profiles, we measured the fibers FFPs which are the projection of their output power distributions and provide a good description of their modal distributions. Thus, we recorded the FFPs for a 1.25 m fiber segment first without pressure as a reference and then, while applying 4 N/mm^2 at 20 cm from the fiber output end using the device described before. The source used was a 635-nm He-Ne laser whose injection angle was changed from −40º to 40º in 1º steps. The experimental set-up to obtain the FFP angular scans has been thoroughly described elsewhere so it is not further explained here [5]. The pressure value of 4 N/mm^2 was chosen to be similar to that needed to fix the fiber on the wall using a staple. These measurements were obtained for the two fibers tested before as well as for another SI-POF with the same size and NA: HFBR-R from Avago (HF).

From the FFPs obtained at different injection angles, the radial profiles have been extracted and introduced as columns into a matrix. These matrices can be represented as images to offer a compact representation of the whole scan. Figure 3 shows these radial profile scan images: on the left and on the right for the SI-POFs (GH and HF, respectively) and in the middle for the GI-POF. On the upper row, the radial profiles obtained without pressure are shown to serve as a reference to reveal the changes in the images obtained when the pressure is applied that are shown on the lower row. On the horizontal axis, the input or injection angle is shown, while the output angle is on the vertical axis. Normalized optical power is color coded ranging from 1 (red) to 0 (dark blue). The images have been all normalized to the maximum value of the pair of measurements corresponding to each fiber.
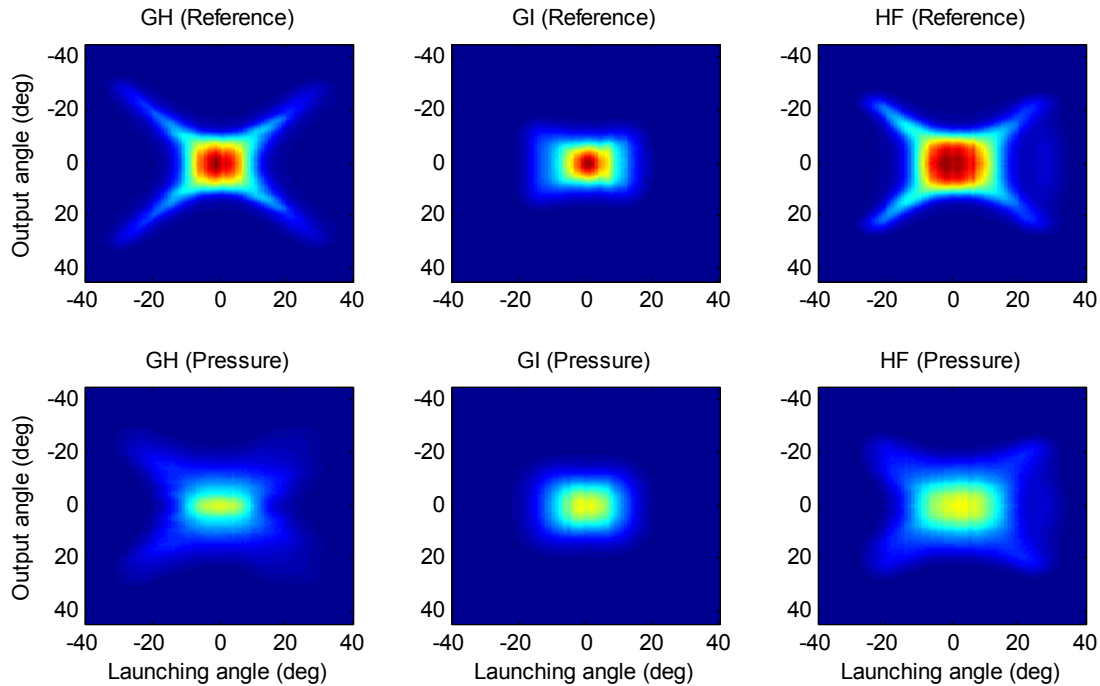
Figure 3. Radial profile scans for the three tested POFs: reference (upper images) and 4-N/mm^2 pressure (lower images).

Notice that the radial profiles for step and graded index POFs are different even before applying pressure. For low input angles, both fibers have radial profiles with a maximum around 0º. At angles higher than 15º, however, the maxima are shifted to higher angles for step-index POFs, but there is no power transmission through the GI-POF. Also, radial profiles are narrower for the GI-POF at all injection angles. Therefore, it is not surprising that the effects of pressure are different for each fiber type. Power loss caused by pressure is revealed by the lower values at all angles and for both fiber types. The GI-POF shows very little power spread as its pattern hardly changes with pressure. On the other hand, the effects of power spread are evident in both SI-POFs, particularly for higher angles where the patterns are smoothed. Thus, the steep loss found for SI-POF at this pressure level can be associated to power transfer from confined to external modes easily radiated.

4. Pressure characteristic matrix

Radial profile scans such as those shown in Figure 3 were used to fit a number of parameters that describe the characteristic matrix for the applied pressure. As the effects of pressure are different for each fiber type, we obtained different sets of parameters for the GH and the GI fibers. Thus, measurements of the scans with and without the pressure for at least six specimens of each fiber type were taken. The parameters determined for each pair were averaged and used to calculate the characteristic matrix for each fiber type shown in Figure 4.

These matrices reveal the different impact of pressure over the behavior of fibers with different profiles. The characteristic matrix for the GH reveals that the power is spread over a very wide angular range, while this effect is much less intense for the GI-POF even though the overall loss at this pressure value is even higher for the latter fiber. For the GI-POF, however, there is not substantial power spread and there is less power loss for angles below 15º. However, power carried at higher angles is totally gone by the sharp filtering effect.
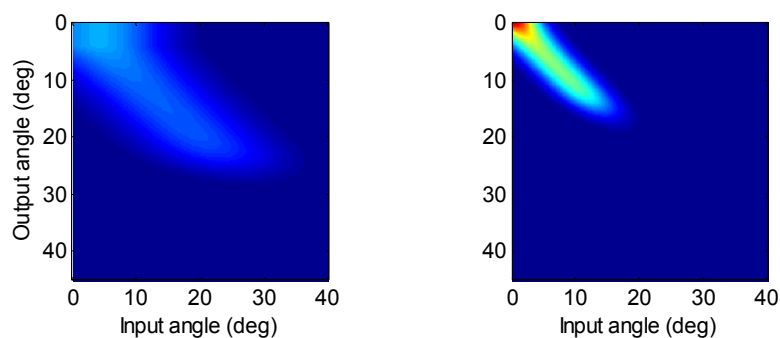
Figure 4. Pressure matrix for step-index (left) and graded-index (right) POFs.

These matrices have been used to calculate power loss when applying a pressure of 4 N/mm^2 simulating the conditions of the experiment described in Section 2. The values obtained are represented as filled black squares together with the experimental results in Figure 2. Error bars are included to show the variability introduced by the matrix parameters found for each fiber specimen. These values are inside the standard deviation of the measurements which validates the characteristic matrix model. In addition, to show that the model can be applied to other POFs, the effects of this pressure over the HF fiber have been simulated using the characteristic matrix obtained for the GH and compared to the actual measurements. Our results show that the standard error is similar to the errors obtained with measurements from different specimens of the same fiber. Therefore, a single matrix for each pressure value can be used to model its effects over all fibers with the same index profile and similar characteristics.

5. Conclusions

We measured power loss for plastic optical fibers of 1-mm core diameter and high numerical aperture with different index profiles which has a strong impact on the variation of loss versus pressure. SI-POFs seem to be more resistant to pressures below 4 N/mm^2, although increasing the pressure above this value produces a sharp increase in power loss. Power loss presents a shallower variation with pressure in GI-POFs but overall loss is higher at high pressures due to a steeper angular attenuation for this fiber type. A matrix to model the global effects of the pressure has been empirically obtained for both index profiles. This characteristic matrix simulates the effects of the localized pressure and can be used to predict its impact over transmission properties in realistic layouts of domestic networks where the fiber has to be held using different fastening systems at several positions throughout the link.

6. Acknowledgements

7. References

[1] International Standard "Optical fibres - Part 2-40: Product specifications – Sectional specification for category A4 multimode fibres", EC60794, IEC 2015.

[2] Japanese Industrial Standard, "Test methods for mechanical parameters of all plastic multimode optical fibres", JIS C6861, Japan, 1992.

[3] M.A. Losada, J. Mateo, J.J. Martinez-Muro, "Assessment of the impact of localized disturbances on SI-POF transmission using a matrix propagation model", *J. Opt.*, 13(5) 055406 (6pp), 2011.

[4] A. Esteban, M.A. Losada, J. Mateo, N. Antoniades, A. López, J. Zubia, "Effects of connectors in SI-POFs transmission properties studied in a matrix propagation framework", *in Proc. Int. Conf. on Plastic Optical Fibers and Application*, 341-346, Bilbao (Spain), 2011.

[5] M.A. Losada, A. López, J. Mateo, "Attenuation and diffusion produced by small radius curvatures in POFs", *Opt. Express*, 24(14), 15710-15720, 2016.

[6] A. López, M.A. Losada, J. Mateo, "Simulation Framework for POF-based Communication Systems", *in Proc. Int. Conf. on Transparent Optical Networks*, Budapest (Hungary), 2015.

Characterization of a Y-coupler for POF

A. López[1*], M. A. Losada[1], J. Mateo[1], N. Antoniades[2], X. Jiang[2], D. Richards[2]

1 GTF, Aragón Institute of Engineering Research (i3A), Department of Electronic Engineering, University of Zaragoza, María de Luna 1, E-50018 Zaragoza, Spain.
2 College of Staten Island, The City University of New York, Staten Island, NY 10314, USA.

*Corresponding author: aliclope@unizar.es

Abstract: Although there are many mature technologies for the manufacture of couplers and splitters for single mode and multimode glass fibers, it is not easy to translate them to similar devices for plastic optical fibers as modal power distribution in POFs is easily modified by spatial disturbances that produce a localized strong power transfer between modes. Here, we experimentally characterize a particular Y-coupler designed for POF. Apart from obtaining the insertion loss of each port as a function of wavelength, we have assessed the impact of the coupler on the angular power distribution, as well as on the frequency response of POF links with different lengths.

1. Introduction

As plastic optical fibers (POFs) are penetrating different scenarios such as home networks and avionics, it increases the need to design and manufacture specific components and, particularly, passive devices. In this context, multi-port couplers are key elements to implement different layouts where combining or splitting optical signals is required, while simpler designs are needed for sensor applications and for power monitoring in network management and testing [1-3]. Thus, depending on their function there is a variety of designs based on different technologies: waveguide plates, fused-tapered or misaligned fibers and beam-splitter cubes [4-6]. The drawback when these devices are inserted in a plastic optical fiber link is that they can modify the fiber modal power distribution, changing its performance so that it is necessary to assess and quantify their impact.

Here, we focus our study on a particular three-port device that splits power asymmetrically. Its main application is to enable the system designer to obtain the optical power value at specific points of a link. In the paper, we describe the experimental set-ups adapted to POFs that have been used to obtain the spectral, spatial and temporal characteristics of the device. Next, we analyze the changes in these properties when the coupler is joined to fibers of several lengths in order to evaluate its impact in a POF system. Finally, we discuss the limits of the device application in real scenarios according to our experimental results.

2. Experimental characterization of the Y-coupler

The device under test is a custom-made pigtail-style POF Y-coupler from OZ Optics Ltd. (FOBS-12P-111) designed to act as a "tap" that splits off a small portion of light. The three pigtails are 1-meter segments of PMMA 1-mm core fiber (GH4002 from Mitsubishi). Light from the input fiber (TRK port), is collimated by a lens, and then sent through a beam-splitter cube with a 5/95 split ratio (12.79 dB). The two resultant beams are then focused back into the output fibers at the T_1 and T_2 ports. This device has been experimentally characterized through the measurement of spectral insertion loss, radial profiles extracted from far field patterns (FFPs) and frequency response as is presented in this section.

2.1 Spectral losses

To obtain the spectral attenuation we implemented the method described in the Japanese Industrial Standard (JIS) [7]. Our experimental set-up was based on a white light source followed by a monochromator to scan the wavelength with a built-in step-motor. This beam was focused onto the input end of the fiber to optimize light injection, while the other end was centered over a Si photodiode (FDS010 from Thorlabs) whose output signal was processed to reduce spurious noise using a lock-in amplifier. The power transmitted by the Y-coupler was measured injecting light into the pigtail fiber at the common input port (TRK) and detecting the power first at T_1 (95%) and then at T_2 (5%). A short segment of GH fiber was used as a reference. From these experimental measurements, the average insertion loss for each output port T_i can be obtained as

$$IL_{TRK,T_i}(\lambda) = 10\log_{10}\left(P_{TRK}(\lambda)/P_{TRK,T_i}(\lambda)\right), \qquad (1)$$

where $P_{TRK}(\lambda)$ is the power at the output of the reference fiber and $P_{TRK,Ti}(\lambda)$ is the power measured at the output of port T_i. The corresponding insertion losses for each output port are represented as a function of wavelength in the left plot of Figure 1 along with their standard deviations shown as error bars. The black line in the plot represents the split ratio at each wavelength ($IL_{TRK,T2}(\lambda) - IL_{TRK,T1}(\lambda)$). On the right plot, the excess loss: $EL_{TRK}(\lambda) = -10\log_{10}(P_{TRK,T1}(\lambda) + P_{TRK,T2}(\lambda))$ is represented along with the loss for a 2-meter GH fiber to visualize the extra loss introduced by the optical components of the coupler.
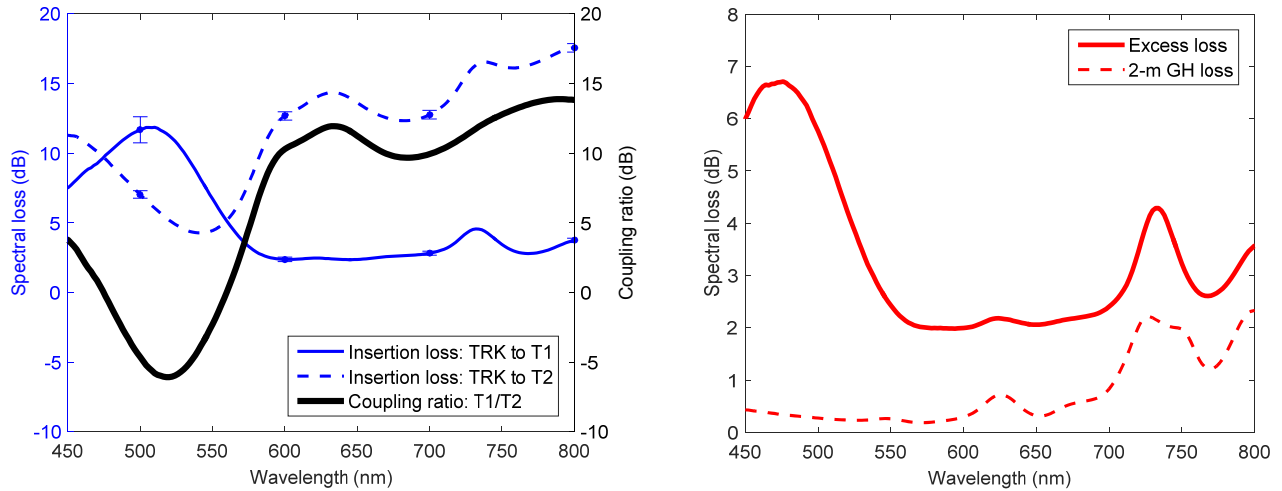
Figure 1. Y-coupler spectral loss measurements: insertion losses for T_1 and T_2 (left) and total excess loss (right).

As the figure shows, the splitting ratio values vary with wavelength from a maximum of 14 dB at 790 nm to a minimum of −6 dB at 520 nm due to the transmission-reflection properties of the beam-splitter cube. At 650 nm, we obtain a split ratio of 11.25 dB, which agrees with the value given at this wavelength in the manufacturer's datasheet. Although the excess loss also has steep variations in the visible spectrum, it is relatively flat from 560 to 690 nm where its value is close to its minimum of 2 dB. Apart from the insertion losses that are represented in the figure, the total loss introduced by the Y-coupler in a POF link should also include the insertion loss of a double connector needed to join the coupler to the fiber [9].

2.2 Spatial power distribution

The fiber far field pattern (FFP) was obtained by recording the image reflected on a white screen placed opposite the fiber at 7.5 cm from its output end using a 12-bit monochrome cooled camera QICAM FAST 1394CCD as has been thoroughly described elsewhere [8]. The radial profile extracted from this pattern and expressed as a function of the propagation angle provides a good representation of the optical power distribution in the fiber. Figure 2 shows the results obtained for a GH fiber of 2 meters and for the Y-coupler to assess the changes introduced by this device. We used two different sources: a He-Ne laser (635 nm)
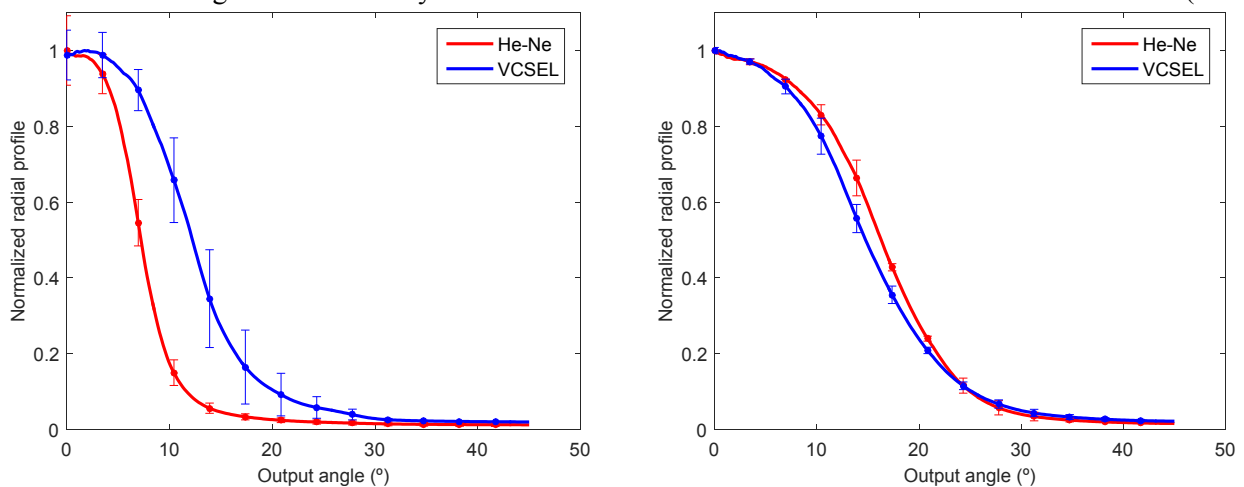
Figure 2. Radial profiles from FFPs for two different optical sources: 2-m of GH fiber (left) and Y-coupler (right).

directly injected into the fiber and the emitter side of the transceiver EDL1000T-EVB from Firecomms[TM] that is based on a VCSEL at 665 nm and is provided with an Optolock® connector. Light was injected directly on the fiber pigtail of the TRK port while the output FFP from the fiber pigtail of T_1 was registered. At least fifteen measurements of each condition were taken to assess variability, so that the graphs show average results as well as standard deviations. As the plots illustrate, the overall effect of the Y-coupler is a widening of the spatial distribution induced by mode coupling. In addition, the changes introduced on the shape of the power distribution produce output patterns that are very similar for both sources as the reduced standard deviation for the measurements with the coupler also confirms.

2.3 Frequency response

We have obtained the frequency response measurements using a set-up based on a Vector Network Analyzer (VNA E5071C from Agilent). For this purpose, an optical link was built modulating directly the emitter in the EDL1000T-EVB transceiver. The receiver was based on a 0.8 mm^2 Si photodetector (DET10A from Thorlabs) followed by an electrical amplifier (ZKL-1R5 from Mini-Circuits). In order to disregard the effect of the measuring system on the results, the frequency response of a very short fiber segment was first measured to serve as a reference that was used to normalize all subsequent measurements. The response for the Y-coupler was obtained by connecting the TRK pigtail to the optical source through the Optolock® and the port T_1 to the detector through an ST connector. As expected (see blue line in Figure 3), a flat frequency response was found, as the coupler is a passive device that has by itself no effect on the frequency. However, when it is placed within a POF link, after or before a fiber segment, it will change the optical power distribution that reaches the detector and thus, modify the fiber frequency response as will be shown in the next section.

3. Impact on the performance of a POF link

The effect of the Y-coupler on the capacity of a communication link has been evaluated by obtaining the frequency responses of several link configurations that include this device. These measurements were carried out using the set-up described in Section 2.3. In particular, we focused our analysis on GH fibers of three different lengths: 10, 20 and 40 meters. We first measured their frequency responses by connecting each fiber end directly to the emitter and the receiver and obtained the normalized frequency responses that are shown in Figure 3 in black (solid line for 10 m, dashes for 20 m and dots for 40 m). Then, we introduced the Y-coupler at the output of the fiber by using a VersaLink (VL) double connector to join the TRK port to the fiber output end and inserting the T_1 pigtail of the Y-coupler into the receiver with an ST connector. These results are shown in the figure as red lines: solid, dashes and dots for the three fiber lengths.
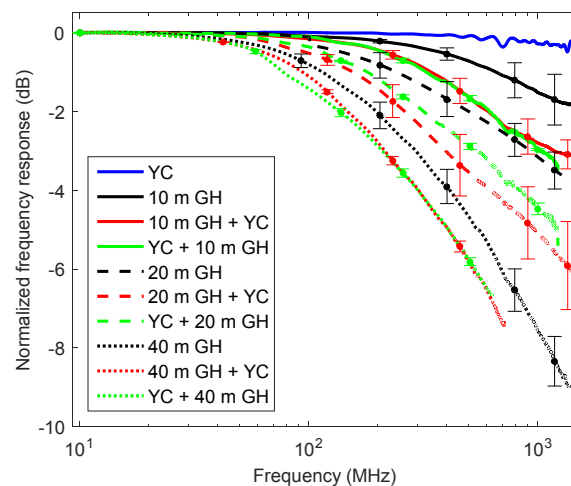
Figure 3. Normalized frequency responses for the Y-coupler (blue), GH-fiber segments of different lengths (black) and several link configurations: coupler at the receiver end (red), coupler at the emitter end (green).

We also tested another useful configuration, placing the Y-coupler directly after the emitter connecting it to the TRK port. The different lengths of fiber were then connected to the T_1 pigtail using the VL connector. This last set of measurements is shown in green. To complete the results, the blue line represents the normalized frequency response of the coupler itself, which was obtained according to Section 2.3. The error bars show the

standard deviation of the measurements as the frequency responses shown in the figure were obtained as the average of at least ten measurements. The relatively large bars reflect the impact of the changes in the connections needed for each particular measurement and are added to the high variability usually found for POFs. Results show that the presence of the Y-coupler both at the emitter and at the receiver degrades the system performance, as it is clear all frequency responses with the coupler show lower values than those obtained with the fiber only. The effect of the Y-coupler is similar in both positions so that its impact on the transmission capacity seems rather independent of its position in the link.

To summarize and taking into account the whole experimental characterization, we have found that the insertion loss of the Y-coupler for port T_1 is relatively low (about 2.5 dB in the region around 650 nm) but that the frequency responses of a fiber link are reduced when introducing the coupler. As we saw from the measured radial profiles, the effect of the coupler is to widen the angular power distribution, increasing power particularly at middle angles (15º – 30º). Thus, when the Y-coupler is right after the emitter, it transforms the optical source into an over-filled input power distribution that lowers the values of the frequency response at higher frequencies. When the Y-coupler is near the receiver, it acts as a mode mixer that also has the same degrading effect.

4. Conclusions

We have thoroughly characterized an Y-coupler based on a beam-splitter that can be used as a "tap" in the wavelength region from 600 to 700 nm where its average split-ratio is 10.72 ± 0.81 dB with maximum excess loss of 2.41 dB. Our measurements show that the fiber modal distribution at the output of the Y-coupler is independent on the input pattern and has a width at half maximum of 15º. Thus, it has an equalizing effect over the power distribution that reduces the frequency responses independently of the device position in the link. The results obtained in this work demonstrate the need to consider carefully the impact of the Y-coupler on the transmission properties of any POF system that requires this or a similar device.

5. Acknowledgements

6. References

[1] Y. Jeong, S. Bae, K. Oh, "All fiber NxN fused tapered plastic optical fiber (POF) power splitters for photodynamic therapy applications", *Curr. Appl. Phys.*, 9, 273-275, 2009.

[2] D. Richards, N. Antoniades, T.K. Truong, "Performance modeling and analytical verification of POF transmissive star couplers for avionics system applications", *in Proc. IEEE Avionics, Fiber-Optics and Photonics Technology Conf.*, 77-78, San Diego (USA), 2011.

[3] A. Ehsan, S. Shaari, M.K. Rahman, "Acrylic-based asymmetric and variable coupling ratio Y-branch plastic optical fiber coupler", *Opt. Rev.*, 19, 13-19, 2012.

[4] K.T. Kim, B.J. Han, "High-Performance plastic optical fiber coupler based on heating and pressing", *Photon. Technol. Lett.*, 23(24), 1848-1850, 2011.

[5] N. S. Mohamed-Kassim, M. K. Abd-Rahman, "High resolution tunable POF multimode power splitter", *Opt. Commun*, 400, 136-143, 2017.

[6] Oz Optics Ltd.: Fiber optic beam splitters, http://www.ozoptics.com/ALLNEW_PDF/DTS0095.pdf.

[7] Japanese Industrial Standard, "Test methods for attenuation of all plastic multimode optical fibres", JIS C6861, Japan, 1992.

[8] J. Mateo, M. A. Losada, I. Garcés, "Global characterization of optical power propagation in step-index plastic optical fibers", *Opt. Express*, 14(20), 9028-9035, 2006.

[9] D. H. Richards, M. A. Losada, N. Antoniades, A. López, J. Mateo, X. Jiang, N. Madamopoulos, "Methodology for Engineering SI-POF and Connectors in an Avionics System", *J. Lightw. Technol.*, 31(3), 468-475, 2013.

Study of Bragg grating inscription mechanisms in PMMA POFs using 400 nm femtosecond pulses

X. Hu[1]*, D. Kinet[1], C.-F. J. Pun[2], H.-Y. Tam[2] C. Caucheteur[1]

1 Electromagnetism and Telecommunication Department, University of Mons (UMONS), Boulevard Dolez, 31, 7000 Mons, Belgium
2 Department of Electrical Engineering, The Hong Kong Polytechnic University, Hong Kong, China

*Corresponding author: xuehao.hu@umons.ac.be

Abstract: We report uniform Bragg grating growth in trans-4-stilbenemethanol (TS)-doped poly(methyl methacrylate) (PMMA) optical fibers. Fiber Bragg gratings (FBGs) were inscribed using a 400 nm femtosecond pulsed laser and a 1060-nm-period uniform phase mask. With a mean laser power of 20 mW, the grating reflectivity reaches 98 % in ~60 seconds. Then, with two mean laser powers (15 mW and 20 mW), reflectivity growth dynamics during the inscription process were demonstrated. After that, the stability of the inscribed gratings was investigated as a function of time, which was explained by the scheme of energy levels involved in the trans-cis photoisomerization process.

1. Introduction

Fiber Bragg gratings (FBGs) in polymer optical fibers (POFs) present several advantages for sensing applications compared to their silica counterparts. Because of the larger thermo-optic coefficient and smaller Young's modulus of polymer materials, polymer optical fiber Bragg gratings (POFBGs) show higher sensitivities for temperature sensing [1,2] and force sensing [1,3], respectively. In addition, the strengthened bending tolerance and biocompatibility make POFBGs suited for biomedical applications [4,5].

Since the first grating manufactured in a step-index POF in 1999 [6], not only the grating quality but also the inscription efficiency has been improved. Among all kinds of POFs made of different materials, poly(methyl methacrylate) (PMMA) POFs are most popular. The POFs based on PMMA were used to produce highly reflective FBGs. Although the refractive index of PMMA varies when irradiated by UV light, photosensitive dopants are usually added in the fiber core in order to make FBG fabrication more efficiently. The dopants Benzyl dimethyl ketal (BDK) and TS are widely used for increasing the photosensitivity in PMMA POFs.

In 2010, Luo et al. reported the first grating inscription in step-index PMMA POFs with a BDK-doped core using a 355 nm nanosecond pulsed laser. BDK acts as a photoinitiator and the refractive index of the BDK-doped core increases under UV irradiation [7,8]. After 16 minutes, the grating (25 % reflectivity) was obtained [7]. In 2004, FBGs were first inscribed in step-index PMMA POFs with a core doped with TS by 325 nm laser pulses. The grating with a reflectivity of 90 % was obtained after 90 minutes [9]. Recently, the grating (25 dB in reflection) was photo-inscribed in step-index TS-doped PMMA POFs in one second [10]. But, the reflectivity is low. TS is a stilbene derivative compound that exhibits a reversible trans–cis photoisomerization [11]. As shown in Figure 1, its structure changes from trans to cis under UV irradiation resulting in a negative refractive index change.
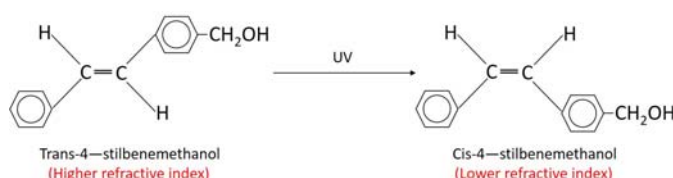
Figure 1. Structure change of 4-stilbenemethanol isomerization (from trans to cis) with UV irradiation [12].

Though the dopants in the fiber core can decrease the inscription time, it is still challenging to make highly reflective gratings in a short time. So, in order to inscribe FBGs much more efficiently, we present an improved FBG fabrication process for step-index TS-doped PMMA POFs. FBGs were inscribed by a

frequency-doubled near-infrared femtosecond pulsed laser emitting at 400 nm through a uniform phase mask. The reflectivity, computed from the measurement of the rejection band in the transmitted amplitude spectrum of the gratings, reached 98 % (17 dB) after ~60 seconds for a controlled mean laser power of 20 mW, confirming the very high efficiency of the FBG inscription process.

2. Experimental set-up

The fiber used in this work was fabricated in the Hong Kong Polytechnic University with a core diameter of 8.2 μm and a cladding diameter of 150 μm. The cladding is in pure PMMA while the core is composed of PMMA doped with diphenyl sulfide (DPS) (5 % mole) and TS (1 % w.t.). Both dopants are used to increase the refractive index and enhance the photosensitivity. DPS facilitates the trans-cis interconversion under UV irradiation [13]. The refractive indices are computed equal to 1.5086 and 1.4904 for the core and the cladding, respectively, at the wavelength of 589 nm.

10-mm-long FBGs were photo-inscribed at the University of Mons using 400 nm femtosecond laser pulses. The information about the 400 nm femtosecond pulsed laser was introduced in our previous report [14]. The mean laser power is adjustable using an attenuator. In order to increase the power density, the output circle beam with a diameter of 10 mm was focused on the fiber core by a 5-cm-focal-length cylindrical lens, yielding a 1 mm beam height in the vertical plane with respect to the fiber axis. Though the laser wavelength is quite far from that of the absorption peak of TS centered at 305 nm [12], a nonlinear multi-photon absorption process can take place [15,16]. This fact is due to the high peak intensity at the laser beam focus in the fiber core. Moreover, the POF absorption losses are much lower at 400 nm than at 325 nm [17]. Because of the higher losses of POFs in the infrared region compared to their silica counterparts, only short POF sections of a few centimeters were used. The two ends of the POF were connected to silica fiber pigtails with an optical UV glue (Norland 86H). Then, both silica fiber pigtails were fixed by standard silica fiber clamps on both sides to monitor the transmission spectrum during the photo-inscription process. To ensure a good stability of the POF section, a slight tension was applied during the whole inscription process. The transmitted amplitude spectrum measurements were obtained with an FBG interrogator (FS2200SA from FiberSensing) that presents a wavelength resolution of 1 pm and a scanning rate of 1 Hz.

3. Experimental results

Figure 2 shows a typical FBG dynamic growth measured from the transmitted amplitude spectrum with a mean laser power of 20 mW. During the inscription process, the FBG rejection band grows very fast and saturates in around one minute. In the meantime, the out-of-band fiber transmission loss level remains almost the same during the photo-writing process, which results from the low power density of the laser beam on the core inducing limited structure change in the fiber core.
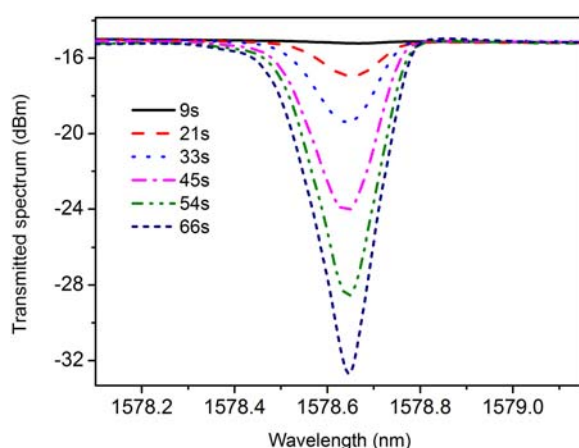
Figure 2. Evolution of a 1-cm-long FBG transmitted amplitude spectrum during the inscription process.
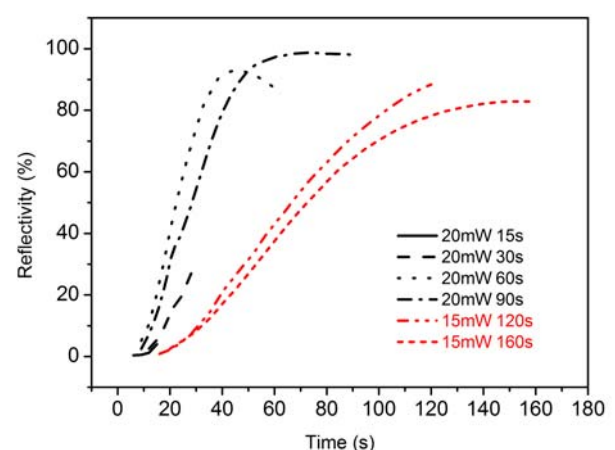
Figure 3. FBG growth dynamics in reflectivity during the inscription process.

Figure 3 shows the dynamics of the reflectivity growth for 6 FBGs made in two regimes with mean output powers (15 mW and 20 mW). This reflectivity is computed from the insertion loss measurement of the core mode resonance in the transmitted amplitude spectrum. The inscription durations are between 15 seconds and 160 seconds. At 20 mW, after 10 seconds, the reflectivity is only ~5 %, and then the reflectivity saturates at ~98 % after an exposition time of ~60 seconds. Its growth between 10 and 40 seconds shows a reflectivity growth rate of 2.5 % reflectivity per second of irradiation. At 15 mW, the growth rate is smaller (0.9 %/s) and the maximum reflectivity is limited to ~90 % reached in ~120 s. Thus, we confirm that the reflectivity growth rate is related to the mean laser power. The distinction in the evolutions between the different expositions obtained for each regime is attributed to the slight fluctuation of the power density reaching the fiber core. The fluctuation mostly results from the fiber alignment in the inscription system.

After that, the stability of the inscribed gratings in the aforementioned conditions was investigated as a function of time by recording their transmitted amplitude spectral evolutions during 15 days after their inscription process. Time 0 in the horizontal axis corresponds to the time right after the inscription. Figure 4 shows that the FBG reflectivity varies as a function of time. For the low reflective gratings produced in short inscription time, the reflectivity strongly increases (> 60 %) as a function of time after the irradiation process, as observed from curve (20mW, 15s) and curve (20mW, 30s). For the latter curve, the reflectivity reaches nearly 100%. Oppositely, highly reflective gratings strongly decay (reflectivity decrease of ~40 %) after the inscription process, as shown from curve (20mW, 60s), curve (20mW, 90s) and curve (15mW, 160s). Curve (15mW 120s) shows an intermediate behaviour with an overall stability.
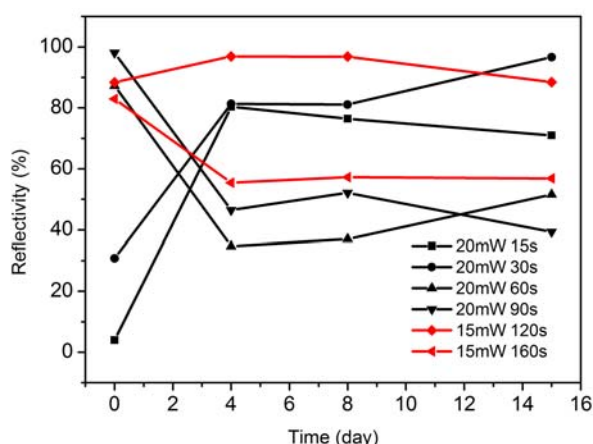
Figure 4. Reflectivity evolutions as a function of time after the inscription process.
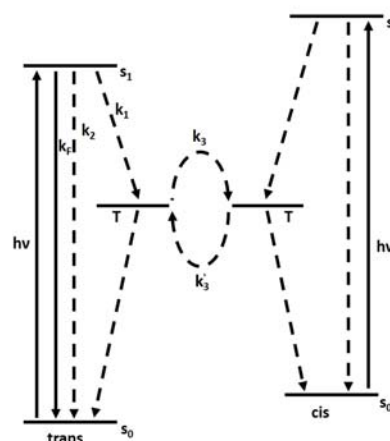
Figure 5. Scheme of energy levels.

We believe that these singular post-irradiation evolutions are related to the strength of the refractive index modulation created in the fiber core [10,18]. Hence, in order to explain these observations, we can rely on the scheme of energy levels involved in the trans-cis photoisomerization process [19], as depicted in Figure 5. Both trans- and cis- isomers have excited intermediate states (T) between the ground states (S_0) and the excited ones (S_1). The left part of the sketch shows the energy levels for trans-isomers, the excited level can be reached with photon absorption. This level is not stable and automatically turns into the trans-isomer intermediate states following the transition rate k_1. Following another transition rate k_3, the trans-isomer intermediate states turns into the cis-isomer intermediate states. These two transition rates increase with increasing temperature [19].

During the FBG inscription process, laser pulses periodically heat the fiber core and consequently generate temperature-induced swelling. Thus, larger space is given for trans-cis transitions, for which trans-isomers on the excited states transit to cis-isomers on the ground states via trans- and cis-isomer intermediate states. Because of the possibility of the reverse transition on both intermediate states, the equilibrium between both states could be established. After the inscription process, part of 4-stilbenemethanol molecules could still be confined on both trans- and cis-isomer intermediate states because of the glassy polymer matrix [12].

Based on this scheme, for the low reflective gratings, their reflectivity increase as a function of time after the irradiation process could be attributed to the continuous isomerization process. This switching process from trans- to cis-forms can take place because there are much more molecules on the trans-isomer intermediate states than those on the cis- ones due to the limited FBG strength related to the limited photon absorption. Then, the k_3 transition occurs as a function of time, which brings the molecules to the cis-isomer intermediate states and consequently enhances the strength of the refractive index modulation amplitude. Oppositely, for the highly reflective gratings, between both intermediate states most of the molecules are on the cis-isomer intermediate states because of the large absorption of photons. Therefore, their decay results from the population inversion between molecules from the cis-isomer intermediate states to the trans- ones (k'_3 transition), resulting in smaller refractive index modulation amplitude. However, after a thermal annealing of 48 hours at 80 °C, the FBG reflectivity can be stabilized to the value reached right after the photo-inscription process. This post-irradiation thermal process allows molecules to transit from both intermediate states to the cis-isomer ground states and prevents the fluctuations illustrated in Figure 4.

4. Conclusion

In this report, we have presented a method to produce highly reflective gratings effectively in step-index TS-doped-core PMMA POFs using 400 nm femtosecond pulses and a phase mask. For a mean laser power of 20 mW, an FBG reflectivity as high as 98 % can be obtained in ~60 seconds in the near-infrared wavelength range. The grating stability as a function of time is corresponded to the trans-cis interconversion process.

5. Acknowledgements

6. References

1. X. Hu, C.-F. J. Pun, H.-Y. Tam, P. Mégret, and, C. Caucheteur, Opt. Express 22, 18807 (2014).
2. J. Bonefacino, X. Cheng, M.-L. V. Tse, and H.-Y. Tam, IEEE J. Sel. Top. Quantum Electron. 23, 5600911 (2016).
3. X. Hu, D. Saez-Rodriguez, O. Bang, D. J. Webb, P. Mégret, and C. Caucheteur, Opt. Express 23, 4581 (2015).
4. X. Hu, C.-F. J. Pun, H.-Y. Tam, P. Mégret, and C. Caucheteur, Opt. Lett. 39, 6835 (2014).
5. X. Hu, P. Mégret, and C. Caucheteur, Opt. Lett. 40, 3998 (2015).
6. Z. Xiong, G. D. Peng, B. Wu, and P. L. Chu, IEEE Photon. Technol. Lett. 11, 352 (1999).
7. Y. Luo, Q. Zhang, H. Liu, and G. D. Peng, Opt. Lett. 35, 751 (2010).
8. D. Sáez-Rodríguez, K. Nielsen, H. K. Rasmussen, O. Bang, and D. J. Webb, Opt. Lett. 38, 3769 (2013).
9. J. M. Yu, X. M. Tao, and H. Y. Tam, Opt. Lett. 29, 156 (2004).
10. X. Hu, D. Kinet, P. Mégret, and C. Caucheteur, Opt. Lett. 41, 2930 (2016).
11. G. H. Brown, Photochromism, Wiley-Interscience, New York (1971).
12. J. M. Yu, X. M. Tao, H. Y. Tam, D. X. Yang, and M. S. Demokan, Opt. Commun. 265, 132 (2006).
13. A. Thalmann, K. Oertle, and H. Gerlach, Org. Synth. 63, 192 (1985).
14. X. Hu, D. Kinet, K. Chah, P. Mégret, and C. Caucheteur, Proc. SPIE 9916, 99161X (2016).
15. A. Baum, P. J. Scully, M. Basanta, C. L. P. Thomas, P. R. Fielden, N. J. Goddard, W. Perrie, and P. R. Chalker, Opt. Lett. 32, 190 (2007).
16. C. Wochnowski, Y. Cheng, K. Meteva, K. Sugioka, K. Midorikawa, and S. Metev, J Opt. A-Pure Appl. Op. 7, 493 (2005).
17. K. Peters, Smart Mater. Struct. 20, 013002 (2011).
18. A. Othonos, Rev. Sci. Instrum. 68, 4309 (1997).
19. S. Malkin, and E. Fischer, J. Phys. Chem. 68, 1153 (1964).

Application of Thermography for Process Control in the Thermal Drawing of Polymer Optical Fibers

R. Evert, D. Zaremba, F. Jakobs, R. Caspary, W. Kowalsky, H.- H. Johannes*

Technische Universität Braunschweig, Institut für Hochfrequenztechnik, 38106 Braunschweig, Germany.
*Corresponding author: h2.johannes@ihf.tu-bs.de

Abstract: A thermographic camera is used to monitor the fabrication process of polymer optical fibers. The camera acts as a temperature control sensor for the furnace. It further records the spatial temperature distribution and the position of the preform in the furnace and it allows to identify process problems online. Special attention needs to be given to the calibration of the absolute temperature.

1. Introduction

The production of polymer optical fibers with a length of a few meters from small material batches is valuable for material research. It allows to examine and compare many different materials and material mixtures. An important parameter is the temperature program for the individual preforms. Measurements using contactless methods are preferred, because they allow online measurements and do not affect the drawing process. Such a method is the utilization of a pyrometer, which allows measurement of a wide range of temperatures but requires a precise adjustment of the measurement spot to the center of the preform. Wrong adjustment will result in the measurement of the furnace background and gives unstable results for different preform diameters. Thermal imaging has been used quite early for investigations of polymer materials [1], but only recently devices became cheap enough for a broader usage in scientific applications. Measurements on polymers have been shown to work in different setups [2,3].

To address these topics a common thermal fiber drawing process is established. A cylindrical bulk polymerized preform with a diameter of up to 16 mm and a length of up to 300 mm is heated and pulled [4]. To circumvent the limitations of the previously used pyrometer an Optris Pi 400 infrared camera is used. The device is installed outside the optical heating furnace monitoring the 20 mm heating zone from a distance of 300 mm, which is equipped with six 500 W halogen lamps radially around the preform. The power is directed to the center with mirror shaped grooves. To seal the camera hole, a 2 mm KBr crystal window with a wide transmittance in the infrared covers the aperture. The camera operates in the spectral range between 7.5 and 13 µm, with 288 x 382 pixels and a telephoto 10° x 13° field of view lens, which gives a resolution of 134 µm per pixel in the heating zone. The temperature measurement range is 0 to 250 °C, which fits the drawing conditions of the polymer.

2. Experimental

2.1 Camera calibration

The measurement layout is shown in figure 1. Due to its temperature, the preform is emitting black-body radiation in the infrared spectrum Φ_M. The emission properties of the object itself are described by the factor ε. This factor may change for different materials, surface properties and geometries. The heating elements in the background emit the radiation Φ_U. Depending on the spectral transparency and reflectance of the object, the thermographic camera additionally captures this emission.

Figure 1. Incident radiation of the temperature measurement, preform top view, ε emission, ρ reflection, τ transmission factor, Φ_M body emission, Φ_U background emission and light reaching the sensor Φ_t (left), PMMA calibration object with black body emission and thermocouple bores (right).

The transmission through the material may be neglected, as measurements with a Perkin Elmer Frontier FT-IR showed no transmission in the measurement region for a sample thickness of 5 mm for *poly*-methyl-methacrylate (PMMA).

Two different ways are used to calibrate the emission factor of the material and the transmission between the object and the camera. The emission factor of a PMMA rod with a diameter of 16 mm is determined by monitoring the temperature of a bore in the polymer object, which acts like a black body emitter (see figure 1). The drilled hole has a diameter of 2 mm and a depth of 12 mm. Surface effects can be neglected at this spot and the emission factor is determined to be 0.93. The effect of the transmission path in the optical system was examined using a calibrated thermocouple ($\pm$1 K) to measure the absolute temperature in the core of the preform. Steady state conditions were reached after 20 minutes and the remaining discrepancy between the thermocouple and the infrared temperature is corrected with a transmission factor of 0.5 for the optical system. Measurements of the absolute values were repeated for preforms with 10 mm and 8 mm.

2.2 Process control

Figure 2 shows relevant measurement spots on the preform. The red lines confine the open aperture of the furnace. Spot A is the middle of the preform. The measured temperature is fed into a PID control loop. Spot B shows the background of the furnace, whose apparent temperature is given by multiple reflections of the lamps on the polished aluminium of the furnace. As the emission properties the aluminium are highly dependent on its surface and the incident angle, absolute measurements are not possible here. The zones marked with C are unsuitable for measurements, as they consist of reflections on the inside of the furnace. In this setup, the temperature of the preform is not the maximum in the thermographic image. This introduces problems for automatic preform identification.
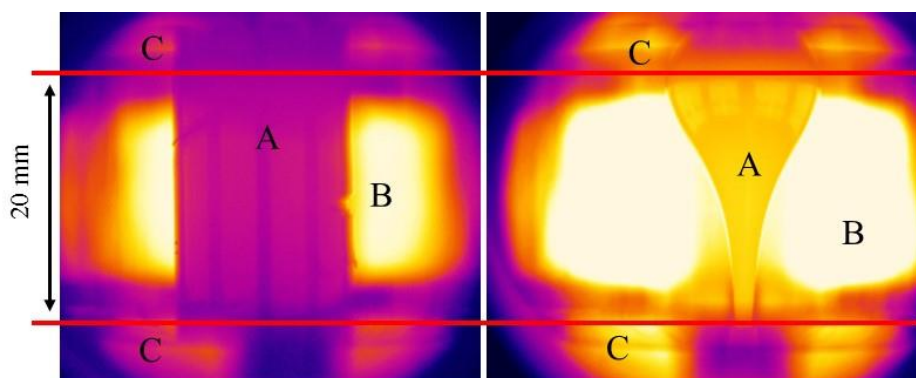
Figure 2. False color camera representation of the camera view with measurement points for the preform (A) and background (B) temperature. The field of view of the camera through the aperture is described by the red area (C), brighter regions are hotter.

Figure 3 shows a horizontal profile through the thermographic image for a preform with a diameter of 10 mm. The edges of the preform appear hotter than the surface and areas of higher and lower temperature appear on the surface of the preform. These are due to the reflection of the lamps on the preform, resulting in an apparent temperature difference of 6 K at 220 °C. As the plateau is flat, the geometry of the preform does not show great effect on the emission properties over the curved part.
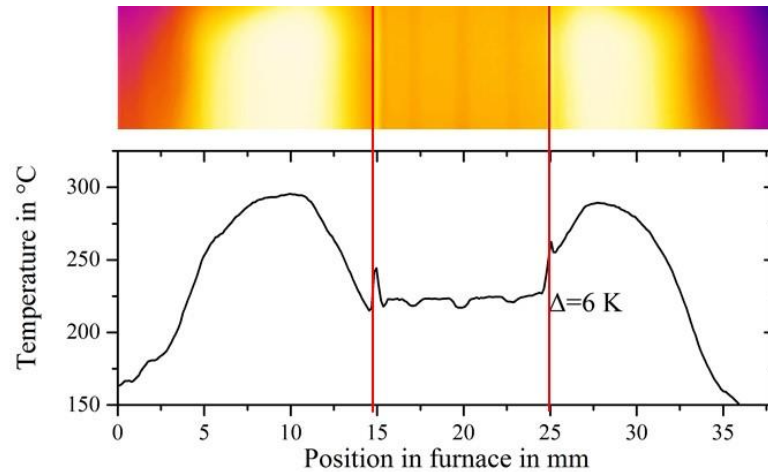
Figure 3. Profile through the thermographic measurement on the preform. Reflections on the outer edges of the preform and on the preform plane are visible.

The calibrated image is used to monitor the neck down region of the fiber preform during a drawing process. Figure 4 shows the profile in the heating zone during warm up of a 8 mm PMMA preform in the 20 mm long heating zone. At temperatures of around 90 °C convection sets in and the upper part of the preform starts to get warmer than the lower part. At around 160 °C the difference is 15 K. Once the drawing starts at 755 seconds, the temperature distribution reaches an equilibrium state with a temperature difference of 5 °C on the upper and lower end.
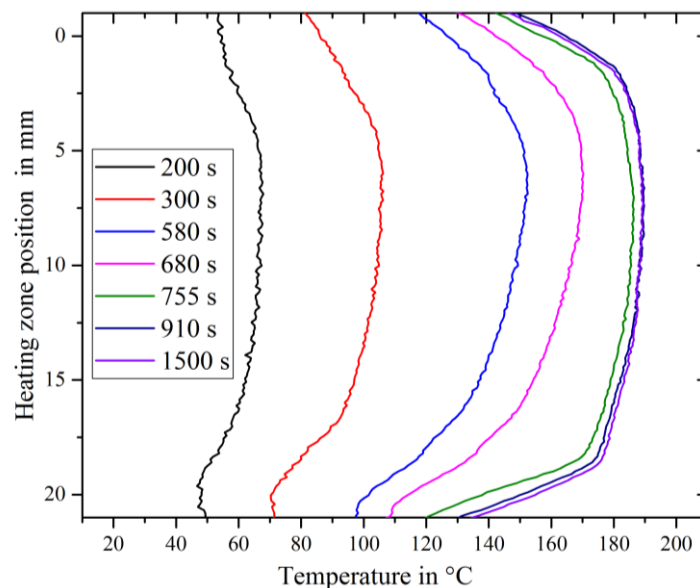
Figure 4. Multiple vertical temperature profiles on the preform during different stages of the drawing process.

2.3 Neck down region monitoring

Usual problems during the drawing process include the formation of bubbles in the preform during drawing. Figure 4 shows this condition with different sizes that are the result of incomplete polymerization, water inclusion or beginning of decomposition processes of the polymer. Recovery from these conditions is possible if they are detected before the fiber breaks by changing drawing parameters.

Additional information may be gathered from monitoring the neck down region. A change of parameters like drawing speed or temperature results in a movement of the neck in the heating zone until stable conditions are reached again. Different models have been shown for silica and microstructured polymer optical fibers [5, 6, 7].
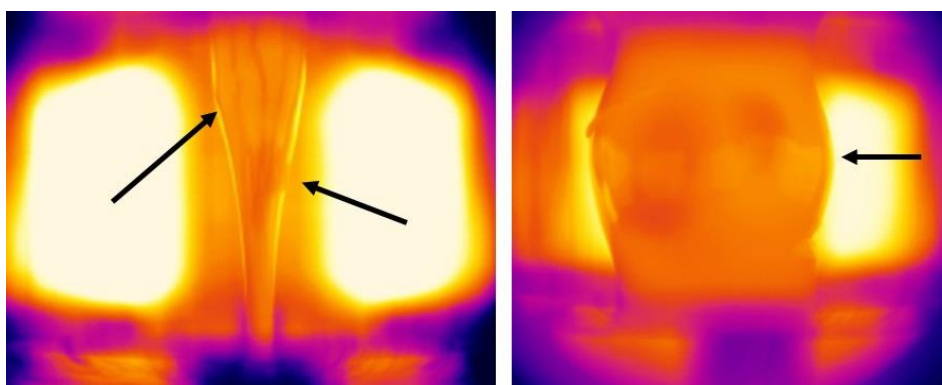
Figure 5. Failed preforms during fiber drawing, formation of small (left) and big (right) bubbles.

3. Conclusion

In this work, a setup for the measurement of the temperature of the preform in the fiber drawing process is shown. The results are used in a control loop to ensure constant drawing conditions. Additionally, this setup gives a better understanding of the conditions in the furnace. Special attention is given to the calibration for absolute temperature measurement, as small calibration errors result in big deviations. The reflections due to the optical heating restrict the measurement area and require additional processing of the temperature data.

The method has been tested with preforms up to a thickness of 16 mm. Preforms with a bigger diameter for the fabrication of microstructured polymer optical fibers may show bigger temperature gradients from the heated outside of the preform to the inside. Selecting different operation wavelengths of the infrared camera in a region with a certain transparency of the polymer may enable thermographic measurements from deeper layers of the material, though these are highly dependent on the spectral material transmission properties and the dimensions of the preform.

4. Acknowledgements

5. References

1. Maher JW, Haward RN, Hay JN, Study of the Thermal Effects in the Necking of Polymers with the Use of an Infrared Camera, Journal of Polymer Science, 18, 1980, 2169-2179, DOI: 10.1002/pol.1980.180181102

2. Marla VT, Shambaugh RL, Papavassiliou DV, Use of an Infrared Camera for Accurate Determination of the Temperature of Polymer Filaments, Ind. Eng. Chem. Res. 2007, 46, 336-344, DOI: 10.1021/ie060703a

3. Wang M, Liao Y, Chen D, Study on the thermal effects of rubbers during loading-unloading cycles by infrared thermogrphy, Polym. Bull., 70, 2013, 171-180, DOI: 10.1007/s00289-012-0795-x

4. Zaremba D, Evert R, Neumann L, Caspary R, Kowalsky W, Menzel H, Johannes HH, Methacrylate-Based Copolymers for Polymer Optical Fibers. Polymers 2017, 9, 34. DOI: 10.3390/polym9020034

5. Mawardi A, Pitchumani, Optical Fiber Drawing Process Model Using an Analytical Neck-Down Profile, IEEE Photonics J., 2010, 2,4, DOI: 10.1109/JPHOT.2010.2052454

6. Barton G, van Eijkelenborg MA, Henry G, Large MCJ, Zagari J, Fabrication of microstructured polymer optical fibres, Optical Fiber Technology, 10, 2004, 325-335, DOI:10.1016/j.yofte.2004.05.003

7. Reeve HM, Mescher AM, Effect of unsteady natural convection on the diameter of drawn polymer optical fiber, Optics Express 11, 2003, 15, 1770-1779, DOI: 10.1364/OE.11.001770

Analytical model for mode based insertion loss in ball-lensed coupling of graded-index silica and polymer fibres

Andy Schreier[1*], Tilman Jeschke[2], Klaus Petermann[2], Aleksander Wosniok[1], Katerina Krebber[1]

1 Bundesanstalt für Materialforschung und –prüfung (BAM), Unter den Eichen 87, 12205 Berlin
2 Technische Universität Berlin, Institut für Hochfrequenztechnik-Photonik, Einsteinufer 25, 10587 Berlin

*Corresponding author: andy.schreier@bam.de

Abstract: In order to calculate mode-based insertion losses within graded-index (GRIN) multimode fibres, simple analytic formulas are considered. An existing ball-lensed coupling between those fibres is taken into account and modal power distributions for axial and longitudinal misalignments in fibre coupling are calculated. All calculations are based on commercially available fibres and lens materials. Finally, the ball-lensed connector is evaluated for coupling between polymer optical and silica based GRIN-fibres with the same core diameter.

1. Introduction

Fibre coupling is crucial for all fibre applications [1]. For further development, applications in sensing and communications with silica optical fibres (SOFs) and polymer optical fibres (POFs) are of special interest. Among the most promising candidates polymer optical fibres are CYTOP based fibres with graded-index profile (PFGI-POFs).

In order to provide an easy handling for customers, ball-lensed coupling systems were developed [2]. However, there is no analytical model for GRIN fibres describing the insertion loss for each optical mode individually. This is crucial for Brillouin-based sensing [3] and modal dispersion in communication systems [4].

2. Description of the model

The developed model offers the potential to calculate insertion loss for each optical mode in GRIN-fibres based of silica and optical polymers. This model utilizes a combination of a Fresnel reflection coefficient and a modal coupling coefficient for each optical mode [5]. The only assumption to be made, is the fact that the ball lens diameter has to be much greater than the diameter of the ray. In this case the surface of the lens can be seen as a plane surface and Fresnel reflections are calculated irrespective of the angle of light incidence [6]. The Fresnel reflection coefficient is based on a difference in refractive index of the components, while the modal coupling coefficient is based on the optical mode size and on the type of misalignment as well as its value.

3. Calculation results

3.1 Results for coupling coefficients

For all calculations the fibre parameters of table 1 were applied. Please note, that these are related to a wavelength of $\lambda = 1319$ nm. The fibre parameter V was calculated by using the relative refractive index difference Δ and the core diameter a of the fibre (see equation 1). The mode field diameter ω_0 was calculated by using V and a (see equations 2 [7] and 3 [8] for graded-index and single-mode fibres, respectively). With the help of the displayed parameters, interconnections between single-mode and multimode fibres as well as between polymer optical and silica-based fibres were estimated.

$$V = \frac{2\pi a}{\lambda} \Delta = \frac{2\pi}{\lambda} a\sqrt{n_2^2 - n_1^2},\tag{1}$$

where n_2 is the maximum refractive index of the core and n_1 corresponds to the refractive index of the homogeneous cladding.

Fibre type	Fibre name	Core radius a [μm]	Numerical aperture	Fibre parameter V	Mode radius ω_0 [μm]
SMF	SMF-28 ®	4.1	0.14	2.734	4.16
GI-MMF	ClearCurve ®	25	0.2	23.82	7.29
PFGI-POF	GigaPOF-50SR ®	25	0.19	22.63	7.49

$$\frac{\omega_0}{a} = \sqrt{\frac{2}{V} + \frac{0.23}{V^{\frac{3}{2}}} + \frac{18.01}{V^6}} \tag{2}$$

$$\frac{\omega_0}{a} = 0.65 + \frac{1.619}{V^{\frac{3}{2}}} + \frac{2.879}{V^6} \tag{3}$$

Table 1: Fibre parameters used for calculations. Note that the mode field radii of the multimode fibres were calculated for fundamental mode only.
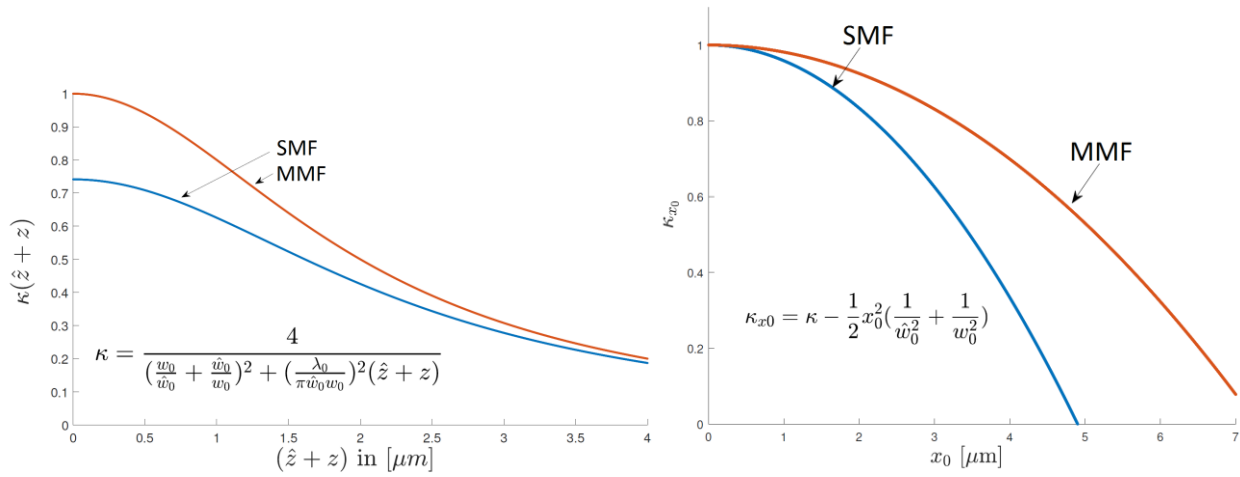
Figure 1: fundamental mode to fundamental mode coupling coefficients κ for longitudinal (left) and axial (right) misalignments. The plots "SMF" and "MMF" are representing the receiving fibres.

Based on the parameter sets in table 1, the coupling efficiencies are plotted as following in figure 1. The GI-MMF fundamental mode launched is injected into the fundamental mode of a receiving fibre such as SMF, GI-MMF and PFGI-POF. Due to the comparable fibre parameter sets of GI-MMF and PFGI-POF the graphs almost progress the same. Therefore, they are displayed as "MMF" in figure 1. However, it should be taken into account, that only the first term of the power series is plotted for the axial misalignment. It is recognisable that the coupling coefficient is decreasing whenever the misalignment increases. Furthermore, the influence on SMF is stronger compared to the MMF due to a smaller mode field diameter.

The coupling coefficient κ represents the transmission of the field amplitude from one fundamental mode to another. Higher order mode power coefficients are a linear combination of κ and are represented as $|c_{m,n}|^2$ in figures 2 and 3 for given misalignments. m and n characterise the mode indexes within the Cartesian coordinates. In addition, $\hat{m}$ describes the launched optical mode and m the received optical mode. Due to the fact that the fibre core is rotationally symmetric follows $m = n$. Thus, only one index is given for each fibre in figure 2. The calculations presented in figure 3 establish that only even mode numbers are feasible in the receiving fibres when the fundamental mode is launched.

All the graphs in figures 2 and 3 indicate that with an increase in misalignment, the number of optical mode in the receiving fibres increase, compared to the decreasing fundamental mode power. Furthermore, the mode conversional behaviour for given misalignments is demonstrated.
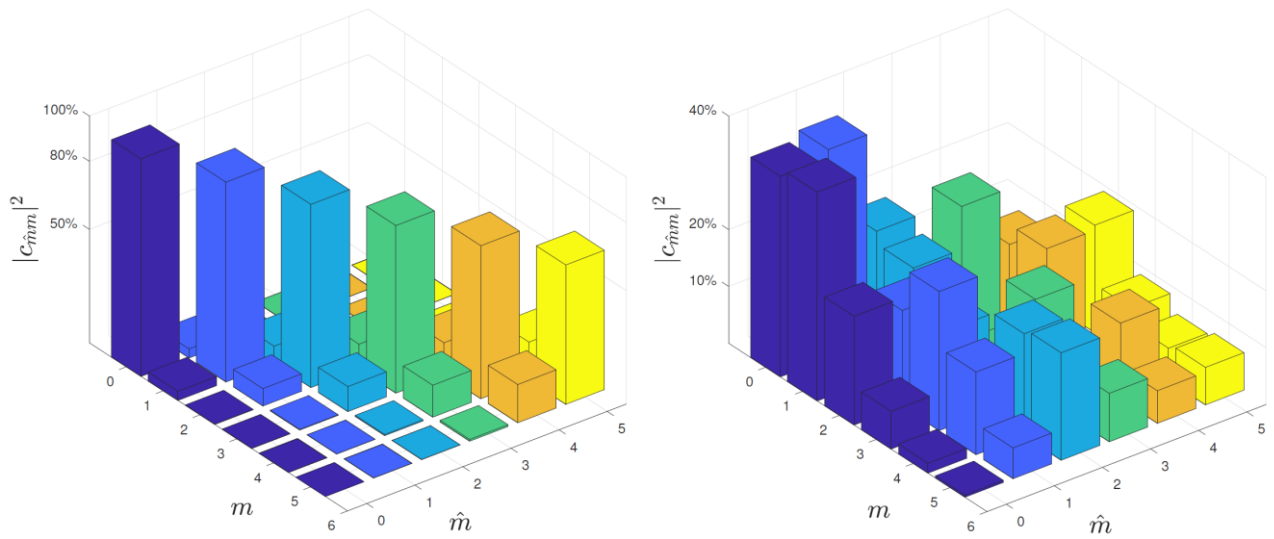
Figure 2: Coupling coefficients for higher order modes by applying an axial misalignment of 1µm (left) and 5 µm (right) for GI-MMF to GI-MMF.
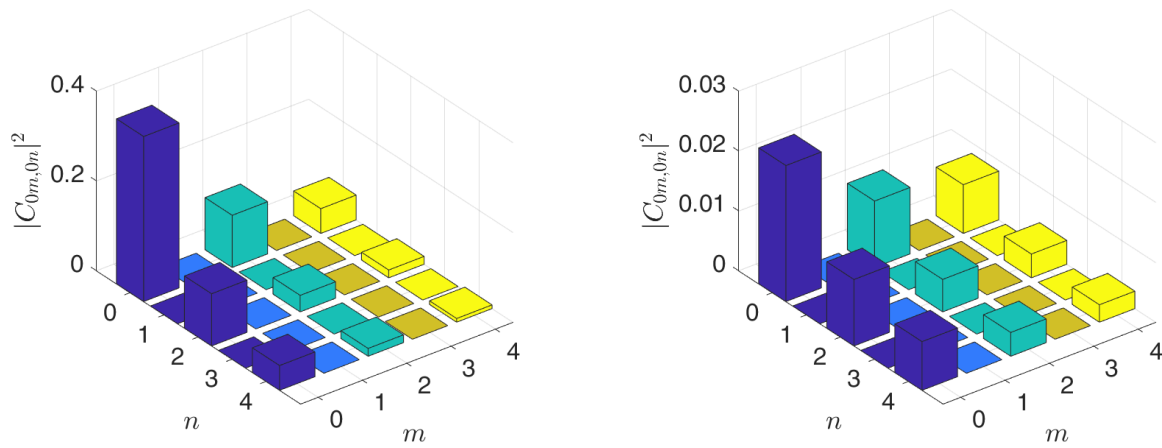
Figure 3: Coupling coefficients for higher order modes by applying a longitudinal misalignment of 365 µm (50 times ω_0, left) and 1822 µm (250 times ω_0, right) for GI-MMF to GI-MMF.

3.2 Results regarding Fresnel reflections

Due to the two ball-lensed fibre couplers, there are 4 air-lens interfaces and 2 fibre-air interface that cause reflections. By using the refractive index of the lens materials and air in-between those, we determined the minimum insertion in table 2. In addition, the calculated reflection loss for butt-coupled fibres with air between the fibre interfaces are 0.25 dB and 0.30 dB for SOF-POF and SOF-SOF, respectively. The refractive index of the lens materials at a wavelength of $\lambda = 1319$ nm were estimated by using the Sellmeier-equation [9].

Table 2: Minimum insertion loss in dB for various lens materials and connector configurations including the SOF-air interfaces.

Lens material	1 lens	2 lenses
Fused silica	2.000	2.485
NBK-7	2.099	2.710
Sapphire	2.606	3.979

For the purpose of calculating a mode dependent insertion loss, the values of table 2 have to be multiplied with the mode dependent coupling coefficients of figure 2 or 3. This process allows for the calculation of all given coupler constellations of lenses and fibres as well as for given misalignments.

3.3 GOF-POF interconnection

Since PFGI-POF and GI-MMF are showing similar fibre parameters in table 1, the coupling conditions between those fibres are comparable. By using two ball lenses (4f imagining system) the magnification factor b was calculated to be $b = 0.97$ %. Thus, by allowing a small imaging fault these ball-lensed couplers are feasible for mode preserving coupling between SOF and PFGI-POF. However, the accurate alignment of the fibres and lenses must be considered critically.

4. Conclusion

We were able to calculate the modal power distributions for axial and longitudinal misalignments in commercially available fibres. In addition to that, the reflection-based insertion losses at optical interfaces were put into perspective. By joining the information of both fields, an easy and powerful tool is achieved to calculate mode power distributions and mode-based insertion losses as well as coupling efficiencies in given optical modes. Finally, it was demonstrated that a 4f imagining system containing of two ball lenses is feasible between SOF and PFGI-POF for mode preserving coupling.

5. References

[1] Wosniok, Aleksander, and Andy Schreier. "Toward investigation of Brillouin scattering in multimode polymer and silica optical fibers." SPIE Optics+ Optoelectronics. International Society for Optics and Photonics, 2017.

[2] Inoue, Azusa, and Yasuhiro Koike. "Proposal of isolator-free optical interconnect using low-noise graded-index plastic optical fiber for pluggable 4K/8K optical interface." IEEE Optical Interconnects Conference (OI), 2017. IEEE, 2017.

[3] Mizuno, Yosuke, and Kentaro Nakamura. "Core alignment of butt coupling between single-mode and multimode optical fibers by monitoring Brillouin scattering signal." Journal of Lightwave Technology 29.17 (2011): 2616-2620.

[4] Shemirani, Mahdieh B., and Joseph M. Kahn. "Higher-order modal dispersion in graded-index multimode fiber." Journal of Lightwave Technology 27.23 (2009): 5461-5468.

[5] Marcuse, D. "Coupled mode theory of round optical fibers." Bell Labs Technical Journal 52.6 (1973): 817-842.

[6] Guenther, B. D. *Modern optics*. OUP Oxford, 2015.

[7] Gloge, D., and E. A. J. Marcatili. "Multimode Theory of Graded-Core Fibers." Bell Labs Technical Journal 52.9 (1973): 1563-1578.

[8] Marcuse, D. "Loss Analysis of Single-Mode Fiber Splices." Bell Labs Technical Journal 56.5 (1977): 703-718.

[9] Schneider, Thomas. *Nonlinear optics in telecommunications*. Springer Science & Business Media, 2013.

Bidirectional Gigabit POF link based on GaN LED and KDPOF Gigabit POF Transceiver

J. Vinogradov[1], R. Kruglov[1], J.-W. Shi[2], R. Engelbrecht[1], O.Ziemann[1]

1 POF-AC, Technische Hochschule Nürnberg Georg Simon Ohm,
  Wassertorstrasse 10, 90489 Nuremberg, Germany

2 Department of Electrical Engineering, National Central University, Taoyuan 32001, Taiwan

*Corresponding author: juri.vinogradov@pofac.th-nuernberg.de

Abstract: This paper shows a bidirectional Gigabit link over 50 m of a 1-mm SI-POF based on novel cyan GaN LEDs and a KDPOF Gigabit POF Ethernet Transceiver (KD-EVK1001MC Evaluation Kit). These LEDs with an active diameter of 75 µm operate at a wavelength of 490 nm and offer a high stability within a wide temperature range. The LEDs provide sufficient fiber-coupled power and a modulation bandwidth to achieve 1 Gbit/s over 50 m SI-POF using KDPOF Gigabit POF Ethernet Transceiver.

1. Introduction

Since some years the company KDPOF offers solutions for Gigabit Fast Ethernet transmission over POF. The KD1000 Family products include Application-Specific Standard Product (ASSP) for home, industrial and automotive networks [1]. The benefit of the KDPOF solution is using a PAM modulation scheme, which allows to use LEDs instead of laser diodes as transmitter. This makes the system cheaper, more robust and complies with eye-safety requirements. To the best of our knowledge the KD-EVK1001MC Evaluation Kit from KDPOF use the optical transceiver from Avago Technologies GmbH, a Broadcom Limited company with the red LEDs operating at the wavelength of 650 nm. [2-4].

Since some years the POF-AC focuses on the data transmission using GaN LEDs operating in the range from 450 nm to 520 nm [5,6]. Operation of POF links within blue and green loss windows can offer a higher power margin due to lower and broader attenuation minima. It provides a better tolerance against spectral drift of the optical source by temperature changes. At the POF Conference 2015 data transmission experiments using KDPOF were shown. The paper [7] shows the use of a green laser diode with KDPOF technology. In this work an error free 1 Gbit/s data transmission over 120 m of MH4002 fiber was achieved. The paper [8] describes the data transmission experiments using 475 nm GaN LEDs with an active diameter of 40 µm. The experiments were carried out with a single media converter operating in loop mode and bit rates up to 850 Mbit/s were achieved over 50 m SI-POF.

This paper describes recent data transmission experiments using novel cyan 490 nm GaN LEDs with active areas of 75 µm. By significantly reducing the number of active $In_xGa_{1-x}N$/GaN quantum wells and the thickness of the barrier layers down to 5 nm, such devices provide a modulation bandwidth up to 1 GHz. [9]. Bit rates of 5.3 Gbit/s and 4.9 Gbit/s over 1 m SI-POF for PAM-4 and NRZ modulation schemes were achieved at 40 mA. This result is not much better than with 40 µm LEDs reported in [5], but the different size of the active area should be taken into account. Compared to the previous LED [8] the new device provides more fiber coupled optical power, which leads to the increase of the output voltage of the receiver. Taking into account the minimum required SNR of 25.4 dB for Gigabit operation at PAM-16 [2], the novel LED provides enough optical power to achieve the given SNR (Table 1). The frequency response of both LEDs is almost identical, but the -3 dB electrical bandwidth is for the new 75 µm LED is slightly higher (Table 1).

Table 1. Parameters of both GaN LEDs

LED	λ [nm]	P_{opt} after 1 m [dBm]	P_{opt} after 50 m [dBm]	Bandwidth [MHz]	SNR [dB]
New GaN	490	-2.16	-6.56	310 [9]	26.2
Old GaN	475	-1.87	-7.00	280 [5]	24.1

Additionally, the chromatic dispersion of a POF at a LED wavelength of 490 nm is slightly lower compared to 475 nm. The pulse broadening after 50 m SI-POF is 1.53 ns [8] and 1.39 ns for 475 nm and 490 nm, respectively. In Table 2 the values for the chromatic dispersion are shown. Since the spectral widths of the both LEDs are identical, the chromatic dispersion depends only on material dispersion, which is lower at 490 nm. For these tests the data transmission in the loop mode and complete bidirectional link using two GaN LEDs was investigated. The LEDs provide a sufficient fiber-coupled power and a modulation bandwidth to achieve 1 Gbit/s over 50 m SI-POF using KDPOF Gigabit POF Ethernet Transceiver.

Table 2. Calculated pulse broadening caused by chromatic dispersion

Distance			50 m	50 m+10 m	50 m+20 m	50 m+30 m	50 m+40 m
LED	$\Delta\lambda$ [nm]	$M_0(\lambda)$ [ps/nm²·km]	Δt [ns]	Δt [ns]	Δt [ns]	Δt [ns]	Δt [ns]
New GaN	35	796	1.39	1.67	1.95	2.22	2.50
Recent GaN	35	875	1.53	1.83	2.14	2.45	2.75

A bit rate of 547 Mbit/s with a 4-PAM modulation format was achieved over 90 m of a 1-mm SI-POF (50 m + 40 m with FSMA connector). In the previous work [8] this distance was unreachable, due to the lower SNR. In order to evaluate the performance, the link was measured with a Gigabit Protocol Tester according to the RFC2544 specification, which allows performing the link at different packet sizes.

2. Setup and measurements

First the link performance was proved in the loop mode according [8]. The GaN LED was modulated over a Bias-T by the KDPOF Media Converter Evaluation Kit at the bias current of 40 mA, Figure 1. The additional attenuator and preamplifier MERA-556+ (Mini Circuits) were required to provide a proper level of the modulation signal. The receiver from Avago Technologies GmbH, [4] was used for this experiment.

The original KDPOF software helps to evaluate the measurements. The system was tested with different lengths of SI-POF Mitsubishi GH-4001 (POF class A4a.2, according IEC 60793-240): 50 m, 50 m+10 m, 50 m+20 m, 50 m+30 m, 50 m+40 m. The fiber segments were connected by FSMA coupling, which adds losses of around 1 dB.
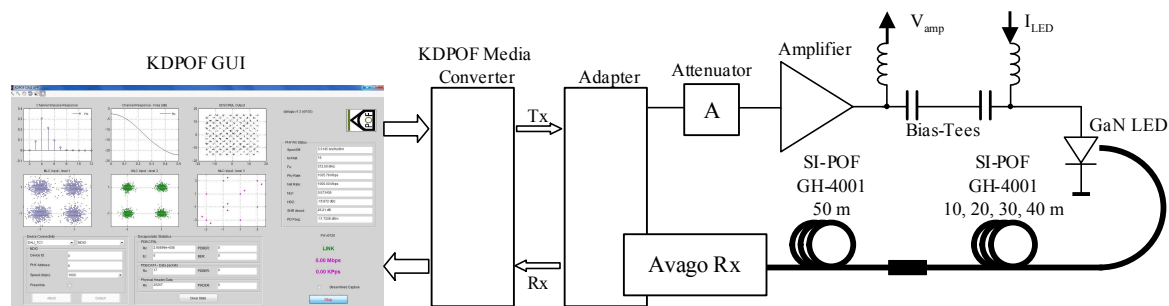
Figure 1. Loop experiment with GaN LED
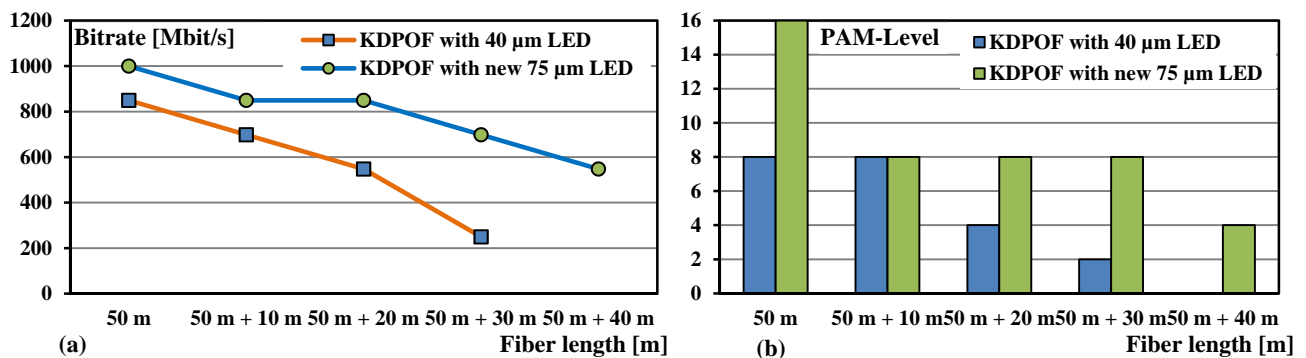
Figure 2. Bit rates (a) and corresponding PAM-level (b)

The measured results are shown in Figure 2. Compared to the previous paper [8] 1 Gbit/s over 50 m SI-POF GH4001 was achieved, which is caused by a higher SNR (Table 1). Even the distance of 90 m offers a moderate bit rate of 547 Mbit/s at the PAM-4 modulation scheme.

The complete bidirectional 50 m link is shown in Figure 3. Other than described above, the additional loss was produced by an optical attenuator. The attenuator was placed after 50 m SI-POF and connected to the receiver from Avago Technologies over the 1 m SI-POF. The received optical power was measured after 1 m SI-POF according to the adjusted value of the attenuator. In this way the link can be characterized depending on the received power.
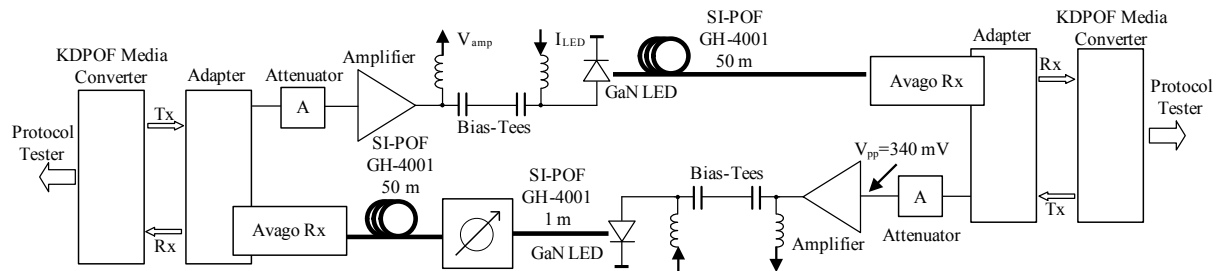
Figure 3. Setup for bidirectional measurements

The Table 2 summarizes the bit rates measured with a protocol tester and the KDPOF software at the different received optical powers. After the distance of 51 m SI-POF and minimal additional loss the received optical power was -7.71 dBm. An increase of attenuation leads to a lower received optical power and thus, decreased PAM modulation level and bit rate. The frame size for the measurement with the protocol tester shown in Table 2 was 1518 Byte and the frame type is according Ethernet II (DIX) [10].

Table 2. Bit rates at different received optical power for the frame size of 1518 Bytes

Fiber coupled optical power [dBm]	Bit rate [Mbit/s] Measured with Prot. Tester at 1518 Byte	Bit rate [Mbit/s] Evaluated with KDPOF Software	KDPOF PAM-Level	Throughput [%]
-7.96	986.99	1000	16	100
-8.93	986.99	1000	16	100
-10.18	838.94	849.15	8	85
-11.94	690.89	698.29	8	70
-14.54	246.74	249.03	2	25

Smaller frame sizes lead to a decrease of the bit rate. Taking into account the overhead of 20 Bits [11] the maximum achieved bit rate for the frame size of 1518 Bytes is 986.99 Mbit/s and for 64 Bytes 761.9 Mbit/s, respectively. These both bit rates correspond to the link throughput of 100 %. Figure 4 shows the bitrates measured by the protocol tester at different received optical powers and frame sizes. At a received optical power between -7.7 dBm and -8.9 dBm the maximum bit rates (throughput 100%) were achieved for any frame size. The bit rates between 220.9 Mbit/s and 246.7 Mbit/s were achieved at the received power of -14.5 dBm depending on the frame size. These correspond to the throughput of around 25%.
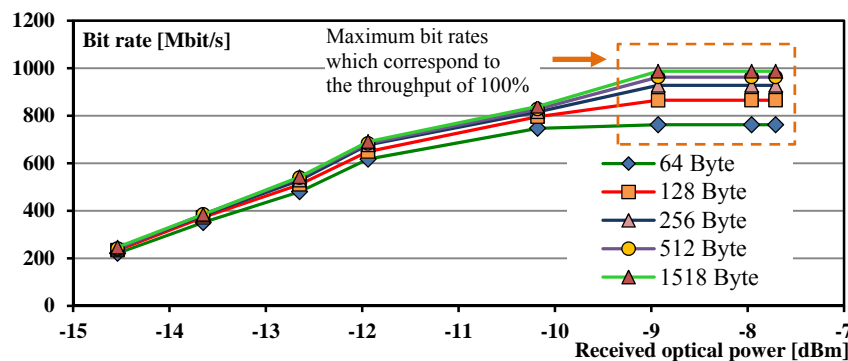
Figure 4. Bit rates measured by protocol tester depending on received optical power and frame size

3. Conclusion

In this paper we have shown the possibility to use GaN 490 nm LEDs for gigabit data transmission using KDPOF technology. The benefit of GaN LEDs is a higher modulation bandwidth and robustness against high temperature [5]. In contrast to the previous publication [8] in this paper the novel GaN LEDs with 75 µm active area were used and 1 Gbit/s over 50 m SI-POF was achieved with 1.2 dB margin. The measurements were carried out with a KDPOF Gigabit POF Ethernet transceiver (KD-EVK1001MC Evaluation Kit) by loop and bidirectional operational mode as well. Using a protocol tester the link was measured taking into account different frame sizes. To the best of the authors' knowledge this is the first demonstration of a bidirectional Gigabit transmission over 50 m SI-POF using GaN LED and KDPOF Gigabit POF Ethernet Transceiver.

4. Acknowledgements

5. Reference

[1] O. Ciordia. C. Esteban. C. Pardo. R. Pérez de Aranda, "Commercial silicon for Gigabit Communication over SI-POF; POF2013; Rio de Janeiro; Brasil

[2] KD-EVK1001-MC Evaluation Kit; User Manual; Revision 2.3; October 2013; www.kdpof.com

[3] http://www.kdpof.com/wp-content/uploads/2012/07/br013e-Automotive_Eval_Kit.pdf

[4] Avago Technologies Data Sheet, "AFBR-59F3Z. Compact 650 nm Transceiver for 1 Gbps Datacommunication MLCC (Multilevel Coset Coded) over POF (Polymer Optical Fiber)", AV02-4655EN - December 17. 2014

[5] J. Vinogradov, R. Kruglov, K.-L. Chi, J.-W. Shi, M. Bloos, S. Loquai and O. Ziemann, "GaN Light-Emitting Diodes for up to 5.5-Gb/s Short-Reach Data Transmission Over SI-POF," IEEE Photon. Technol. Lett.,vol. 26, no. 24, 2473-2475 (2014)

[6] J.-M. Wun *et al.,* "GaN-based miniaturized cyan light-emitting diodes on a patterned sapphire substrate with improved fiber coupling for very high-speed plastic optical fiber communication", *IEEE Photon. J.*, vol. 4, no. 5, pp. 1520–1529, Oct. 2012

[7] V. Goetzfried, T. Lichtenegger, J. Wittl, C. Esteban, Ó. Ciordia: "Gigabit Ethernet over POF (GEPOF) –Latest Status of Technology and Standardization", POF2017. Nürnberg. Germany

[8] J. Vinogradov, R. Kruglov, S.Loquai, J.-W. Shi, O.Ziemann, "GaN optical sources with the KDPOF Gigabit POF Transceiver",POF2017, Nürnberg, Germany

[9] J.Vinogradov et al., "GaN-Based Cyan Light-Emitting Diode with up to 1-GHz Bandwidth for High-Speed Transmission Over SI-POF", IEEE Photonic Journal, Vol. 9, Number 3, June 2017

[10] "Introduction to Ethernet ", The Industrial Ethernet Book, Volume 1, Issue. 3, Fall 1999

[11] IEEE Standard for Etherne, Revision of IEEE Std 802.3-2008, New York, NY 10016-5997 USA. 28 December 2012

WLAN and Multiband LTE-A Simultaneous Transmission over 50m Thick-core GI-POF for In-home Distributed Antenna Systems

F. Forni[1,2*], Y. Shi[2], H.P.A. van den Boom[1], E. Tangdiongga[1], A.M.J. Koonen[1]

1 Institute for Photonic Integration,, Eindhoven University of Technology, P.O. Box 513, 5600MB Eindhoven, The Netherlands.
2 Genexis, Lodewijkstraat 1A, 5652AC Eindhoven, The Netherlands.

*Corresponding author: f.forni@tue.nl

Abstract: An 80MHz, 256-QAM IEEE 802.11ac-compliant WLAN and 9 band 64-QAM LTE-A signals were successfully transmitted over a 50m PMMA GI-POF link. The LTE-A bands were transmitted with radio over POF technique. The WiFi signal was transmitted with an intermediate frequency over POF (IFoPOF) approach due to the POF bandwidth. The IF frequency and the power budget were optimized in order to minimize the EVM penalty induced by the optical link. The total throughput of the LTE-A and WiFi signals were equal to 605 Mb/s and 434Mb/s, respectively. This proves that POF is suitable for multi-standard in-home radio over fiber networks.

1. Introduction

According to CISCO between 2015 and 2020 the share of global Internet traffic generated by PCs is halved to from 67% to 32%, meanwhile the smartphone devices share is triplicated up to 37% and the tablets almost double to 15% [1]. Hence, in few years the smartphones will generate more Internet traffic than PCs and together with the tablet devices, producing more than half of the total traffic. In such scenario the growing momentum of broadband wireless WLAN and mobile networks plays an important role in handling the traffic increase, in particular indoor, where most of the Internet traffic is generated. The present 4G/LTE-A and the envisioned 5G next-generation mobile networks improve the indoor reception, avoiding the poor cell-edge coverage by heterogeneous network technology (i.e. femtocell architecture) and increasing the throughput by multiband transmission. Looking to the WLANs, they play a double role. Firstly, the IEEE 802.11 standard is moving to a wider bandwidth, higher carrier frequency (i.e. 5 GHz and beyond) and higher modulation order (i.e. 256-QAM) to increase the throughput, being considered a wired complement. The latest standard released (IEE802.11ac) is already being supported by more than half of the device nowadays and in 2020 virtually all the devices (96.6%) will support it. Secondly, the data offloading from/to the mobile and WiFi network improves the coverage and throughput of those devices. The 5 GHz carrier frequency of IEEE 802.11ac has nevertheless poor indoor propagation, which results in limited coverage and decreased throughout. The WiFi would take advantage from distributed antenna system spreading the antenna in the in-home building and avoiding the signal propagation through walls. Therefore, it is essential to provide a low-cost wired backbone connecting the centralized residential gateway with the antennas in each room over a cost effective radio over fiber link, as shown in Fig. 1. Plastic optical fibers (POFs) can meet those challenge, bringing the radio signals to each antenna, providing a wired backbone for the wireless connectivity required for in-home networks.
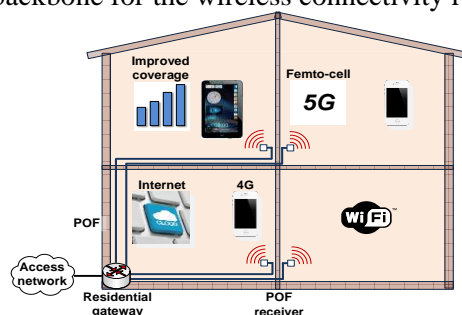
Fig. 1 Illustrative POF network for multi-standard wireless in-home applications.

Our previous work showed that 9 LTE-A bands can be transmitted over a 50m graded index (GI) POF link together with a 4-PAM baseband signal.

In this work, we kept the 9 LTE-A bands and transmitted an IEEE 802.11ac WLAN signal with maximum allowed modulation order and coding rate. The LTE-A bands are transmitted with radio over POF technique, without frequency shifting. The WiFi signal is transmitted with IFoPOF technique due to the POF bandwidth. The downshifted frequency is chosen as such that the interference on the other signals can be reduced and the link gain maximized. The power budget is balanced between the LTE-A and WiFi signal in order to minimize the EVM penalty induced by the optical link.

2. Experimental Setup

We generated 9 LTE-A bands compliant with the 3-GPP test model 3.1 using 64-QAM, as listed in Table 1, and transmitted with the analogue radio-over-POF technique, keeping their original carrier frequencies.

Table 1. LTE-A bands used in the experiments and their most significant parameters.

Parameter	Value								
LTE-A band index	1	2	3	4	5	6	7	8	9
E-UTRA operating band	12	13	14	20	18	19	8	32	24
Carrier Frequency (MHz)	738	751	763	806	868	883	944	1474	1542
Bandwidth (MHz)	10			20	15		10	20	10
Gain of the digital transmitter amplifiers, G_i (dB)	0.4	0.2	0.1	3.45	4.1	4.1	1.25	7.5	5.2
Modulation format	64-QAM								

Hence, the 4G signals are created, equalized, combined, and digital-to-analog converted, as shown in Table 1. The time invariant equalization, described in [2], compensates the low-pass behavior of the POF link, aiming to ensure the same quality of the signal among all the LTE-A bands. The equalization also corrects an impairment on the power of each LTE-A band caused by the LTE-A transmitter.

Table 2. IEEE 802.11ac signal most significant parameters used in the test.

Parameter	Value
Bandwidth (MHz)	80
Modulation format	256-QAM
Coding rate CR	5/6
Guard interval GI (ns)	400
Idle time (µs)	20
Transmitted power (dBm)	-17
IF frequency (MHz)	250

The WiFi signal is generated in accordance with IEEE standard [3], given the parameters in Table 2. The waveform is created by MatLab and generated by the digital-to-analog converter (DAC) of the vector signal generator (VSG), as shown in Fig. 2. A PRBS 2^7-1 sequence is encoded as user data and repeated to fit the payload. The maximum DAC bandwidth limits the WiFi bandwidth to 80MHz. The signal is transmitted over POF with an intermediate frequency. The frequency is has to be within the range of 0-740 MHz before the first LTE-A band. Hence, 250MHz is chosen as IF.
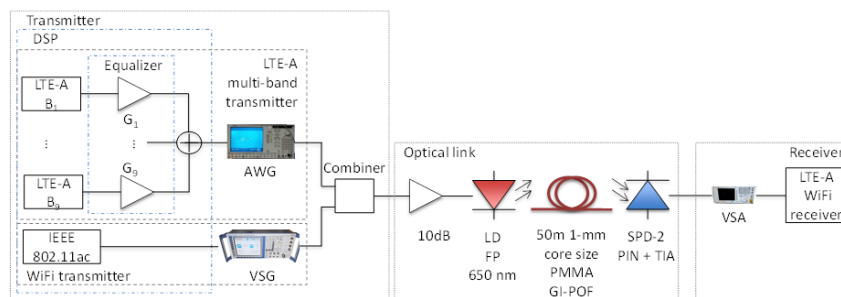
Fig. 2 Experimental setup.

The optical link is an intensity-modulated direct-detection system. The baseband, LTE-A, and WiFi waveforms are combined, boosted by the amplifier in the laser driver, and transmitted by the optical source, as shown in Fig. 2. The optical source is a low-cost Fabry-Perot edge-emitting laser diode (LD). The emitted optical power is 5.7dBm at a wavelength of 650nm and is coupled to 50m of 1mm diameter PMMA GI-POF. The fiber loss is 0.24dB/m at 650nm and the bandwidth distance product is 150MHz · km. The optical receiver is a Graviton SPD-2, consisting of a p-i-n photodiode followed by a transimpedance amplifier.

The received optical power is -8.5dBm and the optical link -3dB electrical bandwidth is 1.1GHz. The signal is given to the vector signal analyzer (VSA), which runs the Keysight VSA software capable to decode both 4G and WiFi ac standards. The WLAN signal is decoded at IF-frequency, the frequency shifting was not implemented. The LTE-A EVM is calculated for each subcarrier and averaged, the measurements are repeated 20 times and the maximum value is considered. The WiFi EVM is route mean square averaged over 21 acquisitions.

3. Experimental Results and Discussion

(a)   (b)
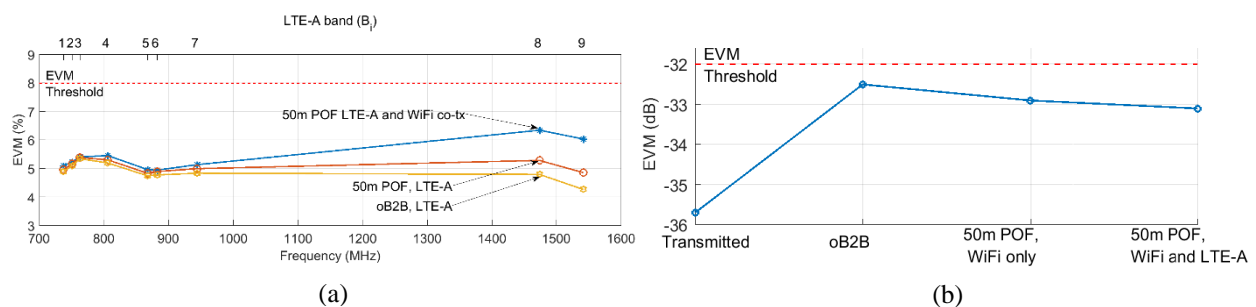
Fig. 3 LTE-A (a) and WiFi (b) EVM experimental results.

The LTE-A experimental results are shown in Fig. 3(a). As indicated by [4], the 64-QAM LTE-A signal is required to have an error vector magnitude (EVM) lower than 8% at the antenna port, which would be after the POF link. The optical back-to-back (oB2B) and 50m POF LTE-A solitary transmissions are also depicted for comparison. In both the cases, the EVM is around 5%, notably the band 8 and 9 have the same EVM as the lower frequency bands, on account of the equalization. The LTE-A bands 8 and 9 have slightly lower EVM in the oB2B than the 50m link, related with the difference frequency response of the links at that frequency.

When the WiFi signal is co-transmitted, 2 different behaviours can the seen for the LTE-A signals: the bands 1, … 7, do not show any EVM degradation while band 8 and 9 show a small EVM penalty of 1%. Still in the same case, the LTE-A EVM is around 5.5 % up to 6.4% for band 8. All the 9 LTE-A bands have EVM lower than 8%. Moving to the WiFi transmission, the IEEE 802.11ac standard defines the EVM performance in logarithmic scale and requires an EVM lower than -32dB to use 256-QAM, coding rate (CR) 5/6 modulation scheme. As depicted in Fig. 3(b), the WLAN solitary transmission has an EVM at the transmitter port close to -36dB, whereas after the oB2B the EVM is slightly higher, up to -33dB. Moving to the 50m POF link, in all the cases the WiFi signal has EVM close to -33dB. No EVM penalty is shown for the 50m POF transmission compared with the oB2B, meanwhile the penalty between the transmitted and received EVM is around 3dB. After the POF link, a 1dB margin is available for further amplification.

(a)   (b)   (c)
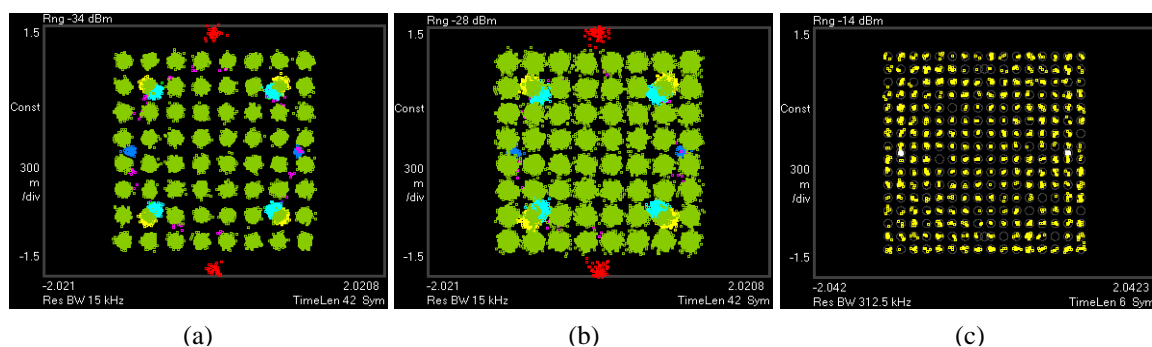
Fig. 4 LTE-A band 1 (a), band 8 (b), and WLAN (c) constellation diagrams. The user downlink channel with 64-QAM (green marks) and control channels (yellow, light blue, purple and dark blue) are shown for the LTE-A signals.

The constellation diagram of the LTE-A and WLAN signals are also considered. As shown in Fig. 4, no phase noise or amplification compression are observed. The broader point spreading of constellation points for the LTE-A in Fig. 4(a) and (b) compared with the WLAN in Fig. 4(c), is related with the higher EVM.

In this paper, we propose a multi-standard distributed antenna system using frequency division multiplexing. 9 LTE-A bands and an IEEE 802.11ac WLAN signal are transmitted with maximum modulation order and coding rate, over 50m of 1mm core diameter PMMA GI-POF. Both the LTE-A and WLAN signals have EVM lower than the respective requirements, according with the standards.

The EVM increase of the LTE-A band 8 and 9 might be related with intermodulation distortion, for which further investigation will be carried out.

Looking to the WLAN transmission, the maximum modulation order and coding rate are used. The transmission bandwidth is limited by the available vector signal generator to 80MHz.

The small penalty between the transmitted and received WiFi EVM might suggest that the VSG might limit the single-to-noise ratio and better EVM could be reached by employing a VSG optimized for the 256-QAM transmission.

Object of further improvement will be the simultaneous transmission of the IEEE 802.11n radio signal to cover the most promising in-home WLAN wireless connectivity standards.

4. Conclusion

In this work, we achieved the successful transmission of 9 LTE-A bands and an IEEE 802.11ac WLAN signal with maximum allowed modulation order and coding rate. The multiband LTE-A signals are transmitted with radio over POF technique. The WiFi signal is transmitted with an intermediate frequency over POF. The total throughput of the LTE-A and WiFi are equal to 605Mb/s and 434 Mb/s, respectively. This work demonstrates the suitability of POF for in-home networks employing next-generation and advanced wireless signal formats.

5. Acknowledgements

6. References

[1]   CISCO, "The Zettabyte Era: Trends and Analysis," *Cisco*, no. May 2015, pp. 1–29, 2015.

[2]   F. Forni, Y. Shi, H. P. A. Van Den Boom, E. Tangdiongga, and A. M. J. Koonen, "SINR-based Equalization for Multiband LTE-A and Gbps 4-PAM Transmission over 50m Thick-core POF and Wireless Link," in *OFC/NFOEC 2017- Optical Fiber Communication and the National Fiber Optic Engineers Conference 2017*, 2017.

[3]   I.-S. S. Board and Authorized, *Specific requirements Part 11 : Wireless LAN Medium Access Control (MAC) and Physical Layer (PHY) Specifications Amendment 4 : Enhancements for Very High Throughput for Operation in Bands below 6 GHz IEEE Computer Society*. New York, NY, 2013.

[4]   3-GPP, "LTE Evolved Universal Terrestrial Radio Access (E-UTRA); Base Station (BS) radio transmission and reception (3GPP TS 36.104 version 9.13.0 Release 9)," 2011.

Low-cost pressure sensor embedded in mattress

D. Sartiano*, J. Madrigal and S. Sales

Institute of telecommunications and multimedia applications (iTEAM), Universitat Politècnica de València, Camino de Vera, s/n 46022 Valencia SPAIN

*Corresponding author: desar@teleco.upv.es

Abstract: The aim of this paper is to report the design of a low-cost plastic optical fiber based pressure sensor, embedded in a mattress. Many research works presented POF sensors based on intensity variations due to bending. In this paper, we report the design of a multipoint sensor, a low-cost alternative to the most common plastic fiber sensors. The sensor is implemented using an Arduino boards, standard LEDs for optical communication in POF (λ=645 nm) and CMOS linear sensors. The Super ESKA® was used to implement the fiber intensity sensor, arranged in a 4x4 matrix.

1. Introduction

The development of optical fiber sensors started during the '70s, since these years, the research was mostly focused on glass optical fiber sensors. Research leads to fiber sensors for strain and temperature, and the developing of distributed sensors through the inscription of gratings or exploiting nonlinear optical effect (e.g. Brillouin scattering based sensors). These sensors have a wide range of applications from structure health monitoring [1] to wearable for medical purposes [2]. Wearable fiber sensors have the advantage to be immune to electromagnetic field, make them useful, for example, to monitor patients during diagnostic procedures in presence of high electromagnetic field, as during magnetic resonance imaging [3]. POF application is growing in wearable sensors field, since their mechanical properties make them completely embeddable in textile; some studies prove that they can be process in high volume textile production, manufactured and integrated as either weft or warp in the weave [4]. Many research works present POF sensors based on intensity variations due to bending, this approach permits to implement low-cost bending sensor [5]; the inscription of gratings is an expensive process as well as the instrumentation to interrogate a fiber in reflection, as it is done in Brillouin/Rayleigh scattering sensors [6], [7]. In this paper, we report the design of a multipoint sensor, embedded in a mattress. Sensors in mattress permit to monitor the patient without requiring the user to wear anything [8], they are commercialised as diagnostic devices capable to monitor sleep phases [9] and patients that suffer of nocturnal apneas [10], [11].

2. Sensor implementation

In the next paragraphs, design and implementation of the fiber sensor are carried out. This section is divided in three subparagraphs: the first describes the light sources and the modulation, the second the photodetectors and the distribution of the fibers in a matrix, and the third the signal processing of the optical power data.

2.1 LED and current driver

The LEDs used are the IF E96E, low-cost visible red LEDs for optical communication in plastic fibers (cross section in figure 1, left). Each LED is driven by a current driver, reported schematically in figure 1 right.
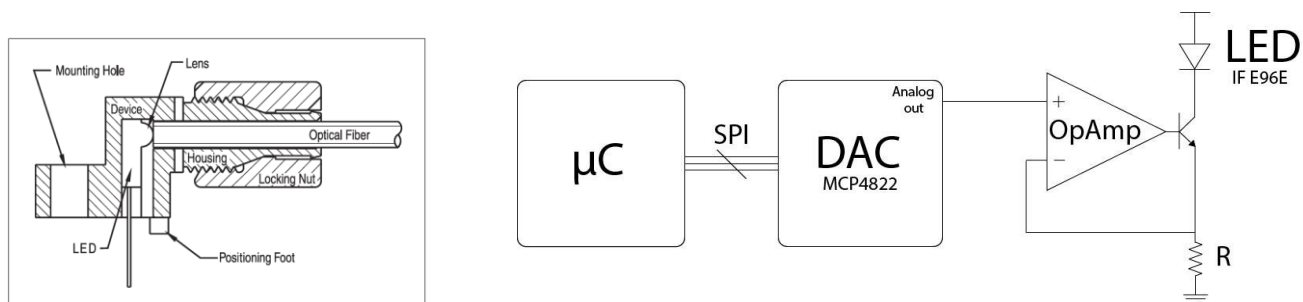
Figure 1: Left, cross section of IF E96E, the LED used to inject light in the fiber. Right, schematic of the LEDs current driver

The microcontroller communicates with an external 12-bit DAC through a SPI interface. The value between 0 and 4096 ($2^{12\ bit}$), is converted in an analog voltage that fix the current flowing into the LED, thanks to the feedbacked analog circuit, implemented with a general-purpose operation amplifier (OpAmp), a bipolar transistor and a resistance. Light is sent into the fibers in the form of a pulse of fixed duration. The duration of the pulses was chosen to maximize the full-scale range of the system. The lower pulse width is limited by the maximum operating frequency of the analog stage and of the LED (maximum operate frequency 50 Mbps); the upper limit of the duration was chosen in order to not saturate the photodiodes.

2.2 Fibers and photodetectors

The photodetectors array is the TSL1402R (figure 2, left), a linear array of 256 photodiodes. The charge of the photodiode is converted to a voltage into the pixel and the single voltage values are outputted serially. The fibers are the industrial plastic fiber manufactured by Mitsubishi, the Super ESKA®. A plastic component was specifically designed to bottom coupled the fibers ends to the light sensor, and therefore 3D printed (figure 2, right, entire piece and cross section).
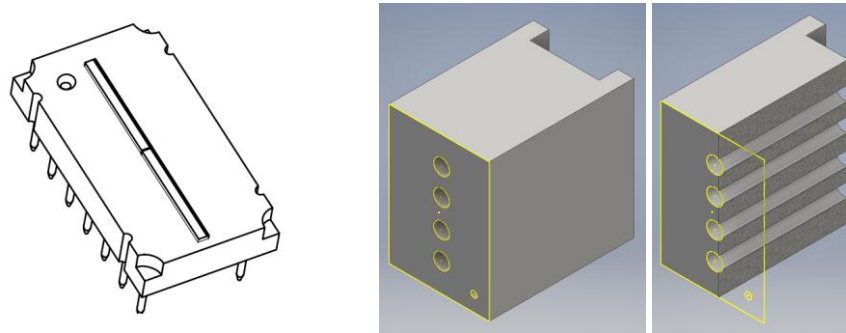
Figure 2: Left, top view of the linear CMOS sensor. Right, plastic support for bottom coupling between POFs and sensitive area of the light sensor.

The customized coupler holds the end of the fiber in front of the sensitive area of the linear sensor and insulates photodiodes from the ambient light that could influence the measurement. Light energy impinging on a pixel generates photocurrent, which is then integrated by the active integration circuitry associated with that pixel. The amount of charge accumulated at each pixel is directly proportional to the light intensity on that pixel and the integration time. The charge stored is sequentially connected to a charge-coupled output amplifier that generates a voltage on analog output. The output voltage of the sensor is converted through the build-in ADC of the Arduino board. The digital value of the 10-bit ADC is directly proportional to the optical power irradiated at the end of the fiber, according to the formula:

$$Digital\ output = (P * R_e * 10^{n\ bit})/V_{DD} \qquad (1)$$

Where P is the optical power density, R_e the responsivity of the sensor, $n\ bit$ is the number of bit of the ADC and V_{DD} the high analog voltage level. Different techniques were presented to make "sensitive" the POFs to bending: abrading part of the cladding [12], [13], using a solvent that can attack the cladding without damaging the core [5]. We focus in finding a technique that can be reproduced in high-volume production; we have developed a cutting technique that allows us to produce cuts in the fibers of approximately the same depth. Therefore, the fibers were arranged in a matrix with the cuts positioned in the crossing points (figure 3) and embedded in a mattress cover sample.
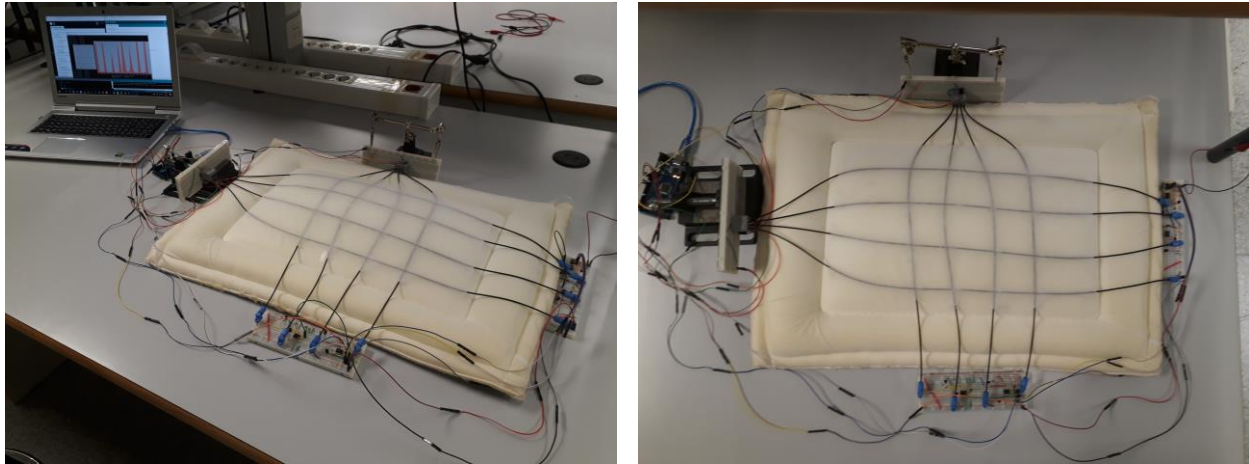
Figure 3: Experimental setup; the fibers were arranged in a matrix with the cuts positioned in the crossing points.

2.3 Data processing and user interface

The figure 4 (right) presents the user interface and the graphic response to a pressure applied in one of the matrix corner. The plot on the right shows the output of the two photodetectors arrays. On the x axis, there are the pixel numbers, on the y axis the output of the ADC. The red peaks are the light detected at the fibers ends; the software implemented in the microcontroller identifies the position of every single fiber coupled to the photodetectors array (e.g. for fiber 1 the initial pixel is number 2 the last is pixel 24 and the average optical power is 686). The software averages the optical power at the fiber end; this permits to implement an intensity sensor more insensitive to the optical power fluctuation due to the electronic noise and to the non-perfect fiber-photodetectors coupling, that could directly influence the voltage level at the input of the ADC. The red numerical values are the threshold for every single fiber, when the optical power goes below this value mean that a pressure is applied on a sensitive point. The plastic fibers, often, do not recover completely after a pressure is applied, a software correction was implemented in order to have dynamic thresholds, that permits to discern between a constant offset in the light power, due to fibers plastic deformation, and a light attenuation due to an applied pressure. The software assigns two fibers to a crossing point, creating the 4x4 pressure matrix. As shown in figure 4, applying a pressure in one of the point of the matrix causes higher losses in the two crossing fibers.
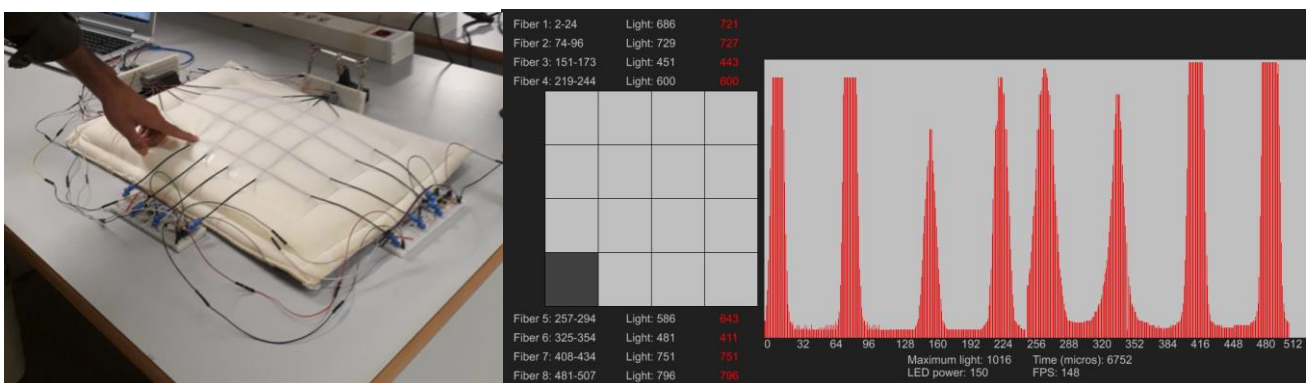
Figure 4: User interface and a demonstration of the effect of a pressure applied to one point of the matrix.

3. Conclusion

This work focuses on finding a cost-effective implementation of a pressure sensor. Finally, it was possible to design a sensor using standard electronic components and an Arduino board. The most common fiber sensors are used for high distance distributed sensor, and expensive and voluminous interrogation systems are needed. This work wants to be part of the actual evolution of fiber sensors for short distance, that is a growing trend for example for wearable application. The compact interrogation system implemented permits to embedded this sensor, not only in a mattress, but even in clothes or used for other applications where volume and weight are important concerns in the sensor design. The microcontroller and the software for the signal processing are the core of the sensor, since permits to adjust the variations in pressure detection due to intrinsic effect in POF (such as the plastic deformation) and to simplify the preparation of the fiber (for example allow a coarser precision cutting the fibers in the sensitive point). Thus, allowing to design a cheap, compact sensor.

Acknowledgment

References

[1] Majumder, Mousumi, et al. "Fibre Bragg gratings in structural health monitoring—Present status and applications." *Sensors and Actuators A: Physical* 147.1 (2008): 150-164.

[2] Grillet, Augustin, et al. "Optical fiber sensors embedded into medical textiles for healthcare monitoring." *IEEE Sensors Journal 8.7* (2008): 1215-1222.

[3] De Jonckheere, Julien, et al. "OFSETH: optical fibre embedded into technical textile for healthcare, an efficient way to monitor patient under magnetic resonance imaging." *Conference proceedings: Annual International Conference of the IEEE Engineering in Medicine and Biology Society. IEEE Engineering in Medicine and Biology Society. Annual Conference.* Vol. 2007. 2006.

[4] Benjamin Mohr, Markus Beckers, "Textile Integration of POF for lighting applications". *Conference proceedings: 25th International Conference on Plastic Optical Fibres (POF 2016)*

[5] Grassini, Sabrina, et al. "Design and deployment of low-cost plastic optical fiber sensors for gas monitoring." *Sensors* 15.1 (2014): 485-498.

[6] Husdi, Irwan Rawal, Kentaro Nakamura, and Sadayuki Ueha. "Sensing characteristics of plastic optical fibres measured by optical time-domain reflectometry." *Measurement Science and Technology* 15.8 (2004): 1553.

[7] Ricchiuti, Amelia Lavinia, et al. "Long fiber Bragg grating sensor interrogation using discrete-time microwave photonic filtering techniques." *Optics express* 21.23 (2013): 28175-28181.

[8] T. Simonite, "Sleep Sensor Hides Beneath the Mattress." Retrieved from https://www.technologyreview.com/s/426073/sleep-sensor-hides-beneath-the-mattress/

[9] *Beddit.* Retrieved from http://www.beddit.com/

[10] Nam, Yunyoung, Yeesock Kim, and Jinseok Lee. "Sleep monitoring based on a tri-axial accelerometer and a pressure sensor." *Sensors* 16.5 (2016): 750.

[11] C. Gullo, "Bam Lab: Mattress monitor for heart rate, sleep apnea." Retrieved form http://www.mobihealthnews.com/14561/bam-lab-mattress-monitor-for-heart-rate-sleep-apnea

[12] Babchenko, Anatoly, and Jonathan Maryles. "Graded-index plastic optical fiber for deformation sensing." *Optics and lasers in engineering* 45.7 (2007): 757-760.

[13] Kuang, Kevin SC, Wesley J. Cantwell, and Patricia J. Scully. "An evaluation of a novel plastic optical fibre sensor for axial strain and bend measurements." *Measurement Science and Technology* 13.10 (2002): 1523.

Angle and Skewness dependent Scattering and Attenuation Measurement of Step-Index Polymer Optical Fibers

T. Becker[1*], B. Schmauss[2], M. Gehrke[1], E. Nkiwane[1], R. Engelbrecht[1] , O. Ziemann[1]

1 Polymer Optical Fiber Application Center, Technische Hochschule Nürnberg, 90489 Nürnberg, Germany
2 Institute of Microwaves and Photonics (LHFT), Friedrich-Alexander-Universität Erlangen-Nürnberg, 91054 Erlangen, Germany

*Corresponding author: thomas.becker@pofac.th-nuernberg.de

Abstract: When light propagates through a step-index polymer optical fiber (SI-POF) its angular power distribution is influenced by attenuation and scattering. Both influences depend on the propagation angle θ_z between the ray and the optical axis. However there is an additional dependency on the angle θ_φ which describes the skewness of a ray. While the skewness of a ray is known to affect attenuation and scattering for that ray, its influence is neglected in common modelling approaches. However the consideration of the skewness is important, since the power distribution in a SI-POF over θ_φ strongly depends on the launching condition. Furthermore no skewness-dependent attenuation and scattering data are available for SI-POF. We present a measurement setup which allows us to retrieve scattering and attenuation data for SI-POF depending on both θ_z and θ_φ along with results that prove the influence of the skewness. The obtained results can be included in a novel propagation model that respects the skewness of a ray.

1. Introduction

1.1 Mode groups

As proposed by Snyder and Love [1] a ray's propagation direction can be defined by a set of angles θ_z, θ_φ and α as depicted in Figure 1. θ_z is the angle between the ray and the fiber's axis. θ_φ defines the ray's skewness and α is the angle between the ray and the normal to the surface at the point of reflection. Since the three angles depend on each other according to

$$\cos(\alpha) = \sin(\theta_z)\sin(\theta_\varphi), \tag{1}$$

considering only two of them is sufficient. Based on these angles every ray can be assigned to a group of modes (Figure 2) which differ from each other in scattering and attenuation. The modes which suffer the lowest attenuation are guided modes which occur for $\alpha > \alpha_{min}$ and $\theta_z < \theta_C$. If α however is larger than α_{min}, the mode is called a tunneling mode. Even though tunneling modes fulfill the critical angle for the total internal reflection, they face a higher attenuation due to an effect called frustrated total internal reflection which is caused by the curvature of the core cladding interface. The last possible group are refracted modes for which α is smaller than the minimum angle for the total internal reflection α_{min}. A part of the ray's power is refracted into the cladding with every reflection and these modes are therefore called refractive modes. The reflected part of the power is so small its contribution to the impulse response of a fiber is negligible even for short fiber lengths.
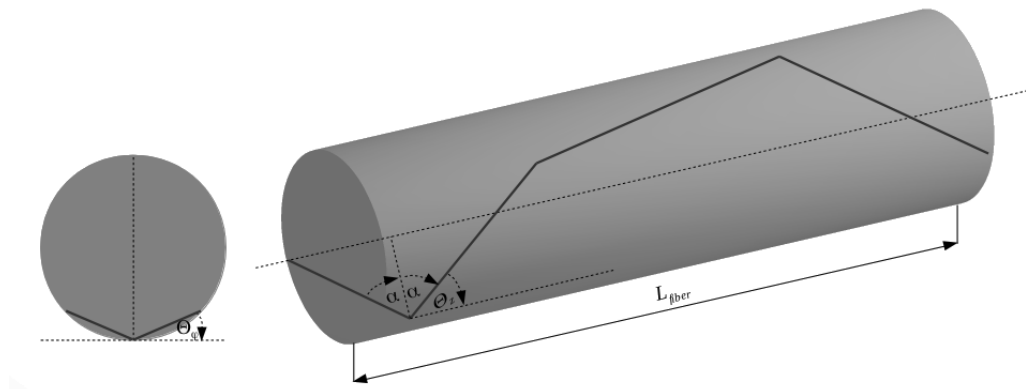
Figure 1. Propagation angles inside a fiber
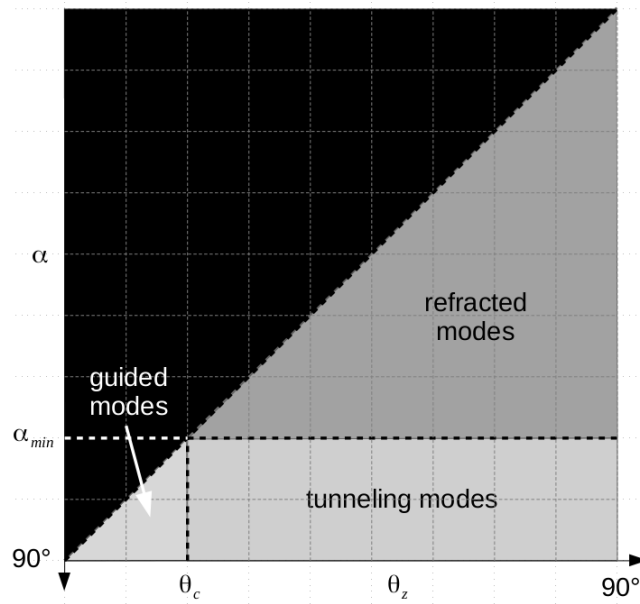
Figure 2. Mode groups

1.2 Intention of the measurement

While the skewness of a ray is known to affect attenuation and scattering for that ray, its influence is usually neglected in common modelling approaches like the power flow equation [2]. Other approaches like ray tracing do not distinguish between guided and tunneling modes. However the proper consideration of the skewness is important as well, since the power distribution in a SI-POF over θ_φ strongly depends on the launching condition as we have shown before [3]. The power distribution in turn affects the impulse response of the whole transmission system and determines the suitability of the system for both data transmission and analog sensing applications [4-5]. A novel fiber model that respects the power distribution over θ_φ is currently being developed at the Polymer Optical Fiber Application Center (POF-AC) in order to improve the modelling of the transmission behavior of SI-POF. This paper presents the measurement technique used to obtain the scattering and attenuation data for that model.

1.2 Separation of scattering and attenuation

While the process of scattering inside a SI-POF contributes to its attenuation, other effects, like absorption, do so as well. It is therefore coherent that scattering and attenuation are usually considered two different effects. For example the power flow equation uses separate coefficients for scattering and attenuation and ray tracing tools like *Synopsis LightTools*[1] expect the user to define scattering and attenuation separately. However since both effects always occur in conjunction, the separate measurement of scattering and attenuation is not feasible and fortunately not important for our purpose. In order to gain a realistic model the distinction between both effects is not necessary since they never occur individually. The results of the presented measurement are therefore combined scattering and attenuation data and the aforementioned novel model is capable of processing this kind of data.

2. Measurement setup

In order to retrieve scattering and attenuation data that depend on both angles θ_z and θ_φ a launching condition, which ideally allows us to excite discrete combinations of both angles, is necessary. If a SI-POF is excited with that kind of launching condition, one can determine the combined scattering and attenuation data for that specific angle combination by evaluating the far field at the end of the fiber. In order to determine correct values for the

---

[1] http://optics.synopsys.com/lighttools/

attenuation, the far field camera has to be able to measure absolute power distributions. For this purpose we use the *Imaging Sphere for Luminous Intensity Measurement (IS-LI)* by *Radiant Vision Systems*[2].

2.1 Basic setup and excitation of discrete θ_z

Figure 3 shows the basic measurement setup. The light source is a laser diode with a wavelength of 660 nm which is used to excite a single-mode glass optical fiber (GOF) with a numerical aperture of $NA = 0.1$. The emitted light at the end of the fiber is collimated with a microscope objective ($f = 10$ mm). The resulting collimated beam has a Gaussian near-field distribution with a full width at half maximum (FWHM) of about 1.5 mm and can therefore be used to excite the full area of the front of a SI-POF whose scattering and attenuation should be examined. The single-mode GOF and the collimating lens are attached to a fiber mount which in turn is mounted on a turntable. The fiber mount is adjusted that the central axis of the collimated beam passes the center of the turntable. The front surface of the fiber under test is also positioned in the center of the turntable. With this setup, the full front surface of the fiber can be excited with discrete angles θ_z. As mentioned before the scattering and attenuation of the examined fiber is evaluated with a far field camera.
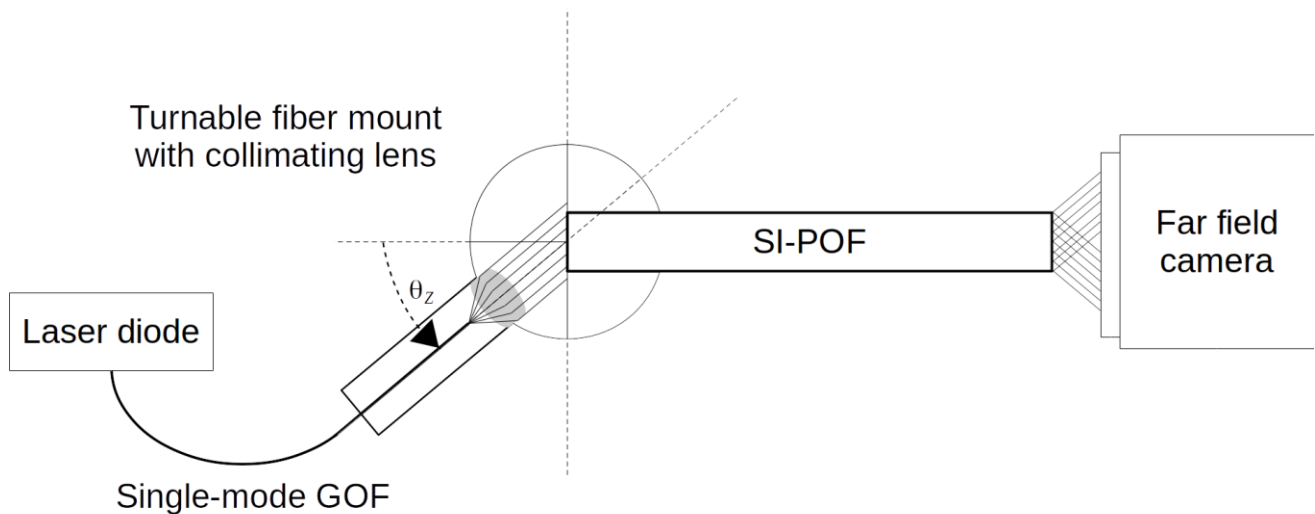
Figure 3. Basic measurement setup

2.2 Variation of θ_φ

The excitation of discrete angles θ_φ is unfortunately not as simple as it is for θ_z. As we have shown in [3] the skewness θ_φ for a ray inside a multimode fiber can be derived from its direction and the position on the fiber's front surface where the ray enters the fiber (see Figure 4). Therefore, the limitation of the excited area results in a limited θ_φ range. One option would be the application of a small diameter circular aperture, which, as a drawback, causes diffraction. The side lobes of the diffraction pattern would not only spoil the narrow θ_φ range but also the discrete angle θ_z. However one detail we can take advantage of can be seen in Figure 4. If we assume that the direction of the incident rays is fixed (from left to right), it can easily be seen that θ_φ depends on the distance a. Therefore, a discrete angle θ_φ can be excited if all incident rays have the same distance a from the top of the fiber. The horizontal position of the ray is not relevant.

If we cover a part of the fiber's front surface with a blade (Figure 5), we can reduce the possible range for θ_φ by moving the blade from the upper edge of the surface to its lower edge. Since the possible θ_φ ranges are symmetric for the upper and the lower half of the surface, it is sufficient to vary the position of the blade only in the lower half of the surface. Of course the lower limit of the θ_φ range is always 0. In order to obtain scattering and attenuation data for arbitrary θ_φ ranges, one can perform two measurements. In the first measurement, the blade is positioned for the desired upper θ_φ limit and in the second for the lower θ_φ limit. The difference between both measurements corresponds to the desired excitation range.

---

[2] http://www.radiantvisionsystems.com/

It should be mentioned that the application of the blade causes a certain amount of diffraction also. The resulting diffraction pattern is not as simple as the ones for small circular apertures or diffraction gratings and can be described by the Cornu Spiral and depend on the distance between the blade and fiber as well as on the distance from the blade in the direction of a. For our measurements we choose a step width for the blade of $a_b = 5$ μm. The distance between the blade and the fiber d_b is set to 50 μm since simulations show that the combination of both values lead to a limited influence of the diffraction.
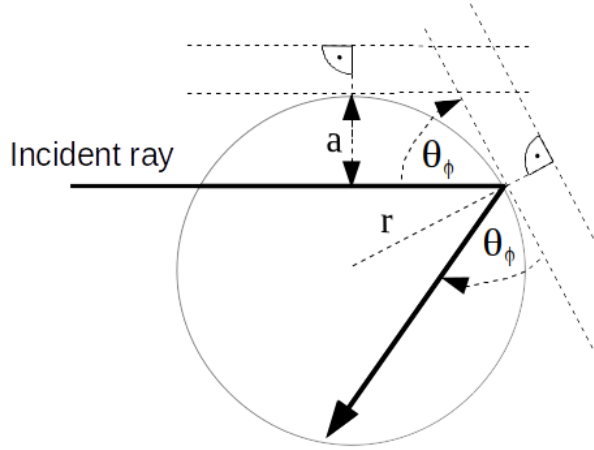
Figure 4. Skewness of an incident ray
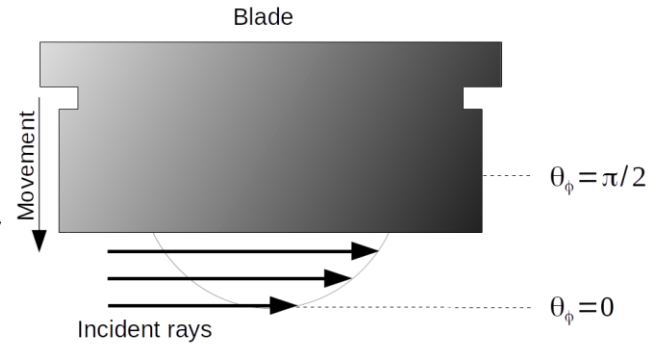
Figure 5. Covering the front surface of the fiber

2.3 Preparation of the fiber

In this paper we want to examine the attenuation and scattering properties that are intrinsic to the fiber. There are however other influences on scattering and attenuation which we want to exclude. Polymer optical fibers are usually shipped and stored on a spool. Therefore, the fiber has a tendency to take a curved shape and forcing it into a straight shape would induce mechanical stress. In both cases the optical properties of the fiber are affected. In order to get rid of these influences the fiber under test is tempered before the measurement. The fiber is hung up with a small weight to straighten it. Then it is heated up to a temperature of 85 °C for three hours. After cutting the weight, the fiber is heated for three more hours to get rid of stress induced by the weight. The result is an almost perfectly straight fiber. The results of the temper process depend on the chosen values for temperature, time and weight and are discussed in [6]. To make sure the fiber stays straight during the measurement, it is embedded in special aluminum fiber mount which has a rectangular notch that fits the fiber's diameter.

Another parameter that has to be defined is the length of the measured fiber. The influence of scattering and attenuation on the angular power distribution has no linear dependency on the length of the fiber. It is therefore not possible to predict the behavior of short fibers from the measurements of long fibers. On the other hand the measurement setup requires a certain minimum length of the fiber due to the mechanical components necessary for the proper alignment of the fiber. The minimum achievable fiber length with our setup is 16 cm.

2.4 Recreation of the θ_φ distribution

So far we have shown how discrete angles θ_z and narrow ranges for θ_φ can be excited. The utilized far field camera however can only capture the resulting angular power distribution over θ_z. The distribution over θ_φ and therefore the difference to the original distribution is unknown. In this paper we limit ourselves to the observation of the θ_z distribution. If the θ_φ distribution has to be maintained, several approaches are conceivable. A simple option would be to assume radially symmetrical scattering around the ray's original direction and consider the measured θ_z distribution to be a two dimensional cross section. A more sophisticated approach would include the measurement of a fiber of double the length of the original fiber (32 cm). It can then be tried to recreate the resulting scatter distributions by combinations of the data retrieved for the 16 cm fiber.

3. Measurement

For this paper we perform the described measurement for a fiber of the type *Asahi DC-1000* with a length of 16 cm.

3.1 Processing the retrieved data

The far field camera captures absolute power density distributions over the solid angle which have to be converted to two dimensional power distributions over θ_z. From the previous chapters it can clearly be seen that not all excited θ_z /θ_φ combinations receive the same power. In order to retrieve correct scattering and attenuation distributions we have to apply a few corrections to the measured data.

Fresnel reflections

Fresnel reflections occur at the front of the fiber as well as at its end. Both contribute to the measured attenuation and have to be taken into account.

Excited area

While the step width of the blade has a constant value of 5 µm, the excitable area of the fiber gets smaller for higher values of θ_φ.

Laser near field

As mentioned before, the radial power distribution of the collimated laser beam has a Gaussian shape. The total power of the laser for each θ_z /θ_φ combination has to be calculated individually.

3.2 Results

Before looking at the results it should be mentioned that besides the angle θ_z also the angle θ_{z0} is used. Since the angle between a ray and the fibers axis changes when it enters the fiber, we use θ_{z0} to describe this angle outside the fiber and θ_z inside the fiber. Figure 6 shows the measured power distributions for different angles θ_z / θ_{z0} and blade positions a. The blade position of $a = 0$ µm means that the blade covers the full upper half of the fiber's front surface. With increasing a values the blade moves downward. The depiction shows the power distribution for $0 \leq \theta_{z0} \leq 85°$ in 5° steps. The measurement was performed with a step width of 1° but for illustration purposes we show only a small set of the retrieved data. While the Fresnel losses are already removed, the data is still affected by the inhomogeneous laser near field and the blade position dependent excitation area.
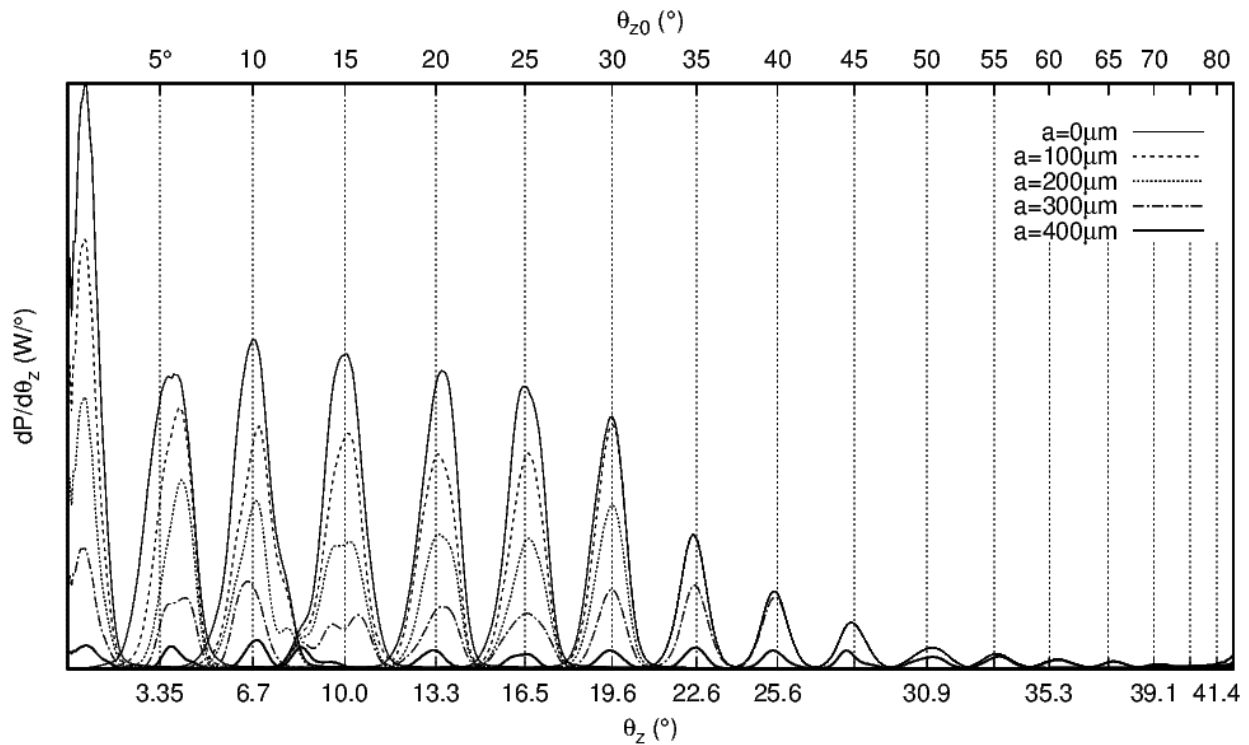
Figure 6. Power distributions over θ_z

The examined fiber has a numerical aperture of $NA = 0.5$ which corresponds to a maximum guided angle $\theta_{c0} = 30°$. As it can be seen, the total power of the scattering distributions drops significantly when this angle is exceeded. By definition rays beyond θ_{c0} are not guided anymore and belong either to the group of tunneling or refracted modes. The higher θ_z, the more power is coupled into refracted modes and the less is coupled into tunneling modes. We have shown in the previous chapter that the possible θ_φ range depends on the blade position a. The corresponding ranges in this example are listed in the Table 1.

a (µm)	$\theta_{\varphi,max}$ (rad)	$\theta_{\varphi,min}$ (rad)
0	$\pi/2$	0
100	1.37	0
200	1.15	0
300	0.91	0
400	0.62	0

Table 1. Blade dependent skewness

An interesting detail is also visible in Figure 6. Despite the fact that higher angles suffer from more attenuation, the shapes of the scattering distributions get smoother and more symmetric. For lower angles the distributions show slight deformations which get worse for increasing blade positions. This is especially pronounced for $\theta_{c0} = 15°$.

3.3 Integrated power distributions

From the two dimensional power distributions shown in Figure 6, we can subtract two measurements for neighboring blade positions to receive the power distribution for a specific $\theta_z / \theta_\varphi$ combination. In a final step the inhomogeneous laser near field and the blade position dependent excitation area are corrected. Figure 7 shows the integrated power of all retrieved power distributions. Since the power distributions are normalized, the maximum power is 1. We can clearly distinguish the three different mode groups. The guided modes have an angle of $\theta_{c0} \leq 30°$ with little attenuation, even down to relatively small values of θ_φ. Only for very skew rays the attenuation increases because of the heavily increasing optical path length. Tunneling modes occur only for $\theta_{c0} > 30°$ and small values for θ_φ and can be observed up to an angle θ_z of about 80°. As expected they face higher attenuation. The group of the refracted modes can easily be identified since their attenuation is so high that every refracted mode lies in the black area in the upper half of the Figure.
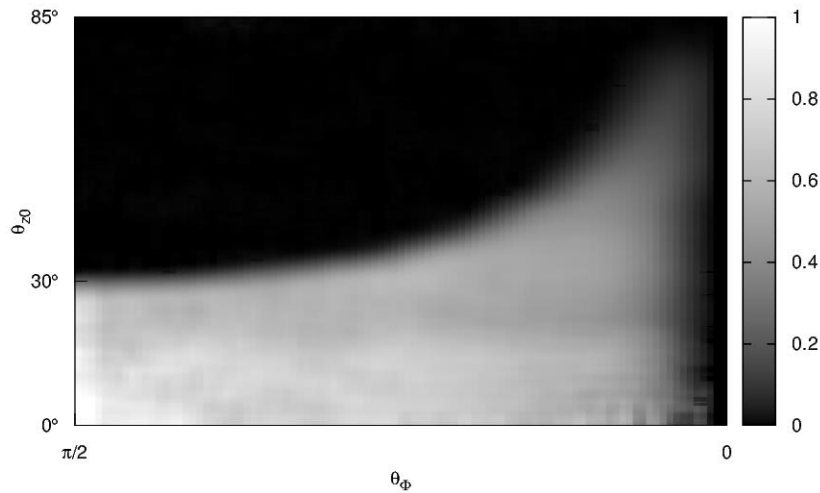
Figure 7. Integrated power distributions

4. Conclusion and outlook

We have presented a measurement technique that allows the retrieval of combined scattering and attenuation data for polymer optical fibers dependent on θ_z and the skewness θ_φ. The results look reasonable and show the

characteristics that are expected from literature. All mode groups and the maximum guided angle θ_c can clearly be identified. The attenuation of the guided and the tunneling modes show the expected dependency on the skewness.

The measurement proves clearly that scattering and attenuation depend strongly on the skewness. Hence, the impulse response of a fiber has a strong dependency on the launching condition. The next step is the inclusion of the obtained data in a new propagation model that is currently being worked on and which allows the prediction of the impulse response for a fiber of an arbitrary length and launching condition. The new model will allow us to evaluate the suitability of a specific fiber for a particular application in combination with the launching condition more precisely.

Another interesting approach is the derivation of coefficients for the power flow equation from the performed measurements which is also currently investigated at the POF-AC.

5. Acknowledgements

6. References

[1]   A. W. Snyder, J. D. Love. Optical Waveguide Theory. Kluwer Academic Publishers Massachusetts; 2000, ISBN: 978-0-41209-950-2.

[2]   D. Gloge, "Optical Power Flow in Multimode Fibers", Bell System Technical Journal 51.8, pp. 1767-1783, 1972

[3]   T. Becker, B. Schmauss, M. Gehrke, E. Nkiwane, and O. Ziemann, "Analytical model for the angle-dependent power distribution in optical multimode fibers," in The 25th International Conference on Plastic Optical Fibers - Conference Proceedings, Birmingham, September 2016, ISBN: 978-1-85449-408-5.

[4]   T. Becker, S. Loquai, H. Poisel, O. Ziemann, M. Luber, and B. Schmauss, "Influence of modal dispersion on impulse and frequency response of step-index polymer optical fiber," in POF Simulation beyond Data Transmission - Summary of the 3rd International POF Modelling Workshop 2015, C. A. Bunge and R. Kruglov, Eds. Norderstedt: Books on Demand, September 2015, p. 23ff, ISBN: 978-3-73921-499-3.

[5]   T. Becker, B. Schmauss, E. Nkiwane, M. Gehrke, and O. Ziemann, "Non-linear relation between modulation frequency and phase response of step-index polymer optical fiber," in The 25th International Conference on Plastic Optical Fibers – Conference Proceedings, Birmingham, September 2016, ISBN: 978-1-85449-408-5.

[6]   M. Gehrke, B. Schmauss, T. Becker, E. Nkiwane, R. Engelbrecht, O. Ziemann, "Experimental Investigation of the Influence of Tempering Processes on the Scattering Behavior of Step-Index Polymer Optical Fibers" in The 26th International Conference on Plastic Optical Fibers – Conference Proceedings, Aveiro, September 2017.

Experimental Investigation of the Influence of Tempering Processes on the Scattering Behavior of Step-Index Polymer Optical Fibers

M. Gehrke[1*], B. Schmauss[2], T. Becker[1], E. Nkiwane[1], R. Engelbrecht[1], O. Ziemann[1]

1 Polymer Optical Fiber Application Center, Technische Hochschule Nürnberg, 90489 Nürnberg, Germany
2 Institute of Microwaves and Photonics (LHFT), Friedrich-Alexander-Universität Erlangen-Nürnberg (FAU), 91054 Erlangen, Germany

*Corresponding author: martin.gehrke@th-nuernberg.de

Abstract: This paper presents an analysis of the scattering behavior of step-index polymer optical fibers. The major focus of the experiments lies on the measurement of far field patterns. For this purpose the fibers have been excited with a collimated light beam under different launching angles. After the light waves have propagated along the fibers the resulting patterns are recorded with a far field measurement device. In order to investigate the dependence of the far fields on the short-term climatic conditions the fibers have previously been subjected to reasonably high temperatures for specific time frames, which is called a tempering processes. We can subsequently clearly show a relation between the time the fibers have been exposed and their respective far field output.

1. Introduction and state of the art

Polymer optical fibers (POFs) are optical waveguides with their lowest attenuation within the visible light spectrum. They have been researched and manufactured for long enough so many different applications have been created over time. These include, but are not limited to, short to medium range data transmission, sensor applications, and illumination purposes. Generally considered to be reliable and inexpensive, POFs are primarily used either in home networks, automotive applications, or in areas where electromagnetic interference is a significant problem. [1]

During their use in the aforementioned applications POFs are subjected to various kinds of environmental influences such as varying temperature, humidity, and mechanical stresses. It is well established that optical, physical and chemical parameters of polymer materials degrade as a result of such an exposure. Oxidation has been reported as a possibility as well. [2, 3]

In order to guarantee a satisfactory performance of the optical fibers during their time of use a significant amount of work has already been invested in the attempt to determine the effects ageing has on POFs and to try to standardize tests in order to define quantifiably measurable parameters [4-8]. These publications mainly focus on transmission loss in regards to the application of POF in data communications and do not investigate the scattering properties themselves. In [9-11] a method is proposed to investigate the degradation of POF and its corresponding spectral transmission loss using chemiluminescence measurements. In conjunction with this work [12] tried to model light scattering using raytracing simulations based on aged far field measurements. Another problematic aspect of climatic influences on optical fibers is the variation of the physical length, which can cause the fibers to expand or retract from their connector, which is called pistoning. This has been observed by [13, 14].

All the mentioned research tries to specify ageing in a time frame of several thousand hours to quantify slow degradation processes. It is not however investigated what impact short-term climatic influences can have on the fibers. Additionally the parameters investigated usually are focused on attenuation. To gauge the climatic effects we propose a method to characterize scattering behavior of the fibers by analyzing the resulting far field shapes of different fibers with varying climatic exposure times. In this work we specifically investigate time frames of less than ten hours. We also measure shorter fibers than shown in the previously published results, and we also expand the observed angular range of the far field measurements. Special care was taken to minimize the influence of bends on the measurements.

With these specifications the goal is to improve the accuracy of the determination of scattering processes depending on climatic influences in order to enhance existing sensor concepts and data transmission applications by gaining a greater understanding of scattering processes and by using the results to improve upon current fiber modeling theories [15-19] by significantly improved determination of simulation parameters.

2. Scattering and climatic influences

During the propagation along a fiber any travelling light is subjected to different fiber influences, such as mode dispersion, mode dependent attenuation, and mode mixing. While dispersion is an effect caused simply by the different inclination angles of the different mode groups in conjunction with the geometric properties of a cylindrical waveguide [20], the latter two effects are primarily caused by scattering in the core material and at the core-cladding interface. Different types of absorption are contributing to the attenuation as well.

Due to the mentioned effects, any propagating light signal will experience changes to both its temporal and angular shape which subsequently affects applications such as data transmission or sensors and thus need to be accounted for.

In terms of influence a tempering process has on the scattering characteristics of POF, a couple of effects are mentioned. The primary sources of absorption within POF are vibrations and electronic transitions. Without providing too much detail on the chemical properties, it is clear POF, being made from organic materials, is comprised of many different molecular groups with varying absorption lengths. These could certainly be influenced by exposure to different climatic conditions. One of the main scattering processes within POF is Rayleigh scattering [21], which is caused by sub-wavelength density fluctuations, thus resulting in a slightly irregular composition of the transport medium. This form of scattering is an intrinsic process inherent to amorphous materials like polymers [2]. In order to quantify light scattering due to density fluctuations the formula [22] for turbidity (τ) given by equation (1) for an amorphous material, which is considered to be a supercooled liquid, thus keeping its liquid molecular structure from the melting process during manufacturing, can be used:

$$\tau = C \cdot \frac{8\pi}{3\lambda^4} \cdot \left(\frac{\left(n^2 - 1 \right)\left(n^2 - 2 \right)}{3} \right) \cdot kT_{gt} \beta_T \tag{1}$$

A strong dependency on the wavelength of the incident light can be seen by the inverse proportionality to the fourth power of λ. T_{gt} is the glass transition temperature (378 K) [23], k the Boltzmann constant, n the refractive index (1.492), β_T the isothermal compressibility ($3.6 \cdot 10^{-10}$ m^2/N) [24] and C the Canbannes factor (1.1). It is used to correct for the molecular anisotropy of the polymers contained in the fiber. Again it is not unreasonable to assume temperature exposure to have influence on the structure and the resulting turbidity.

In addition to those intrinsic properties extrinsic effects can also be observed. A significant contributor to scattering is the shape the coiled fiber assumes after production. During manufacturing the fibers are drawn in a straight line in the drawing tower, but they are stored and shipped coiled on spools. The natural relaxed shape of a POF is thus not straight but actually circular with a radius in the vicinity of 20 cm. This significantly affects the propagation of light, since scattering at a curved cylinder differs from a straight one. Should the fiber be straightened forcefully strain is introduced which also influences light propagation. This effect can also be influenced by tempering processes since a shape change can be observed during the procedure.

3. Measurement setup and preparation

In order to determine the dependence of the scattering on tempering processes far field patterns of fibers, which have previously be subjected to varying climatic conditions, have to be measured. For the measurements two different sets of *Toray PFU CD1001 22 E* fibers with differing production dates have been prepared prior. For the necessary tempering process a climate chamber (*CTS C-70/200*) is used. The fiber samples of two lengths (16 cm and 32 cm) are mounted inside the climate chamber with their orientation pointing straight down, so the fibers will straighten during the tempering process due to the gravitational force. The temperature of the climate chamber was set to 85 °C and the relative humidity to 0%. The parameters

were chosen to remove absorbed water from the fiber gently without reaching temperatures too close to T_{gt}. After 0.25, 0.5, 0.75, 1.0, 2.0, 3.0, 5.0, and 8.0 hours one fiber sample of each length has to be removed. The fibers inside the climate chamber can be seen in Fig. 1a while the collection of all 16 cm samples (fibers not yet cut exactly to the specified length) can be seen in Fig. 1b. After the tempering processes the fibers are cut to exact length with a razor blade cutter and polished using abrasive polishing papers of successively larger grits with particle sizes down to 0.3 μm.

| (a) | (b) |
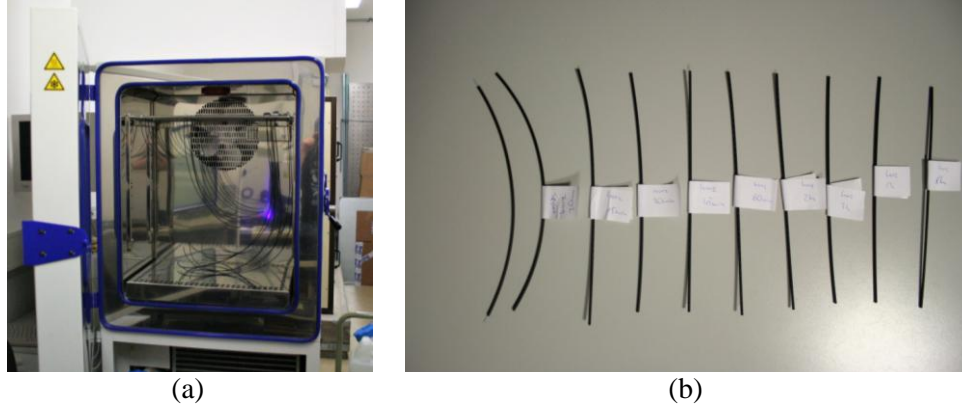
Fig. 1: Fiber test samples in a climate chamber (a) and 16 cm fiber samples after tempering processes (b)

The far field measurements themselves are performed with a *Radiant Vision Systems Imaging Sphere*. The two main optical components of the measurement device are a CCD camera and a hemispherical measurement chamber arranged so the imaging device observes the full inner surface of the measurement sphere with the aid of a convex mirror [25]. The fiber's end surface is placed in the center of the half sphere using a specifically designed mount, which guarantees a straight guidance of the fiber and also allows for easy and precise alignment between the center of the sphere and the fiber. The beginning of the fiber is placed in the rotary center of a collimated laser beam provided by a single mode fiber coupled *PDL-800* laser with collimating optics. The rotation can be used to excite the fiber under different angular launching conditions. The full fiber front face is illuminated, which guarantees a maximum of coverage of the propagating modes' skewness range. This measurement is a simplification of [26] where the skewness composition of the propagating modes can additionally be limited. A schematic of the measurement setup is shown in Fig. 2a and the physical setup itself is shown in Fig. 2b.

| (a) | (b) |
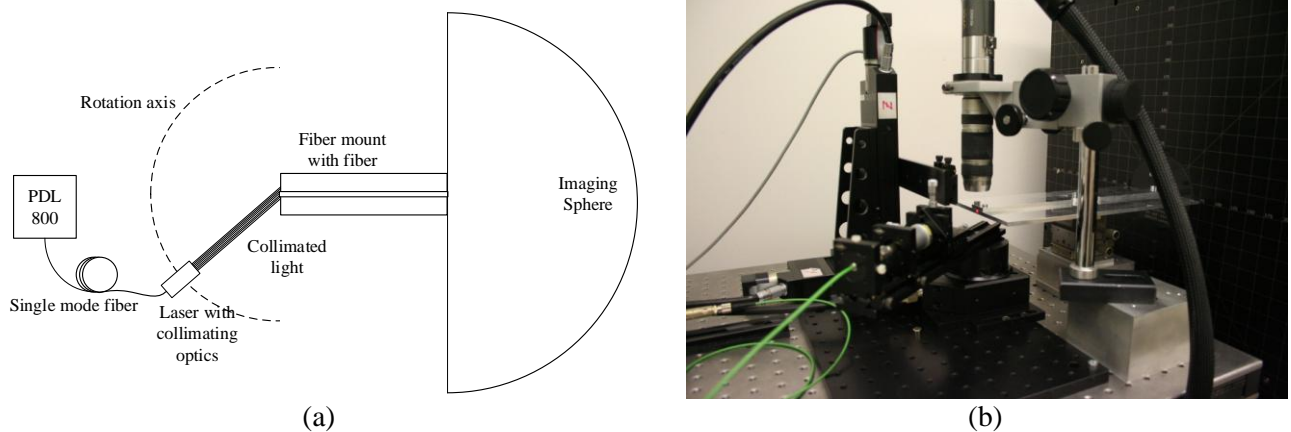
Fig. 2: Far field measurement schematic (a) and measurement setup (b)

4. Measurement results

First a series of far field measurements for the 32 cm fibers are shown in Fig. 3. The prepared fibers with different tempering durations were excited under 15°. In the provided images one can clearly see the ring pattern caused by the cylindrical waveguide even after this short fiber length. Additionally it is evident even at first glance without further quantification that the tempering duration has a significant impact on the far fields. Fig. 3a, which corresponds to an untreated fiber, shows significantly more severe scattering into inclination

angles further removed from the original center angle of 15°. Fig. 3b shows a clear reduction in the scattering severity, with Fig. 3c as an even further improved result. This correlates with increased tempering time. However Fig. 3d, which was the longest measured time, shows a significant deterioration of the results.

(a) Untempered

(b) 60 minutes

(c) 180 minutes

(d) 480 minutes
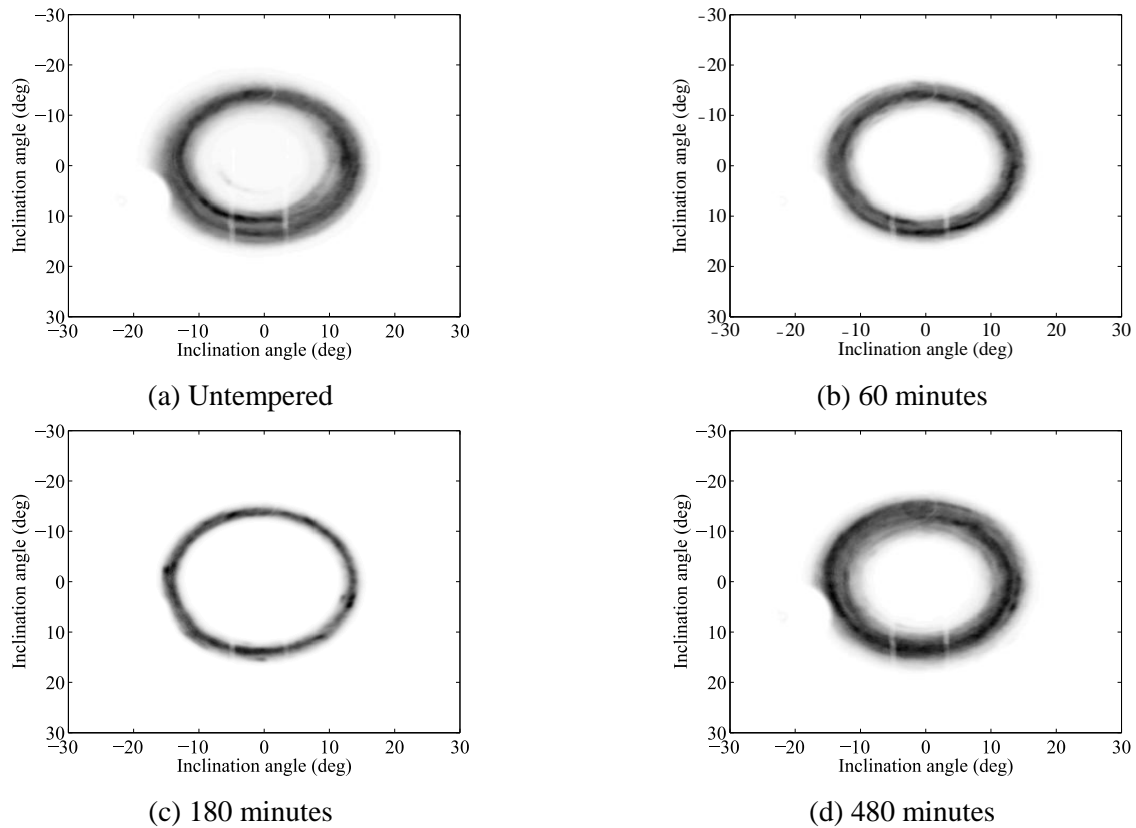
Fig. 3: Far field measurements of 32 cm fibers for different tempering durations

This only gives a brief excerpt of the measurements since they were performed for two fiber lengths (16 cm and 32 cm), two different fiber production samples, 25 excitation angles, and nine different tempering durations. All of which show the same behavior within reason. Providing more results is not feasible within the scope of this paper.

5. Evaluation and discussion

Although it seems clear that there is a certain correlation between tempering duration and scattering intensity judging by Fig. 3, further investigations are provided to illustrate the effect. A first step to improve the quantification is the analysis of the 1D far field. This can be obtained from the 2D far field patterns by integrating over the azimuthal angle. This yields the total power present in each inclination angle. Fig. 4 shows a collection of such power over angle graphs. Each plot shows eight graphs for the different tempering durations. All the different inclination angles show very similar results. The solid black line represents the untempered fiber and it is clearly the worst sample out of all the measured fibers. It scatters significant power into angles of more than 5° difference from the true propagation angle even after such short fiber lengths of 16 and 32 cm. The dashed black line represents a fiber after 15 minutes tempering process whose behavior is still very similar to the untempered case. However a slight improvement can be observed with slightly less scattering and more concentrated power in the original propagation angle. The black "x", dotted and grey solid line can subsequently be grouped together. They represent 30, 45, and 60 minutes of tempering. Here a clear improvement between this and the first group can be identified immediately. The maximum power in the central angle is increased and the width of the scattered power is clearly reduced. The final group is comprised of the fibers tempered 120 and 180 minutes represented by grey dashed line and "x". The curves are even steeper and narrower, signaling even less scattering. Interestingly the fiber exposed for 300 minutes shows significantly worse results more akin to the first group suggesting the beginning of another process degrading the fibers.

There is hardly any difference between the total power carried by the different fiber samples. The differences are thus caused mainly by scattering and not by significant absorption processes. The 16 cm fiber shows slightly more variance in its results but still follows the general trend.

(a) 32 cm 5°

(b) 32 cm 25°

(c) 32 cm 35°

(d) 16 cm 25°
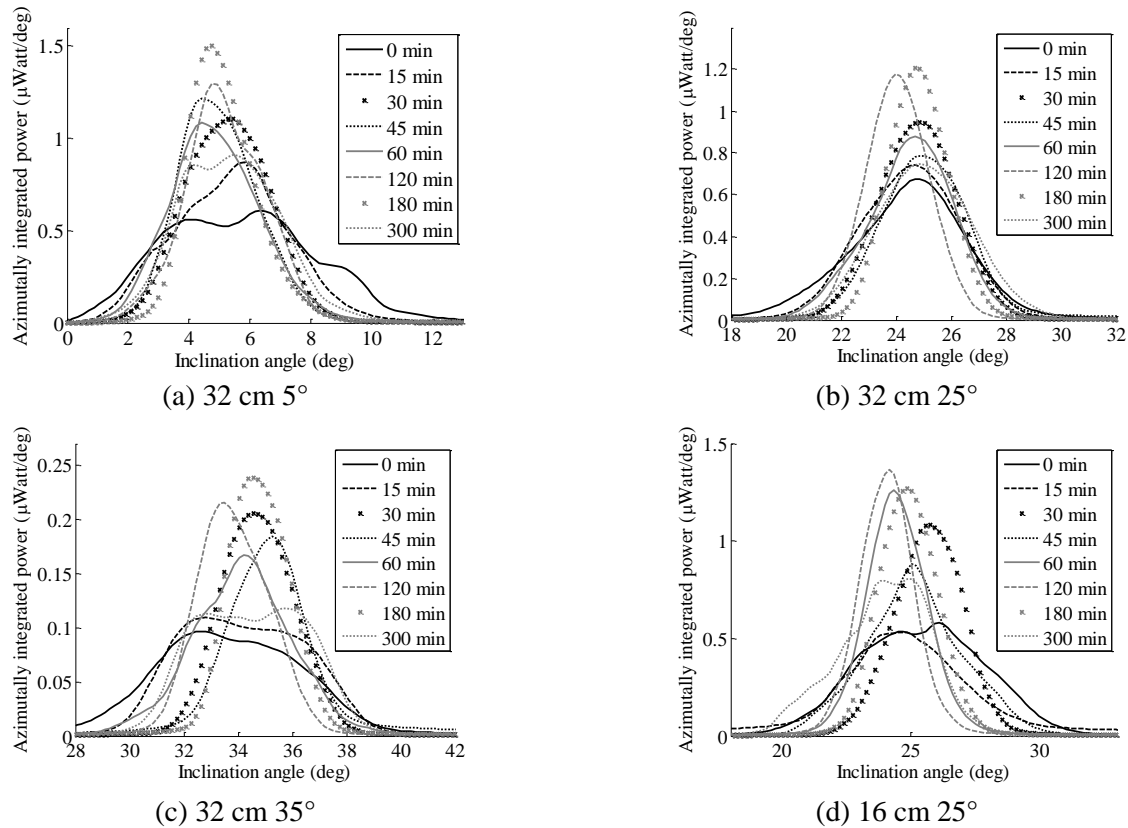
Fig. 4: Integrated power over inclination angle

While the 1D far field graphs show great detail, a much simpler correlation between tempering process duration and scattering can be obtained by looking at the full width at half maximum (FWHM) values of the Gaussian power profiles. Such an analysis is depicted in Fig. 5. Again three different, interesting excitation angles (15°, 25°, and 60°) for the 32 cm fibers and one excitation angle (25°) for the 16 cm fibers are shown. The FWHM values of the measured far field patterns are plotted over the corresponding tempering process duration. Additionally the best 2nd degree polynomial fit is shown for each set of data. The aforementioned behavior can be observed clearly. In all cases the untempered fiber has the largest width with up to 7°. The width then correlates inversely with the increased tempering process duration and thus decreases until 300 minutes, where a local minimum is apparently reached. Towards even longer exposure times degradation with correlating increase of the width can be observed. However the number of measurement points is limited for the longer exposure times.

Fig. 5c, which shows the 32 cm fiber under 60° of excitation shows a slightly less conclusive result with more variance between the FWHM and the tempering duration. For such steep angles outside the numerical aperture the fiber does not guide light perfectly and propagation is based on leaky rays with significantly increased number of reflections at the core-cladding interface. This can certainly lead to slightly less conclusive results. However the general trend can still be observed even for this case.

An interesting confirmation of the results is given by optical inspection of the fibers in regards to their straightness. A set of fibers is shown in Fig. 1b. They are ordered by tempering duration from left (untempered) to right (480 minutes). The remnant curvature of the fibers decreases towards the center where the 60, 120, and 180 minute fibers are located before the curvature slightly increases again for the 300 and 480 minute fiber. This correlates well with the results seen in Fig. 5.

(a) 32 cm 15° (b) 32 cm 25°

(c) 32 cm 60° (d) 16 cm 25°
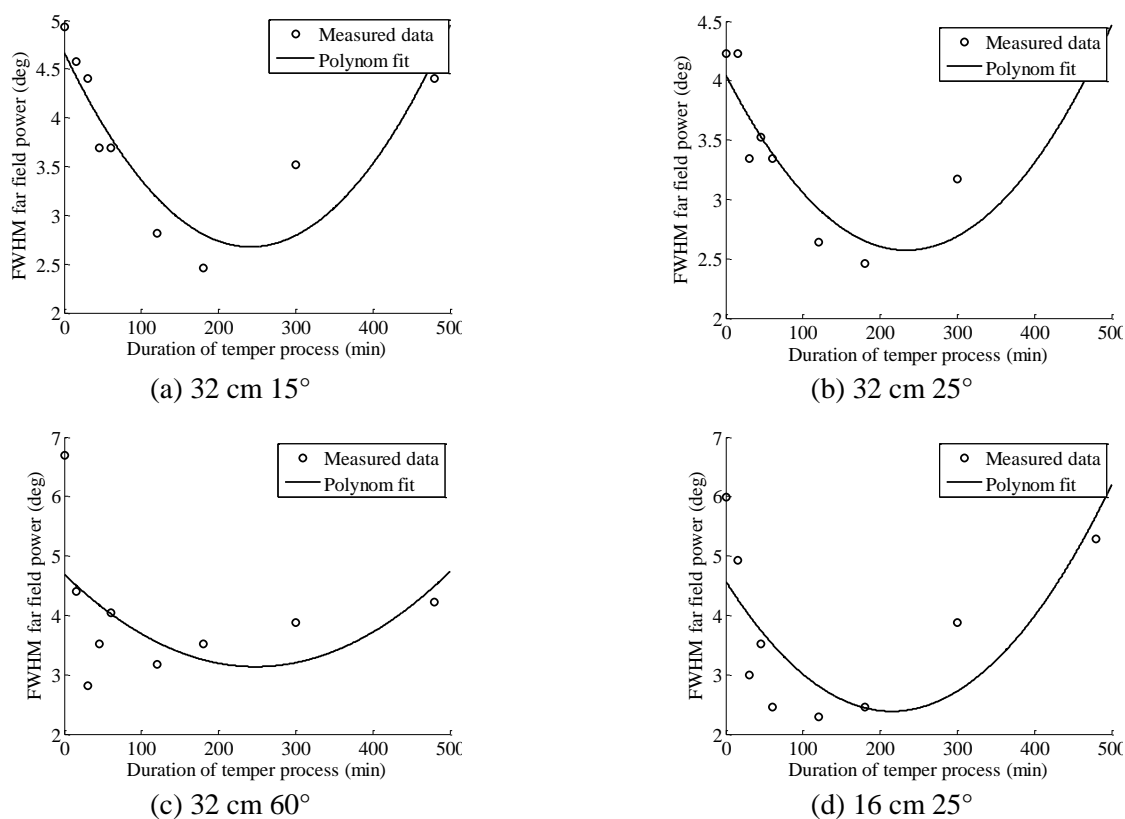
Fig. 5: FWHM of the power over inclination angle over tempering

6. Conclusion

We have proposed an investigation into the effects of short duration tempering on the scattering properties of POF. At first reasonable climatic conditions have been defined, before a set of fibers of different lengths were tempered for varying durations between 15 minutes and 8 hours. Afterwards a measurement setup has been described, which was subsequently used to record far field profiles of the tempered fibers under different launching conditions. During the evaluation we have shown a clear correlation between the scattering propensity of POF and the tempering duration. The scattering first decreases with longer exposure time until 180 minutes before some degradation sets in. For further research fibers from other manufacturers should be measured as well. Additionally different climatic conditions could be analyzed as well to find a possibly better value. Longer fibers might also yield some results and should be considered for measurement. Finally the ageing properties of such a treated fiber should be monitored to see whether the effects are permanent or reversible.

7. Acknowledgements

8. References

[1] O. Ziemann, J. Krauser, P. E. Zamzow and W. Daum, POF-Handbuch: optische Kurzstrecken-Übertragungssysteme, Berlin: Springer Verlag, 2007.

[2] C. Emslie, "Polymer Optical Fibers," *Journal of materials science 23(7),* pp. 2281-2293, 1988.

[3] R. L. Feller, Accelerated Aging: Photochemical and Thermal Aspects, The J. Paul Getty Trust, 1994.

[4] O. Ziemann, W. Daum, A. Bräuer, W. Schlick and W. Frank, "Results of a German 6000 hours

accelerated aging test of PMMA POF and consequences for the practical use of POF," *Proceedings 9th International Conference on Plastic Optical Fibers,* 2000.

[5] W. Frank, A. Bräuer, W. Daum, H. J. Tessmann, A. Weinert and O. Ziemann, "Polymer optical fibres in Germany: reliability test for use in premise wiring," *Proceedings of the 7th International Conference on Plastic Optical Fibers,* 1998.

[6] M. Sato, T. Ishigure, E. Nihei and Y. Koike, "Thermal and Humidity resistant GI POF," *Proceedings of the 7th International Conference on Plastic Optical Fibers,* 1998.

[7] W. Daum, W. Hammer and K. Mäder, "Spectral Transmittance of polymer optical fiber before and after accelerated aging," *Proceedings of the 6th International Conference on Plastic Optical Fibers,* 1997.

[8] J. Marcou, G. Boutinaud, P. Faugeras, K. Etorneau, G. Roblin, G. Roger, M. Dequenne, J. Dugas and P. Zimmermann, "Study of the POF behaviour under mechanical and thermal constraints," *Proceedings of the 4th International Conference on Plastic Optical Fibers,* 1995.

[9] A. Appajaiah, Climatic stability of polymer optical fibers (POF), Wirtschaftsverl. NW, Verlag für neue Wiss., 2006.

[10] A. Appajaiah, V. Wachtendorf and W. Daum, "Characterization of thermo-oxidative stability of polymer optical fibers using chemiluminescence technique," *Polymer degradation and stability 91.11 ,* 2006.

[11] A. Appajaiah, V. Wachtendorf and W. Daum, "Thermooxidative stability characterization by chemiluminescence," *Journal of applied polymer science 103.3,* 2007.

[12] Ł. Jankowski, Modelling and simulation of light propagation in non-aged and aged step-index polymer optical fibres, Berlin: BAM-Dissertationsreihe, 2005.

[13] R. Beuth, "Polymeric optical conductors". USA Patent 6,766,091, 2004.

[14] T. Kibler, S. Poferl, G. Bock, H.-P. Huber and E. Zeeb, "Optical data buses for automotive applications," *Journal of lightwave technology 22.9,* 2004.

[15] D. Gloge, "Optical Power Flow in Multimode Fibers," in *Bell System Technical Journal 51.8*, 1972, pp. 1767-1783.

[16] M. Gehrke, S. Loquai, O. Ziemann and B. Schmauss, "Time-domain solution to the power flow equation and possible applications," in *POF Simulation beyond Data Transmission - Summary of the 3rd International POF Modelling Workshop*, Norderstedt, Books on Demand, 2015, p. 277ff..

[17] M. Gehrke, B. Schmauss, T. Becker, E. Nkiwane and O. Ziemann, "Improving OTDR Spatial Resolution using signal processing based on Power Flow Equation simulation data," in *25th Conference on Plastic Optical Fibers*, Birmingham, 2016.

[18] M. Gehrke, B. Schmauss, T. Becker, E. Nkiwane, O. Ziemann and R. Engelbrecht, "Influence of Scattering Characteristics on the Angle and Time Dependent Backscattered Power in Polymer Optical Fibers," *Fiber Society Spring Conference,* 2017.

[19] M. Gehrke, O. Ziemann, S. Loquai and B. Schmauss, "Polymer optical fiber backscatter simulation model using the power flow equation solved in the time domain," in *24th International Conference on Plastic Optical Fibers*, Nürnberg, 2015.

[20] A. W. Snyder and J. Love, Optical Waveguide Theory, Springer Science & Business Media, 1983.

[21] C. A. Bunge, R. Kruglov and H. Poisel, "Rayleigh and Mie scattering in polymer optical fibers," *Journal of lightwave technology 24(8),* p. 3137ff, 2006.

[22] T. Flipsen, Design, synthesis and properties of new materials based on desely crosslinked polymers for polymer optical fiber and amplifier applications, Groningen: Rijksuniversiteit, 2000.

[23] J. Bandrup, E. H. Immergut, E. A. Grulke, A. Abe and D. R. Bloch, Polymer handbook, New York: Wiley, 1989.

[24] N. Tanio and Y. Koike, "Estimate of light scattering loss of amorphous polymer glass from its molecular structure," *Japanese journal of applied physics 36.2R,* 1997.

[25] R. Yeo, R. Rykowski, D. Kreysar and K. Chittim, "The imaging sphere—the first appearance meter?," *The 5th Oxford Conference on Spectroscopy,* 2006.

[26] T. Becker, B. Schmauss, M. Gehrke, E. Nkiwane, R. Engelbrecht and O. Ziemann, "Angle and Skewness dependent Scattering and Attenuation Measurement of Step-Index Polymer Optical Fibers," *Proceedings 26th International Conference on Plastic Optical Fibers and Applications,* 2017.

Review of Optical Frequency Domain Reflectometry Methods for Optical Fiber Sensors

R. Engelbrecht[1*], S. Werzinger[2], M. Koeppel[2], G. Saur[2], B. Schmauss[2]

1: Polymer Optical Fiber Application Center (POF-AC), Technische Hochschule Nürnberg Georg Simon Ohm, Wassertorstraße 10, 90489 Nürnberg, Germany.

2: Institute of Microwaves and Photonics (LHFT), Friedrich-Alexander-Universität Erlangen-Nürnberg, Cauerstraße 9, 91058 Erlangen, Germany.

*Corresponding author: rainer.engelbrecht@th-nuernberg.de

Abstract: Optical frequency domain reflectometry (OFDR) is widely used to achieve spatial resolution in optical fiber sensors using singlemode silica-glass fibers (SMF) as well as multimode polymer optical fibers (POF). In this contribution, OFDR principles and applications are reviewed, including sensing and measurements with Rayleigh backscatter, multiplexing of fiber Bragg grating (FBG) sensors and Raman distributed temperature sensing (DTS). Problems in iOFDR systems arising from residual optical coherence and manifold mutual reflections between discrete locations along the fiber are addressed as well as possible solutions.

1. Introduction

Many fiber-optic sensor systems rely on the spatial resolution of reflections and backscatter along a single fiber. Different sensor principles can be employed [1, 2]. Examples are (typical fiber types in parentheses):

- Fresnel reflections at one or more fiber discontinuities, e.g. for measurement of strain (POF and SMF),

- Rayleigh backscatter, where the spatial reflection fingerprint can be used for fiber identification or strain and temperature sensing (SMF), or where an increased scattering detects strain (POF) [3],

- Spontaneous Raman scattering for distributed temperature sensing (DTS) by comparing the power of Stokes and Antistokes scattering after spectral optical filtering (SMF) [4],

- Spontaneous or stimulated Brillouin scattering for strain and temperature sensing by measuring the Brillouin frequency shift of the backscatter with microwave photonics (SMF) [5],

- Fiber Bragg gratings (FBG), where the Bragg wavelength of reflection depends on strain and temperature (SMF, POF) [6]. Although typically multiplexed in the wavelength domain, spatial multiplexing is of interest for long chains of many similar FBGs [7].

The most straightforward method to achieve a spatial resolution for these principles is optical time-domain reflectometry (OTDR), where a short light pulse is launched into the fiber. Reflections and backscatter are then detected with a high temporal resolution, and time is mapped to range information simply by $z = t\, c_0/(2n)$, where c_0 is the speed of light in vacuum, and n is the effective index of refraction of the propagating mode of the lightwave. Spatial resolution is usually defined by $\Delta z = \Delta t\, c_0/(2n)$, where Δt is the optical pulse length. Typical values are $\Delta z = 10$ cm for $\Delta z = 1$ ns, requiring opto-electronic components and circuits having a bandwidth of roughly $B = 1/(2\,\Delta t)$, or from DC to 500 MHz, respectively. The DC and low-frequency content is of particular importance for all distributed scattering processes like Rayleigh, Raman or Brillouin, because of the low-pass signal characteristics of their OTDR impulse responses. The maximum range is limited by the dynamic range of the detector and the fiber attenuation, yielding typically 100 m in POF and many 10s of km in SMF.

One disadvantage of OTDR methods is the low average energy launched into and received from the fiber. This is because of the short optical pulse width Δt required for spatial resolution compared to the time T required for the detection of the most distant reflection, i.e. at the fiber end. As SNR and thus, measurement precision, is proportional to the signal energy, long measurement times with lots of averaging are required for precise OTDR sensor read-out and to achieve low standard deviations for the quantities to be measured. This limitation can be overcome with methods in the frequency domain as briefly reviewed in the next sections.

2. Theory

From a signals and systems perspective, the ideal OTDR result defined as the true reflection profile over range $R(z)$ is simply the impulse response of a linear system $h(t)$, when the time t is mapped to range z as described, and a proper normalization is applied, e.g. by using a reference reflector R_0. This holds as long as there are no multipath or mutual reflections. This is typically the case given the low backscatter coefficients per unit length of distributed scattering. Additionally, this condition can be satisfied approximately by using low Fresnel and FBG reflectivities. The impulse response $h(t)$ is related to a corresponding frequency response $H(f)$ by the Fourier transforms:

$$H(f) = \mathcal{F}\{h(t)\}, \; h(t) = \mathcal{F}^{-1}\{H(f)\}. \tag{1}$$

Thus, optical frequency-domain reflectometers (OFDR) measure a frequency response, typically a complex-valued, frequency-dependent transmission function $H(f)$, and by applying an inverse Fourier transform the impulse response $h(t)$ is reconstructed and scaled to the reflection or backscatter over range profile $R(z)$, finally. Two different methods for obtaining such a frequency-dependent transmission function $H(f)$ are commonly used:

- **Coherent optical frequency-domain reflectometry (cOFDR):** Here, the optical frequency f of a narrow-linewidth tunable laser is swept and an optical interferogram between a reference lightwave and the backscattered light is recorded, yielding $H(f)$ as discussed in section 3.
- **Incoherent optical frequency-domain reflectometry (iOFDR):** A light source is electronically modulated in its intensity by varying RF frequencies f and an electrical transmission function $H(f)$ in respect of the photocurrent of an intensity detector for the reflected light is measured, as described in section 4.

The main advantage of both methods is a permanent input and measurement of light into and out of the fiber, resulting in a higher average light energy and a higher SNR for a given measurement time compared to OTDR. Whereas the system complexity of a cOFDR results from a widely and precisely tunable laser source, RF or microwave components and circuits for modulation and detection of light are required for iOFDR. Although having the same theoretical framework, both methods have unique and distinct features and limitations.

3. Coherent Optical Frequency Domain Reflectometry (cOFDR)

Fig. 1 shows a basic cOFDR setup. A narrow-linewidth tunable laser is swept in its optical wavelength λ, and thus, in its optical frequency f over a total optical bandwidth B_{opt}. The light is launched into the sensor fiber, and the backscattered as well as reflected light is coherently superimposed with a reference lightwave directly from the laser source.
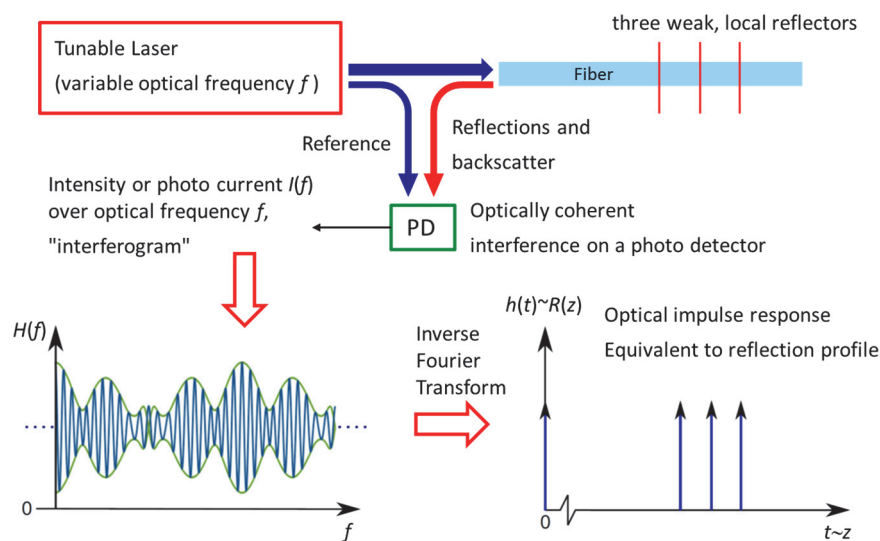

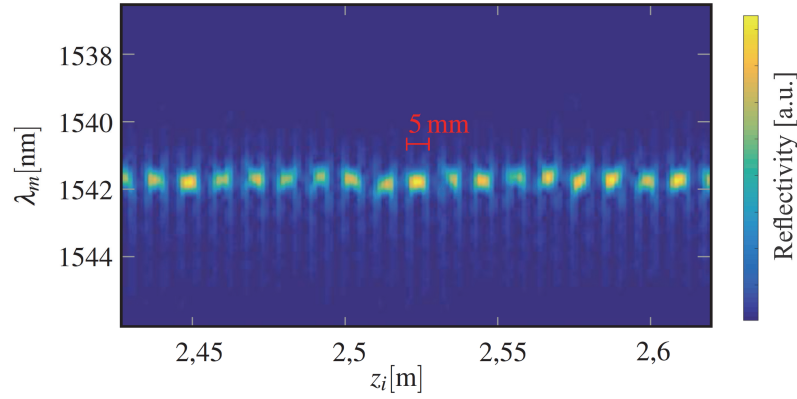Figure 1. Principle of a coherent OFDR [2]

Figure 2. Spatially and spectrally resolved reflection profile of a FBG chain measured with cOFDR [8].

The resulting intensity $I(f)$ is measured with a photo detector yielding a frequency dependent interference pattern called interferogram. This interferogram is used as optical frequency response $H(f)$ and by an inverse Fourier transform, the optical impulse response $h(t)$ is reconstructed and scaled to the reflection over range profile $R(z)$. By the properties of the Fourier transform, the spatial resolution is given by

$$\Delta z = \frac{c_0}{2nB_{\text{opt}}} \; .$$

(2)

As an example, if a light source centered at 1550 nm is tuned over 50 nm or $B_{\text{opt}} = 6200$ GHz, respectively, this yields a spatial resolution Δz of 16 µm. This extremely high spatial resolution is the main benefit of employing cOFDR, which essentially the same technology is called Fourier-Domain Optical Coherence Tomography (FD-OCT) for medical imaging. A second advantage is the heterodyne detection of the electric field of the weak backscattered light by coherently mixing with a strong reference light wave acting as local oscillator (LO), yielding a stronger signal in the photo current compared to direct non-coherent intensity detection with no LO.

The temporal tuning properties of the laser source are of no importance for this simple cOFDR theory presented here. Of course, the optical wavelength sweep requires some time and thus, the interferogram is sampled at discrete times t_i at first. When the corresponding frequency f_i at each time t_i is known, the interferogram can be directly mapped to $H(f)$ and processed as described. Therefore, wavelength references are typically integrated in a cOFDR system to correct any non-ideal tuning behavior of the laser by digital post-processing.

A third interesting feature of cOFDR is that the spectral properties of reflectors are also encoded in the interferogram. The cOFDR range information $R(z)$ or the optical impulse response $h(t)$ consists of typically millions of data points spaced by Δz and distributed over the total measured range L. If a subset of N of these data points centered at a range z_0 is transformed back into the optical frequency domain by a Fourier transform, the spectral reflection $R(f, z_0)$ and thus, $R(\lambda, z_0)$ averaged over a span of $N \cdot \Delta z$ centered at z_0 is calculated. In principle, any compromise between spatial and spectral resolution can be realized by choosing N within the theoretical limits defined by the total optical bandwidth and the properties of the Fourier transform. As an example, Fig. 2 shows a both, spatially and spectrally resolved reflection measurement of a chain of closely spaced FBGs having the same Bragg wavelength [8]. Thus, multi-point or quasi-distributed temperature and strain sensing can be realized by evaluating the Bragg wavelengths of these FBGs.

Finally, due to the high sensitivity and spatial resolution, the Rayleigh backscatter can be measured with such high fidelity that individual reflection patterns are recorded that are unique for any piece of fiber ("fingerprint"). Once a reference pattern has been acquired for a fiber segment, a displacement $\Delta z(T, \varepsilon)$ of this segment by temperature T and strain ε can be measured by correlation techniques either in the spatial or in the wavelength domain (Fig. 3). Thus, distributed temperature and strain sensing is possible with cODFR with bare fibers and without any FBGs [9].
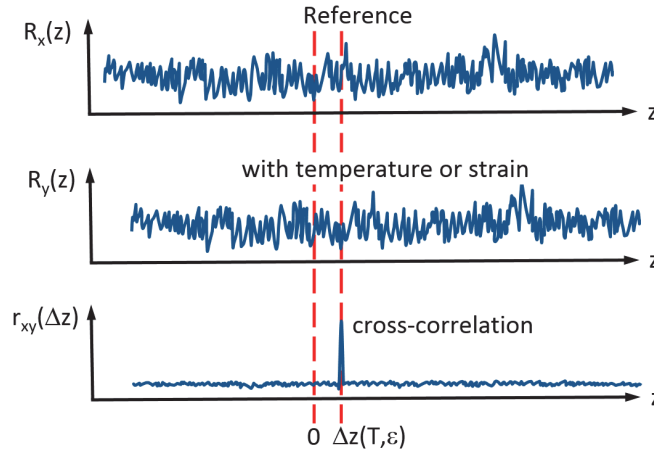
Figure 3. Strain or temperature sensing by fingerprint correlation of Rayleigh backscatter with cOFDR [2].

The total measurement range L_{max} of a cOFDR is limited for some reasons. First, the optical phase noise of the laser and thus, the finite coherence length sets an upper limit to the maximum distance before the interference visibility fades. Secondly, if the laser optical frequency is swept at a rate of $\mu = \Delta f / \Delta t$, and the interferogram is sampled electronically at a rate of f_S, then the maximum range of a detector is given by

$$L_{max} = \frac{c_0 \, f_S}{4n \, \mu} \, . \qquad (3)$$

At larger distances, the interference pattern would oscillate so fast during wavelength tuning that Nyquist's sampling theorem would be violated.

The combination of both effects limit the maximum sensing range for cOFDR to typically a few 100 m.

As cOFDR is an optically coherent technique and thus sensitive to path length changes in the order of an optical wavelength, singlemode fibers are typically used. Multimode fibers like a typical POF would wash out the interference contrast by superposition of many modes with different path lengths due to modal dispersion. Even in SMF, chromatic dispersion over the laser's tuning range needs to be compensated for highest resolution.

3. Incoherent Optical Frequency Domain Reflectometry (iOFDR)

Fig. 4 shows the principle of an incoherent OFDR system. As optical coherence or wavelength tuning are not required for iOFDR, any light source like laser diodes (LD), super-luminescence diodes (SLED) or LEDs can be used, provided they are suitable for coupling enough light into a SMF or POF for sensing. In fact, a sufficiently low optical coherence is advantageous to minimize multipath interference from mutual reflections and to suppress stimulated Brillouin scattering (SBS) [10]. The intensity of the light source is electronically modulated with a variable frequency f from DC (ideally) up to RF (radio frequency) or microwave frequencies, having a total bandwidth B_{RF}. This is done by direct modulation of the injection current or by external modulation as shown in Fig. 4. A photo diode detects the intensity of the backscattered light. The photo current is amplified and the magnitude and phase of the modulation present in this current in respect to the modulation applied to the light source is measured with an RF vector network analyser (VNA). Thus, a frequency-dependent transfer function $H(f)$ is measured at a previously calibrated reference plane as shown in Fig. 4. Again, an inverse Fourier transform is applied to $H(f)$ yielding an impulse response $h(t)$ that is directly comparable to a conventional OTDR. Further calibration with an optical reference reflector helps to scale the impulse response to a true reflection profile $R(z)$ and to shift to range zero relative to a reference location along the fiber. The details of signal processing and calibration for an iOFDR are described in detail in [11], for example.

iOFDR is very similar to techniques well-known from radar systems. If the RF modulation frequency f is swept continuously, it would resemble a classic analogue FMCW (frequency-modulated continuous wave) radar.

Figure 4. Principle of an incoherent OFDR [2]

If the frequency f is applied at discrete steps as it is usually the case with a VNA, it would be called stepped-frequency radar. As all modern sensing systems apply some kind of time-discrete data sampling, both techniques are essentially similar. Again, the temporal speed of frequency tuning is of no particular importance for the basic iOFDR theory. In iOFDR, the lightwave acts as a carrier like a virtual "aether" for the RF wave which propagates on top of the light wave as intensity modulation of the light. Thus, all known techniques and signal processing known from radar system can be applied, but at propagation properties defined by a lightwave, for example using low-divergence free-space light beams or low-loss silica fibers for long-range sensing.

Similar to cOFDR, the spatial resolution of an iOFDR for clearly resolving two distinct reflectors is given by

$$\Delta z = \frac{c_0}{2nB_{\text{RF}}} \ . \tag{4}$$

For example, if the VNA and the RF electronics provide a bandwidth of 5 GHz, Δz is 2 cm. Alternatively, the separation of two discrete points in the range data after IFFT can be defined as spatial resolution by

$$\Delta z_{\text{IFFT}} = \frac{c_0}{4nB_{\text{RF}}} \ , \tag{5}$$

which is essentially the same as of an OTDR system described in section 1 with equal bandwidth B. If the same noise properties of the electronics for an OTDR and an iOFDR are assumed, and comparable measurement times or effective noise bandwidths by filtering or averaging are used, iOFDR has no principal advantage over OTDR. As mentioned already, the main advantage of iOFDR is a much higher average signal energy by the permanent light injected into and received from the fiber which provides a better SNR in less time, typically. An OTDR having the same average light energy in the fiber would have the same SNR in same time, but the extremely high peak power of the short light pulse that would be required is not feasible in practice. Additionally, signal processing known from radar systems can be applied to iOFDR for making best use of the given system bandwidth and SNR.

Modern RF and microwave oscillators have such a low relative phase noise and large coherence length, that these are no primary concerns limiting the maximum sensing range. The maximum unambiguous sensing distance is simply given by the cyclic properties of the Fourier transform by

$$z_{\text{max}} = \frac{c_0}{2n \, \Delta f_{\text{RF}}} = \frac{c_0}{2nB_{\text{RF}}} \ (N-1), \tag{6}$$

where Δf_{RF} is the frequency step between two measurement frequencies of the VNA, or N is the total number of measurement frequencies within Δf_{RF}, respectively.
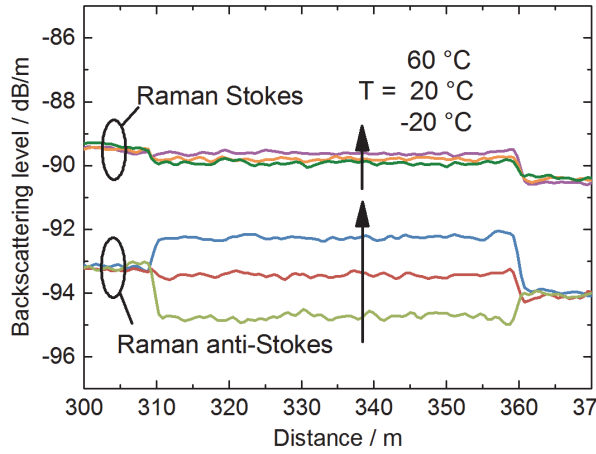
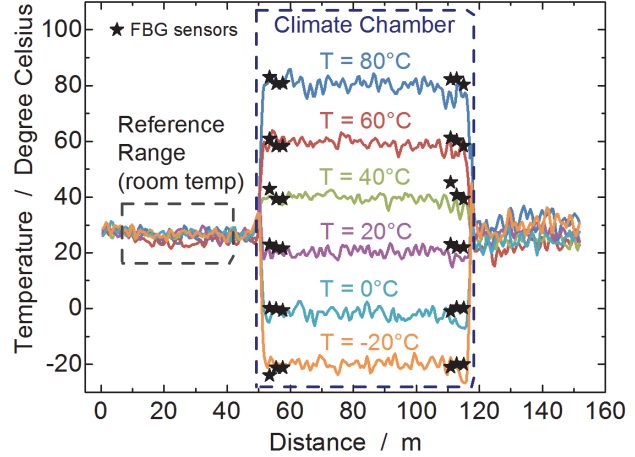Figure 5a. Spatially resolved Raman scattering in a SMF measured with iOFDR at different temperatures [13].

Figure 5b. Combined Raman distributed temperature sensing (DTS) with simultaneous FBG sensing using wavelength-stepped iOFDR [13].

With a bandwidth of 5 GHz and $N = 100.000$ the maximum distance is 2 km. Reflections at larger distances would still be measured but would be mapped into the same interval between 0 and z_{max} in the iOFDR result.

As iOFDR does not rely on optical coherence and the range resolution is limited to a few cm, modal dispersion in multimode fibers is not as detrimental as for cOFDR. Thus, iOFDR is widely employed for both singlemode and multimode fibers made of silica or polymers. For example, iOFDR with POF for strain sensing was examined in detail in [12].

iOFDR can be used for spatial resolution of any sensing effects described in section 1. For distributed temperature sensing (DTS) using spontaneous Raman scattering in silica fibers, the backscattered light is spectrally filtered into a Raman-Stokes spectral region and a Raman Antistokes region and measured with two photo detectors, typically avalanche photo diodes because of the low power per unit length of Raman scattering. Both spectral regions are than measured with iODFR as shown in Fig. 5a [13]. By theory of Raman scattering [9] and after a calibration, the spatially resolved temperature profile can be achieved. Raman DTS is widely employed for fire detection in highway tunnels, for example.

If iOFDR spatial resolution is combined with a wavelength tunable light source (TLS) as shown in Fig. 6, spatial multiplexing and simultaneous spectral interrogation of FGB chains in a SMF having similar Bragg wavelengths is possible [11]. Note that the TLS here does not need to have special coherence properties or very narrow wavelength step sizes as required for cOFDR. In fact, the coherence has to be reduced with broadband noise from a noise source (BBNS) and an optical phase modulator (PM) to avoid interference fringes and SBS.
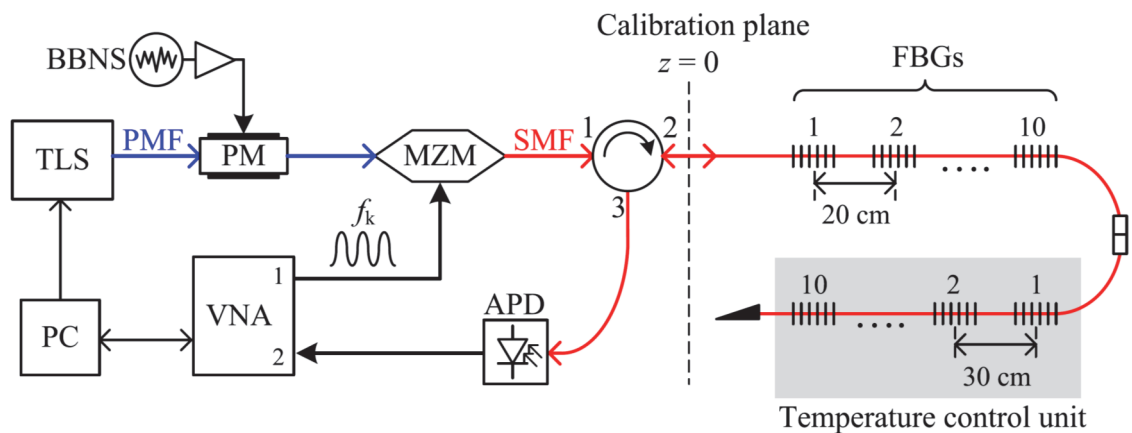

Figure 6. Setup for multiplexing of fiber Bragg grating (FBG) sensors using iOFDR [11]
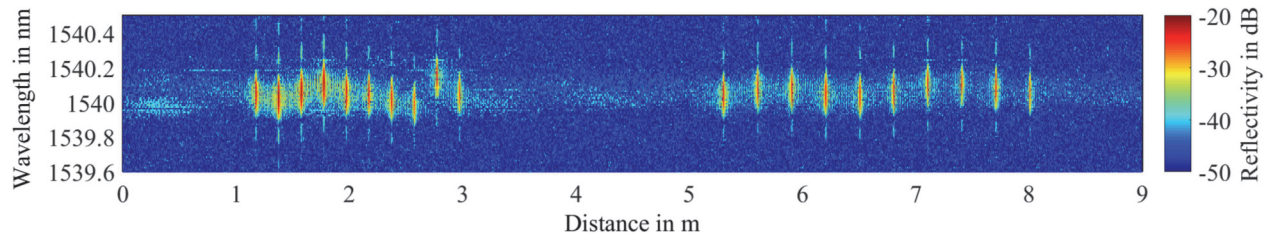
Figure 7. Measured reflectivity over distance and wavelength at room temperature of two concatenated FBG arrays, each containing ten gratings with 20 cm and 30 cm separations, respectively [11].

Fig. 7 shows results for such quasi-distributed fiber Bragg grating sensors using iOFDR. The FBGs are well resolved in both their spectrum and range. Some artifacts from residual coherent interference and mutual reflections between different FBGs can still be seen. The measurement time of such a system is quite large because of measuring many iOFDR traces at each wavelength of the TLS. The measurement time can be largely reduced by applying methods from radar systems like compressed sensing. As the position of the FBGs are known, this information can be used to apply less and unevenly spaced RF frequencies und thus, requiring less time than a conventional iOFDR, and still achieving almost the same precision in Bragg wavelength measurement of the FBGs [14]. Model-based processing of the measured transfer function $H(f)$ instead of an inverse Fourier transform can include and mitigate mutual reflections for such iOFDR applications, which is hardly possible for OTDR.

Finally, Raman DTS and spatial FBG multiplexing can be combined in a single fiber-optic sensor system, for simultaneous detection of anomalous temperatures anywhere of large structures and precise multi-point strain or temperature sensing at known critical spots. An example measurement result from [13] is shown in Fig. 5b. This has great potential for surveillance of large facilities in energy systems, for example high-voltage direct-current (HVDC) switchyards.

5. Conclusion and outlook

Optical frequency-domain reflectometry is a powerful technique for achieving spatial resolution in fiber optic sensing. Coherent OFDR with tunable lasers provide superior range resolution of a few 10 μm and optional spectral interrogation. Incoherent OFDR generates reflection profiles similar to conventional OTDR but in less time or with better SNR because of a higher average light energy in the fiber. Radar signal processing techniques improve the performance of such iOFDR systems, with a full discussion being beyond the scope of this paper. In the future, novel wavelength-agile, compact and economic tunable lasers will foster cOFDR applications. With the availability of ultra-high-speed and high-resolution digital-to-analog converters for modulation signal generation and analog-to-digital convertors for backscatter signal acquisition, more capable and cost-effective iOFDR systems can be realized compared to conventional microwave electronics. Moreover, this offers the possibility of using different modulation waveforms than simple single pulses in OTDR or harmonic oscillations in iOFDR, washing out the limitations and combining the features of this both worlds in the future. Combined with a massive digital signal processing in high-speed FPGAs, this gives a bright outlook for innovative fiber sensing systems using both, singlemode silica fibers and multimode polymer optical fibers.

6. Acknowledgements

7. References

[1]   X. Bao, L. Chen: "Recent progress in Distributed Fiber Optic Sensing," Sensors, vol. 12 no. 7, pp. 8601-8639 (2012).

[2]   R. Engelbrecht. „Fiber Optic Strain and Temperature Sensing: Overview of Principles," 18th Int. Conf. on Sensors and Measurement Technology (SENSOR 2017), 30. Mai – 1. Juni 2017, Nürnberg. In: Proceedings. AMA Verband für Sensorik und Messtechnik e.V., paper no. B6.1 (2017).

[3]   S. Liehr and K. Krebber, "Application of quasi-distributed and dynamic length and power change measurement using optical frequency domain reflectometry," IEEE Sensors J., vol. 12, no. 1, pp. 237–245 (2012).

[4]   E. Karamehmedovic, U. Glombitza: "Fiber-optic distributed temperature sensor using Incoherent Optical Frequency Domain Reflectometry," Proc. SPIE 5363, pp. 107-115 (2004).

[5]   S. M. Foaleng, M. Tur, J.-C. Beugnot, L. Thévenaz: "High spatial and spectral resolution long-range sensing using Brillouin echoes," J. Lightwave Technol., vol. 28, no. 20, pp. 2993-3003 (2010).

[6]   M. Majumder, T. K. Gangopadhyay, A. K. Chakraborty, K. Dasgupta, D.K. Bhattacharya: "Fibre Bragg gratings in structural health monitoring-Present status and applications." Sensors and Actuators, A: Physical, vol. 147, no. 1, pp. 150-164 (2008).

[7]   M. Rothhardt, C. Chojetzki, H. R. Mueller: "High mechanical strength single-pulse draw tower gratings," Proc. SPIE 5579-1, pp. 127-135 (2004).

[8]   G. Saur: „Aufbau und Charakterisierung eines polarisationsaufgelösten kohärenten Frequenzbereichsreflektometers für die verteilte faseroptische Sensorik," Master Thesis, Institute of Microwaves and Photonics (LHFT), Friedrich-Alexander-Universität Erlangen-Nürnberg (2016).

[9]   A. K. Sang, M. E. Froggatt, D. K. Gifford, S. T. Kreger, B. D. Dickerson: "One centimeter spatial resolution temperature measurements in a nuclear reactor using Rayleigh scatter in optical fiber," IEEE Sensors J., vol. 8, no. 7, pp. 1375-1380 (2008).

[10] R. Engelbrecht: „Nichtlineare Faseroptik," Springer Vieweg, Berlin Heidelberg (2014).

[11] S. Werzinger S. Bergdolt, R. Engelbrecht, T. Thiel, B. Schmauss: „Quasi-Distributed Fiber Bragg Grating Sensing Using Stepped Incoherent Optical Frequency Domain Reflectometry," J. Lightwave Technol., vol. 34, no. 22, pp. 5270-5277 (2016).

[12] S. Liehr, N. Nöther, K. Krebber: "Incoherent optical frequency domain reflectometry and distributed strain detection in polymer optical fibers," Meas. Sci. and Technol., vol. 21, no. 1, paper no. 017001 (2010).

[13] M. Köppel, S. Werzinger, J. Sutter, S. Bergdolt, B. Schmauss: "Incoherent Optical Frequency Domain Reflectometry for Distributed Raman and Bragg Fiber Temperature Sensors," 18th Int. Conf. on Sensors and Measurement Technology (SENSOR 2017), 30. Mai – 1. Juni 2017, Nürnberg. In: Proceedings. AMA Verband für Sensorik und Messtechnik e.V., paper no. B6.2 (2017).

[14] S. Werzinger, M. Gottinger, S. Gussner, S. Bergdolt, R. Engelbrecht und B. Schmauss: „Model-based compressed sensing of fiber Bragg grating arrays in the frequency domain," 25th Int. Conf. Optical Fiber Sensing (OFS-25), Jeju, Korea. In: Proc. SPIE. 10323, paper no. 103236H (2017).

Surface Plasmon Resonance sensor read out system based on the Field Programmable Gate Array

Y.S. Ong[1*], I. Grout[1], E. Lewis[1] and W. Mohammed[2]

1 Department of Electronic and Computer Engineering, University of Limerick, Limerick, Ireland
2 BU-CROCCS, School of Engineering, Bangkok University - Rangsit Campus, Bangkok, Thailand

*Yong Sheng Ong: Yong.Ong@ul.ie

Abstract: In this paper, the design and operation of plastic optical fibre (POF) based surface plasmon resonance (SPR) sensor read out system is presented. The design is based on the use of the field programmable gate array (FPGA) which is aimed to provide a flexible, portable and low cost platform for this type of sensor. The light source is an RGB – red, green, blue – light emitting diode (LED) and the detector is a silicon photodiode for intensity interrogation. The LED is used with a single photodiode to provide a pseudo-wide spectrum and self-referencing capability. The system is interfaced to a computer running a Python open-source language script using Zigbee wireless connection. The script provides FPGA control, sensor data capture and visualisation, and database interfacing.

1. Introduction

In typical optical fibre sensor (OFS) systems, an optical fibre cable is used either as a medium for signal propagation between the sensor and the sensor electronics or becomes part of the sensing device. In both cases, light is used rather than electrical signals. Recently, a range of different optical fibre sensors have been developed and demonstrated for applications such as environmental monitoring and biomedical sensors [1, 2]. Any particular application requires a specific system implementation. The common ground between all the OFS systems is that a fibre (fiber) is used to deliver the light signal between the sensor and the system electronics. This approach requires the use of electro-optical components to generate a modulated optical beam and convert the detected change of intensity into an electrical signal [1]. For the optical link, several types of fibres are commonly used: single mode fibre, silica based multimode fibre and POF are commonly used [1]. Here, POF is selected as it is commonly used in many lower cost sensor designs [3]. To develop a working OFS, an interface needs to be developed to control the light source, provide sensor output signal detection and analyse results obtained. Interfacing with the sensor can be typically realised using a computer based software application and data acquisition (DAQ) module, or by using software programmed processor such as a microcontroller programmed using a suitable programming language such as C [4-6]. In this paper, an alternative approach is discussed, where a hardware configured programmable logic device (PLD) such as the FPGA or complex programmable logic device (CPLD) is used. Unlike a processor, programmed to implement a software program, the PLD is configurable (programmable) in hardware. It can be configured to implement different digital logic circuits and as such, it can be used to develop custom and optimised digital logic for the required application. The FPGA provides the core digital functions in hardware using a synthesised design description written in a hardware description language (HDL) such as VHDL or Verilog-HDL [7]. It can be seen as a complement to the software programmed processor (e.g., a microcontroller). The paper discusses the design and operation of an OFS system based on the Xilinx Artix-7 FPGA [8] which forms the core functions of the system as shown in figure 1. The design approach adopted in hardware using the FPGA can be compared with the software programmed processor approach. The sensor used is the Bangkok University Surface Plasmon sensor (BU-SPR) [9] which is excited using an RGB LED. Test results from the RGB LED light source and the SPR sensor are gathered, visualised and stored on the host computer for analysis through the use of a Python open-source language script for computer side software operations. The FPGA controls the R, G and B colours independently using current control (voltage-to-current (VI)) circuits that derive their inputs directly from the FPGA digital output pins. The optical power synchronised to each particular colour light pulse is recorded using a photodiode, current-to-voltage (IV) converter circuit and the internal 12-bit resolution analogue-to-digital converter (ADC) embedded within the FPGA (referred to as the XADC). A Zigbee wireless serial interface allows for two-way communication between the FPGA and an external computer.
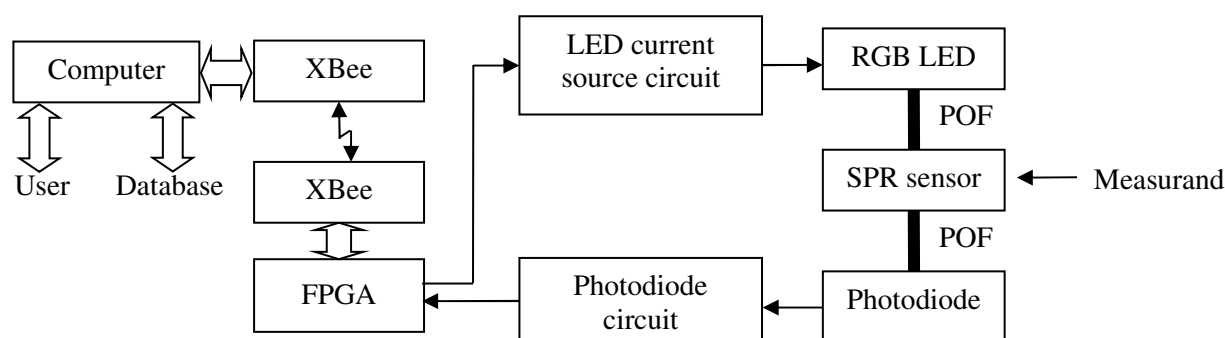
Figure 1. FPGA based sensor system overview.

The following section, section two, will introduce the use of the FPGA as the configurable digital core within an OFS system. The use of the FPGA with a single sensor will be presented as a proof of concept. Section three extends the idea introduced in section two to include the interfacing to multiple sensors within a "distributed" OFS system based on 'single point' sensors. Section four will conclude the paper.

2. OFS system based on the FPGA

The FPGA is a reprogrammable (configurable) integrated circuit (IC) that is capable of forming different custom hardware circuits and systems. It consists of an array of logic blocks that are linked together through programmable interconnect. The digital circuit to configure within the FPGA would be designed by the user using different design entry approaches familiar to digital circuit designers, but typically an HDL description to implement the required functions would be created. The reprogrammable capability ensures long term value as it requires minimal cost or time for system improvement (i.e., no hardware changes are required when upgrading the digital design as a new configuration is just downloaded into the existing device). To interact with external circuitry, input/output (I/O) blocks are used as an interface that can be configured to operate with different I/O standards. FPGA devices typically have a high number of programmable I/O pins. For the desired sensor application, having multiple pins means that there is a potential to interface to multiple units with a single FPGA. In addition, the concurrent processing capabilities of the implemented hardware means that it can process a large amount of incoming data from multiple devices simultaneously. These two device features make the FPGA useful in an embedded sensor arrangement. The proposed FPGA based optical sensor would be capable of performing high speed signal modulation, collection and data processing. In addition, functional blocks such as DSP (digital signal processing) slices commonly integrated into modern FPGAs can be used. Combined with a high clock frequency, demanding algorithms or tasks can be created within the FPGA. This makes the FPGA a suitable device for use in sensor systems [10] to act as digital core for an OFS system requiring real-time operation, embedded DSP operations and multiple nodes. Different sensing mechanisms can be supported using combination of light sources and receivers with appropriate digital circuitry within FPGA. In the system arrangement considered here, the LED current source circuit and photodiode circuit are used to interface with the light source and receiver. Wireless communication between a host computer and the sensor system is implemented using the Digi XBee communication module. System control and database (MySQL) entry operations are performed using a Python script operating on the host computer. A graphical user interface (GUI) was created to facilitate such operations. To demonstrate readout system operation, the BU-SPR system is used. A single photodiode (Industrial FiberOptics IF-D91) is used to convert the optical signals into analogue electrical signal. The XADC within the FPGA is then used to convert the analogue signal into a 12-bit digital value. In the SPR system, the reflected spectrum from the sensor exhibits an obvious dip (around 650 nm) when water is present for polarised light in Transverse magnetic (TM) mode under the designed incidence angle of $20°$ as shown in the inset in figure 2. In terms of RGB values, the presence of the dip corresponds to the change of the three colour values in different manners. With the given spectrum, the value of the blue light experiences a minimal change due to the presence of the dip in the red region. Hence, the blue signal can be used as a reference to compensate for the optical signal fluctuation. Practically, a series of red, green, and blue colour light pulses are generated by the LED using a current driver circuit and individual modulated light pulses intensity gives measurand information. A POF is used as a link to guide the

colour pulses into the SPR sensor as shown in figure 2. Different colour pulses attenuate differently. The modulated light pulses then reach the photodiode through another fibre.
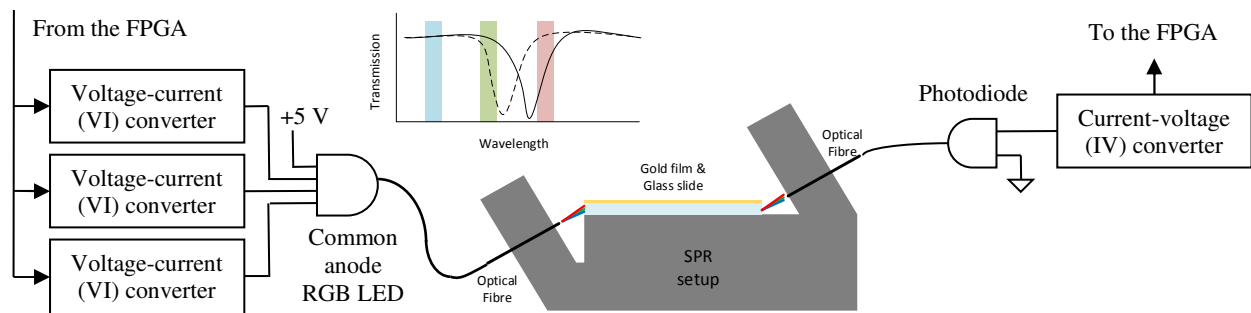

Figure 2. Surface Plasmon resonance sensor arrangement.

The modulated light intensity is transformed into electrical information and then digitised using the XADC. A data processing unit within the FPGA is tasked to minimise signal noise by averaging multiple samples. The processed data is stored in internal memory before transmission to the host computer. Transmission is performed by serial communication unit using the UART (universal asynchronous receiver transmitter) protocol. This unit also receives system commands from the user to regulate LED pulse generation and control the XADC unit. These functions are executed by a few components within the FPGA as shown in figure 3. The Digilent Arty development board [8] houses the Artix-7 FPGA.
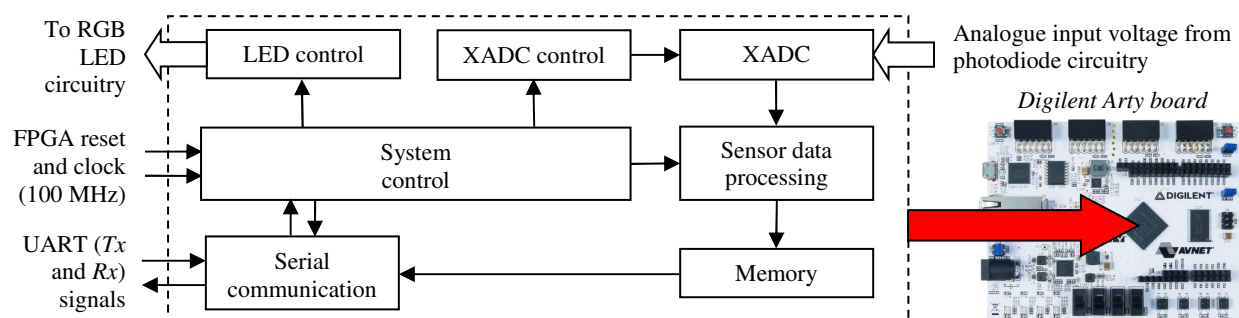

Figure 3. Embedded operations with the FPGA.

Preliminary test results from the SPR sensor are shown in figure 4. In figure 4(a), the bar plot shows the results for two measurands, water and air. The red, green, and blue intensity bars are placed at the peak wavelength positions. The plot shows that the red and green light data produce a large change when compared to blue data which is relatively stable for both measurands. Currently data analysis is still largely dependent on the host computer, although analysis operations within the FPGA are possible. Nearest centroid analysis method is considered by using red and green colour intensity, whilst blue colour used as reference, as shown in figure 4(b). Centroids are generated using training data and few measurands are categorised through colour.
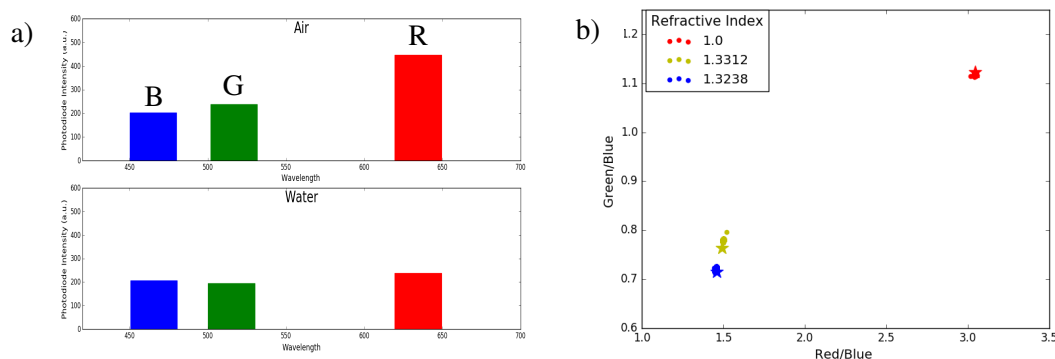

Figure 4. a) Elementary data b) Data analysis using nearest centroid method (star: centroid, dot: data).

3. Distributed OFS system based on multiple 'single point' sensors and the FPGA

A distributed sensor system aims to support many sensing instruments utilising a single core module that can remotely monitor multiple locations and parameters. This sensing method is important in both small and large scale application in numerous fields which include: electrochemical and environmental [4, 11] in order to collect and process information in real time. Figure 5 depicts a schematic of a proposed multi sensor arrangement that govern multiple light sources and light receivers that connected to sensors using the FPGA. This multi-sensor arrangement is a projection of the FPGA based single sensor arrangement that is capable of communicating with other devices and would also incorporate a human-computer interface. Its parallel processing ability allows the user to deploy multiple optical fibre sensors with different light source requirements. Essentially, different sensing mechanisms can be assembled within single core module.
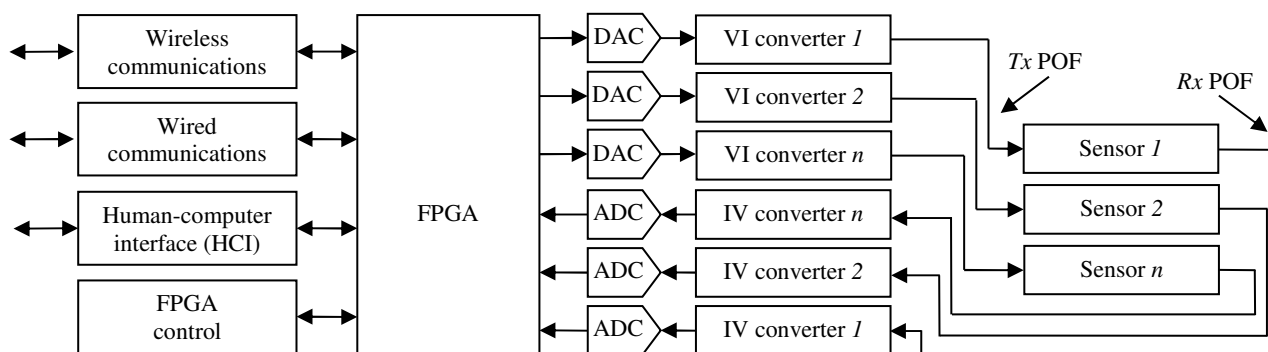

Figure 5. Distributed, multi-sensor arrangement based on 'single point' sensors and the FPGA.

4. Conclusion

In this paper, the design and operation of a POF based SPR sensor read out system was presented. The FPGA was used as the digital core providing interfacing to the sensor, the user and an external computer. The computer provided FPGA control and sensor data analysis, along with data visualisation and access to a MySQL database. A prototype system based on a single SPR with RGB LED light stimulus was presented and this acted as a "proof of concept" for this type of sensor system, along with considerations for the use of the FPGA in a multi-sensor, distributed application based on 'single point' sensors.

5. Acknowledgements

6. References

1. Yasin, M., S.W. Harun, and H. Arof, *Fiber optic sensors*. 2012: InTech.
2. Udd, E. and W.B. Spillman Jr, *Fiber optic sensors: an introduction for engineers and scientists*. 2011: John Wiley & Sons.
3. Grassini, S., et al., *Design and deployment of low-cost plastic optical fiber sensors for gas monitoring*. Sensors, 2014. **15**(1): p. 485-498.
4. He, Y., et al. *Study on Mash Gas Monitoring with Distributed Multipoint Fiber Optic Sensors System in Coal Mine*. in *Photonics and Optoelectronics (SOPO), 2012 Symposium on*. 2012. IEEE.
5. Nenninger, G.G., M. Piliarik, and J. Homola, *Data analysis for optical sensors based on spectroscopy of surface plasmons*. Measurement Science and Technology, 2002. **13**(12): p. 2038.
6. Van Hoe, B., et al., *Ultra small integrated optical fiber sensing system*. Sensors, 2012. **12**(9): p. 12052-12069.
7. Laskar, S. and S. Bordoloi, *Microcontroller-based instrumentation system for measurement of refractive index of liquid using bare, tapered and bent fibre as sensor*. IET Optoelectronics, 2013. **7**(6): p. 117-124.
8. Xilinx. *Artix-7 35T Arty FPGA Evaluation Kit*. [cited 2017 17 July]; Available from: https://www.xilinx.com/products/boards-and-kits/arty.html.
9. Somarapalli, M., et al., *Demonstration of low cost and compact SPR optical transducer through edge light coupling*. Micro & Nano Letters, 2017.
10. De La Piedra, A., A. Braeken, and A. Touhafi, *Sensor systems based on FPGAs and their applications: a survey*. Sensors, 2012. **12**(9): p. 12235-12264.
11. Cao-Paz, A.M., et al., *A multi-point sensor based on optical fiber for the measurement of electrolyte density in lead-acid batteries*. Sensors, 2010. **10**(4): p. 2587-2608.

Sectorial-Perturbation Analysis of Fiber Specklegram Using Machine Learning Techniques

M. Fontana[1], A. Rodríguez-Cuevas[1], L. Rodríguez-Cobo[1,2,3], J. Mateo[4], M. Lomer[1,2,3*]

1 Grupo de Ingeniería Fotónica, Universidad de Cantabria, Santander, Spain
2 Centro de Investigación Biomédica en Red en Bioingeniría, Biomateriales y Nanomedicina (CIBER-BBN), Cantabria, Spain
3 Instituto de Investigación Sanitaria Valdecilla (IDIVAL), Cantabria, Spain
4 Department of Electronic Engineering, University of Zaragoza, Spain

*Corresponding author: lomerm@unican.es

Abstract: Fiber-optic specklegram patterns are highly sensitive to external perturbations such as vibrations, temperature, or strain. However, due to its highly random behaviour using this kind of system for distributed sensing remains. In this work, a distributed sensing speckle system has been designed. This proof-of-concept has been developed by perturbating a multimode plastic optical fiber in three different places, recording the videos of these perturbations and using them for training and testing machine learning algorithms. The results show classifications over 99% of accuracy when testing new data under certain conditions.

1. Introduction

The importance of the fiber-optic sensors has been growing strongly in the last years. Among the different sensors, many authors have studied the speckle phenomenon produced in fiber optics since Spillman et al. first realised about the utility of the phenomenon [1]. Some of the most important applications are medical [2], and security ones [3].

This phenomenon occurs when coherent light is conducted towards a multimode optical fiber. At the other end of the fiber a specklegram pattern is generated [1]. Eventually the speckle pattern is highly sensitive to external perturbations such as vibrations, temperature, or strain. Nonetheless, whenever a speckle system in fiber optic is used for sensing purpose, the specklegram study is always statistical.

The current state-of-the-art shows that there are almost no publications about the speckle system in fiber optic used as a distributed sensing method. This is fundamentally explained because of the fact that the speckle phenomenon in fiber optic is highly random and therefore obtaining a relation between the behaviour of the modes and the kind or place of the perturbation is extremely complex in a mathematical way. However, some authors have study this behaviours in rather small segments of fiber optic [4].

In this work, we set up a system able to detect a perturbation occurring along the fiber and to recognize if it has taken place at the beginning, at the end or in the middle of it. The proposed system has been set in a very basic way under laboratory conditions and as a proof-of-concept.

2. Set up and Processing method

2.1 Set up:

In this work, a sectorial distributed sensing specklegram system has been propose and tested. A setup, consisting of a 6-meters-long plastic optical fiber, a CCD camera, a coherent light source (638 nm wavelength), and a linear stepper motor has been used, as it is shown in the Figure 1 (see Figure 1). By hitting the fiber in three different equidistant points (1,5 meters from each other), perturbations lasting around 8 frames (8/30 seconds) were generated, and recorded. Additionally, some other videos were recorded too, but in these occasions the perturbations were caused manually using short sticks or just the fingertip. All these short videos have been processed normalized and labelled.

The videos were recorded individually but they were captured in groups on different days. Each of these groups was identified as a different dataset.
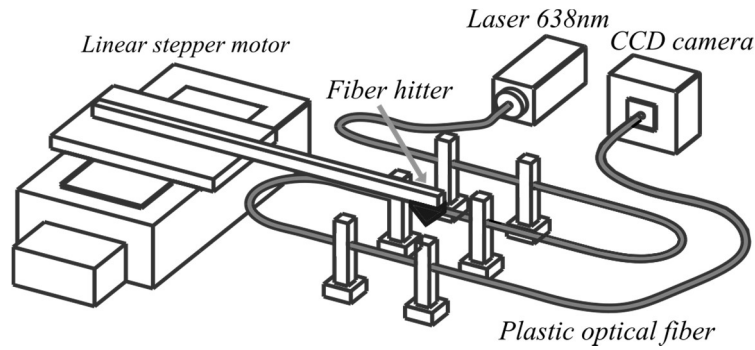
Figure 1. Set up used for automatic recording videos of perturbations on a multimode plastic optical fiber.

2.2 Pre-Processing method:

The processing method consist of a pre-processing of the videos converting them into images and afterwards two different classification methods.

After the acquisition, the nine frames of a perturbation look like in figure 2.a. Then, the video is converted to a grayscale. Later, a differential processing is done by subtracting one frame from the previous one (see figure 2.b) and then obtaining the total of intensity in every of them. In this way, we obtain a 1D sequence of values which every one of them represents how much the image speckle pattern is changing respect to the previous image. In the next step, the maximum value of the 1D sequence is obtained. Later the frame corresponding to this value plus the four previous and the four next are sum (Equation 1). The outcome images (see figure 2.c) are pondered by dividing every pixel value by the sum of the values of all pixels (Equation 2).

$$Frame\_sum = \sum_{K=1}^{9} Diff\_frames(K) \qquad (1)$$

$$Frame\_norm = \frac{Frame\_sum}{\sum pixel(Frame\_sum)} \qquad (2)$$

In this equations *Frame_sum* is the sum of all the 9 frames about a certain peak, *Diff_sum* is the vector containing all the differential frames related to a peak, *pixel()* is a function that returns the intensity of a pixel and *Frame_norm* is the normalized image.

The reason of this pre-processing method is making sure that the classification obtained is based on the changes generated in the pattern and no based of the fact that all the perturbations of one category follow the same temporal pattern or that all the perturbations are slightly more intense in one category than in the other.
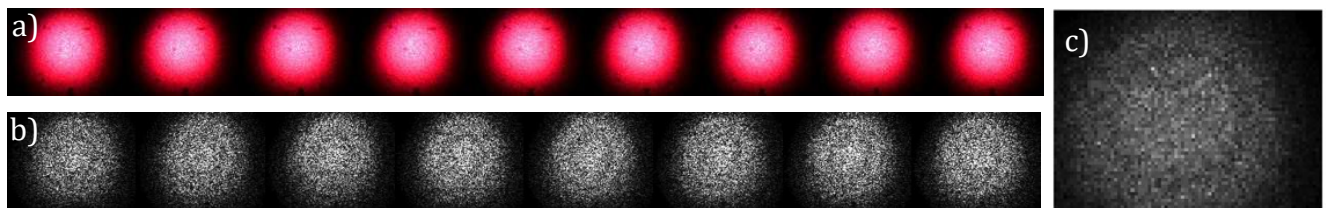

Figure 2. a) Frames related to a detected perturbation in 50nm optical fiber; b) Differential frames of the ones in Figure 2.a; c) Example of the result of the sum and the normalization of the nine differential frames.

2.3 Machine learning:

Using supervised machine learning techniques, two different approaches have been implemented to predict where the perturbations were being caused. The first and the simplest one was a feedforward neural network, which in this case consisted of three layers of neurons. The data initially flows through an input layer, where each pixel on the input image is associated to a neuron. Then, the information has to pass through a hidden layer, that in our case had dimension of 10 and 20 neurons, depending on the types of input data. In this layer, each neuron is connected to each neuron of the previous layer, that is the input one. So, the output of a neuron belonging to this layer is a function of all the pixel at the input, which contribute to the output according to a set of weights calculated during the training process (see figure 3.a). In our case, we chose to use the scaled

conjugate gradient backpropagation training function provided by the Matlab R2016a. The neurons of the hidden layer are fully connected with the final layer, in which are the neuron that will represent the result of the classification.

The second and more advanced method of analysis was a deep convolutional neural network (CNN) [5]. It was constituted by a greater number of layers, able to analyse a wider set of characteristics of the input images and to summarize the information extract through the network up to the output, represented by the classification of the position in our case (see figure 3.b). In particular, the structure used for this analysis includes two convolutional layers, which have the aim of learn a set of parameters, often called "filters", to point out a certain number of features present through the images. The output of a convolutional layer is then passed through a "Rectifier Linear Unit" (ReLU), that is simply an activation function which performs a threshold operation to each element, without changing the number of them. After this operation, a Max Pooling layer is used to down-sample the representation of the data coming out from the previous layer, reducing the number of parameters by dividing the input in non-overlapping subregions and taking the maximum element to represent the entire subregion at the output. The matrix built in this way pass to another set of the layers described above, and then it is analysed by the Full Connected Layer to compute the class scores, where each of the three neurons that belong to this layer correspond to a category.
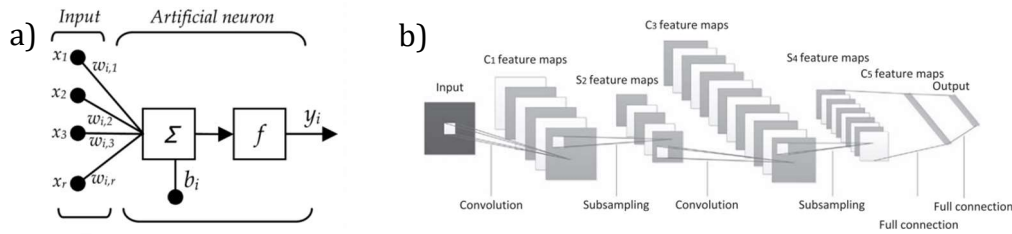

Figure 3. a) Inputs and outputs of a neuron in the network; b) Structure of the deep convolutional neural network, exposed by Liu, W. et al. in [5].

3. Results:

The results are divided in two different tables. In the first one (Table 1 a)) all the datasets are mixed. Then 75 percent of the videos are used for testing and the additional 25% are used for testing. The second table (Table 1 b)) shows the results when the data sets for testing and training are different.

Table 1: a) Results when using parts of the same datasets for training and for testing. b) Results when using different datasets from training than testing. The type of data is described depending whether it is acquired using the linear or manually. Also the number the number of videos (nº) used for testing and training are represented.

a) Type of Fiber	Train	Test	Classification Neural Network	Classification Deep Learning
50μm Diameter Core	Linear nº 112500	Linear nº 37500	99.8 %	99.71 %
	Manual nº 17050	Manual nº 5680	79.1 %	78.3 %
240 μm Diameter Core	Linear nº 43020	Linear nº 14340	79.1 %	80.08 %
	Manual nº 14550	Manual nº 4850	78.7 %	72.26 %

b) Type of Fiber	Train	Test	Classification Neural Network	Classification Deep Learning
50μm Diameter Core	Linear nº 112500	Linear nº 37500	96.9 %	90.34 %
	Manual nº 17050	Manual nº 5680	53.4 %	48.91 %
240 μm Diameter Core	Linear nº 43020	Linear nº 14340	73.7 %	71.01 %
	Manual nº 14550	Manual nº 4850	75.6 %	66.07 %

The number of videos for testing and training is the same than in the previous cases but they were acquired in different days. Therefore, the environmental conditions were slightly different (camera temperature, air currents,

alignment of the CCD and the fiber, or noise). Additionally, to proceed with the best possible data some of the videos were deleted beforehand since they had some problems related with some external perturbations like vibration, air streams or some other problems that were generating noise in the signal. That's the reason why the datasets are not equal. However, it should be emphasized that in any case the videos used for testing are previously used for training.

As it is shown in both tables classifications are very precise over 99% when the 50μm plastic fiber optic is used, while only 80% accuracy is obtained when using a 240μm plastic fiber optic. Above all this fact mean that classifying the perturbation by the section it is caused is possible.

On the other hand, it is not clear why the accuracies are considerably better in the case of the 50μm fiber than in the case of 240μm. Nevertheless, the amount of modes generated in a 240μm fiber is considerably greater than the amount of modes of a 50μm fiber, so that could mean that the size of the dataset required is significantly larger and probably the camera resolution needs to be higher as well.

When analysing the results of the perturbations obtained manually, in every case the classifications are worst, probably because everything is more random. Furthermore, the differences become clearer when different datasets are used. Comparing the results of the handmade perturbations, the differences between the datasets are more important because the way the fiber was disturbed was different from dataset to dataset so it seems logical that the classification is worse than the combinate datasets.

Finally, both machine learning methods are rather accurate, although the neural network method is slightly more precise.

4. Conclusions:

The pre-processing method makes sure that the videos are not classified for the differences in the perturbation; whether this is a little bit more intense in one segment than in the other or the temporal evolution of the perturbation is more similar intra-categories than inter-categories. Following this statement, it is possible to assert that, based on the results obtained in this work, the perturbations caused in the speckle pattern in a multimode plastic fiber optic can be classified, with some degree of accuracy, according to the distance where the perturbation is caused. However, any slightly modification in the conditions of the environment or in the alignment of the fiber respect to the camera will generate an important degree of confusion in the machine learning method. So therefore, it is important to keep the external conditions as similar as possible when generating the datasets.

This work was done as a proof-of-concept, so future works need to be done changing the parameters, increasing the number of categories, or modifying the processing method in order to corroborate the conclusions here exposed.

5. Acknowledgments

6. References:

1. Spillman W, Kline B, Maurice L, Fuhr P. Statistical-mode sensor for fiber optic vibration sensing uses. Appl Opt. 1989;28(15):3166-76.
2. Rodriguez-Cuevas A, Peña ER, Rodriguez-Cobo L, Lomer M, Higuera JM. Low-cost fiber specklegram sensor for noncontact continuous patient monitoring. J Biomed Opt. 2017 Mar 1;22(3):37001.
3. Rodriguez-Cuevas, A., Rodriguez-Cobo, L., Lomer, M., & Lopez-Higuera, J. M. (2017, April). Safe and private pedestrian detection by a low-cost fiber-optic specklegram. In *Optical Fiber Sensors Conference (OFS), 2017 25th* (pp. 1-4). IEEE.
4. Plöschner M, Tyc T, Čižmár T. Seeing through chaos in multimode fibres. Nature Photonics. 2015;9(8):529-35.
5. Liu, W., Wang, Z., Liu, X., Zeng, N., Liu, Y., & Alsaadi, F. E. (2017). A survey of deep neural network architectures and their applications. *Neurocomputing, 234,* 11-26.

Integrated POF Illumination & Data Communication System

Mark Li - (General Manager of Hakko Opto Limited)

Address : Unit 4, 3/F, Sun Cheong Industrial Bldg., No.1 Cheung Shun Street, Cheung Sha Wan,

Kowloon, Hong Kong

*Corresponding author: markli@hakko-opto.com

Abstract: This paper is to analyse briefly the opportunity of combining the illumination as well as the data communication sectors of using Polymer/Plastic Optical Fiber (POF). It also reports the preliminary research results of the individual sector. This paper also indicates the significance of this Integrated POF Illumination & Data Communication Platform and how the general public may be beneficial from deploying this innovative integrated system.

1. Introduction

Optical fiber made of glass has been using for long distance data communication since the invention of optical communication by Professor Charles Kao and others in 60's of last century. Optical fiber made of polymer (or is also called "plastic) has also been investigated as the transmission media for data communication . However, due to the high transmission loss (typical 0.8dB/m), it can only be used for short-distance applications such as in-building or household installations. The main advantage of Polymer Optical Fiber (POF) is its flexibility and easiness of installation. Both glass and polymer optical fiber for data communication application use laser of invisible spectrum from 850nm ~ 1700nm as the light source.

2. POF For Illumination

POF has also been using for video application in medical diagnosis industry for many years. They insert one end of the POF inside the patient's body and watch the organs from another end searching for any abnormality of the patient's organs. People start to use POF for illumination not long ago mainly for decoration only. They use either thin solid core POF (side-glow or end-glow) or bundle of very tiny thin POF. The light source for POF illumination is basically LEDs due to rich availability of colours. However, the illuminating length is limited to few meters only due to the incoherent light characteristics of LED that makes the very high transmission loss over the POF. Until recently, few companies start to use high power lasers of visible spectrum as the light source to illuminate a thicker diameter side-glow POF for real linear lighting applications.

2.1 Advantages

There are many advantages of using POF for linear lighting applications such as:- (see figure 1)

- non-combustible
- submersible
- weatherproof and impact resistant
- malleable, non-current conducting
- super energy efficient
- Very long life expectancy
- Homogenous brightness along the POF (see figure 2)
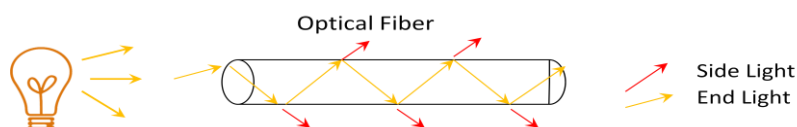- Low initial setup costs
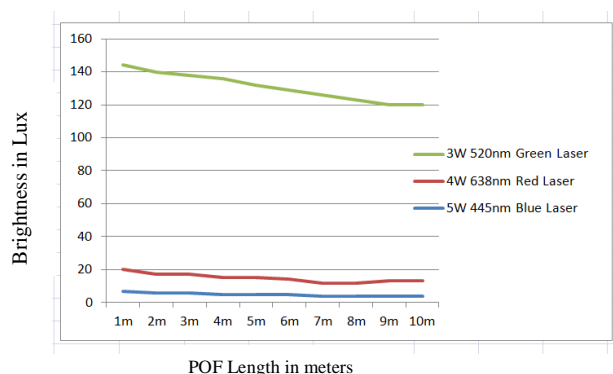

Figure 1. POF Lighting

Figure 2. Brightness vs. Length of POF Away From Laser Source Of Different Colours

2.2 Costs Comparison

POF/Laser lighting is more cost effective and energy efficient than corresponding neon lamp and LED lighting solutions. Presently, two 2.5W green lasers can light up 80m long and 14mm diameter cross-section side-glow POF with reasonable brightness in Lumen. For blue and red lasers, higher laser power output (4W~6W) are required to produce similar lumen for the same POF length. The following is a brief costing comparison:-

- Setup Cost Saving (see figure 3)

Optical Fiber Laser System BOM	QTY	Cost	Total
Side Light Fiber Optics 1/2" 14mm diameter (ft)	350	$9.74	$3,409.98
UV 2 Part Mounting Channel (per 6ft)	58	$24.90	$1,452.50
4W Blue Laser Illuminator	3	$2,577.00	$7,731.00
TOTAL			$12,593.48

Neon Lighting BOM	QTY	Cost	Total
15mm Neon Tubing CO_2 gas White Light (ft)	350	$75.00 [1]	$26,250.00
*8ft max single run [2]			
5000V 60mA Electronic Transformer	3	$187.13 [3]	$561.39
7500V 60mA Electronic Transformer	1	$263.60 [3]	$263.60
TOTAL			$26,811.39

LED Linear Lighting BOM	QTY	Cost	Total
24VDC 5700K White LED Cold Neon Lighting (ft)	350	$41.61	$14,563.50
*32ft max single run			
Cold Neon Termination Kit	11	$17.00	$185.94
Aluminum Mounting Track per 39"	108	$13.00	$1,400.00
150W DC Transformer	11	$176.00	$1,925.00
Surge Protectors	11	$31.60	$345.63
TOTAL			$18,420.06

Figure 3. Setup Cost Comparison

- Energy Cost Saving (see figure 4)

	Laser	Neon	LED
Vancouver 11.27 cents per kWh [7]			
1 day cost ($)	$0.16	$1.66	$1.73
1 year cost ($)	$58.40	$604.69	$632.33
Los Angeles 22.3 cents per kWh [8]			
1 day cost ($)	$0.32	$3.28	$3.43
1 year cost ($)	$115.55	$1,196.51	$1,251.20

	Laser	Neon	LED
Initial Cost	$12,593.48	$26,811.39	$18,420.06
Annual Operating Cost			
Equipment Replacement *	$2,473.92	$2,298.00	$1,641.96
Maintenance	$0.00	$1,800.00 [9]	$0.00
Energy	$115.55	$1,196.51	$1,251.20
TOTAL	$2,589.47	$5,294.50	$2,893.16

Figure 4. Energy Cost Saving & Total Cost Analysis

3. POF For Data Communication

As mentioned earlier in this article, thin POF has been using as a transmission media for short distance data communication such as the home network. But it still not very common in the general public. In car industry and aviation industry, using POF for data networking between sensors is also seen in limited scenario. The main reason for using POF for data networking in car/aviation industries is its light weight and immunity to electromagnetic interference. In our on-going research, the goal is to use the same POF and the same laser that are for illumination to perform the data communication simultaneously. Therefore, it is an integrated platform for both illumination and data communication application. There are two directions for our research work namely 1) End-To-End Data Communication, and 2) Wireless Visible Light Communication (VLC).

3.1 End-To-End Data Communication

Analogous to the long distance data communication using glass optical fiber and laser of invisible light spectrum, the end-to-end data communication using POF and laser of visible light spectrum (mainly blue, green or red) deploys a similar approach. The digital data being transmitted over the POF from one end modulates the laser light source. The receiver demodulates the digital data from the other end. Since human eyes cannot distinguish light intensity variation of frequency over 25 Hertz, the end-to-end modulated data transmission will not affect the illumination of the POF. Of course, this application cannot extend to long distance. But the current maximum length for POF illumination of reasonable brightness (lumen/lux) is only 80 meters presently and therefore end-to-end data communication of POF is not necessary to exceed this limit. The target data rate for this application is over 1Gbps. (see figure 5)
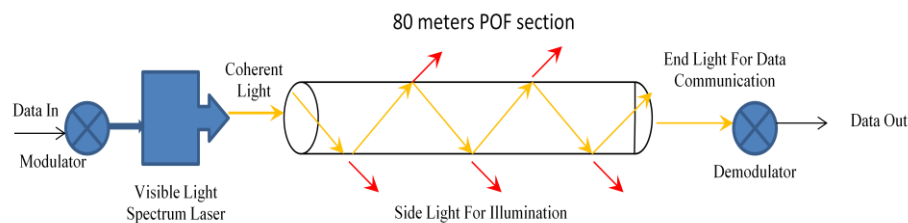

Figure 5. POF Illumination & End-To-End Data Communication Integrated Platform

3.2 Wireless Visible Light Communication (VLC)

With the emerging of the LiFi technology using LED, VLC will be more popular and has advantages over traditional WiFi. The POF with laser illumination platform integrated with theLiFi technology will be a very attractive research direction. (see figure 6). The POF Wireless VLC solution can be considered as the analogy to Radio Frequency (RF) Coaxial Leaky Cable. The RF Leaky Cable is being widely used for mobile communication in special locations such as tunnels, mining,…,etc. where normal RF signal from antenna cannot reach. POF VLC does not only provide a similar solution for mobile communication. It can also provide illumination simultaneously as a prominent advantage over traditional RF Coaxial Leaky Cable. However, the LiFi technology is still under development and does not have large scale public deployment. The wireless VLC application with POF will come later in the product development road map.
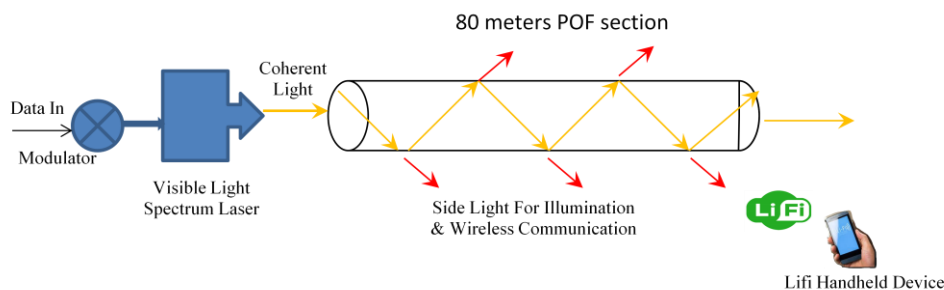

Figure 6. POF Illumination & Wireless Visible Light Communication Integrated Platform

4. Applications & Technical Challenges

4.1 Applications

There are quite a number of applications for POF Illumination alone and for the Integrated Platform for both Illumination and Data Communication. To mention a few of them as below:-

- Replacing traditional RF coaxial leaky cable in concealed areas
- Architectural linear lighting
- Pathway lighting
- Smart city street lighting with LiFi capability
- Hazardous environment lighting and communication such as mining

4.2 Technical Challenges

Since combining the illumination and data communication in a single platform using POF and laser is a completely innovative idea, there still have a lot of technical challenges for the successful and large public deployment such as below:-

- Extend the current 80 meters illumination length limit
- Enrich the colour variation of the laser light source at lower cost (presently only expensive RGB laser can provide full colour spectrum)
- Increase the brightness (lumen) of the side-glow POF
- Increase the data rate of the end-to-end communication
- Solve the unidirectional nature of the POF wireless visible light communication
- Solve the safety issues for high power laser being used in public areas

5. Conclusion

Despite the fact that there are still many obstacles and challenges that the researchers and developers face, the future of this innovative idea "Integrated POF Illumination & Data Communication Platform" is very promising. The nature of POF and laser have many advantages over traditional neon and LED lighting solutions. Some experts anticipate that POF lighting will replace a significant portion of the neon and LED linear lighting solutions in the future ten years. The present situation of POF illumination is very similar to that for LED lighting which started 20 years ago. And now, LED illumination products have dominated the market place. The future of POF illumination will be the same scenario and the integrating the data communication application just accelerates the development speed and widens the application areas !

Double-Doped Polymer Optical Fibers for High Performance Fluorescent Fiber Applications

Itxaso Parola[2,1], Daniel Zaremba[1], Robert Evert[1], Jana Kielhorn[1], Florian Jakobs[1], M. Asunción Illarramendi[2], Joseba Zubia[3], Wolfgang Kowalsky[1] and Hans-Hermann Johannes[1]

1 Technische Universität Braunschweig, Institut für Hochfrequenztechnik, 38106 Braunschweig, Germany.
2 Department of Applied Physics I, University of the Basque Country (UPV/EHU), Engineering School of Bilbao (EIB), Plaza Ingeniero Torres Quevedo 1, E-48013 Bilbao, Spain.
3 Department of Communications Engineering, University of the Basque Country (UPV/EHU), Engineering School of Bilbao (EIB), Plaza Ingeniero Torres Quevedo 1, E-48013 Bilbao, Spain.
*Corresponding author: h2.johannes@ihf.tu-bs.de; itxaso.parola@ehu.eus

Abstract: In this work, we have fabricated four different double-doped polymer optical fibers employing *poly*(methyl-methacrylate) as host material and a combination of two dopants (Eu(TTFA)$_3$Phen /Perylene/Lumogen Orange/Coumarin-1/Coumarin-6), with the aim of investigating their performance for fluorescent fiber applications, specially focusing on their potential as solar concentrators. Their optical properties have been studied under solar-simulator excitation, and the results are presented and discussed.

1. Introduction

Active polymer optical fibers (POF) mixing two different dopant materials (organic dyes/metal-organic materials) appear to be a promising route to produce high performance luminescent hybrid systems. These hybrid systems could provide a suitable luminescent material for, as an example, fluorescent fiber solar concentrators or remote energy harvesting systems, combining the benefits of both, organic and metal-organic dopants. The high absorption and emission bands of the organic dyes permit a broad utilization of the solar spectrum, and the large emission wavelength of metal-organic materials contribute to minimize the reabsorption losses. Moreover, the cylindrical waveguide structure of the POFs has several added benefits. On the one hand, they are light-weight, thin and flexible, which permits an easy manipulation. On the other hand, they can easily be attached to transparent optical fibers for light waveguiding, which allows spatial separation between the light harvesting system and the final system placement. The latter, leads to a positive feature for solar concentrator applications since no precise tracking systems are required, overcoming one of the traditional Si-cell harvesting system limitations [1–6].

In this study, methyl-methacrylate (MMA) has been polymerized combining two different organic dyes and metal-organic dopants in a bulk process. From the preforms obtained, double-doped POFs have been fabricated. An analysis of the optical properties of these new fibers have been carried out under solar simulator excitation. Applications in the field of fluorescent fibers, such as highly efficient Fluorescent Fiber Solar Concentrators (FFSCs) are targeted.

2. Experimental

2.1 Preform and fiber fabrication

The combination of two different dopants (Eu(TTFA)$_3$Phen/Perylene/Lumogen Orange/Coumarin-1/Coumarin-6), lauroylperoxide (0.03 mol%) and 1-butyl-mercaptan (0.1 mol%) were solved in a nitrogen saturated MMA solution at room temperature. The monomer solution was then filtered into 8 mm diameter borosilicate tubes. The tubes were sealed with silicon plugs and transferred into a heating cabinet. The preforms were heated for five days to 100 °C, then, kept at this temperature for 1 day, and finally cooled down to room temperature (20 °C) along 24 hours. After that, the glasses were carefully removed and the obtained PMMA+dopant preforms were cleaned with isopropanol (see Figure 1 (a)). Afterwards, they were drawn to fiber employing a fiber drawing tower, heated to 210 °C pulled by applying a constant force. A core diameter

of 980 μm was targeted. In a second step, a 20 μm film of Efiron PC404F-AP (Luvantix) was applied and UV cured to create a cladding material. One of the final fibers exposed to sun radiation is shown in Figure 1 (b).

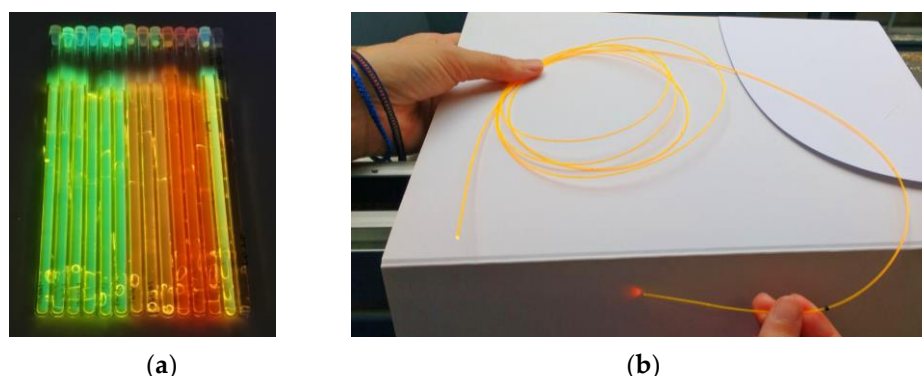(**a**)   (**b**)

Figure 1. (a) Polymerized preforms under UV radiation. (b) One of the fabricated fibers exposed to sun radiation.

The assigned code and the dopant combinations of the fabricated fibers are shown in the following table:

Table 1. Double-doped combinations and dopant concentrations.

Code	Dopant 1	c Dopant 1 (mol%)	Dopant 2	c Dopant 2 (mol%)
F1[Eu/P]	Eu(TTFA)$_3$Phen	0.003	Perylene	0.007
F2[Eu/L]	Eu(TTFA)$_3$Phen	0.003	Lumogen Orange	0.003
F3 [Eu/C6]	Eu(TTFA)$_3$Phen	0.003	Coumarin-6	0.01
F4[C1/C6]	Coumarin-1	0.02	Coumarin-6	0.003

2.2 Setup

As excitation source, a solar-simulator (Newport Oriel Desktop 91160-1000) was used under the standard 1 Sun AM 1.5 G simulated solar irradiation. The fibers were placed perpendicularly to the light source, allowing side excitation with a calibrated intensity of 34.5 mA. The emission spectra were recorded with a fiber-optic spectrometer (Ocean USB2000), and the output power at one of the fiber ends was measured employing a silicon photodetector (Thorlabs S120VC) and a double-channel power meter (Thorlabs PM320E). The recorded values were corrected employing the responsivity curve of the photodetector and the emission spectra of the fibers. Figure 2 shows a schematic of the setup employed (a), and a photograph of one of the fibers under solar-simulator exposure (b).
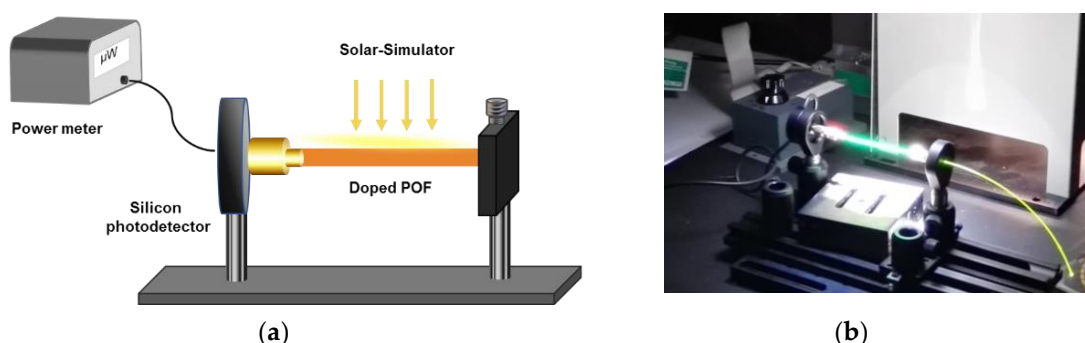

(**a**)   (**b**)

Figure 2. (a) Schematic of the experimental setup. (b) Photograph of one of the fabricated fibers under solar-simulator radiation.

3. Results and discussion

3.1 Absorption and emission bands

Eu(TTFA)$_3$Phen has a broad wavelength range of around 130 nm in the near-UV region. Combining its absorption with those of the organic dyes, a remarkable broad absorption band is obtained, with a small overlap between the absorption and emission spectrum (see Figure 3). Also with the combination of two

organic dyes, a considerably broad absorption band is obtained, but with higher reabsorption losses. As it is widely known, the external quantum efficiency of a silicon solar cell (Si-cell), covers a wavelength range from 400 to 1000 nm. With these double-doped POFs we propose, the near-UV part of the solar radiation can be collected and down-converted to longer wavelengths where the Si-cells are more efficient, improving the performance of the solar energy harvesting system.
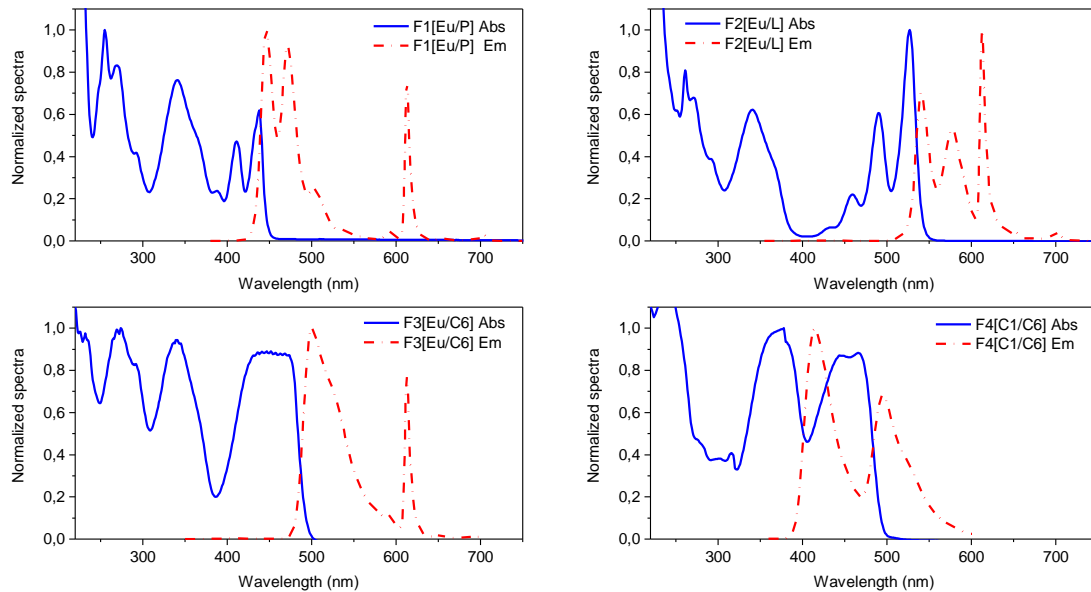

Figure 3. (a) Absorption and emission bands of the four dopant combinations.

3.2 Conversion efficiency

The conversion efficiencies of each of the fibers have been calculated for an excited length of 6 cm and a non-excited length of 3.3 cm (SMA connector). We define the conversion efficiency as follows:

$$\eta_{eff} = \frac{P_{fiber}}{P_{ex}} \cdot 100 \ (\%)$$

where, P_{fiber} corresponds to the power value measured at the fiber end closer to the detector, and P_{ex} is the power of the incident radiation for an area of 6x0.1 cm. The values obtained are gathered in Table 2. The best results are obtained for F2[Eu/L] and F3[Eu/C6], with power values around 125 µW and conversion efficiencies of around 0.2%. The combination of C1/C6 also demonstrates good potential as FFSC with power values of around 95 µW. These results can be greatly improved employing higher dopant concentrations, using reflective surfaces below the fiber, and in real-sun conditions expecting a higher irradiance in the near-UV where the dopant combinations absorb.

Table 2. Dopant combinations and dopant concentrations.

	F1[Eu/P]	F2[Eu/L]	F3[Eu/C6]	F4[C1/C6]
P_{fiber} (µW) 6 cm	52	125	121	95
η_{eff} (%)	0.09	0.21	0.2	0.16

3.3 Power saturation fiber length

For studying the evolution of the output power as a function of the illuminated fiber length, the fiber was rolled step by step into loops, increasing the illuminated area (see Figure 4 (a)), and the output power at the fiber end closer to the detector was measured for each of the steps. The curves obtained for 3 samples are shown in Figure 4(b). As can be seen, for the first steps the output power increases quite abruptly for all samples, but, afterwards, it starts saturating. The saturation fiber length, L_{sat}, corresponds to the length were the variation of the output power is less than 0.5%. We called this saturation level as P_{sat}. The values obtained are gathered in Table 3. F3[Eu/C6] and F4[C1/C6] fibers obtained the best performance with distance,

reaching effective lengths longer than 4 m in both cases. Moreover, F3[Eu/C6] sample achieves a power saturation level of 736 µW, which leads an intensity value at the output of a single 1 mm diameter fiber of 0.96 mW/mm^2. Knowing that the intensity of the sun-light is estimated to be around 1 mW/mm^2 at the earth surface, these results are of high interest in the field of solar energy harvesting.

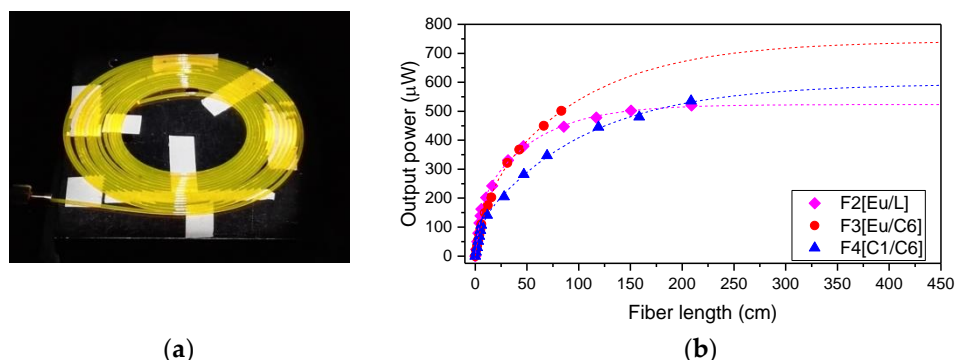(**a**)   (**b**)

Figure 4. (a) Photograph of a fiber sample rolled into several loops under the solar simulator excitation. (b) Evolution of the output power in one of the fiber ends as a function of the illuminated fiber length.

Table 3. Values of saturation fiber length, power saturation and the equivalent intensity.

Code	L_{sat} (cm)	P_{sat} (µW)	Intensity (mW/mm^2)
F2[Eu/L]	243	519	0.66
F3[Eu/C6]	428	736	0.94
F4[C1/C6]	415	586	0.75

4. Conclusions

We have successfully fabricated four different polymer optical fibers doped with a combination of two dopants (organic dyes/metal organic materials), from the preform polymerization to the fiber drawing process. The obtained 1 mm diameter double-doped fibers have been analysed under solar-simulator excitation, obtaining light conversion efficiencies of around 0.2%, saturation fiber lengths longer than 4 m and an output intensity value of 0.94 mW/mm^2 for the best sample combining Eu(TTFA)$_3$Phen with Coumarin-6. The results obtained are of great interest for fluorescent fiber based solar-light concentration applications.

5. Acknowledgements

6. References

1.   Huang X, Han S, Huang W, Liu X. Enhancing solar cell efficiency: the search for luminescent materials as spectral converters. Chem Soc Rev [Internet]. 2013 [cited 2017 May 10];42(1):173–201. Available from: http://xlink.rsc.org/?DOI=C2CS35288E

2.   Colantuono G, Buckley A, Erdelyi R. Ray-Optics Modelling of Rectangular and Cylindrical 2-Layer Solar Concentrators. J Light Technol [Internet]. 2013 Apr [cited 2016 Dec 12];31(7):1033–44. Available from: http://ieeexplore.ieee.org/document/6412695/

3.   McIntosh KR, Yamada N, Richards BS. Theoretical comparison of cylindrical and square-planar luminescent solar concentrators. Appl Phys B [Internet]. 2007 Jul 7 [cited 2016 Dec 12];88(2):285–90. Available from: http://link.springer.com/10.1007/s00340-007-2705-8

4.   Wang T, Yu B, Chen B, Hu Z, Luo Y, Zou G, et al. A theoretical model of a cylindrical luminescent solar concentrator with a dye-doping coating. J Opt [Internet]. 2013 May 1 [cited 2017 Jan 3];15(5):55709.Available from: http://stacks.iop.org/2040-8986/15/i=5/a=055709?key=crossref.623053742b28d92546c16ee34861d8f2

5.   Wang C, Abdul-Rahman H, Rao SP. Daylighting can be fluorescent: Development of a fiber solar concentrator and test for its indoor illumination. Energy Build. 2010;42(5):717–27.

6.   Correia SFH, Lima PP, André PS, Ferreira MRS, Carlos LAD. High-efficiency luminescent solar concentrators for flexible waveguiding photovoltaics. Sol Energy Mater Sol Cells. 2015;138:51–7.

Versatile Hardware Platform for Polymer Fibre Sensors

Bernd Offenbeck [1*], Hans Kragl [2]

1 OBTIS GmbH, Rossbachstr. 5, D-93057 Regensburg, Germany
2 DieMount GmbH, Giesserweg 3, D-38855 Wernigerode, Germany
*Corresponding author: bernd.offenbeck@obtis.de

Abstract: This document shows the development of a versatile, processor controlled hardware platform for polymer fibre based sensors named "POF LINK ANALYZER". The hardware is capable of driving up to 3 LEDs and offers 2 receiver channels with a high dynamic range and fast acquisition rate. The receivers are locked to the modulated signals of the LEDs to suppress ambient light. Depending on the application different LEDs and receivers can be installed. The integration of low crosstalk splitters allows transmitting and receiving on a single fibre, making unique sensor applications possible. This allows the development of various, all optical POF based sensors.

1. Introduction

Many interesting 1 mm PMMA-POF based sensor projects fail, due to lack of the necessary measurement system. Out of this necessity a flexible hardware platform was developed, that is adaptable for most scenarios.

Goal was to cover applications with a sensor in a fibre loop, optional with a second photodiode - as well as sensors working in reflective mode over a single fibre with the use of low-crosstalk splitters.

In addition multi wavelength configurations with up to three LEDs should be covered.

This enables the use in most sensor systems, like mechanical sensors for shock and vibration as well as bio- and chemical sensors working on multiple wavelengths.
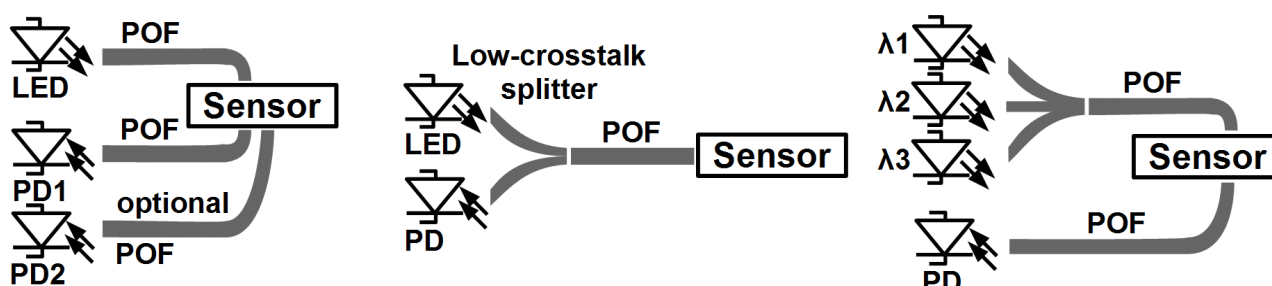
left: sensor device in POF loop   middle: single fibre sensor with splitter   right: multi wavelength sensor
Figure 1. Typical application scenarios

In addition the measurement device should provide a fast measure rate of 10 msec, a high dynamic range to deal with fibre and sensor attenuation, low noise floor, suppression of ambient light and the possibility to interface it with a PC or process control system.

2. Measurement system

The only option to satisfy all these demands was a modular, microprocessor controlled platform.

It consists of a microcontroller, that is running code for generating the LED modulation at typically 5 kHz, a synchronized digital lock-in amplifier with good noise performance and high DC suppression to eliminate ambient light, as well as control options for the receiver blocks and digital interfaces for the user section.

The two receiver blocks feature specially designed variable gain transimpedance-amplifier (TIA) with a controllable gain from typically 3 kΩ to 4.8 MΩ, optional changeable up to 300 kΩ to 480 MΩ (low-noise

configuration). The amplifiers use a DC cancellation technique that allows suppression of a huge part of the ambient light, before feeding the signal to a high resolution ADC and the digital lock-in amplifier. Inside the microcontroller an individual ADC and lock-in block is present for each photodiode. Both large-area photodiodes measure simultaneously, allowing sensor systems with two optical paths. The gain setting is so fast, that within one period of the 5 kHz modulation signal (200 µsec) the gain can be switched from 3 kΩ to 4.8 MΩ (full scale) with an accuracy of typically better 1%. Within a single 10 msec measurement block the microprocessor adopts the gain various times to give the best performance regarding noise, linearity and ambient light suppression using a special algorithm.

An additional fixed gain input can be used as monitor to supervise the LED operation.

Finally up to three LEDs can be installed on current drivers, capable of driving a modulation of 0.5 to 30 mA, even for devices with higher forward voltage as blue and UV LEDs. With some increase in noise the system is fast enough to switch and measure all three LEDs in one 10 msec timeslot, allowing multi spectral sensing.

A temperature sensor close the LEDs allows compensation of power drift as well as future use for digital compensation of the spectral change over temperature.
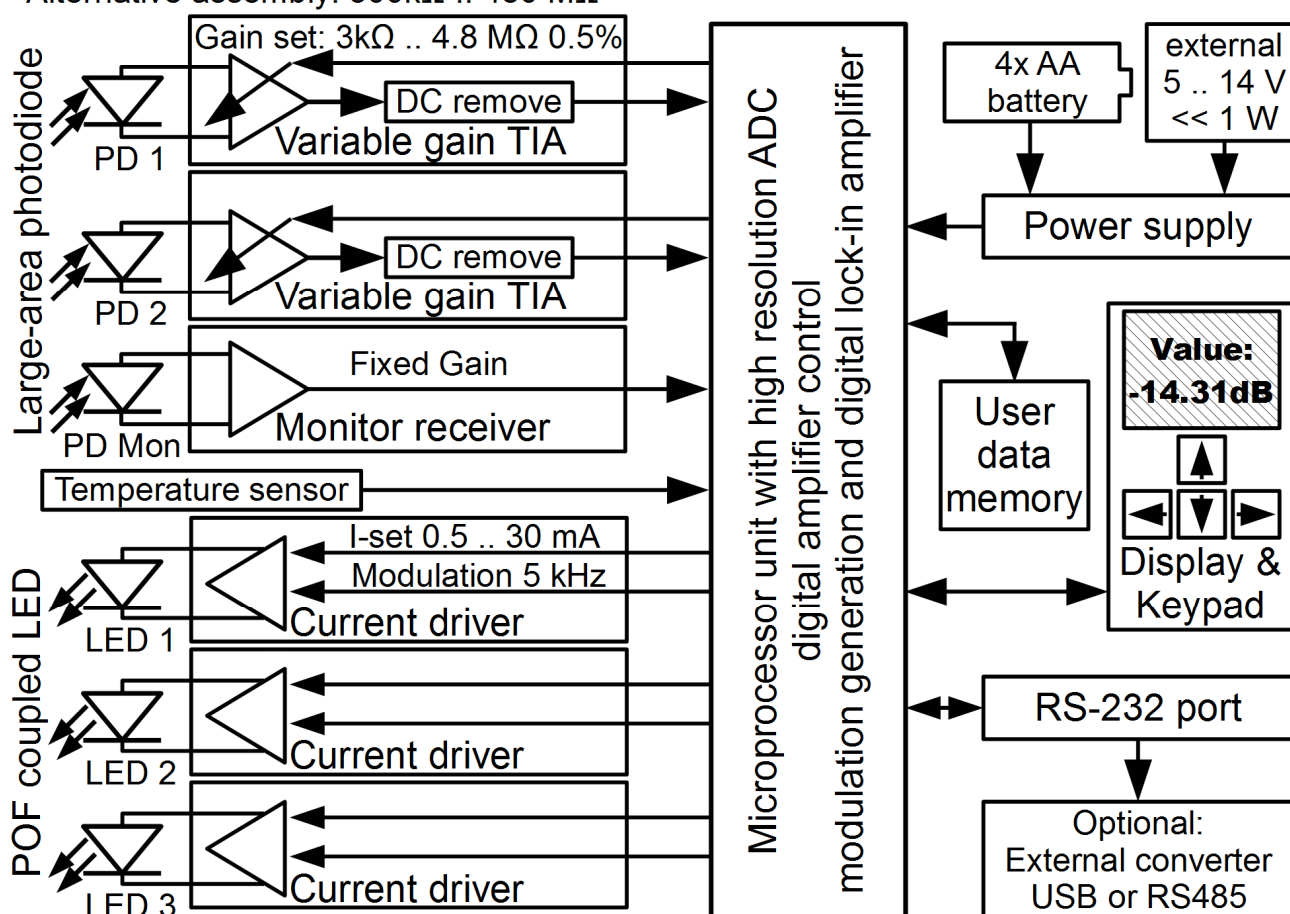

Figure 2. Block diagram of the measurement system in maximal configuration

On user side the system can be configured over a large-area display and keyboard. In addition an RS-232 port allows interfacing the device to a PC, e.g. by a USB converter or to a process control system, e.g. by a RS-485 converter. The configuration data is stored inside a device internal memory.

The software can be updated and changed by a bootloader, e.g. to a special firmware for custom applications.

Power supply runs from either 4 AA batteries or an external power supply from 5 to 14V. The power consumption is far below 1 W, even with all three LEDs installed at maximum current and display backlight. In normal configuration with one LED the typical power consumption is only ~250 mW including display.

3. System performance

The left diagram of figure 3 shows the maximum RMS noise in dB of the standard TIA assembly, reading one LED with 10 msec measurement rate. It is referenced to the average optical input signal in dBm. An optical attenuator was used to reduce the optical power of the LED. The noise floor is very flat with an increase below -50 dBm. If a lower measure rate as 10 msec is acceptable, the system can be used even beyond -60 dBm. Saturation of this receiver type is about +2 dBm. The optional low-noise receiver is 20 dB more sensitive with a little higher noise and saturation at -20 dBm.

The right diagram shows the immunity to ambient light, coupled in by a splitter in the fibre loop. Even with 10000x more external light than signal (-10 vs. -50 dBm) the influence on the measurement is near zero.

Figure 3. Left: Maximum RMS noise vs. optical input signal   Right: Influence of external light on the measurement

4. Example Applications:

4.1 POF Installation Tester

A very common problem we encountered was the measurement of POF cables itself. The specialized "POF Installation Tester" uses a 650 nm LED, running at absolute eye-safe 200 µW optical power. With a 300 msec measurement rate it allows to measure link attenuations up to -45 dB and external light up to -25 dBm with high accuracy. In addition it features the option to log and document measurements.

Figure 4. POF Link Analyzer in configuration as "POF Installation Tester" with USB cable and protective cover

4.2 Simplex Fibre System (Reflectometer) with low-crosstalk splitters

During the POF 2015 conference in Nuremberg we presented the paper "Polymer optical fiber (POF) based sensors for the measurement of elongation via a single fiber", evaluating mechanical movement and vibration.
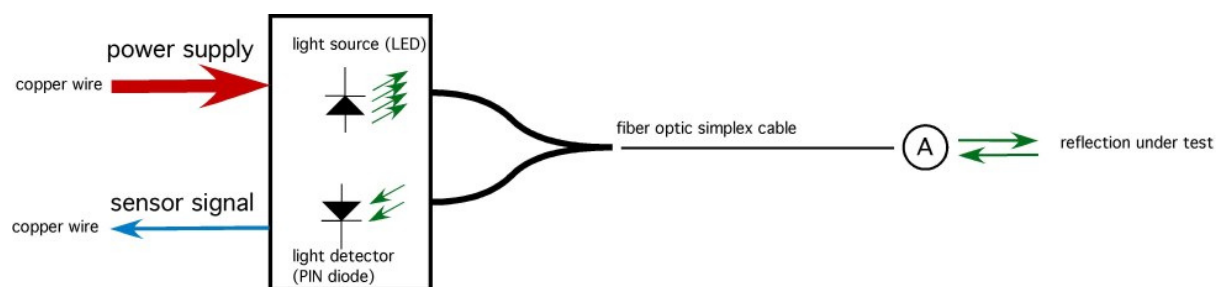

Figure 5. Simplex fibre optical sensor system

The new hardware platform is perfectly suited for this application, as it offers the possibility to further reduce crosstalk electronically as well as the use multiple LEDs and photodiodes.

Currently we are developing the option to measure the attenuation of a single POF from only one side, using a reflector on the fibre end, to save lots of time for qualification of POF data networks.

4.3 Multi LED configuration for wavelength depending sensor principles

With up to three LEDs and two optionally colour filtered photodiodes the POF Link Analyzer allows sensor principles using spectral effects and colour changes. These are for example colour measurement, chemical and biological analysis or even splitting the light and using multiple single wavelength sensors in one fibre loop.
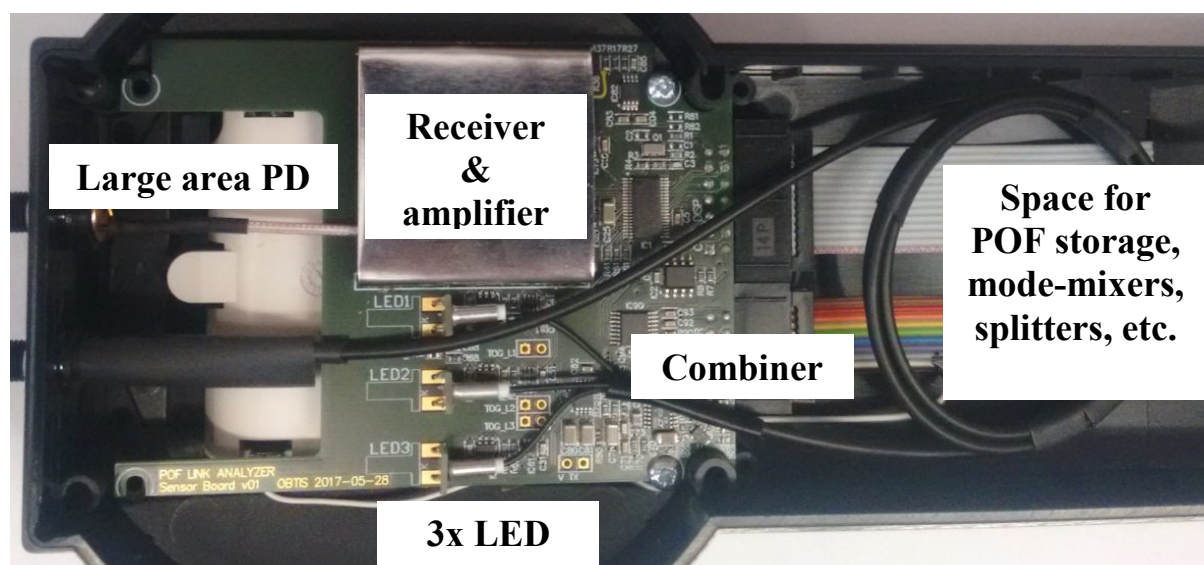

Figure 6. Hardware assembly of a three LED setup with red, green and blue LED and a combiner

One example of an all-optical temperature measurement was presented by Dr. Wolfgang Wildner in his paper "A Fiber Optic Temperature Sensor Based on the Combination of Epoxy and Glass Particles With Different Thermo-Optic Coefficients" [PHOTONIC SENSORS / Vol. 6, No. 4, 2016: 295–302].

5. Conclusion & Outlook

The presented measurement system "POF Link Analyzer" allows a very wide range of configurations for various applications. For example we are investigating the option to use a splitter and two receivers with different gains to boost the dynamic range over 80 dB while keeping the measurement performance.

With our partners we hope to be able to present even more challenging sensor applications in the future.

POF Immunosensor with Antibodies Immobilization for *Escherichia coli*

R.N. Lopes[1*], D.M.C. Rodrigues[1], A.S. Allil[1], R.C.S.B. Allil[1], M.M. Werneck[1]

1: Photonic and Instrumentation Laboratory, Electrical Engeineering Program, Universidade Federal do Rio de Janeiro, Rio de Janeiro, Brazil

* Corresponding author: rafaela@lif.coppe.ufrj.br

Abstract: The immunosensors are characterized by antibodies as biological recognition element, responsible for the specificity of the biosensor. For the development of immunsensors based on plastic optical fiber (POF) technology, it is necessary the amination of the fiber core surface, which is made of polymethylmethacrylate (PMMA). In this study we compared four functionalization protocols of PMMA and immobilization of antibodies on the surface of the immunosensor development for the detection of *Escherichia coli*. Tests with bacterial suspensions in 10^8 CFU/mL concentrations were carried out to evaluate the response of the immunosensors functionalization with different protocols.

1. Introduction

The Imunosensors are compact analytical devices in which the formation of antigen-antibody complexes are detected and converted, by means of a transducer, an electrical signal that can be processed, recorded and displayed [1]. The use of optical fibers as transducer allowed the expansion of biosensors. An optical fiber sensor can be defined as a device through which a measuring physical, chemical or biological, interacts with light guided by fibre optics (intrinsic) or with light guided to the interaction region by optical fiber (extrinsic), to produce an optical signal that will be analogous to the parameter one wants to measure [2]. The physical principle fundamental to the functioning of the sensors for plastic optical fiber (POF), developed in this paper, is the interaction of the sample with a curved fiber. The curve on POF creates a region sensitive to the external environment, causing changes in the amplitude of light guided in accordance with the index of refraction of the external environment in which the sensor is immersed [3].

A key step in the construction of the biosensor is the reconnaissance element immobilization onto the surface that will be read by the transducer. A large amount of biological element must be connected to the sensor surface so that the immobilized biomolecules exhibit greater stability. There is a very great interest in the study of adsorption of proteins on polymeric particles because of the importance of these materials in biomedical and biotechnological applications. Because of the flexibility, high polymer chemistry can be modified with biological macromolecules, allowing the application of materials for production of biosensors [4]. Most of the immobilization methods are based on a surface considered activated for the coupling, that is, the surface of the material must have reactive chemical groups such as hydroxyls (-OH), amines ($-NH_2$) and carboxylic acids (-COOH) [5]. For the immobilization of the antibody at the surface of the POF it is necessary the amination of the fiber core surface, which is made of polymethylmethacrylate (PMMA).

In the present study, we used the technique of chemical modification, through chemical reaction, so that the present primary amino groups of the PMMA be suitable for immobilization of antibodies. The adsorption of the ligands occurs through chemical interactions between the antibody to be immobilized and the functionalized surface.

2. Material and Methods

2.1 Manufacture of sensors of POF in U

The sensors were manufactured in U-shape through the method of flame-blush, where a jet of heat is applied so that it occurs a partial melting of the fiber [3].

2.2 Cladding removal

The POFs used for manufacturing the sensor presents a core of 980 μm in diameter, made of PMMA, and a cladding with 10 μm in thickness (Mitsubishi Rayon Eska CK-40). The chemical nature of the components of the cladding is not informed by the manufacturers, so that we applied a procedure for removing the cladding of the fiber: the curve of the sensor was placed between the folding of a tissue of 30 mm^2, and applied 50 μL of acetone and 50 μl of distilled water to neutralize the effect of corrosion [6].

2.3 Functionalization the surface of the sensor and immobilization of antibodies

Four protocols were tested for the functionalization of the sensor surface using sulfuric acid (H_2SO_4) at 60°C, hexamethylenediamine (HMDA) at 37°C and glutaraldehyde (GLU) at 37°C for activation of the amine group as shown in table 1:

Table 1: Adjustment made in PMMA functionalization protocols and activation of amine

Steps	Protocols			
	1	2	3	4
Functionalization	HMDA 24h	H_2SO_4 2h + HMDA 2h	H_2SO_4 2h + HMDA 24h	H_2SO_4 4h+ HMDA 24h
Activation	GLU 24h	GLU 2h	GLU 24h	GLU 24h

After amination and activation, sensors were incubated with protein A (Sigma-Aldrich, St. Louis, USA) for 1 hour at 30°C, followed by incubation for 4 hours in a solution of 0.1 mg/mL of anti-*E.coli* antibodies (BIORAD, United Kingdom).

2.4 *Instrumentation and electronic setup*

For the measures undertaken with the immunosensor, it was necessary to eliminate the influence of other parameters that may mask the results. We used a similar reference sensor manufactured on the same conditions, however, not functionalized. Figure 1 shows the optoelectronic setup.
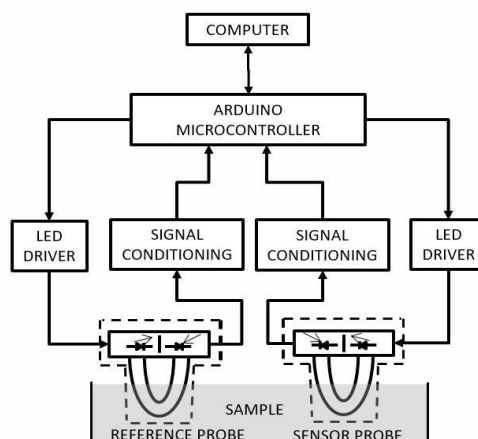

Figure 1: Block diagram of the setup for the optoeletronic system implemented

3. Results and Discussion

For the PMMA functionalization analysis, four protocols were tested for the detection of *E.coli* at 10^8 CFU/mL concentrations. Figure 2 shows the graph of the results obtained with the four protocols. For each protocol, 5 sensors were tested. Protocol 1 was not satisfactory, presenting a great irregularity in the reading of the sensors. In protocol 2 an improvement in sensor sensitivity was obtained with the acid hydrolysis process of PMMA with H_2SO_4, but the deeps were not significant. Protocol 3 presented a greater sensitivity and regularity in the measurement with the 5 sensors showing decrease in the same period of time. Protocol 4

presented a significant but irregular decrease in the measurement of all sensors, besides presenting great difficulty in washing the residues by the incubation time with H_2SO_4.
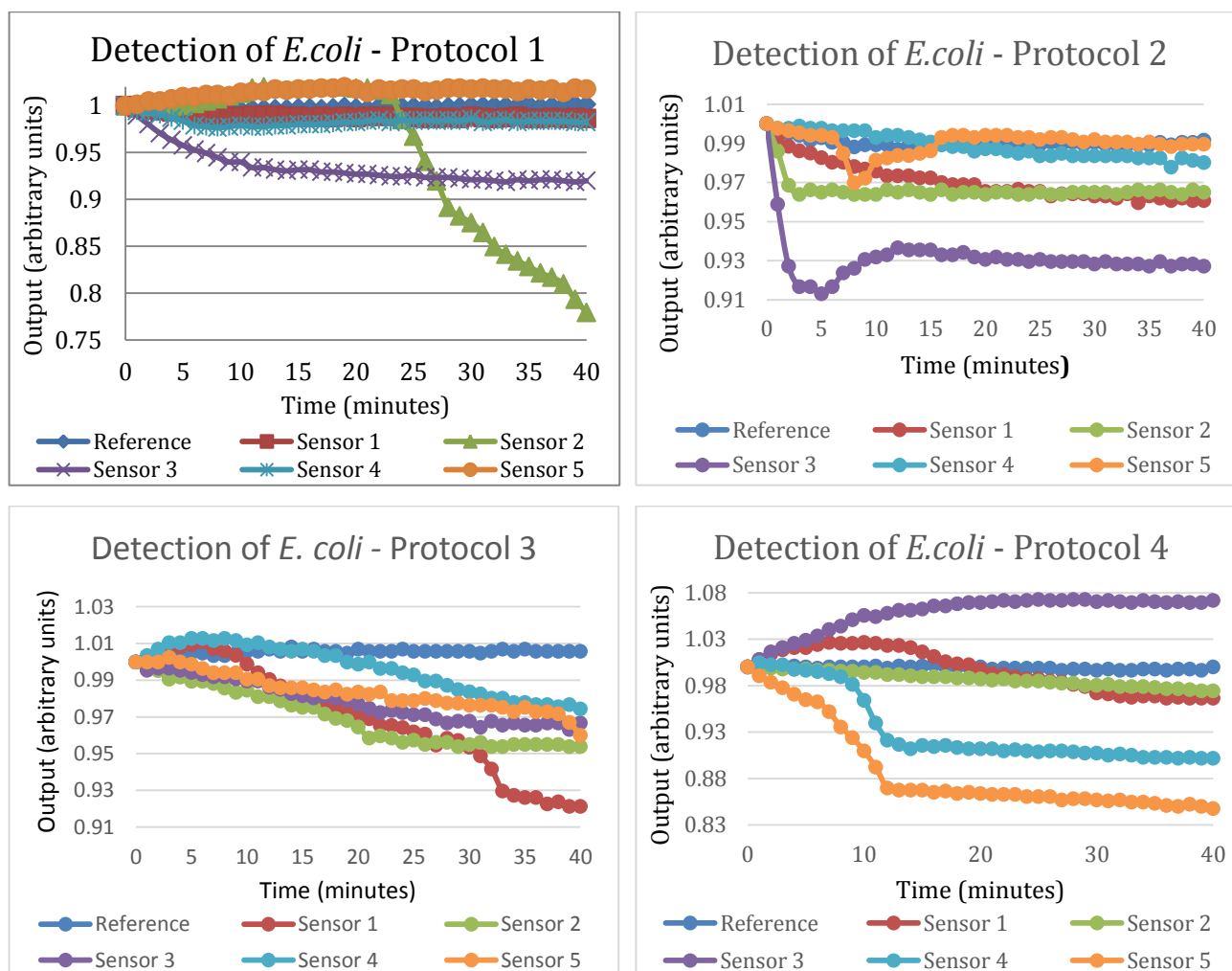

Figure 2: Graphs of the results obtained in the detection of *E. coli* by the 4 functionalization protocols tested.

With all the experiments performed on the evaluation of the protocols, it was observed that protocol 3 was the most efficient for the immobilization of the antibodies due to its regularity in the reading of the sensors, which gives a greater reproducibility, and for optimizing the time in the whole process.

To confirm the formation of amine group on the surface of POF after functionalization with Protocol 3, a disc of PMMA was aminated and the contact angle formed with the water was measured by a goniometer (NRL A- 100-00, Ramé-Hart Instruments Co., USA), and compared with the contact angle obtained from a disc of pure PMMA. The angle obtained with PMMA functionalized is smaller than the angle obtained with pure PMMA [7]. Table 2 shows averaged values of angles obtained confirming the presence of amine group after functionalization.

Table 2: Average angle derived from the goniometer in pure PMMA discs and functionalized disks

Sample	Average of the angles
Pure PMMA	86°
PMMA funcionalizado with the 3 Protocol	74°

A good way to check the immobilization processes is by the use of a scanning electron microscope (SEM) for detecting the presence of the cels immobilized at the sensor surface. Figure 3 shows one micrographs taken by a SEM (FEI Quanta 250, USA) of a functionalized sensor after being in contact with *E.coli* in a concentration of 10^8 CFU/mL. It is possible to observe the bacteria sparsely distributed along the surface of the sensor. The micrographs help to evaluate the adhesion of bacteria on the fiber surface, demonstrating the successful capture of *E.coli* by immobilized antibodies on the fiber surface.
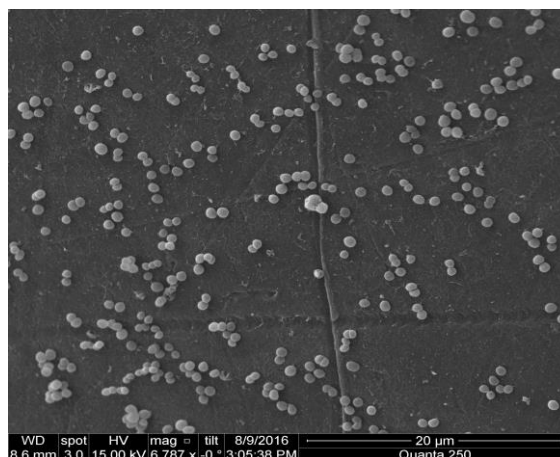

Figure 3: SEM of the surface of the sensor with immobilized antibodies and covered by *E.coli* in an increase of 6.787x.

4. Conclusions

Plastic optical fibers, made of PMMA, are an excellent optical instrument for the rapid detection of *E. coli* and can also be used for a wide range of biological agents. New PMMA functionalization protocols were tested and it was concluded that hydrolyzing the fiber with sulfuric acid solution prior to incubation with HMDA made the sensor more sensitive and efficient. The ideal hydrolysis is 2 hours, followed by incubation to HMDA and Glutaraldehyde for 24 hours.

5. References

[1] Geng, T.; Morgan, M.T.; Bhunia, A.K., Detection of Low Levels of *Listeria Monocytogenes* Cells by Using q Fiber-Optic Immunosensor Applied Environm Microbiol.. v. 70 (10), p. 6138–6146, 2004

[2] Gouveia, C.A.V.J., Sensores em Fibra Óptica para Monitorização Ambiental. Dissertação de Mestrado em Engenharia de Comunicações e Redes. Departamento De Matemática e Engenharias Universidade De Madeiras, Portugal, 2008

[3] Wandermur, G.L.; Rodrigues, D.M.C.; Allil, R.C.S.B.; Queiroz, V.M.; Peixoto, R.; Werneck, M.M.; Miguel, M., Plastic Optical Fiber-Based Biosensor Platform for Rapid Cell Detection. Biosensors & Bioelectronics, v. 54, p. 661- 666, 2013

[4] Oréfice, R.L., Materiais Poliméricos: Ciência e Aplicação como Biomateriais. Biomateriais: Fundamentos E Aplicações. 1ª Ed. Rio De Janeiro: Cultura Médica. v. 1, p. 83-156, 2006.

[5] Tian, H.; Tang, Z.; Zhuang, X.; Chen, X.; Jing, X.. Biodegradable Synthetic Polymers: Preparation, Functionalization and Biomedical Application. Progress in Polymer Science. 2011.

[6] Merchant, D.F.; Scully, P.J.; Schmitt, N.F., Chemical Tapering of Polymer Optical Fiber. Sensors and Actuators. v. 76, p. 365–371, 1999.

[7] Growri, A.; Sai, V.V.R: Development of LSPR Based U-Bent Plastic Optical Fiber Sensors. Sensor and Actuators B: Chemical. v. 230, p. 536-543, 2016.

Low-Cost Sensitive Liquid Level Monitoring Using Polymer Optical Fibers

M. Bär[1*], S. Werzinger[1], M. Köppel[1] and B. Schmauss[1]

1 Institute of Microwaves and Photonics, Erlangen Graduate School for Advanced Optical Technologies (SAOT),
Friedrich-Alexander University Erlangen-Nuremberg, Germany

*Corresponding author: matthias.baer@fau.de

Abstract: In this paper we propose low-cost solutions for sensitive optical liquid level monitoring, using standard polymer optical fibers (POF). Further we present a simple technique to reduce noise introduced by other light sources. The whole system can be integrated using six electronic components including a microcontroller. A simple circuit diagram is given. To determine the required dynamic range of the used analog-to-digital converter, measurements have been performed.

1. Principle of operation

The two sensors presented, are both based on total internal reflection on one or more surfaces. A light beam is totally reflected on a junction between the sensor material and the surrounding medium. In this case the sensor material is either the POF itself or another transparent plastic. The liquid that will be detected changes the refractive index step between the sensor material and the surrounding and thus supresses the total internal reflection. This leads to a change of the reflected light's intensity.

One presented sensor (Sensor A) is mounted outside a transparent fluid container and thus doesn't get into contact with the liquid. This is an advantage if the fluid is highly aggressive or the risk of contamination has to be reduced (inspired by [1]). The second sensor (Sensor B) gets directly in contact with the fluid but can be used for any kind of container.

1.1 Sensor A

This sensor (Fig. 1) consists of two POFs glued to the outside of a transparent container in an angle in respect to the perpendicular of the containers inner surface. The POFs have to be in the same plane. The distance of the end faces glued to the surface has to be in such a way that light coupled out of one fiber, reflects on the containers inner surface and couples into the other fiber. The glue acts as an index matching material between the end faces of the POFs and the container. The angle of incidence on the inner container surface has to be above the critical angle when the container is empty ($n_{air} = 1$) but below if the container is filled with a liquid ($n_{liquid} > 1$). In the case that the container is empty, the light is reflected at the inner container surface and a relatively high proportion is coupled from one fiber into the other fiber. For the case that the container is filled with a liquid, most of the incident light is transmitted.
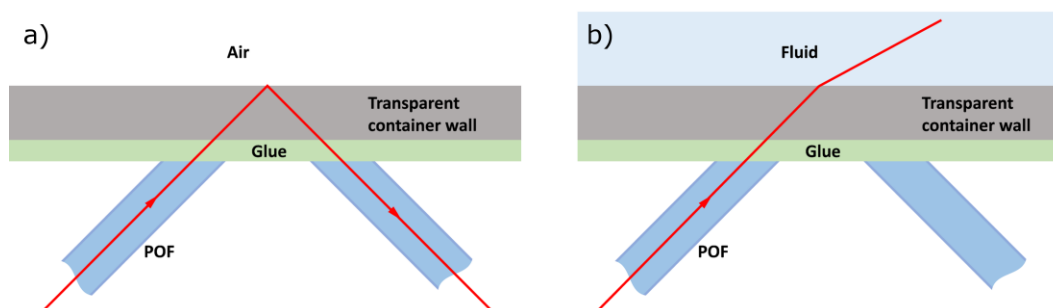

Figure 1: Operation principle of the first proposed sensor, which is mounted at the outside of a transparent container

Our sample setup (Fig. 2) consists of a transparent polystyrene container with a refractive index n_{PS} of 1.59 [2] for the used LED light source ($\lambda = 585$ nm) and standard PMMA POFs with a diameter of 1 mm. The POFs are held in place using two plastic plates. The POFs and plastic plates are glued to the container with hot glue. The angle of the POFs in respect to the container surface is 45°. As liquid, water with a refractive index n_w of 1.33 [3] is used. The critical angle for the empty container (polystyrene – air junction) is 39° for the given wavelength.

Thus with an angle of incidence of 45°, total internal reflection is obtained. In the case that the container is filled with water (polystyrene – water junction) the critical angle calculates to 56.8° and a large portion of the light is transmitted into the water.
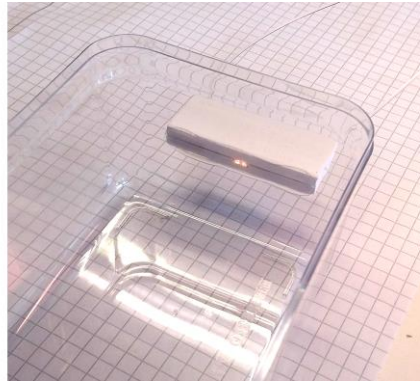

Figure 2: Test setup for sensor A. The position of the fiber ends is clarified by white light coupled into the fibers

1.2 Sensor B

This sensor (Fig. 3) consist of two parallel oriented POF tips glued together with transparent epoxy resin. The resulting epoxy block is sanded and polished to an angle of 45°. The working principle is similar to the first sensor. With air as surrounding material, light gets totally reflected on the angled POF end face. The reflected light couples into the second POF by being again reflected on the angled end face of the second POF. When the sensor is immersed in a fluid the critical angle increases and the light is partially transmitted into the fluid.
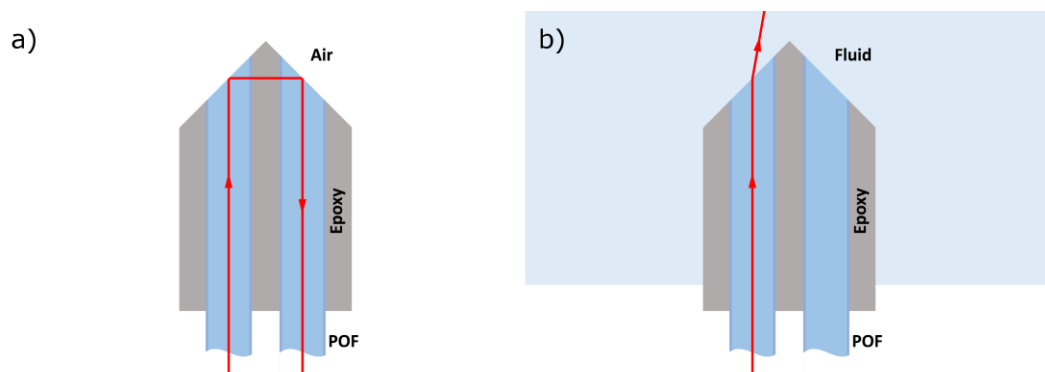

Figure 3: Operation principle of the second proposed sensor. In subfigure a) light gets totally reflected on the PMMA-air junction and thus is coupled from one fiber into the other one. Subfigure b) shows the case if the sensor is dipped in a fluid. The light is mainly transmitted due to the fluids' higher refractive index.

For the case that a PMMA POF with a refractive index n_{PMMA} of 1.49 [4] is used, the critical angle of the PMMA – air junction calculates to 42.6°. This is quite close, but still below the angle of 45° required for the setup. For a PMMA – water junction the critical angle increases to 63.2°. Our sample setup for this type of sensor is shown in Fig. 4.

Figure 4: This figure shows the implementation of sensor B. In the right image the position of the POFs within the epoxy resin and the angled tip can be seen clearly.

2. Sensor evaluation

The sensor signal can easily be evaluated by measuring the intensity of the light that couples from one fiber into the other. An issue that has to be taken into account, is ambient light that couples into the open end faces of the fibers and superimposes the sensor signal. To suppress ambient disturbances, the lock-in principle should be applied by modulating the light source and synchronously detecting the sensor signal. Fig. 5 shows the main principle of a digital synchronous detector using a switched mixer [5].
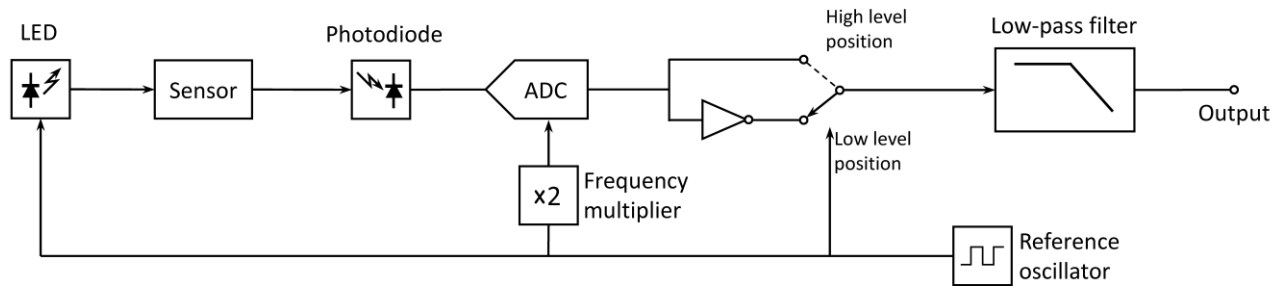

Figure 5: Digital implementation of a lock-in amplifier as it can easily be done with a microcontroller.

Disturbances of the detector signal are mainly caused by room illumination (100 Hz), but also electrical noise, especially 50 Hz disturbance by power lines and its harmonics interfere with the sensor signal. The lock-in principle is perfectly suited to suppress such types of noise, in the case the reference frequency is chosen with care. Also the design of the subsequent low-pass filter has an influence on the performance. For simplicity and for easy implementation in a microcontroller, the low-pass filter can be designed as moving average filter.

3. Implementation using a microcontroller

To demonstrate the simplicity of implementation of the system, the schematic in Fig. 6 was successfully tested with an ATMEL microcontroller [6].
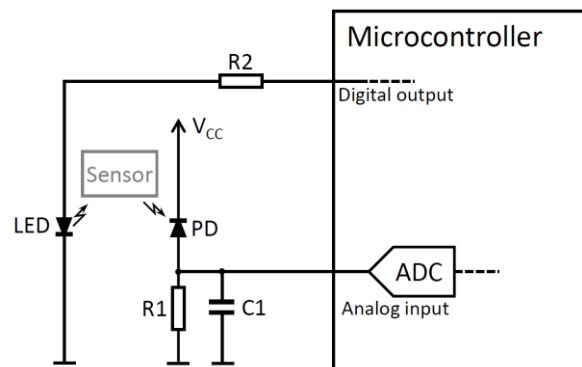

Figure 6: Hardware integration for low-cost applications.

The Resistor R1 has to be chosen in the way that ambient light doesn't overdrive the microcontroller's ADC, but that the sensor's LED still causes a measurable change of the signal amplitude. The capacitor C1 combined with R1 reduces the signal bandwidth and thus helps to reduce noise. The sensor's light source was a yellow SMD LED (λ_{LED} = 585 nm), which was driven with a maximal current of 10 mA and fairly coupled to the POF. To determine which amplitude change of the sensor signal, induced by the sensor's light source can be considered as measurable, a test setup using sensor A was done. To introduce some additional noise, a strong flickering light source (a 9 W energy-saving lamp) placed right in front of the sensor. This scenario was assumed to be the worst case for such a device. The setup is shown in Fig. 7. The sensor's signal was sampled with a high resolution multifunctional I/O device (USB-6281 by National Instruments).
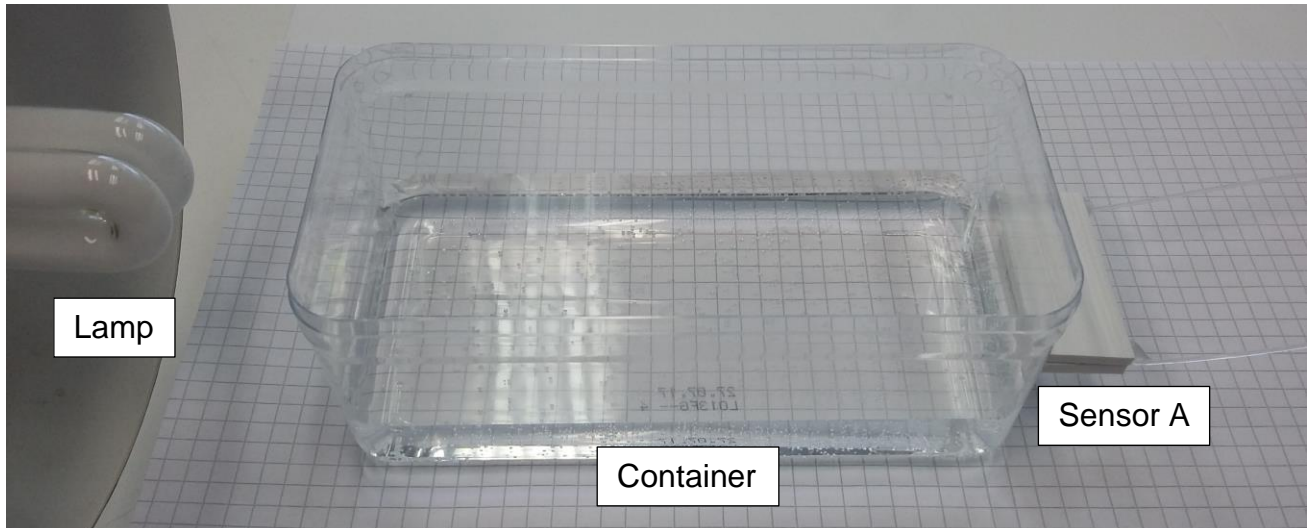
Figure 7: Setup for testing the robustness of the system towards noise caused by other light sources. A 9 W energy-saving lamp with high 100 Hz flicker was positioned close to the sensor to overlay the optical sensor signal with noise. The shown scenario can be assumed to be the worst case.

Fig. 8 (left) shows the measured sensor signal, sampled with high resolution. In a next step, the resolution of the amplitude range was reduced to N bits. In other words, the performance of the system was tested, for the case that the modulated light source plus noise leads to a detector signal that changes the last N bit of the ADC result. Then the synchronous detection was applied. The right plot of Fig. 8 shows the output after synchronous detection and low-pass filtering using a moving average filter. The reference frequency was set to 75 Hz as it is right in between the 50 Hz electrical disturbance and the 100 Hz optical disturbance. The moving average filter had an averaging time of 1/25 s, which leads to a complete suppression of 25 Hz frequency components [7]. This is important, because 25 Hz frequency components are a result of multiplying the reference frequency with 50 Hz or 100 Hz disturbances in the synchronous detector. It can be seen that even with a resolution as low as 4 bits, the output signal of the system is well suited to give a reliable indication of the liquid level in the container. This means that using only 1/16 of the dynamic range of an 8-bit ADC is sufficient to produce reliable results.
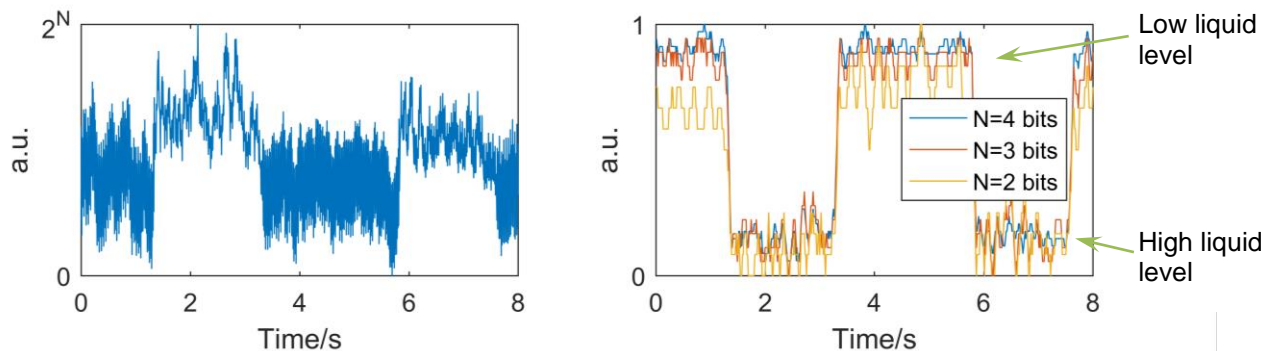

Figure 8: Measured noisy sensor signal (left) and output signal after synchronous detection and low-pass filtering (right). The number of bits indicates the number of discrete amplitude steps with which the noisy input signal was sampled.

4. Conclusion

In this paper two simple but well performing liquid level detectors were presented. Combined with a fully digital synchronous detector, constraints concerning signal to noise ratio and hardware effort could be reduced to a minimum. It has been shown, that a simple electrical circuit combined with a low resolution ADC is sufficient to reliably indicate the liquid level in a container.

5. References

[1] D. S. Montero and C. Vázquez, "Polymer Optical Fiber Intensity-Based Sensor for Liquid-Level Measurements in Volumetric Flasks for Industrial Application," ISRN Sensor Networks, vol. 2012, Article ID 618136, 7 pages, 2012. doi:10.5402/2012/618136

[2] N. Sultanova, S. Kasarova, I. Nikolov; "Dispersion Properties of Optical Polymers", Acta Physica Polonica A 2009, Vol. 116:585

[3] G. M. Hale and M. R. Querry. Optical constants of water in the 200-nm to 200-µm wavelength region, Appl. Opt. 12, 555-563 (1973)

[4] G. Beadie, M. Brindza, R. A. Flynn, A. Rosenberg, and J. S. Shirk. Refractive index measurements of poly(methyl methacrylate) (PMMA) from 0.4-1.6 µm, Appl. Opt. 54, F139-F143 (2015)

[5] EG&G Princeton Applied Research, "Explore the Lock-In Amplifier", http://cpm.uncc.edu/sites/cpm.uncc.edu/files/media/Explore_1.pdf (7/17)

[6] ATMEL 8-bit microcontroller product list, http://www.atmel.com/products/microcontrollers/avr/megaavr.aspx (7/17)

[7]James M. Masciotti, Joseph M. Lasker, Andreas H. Hielscher; "Digital Lock-In Detection for Discriminating Multiple Modulation Frequencies With High Accuracy and Computational Efficiency", IEEE Transactions on Instrumentation and Measurement, VOL. 57, NO. 1, JANUARY 2008

[8] O. Ziemann,J. Krauser,P. E. Zamzow,W. Daum; POF Handbook - Optical Short Range Transmission Systems, 2nd edition; Springer

U-Bent POF biosensor coated with gold thin film for *E. coli* detection

A.S.Arcas[1*], R. C. S. B. Allil[2], M. M. Werneck[2]

[1]Federal University of Rio de Janeiro, Nanotechnology Program/COPPE, RJ, Brazil
[2]Federal University of Rio de Janeiro, Electrical Engineering Program/COPPE, RJ, Brazil

*Corresponding author: ariadny@lif.coppe.ufrj.br

ABSTRACT

Escherichia coli (*E. coli*) is a bacterial type that inhabits the intestinal tract of humans and animals and its presence in water and food is an indication of fecal contamination. This work presents the development of a fiber-optic sensor coated with gold thin film for E. coli detection as a portable, fast response and low cost alternative to conventional methodologies. The sensor operation is based on intensity modulation excited by a monochromatic light. Bacterial selectivity is guaranteed by anti-*E. coli* antibody immobilization on the fiber surface. The sensor was able to detect 1.5×10^3 CFU/mL of bacteria concentration.

1. INTRODUCTION

Escherichia coli (*E. coli*) is a bacterial type that inhabits the intestinal tract of humans and some animals and it can be harmful to health if ingested. The most common routes of *E. coli* contamination are drinking water, eating vegetables, undercooked meat, unpasteurized milk, and bathing in polluted rivers and seas [1] [2]. Its importance as a public health is evident when there are outbreaks such as occurred in 1982 in which 8,598 people were infected in the Oregon and Michigan cities at United States [3]. Food quality is a matter of global importance that shall be ensured by constant monitoring and in order to prevent new outbreaks, novel rapid and reliable detection methods are needed [4].

This work presents the development of a biosensor based on an U-bent POF coated with gold thin film for *E. coli* bacteria detection. The biosensor works by monochromatic light intensity modulation imposed by Surface Plasmon Resonance (SPR) phenomenon which absorbs light due to interaction with gold thin film. Light absorption depends on the surrounding RI variations. The gold thin film also has the function of improving the antibodies immobilization. Preferred use of gold instead of silver or copper is due to its high chemical stability. U-shaped geometry does not require removing fiber cladding for using intensity-modulated SPR, which is difficult in practice. In straight fibers, the evanescent wave does not reach the gold film because of cladding thickness, however, in a bent fiber, higher-order propagation modes go through to the cladding producing evanescent field in the gold and medium.

This scheme reduces the cost because it requires no optical spectrum analyzer (OSA) to measure the output spectrum of the transmitted light which goes through the U-bent probe. With a simple and easy-to-fabricate detection system, this scheme has a larger possibility of ending up in a commercial and large-scale production.

2. MATERIALS AND METHODS

2.1 U-bent Probes Fabrication

Multi-mode Mitsubishi Rayon Eska GH 4001 POF with 1-mm diameter made of polymethyl methacrylate (PMMA) core and fluorinated polymer cladding with 10 μm in thickness was used. The refractive index in the visible range of interest is about 1.49 for PMMA and 1.41 for fluorinated polymer. The POF was cut into several 10-cm-long sections and both end surfaces were cleaved and polished with 3 μm polishing paper for better light coupling [5]. Then the 10-cm-long sections were bent around a mold and heated at about 70 °C for 15 s to produce U-bent probes with 25 mm length and 8 mm waist diameter.

2.2 Gold Thin Film Deposition

A sputtering system (Aja International, USA) with RF magnetron was used for gold depositon over the U-bent probe. Prior to gold coating, the probes were cleaned in isopropyl alcohol 100 % for 2 minutes, and then washed in ultrapure water and dried with ultrapure nitrogen. The sputtering process was done with argon flow rate of 12sccm (standard cubic centimeters per minute) at a pressure of 4×10^{-3} mbar. A 40 W RF power was applied to ionize the gas (plasma). The gold deposition rate in these conditions is about 3.5 nm/min. Probes were exposed

to the sputtering process for 8, 14, 20 and 28 minutes to produce probes coated with 30, 50, 70 and 100 nanometer of gold thickness, respectively.

2.3 Sucrose Solutions and Bacterial Suspensions

Aqueous solutions with RI varying from 1.333 to 1.375 were prepared by dissolving sucrose in ultrapure water. Sucrose solutions refractive indexes were measured by Abbe refractometer (Quimis, Brazil, Model Q767BD).

E. coli O55 was obtained from Oswaldo Cruz Institute (FIOCRUZ) in Rio de Janeiro, Brazil. Bacterial cultures were prepared on a plate containing tryptic soy agar (TSA), incubated at 37 °C for 24 hours. The bacterial suspensions for sensor testing were prepared in a saline water solution at 0.85 %. Bacteria concentrations were obtained by dilution and confirmed by two methods: McFarland turbidity standards and absorption spectroscopy (Pro-Tools UV-1800 spectrophotometer). The absorbance of *E. coli* concentration of $1,5 \times 10^8$ CFU/mL (colony forming unit) should be beetwen 0.08 and 0.1 at 625 nm wavelength [6].

2.4 Antibody Immobilization

Polyclonal anti-*E. coli* antibody from rabbit (Bio-Rad Labs, Brazil) was diluted to the concentration of 10 mg/mL in phosphate-saline buffer (PBS). After gold coating, the probes were immersed into ethanol solution containing cysteamine 4 mM at 25 °C for 2 hours. Then they were rinsed with ethanol 100 % and treated with a 40 mM N-Hydroxysuccinimide (NHS) /100 mM N-Ethyl-N′-(3-dimethylaminopropyl) carbodiimide hydrochloride (EDAC) solution in PBS buffer for 1 hour at room temperature. They were further rinsed with PBS buffer and ultrapure water. The sensors prepared with cysteine, NHS and EDAC were immersed in antibody solution with PBS for 1 hour at 20 °C. Unbound antibody molecules were removed by washing with PBS and subsequent immersion in Bovine serum albumin (BSA) solution for 30 minutes.
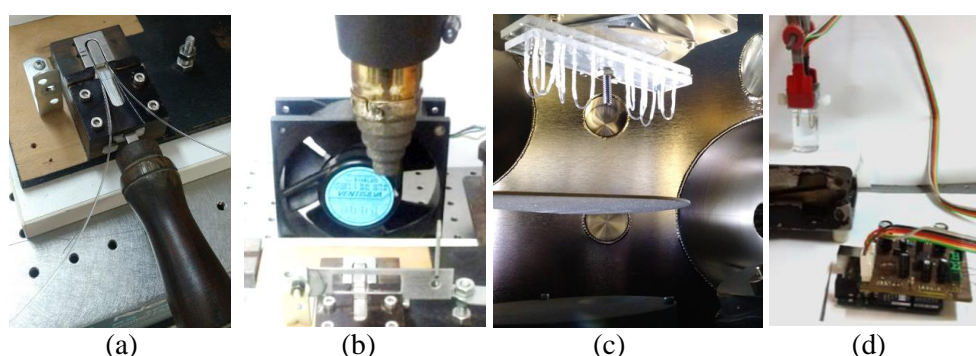

(a) (b) (c) (d)

Figure 1: (a) Custom-made device for molding U-bent probes. (b) Hot-air gun and cooler used for heating and cooling the probes. (c) bare U-shaped probes installed inside the sputtering chamber. (d) Optical setup photo. Immobilized and reference U-bent probes immersed into bacteria suspension.

2.5 Optical Setup

The optical setup consisted of two sets of 880 nm LED powered by a current source controlled by an Arduino Microcontroller and connected to the end of the bent fiber. The light is received by the photodiode located on the opposite fiber end. The light intensity is modulated by SPR absorption in function of the RI variation in the U-bent surface due to bacteria adhesion. For wavelengths around 880 nm, the photodiode achieves maximum gain. The optical setup (Fig. 1.d) allows using two U-bent probes at the same time. This is useful for checking immobilization effect referencing during tests.

3 RESULTS AND DISCUSSION
3.1 RI Sensitivity

The biosensors were tested with sucrose solutions under different RI into the operation range (1.33 to 1.39) for bacteria detection in order to verify their linearity and sensitivity. Six sensors were fabricated and tested for each gold thickness. For 30-nm and 50-nm gold thin film coated probes, the sensors showed a non-linear behaviour and no sensitivity to RI variation. Therefore, theses sensors are definitely not useful for bacteria detection.

The 70-nm and 100-nm gold thin film coated probes were tested in sucrose solutions with RI from 1.33 to 1.38. The results are shown in Fig. 2. Each point in the plot is the average value of twenty measures. The

sensor output voltage was set to be 3 V for water refractive index. In this operating range, both sensors showed linear response as a function of the RI. The average sensitivities of 70-nm and 100-nm gold coated probes were respectively 6.01 V/RIU and 8.25 V/RIU. The highest standard deviation was the order of 10^{-3} RIU for both gold film thickness. Notice that the output signal is proportional to the RI variation. This behaviour is in accordance with results from [7]. A simple explanation for this phenomenon is that the light incident on the metal-dielectric surface will be more or less absorbed by the plasmon ressonance effect generated by the incident beams with angle greater than the critical one. The curvature of the U-bent probes allows high order propagation modes to go to the cladding and senses the external medium.
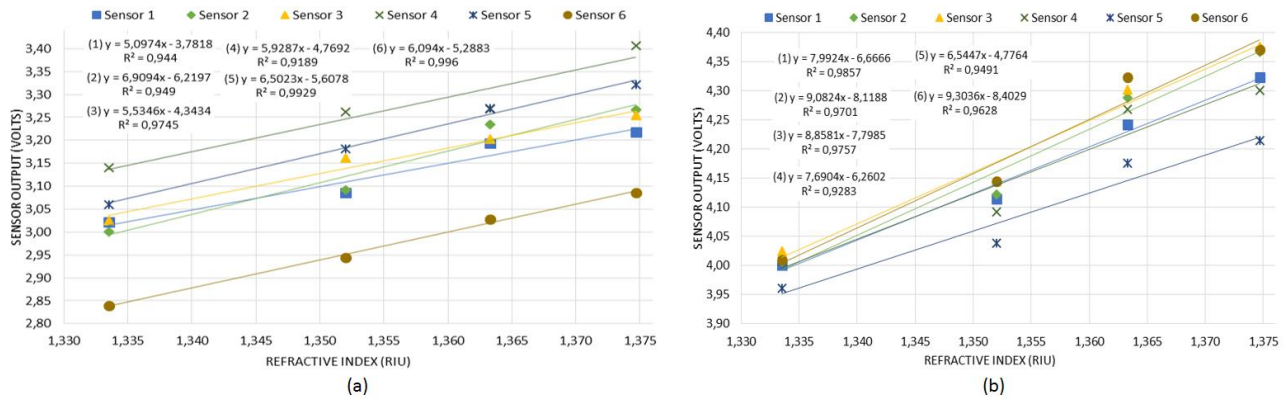

Figure 2: Results of: a) 70 and b) 100-nm gold thin film coated sensors measuring refractive index of sucrose solutions.

3.2 Bacteria Detection Tests

In this section, we present the results obtained with immobilized 70-nm gold thin film coated U-bent sensors for bacteria detection. This thickness was chosen instead of 100-nm just for saving the gold target. Fig. 3 shows the results of 70-nm gold coated sensor in a suspension with 1.5×10^{8} CFU/mL bacteria concentration. The immobilized sensor showed an increase in output voltage in time due to the increase in the surrounding RI caused by immunocapture effect as the antibody layer keeps capturing the bacteria present in the water. The output of reference sensor remained constant which confirms the properly operation of the immobilized sensor for *E. coli* detection. However, at lower concentrations, the sensor was not able to measure the small changes in the surrounding RI. It was supposed that the optical setup did not have enough sensitivity at this extreme of the range. In order to verify the functionality of the sensor, tests were carried out with a spectrophotometer (Model HR-400, Ocean Optics) and a white light source. The wavelength of interest is 845 nm (as close as possible to 880 nm, the peak of Si photodiode sensitivity). It was not possible to test at 880 nm because this wavelelngth is outside the spectrometer range.

Figure 3: Results of the 70-nm gold coated U-bent sensor in bacteria concentrations of: a) 1.5×10^{8} CFU/mL. b) 1.5×10^{3} CFU/mL obtained with the spectrophotometer for 845 nm.

In this optical configuration, the 70-nm gold coated U-bent sensor was able to measure an *E. coli* concentration of 1.5×10^{3} CFU/mL. Fig. 3.b shows the results for operation time of 70 min.

4 CONCLUSION

The 30-nm and 50-nm gold thin film coated biosensors showed a non-linear behavior and no sensitivity to the surrounding RI variation and thus they are not useful for sensing. Nonetheless, 70-nm and 100-nm gold thin film coated biosensors showed properly linear responses for the range from 1.333 to 1.375 RIU. Experimets with *E. coli* showed that the biosensor is able to detect concentration of 1.5×10^8 CFU/mL in the optical setup used and 1.5×10^3 CFU/mL in the spectophotometer.

In order to improve the limit of detection, the following solutions shall be adopted: to fabricate a highest sensitivity optical and electronic set-up, to investigate more efficient protocols for bacterial adhesion, and to choose a led wavelength with higher response in SPR.

5 REFERENCES

[1]   B. Gordon, P. Callan, and C. Vickers, "WHO guidelines for drinking-water quality.," *WHO Chron.*, vol. 38, no. 3, p. 564, 2008.

[2]   A. Vranjac, "Síndrome Hemolítico - Urêmica e *Escherichia coli O104:H4* e o surto na Alemanha," *Vigilância Epidemiolõgica*, pp. 1–17, 2011.

[3]   J. M. Angel, P. H. Sparling, C. Crowe, P. M. Griffin, and D. L. Swerdlow, "Epidemiology of *Escherichia coli O157:H7* Outbreaks, United States, 1982–2002," vol. 11, no. 4, 2005.

[4]   H. Baccar, M. B. Mejri, I. Hafaiedh, T. Ktarli, M. Aouni, and A. Abdelghani, "Surface plasmon resonance immunosensor for bacteria detection," *Talanta*, vol. 82, no. 2, pp. 810–814, 2010.

[5]   G. Wandermur *et al.*, "Biosensors and Bioelectronics Plastic optical fiber-based biosensor platform for rapid cell detection," *Biosens. Bioelectron.*, vol. 54, pp. 661–666, 2014.

[6]   McFarland, "Padrão de Turvação preparado BBL," p. 3, 2010.

[7]   K. Kurihara, K. Nakamura, and K. Suzuki, "Asymmetric SPR sensor response curve-fitting equation for the accurate determination of SPR resonance angle," *Sensors Actuators, B Chem.*, vol. 86, no. 1, pp. 49–57, 2002.

Long-term stability enhancement of POF-based Brillouin measurement by mitigating multiple Fresnel reflections using CYTOP

N. Matsutani, H. Lee, Y. Mizuno[*], and K. Nakamura

Institute of Innovative Research, Tokyo Institute of Technology, Yokohama 226-8503, Japan
*Corresponding author: ymizuno@sonic.pi.titech.ac.jp

Abstract: For Brillouin-sensing applications, we develop a method of mitigating the Fresnel reflection at the end of perfluorinated plastic optical fibers by covering there with amorphous fluoropolymer (CYTOP; material of the fiber core) dissolved in volatile solvent. Even after the solvent evaporates, the CYTOP layer remains, leading to long-lasting Fresnel reduction. The effectiveness of this method is experimentally proved.

1. Introduction

Brillouin scattering in optical fibers has attracted significant attention in sensing community due to its measurability of strain and temperature distributions [1–5]. In 2010, Brillouin scattering in plastic optical fibers (POFs) was first observed [6], and since then, many research groups have been developing POF-based Brillouin sensors [7–9], which have large-strain measurability, ease of handling, and so-called memory functions of strain and temperature. Unlike the other groups studying POF-based Brillouin sensing with two-end-access configurations (such as Brillouin optical time-domain analysis and Brillouin optical frequency-domain analysis), we have been developing POF-based single-end-access distributed sensing systems using a technique called Brillouin optical correlation-domain reflectometry (BOCDR) [3–5]. Recently, several high-speed configurations of BOCDR have been implemented and successfully applied to POF-based sensing.

To date, various types of POFs have been developed. For instance, the most common POF composed of polymethyl methacrylate is optimized for visible light transmission, but its propagation loss at telecom wavelength is so high (>>100 dB/m) that it is not suitable for Brillouin applications. Actually, the only type in which Brillouin scattering has been experimentally observed is a perfluorinated graded-index (PFGI-) POF [6,10] with relatively low propagation loss even at telecom wavelength.

In BOCDR using a PFGI-POF (core refractive index n = ~1.36) as a fiber under test (FUT), when the Fresnel reflections at both ends of the POF (boundary with a silica single-mode fiber (SMF; n = ~1.46) and that with air (n = ~1.00)) are significant, the Brillouin gain spectrum (BGS) is generally overlapped with the interference noise [11], which is temporally unstable. Consequently, the measurement accuracy of the Brillouin frequency shift (BFS), which provides the information on strain and temperature, is deteriorated, especially at high-speed operations [4,5].

When the FUT is a silica SMF, besides the fact that the Fresnel reflection at the proximal end of the FUT is weak, the Fresnel reflection at the distal open end of the FUT can also be sufficiently reduced by applying considerable bending loss near the end. However, when the FUT is a PFGI-POF, it is difficult to apply sufficient bending loss near the open end of the FUT, because the PFGI-POF is a multimode fiber with a core diameter of at least 50 μm and quite insusceptible to bending loss [10]. Conventionally, the Fresnel reflection at the open end of the PFGI-POF was suppressed by dipping the end in water, the refractive index of which (n = ~1.33) is close to that of the PFGI-POF core. However, when the tip of the PFGI-POF is taken out of water, as high-power light is radiated at the open end, water evaporates in a short period, and thus it was not easy to use this method for long-term measurement.

In this work, we develop a new method of mitigating the Fresnel reflection at the open end of the PFGI-POF by covering there with amorphous fluoropolymer (cyclic transparent optical polymer (CYTOP®; Asahi Glass Co., Ltd.); same material as the core of the PFGI-POF) dissolved in volatile solvent. Even after the solvent evaporates, the CYTOP layer remains attached to the open end, leading to long-lasting Fresnel reduction. In addition, as the materials of the core and CYTOP are the same, refractive index matching can be performed more ideally than in the case of water. Here we experimentally show the effectiveness of this method.

2. Experimental setup

A 2.6-m-long PFGI-POF was employed as an FUT. It consists of a core (50 μm diameter), cladding (100 μm

diameter), and overcladding (750 μm diameter). The core and cladding layers are composed of doped and undoped CYTOP, respectively. The refractive index at the center of the core is 1.356, whereas that of the cladding layer is 1.342; these values are not strongly dependent on optical wavelength. The propagation loss at 1.55 μm is ~0.25 dB/m.

The experimental setup for measuring the temporal variations of the Fresnel-reflected light power before and after covering the open end of the PFGI-POF with water and CYTOP is depicted in Fig. 1. The output of a semiconductor laser at 1.55 μm was injected into one end of a PFGI-POF via an optical circulator (OC) composed of silica SMFs. Using an erbium-doped fiber amplifier, the incident power was kept at 23.5 dBm. The polarization state was
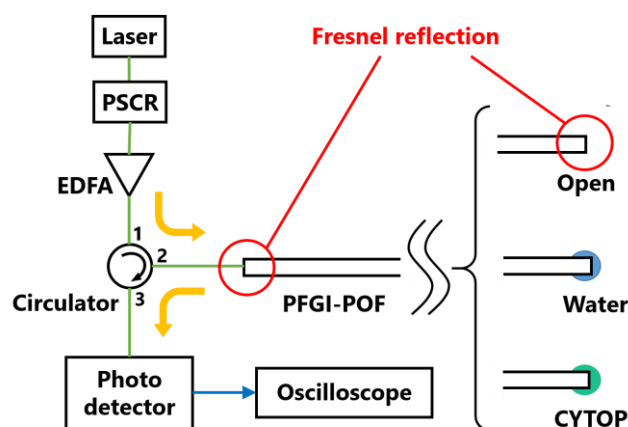

Fig. 1. Experimental setup. EDFA: erbium-doped fiber amplifier; PFGI-POF: perfluorinated graded-index plastic optical fiber; PSCR: polarization scrambler.

scrambled to suppress the polarization-dependent signal fluctuations. The SMF (2nd port of the OC) was butt-coupled to the PFGI-POF [6]; this part was fixed during all the measurements, leading to constant Fresnel reflection (consequently, the power change was attributed to the Fresnel reflection at the other end of the PFGI-POF). With a photo detector (PD), the reflected light was converted into an electrical signal, which was observed using an oscilloscope on a real-time basis. The tip of the PFGI-POF, perpendicularly cut and polished, was first completely dipped in water or CYTOP solution (CTX-809SP2; concentration: 9%; solvent: CT-SOLV180 (n = ~1.29)), and then it was taken out. The measurement of the BGSs was also performed using the setup shown in Fig. 1, by simply replacing the PD with an electrical spectrum analyzer. In this configuration without using an explicit reference light path, the Fresnel-reflected light operates as reference light for BGS detection [12].

3. Experimental results

The temporal variations of the Fresnel-reflected light power before dipping the open end of the PFGI-POF in water, during dipping, and shortly (1 min) after taking it out are shown in Fig. 2(a), (b), and (c), respectively. The vertical axis was normalized so that the average power of Fig. 2(a) (–54.2 dBm) became 0 dB. In Fig. 2(a), the Fresnel reflection at the open end was temporally unstable with a standard deviation (SD) of +/–1.67 dB. Then, when the open end was dipped in water, the temporal signal fluctuations were suppressed down to an SD of +/–0.94 dB thanks to the refractive index matching. However, 1 min after taking the PFGI-POF end out
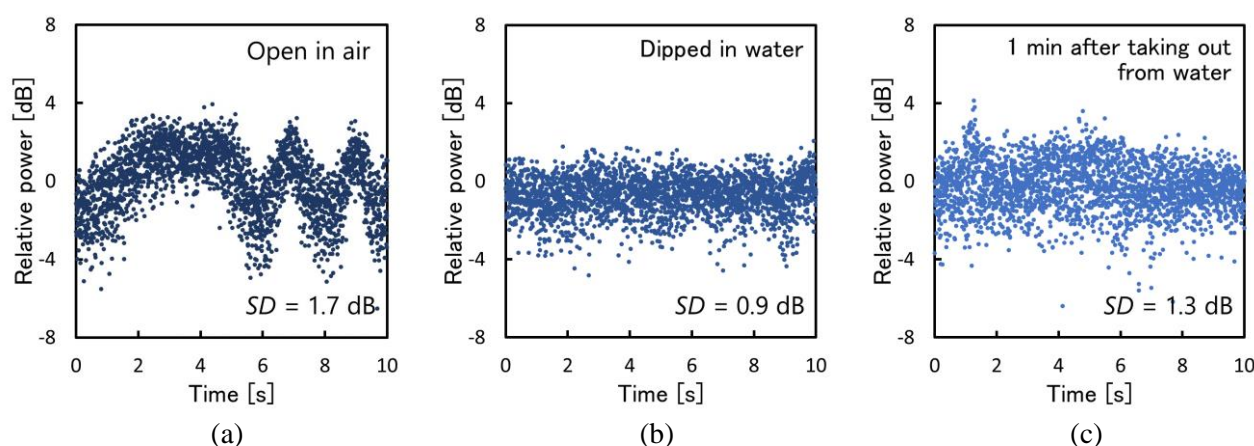

Fig. 2. Temporal variations of the Fresnel-reflected light power (a) before dipping the open end of the PFGI-POF in water, (b) during dipping in water, and (c) 1 min after taking it out from water. The standard deviations (SD) of the signal fluctuations are indicated.
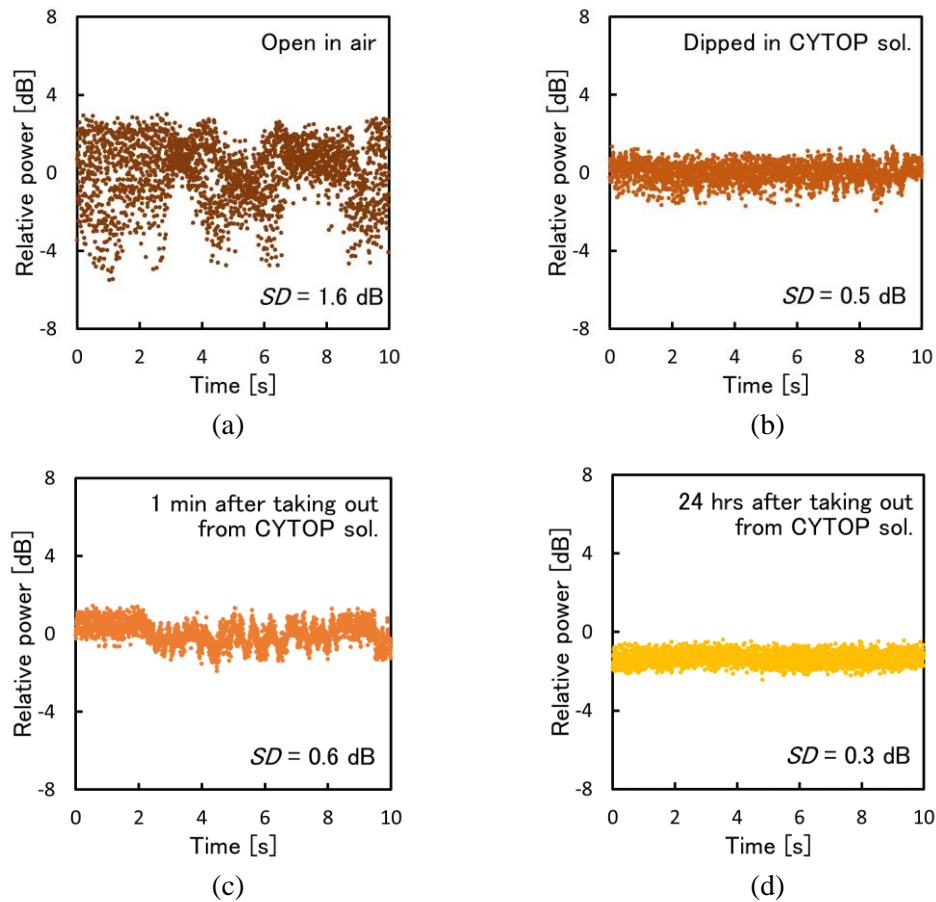
Fig. 3. Temporal variations of the Fresnel-reflected light power (a) before dipping the open end of the PFGI-POF in CYTOP solution, (b) during dipping in CYTOP solution, (c) 1 min after taking it out from CYTOP solution, and (d) 24 hrs after taking it out from CYTOP solution. The standard deviations (SD) of the signal fluctuations are indicated.

from water, the signal fluctuations became as large as before dipping, with an SD of +/–1.29 dB. This is because the water left on the core quickly evaporated because of the high-power light radiation, and the index matching became no longer active. Thus, covering the PFGI-POF end with water was shown to be not suitable for reducing the Fresnel reflection for a long term.

Subsequently, the same measurements were performed using CYTOP solution. The temporal variations of the Fresnel-reflected light power before dipping the open end of the PFGI-POF in CYTOP solution, during dipping, 1 min and 24 hrs after taking it out are shown in Fig. 3(a), (b), (c), and (d), respectively. In Fig. 3(a), the signal fluctuations were relatively large with a standard deviation (SD) of +/–1.64 dB, which is comparable to that in Fig. 2(a) (basically the same measurement condition). When the open end was dipped in CYTOP solution for refractive index matching, the signal fluctuations were suppressed down to an SD of +/–0.52 dB, just in the same way as in water. Then, 1 min after taking the PFGI-POF end out from CYTOP solution, the signal fluctuations were still suppressed with an SD of +/–0.58 dB partially thanks to the high viscosity of the solution. Moreover, 24 hrs after taking it out from CYTOP solution, the signal fluctuations were even more suppressed with an SD of +/–0.33 dB. Unlike the case of water, after the solvent evaporated, the CYTOP was solidified and remained on the core. The enhanced suppression of the signal fluctuations was probably caused by more ideal refractive index matching between the PFGI-POF core (n = ~1.36) and the CYTOP (n = ~1.35) (note that n of CYTOP solution is lower than ~1.35 because n of its solvent is ~1.29). Thus, covering the PFGI-POF end with high-viscosity CYTOP solution was shown to be suitable for long-term Fresnel reduction.

Finally, we measured the BGSs of the same PFGI-POF before dipping its open end in CYTOP solution and 25 hrs after taking it out, as shown in Fig. 4. Before dipping, the BGS was overlapped with the interference noise

caused by the multiple Fresnel reflections at both ends of the PFGI-POF. The peak interval of the noise was approximately 40 MHz, which well corresponds to the theoretical value calculated using the PFGI-POF length [11]. On the other hand, it is clear that the noise was reduced by use of CYTOP, leading to the improved long-term measurement accuracy of the BFS.

4. Conclusion

To improve the long-term measurement accuracy of PFGI-POF-based single-end-access Brillouin sensors, we developed a new Fresnel suppression method using CYTOP dissolved in volatile solvent. We experimentally proved that, by covering the open end of the PFGI-POF with CYTOP solution, even after the solvent evaporates, the Fresnel reflection can be permanently mitigated. The high viscosity of CYTOP is also advantageous over a conventional water-based method. Thus, we believe that this method will be a standard technique for improving the performance of PFGI-POF-based Brillouin sensing systems.

Fig. 4. BGSs measured before dipping the PFGI-POF end in CYTOP solution (blue) and 25 hrs after taking it out (orange).

5. Acknowledgements

6. References

[1]   A. H. Hartog, *An Introduction to Distributed Optical Fibre Sensors*, CRC Press (2017).
[2]   K. Hotate and T. Hasegawa, "Measurement of Brillouin gain spectrum distribution along an optical fiber using a correlation-based technique: Proposal, experiment and simulation," IEICE Trans. Electron. **E83-C**, 405 (2000).
[3]   Y. Mizuno, W. Zou, Z. He, and K. Hotate, "Proposal of Brillouin optical correlation-domain reflectometry (BOCDR)," Opt. Express **16**, 12148 (2008).
[4]   H. Lee, N. Hayashi, Y. Mizuno, and K. Nakamura, "Slope-assisted Brillouin optical correlation-domain reflectometry: proof of concept," IEEE Photon. J. **8**, 6802807 (2016).
[5]   Y. Mizuno, N. Hayashi, H. Fukuda, K. Y. Song, and K. Nakamura, "Ultrahigh-speed distributed Brillouin reflectometry," Light: Sci. Appl. **5**, e16184 (2016).
[6]   Y. Mizuno and K. Nakamura, "Experimental study of Brillouin scattering in perfluorinated polymer optical fiber at telecommunication wavelength," Appl. Phys. Lett. **97**, 021103 (2010).
[7]   A. Minardo, R. Bernini, and L. Zeni, "Distributed temperature sensing in polymer optical fiber by BOFDA," IEEE Photon. Technol. Lett. **26**, 387 (2014).
[8]   Y. Dong, P. Xu, H. Zhang, Z. Lu, L. Chen, and X. Bao, "Characterization of evolution of mode coupling in a graded-index polymer optical fiber by using Brillouin optical time-domain analysis," Opt. Express **22**, 26510 (2014).
[9]   N. Hayashi, Y. Mizuno, and K. Nakamura, "Distributed Brillouin sensing with centimeter-order spatial resolution in polymer optical fibers," J. Lightwave Technol. **32**, 3397 (2014).
[10]   Y. Koike and M. Asai, "The future of plastic optical fiber," NPG Asia Mater. **1**, 22 (2009).
[11]   Y. Mizuno, N. Hayashi, and K. Nakamura, "Fiber-optic interferometry using narrowband light source and electrical spectrum analyzer: influence on Brillouin measurement," J. Lightwave Technol. **32**, 4132 (2014).
[12]   Y. Mizuno, N. Hayashi, and K. Nakamura, "Fresnel-assisted self-heterodyne detection for Brillouin gain spectrum characterisation in polymer optical fibres," Electron. Lett. **50**, 1153 (2014).
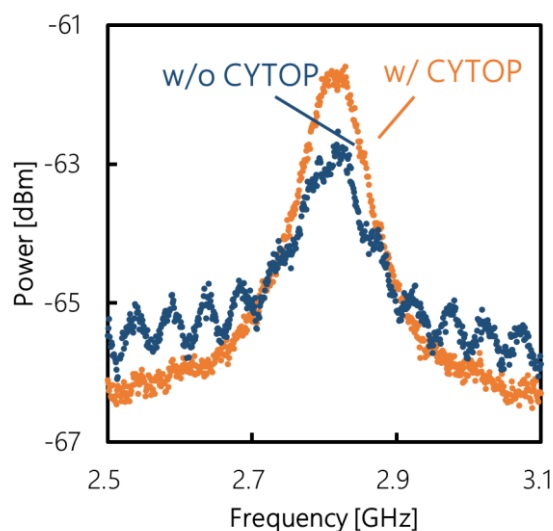
Hydrostatic pressure dependence of FBG inscribed in perfluorinated GI-POF

R. Ishikawa[1], H. Lee[1], A. Lacraz[2], A. Theodosiou[2], K. Kalli[2], Y. Mizuno[1*], and K. Nakamura[1]

[1]Institute of Innovative Research, Tokyo Institute of Technology, Yokohama 226-8503, Japan
[2]Nanophotonics Research Laboratory, Cyprus University of Technology, Limassol 3036, Cyprus

*Corresponding author: ymizuno@sonic.pi.titech.ac.jp

Abstract: We investigate the hydrostatic pressure dependence of the Bragg wavelength of a fiber Bragg grating (FBG) inscribed in a perfluorinated POF at 1550 nm. At 0.5 MPa, the Bragg wavelength increased with time and became almost constant ~150 min later. The pressure-dependence coefficient without considering the time constant was calculated to be 1.3 nm/MPa, which is over 5 times the values of other types of POF-FBGs. The pressure-dependence coefficient was then measured to be –0.13 nm/MPa, the absolute value of which was comparable to those of other POF-FBGs, but the sign was opposite.

1. Introduction

Fiber Bragg gratings (FBGs) have been exploited to develop fiber-optic sensors for strain, temperature, humidity, refractive index, and many other physical parameters [1]. Pressure sensing is one of the major targets in FBG research community, and a number of relevant results have been reported using FBGs inscribed in glass optical fibers [2–5]. In the meantime, as polymeric materials are generally softer than glass materials, higher pressure sensitivities have been achieved using FBGs inscribed in some types of plastic optical fibers (POFs) [6–8]. For instance, at telecom wavelength, FBGs in a single-mode (SM-) poly(methyl methacrylate) (PMMA-) POF [7] and a multimode microstructured (MM-m) POF [8] are reported to have pressure sensitivities of ~0.25 nm/MPa (corresponding to a fractional sensitivity (Bragg wavelength shift divided by the initial Bragg wavelength for fair comparison) of ~163×10^{-6}/MPa) and ~0.1 nm/MPa (corresponding to ~64×10^{-6}/MPa), respectively, the absolute values of which are approximately ~82 and ~32 times larger than the typical value of an FBG in a silica single-mode fiber (SMF) (–3.1 pm/MPa, corresponding to –2.0×10^{-6}/MPa) [9]. However, such conventional POF-FBGs suffer from extremely high propagation loss at 1550 nm.

Recently, in order to tackle this problem, some research groups [10,11] have developed an FBG inscription technique in perfluorinated graded-index (PFGI-) POFs [12] with relatively low propagation loss even at 1550 nm, where amplified spontaneous emission (ASE) can be directly used as a wideband light source for interrogating the Bragg wavelength. Besides, the core refractive index of PFGI-POF-FBGs is close to that of water, which is beneficial for some bio-sensing applications [13]. To date, the strain, temperature, and humidity sensing characteristics of PFGI-POF-FBGs have been investigated [10,14], but no reports have been provided regarding their pressure dependence.

In this paper, at 1550 nm, we investigate the hydrostatic pressure dependence of the Bragg wavelength of a PFGI-POF-FBG for the first time to the best of our knowledge. At 0.5 MPa, the Bragg wavelength increases with time and, ~150 min later, becomes almost constant. The pressure-dependence coefficient is then measured to be –0.13 nm/MPa, which is compared with those of a silica fiber and other types of plastic fibers.

2. FBG inscription and measurement setup

A 2-mm-long FBG was inscribed in a 1.3-m-long PFGI-POF. The PFGI-POF (GigaPOF-50SR, Chromis Fiberoptics) has a three-layered structure: core (diameter: 50 μm; refractive index: ~1.35), cladding (diameter: 70 μm), and overcladding (diameter: 490 μm). The core and cladding consist of doped and undoped amorphous fluoropolymer (CYTOP®), respectively, the water absorption of which is negligibly small [15], and the overcladding is composed of
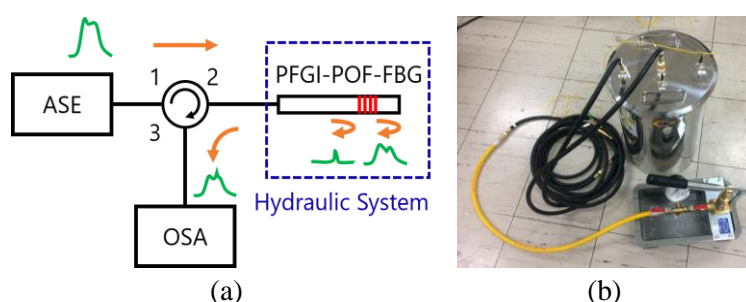

Fig. 1. (a) Experimental setup. ASE: amplified spontaneous emission; OSA: optical spectrum analyzer. (b) Photograph of hydraulic system.
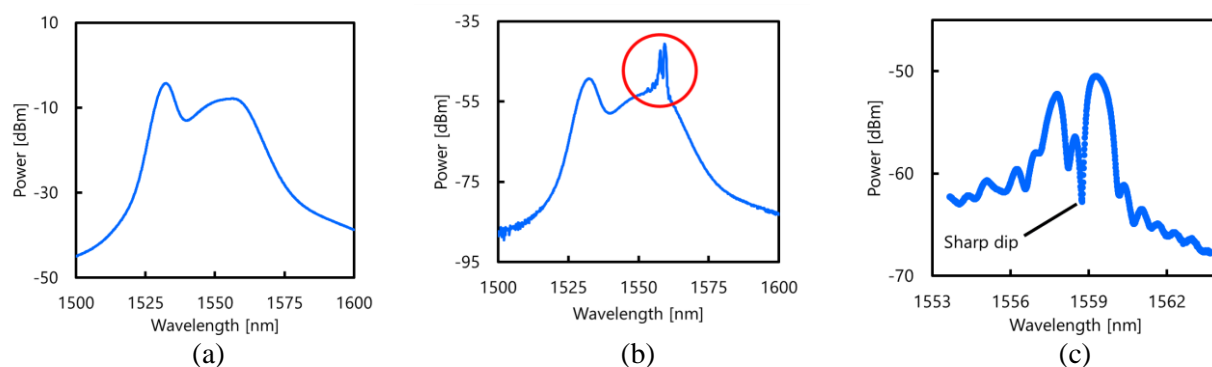
Fig. 2. (a, b) Measured optical spectra of the ASE output and the reflected light, respectively. (c) Magnified view of the red-circled part in (b), around the FBG-induced peaks.

polycarbonate. The optical propagation loss is relatively low (~0.25 dB/m) even at 1550 nm. The FBG was inscribed without removal of the overcladding using a femtosecond laser system (High Q femtoREGEN) operating at 517 nm, with a 220-fs pulse duration, 1-kHz repetition rate and laser pulse energy of ~100 nJ [10]. The PFGI-POF was mounted on an air bearing translation system (Aerotech) for accurate two-axis motion and the laser beam was focused from above using a long working distance x50 objective (Mitutoyo). Accurate synchronization of the laser pulse repetition rate and stage motion allowed for plane-by-plane grating inscription, writing the grating to the desired length and index modulation value.

Figure 1(a) shows an experimental setup for measuring the Bragg wavelength of the FBG. All the optical paths except the PFGI-POF were silica SMFs. The output from an ASE source was injected into

Fig. 3. FBG-reflected spectra around the sharp dip measured at 0.1 MPa (blue) and 0.5 MPa (red).

the PFGI-POF, and the reflected light from the FBG was guided via an optical circulator to an optical spectrum analyzer. The PFGI-POF was placed in a hydraulic system (Fig. 1(b)), in which the hydrostatic pressure P can be controlled from 0.1 MPa (atmospheric pressure) to 0.5 MPa. One end of the PFGI-POF was connected to a silica SMF using a so-called butt-coupling technique [16], and the other end was kept open.

3. Experimental results

First, we measured the optical spectra of the ASE output and the FBG-reflected light, as shown in Figs. 2(a) and (b). The spectrum of the light Fresnel-reflected at the open end of the POF was overlapped with the FBG-reflected spectrum, which was still clearly observed at 1559 nm. The magnified view of the FBG-reflected spectrum around its peaks is shown in Fig. 2(c). Multiple peaks and dips, caused by the multimode nature of the POF [17], were observed in the spectrum. The wavelength of any peak or dip (including the highest peak) could be selected as a Bragg wavelength, but here, the clear and sharpest dip at 1558.97 nm was used to enhance the measurement accuracy.

Subsequently, we measured the FBG-reflected spectra around the dip before and after the pressure P was abruptly (within 20 s) increased from 0.1 MPa (atmospheric) to 0.5 MPa, as shown in Fig. 3. Although the linewidth of the dip was slightly reduced, the Bragg wavelength shift was negligibly small. After that, however, when the pressure P was maintained at 0.5 MPa, the Bragg wavelength shifted as time proceeded, as shown in Fig. 4(a). Figure 4(b) shows the temporal dependence of the Bragg wavelength at 0.5 MPa. The Bragg wavelength increased with time and, approximately 150 min later, became almost constant. A total Bragg wavelength shift was approximately 0.5 nm. The positive dependence of the Bragg wavelength on pressure was the same as those of other types of POFs [7,8], but the wavelength shift accompanying a time constant of over several tens of minutes was first observed in this measurement. Such a long time constant appears to be caused by the structure of the PFGI-POF, which is composed of two different polymer materials (CYTOP and polycarbonate). Suppose that the Bragg wavelength dependence on pressure without considering
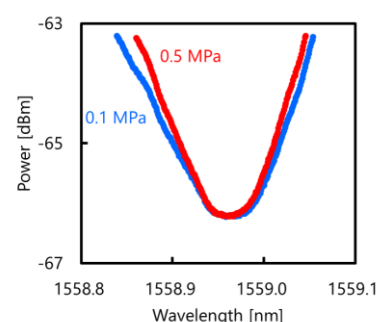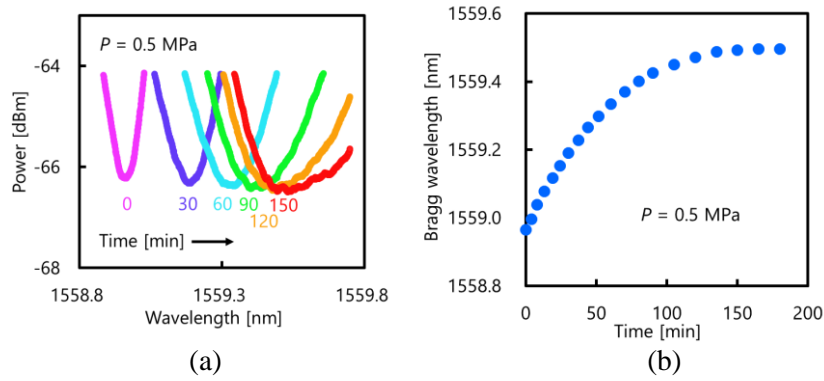
(a)

(b)

Fig. 4. (a) Temporal dependence of the FBG-reflected spectrum at 0.5 MPa. (b) Temporal dependence of the Bragg wavelength at 0.5 MPa.
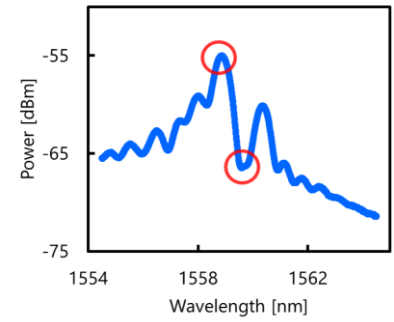
Fig. 5. FBG-reflected spectrum measured after 0.5-MPa pressure was applied for 240 minutes.
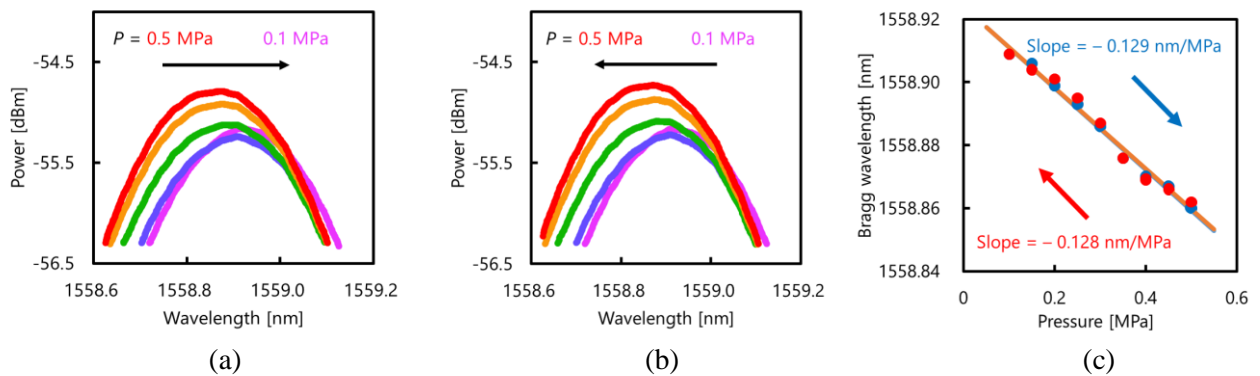

(a)

(b)

(c)

Fig. 6. (a, b) Pressure dependences of FBG-induced spectra around the sharp peak when the pressure was decreased from 0.5 MPa to 0.1 MPa and when the pressure was then increased from 0.1 MPa to 0.5 MPa. (c) Measured Bragg wavelength dependence on pressure; the red points indicate the data when the pressure was decreased, and the blue points are the data when the pressure was then increased. The two lines are their linear fits, which are overlapped and appear to be one line in this figure.

the time constant (i.e., when the Bragg wavelength is measured at each pressure after waiting for a sufficiently long time for the signal to be constant) is linear, the dependence coefficient is calculated to be ~1.3 nm/MPa (corresponding to ~860×10^{-6}/MPa). This value is ~5.2 and ~13 times larger than those of the FBGs in an SM-PMMA-POF [7] and MM-mPOF [8], respectively. Note that the linewidth of the dip increased with time, and compared with Fig. 2(c), the FBG-reflected spectrum was so much changed (Fig. 5) that the dip was no longer sharp, therefore we used the highest peak for the following measurements.

Finally, the pressure dependence of the Bragg wavelength (measured using the highest peak, as discussed above) was measured in a short period (< 1 min). Figures 6(a) and (b) show the pressure dependences of the FBG-reflected spectra when the pressure P was decreased from 0.5 MPa to 0.1 MPa and when P was then increased from 0.1 MPa to 0.5 MPa, respectively. In both cases, as the pressure became higher, the Bragg wavelength grew shorter. The spectral power change seems to have been caused by the multimode nature of the POF. The Bragg wavelength was then plotted as a function of pressure P, as shown in Fig. 6(c). Irrespective of the direction of the pressure change, the Bragg wavelength exhibited a negative dependence on pressure with a coefficient of –0.13 nm/MPa (corresponding to a fractional sensitivity of -84×10^{-6}/MPa). This absolute value is ~42, ~0.52, and ~1.3 times larger than those of the FBGs in a silica SMF [9], SM-PMMA-POF [7], and MM-mPOF [8], respectively. The negative dependence, which is opposite to those of other types of POFs [7,8], will be discussed elsewhere (due to the space limitation).

4. Conclusion

The hydrostatic pressure dependence of the Bragg wavelength of an FBG inscribed in a PFGI-POF was

investigated at 1550 nm. The Bragg wavelength shift was negligibly small shortly after the pressure was abruptly increased to 0.5 MPa. However, when the FBG was maintained at 0.5 MPa, the Bragg wavelength increased with time and became almost constant ~150 min later. A simply calculated pressure-dependence coefficient was 1.3 nm/MPa, which is over 5 times the values of other types of POF-FBGs. The pressure-dependence coefficient was then measured to be –0.13 nm/MPa, the absolute value of which was not largely different from those of other POF-FBGs, but the sign of the pressure-dependence coefficient was negative unlike other POF-FBGs. Our results indicate the feasibility of high-sensitivity pressure sensing with a short response time by removing the overcladding of the PFGI-POF-FBG.

5. Acknowledgements

6. References

[1]   A. Othonos and K. Kalli, *Fiber Bragg Gratings: Fundamentals and Applications in Telecommunications and Sensing* (Boston, Artech House Publishers, 1996).

[2]   V. R. Pachava, S. Kamineni, S. S. Madhuvarasu, K. Putha, "A high sensitive FBG pressure sensor using thin metal diaphragm," J. Opt. **43**, 117 (2014).

[3]   J. Huang, Z. Zhou, X. Wen, D. Zhang, "A diaphragm-type fiber Bragg grating pressure sensor with temperature compensation," Measurement **46**, 1041 (2013).

[4]   G. Rodriguez, M. Jaime, F. Balakirev, C. H. Mielke, A. Azad, B. Marshall, B. M. L. Lone, B. Henson, and L. Smilowitz, "Coherent pulse interrogation system for fiber Bragg grating sensing of strain and pressure in dynamic extremes of materials," Opt. Express **23**, 14219 (2015).

[5]   Y.-F. Gu, Y. Zhao, R.-Q. Lv, Y. Yang, "A practical FBG sensor based on a thin-walled cylinder for hydraulic pressure measurement," IEEE Photon. Technol. Lett. **22**, 2569 (2016).

[6]   D. J. Webb, "Fibre Bragg grating sensors in polymer optical fibres," Meas. Sci. Technol. **26**, 092004 (2015).

[7]   K. Bhowmik, G. D. Peng, Y. Luo, E. Ambikairajah, V. Lovric, W. R. Walsh, and G. Rajan, "Experimental study and analysis of hydrostatic pressure sensitivity of polymer fibre Bragg gratings," J. Lightwave Technol. **33**, 2456 (2015).

[8]   I. P. Johnson, D. J. Webb, and K. Kalli, "Hydrostatic pressure sensing using a polymer optical fibre Bragg gratings," Proc. SPIE **8351**, 835106 (2012).

[9]   M. G. Xu, L. Reekie, Y. T. Chow, and J. P. Dakin, "Optical in-fibre grating high pressure sensor," Electron. Lett. **29**, 398 (1993).

[10] A. Lacraz, M. Polis, A. Theodosiou, C. Koutsides, and K. Kalli, "Femtosecond laser inscribed Bragg gratings in low loss CYTOP polymer optical fiber," IEEE Photon. Technol. Lett. **27**, 693 (2015).

[11] M. Koerdt, S. Kibben, J, Hesselbach, C. Brauner, A. S. Herrmann, F. Vollertsen, and L. Kroll, "Fabrication and characterization of Bragg gratings in a graded-index perfluorinated polymer optical fiber," Proc. Technol. **15**, 138 (2014).

[12] Y. Koike and M. Asai, "The future of plastic optical fiber," NPG Asia Mater. **1**, 22 (2009).

[13] G. Zhou, C. F. J. Pun, H. Y. Tam, A. C. L. Wong, C. Lu, and P. K. A. Wai, "Single-mode perfluorinated polymer optical fibers with refractive index of 1.34 for biomedical applications," IEEE Photon. Technol. Lett. **22**, 106 (2010).

[14] P. Stajanca, A. Lacraz, K. Kalli, M. Schukar, and K. Krebber, "Strain sensing with femtosecond inscribed FBGs in perfluorinated polymer optical fibers," Proc. SPIE **9899**, 989911 (2016).

[15] S. Ando, T. Matsuura, and S. Sasaki, "Perfluorinated polymers for optical waveguides," Chemtech **24**, 20 (1994).

[16] Y. Mizuno and K. Nakamura, "Experimental study of Brillouin scattering in perfluorinated polymer optical fiber at telecommunication wavelength," Appl. Phys. Lett. **97**, 021103 (2010).

[17] T. Mizunami, T. V. Djambova, T. Niiho, and S. Gupta, "Bragg gratings in multimode and few-mode optical fibers," J. Lightwave Technol. **18**, 230 (2000).

A study on simulation of a high-speed optical space transmission system for rail guided vehicles

H. Takizuka[1*], M. Ishibashi[2], A. Mitsui[3], H. Suzuki[3], T. Toma[1], S. Haruyama[1], Y. Koike[2]

1: Keio University, 3-14-1 Hiyoshi, Kohoku-ku, Yokohama-shi, Kanagawa 223-8522 Japan
2: Murata Machinery, 136, Takedamukaidaicho, Fushimi-ku, Kyoto-shi, Kyoto 612-8686, Japan
3: Mitsubishi Pencil, 2-5-12 Irie, Kanagawa-ku, Yokohama, Kanagawa 221-8550, Japan

*Corresponding author: takizuka@kpri.keio.ac.jp

Abstract: We have proposed a new optical space transmission system using the GI-POF and the Ballpoint-pen collimators [1] that enables high-speed, highly stable communication with respect to remote control of rail guided vehicle used in factories and warehouses, compared to existing, mainly used wireless communication systems. As a conclusion, depending on the coupling structure of the GI-POF and the combination of lenses, the loss of the simulation results was in the range of about -27 dB to -33 dB.

1. Introduction

Several communication methods are adopted for the remote control of rail guided vehicles used in factories and warehouses. Main communication methods include wireless, wireless LAN, leaky coaxial cable, etc. These radio systems have disadvantages such as hindrance of running due to electromagnetic noise and interference, and slow transmission speed. In recent years, it has been desired to increase the communication speed in accordance with improvement of maintainability by moving images, increase of the number of vehicles accommodated, and improvement of efficiency by refinement of control. Therefore, we investigated a new optical space transmission system for Factory Automation which can overcome the shortcomings of wireless transmission and can realize high speed real time.

The goals are 1) the data transmission speed of 100 Mbps or more, 2) the maximum distance of 100 m between the vehicle and the controller, and 3) the maximum number of vehicles of 100.

The system configuration is shown in Figure1. Data transmission is a downlink sent from the controller to the vehicles and an uplink from the vehicles to the controller. In order to lower the cost by reducing the number of optical parts in the downlink, the controller broadcasts data to all vehicles. And in the uplink, only designated vehicles transmit data to the controller. Time division multiplexing system is assumed to be used. Also, the same medium is used by different wavelengths of the laser used for downlink and uplink.
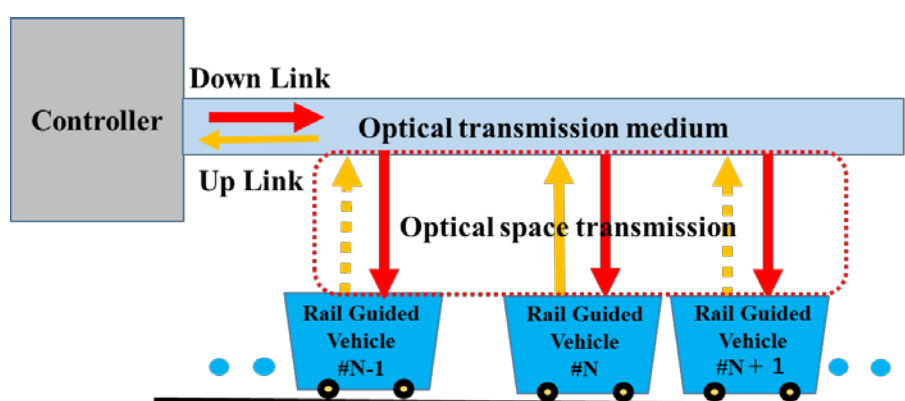

Figure 1. system configuration

Using a GI-POF that is strong against bending, and has low loss, and good high-frequency characteristics up to the vicinity of each vehicles, and a ballpoint-pen collimator that is effective for optical space transmission and an optical system between the GI-POF and the vehicle (see Figure2). In this paper, we simulated the optical system related to optical space transmission (Lighttools 8.5[2] Synopsys, Inc) and evaluated the results.
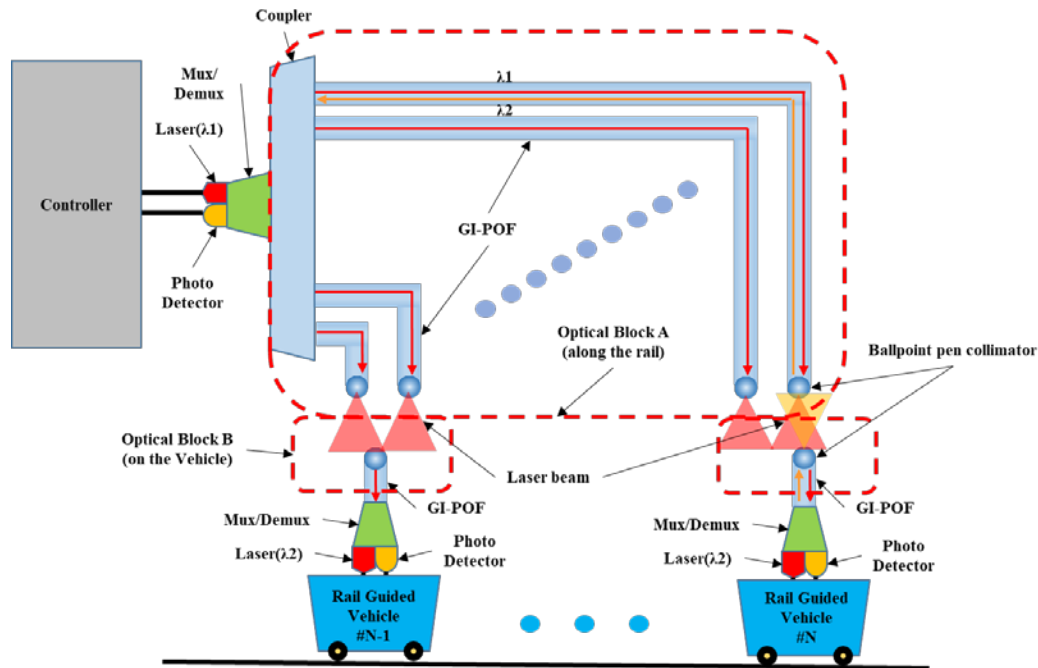
Figure 2. optical system
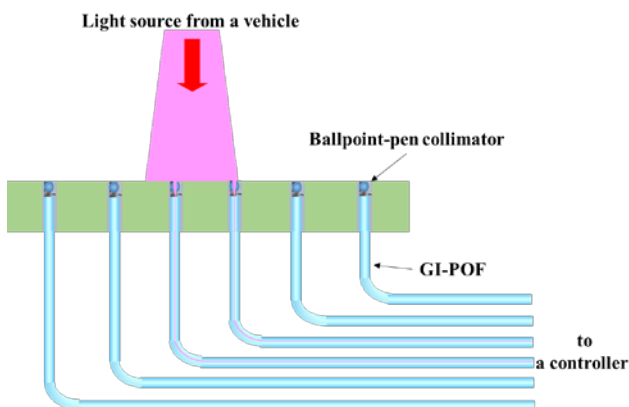
2. Optical system for space transmission
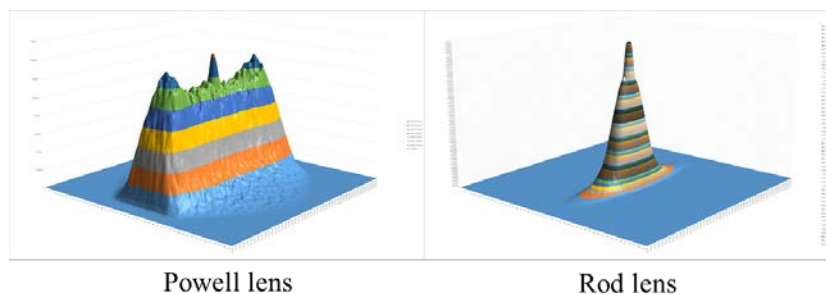

Figure 3. optical block along the rail

The optical system is composed of an optical block (A) including a GI-POF with a ball-point collimator laid along a track and an optical block (B) attached to a vehicle. The optical block (A) is arranged in the vicinity of the track at certain intervals (Figure 2, 3). The wider the interval, the smaller the number of optical components including GI-POF, and the more the loss of light increases. An appropriate relationship between the number of components and the loss is obtained by simulation.

2.1 Enlargement of light

Figure 4. light power distribution of cylindrical lens and powell lens

As a means for expanding the light, there are a cylindrical lens, a Powell lens. The light power distribution of a cylindrical lens (Rod lens, Outer diameter 5 mm, material: N-BK7) and Powell lens (60° narrow beam, material: SF6) is shown in the figure 4. The enlargement by the cylindrical lens becomes a Gaussian distribution shape and is not uniform. On the other hand, the enlargement by the Powell lens has a uniform distribution and conforms to this purpose.

2.2 Incident light angle and loss of ballpoint-pen collimator
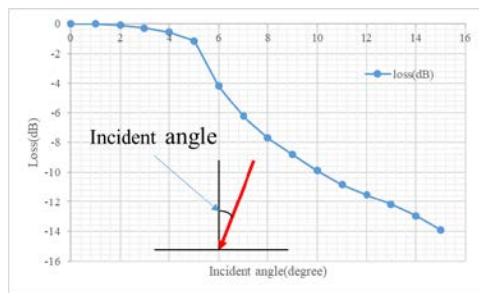
When light is enlarged, the incident angle of light with respect to the ball-point collimator becomes sharper at both ends. The relation between the incident angle and the loss was obtained by simulation. When the incident angle becomes 5 degrees or more, the loss rapidly increases. (see Figure 5)

Figure 5. The relation between the incident angle and the loss

2.3 Lens composition and loss

Plano Convex Cylindrical Lens (diameter 220 mm, length 120 mm, material: N-BK7) for vertically entering the ball lens collimator in order to not increase the loss due to the incident angle of light, and light spreading in directions other than the arrangement direction is composed of two pieces of Plano Convex Cylindrical Lens (120 mm in diameter, 200 mm in length, material: N-BK7) for focusing, and the loss was evaluated by simulation. In the range of 130 mm, the loss was -41 to -45 dB. (see Figure 6)
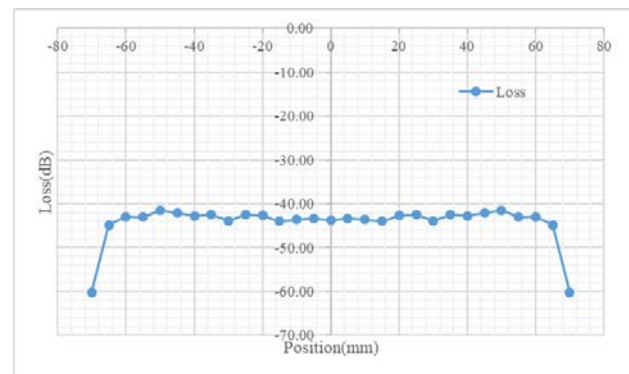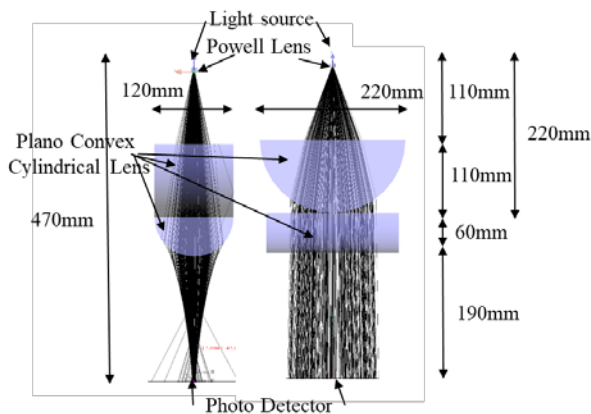

Figure 6. Optical block composed of two Plano Convex Cylindrical Lens
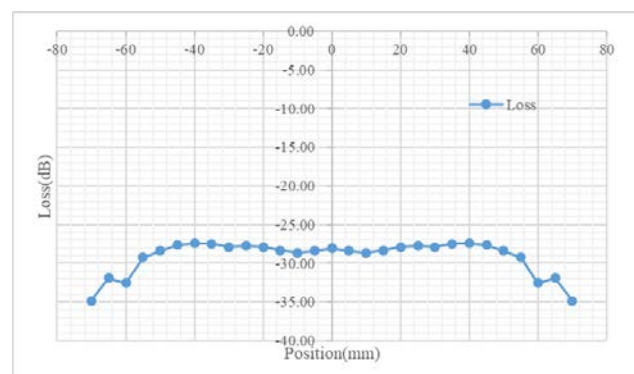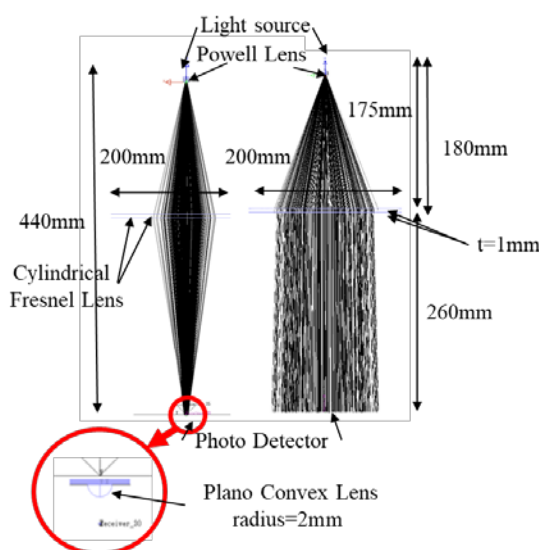

Figure 7. Optical block composed of two Cylindrical Fresnel Lens

Because Plano Convex Cylindrical Lens is large and heavy, it was replaced with Cylindrical Fresnel Lens (200 mm x 200 mm, 1 mm thickness, material: PMMA) respectively. Moreover, in the previous result, the loss was large, because the light was still spreading in the direction perpendicular to that of the path of vehicle. Plano Convex Lens (radius 2 mm, material: N-BK7) for converging was further added. In the range of 130 mm, the loss was -27 to -33 dB. (see Figure 7)
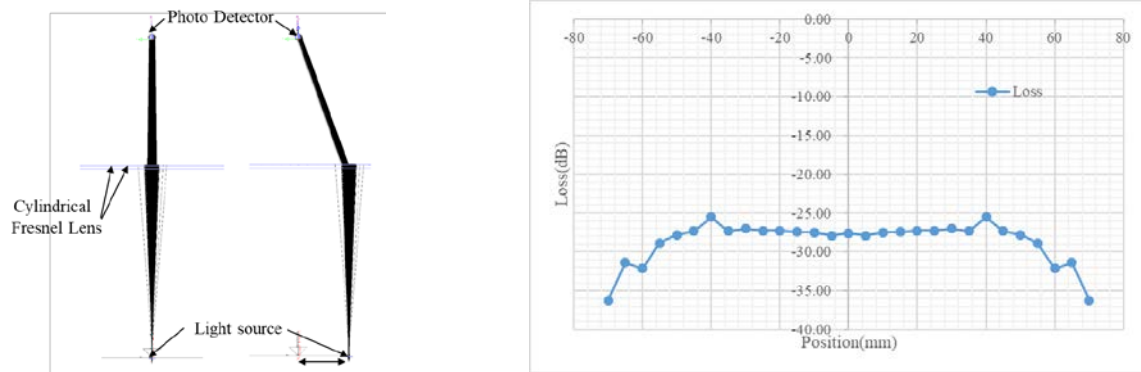
2.4 Downlink evaluation

Figure 8. The characteristics of the downlink

The characteristics of the downlink were simulated by reversing the light source and light receiving side. In the range of 130 mm, the loss was -26 to -32 dB.(see Figure 8)

3. the loss of coupler

When the optical system is constructed using the optical system described above, the number of collimators covering the length of 100 m is 770(=10000/13) or the same number of photoelectric conversion modules are required for the controller. In the case of using a photoelectric converter having a margin for loss, it becomes possible to reduce the number of cables bundled by a coupler. The simulation results in the case of using a coupler structured to bundle a plurality of ball-point pen collimator-equipped cables and converge on a single ballpoint-pen collimator equipped cable opposed to each other will be described below. When a 10: 1 coupler is used, the number of collimators and the photoelectric converter of the controller are reduced to 77, but the insertion loss is -18 dB.(see Figure 9)
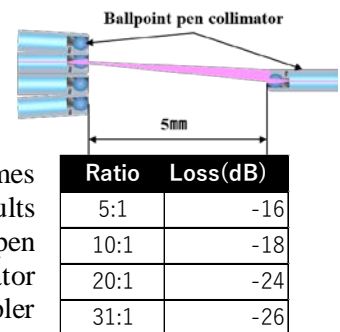

Ratio	Loss(dB)
5:1	-16
10:1	-18
20:1	-24
31:1	-26

Figure 9. the loss of the coupler

4. Conclusion

We have studied a new optical space transmission system for high - speed real - time tracked vehicles. It was realized by using ballpoint pen collimator, Powell lens, Cylindrical Fresnel Lens. When the collimator spacing was arranged at 130 mm, the loss was -27 to -33 dB on the uplink and -26 to -32 dB at the downlink. The transmission speed of the GI-POF 100 m is 10 Gbps or more, but it was about 1 Gbps transmission rate due to the arrangement interval of the collimator (in the case of 130 mm).The number of photoelectric converters of the collimator and the controller can be reduced by using a coupler, but a high-power laser and a light reception element with excellent light reception sensitivity are required.

5. References

[1] Tetsuya Toma, Hiroshi Takizuka, Toshitaka Torikai, Hitoshi Suzuki, Tetsuro Ogi and Yasuhiro Koike, "Development of a household high-definition video transmission system based on ballpoint-pen technology", Synthesiology 05/2014; 7(2):118-128.

[2] Hideki Urabe, Shinichiro Haruyama, Tomohiro Shogenji, Shoichi Ishikawa, Masato Hiruta, Fumio Teraoka, Tetsuya Arita, Hiroshi Matsubara, Shingo Nakagawa, "High data rate ground-to-train free-space optical communication system",SPIE Proceedings Vol. 51, Optical Engineering 51 (03), March 2012

Low-noise Graded-index Plastic Optical Fiber
Enabling Low-cost Optical Modules for Consumer-friendly 4K/8K Interfaces

A. Inoue[*] and Y. Koike

Keio Photonics Research Institute (KPRI), Keio University,
7-1 Shin-Kawasaki, Saiwai-ku, Kawasaki-shi, Kanagawa 212-0032, Japan

*Corresponding author: inoue@kpri.keio.ac.jp

Abstract: We demonstrate that a low-noise graded-index plastic optical fiber (GI POF) can significantly increase fiber alignment tolerance for error-free data transmission without optical isolators and/or angled fiber facets in a consumer-friendly multimode fiber (MMF) link based on a vertical cavity surface emitting laser (VCSEL). This improvement can be achieved by reflection noise reduction effects of the low-noise GI POF through its strong mode coupling because of microscopic heterogeneities in the core materials, which have much larger-scale density fluctuations than silica glasses. The novel GI POF allows for low-cost optical modules for various consumer applications in the upcoming 4K/8K era.

1. Introduction

Recently, ultra-high definition (UHD) displays with 4K (3840x2160) and 8K (7680x4320) resolutions have been rapidly developed. In Japan, full-scale 4K/8K TV broadcastings are scheduled to be started towards the 2020 Tokyo Olympics and Paralympics. This has been accelerating various distributing technologies with satellite, cable television network, and internet protocol television network. For any distributing systems, uncompressed video data transfer is required around 4K/8K TV. For the 8K video transmission, the data rates become well above 100 Gb/s. This suggests that the interface cables for consumers have extremely high transmission bandwidths in the upcoming 4K/8K era. Conventional metal interfaces such as serial digital interfaces are not suitable for the in-home applications because they require so many thick cables and electromagnetic interference preventions. Therefore, consumer-friendly optical interface cable has been demanded.

In the consumer applications, low-cost optical interconnects without precise alignments, optical isolators, angled fiber end-faces are essential for optical modules and connectors. Moreover, optical fiber cables should be frequently plugged in and out in extremely short links below several meters. In such conditions, transmitted signal qualities are degraded by optical external feedback and modal noises in the consumer-friendly optical link, which depend on alignments of optical components such as lasers, fibers, and photodiodes (PDs). This becomes more pronounced for more noise-sensitive multilevel modulation schemes which are invaluable for the uncompressed 8K video transmission. Therefore, it is required to improve worst-case data transmission quality in the consumer-friendly link where the optical components are easily coupled.

A graded-index plastic optical fiber (GI POF) has been a promising optical interface cable for the consumer applications because of its flexibility, safety, and high bandwidth [1,2]. The bandwidths of GI POFs have been increased by developing low-dispersion polymers, allowing for 40 Gb/s data transmission for a length of 100 m. Recently, we have developed GI POFs with noise reduction effects [3] because of their strong mode couplings which are closely related to microscopic polymer properties [4,5]. Here, we demonstrate that the low-noise GI POF can significantly increase fiber alignment tolerance for error-free data transmission without optical isolators and/or angled fiber facets to improve the worst-case bit error rate (BER) in multimode fiber (MMF) link based on a multimode vertical cavity surface emitting laser (VCSEL). This allows for low-cost optical modules for consumer applications in the upcoming 4K/8K era.

2. Experimental

Figure 1 (a) shows experimental setup composed of 1-m multimode fiber (MMF), a 12 GHz GaAs photodiode (PD) with TIA, and a 14Gb/s 850-nm multimode VCSEL whose LIV characteristics are shown in Fig. 1 (b). The output beam from the VCSEL was focused on a fiber input face. The output beam from a fiber was

collimated and focused on the PD. All the coupling lenses were antireflection-coated. These allowed for evaluation of transmission qualities with little coupling loss and little modal noise, as confirmed in the insets of Fig. 1 (a).
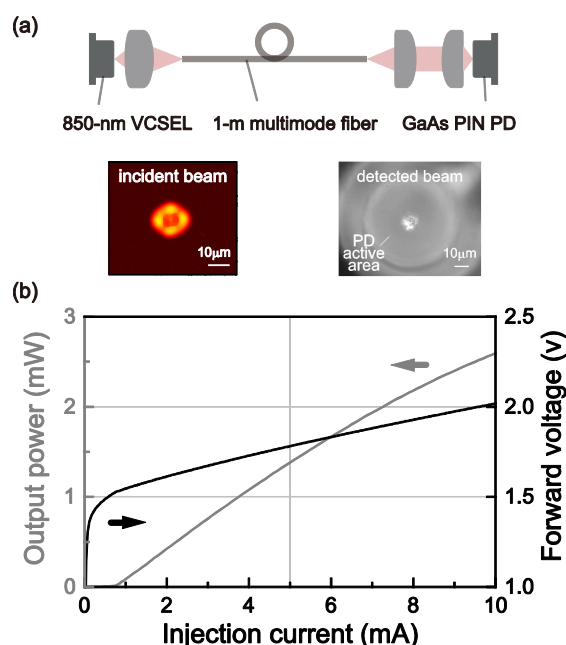

Figure 1. (a) Experimental setup. The insets show incident beam pattern on a fiber input face and irradiated beam pattern on the PD. The injection current was 5 mA. (b) LIV characteristics of the 850-nm multimode vertical cavity surface emitting laser (VCSEL).

Table 1. Properties of evaluated fibers

	GI MMF	GI POF A	GI POF B
Core dia. (μm)	~ 50	~ 50	~ 50
NA	~ 0.2	~ 0.2	~ 0.2
Attenuation (dB/m)	2.3×10^{-3}	6.0×10^{-2}	2.4×10^{-1}
Intrinsic mode coupling	little	weak	strong
Light scattering of core material	Rayleigh scattering	Forward scattering	Forward scattering

For evaluation of the MMF link, the VCSEL was directly modulated at a bit rate of 10 Gb/s with an NRZ data (2^{31}-1 PRBS pattern length). We measured bit error rates (BERs) of transmitted data through 1-m fibers shown in Tab. 1. In this extremely short link without optical isolators for consumer applications, transmission qualities are limited by noise and modulation instability rather than fiber bandwidth and attenuation, which are sufficiently high and low for a fiber length of 1 m, respectively. Actually, the MMF links with all the evaluated fibers have almost the same frequency responses which are dominantly determined by those of the VCSEL and the PD. The dominant noise mechanism may be external optical feedback from the fiber output faces and the PD. Note that optical feedback from the fiber input face barely influences on the VCSEL stability because the corresponding external cavity mode spacing of ~ 15 GHz is much higher than the VCSEL

relaxation frequency of ~ 9 GHz at a bias current of 5 mA [6-8]. In this study, we evaluated the worst-case BER by precisely aligning the VCSEL, the fiber, and the PD in the MMF link.

Table 1 shows properties of evaluated fibers, whose GI profiles are optimized for a wavelength of 850 nm. The low-noise GI POFs have intrinsic mode coupling which is closely related to microscopic heterogeneous structure with much larger-scale density fluctuation in core polymers than silica glasses [9-10]. The microscopic heterogeneities in GI POF core result in random mode coupling through Rayleigh-Debye's forward scattering. The resultant coupling strength depends on correlation length and mean square of the dielectric constant fluctuation. In this study, we prepared low-noise GI POF A and B with the different microscopic properties or different coupling strengths. Note that scattering loss due to the intrinsic mode coupling can be sufficiently lowered in the extremely short link for consumer applications.

3. Results and discussion

Figure 2 shows dependence of BERs on launching condition which was changed by moving the position of the core center on the input end-face in the vicinity of the focal position of the coupling lens. The VCSEL modulation voltage was 0.1 V. For all the fibers, measured BER became higher for closer fiber axes to the optical axis of the incident light which result in higher self-coupling efficiencies of backreflected lights through the fibers into the VCSEL. For the silica GI MMF, transmission quality was significantly degraded by the optical feedback-induced instability and the resulting BER strongly depended on launching position, being more pronounced in the vicinity of the focal position where the worst-case BER was ~ 10^{-4}. This indicates that the precise fiber alignment is required to achieve error-free data transmission for the silica GI MMF. However, alignment tolerance for error-free data transmission and the worst-case BER could be significantly improved just by using the low-noise GI POFs, where the reflected beam pattern was greatly changed from the VCSEL modes with weak dependence on launching condition, even for the lowest modulation voltage of 0.1 V which is comparable to 4-level pulse amplitude modulation. This effect was more pronounced by using the GI POF B with stronger mode coupling than GI POF A. These results show that mode coupling of the low-noise GI POF results in highly-stable data transmission without dependence on launching condition, allowing for optical modules without optical isolators, angled fiber facets, and precise alignment or machining accuracy for the consumer applications.
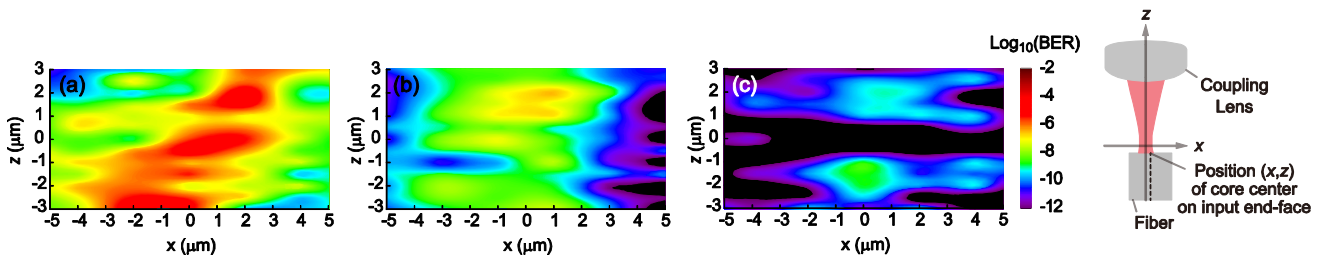

Figure 2. Launching-position dependence of BERs for (a) the silica GI MMF (little mode coupling), (b) the GI POF B (weak mode coupling) and (b) the GI POF C (strong mode coupling) with same core diameters of ~ 50 μm and NAs of ~ 0.2. BER was measured by using the 1-m MMF link with modulated 850-nm VCSEL at 10 Gb/s with an NRZ data. Black regions correspond to error-free data transmission with BERs below 10^{-12}.

4. Conclusion

In conclusion, we demonstrate that the GI POF can significantly increase fiber alignment tolerance for error-free data transmission without optical isolators and/or angled fiber faces in a launching optical system or an optical module. This significant stabilization is attributed to decrease of instabilities due to external optical feedback through strong mode coupling which is closely related to microscopic heterogeneities in the core materials. Moreover, it was suggested that this stabilization effect can be controlled by material properties of correlation length and mean square of dielectric constant fluctuation of the core polymers. The low-cost GI POFs are paving the way for low-cost optical modules for consumer applications in the 4K/8K era.

5. Acknowledgements

6. References

[1] Y. Koike, *Fundamentals of plastic optical fibers*, Wiley (2015).

[2] Y. Koike and A. Inoue, "High-speed graded-index plastic optical fibers and their simple interconnects for 4K/8K video transmission," J. Lightwave Technol., **34**, 1551 (2016).

[3] A. Inoue, R. Furukawa, M. Matsuura, and Y. Koike, "Reflection noise reduction effect of graded-index plastic optical fiber in multimode fiber link," Opt. Lett., **39**, 3662 (2014).

[4] A. Inoue, T. Sassa, K. Makino, A. Kondo, and Y. Koike, "Intrinsic Transmission Bandwidths of Graded-Index Plastic Optical Fiber," Opt. Lett., **37**, 2583 (2012).

[5] A. Inoue, T. Sassa, R. Furukawa, K. Makino, A. Kondo, and Y. Koike, "Efficient group delay averaging in graded-index plastic optical fiber with microscopic heterogeneous core," Opt. Express, **21**, 17379 (2013).

[6] K. Petermann, *Laser diode modulation and noise*, Kluwer (1991).

[7] G. P. Agrawal and N. K. Dutta, *Semiconductor Lasers*, van Nostrand Reinhold (1993).

[8] J. Ohtsubo, *Semiconductor lasers: stability, instability and chaos*, Springer (2012).

[9] P. Debye and A. M. Bueche, "Scattering by an Inhomogeneous Solid," J. Appl. Phys., **20**, 518 (1949).

[10]   Y. Koike, N. Tanio, and Y. Ohtsuka, "Light scattering and heterogeneities in low-loss poly (methyl methacrylate) glasses," Macromolecules, **22**, 1367 (1989).

[11]   Y. Koike, S. Matsuoka, and H. E. Bair, "Origin of excess light scattering in poly (methyl methacrylate) glasses," Macromolecules, **25**, 4807 (1992).

Encircled Angular Flux (EAF): A proposed reproducible representation method for MMFs and its application to POF system characteristics

M. Kagami[1,2*], A.Kawasaki[1], T. Yamashita[1], M. Ogawa[1]

1: Toyota Central R&D Labs., 41-1 Yokomichi, Nagakute, 480-1192, Japan,
2: Toyota Technological Institute, 2-12-1 Hisakata, Tempaku, Nagoya, 468-8511, Japan
*Corresponding author: kagami@mosk.tytlabs.co.jp

Abstract: To realize a stable data transmission along MMF even in complex wiring harnesses like an in-vehicle network, management of transmitted optical modal power distribution (MPD) is very important. We measured MPD variance over a POF transmission system including an in-line connector and/or tight fiber bend in terms of Encircled Angular Flux (EAF). Since EAF is a very useful index for understanding MPD power flow, we implemented EAF in an optical communication simulator as an interface specification. As a result, we confirmed that signal waveform prediction is possible, as is total MPD management from Tx to Rx over the POF system.

1. Introduction

Large-core multimode optical fiber (MMF) has been promising in very short reach communication systems in terms of cost and connector tolerance. In automotive area, in-vehicle optical Ethernet standard[1] using a SI-POF has published this year. However, modal power distribution (MPD) management is very important in such systems for maintaining system performance. For this purpose, we previously proposed[2] the concept of total MPD management, which observes the MPD behaviour from Tx to Rx over an MMF system. Changes of MPD in MMF can be caused not only by propagation length but also bends and connector insertions. To quantify MPD transformation, we have previously developed a reproducible representation method, named Encircled Angular Flux (EAF)[2], and standardized it in IEC[3].

1.1 EAF definitions

EAF expresses power flow in terms of MPD and is defined by the encircled flux (EF[4]) on an FFP screen. By linking this EF with the radiation angle θ from the MMF, the obtained EAF(θ) curve shows the relative optical power flow within a radiated cone angle of θ, as shown in Figure 1 and eq. (1).
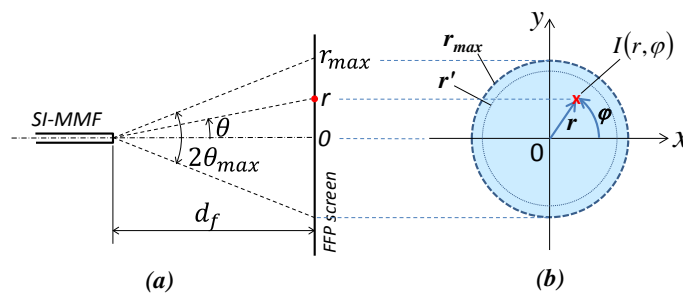

Figure 1 Coordinate system for FFP measurements, (a) Measurement parameters in the meridional plane including the measurement point r and the optical fiber axis. The maximum angle of radiation from the SI-MMF is 2θ_max. Note that, θ is not a projection angle but an angle in the meridional plane, (b) polar coordinate system (r,φ) on the FFP screen.

$$EAF(\theta') = \frac{\int_0^{2\pi} \int_0^{\theta'} I(\theta, \varphi) \cdot \frac{sin(\theta)}{cos^3(\theta)} \cdot d\theta d\varphi}{\int_0^{2\pi} \int_0^{\theta_{max}} I(\theta, \varphi) \cdot \frac{sin(\theta)}{cos^3(\theta)} \cdot d\theta d\varphi} \qquad (1)$$

1.2 EAF propagation along POF

Flat polished SI-POFs (Mitsubishi) with lengths from 1 to 300 m were prepared and the EAF measured at wavelengths of 659 nm, as shown in Figure 2. From the various experiments, we found the EAF curve at 300m is the SI-POF's intrinsic EMD for the wavelength.
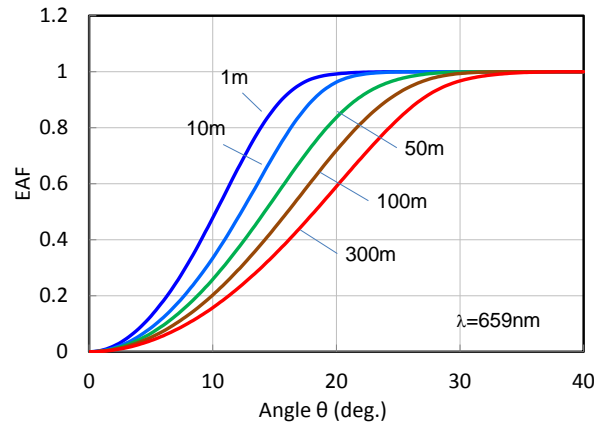

Figure 2. EAF of various lengths of SI-POF for restricted mode launching condition.

1.3 EAF transformation at an in-line connector

Figure 3 shows example EAF curve shifts caused by inserting an in-line optical connector for an angular misalignment of θax and a constant 3 mm of end-to-end separation into plastic optical fiber (POF). As shown, a degree of modal power flow transfers to higher order groups at this misalignment connection in quantity. Similar experiments for hard polymer cladding fiber (HPCF) are demonstrated in previous paper. [5]
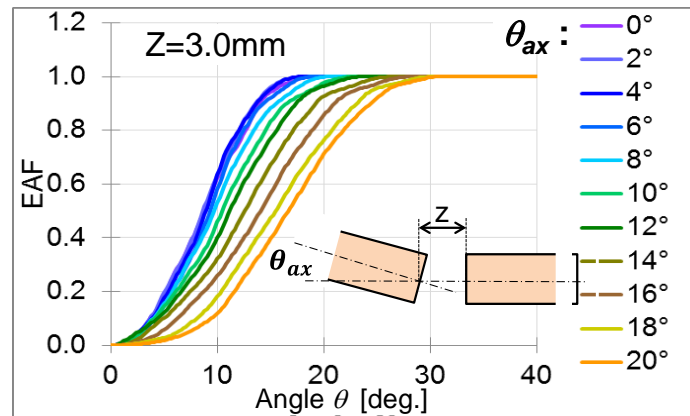
Figure 3. EAF shifts after passing the angularly misaligned in-line connection.

1.4 EAF implementation to an optical communication system simulator

We implemented EAF based on total MPD management in a commercial optical communication system simulator. Under the 16-PAM and restricted modal launch (RML) condition, for example, 1 Gbps data transmission can be achieved by employing the SI-POF-MMF with core radius 980 μm, NA 0.50, length 15 m and an in-line connecter with large misalignment, as shown in Figure 4.

Figure 4. 16-PAM simulation results in a case of axis misalignment (z=1 mm and x=0.2mm). SI-POF and red LED (λ=659nm) are used for this simulation.
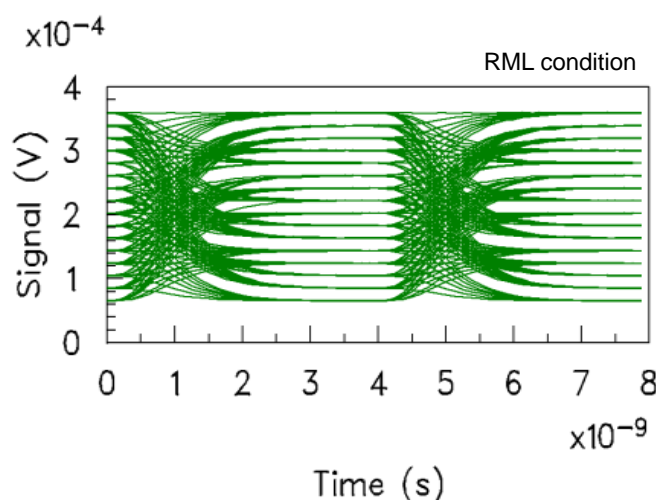
2. Conclusion

In this paper, we studied the change of EAF in a POF system including an axis and/or angular misalignment occurring at an in-line connector based on EAF. We are in great hopes that the concept of total MPD management based on EAF enables accurate performance prediction that considers the complex optical propagation peculiar to MMF.

3. Acknowledgements

4. References

1) IEEE Std 802.3bv™-2017, "Amendment 9: Physical Layer Specifications and Management Parameters for 1000 Mb/s Operation Over Plastic Optical Fiber"
2) M. Kagami, et al., "Encircled angular flux representation of the modal power distribution and its behavior in a step index multimode fiber" J. Lightwave Technol., vol. 34, no. 3, pp. 943-951, 2016.
3) IEC 61300-3-53, 1st ed., Feb. 2015. Examinations and measurements – Encircled angular flux (EAF) measurement method based on two–dimensional far field data from step index multimode waveguide (including fibre).
4) P. Pepeljugoski, M. J. Hackert, J. S. Abbott, S. E. Swanson, S. E. Golowich, A. J. Ritger, P. Kolesar, Y. C. Chen, and P. Pleunis, "Development of system specification for laser-optimized 50 µm multimode fiber for multigigabit short-wavelength LANs," J. Lightw. Technol., vol. 21, no. 5, pp. 1256-1275, 2003.
5) S. Kobayashi and O. Sugihara, "Launch light dependency of step-index multimode fiber connections analyzed by modal power distribution using encircled angular flux," Appl. Opt., vol. 54, no. 4, pp.876-883, 2017.

Detection of 5-mm-long heated section in plastic optical fiber using slope-assisted BOCDR

H. Lee[*], Y. Mizuno, and K. Nakamura

Institute of Innovative Research, Tokyo Institute of Technology,

4259, Nagatsuta-cho, Midori-ku, Yokohama 226-8503, Japan

*Corresponding author: hylee@sonic.pi.titech.ac.jp

Abstract: Slope-assisted (SA-) Brillouin optical correlation-domain reflectometry (BOCDR) is known as a single-end-access distributed Brillouin sensing technique with high spatial resolution, high-speed operation, and cost efficiency. Using SA-BOCDR, we have already demonstrated the detection of a 100-mm-long heated section along a plastic optical fiber (POF). In the meantime, a so-called "beyond-nominal-resolution" effect of SA-BOCDR has been recently discovered, but its details have not been clarified yet. In this work, we experimentally investigate this effect, and using this effect we demonstrate the detection of a 5-mm-long heated section along a POF in a distributed manner.

1. Introduction

Optical fiber sensing based on Brillouin scattering [1] is a promising technique for structural health monitoring due to its distributed measurement capability of strain and temperature change. Hence, many types of Brillouin-based measurement schemes have been developed. They include Brillouin optical time-domain reflectometry (BOTDR) [2]–[5], Brillouin optical frequency-domain reflectometry (BOFDR) [6], Brillouin optical correlation-domain reflectometry (BOCDR) [7]–[10], Brillouin optical time-domain analysis (BOTDA) [11]–[15], Brillouin optical frequency-domain analysis (BOFDA) [16]–[18], and Brillouin optical correlation-domain analysis (BOCDA) [19]–[23]. While each scheme has its own merit and demerit, BOCDR is the only technique that has high spatial resolution and cost efficiency and operates by single-end light injection.

A variety of BOCDR configurations have been implemented to improve the performance [24]–[27] since the first development of its original configuration in 2008 [7]. As for the operating speed, the sampling rate of BOCDR had been limited to approximately 20 Hz [8], resulting in the difficulty in real-time distributed measurement. In 2016, however, we developed two high-speed configurations of BOCDR: phase-detected (PD-) BOCDR [28] and slope-assisted (SA-) BOCDR [29]. In PD-BOCDR, the Brillouin gain spectrum (BGS) is converted to time-domain signal, and it is approximated by a sinusoidal waveform, the phase delay of which is directly obtained. With this technique, a 100-kHz sampling rate was achieved, and real-time distributed strain sensing was demonstrated. However, the limited strain dynamic range was a major problem, though some efforts to mitigate this limitation have been performed [30]. Thus, here we focus on SA-BOCDR.

In SA-BOCDR, the spectral power of the BGS is used to obtain the Brillouin frequency shift (BFS) by exploiting their one-to-one correspondence. The basic operations of SA-BOCDR have been demonstrated using not only silica glass optical fibers [29] but also plastic optical fibers (POFs) [31]. In the case of POFs, the detection of a 100-mm-long heat section was demonstrated [32]. Recently, the relationship between the final system output (i.e., power-change distribution) and the actual BFS distribution has been investigated [33]. In addition, it has been proved that, even when the strained (or heated) section is shorter than the nominal spatial resolution, some shift in the power change can be observed [33]. Although this "beyond-nominal-resolution" effect unique to SA-BOCDR is potentially useful for practical applications, no detailed characterization has not been performed yet.

In this work, first, we experimentally characterize the beyond-nominal-resolution effect of SA-BOCDR using a silica single-mode fiber (SMF). We find that a hot spot up to 50 times shorter than the nominal spatial resolution can be detected. Then, using this effect, we demonstrate the detection of a 5-mm-long heated section along a POF. This value is the shortest ever, 20 times shorter than the previous record.

2. Experimental setup

Figure 1 depicts the experimental setup of SA-BOCDR used in this experiment, which is basically the same as that of the previous report [29]. First, to characterize the beyond-nominal-resolution effect, we employed a
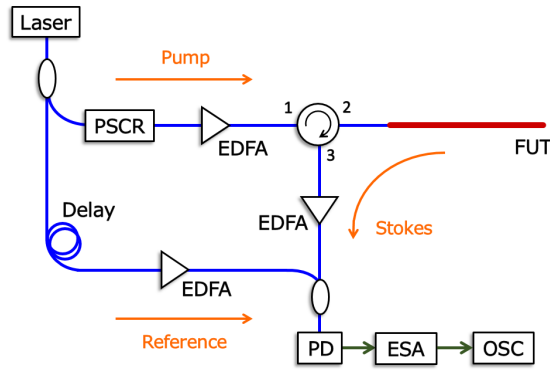
Fig. 1. Experimental setup for SA-BOCDR. EDFA: erbium-doped fiber amplifier, ESA: electrical spectrum analyzer, FUT: fiber under test, OSC: oscilloscope, PD: photo diode, PSCR: polarization scrambler.
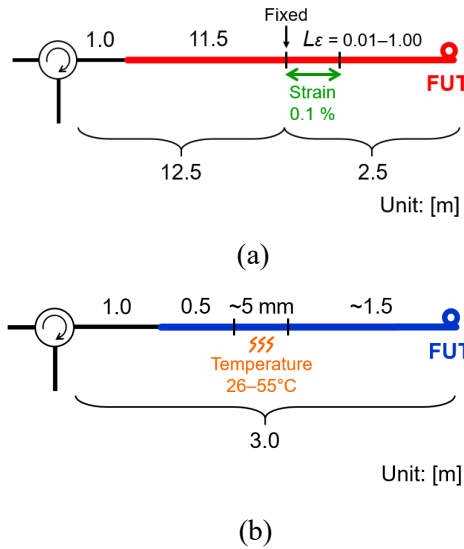

Fig. 2. (a) Structure of a silica SMF under test. The length of the strained section L_ε was set to 0.01, 0.02, 0.05, 0.10, 0.20, 0.50, and 1.00 m. (b) Structure of a POF under test, which was locally heated to 26, 35, 45, and 55°C.

14.0-m-long silica SMF as a fiber under test (FUT). The BFS of the FUT was 10.89 GHz at 1.55 μm at 26°C (room temperature). The open end of the FUT was bent to suppress the Fresnel reflection. The spectral power-change at 10.87 GHz (determined by differentiating the BGS [29]) was monitored using an oscilloscope (OSC). The modulation frequency f_m and the modulation amplitude Δf were set to 5.10–5.26 MHz and 0.19 GHz, respectively, leading to the measurement range of 20.1 m and the nominal spatial resolution of 1.01 m [8]. A strain of 0.1% was applied to 0.01-, 0.02-, 0.05-, 0.10-, 0.20-, 0.50-, and 1.00-m-long sections of the FUT, as shown

(a)

(b)
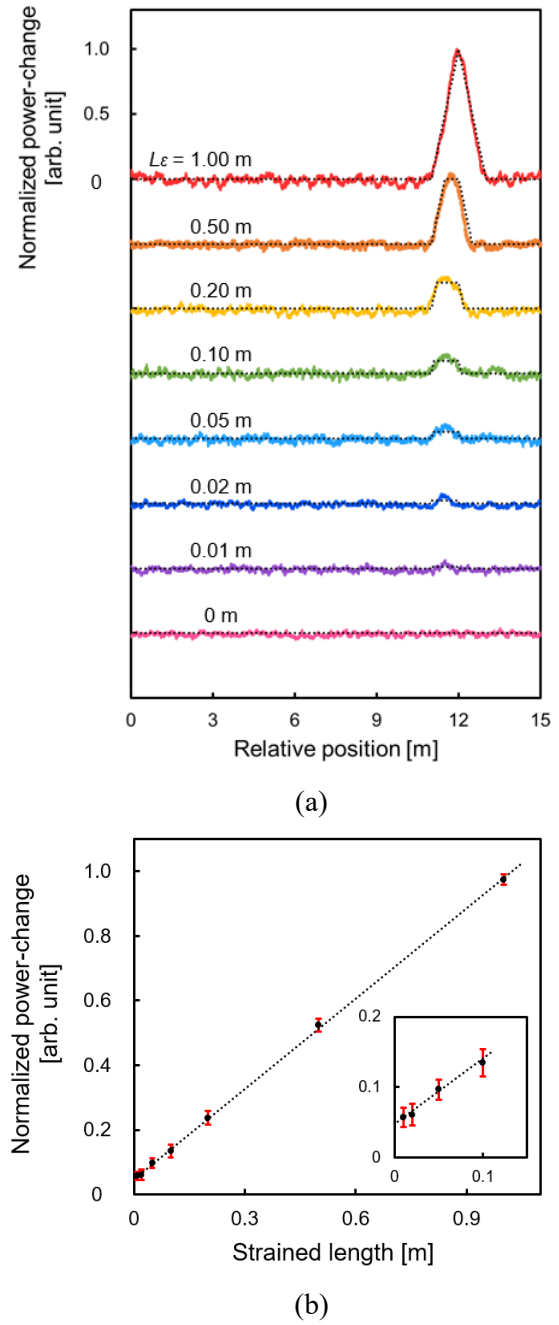
Fig. 3. (a) Normalized power-change distributions measured when the length of the strained section L_ε was reduced from 1.00 m to 0.01 m; each distribution was shifted by 0.5. Dotted lines indicate the theoretical trends. (b) Maximal power-changes plotted as a function of L_ε. The error bars are calculated as standard deviations of the signal fluctuations at non-strained sections. The dotted line is a linear fit. The inset shows the magnified view at L_ε shorter than 0.1 m.

in Fig. 2(a). When the length of the strained section was changed, the position of its proximal end was fixed. The repetition rate was 100 Hz, and averaging was performed 1024 times on the OSC to obtain a higher signal-to-noise ratio.

Subsequently, exploiting the beyond-nominal-resolution effect, we attempted the detection of shortest-ever hot spots using a silica SMF and a POF. Here we describe only the latter result; the former will be presented elsewhere. The POF used in the experiment was a 2.0-m-long perfluorinated graded-index (PFGI-) POF (core diameter: 50 μm; propagation loss at 1.55 μm: 0.25 dB/m; BFS at 1.55 μm: 2.75 GHz). The modulation frequency f_m and amplitude Δf were set to 24.70–24.84 MHz and 0.69 GHz, respectively, corresponding to the measurement range of 4.5 m and the nominal spatial resolution of 0.21 m. As shown in Fig. 2(b), a 5-mm-long section (~1.5 m away from a circulator) of the POF was heated to 35, 45, and 55°C. Note that the length of the heated section was over 40 times shorter than the nominal spatial resolution. The change in the spectral power at 2.78 GHz was monitored. The repetition rate was 100 Hz, and the averaging count was 1024.

3. Experimental results

The power-change distributions measured when the length of the strained section L_ε was reduced from 1.00 m to 0.01 m are shown in Fig. 3(a). Note that the nominal spatial resolution was 1.01 m throughout the measurement. The vertical axis was normalized so that the maximal power-change became 1 when L_ε was 1.00 m. Each distribution was displayed with a vertical interval of 0.5. When L_ε was 1.00 m, the power-change distribution showed a triangular shape, which is natural considering the operating mechanism of SA-BOCDR [29]. As L_ε decreased, the maximal power-change also decreased. When L_ε was 0.02 m, the power-change was still clearly detected, but it became comparable to the signal fluctuations when L_ε was 0.01 m. Thus, in this experimental condition, it was shown to be feasible to detect a strained section at least 50 times shorter than the nominal spatial resolution. Figure 3(b) shows the normalized maximal power-change plotted as a function of L_ε. The error bars were calculated as standard deviations of the signal fluctuations at non-strained sections. The maximal power-change decreased almost linearly with decreasing L_ε, which agrees well with the theory [X]. The relationship between the actual value of L_ε and the observed length of non-zero-power-change section will be discussed somewhere else.

Finally, exploiting the beyond-nominal-resolution effect verified above, we attempted the detection of a 5-mm-long heated section along a POF with a nominal spatial resolution of 0.21 m. Figure 4(a) shows the normalized power-change distributions measured when the section was heated to 26 (room temperature), 35, 45, and 55°C. The local power-changes corresponding the temperature changes were observed at the correct position in the POF. The maximal power-change of each distribution in Fig. 4(a) was plotted as a function of temperature (Fig. 4(b)). With increasing temperature, the maximal power-change also increased almost linearly. Thus, we succeeded in detecting the shortest-ever heated section along the POF. By combining the abovementioned results, we can conclude that, if the nominal spatial resolution of the SA-BOCDR system is
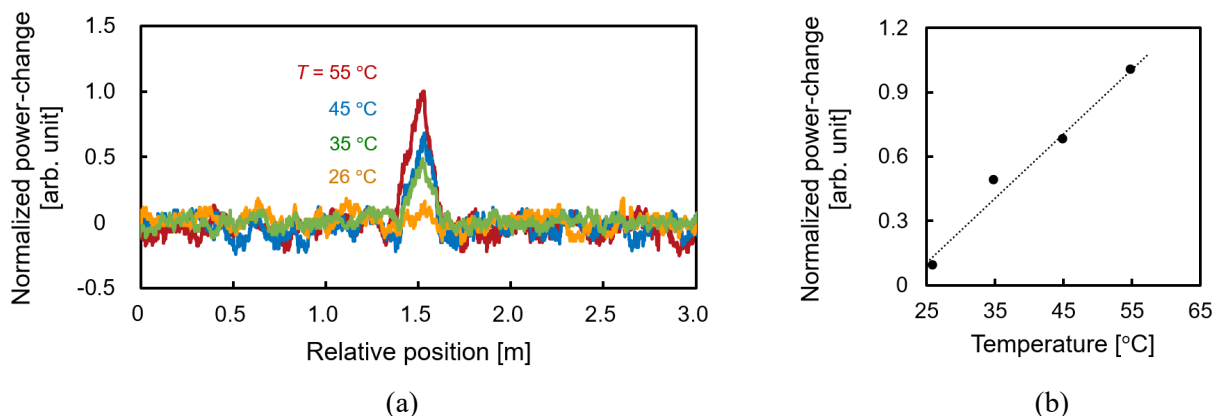

Fig. 4. (a) Normalized power-change distributions along a POF; measured at four temperatures. (b) Maximal power-changes plotted as a function of temperature. The dotted line is a linear fit.

known, the length of the hot spot and the magnitude of strain (or temperature change) can be deduced from the measured power-change distribution, even when the beyond-nominal-resolution effect is exploited.

4. Conclusion

First, we experimentally investigated the "beyond-nominal-resolution effect" of SA-BOCDR using an SMF. When the nominal spatial resolution was kept constant, the measured maximal power-change decreased almost linearly with decreasing length of the strained section. Even when the strained length was 50 times shorter than the nominal spatial resolution, power-change was still clearly observed at a correct position. Subsequently, by exploiting this effect, we demonstrated the detection of a 5-mm-long—shortest ever—hot spot in a POF. The power-change distributions at four temperatures were measured, and the maximal power-changes at each distribution increased almost linearly with increasing temperature. These results indicate that, even when the hot spot is much shorter than the nominal spatial resolution, the length of the hot spot and the magnitude of applied strain (or temperature change) can be calculated from the measured power-change distribution using the nominal resolution. Thus, we anticipate that this paper will greatly enhance the practical applicability of SA-BOCDR by showing its capability of detecting an extremely short hot spot along an optical fiber.

5. References

[1]   G. P. Agrawal, *Nonlinear Fiber Optics* (Academic Press, California, 1995).
[2]   T. Kurashima, T. Horiguchi, H. Izumita, S. Furukawa, and Y. Koyamada, IEICE Trans. Commun. **E76-B**, 382 (1993).
[3]   D. Iida and F. Ito, J. Lightwave Technol. **26**, 417 (2008).
[4]   M. Ohsaki, M. Tateda, T. Omatsu, and H. Ohno, IEICE Trans. Commun. **E85-B**, 1636 (2002).
[5]   N. Nitta, M. Tateda, and T. Omatsu, Opt. Rev. **9**, 49 (2002).
[6]   A. Minardo, R. Bernini, R. Ruiz-Lombera, J. Mirapeix, J. M. Lopez-Higuera, and L. Zeni, Optics Express **24** 29994 (2016).
[7]   Y. Mizuno, W. Zou, Z. He, and K. Hotate, Opt. Express 16, 12148 (2008).
[8]   Y. Mizuno, W. Zou, Z. He, and K. Hotate, J. Lightwave Technol. 28, 3300 (2010).
[9]   N. Hayashi, K. Minakawa, Y. Mizuno, and K. Nakamura, Appl. Phys. Lett. **105**, 091113 (2014).
[10]   N. Hayashi, Y. Mizuno, and K. Nakamura, Opt. Express **20**, 21101 (2012).
[11]   T. Horiguchi and M. Tateda, J. Lightwave Technol. **7**, 1170 (1989).
[12]   A. Minardo, R. Bernini, and L. Zeni, Opt. Express **19**, 19233 (2011).
[13]   Y. Dong, L. Chen, and X. Bao, Opt. Lett. **36**, 277 (2011).
[14]   Y. Peled, A. Motil, I. Kressel, and M. Tur, Opt. Express **21**, 10697 (2013).
[15]   W. Li, X. Bao, Y. Li, and L. Chen, Opt. Express **16**, 21616 (2008).
[16]   D. Garus, T. Gogolla, K. Krebber, and F. Schliep, Opt. Lett. **21**, 1402 (1996).
[17]   R. Bernini, A. Minardo, and L. Zeni, IEEE Photonics J. **4**, 48 (2012).
[18]   A. Minardo, R. Bernini, and L. Zeni, IEEE Photon. Technol. Lett. **26**, 387 (2014).
[19]   K. Hotate and T. Hasegawa, IEIECE Trans. Electron. **E83-C**, 405 (2000).
[20]   W. Zou, C. Jin, and J. Chen, Appl. Phys. Express **5**, 082503 (2012).
[21]   K. Y. Song, M. Kishi, Z. He, and K. Hotate, Opt. Lett. **36**, 2062 (2011).
[22]   C. Zhang, M. Kishi, and K. Hotate, Appl. Phys. Express **8**, 042501 (2015).
[23]   W. Zou, Z. He, and K. Hotate, IEEE Sens. J. **14**, 244 (2013).
[24]   Y. Mizuno, Z. He, and K. Hotate, Opt. Express **18**, 5926 (2010).
[25]   N. Hayashi, Y. Mizuno, and K. Nakamura, IEEE Photon. J. **7**, 6800407 (2015).
[26]   Y. Mizuno, Z. He, and K. Hotate, Opt. Commun. **283**, 2438 (2010).
[27]   N. Hayashi, Y. Mizuno, and K. Nakamura, IEEE Photon. J. **6**, 6803108 (2014).
[28]   Y. Mizuno, N. Hayashi, H. Fukuda, K. Y. Song, and K. Nakamura, Light: Sci. Appl. **5**, e16184 (2016).
[29]   H. Lee, N. Hayashi, Y. Mizuno, and K. Nakamura, IEEE Photon. J. **8**, 6802807 (2016).
[30]   Y. Mizuno, N. Hayashi, H. Fukuda, and K. Nakamura, Jpn. J. Appl. Phys. **56**, 072501 (2017).
[31]   H. Lee, N. Hayashi, Y. Mizuno, and K. Nakamura, J. Lightwave Technol. **35**, 2306 (2017).
[32]   N. Hayashi, Y. Mizuno, and K. Nakamura, J. Lightwave Technol. **32**, 3999 (2014).
[33]   H. Lee, N. Hayashi, Y. Mizuno, and K. Nakamura, Opt. Express **24**, 29190 (2016).

Significant Improvement of durability for Repeated Plugging in and out By Ballpoint-pen Interconnect of Graded-index Plastic Optical Fiber

Y. Kaseda[1*], A. Inoue[1], A. Mitsui[2], H. Suzuki[2] and Y. Koike[1]

1 Graduate School of Science and Technology, Keio University, 3-14-1 Hiyoshi, Kohoku-ku, Yokohama, Kanagawa 223-0061, Japan.

2 Mitsubishi Pencil, 2-5-12 Irie, Kanagawa-ku, Yokohama, Kanagawa 221-8550, Japan

*Corresponding author: yugo.kaseda@gmail.com

Abstract:

We investigate influence of repeated plugging in and out processes on data transmission quality through ballpoint-pen interconnect where ball lens can be precisely mounted on graded-index plastic optical fiber (GI POF) end-face using ballpoint-pen production technology. By using the ballpoint-pen interconnect, data transmission quality is barely degraded with repeated plugging in and out, resulting in its better transmission after 2500 cycles of plugging in and out without any cleanings than butt-coupling. This is because coupling loss increment due to dusts and scratches caused by plugging in and out are suppressed owing to protected GI POF end-face from dusts and scratches by ball lens and increased ratio of dusts and scratches to beam width.

1. Introduction

A graded-index plastic optical fiber (GI POF) with a high bandwidth and flexibility is expected to be a transmission medium for short-reach communication [1, 2]. Moreover, GI POF has noise reduction effects which are closely related to the strong mode coupling [3]. These allow for high-speed data transmission in home networks without an optical isolator. For consumers, the pluggable interconnects have been demanded. Conventional butt-coupling has problem of the deterioration of data transmission quality by frequent plugging in and out owing to the coupling loss increments which are caused by some dusts and scratches. This suggests that the butt-coupling is not suitable for consumer applications because of requirement for cleanings and careful handling of fiber end-faces. For pluggable interconnects of GI POFs, we have developed ballpoint-pen interconnects where ball lens can be precisely mounted on GI POF end-face using ballpoint-pen production technology [4, 5]. The ballpoint-pen connector significantly can increase the misalignment tolerance for connection of GI POFs because of the expanded and collimated output beam [6, 7]. Furthermore, this connector can protect GI POF end-faces from dusts and scratches with ball lenses and enables large ratio of dusts and scratches to beam width, resulting in decreasing the degradation of coupling losses. Here, we investigated influence of repeated plugging in and out processes on data transmission quality through ballpoint-pen interconnect of the GI POFs in a multimode fiber link.

2. Data transmission through the ballpoint-pen interconnect

2.1 Experiment

Figure 1 shows the ballpoint-pen interconnect whose production is based on the simple and low-cost ballpoint-pen technology. This ballpoint-pen connector significantly increases tolerance for misalignments of the GI POF axes, resulting from the expanded and collimated output beam. The ball lens in the ballpoint-pen connector has a refractive index of 1.51, a diameter of 550 μm, and an effective focal length of 407 μm. The core diameter and the numerical aperture (NA) of the GI POF were 80 μm and 0.25, respectively.
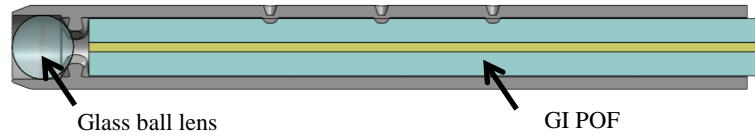
Fig. 1 Schematic structure of ballpoint-pen interconnect.

As shown in Fig. 2, we measured BERs versus plugging in and out cycles for coupled 1-m GI POFs with ballpoint-pen interconnect. As a reference, conventional butt-coupling of GI POFs was also evaluated. A bias current and a modulation voltage were 5 mA and 0.1 V, respectively. The transmission experiments were performed using a 10 Gbps non-return to zero data pattern with a 2^{31}-1 pseudorandom binary sequence. An 850-nm vertical cavity surface emitting laser (VCSEL) was directly modulated. The output beam from the GI POF was received by the photo diode (PD), as shown in Fig. 2.
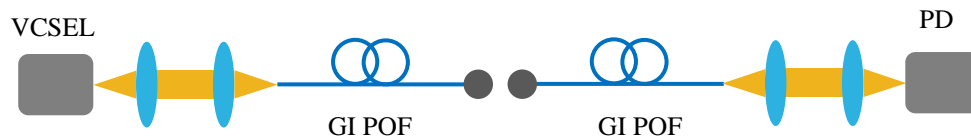

Fig. 2 Experimental setup for measuring BERs versus plugging in and out cycles for coupled 1-m GI POFs.

2.2 Influence of repeated plugging in and out processes on transmission quality

Figure 3 (a) shows BERs as a function of the plugging in and out cycles of GI POFs coupled with the ballpoint-pen interconnect and the butt-coupling in optical links. When one plugging in and out process increases coupling loss over 6 dB, some dusts on the GI POF end-faces were removed by cleaner. For the butt-coupling, BERs changed and gradually degraded owing to repeated plugging in and out. However, by using the ballpoint-pen interconnect, data transmission quality was barely degraded with repeated plugging in and out. This resulted in its better transmission after 2500 cycles without cleanings than butt-coupling whereas the BERs for ballpoint-pen coupling were worse than butt-coupling because of Fresnel losses at the beginning of the cycles.
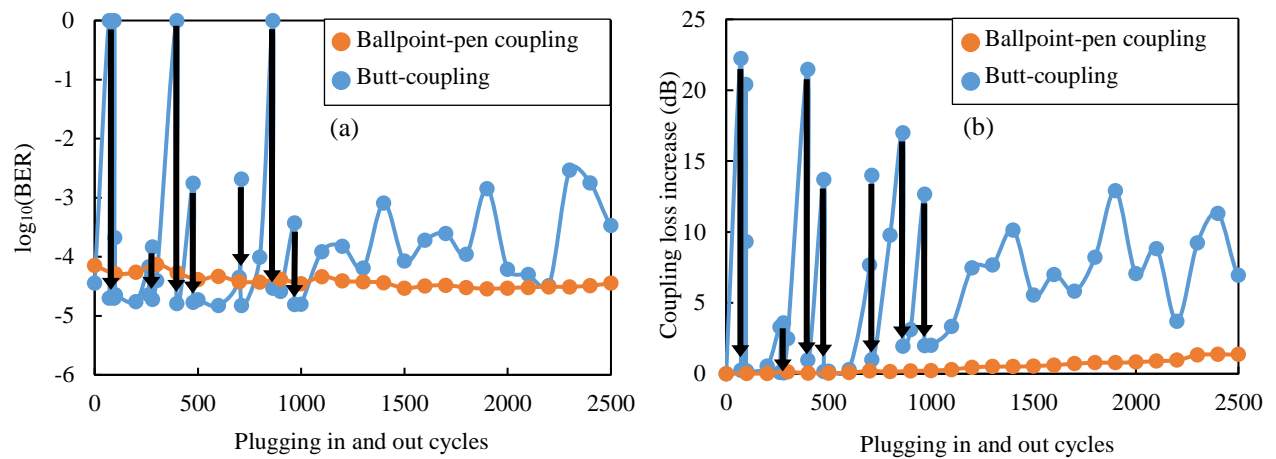
Fig. 3 (a) BERs and (b) coupling loss increase for the butt-coupling and the ballpoint-pen interconnect of connected 1-m GI POFs as a function of the plugging in and out cycles. The black arrows correspond to cleanings the connectors.

We also evaluated the coupling losses as a function of plugging in and out cycles for the ballpoint-pen interconnect and conventional butt-coupling, as shown in Fig. 3 (b). For the butt-coupling, coupling losses changed and increased as plugging in and out cycles increased. Figure 4 (a), (b), and (c) show microscopic images of fiber end-faces in butt-coupling before plugging in and out cycles, after 2500 cycles without cleanings and after 2500 cycles with cleanings, respectively. These suggest that repeated plugging in and out processes resulted in not only dust but also scratch increase on fiber end-face. The coupling losses caused by scratches cannot be decreased without repolishing fiber end-faces. The change and increment of coupling losses due to repeated plugging in and out in butt-coupling may be attributed to the increase of scratches and dusts on fiber end-faces, as shown in Fig. 4 (a)-4 (c). However, by using the ballpoint-pen interconnect, the coupling loss increment due to plugging in and out were significantly decreased. Moreover, the coupling loss increase was only 1.37 dB at 2500 plugging in and out cycles without cleanings in the ballpoint-pen interconnect. As shown in Fig. 4 (d), (e), and (f), microscopic images of the glass lens in ballpoint-pen connector before plugging in and out cycles, 2500 cycles without cleanings and 2500 cycles with cleanings, respectively. As shown in Fig. 4 (f), there is no dust and scratch on the glass ball lens after 2500 cycles with cleanings. In the ballpoint-pen interconnect, the coupling loss increment suppression with the increase in plugging in and out cycles than butt-coupling may result from no scratch and decreased dusts because of non-physical contact interconnect, as shown in Fig. 4 (d)-4 (f). Moreover, ratio of dusts to beam width of the output beam from GI POF is significantly larger by using ballpoint-pen interconnect than butt-coupling, resulting in its lower influence of plugging in and out on the coupling loss increment.
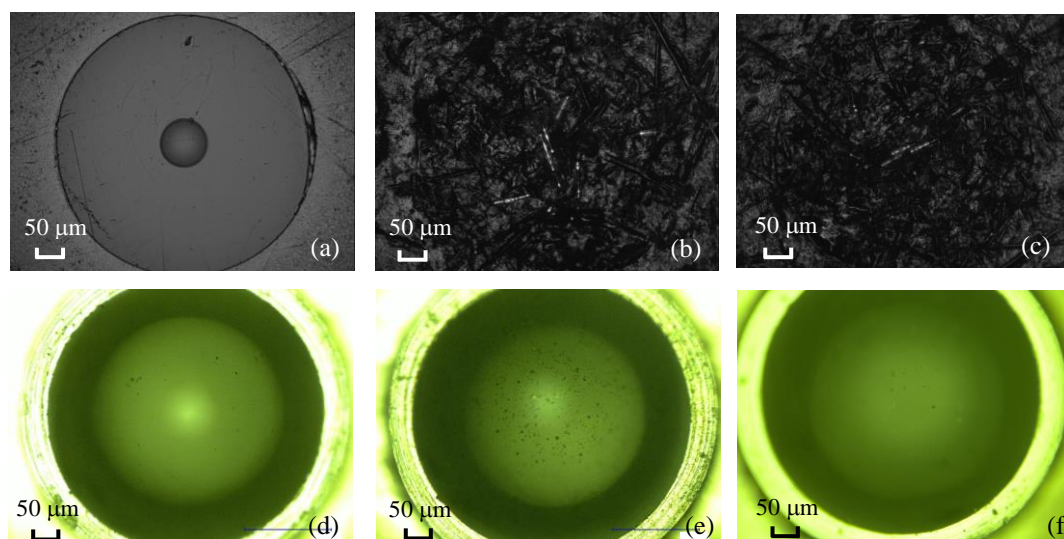
Fig. 4 Microscopic images of fiber end-faces in butt-coupling (top) and glass ball lens in ballpoint-pen interconnect (bottom). (a) and (d) before plugging in and out. (b) and (e) after 2500 plugging in and out cycles without cleanings. (c) and (f) after 2500 plugging in and out cycles with cleanings.

3. Conclusion

We investigated influence of repeated plugging in and out processes on data transmission quality through ballpoint-pen interconnect where ball lens can be precisely mounted on GI POF end-face using ballpoint-pen production technology. By using the ballpoint-pen interconnect, data transmission quality was barely degraded with repeated plugging in and out, resulting in its better transmission after 2500 cycles without cleanings than butt-coupling. This was because coupling loss increment due to dusts and scratches caused by plugging in and out were suppressed owing to protected GI POF end-face from dusts and scratches by ball lens and increased ratio of dusts and scratches to beam width. These results show that ballpoint-pen interconnect is much more suitable than conventional butt-coupling for consumer applications where pluggable interconnects are essential.

References

[1] Y. Koike, Fundamentals of plastic optical fibers, Wiley, New York, 2015.

[2] I. Mollers, D. Jager, R. Gaudino, A. Nocivelli, H. Kragl, O.Ziemann, N. Weber, T. Koonen, C. Lezzi, A. Bluschke, and S. Randel, "Plastic optical fiber technology for reliable home networking: overview and results of the EU project POF-ALL," *IEEE Commun. Mag.*, Vol. 47, no. 8, pp. 58-68, 2009.

[3] A. Inoue, R. Furukawa, M. Matsuura, and Y. Koike, "Reflection noise reduction effect of graded-index plastic optical fiber in multimode fiber link," *Opt. Lett.*, Vol. 39, no. 12, pp. 3662-3665, 2014.

[4] T. Toma, H. Takizuka, T. Torikai, H. Suzuki, T. Ogi, and Y. Koike, "Development of household high-definition video transmission system based on ballpoint-pen technology," *Synthesiology*, Vol. 7, no. 2, pp. 118-128, 2014.

[5] Y. Koike and A. Inoue, "High-speed graded-index plastic optical fibers and their interconnects for 4K/8K video transmission," *J. Lightw. Technol.*, Vol. 34, no. 6, pp. 1551-1555, 2016.

[6] A. Nicia, "Practical low-loss lens connector for optical fibres," *Electron. Lett.*, Vol. 14, no. 16, pp. 511-512, 1978.

[7] M. Hughes, D. Childers, J. Graham, "Next-generation high-density low-cost multimode optical interconnect," Proc. SPIE, Vol. 8267, Optoelectronic Interconnects XII, 2012.

The Noise Reduction Effect of Graded-index Plastic Optical Fiber

Based on Acrylic Polymer

T. Omuro[1*], A. Inoue[1], Y. Koike[1]

1 Graduate school of Science and Technology, Keio University, 7-1 Shinkawasaki, Saiwai-ku, Kawasaki 212-0032, Japan

*Corresponding author: takaya-omuro@keio.jp

Abstract: We investigate characteristics of graded-index plastic optical fiber (GI POF) based on a partially fluorinated acrylic polymer. This suggests that the GI POF would significantly reduce reflection noise. By evaluating the angle dependence of scattering intensity for the polymer bulk, we show that the polymer has intrinsically directional forward scattering because of the microscopic heterogeneities. The noise reduction is closely related to the intrinsic scattering because of the microscopic heterogeneities. The low-noise GI POF improves transmission quality in spite of the partial detection with photodetector that increases loss and noise. The GI POF based on the partially fluorinated acrylic polymer could be candidate for multilevel transmission with higher signal-to-noise ratio.

1. Introduction

The growing demand for increased transmission speed in application such as 4K/8K television motivates the development of optical cables for the high-speed data transmission. Recently, the optical interface cable for 8K display has been proposed, using twenty-four glass multimode fibers (MMFs) [1]. However, the optical cable requires highly precise alignment and connection because of the many number of fibers. To decrease the number of the fibers for transmission media, multilevel modulation scheme has been studied. The multilevel transmission can increase bit rate over 2-level transmission [2], but is subject to noise problems because signal-to-noise ratio (SNR) decreases with an increase in number of levels.

The graded-index plastic optical fiber (GI POF) has been a promising transmission medium for home and building networks because of its flexibility, high bandwidth, and low installation cost [3, 4]. Moreover, we experimentally demonstrated that the GI POF can intrinsically reduce reflection noise in a MMF link with a vertical-cavity surface-emitting laser (VCSEL) [5]. The noise reduction effect results from mode coupling of GI POF. The mode coupling changed the backreflected beam pattern so that it has less influence on VCSEL stability. For lower-noise GI POF, we focused on acrylic polymer as base material which can be easily synthesized at low cost. Moreover, it is likely that the acrylic-polymer-based GI POF has microscopic heterogeneities or large-scale density fluctuation which results in strong mode coupling [6] and thus noise reduction effect. In this report, we investigate the reflection noise reduction effect of the GI POF based on acrylic polymer.

2. Experimental section

We selected the partially fluorinated acrylic polymer as new base material to achieve low attenuation at 850 nm [7] and evaluated its noise reduction effect of the GI POF based on the polymer. Using the partially fluorinated acrylic polymer, we fabricated a GI POF with a core diameter of 400 μm by the rod-in-tube method. The GI POF has an attenuation of 1.3 dB/m at a wavelength of 850 nm, which has potential for further reduction in an attenuation.

Figure 1 shows the experimental setup for evaluation of reflection noise in MMF links. The laser is a multimode VCSEL with an oscillation wavelength of 850 nm. The photodetector is a PD with TIA. The output beam from the VCSEL was collimated and focused on a fiber end-face using an antireflection coated (AR-coated) lens. The output beam from the fiber was collimated and focused on the PD with TIA using an AR-coated lens. Under restricted mode-launching condition, we measured the noise floor spectra of the 2-m MMF links with an unmodulated VCSEL, which was operated at a drive current of 5.0 mA. All the output beam from the GI POF could not be detected with PD because of the larger beam diameter than PD active area,

whereas all the output beam from the glass GI MMF could be detected with PD (Fig. 2). Also, because of the partial detection and higher attenuation of the fiber, the averaged received power of the GI POF was much lower than that of the glass GI MMF (Table 1).
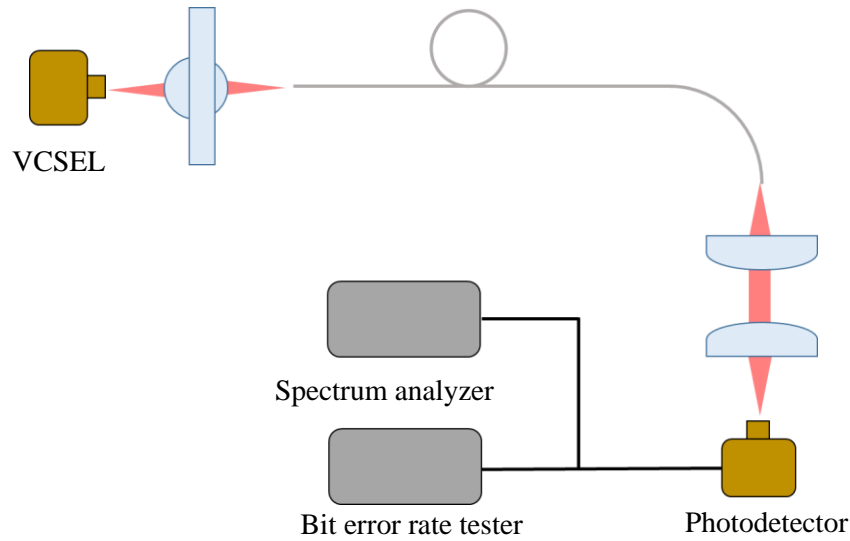

Fig. 1 Schematic diagram of experimental arrangement.
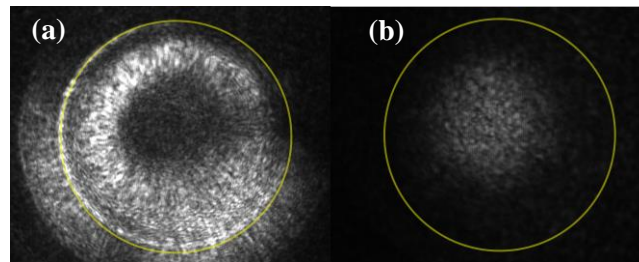

Fig. 2 Microscopic images of the output beam pattern on the PD irradiated for (a) a 2-m GI POF and (b) a 2-m glass GI MMF imaged on the PD. The yellow circle shows active area of the PD.

Table 1 The averaged received power of the GI POF and the glass GI MMF.

	GI POF	Glass GI MMF
Avaraged received power (dBm)	-9.6	-1.5

As shown in Fig. 3, the noise floor spectrum of the acrylic-polymer-based GI POF was lower than that of the glass GI MMF for all the frequencies. The glass GI MMF has peaks with an equal spacing of 50 MHz, which corresponds to the round-trip frequencies of the external cavities with the reflector of the fiber output face and PD [8]. However, using the GI POF, we can significantly reduce the reflection noise corresponding to periodic peaks. The decreasing the noise floor levels of the GI POF for all the frequencies would be caused by the excess loss of the received power and the reflection noise reduction of the GI POF might be related to the characteristics of the polymer.

To investigate the characteristics of the partially fluorinated acrylic polymer, we evaluated the angle dependence of scattering intensity (Fig. 4). It is worth stressing that the polymer has intrinsically directional forward scattering, which may cause strong mode coupling because of the microscopic heterogeneities. For GI POF with strong mode coupling, the backreflected beam patterns have significantly different beam patterns from the glass GI MMF, lowering self-coupling efficiencies into the VCSEL cavity. Thus, the significant

reflection noise reduction is closely related to the intrinsic scattering because of the microscopic heterogeneities.
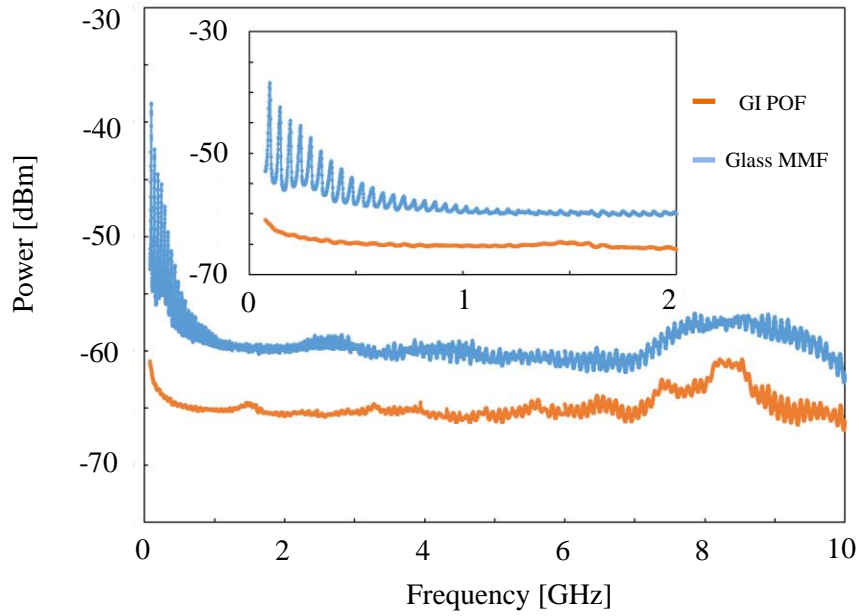

Fig. 3 Noise floor spectra of 2-m GI POF and 2-m glass GI MMF. The VCSEL drive current is 5.0 mA. Insert: enlarged figure for frequencies between 0 GHz and 2 GHz.
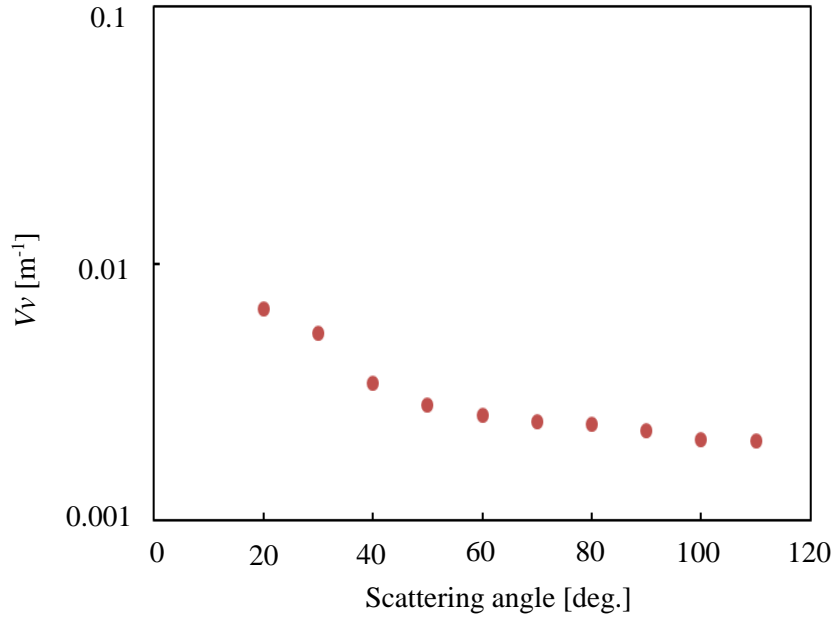
Fig. 4 Angle dependence of scattering intensity for partially fluorinated acrylic polymer.

  We investigated the bit error rate (BER) of the MMF links with modulated VCSEL with a voltage of 0.1 V (peak to peak) and 10 Gb/s NRZ-coded pseudo random bit sequence pattern. The measurement time was ten minutes. As shown in table 2, the BER for the acrylic-polymer-based GI POF was lower than that for the glass GI MMF though all the output beam pattern of the GI POF could not be detected with PD and thus loss and

modal noise were increased [9-11]. Therefore, under the condition that all the beam from the fiber is received by using the GI POF with smaller core diameter, the BER can be further improved. These results suggest that the GI POF can be candidate for multilevel transmission with higher signal-to-noise ratio.

Table 2 BER of the GI POF and the glass GI MMF.

	GI POF	Glass GI MMF
BER	6.2×10^{-10}	4.6×10^{-9}

3. Conclusion

We have experimentally demonstrated that a GI POF based on the partially fluorinated acrylic polymer can significantly reduce the noise level. By evaluating the angle dependence of scattering intensity for the polymer bulk, we show that the polymer has intrinsically directional forward scattering because of the microscopic heterogeneities. The significant noise reduction is closely related to the intrinsic scattering because of the microscopic heterogeneities. These characteristics of the GI POF would allow for the BER improvement though all the output beam from the GI POF could not be detected with PD. These results suggest that the GI POF based on the partially fluorinated acrylic polymer can be candidate for multilevel transmission with higher signal-to-noise ratio.

4. Acknowledgements

5. References

[1] ARIB STD-B58 (1.0), Interface for UHDTV Production System (2014)

[2] Krzysztof Szczerba et al., "30 Gbps 4-PAM transmission over 200 m of MMF using an 850 nm VCSEL," OSA, 19, B203-B208 (2011).

[3] Y. Koike and A. Inoue., "High-speed graded-index plastic optical fibers and their simple interconnects for 4K/8K video transmission," J. Lightwave Technol., 34, 1551-1555 (2016).

[4] Y. Koike., *Fundamentals of plastic optical fibers.*, John Wiley & Sons, (2014).

[5] A. Inoue et al., "Reflection noise reduction effect of graded-index plastic optical fiber in multimode fiber link," Opt. Lett., 39, 3662-3665 (2014).

[6] T. Kashiwazaki and A. Inoue et al., "Correlation between mode coupling and light scattering caused by microscopic heterogeneous structure in graded-index plastic optical fiber," in *Proceedings of the POF 2014*, 147-150 (2014).

[7] Werner Groh., "Overtone absorption in macromolecules for polymer optical fibers," Makromol. Chem., 189, 2861-2874 (1988).

[8] I. Ikushima and M. Maeda., "Self-coupled phenomena of semiconductor lasers caused by an optical fiber," J. Quantum Electron., 14, 331-332 (1978).

[9] B. Daino et al., "Analysis and measurement of modal noise in an optical fibre," Electron. Lett., 15, 755-756(1979).

[10] T. Kanada., "Evaluation of modal noise in multimode fiber-optic systems," J. Lightwava Technol., 2, 11-18 (1984)

[11] K. Petermann., *Laser diode modulation and noise.*, Kluwer Academic Publishers, (1988)

A STUDY ON THE EFFECT OF MISALIGNMENT ON A SYSTEM COMPRISING GI-POF INTERCONNECTED WITH BALLPOINT PEN COLLIMATORS.

Bach T. [2*], Mitsui, A.[2],Koike,Y[1]

1: Keio University, 3-14-1 Hiyoshi, Kohoku-ku, Yokohama-shi, Kanagawa 223-8522 Japan
2: Mitsubishi Pencil, 2-5-12 Irie, Kanagawa-ku, Yokohama, Kanagawa 221-8550, Japan
*Corresponding author: t-bach@mpuni.co.jp

Abstract: It has been verified that ball point pen collimators, have an effect on the modal distribution of light traveling through GI-POF. It is reasoned that the spherical lenses act as low pass filters, preventing higher modes of being reaccepted into the system. A possible explanation for this effect could be spherical aberration due the combination spherical lens diameter and beam size. The positive effects on misalignment responsiveness are investigated and discussed.

1   Introduction

As optical data transmission systems are expanding into areas such as infrastructure, medical care, industrial equipment and many others, a simple, easy and yet reliable optical connection is necessary. The amount of electronic devices around us is increasing exponentially, and so is the amount of data that has to be transmitted. A standardized copper interconnection such as HDMI has the capability of transmitting up to 10.2Gb/s, but as speed requirements keep increasing, copper based interconnects are reaching the practical limit. [1]

Optical fibers and waveguides have become increasingly important, since they can overcome the before mentioned limitations of copper cables. Within optical fibers, GI-POF`s are attracting attention due to the high achievable bandwidth, low bending loss, high flexibility and large core size. [2] It is expected that such fibers will proliferate into applications where plastic fibers are preferred over its glass counterparts.

Harsh applications environments such as those found in consumer electronics and automotive applications require interconnection strategies that account for dust, vibration and misalignment. In large cored GI-POF`s direct fiber-to-fiber interconnects are simple, cheap and present low insertion loss, but due to the softness of plastic fibers this interconnection method is not ideal for application with either vibrations or high mate-demate cycles.

Expanded beam interconnects (EB) are the natural choice for those kind of applications. The larger beam diameter allows for a lower sensitivity to dust and misalignments [3] allowing this interconnection strategy to be used by a wide range of applications. Yet another advantage of EB is the fact that the end faces are not in direct contact, thus eliminating the negative effects of vibration.

Previously, a novel approach to producing EB interconnects using ball point pen technology has been proposed [4]. A spherical lens is fixated in a metallic pipe, and the GI-POF fiber is inserted from the opposite end of the pipe. The distance between fiber and lens is controlled through indentations in the pipe, as can be seen in Figure 1.
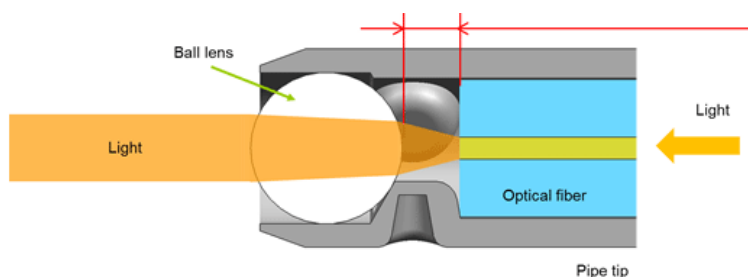

Figure 1 - Schematic of a ball point pen collimator

The combination GI-POF and ball point pen collimator allows for an interconnection strategy that favors the strong points of both technologies, and therefore makes it the perfect choice for demanding applications.

This paper will investigate the changes in modal distribution after a Ball point pen collimators interconnect. Under certain launch conditions it has observed that the modal distribution of light is affected and the change in modes traveling in the fiber is enough to change the sensibility of such system to misalignments.

2   Experimental details
2.1   Mode propagation analysis

A set of GI-POF`s interconnected with ball point pen collimators was assembled such as the schematic shown in Figure 2.
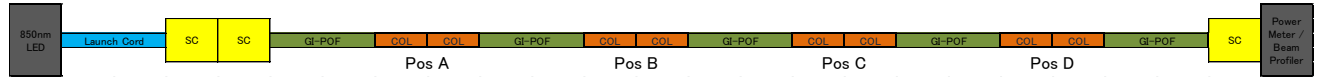

Figure 2 - Experimental set-up schematic

The light source is a 850nm LED source (Graytechnos Co., Ltd. Model 351). Three different kinds of launch conditions have been tested, namely GI-POF with $80\,\mu$ m core diameter, a Mode Scrambler GI50 and a GI50 encircled flux patch cord from Fluke. The respective Near Field Patterns are shown in Figure 3 below.
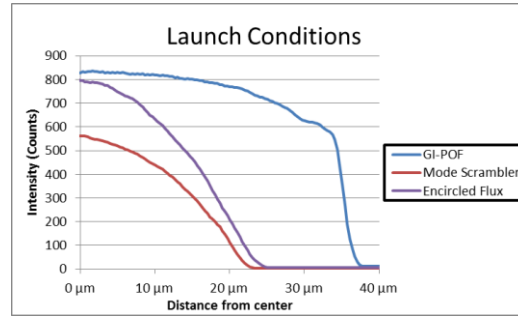

Figure 3 - Modal distribution for each launch condition

The fiber used is Asahi Glass Fontex 80μm with an NA of 0.245, connected with ball point pen collimators equipped with a 0.5mm ball lens. The collimators are aligned using a split sleeve adaptor. The beam profile is measured after each connection point (Position A to D on figure 2) by using a 0.5m cable with a ball point pen collimator on one side and a SC connection on the opposite side.

Studies have shown [5] that the length of the fiber and its NA change the mode coupling behavior of GI-POF. In order to evaluate this effect in this experimental setup, a slightly different setup using only GI-POF and physical connections was used, as depicted in figure 4.
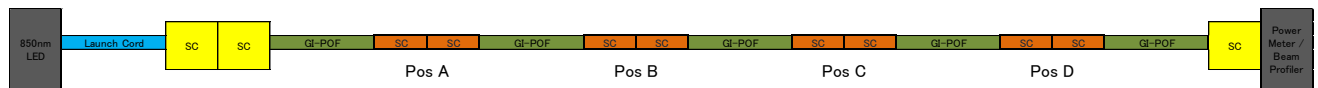
Figure 4 - Experimental setup to evaluate mode coupling in GI-POF

Since fiber NA also plays a role in modal coupling, the refractive index within the core was calculated according the power law equation shown by

$$n(r) = n_1 \left[1 - 2\Delta \left(\frac{r}{a} \right)^g \right]^{\frac{1}{2}} \qquad (2.1.1)$$

where n^1 and n_2 are respectively the refractive indexes of core center and cladding, a is the core radius and Δ is the relative index difference defined as

$$\Delta = \frac{n_1^2 - n_2^2}{2n_1^2} \qquad (2.1.2)$$

g is index exponent and it determines the refractive index profile. [5] The values used are n_1=1.354, n_2=1.342, a=55 and g=2.
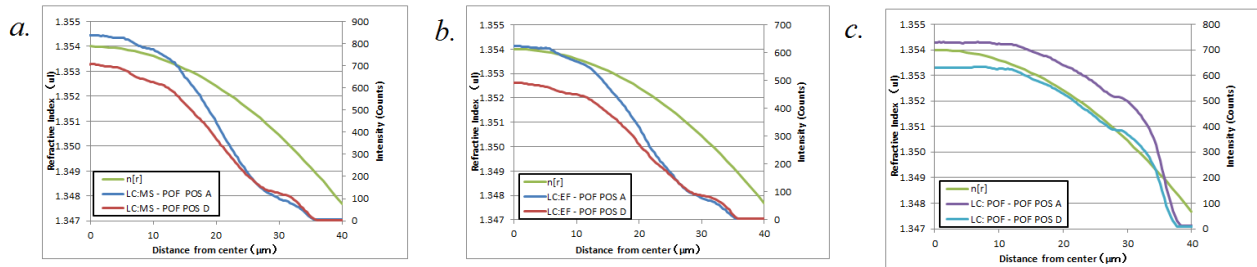

Figure 4 - Modal distribution of a GI-POF system interconnected with physical SC-SC connections. a. GI50 mode scrambler as launch cord. b. Fluke Encircled flux as launch cord. c. Fontex80 as launch cord.

It is possible to verify that the modal distribution tend to approximate to the refractive index distribution of the used fiber. Conducting the same experiment with ball point pen collimators (as in Figure 2) shows a slightly different behavior. In figure 6 is possible to see that when using under filled launch conditions (UFL) such as the ones obtained with mode scrambles and Encircled flux (Figure 6a and b respectively), the modal distribution does not change among the system whereas if launched from an over filled launch conditions (OFL) such as the one obtained from using GI-POF as launch cord, high modes are filtered out (Figure 6c).
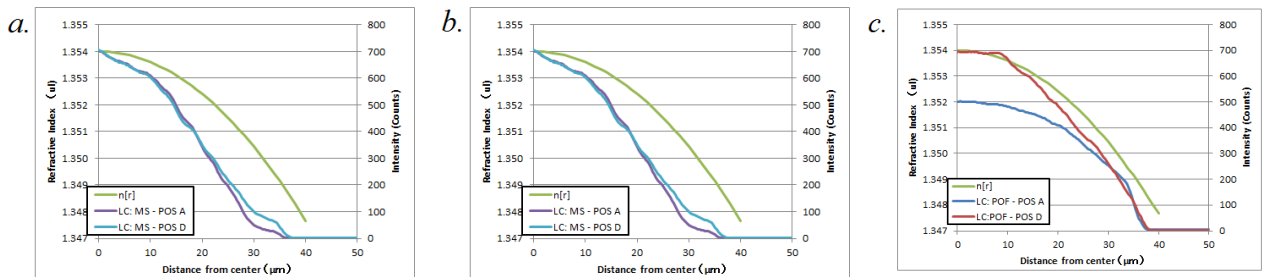

Figure 5 - Modal distribution of a GI-POF system interconnected with Ball point pen collimators. a. GI50 mode scrambler as launch cord. b. Fluke Encircled flux as launch cord. c. Fontex80 as launch cord

Systems that start with OFL conditions or that due to misalignments have higher modes populated benefit from ball point pen collimator since these high propagation modes are supressed.

The authors believe that this effect is due to spherical aberration caused by the use of lenses with curvature radius in the same size magnitude as the beam size. Modes that travel in the periphery of the core will have a slightly different focal point and therefore will be focused slightly before the geometrical focal point. If the difference between those two points is large enough, higher modes are not reaccepted into the receiving fiber.
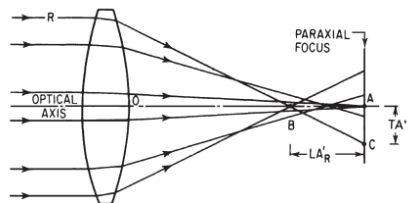

Figure 6 - Spherical Aberration schematic. [6]

The combinations of the effects of GI-POF and the collimator lens on the modal distribution have some practical implication that will be discussed in the next section.

2.2   *Practical implications of the observed effects*

This section will briefly discuss the practical implications of the effect observed in the previous section. Experiments conducted show that this beam shaping reduces the interconnection sensibility to misalignments.
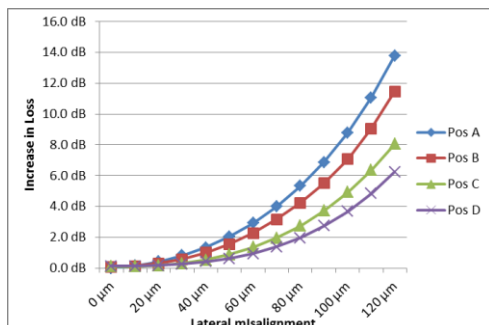

Figure 7 - Increase in IL due to axial misalignment among the system. Launch cord: Encircled flux
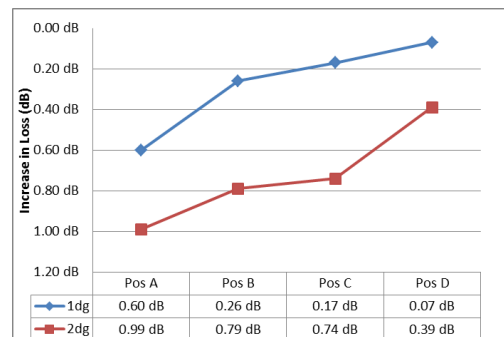

Figure 8 - Increase in IL due to angular misalignment among the system. Launch cord: Encircled flux

Figure 8 shows the measurement results for the influence of lateral misalignment. At $120\,\mu$ m misalignment was verified that Position A insertion loss is 7.55dB higher than Position D. From figure 9 it is possible to see an improvement of 0.60dB from Position A to Position D. Since higher modes are filtered out by the spherical lens in the collimator, the coupling performance under misalignment of such a beam is increased.

One could also argue that the low pass filter system as the one obtained by the combination of GI POF and ball point pen collimator would lead to smaller pulse dispersion and thus allowing for higher system bandwidth.

3   Conclusions

It has been verified that the ball point pen collimator using spherical lenses influences the beam favoring light traveling in lower modes. Although GI-POF has shown the same behavior it was found to be limited to the refractive index distribution of the core. By employing ball point pen collimators, the modal distribution is sharper than the one obtained by using just GI-POF. A possible explanation could be the effect of spherical aberration since the employed lens size is similar to the beam diameter.

This beam shaping effect has some positive effects, among them the fact that a more concentrated beam is less susceptible to loss generated by misalignments. Under certain conditions an increase in bandwidth could also be achievable.

4   References

[1] P. Dainese, S. Bickham et.al "Novel optical design for low-cost optical interconnects in consumer applications", Optics Express 24(20) 2012.

[2] K. Makino, T. Kado et.al "Low loss graded index polymer optical fiber with high stability under damp heat condiions", Optics express 12(20) 2012.

[3] J.C Baker and D.N Payne "Expanded beam connector design study", Appl. Opt. 20(16),2861-2867 (1981)

[4] T. Torikai, T. Yamauchi et.al "Optical I/O connectors employing ball-point pen type optical collimator lenses suitable for plastic optical fiber communications". Proceeding of the 21st Int. Conf. Plastic Optical Fibers 2012

[5] K. Ohdoko, T. Ishigure et.al "Propagating Mode Analysis and Design of Waveguide Parameters of GI POF in Very Short-reach Network Use". IEEE Photonics Technology Letters 17(1) 2005.

[6] Smith, Warren, Modern Optical Engineering,3d Ed, McGraw-Hill, New York, 2000

Fiber-length Dependence of Noise Reduction Effects of
Low-noise Graded-Index Plastic Optical Fiber

H. Suzuki[1*], A. Inoue, Y. Koike

1 Graduate school of Science and Technology, Keio University, 7-1 Shinkawasaki, Saiwai-ku, Kawasaki-shi 212-0032, Japan

*Corresponding author: hikari.suzuki.1225@keio.jp

Abstract: We investigate the link-length-dependence of noise reduction effects for a graded-index plastic optical fiber (GI POF). This shows that the GI POF with noise reduction effects can significantly improve data transmission quality in multimode fiber link for consumer applications with lengths below 30 m. This can be resulted from strong mode coupling because of microscopic heterogeneities with larger-sized density fluctuations than silica glasses. The transmission quality improvement becomes more pronounced as fiber-length increases despite scattering loss increase for link lengths below 10 m, where mode coupling has more influence of noise reduction effects than scattering loss increase on transmission quality. These results suggest that the data transmission quality can be improved further by optimizing the noise reduction effects for various lengths.

1. Introduction

A graded-index plastic optical fiber (GI POF) with a flexibility and high bandwidth is expected to be a transmission media for home-area networks [1, 2]. Recently, we experimentally demonstrated that a GI POF with noise reduction effects can significantly improve data transmission quality in an extremely-short optical-isolator-free optical link with a vertical-cavity surface-emitting laser (VCSEL) for consumer applications [3]. The noise reduction effects can be resulted from mode coupling because of intrinsic properties of the core material. Polymers have microscopic heterogeneities with larger-sized density fluctuations, resulting in more directional forward scattering than Rayleigh scattering in silica glasses [4]. However, the mode coupling also increases scattering loss, which can degrade transmission quality. In the longer fiber link, transmission quality can be determined by both noise reduction effects and the scattering loss increase due to mode coupling, but the influence of the scattering loss increase on resultant transmission quality has not been quantified. In this report, we investigate the fiber-length dependence of transmission quality in multimode fiber (MMF) links with a VCSEL.

2. Fiber-length dependence of transmission quality

2.1 Experiments

The basic experimental setup is shown in Fig. 1. The laser is a multimode VCSEL with an oscillation wavelength of around 850 nm. The output beam from the VCSEL was collimated and focused on a fiber end-face using an antireflection-coated lens. The output beam from the optical fiber was received by the photo detector (PD) with TIA. Under restricted mode-launching condition, we measured the bit error rates (BERs) of the MMF links with a directly modulated VCSEL. The transmission experiments were performed at a VCSEL drive current of 5 mA
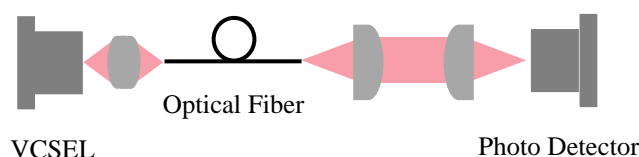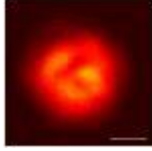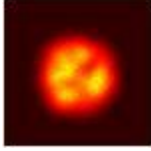

Figure 1. Experimental setup.

Table 1. Characteristics of evaluated fibers. Output beam patterns were measured for length of 1 m. The scale bars are 10 μm.

	low-noise GI POF	silica GI MMF
Numerical aperture	0.19	0.20
Core diameter (μm)	50	50
Output beam pattern		
Attenuation (dB/m)	0.054	0.0033

using a 10 Gbit/s non-return to zero data pattern with a 2^{31}-1 pseudorandom binary sequence. A modulation voltage was 0.1 V, which is much lower than the conventional voltage for 2-level modulation.

The characteristics of evaluated fibers are listed in Table 1. The microscopic images show the near field patterns of output beams after propagation through 1-m optical fibers. The output power distribution of a silica GI MMF is similar to initial distribution for launched modes. On the other hand, a low-noise GI POF has a more changed beam pattern with a large beam width than the silica GI MMF. This may result from strong mode coupling, which induces a power transition from launched modes to the other guided modes. Strong mode coupling also increases scattering loss, resulting in higher attenuation of the low-noise GI POF (0.054 dB/m) at a wavelength of 850 nm than the silica GI MMF (0.0033 dB/m) with little mode coupling.

2.2 Results and discussions

Figure 2 shows the fiber-length dependence of bit error rates (BERs) of transmitted signal through the low-noise GI POF and the silica GI MMF. By using the low-noise GI POF, we could significantly improve BERs compared with the silica GI MMF for all the fiber lengths. For MMF link below 10 m, the BER improvement of low-noise
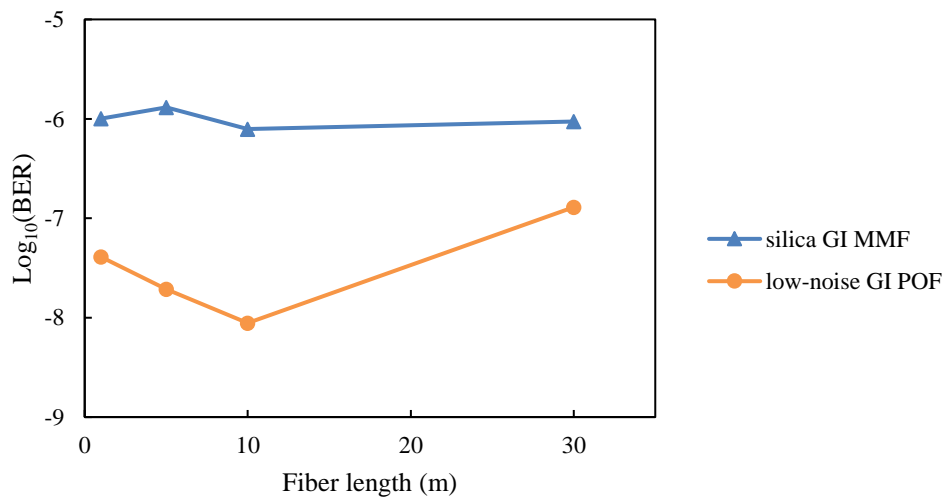

Figure 2. Fiber-length dependence of BERs of transmitted signal through the low-noise GI POF and silica GI MMF. A bias current and a modulation voltage were 5 mA and 0.1 V, respectively.

GI POF became more pronounced as fiber length increases, even though scattering loss increases. This suggests that the mode coupling has more influence of noise reduction effects than scattering loss increase on data transmission quality for link lengths below 10 m, whereas the influence of scattering loss increase on the transmission quality was stronger than the noise reduction effects for length of 30 m.

Figure 3(a)-(d) show the noise power spectra of optical links for lengths of 1 m, 5 m, 10 m, and 30 m with unmodulated VCSEL using PD without TIA. Both the spectra of the low-noise GI POF and the silica GI MMF have periodic peaks, which have equal spaces to the round-trip frequencies of the external cavities with the reflector of the fiber output face or PD [5], and the noise levels of the low-noise GI POF were lower than those of the silica GI MMF.

To investigate the mechanism for reflection noise reduction, backreflected beams from the fibers were observed as shown in Fig. 4. For all the fiber lengths, the silica GI MMF with little mode coupling has almost the same backreflected beam pattern as incident beam. This suggests that the backreflected beam from the silica GI MMF can be self-coupled with higher coupling efficiency into the VCSEL cavity, resulting in higher reflection noise levels. On the other hand, the low-noise GI POF with strong mode coupling has a significantly changed backreflected beam pattern from incident beam pattern, while the backreflected beam pattern after propagation through 30 m could not be clearly captured because of too weak power and the camera limited dynamic range. This can be attributed to power transitions from launched modes to the other guided modes because of more directional forward scattering by intrinsic

Figure 3. Noise power spectra of optical links for length of (a) 1 m, (b) 5m, (c) 10 m, and (d) 30 m. The insets show enlarged figure between 0.05 GHz and 0.15 GHz.

core heterogeneities. The changes from incident beam could reduce self-coupling efficiency into the VCSEL cavity, resulting in reduction of reflection noise. This effects can lead to transmission quality improvement. However, the pronounced beam width change depending on fiber length could not be observed. Also both the noise floor levels of the low-noise GI POF and the silica GI MMF increased for length of 30 m as shown in Fig. 3. To clarify the mechanism for the influence of mode coupling on fiber-length-dependent transmission quality, more detailed analyses for transmission characteristics of the low-noise GI POF and stability of a VCSEL coupled with the low-noise GI POF are required.
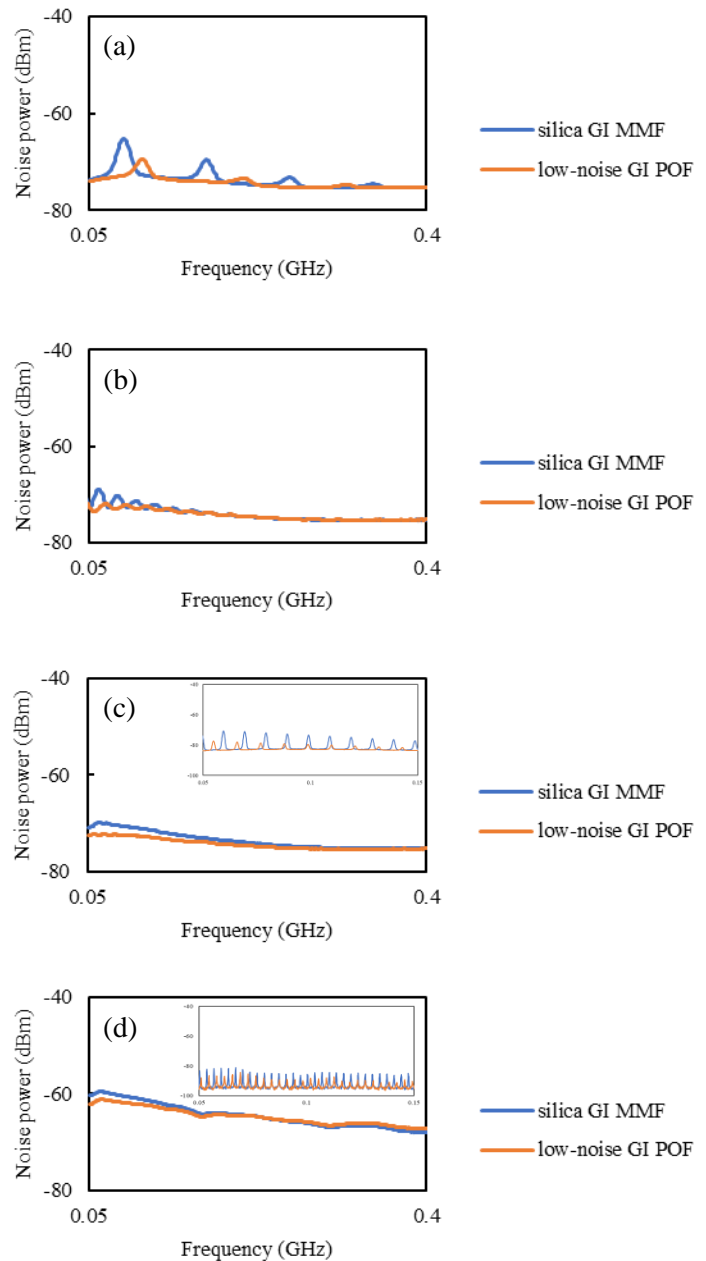
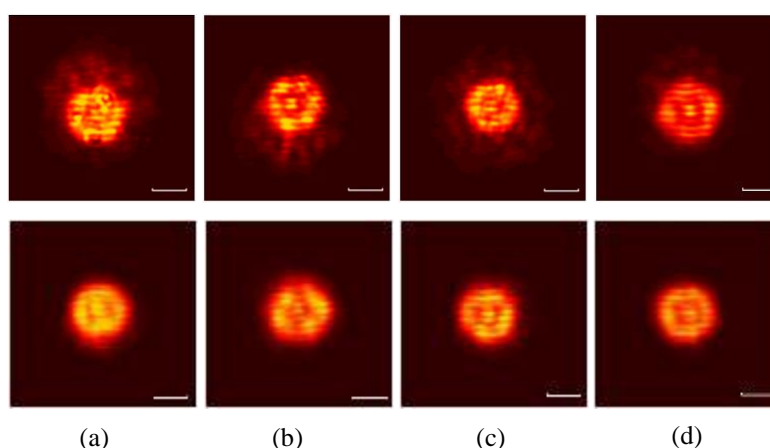| | | | |
| (a) | (b) | (c) | (d) |

Figure 4. Microscopic images of backreflected beam patterns from low-noise GI POF (top) and silica GI MMF (bottom) on the fiber-input faces. The beam patterns were observed for length of (a) 1 m, (b) 5 m, (c) 10 m, and (d) 30 m. The scale bars are 10 μm.

3. Conclusion

We investigate the link-length-dependence of noise reduction effects for the low-noise GI POF. This shows that the low-noise GI POF can significantly improve baseband transmission quality in MMF link with a VCSEL for all the fiber lengths below 30 m. This may result from reflection noise reduction effects because of strong mode coupling by intrinsic core heterogeneities. Moreover, the transmission quality improvement became more pronounced as fiber length increases in spite of scattering loss increase with lengths below 10 m, where the mode coupling has more influence of noise reduction effects than scattering loss increase. These results suggest that the data transmission quality can be improved further by optimizing mode coupling effects.

4. References

[1] Y. Koike, "Fundamentals of plastic optical fibers," Wiley, New York, 2015.

[2] A. Inoue and Y. Koike, "High-Speed Graded-Index Plastic Optical Fibers and Their Simple Interconnects for 4K/8K Video Transmission," J. Lightw. Technol., vol. 34, no. 6, pp. 1551-1555, 2016.

[3] A. Inoue and Y. Koike, "Stabilized Multimode Fiber Link Using Graded-Index Plastic Optical Fiber with Strong Mode Coupling," The 25th International Conference on Plastic Optical Fibres, presented on Sept. 13, 2016.

[4] A. Inoue, T. Sassa, R. Furukawa, K. Makino, A. Kondo, and Y. Koike, "Efficient group delay averaging in graded-index plastic optical fiber with microscopic heterogeneous core," Opt. Express, vol. 21, no. 14, pp. 17379-17385, 2013.

[5] J. Otsubo, "Semiconductor lasers Stability, instability and chaos," Springer, New York, 2007.

Design of Launching Condition in Optical Module through Ballpoint-Pen Interconnect for Graded-Index Plastic Optical Fiber

T. Yagi[1*], A. Inoue[1], A. Mitsui[2], H. Suzuki[2], and Y. Koike[1]

1 Graduate school of Science and Technology, Keio University, 7-1 Shinkawasaki, Saiwai-ku, Kawasaki-shi, Kanagawa 212-0032, Japan
2 Mitsubishi Pencil, 2-5-12 Irie, Kanagawa-ku, Yokohama, Kanagawa 221-8550, Japan
*Corresponding author: t.inrrtl_t@keio.jp

Abstract: We investigate the launching condition dependence of the data transmission quality for the ballpoint-pen interconnect of the graded-index plastic optical fibers (GI POFs) to obtain design guidelines for its optimum optical module. The result shows that bit error rates can be significantly improved by using 30-μm offset launching condition for the core diameter of 80 μm despite decrease of detected power. This is attributed to the reflection noise reduction because of decreased self-coupled power to laser cavity, which is caused by different propagation axis between incident beam and backreflected beam. This suggests that sufficient offset launching is suitable for the optical module for the ballpoint-pen interconnect of the GI POF.

1. Introduction

For the upcoming 2020 Tokyo Olympics and Paralympics, 8K (7680x4320 pixel) television will be developed. The presently used metal cable causes deterioration of bandwidth due to a dielectric loss and skin effect increased for higher frequency. As such, so many thick metal cables are required to transmit the large amount of uncompressed 8K video data over 100 Gb/s. Moreover, the throughput of Wi-Fi could be degraded by electro-magnetic interference because of radiation leakage from metal cable.

A graded-index plastic optical fiber (GI POF) with a high bandwidth, low reflection noise, and flexibility is expected to be a transmission media for short-reach communication in-home networks where many connections and bends would be required [1,2]. In order to realize the simple GI POF connection for consumers, we have developed ballpoint-pen interconnect, where GI POFs are coupled with ball lens mounted on their end faces [3-5]. This ballpoint-pen connecter significantly increases tolerance for misalignments of the GI POF axis, caused by the expanded and collimated output beam. In actual consumer-friendly link, however, the misalignment tolerance for connection depends on launching conditions which also change the influence of reflection noise due to some discontinuities [6]. Therefore, the launching optical system requires optimization to improve the transmission quality. In this report, we investigated the launching condition dependence of the data transmission quality through the ballpoint-pen interconnect to obtain design guidelines for its optimum optical module.

2. Method

2.1 Experiment

In ballpoint-pen interconnect, a ball lens is mounted on a GI POF end face through a metal sleeve (see Fig. 1). The connector fabrication technology is based on the ballpoint-pen producion process. A metal ball and ink cartridge are replaced with a glass ball lens and a GI POF, respectively. The output beam expanded and collimated by ball lens can increase tolerance for lateral misalignment, compared with conventional butt coupling. As shown in Fig. 2, we evaluated launching condition dependence of data transmission quality for ballpoint-pen interconnect of GI POFs using a multimode vertical cavity surface emitting laser (VCSEL) with oscillation wavelengths around 850 nm. The transmission experiments were performed using a 10 Gb/s non-return to zero pulse pattern with a $2^{31} - 1$ pseudo-random bit sequence. A bias current and modulation voltage were 5 mA and 0.8 V, respectively. The output beam from the GI POF was detected by the photo-diode (PD). The ball lenses in ballpoint-pen interconnect have a refractive index of 1.51 and a diameter of 550 μm. The core diameter and the numerical aperture of GI POF were 80 μm and 0.25, respectively.
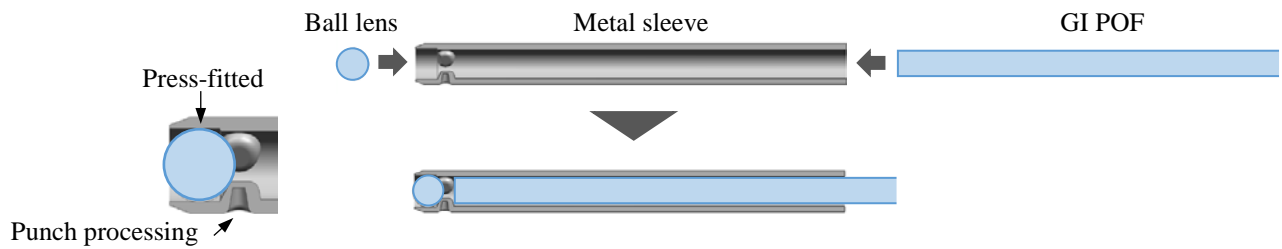
Figure 1. Schematic fabrication process of ballpoint-pen connector.
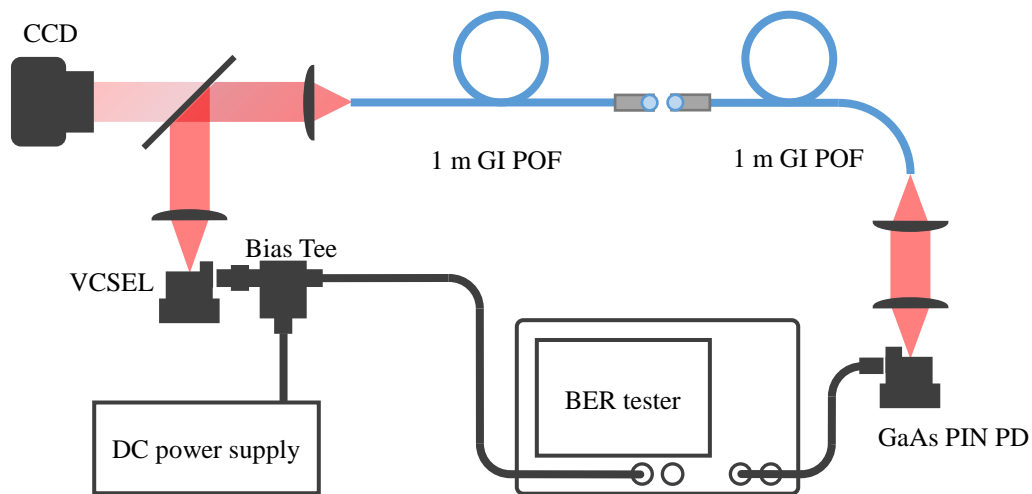
Figure 2. Experimental setup for measuring launching condition dependence of BER for ballpoint-pen interconnect of GI POFs.

2.2 Launching condition

In this report, we evaluated the influence of offset launching condition on data transmission quality for the lateral ballpoint-pen connector misalignment. In the fiber input face, we changed the launching position from center core to radial direction up to 30 μm. Figure 3 shows the microscopic images of focused output beams from the VCSEL on input fiber end face.

(a)   (b)   (c)   (d)

Figure 3. Microscopic images of focused output beams from the VCSEL on an input fiber end face for different incident positions where (a)0, (b)10, (c)20, and (d)30 μm. For the fibers with flat-polished output faces, the backreflected beam was also observed. The driving current was 5 mA.

3. Results and discussions
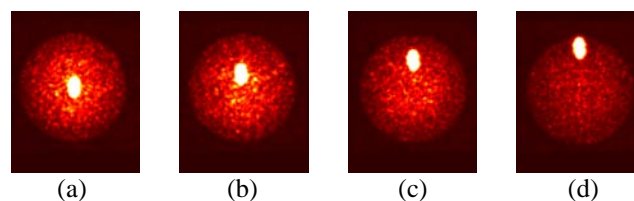
3.1 Offset launching condition dependence of BER for ballpoint-pen interconnect of GI POFs

Figure 4 (a) and (b) show BER and detected power as a function of lateral connector misalignment for the different launching positions r in the fiber input face, respectively. BERs could be significantly improved for offset launching with r value of 30 μm. In order to clarify the mechanism for transmission quality improvement by using the offset launching, we evaluated the noise floor spectra under the different launching positions without lateral connector misalignment (see Fig. 5). As shown in Fig. 5, the periodic peaks with an equal spacing of ~0.1 GHz corresponded to the round-trip frequencies of the formed external cavities which were composed of the laser output mirror and some discontinuities in the connectors [7]. For 30-μm offset launching, these reflection noises were significantly reduced. This was attributed to the reduction of backreflected beam self-coupled into VCSEL cavity because of different propagation axis between incident beam and backreflected beam. This result suggests that using the offset launching is suitable for the optical module for the ballpoint-pen interconnect of the GI POFs. Moreover, in all the launching positions, BERs decreased as the lateral connector misalignment was larger despite detected power decrease. This may result from reduction of some noises (e.g. reflection noise) because of lateral connector misalignment.
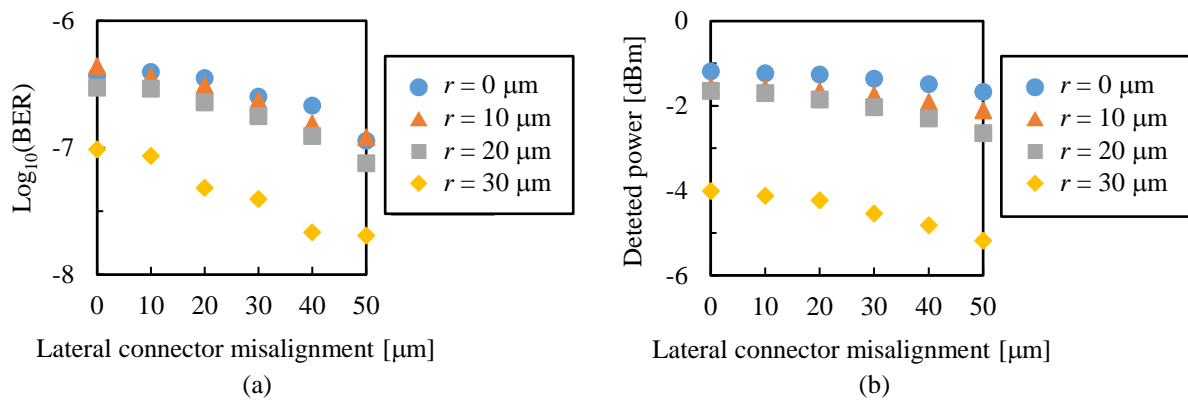
Figure 4. Dependence of (a) BERs and (b) detected optical powers on the lateral misalignments of the coupled 1-m GI POFs with the ballpoint-pen interconnect for the different launching conditions. The bias current and the laser modulation voltage were 5 mA and 0.8 V, respectively.
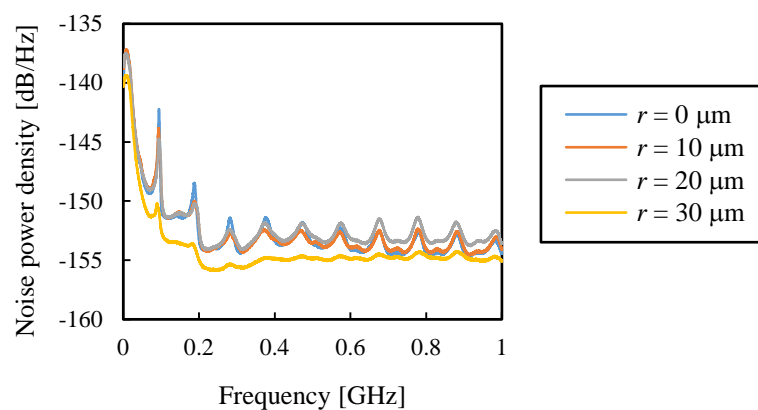

Figure 5. Noise power density spectra for ballpoint-pen connector of the coupled 1-m GI POF without lateral connector misalignment under the different launching conditions.

4. Conclusion

The influence of the launching position on the data transmission quality with the ballpoint-pen interconnect of the GI POF based on the multimode VCSEL system was investigated. The transmission quality was significantly improved by using for 30-μm offset launching although the detected power was decreased. This was attributed to the reflection noise reduction owing to the decrease of backreflected beam self-coupled into the VCSEL cavity because propagation axes were different between incident beam and backreflected beam from some discontinuities such as ballpoint-pen connectors. This suggests that, by using appropriate offset launching condition, the data transmission quality can be improved for consumer short-reach system with ballpoint-pen interconnects of GI POFs.

5. References

[1] Y. Koike and A. Inoue, "High-speed graded-index plastic optical fibers and their interconnects for 4K/8K video transmission," J. Lightw. Technol., vol. 34, no. 6, pp. 1551-1555, Mar. 2016.

[2] Y. Koike, "Fundamentals of Plastic Optical Fibers," Wiley-VCH: New York, pp. 50-55, Jan. 2015.

[3] T. Torikai, T. Yamauchi, S. Mine, N. Moriya, A. Mitsui, H. Suzuki, Y. Watanabe, M. Kanou, H. Takizuka, T. Toma, and Y. Koike, "Optical I/O connectors employing ball-point pen type optical collimator lenses suitable for plastic optical fiber communications," Proc. 21st Int. Conf. Plastic Optical Fibers, Atlanta, USA, pp. 227-231, Sep. 2012.

[4] H. Takizuka, T. Torikai, A. Mitsui, H. Suzuki, Y. Watanabe, T. Toma, and Y. Koike, "A proposal of novel optical interface to transmit 8K-UHDTV for consumer applications," Proc. 18th Microoptics Conf., Tokyo, Japan, pp. 1-2, Oct. 2013.

[5] T. Toma, H. Takizuka, T. Torikai, H. Suzuki, T. Ogi, and Y. Koike, "Development of household high-definition video transmission system based on ballpoint-pen technology," Synthesiology, vol. 7, no. 2, pp. 118-128, May 2014.

[6] A. Inoue and Y. Koike, "Misalignment Tolerance of Pluggable Ballpoint-Pen Interconnect of Graded-Index Plastic Optical Fiber for 4K/8K UHD Display," IEICE Transactions on Electron., vol. E99-C, no. 11, pp. 1271-1276, Nov. 2016.

[7] I. Ikushima and M. Maeda, "Self-Coupled Phenomena of Semiconductor Lasers Caused by an Optical Fiber," J. Quantum Electron., vol. QE-14, no. 5, pp. 331-332, May 1978.

Stabilization Mechanism Analyses of Consumer-friendly Optical Link
Based on Low-noise Graded-index Plastic Optical Fiber

K. Muramoto[*], A. Inoue, Y. Koike

Graduate school of Science and Technology, Keio University, 7-1 Shin-kawasaki, Saiwai-ku, Kawasaki-shi Kanagawa 212-0032, Japan
*Corresponding author: kenta.m051038@gmail.com

Abstract: We investigate the bit-rate dependence of transmitted signal quality through a low-noise graded-index plastic optical fiber (GI POF) in the consumer-friendly optical link without an optical isolator. By using the low-noise GI POF, the transmission quality is significantly improved compared with a silica GI multimode fiber for all the evaluated bit rates under the modulation conditions in this study. This improved transmission quality by the low-noise GI POF is related to reduced distortion of frequency response, which is caused by the self-coupled power reduction of the backreflected beam into the VCSEL cavity owing to strong mode coupling in the low-noise GI POF. This suggests that the low-noise GI POF allows for high-quality multilevel transmission for consumer-friendly 8K interface.

1. Introduction

The growing demand for high-speed data transmission in consumer applications such as 4K/8K television motivates the development of multilevel modulation [1, 2]. Multilevel modulation can increase bit rate over 2-level modulation for same symbol rate. However, signal-to-noise ratio of the multilevel modulation deteriorates compared with the 2-level modulation for same noise level because of its reduced minimum symbol-level difference. Recently, we experimentally demonstrated that a graded-index plastic optical fiber (GI POF) significantly improved the transmission signal quality compared with a silica GI multimode fiber (MMF) in the consumer-friendly MMF link without an optical isolator, where laser and optical fiber easily coupled [3]. This high-quality transmission is related to reflection noise reduction because of strong mode coupling in the GI POF [4]. However, the details of the link stabilization mechanism have not been clarified. Moreover, the transmission quality in the MMF link changes depending on modulation conditions of the vertical-cavity surface-emitting laser (VCSEL) such as bias current, modulation amplitude, and modulation frequency spectrum [5]. Here, we investigate the bit-rate dependence of data transmission quality through the low-noise GI POF in the consumer-friendly MMF link. We also evaluate the frequency response of the VCSEL coupled with the low-noise GI POF to investigate the stabilization mechanism.

2. Experimental setup

Figure 1 (a) shows the experimental setup for evaluation of bit error rate (BER). The laser was a multimode VCSEL with an oscillation wavelength of 850 nm and a -3 dB bandwidth of 9 GHz at an injection current of 5 mA. The output beam from the VCSEL was focused on a center of an optical fiber end-face using an antireflection-coated (AR-coated) aspherical lens. Evaluated optical fibers were a low-noise GI POF and a silica GI MMF with roughly the same fiber length (1 m), NA (~ 0.2), and core diameter (~50 μm). The output beam from the optical fiber was collimated and focused on a photodiode (PD) with a -3 dB bandwidth of 12 GHz using two AR-coated aspherical lenses. Under this restricted mode-launching condition, we measured the bit-rate dependence of BER by using bit error rate tester (BERT). The transmission signal was non-return to zero data pattern with a $2^{31}-1$ pseudo-random bit sequence (PRBS). The bias current and the modulation voltage of the VCSEL were, respectively, 5.0 mA and 0.10 V (peak-to-peak voltage), which is comparable to minimum symbol-level difference of PAM4. Figure 1 (b) shows the experimental setup for evaluation of frequency response of the VCSEL coupled with the low-noise GI POF. The output beam from the optical fiber was received by the PD built in a Lightwave Component Analysers (LCA). For consumer applications, plugging and unplugging of optical cable may change the alignment of the optical components, being affected by backreflected beam from some discontinuities. Therefore, in this study, we precisely aligned the optical axis of the MMF link to evaluate the worst-case quality.
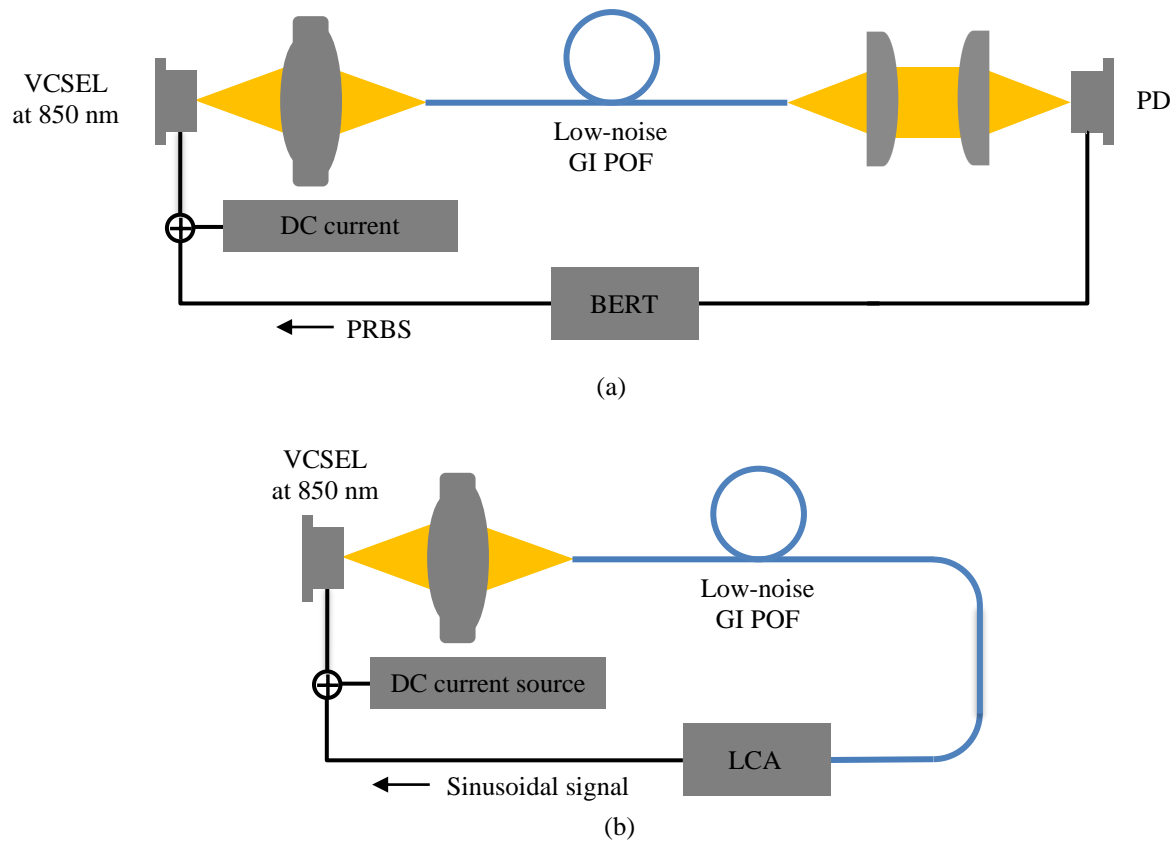
Fig. 1   Experimental setups for evaluation of (a) BER for transmitted signal through the low-noise GI POF and (b) frequency response of the VCSEL coupled with the low-noise GI POF.

3. Results and discussions

Figure 2 shows bit-rate dependence of BER for transmitted signal through the low-noise GI POF and the silica GI MMF in the MMF link. We observed the tendency of BER degradation with increasing bit rate. By using the low-noise GI POF, transmission quality in the MMF link was significantly improved compared with the silica GI MMF for all the evaluated bit rates. To clarify the link stabilization mechanism by using the low-noise GI POF, we evaluated the frequency response of the VCSEL coupled with the low-noise GI POF and the silica GI MMF. As shown in Fig. 3, we observed periodic peaks with an equal spacing of 100 MHz, which corresponds to the round-trip frequencies of the external cavities with the reflector of the optical fiber output face [6]. By using the low-noise GI POF, this peak level and frequency response distortion was decreased compared with the silica GI MMF. This decreased distortion of the frequency response is related to strong mode coupling in the low-noise GI POF, which reduces self-coupling efficiency of the backreflected beam into the VCSEL cavity. This suggests that the BER improvement in the MMF link is attributed to low-distortion frequency response by using the low-noise GI POF. Also, as bit rate increased, the difference of BER between using the low-noise GI POF and the silica GI MMF decreased (Fig. 2). As shown in Fig. 3, both MMF links using the low-noise GI POF and silica GI MMF had comparable frequency response with almost the same bandwidths. This suggests that, in the short-reach optical communication, the bandwidth of the MMF link is mainly affected by the bandwidth of the VCSEL because the bandwidth of the optical fiber is sufficiently higher than the VCSEL bandwidth. Therefore, as bit rate increased, the BER improvement effect by the low-noise GI POF decreased since the signal degradation due to the VCSEL bandwidth limitation became larger than the optical feedback.
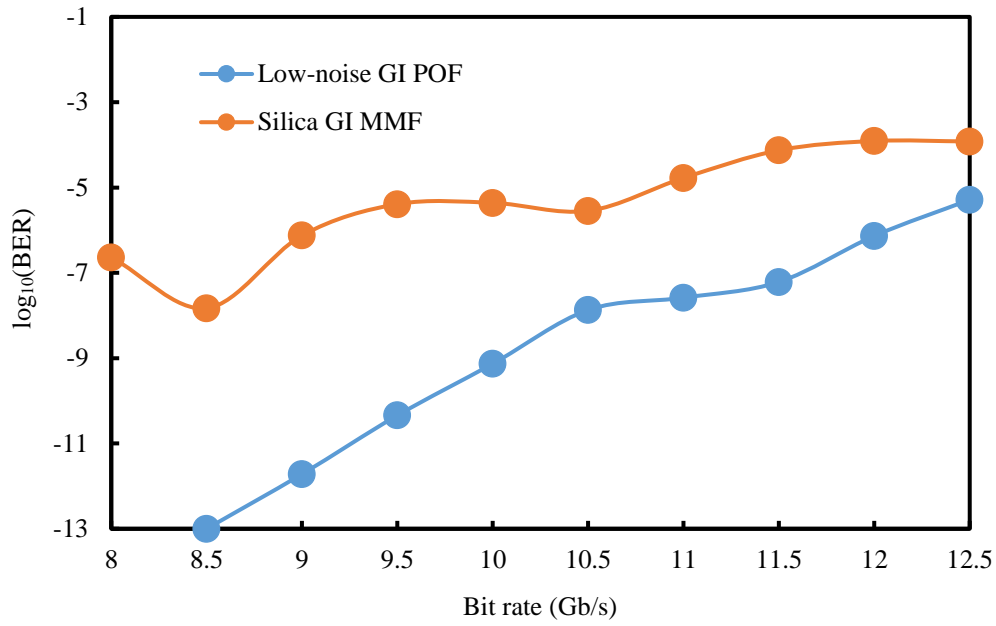
Fig. 2　Bit-rate dependence of BER of transmitted signal through the 1 m low-noise GI POF and the 1 m silica GI MMF in the MMF link whose optical components are precisely aligned. The bias current and the modulation voltage of the VCSEL were, respectively, 5.0 mA and 0.10 V (peak-to-peak voltage) which is comparable to minimum symbol-level difference of PAM4.

Fig. 3　Frequency responses of the VCSEL coupled with the 1 m low-noise GI POF and the 1 m silica GI MMF. The bias current and the modulation voltage of the VCSEL are 5.0 mA and 0.10 V, respectively. The inset shows frequency response on an enlarged scale.
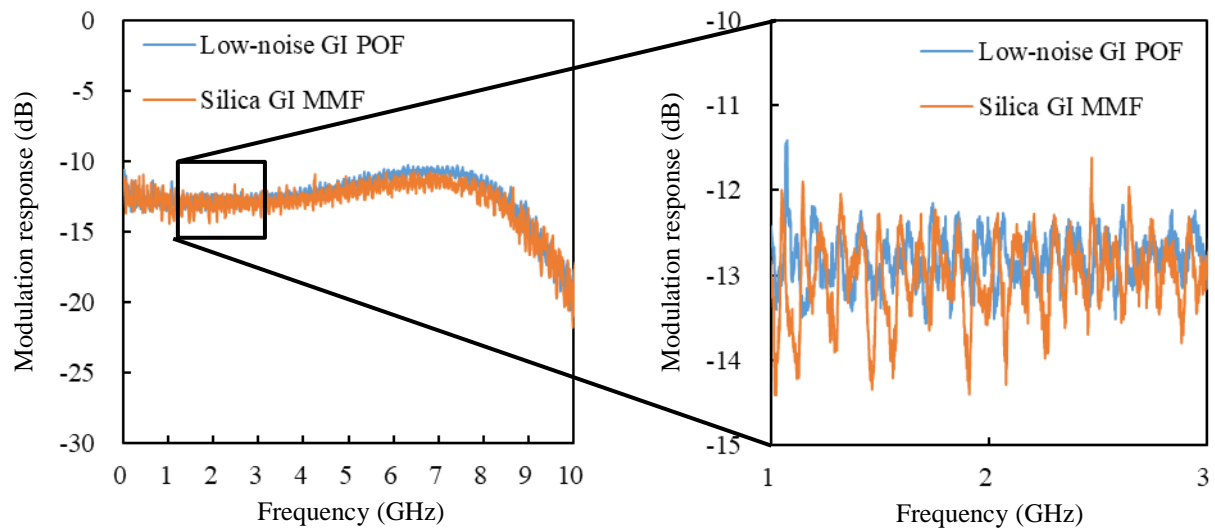
4. Conclusion

  We investigated the bit-rate dependence of transmitted signal quality through the low-noise GI POF in the consumer-friendly optical link without an optical isolator. By using the low-noise GI POF, the transmission quality was significantly improved compared with the silica GI MMF for all the evaluated bit rates under the modulation conditions in this study. This improved transmission quality by the low-noise GI POF is related to reduced distortion of frequency response, which is caused by the self-coupled power reduction of the backreflected beam into the VCSEL cavity owing to strong mode coupling in the low-noise GI POF. This suggests that the low-noise GI POF allows for high-quality multilevel transmission for consumer-friendly 8K interface.

5. References

[1] Y. Koike and A. Inoue, "High-speed graded-index plastic optical fibers and their simple interconnects for 4K/8K video transmission," J. Lightw. Technol., vol. 34, no. 6, pp. 1551-1555, Mar. 2016.

[2] K. Szczerba, P. Wastbergh, J. Karout, J. Gustavsson, A. Haglund, M. Karlsson, P. Andrekson, E. Agrell, and A. Larsson, "30 Gbps 4-PAM transmission over 200 m of MMF using an 850 nm VCSEL," Opt. Exp., vol. 19, no. 26, pp. B203-B208, Dec. 2011.

[3] A. Inoue and Y. Koike, "Stabilized multimode fiber link using graded-index plastic optical fiber with strong mode coupling," presented at the 25th Int. Conf. Plastic Optical Fibres, Birmingham, UK, Sept. 13-15, 2016.

[4] A. Inoue, R. Furukawa, M. Matsuura, and Y. Koike, "Reflection noise reduction effect of graded-index plastic optical fiber in multimode fiber link," Opt. Lett., vol. 39, no. 12, pp. 3662-3665, Jun. 2014.

[5] A. Haglund, C. Carlsson, J. S. Gustavsson, J. Halonen, and A. Lasson, "A comparative study of the high-speed digital modulation performance of single- and multimode oxide confined VCSELs for free space optical interconnects," Proc. SPIE, vol. 4649, pp. 272-280, Jun. 2002.

[6] J. Helms and K. Petermann, "Microwave modulation characteristics of semiconductor laser with optical feedback," Electron. Lett., vol. 25, no. 20, pp. 1369-1371, Sept. 1989.

Syntheses of New Polymerizable Organic Dyes for Fibre-Laser Applications

Jana Kielhorn[1], Daniel Zaremba[1], Itxaso Parola[2], Wolfgang Kowalsky[1] and Hans-Hermann Johannes[1]

1 Technische Universität Braunschweig, Institut für Hochfrequenztechnik, Labor für Elektrooptik, Bienroder Weg 94, D-38106 Braunschweig, Germany.

2 University of the Basque Country (UPV/EHU), Faculty of Engineering of Bilbao (EIB), Plaza Ingeniero Torres Quevedo 1, E-48013 Bilbao, Spain.

*Corresponding author: h2.johannes@ihf.tu-bs.de

Abstract: The main goal of this study lies in the syntheses of new organic dyes based on Perylene and 4-(dicyanomethylene)-2-methyl-6-(*p*-dimethyl-aminostyryl)-4*H*-pyran (DCM) for fibre-lasers, which are achieved by integrating functional groups. Deep spectral characterizations and a successful preform and fibre drawing process have shown promising results.

1. Introduction

Over the last years the incorporation of active materials into specific hosts has attracted a great attention due to their potential applications in areas such as organic-based lasers and amplifiers. For instance, Polymer Optical Fibres (POF) doped with organic dyes have demonstrated to have potential qualities for fibre-based laser applications in the field of medical lasers, communication links and a wide variety of sensors [1].

In this work new organic dyes based on Perylene and DCM dyes have been synthesised by integrating functional groups. Deep spectral characterization of these dyes have been carried out.

The main goal of this study is the syntheses of new active materials for fibre-laser applications.

2. Experimental

2.1 Syntheses

Perylene dye: Based on the Murai–Chatani–Kakiuchi protocol we have synthesised a Perylene Bisimide with chlorophenethyl groups **2** (see Figure 1). Via these ruthenium-catalyzed C-H bond activation, an alkylation of the bay area at the 2,5,8,11-positions is possible [2].
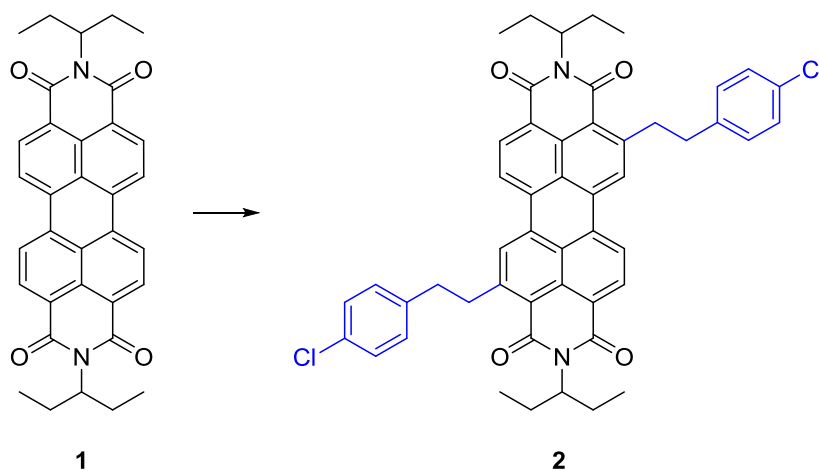

Figure 1: Schematic of the syntheses of **2**-dye in a ruthenium-catalyzed process.

DCM dye: Through a condensation reaction, the compound **4** is prepared (see Figure 2). Because of small amount of the substance, the second step, which is a functionalization with methacryloyl chloride, wasn't yet possible.
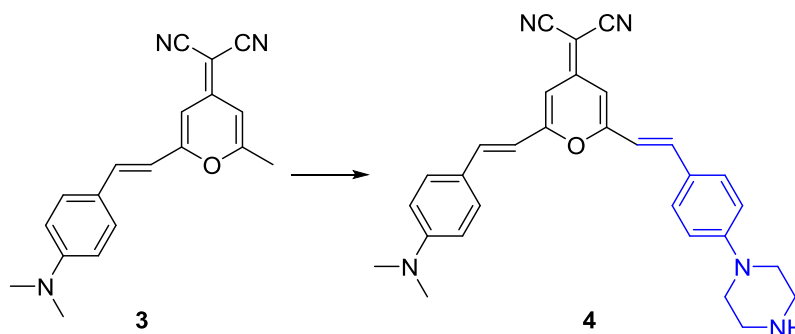

Figure 2: Schematic of the syntheses of **4**-dye in a condensation reaction.

2.2 Polymerization with dyes

At room temperature the dyes (Sigma Aldrich *N,N′*-Bis(3-pentyl)perylene-3,4,9,10-bis(dicarboximide), **2**, Radiant DCM and **4** in each case 0.0005 mol%), lauroylperoxide (0.03 mol%) and *n*-butyl-mercaptan (0.1 mol%) were solved in a nitrogen saturated MMA solution.

For the preform fabrication, the monomer solution was filtered into glass tubes and sealed with silicon plugs. The polymerization was temperature induced via a temperature ramp from 20 to 100 °C during 5 days. This temperature will be kept for 24 hours and finally cooled down to room temperature (20 °C) over 1 day. For the bulk samples fabrication, the monomer solution was filtered into small glasses and treated with the same temperature program as the preforms[3].

After release from the glasses the preforms were cleaned and drawn to fibre using a fibre drawing tower. The preforms were heated up to 210 °C and pulled by applying a constant force. A fibre with core diameter of 980 μm was received and a cladding of a 20 μm film of Efiron PC404F-AP (Luvantix) was added. One of the obtained fibres with synthesised **2**-dye is shown in Figure 3.
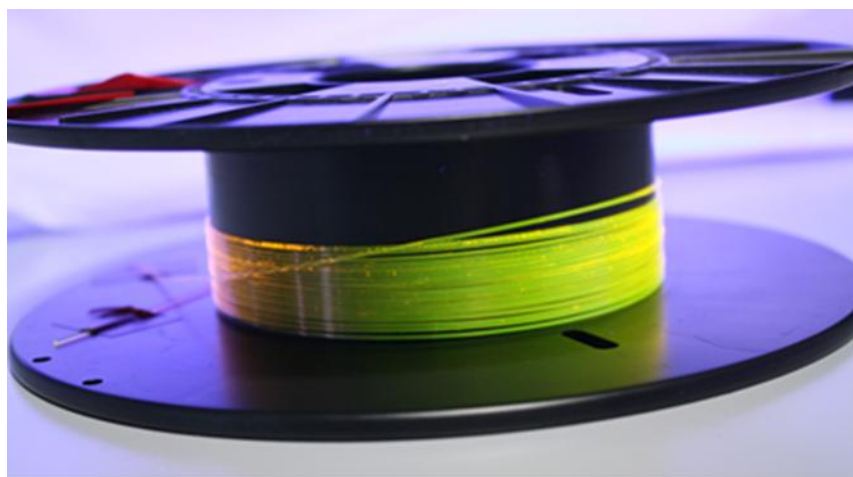
Figure 3: Photograph of one of our **2**-dye doped POF under UV light.

3. Results and discussion

Dye Characteristics: Figure 1 also shows the fluorescent Perylene-dyes **1** and **2**. Both of them have a characteristical Perylene basic structure. This substructure is responsible for their high chemical, thermal and photochemical stability. Therefore, a high reaction temperature is necessary for the syntheses and temperature induced polymerization will be possible. Moreover, Perylene derivatives exhibit excellent photophysical

properties like high absorption coefficient, low photo bleaching and high fluorescence quantum yield. The optical and electrochemical properties of Perylene dyes can be achieved by functionalizing different substituent groups in *peri* and *bay* positions of Perylene core. Broadly speaking, a tuning of the spectroscopic and electrochemical properties is reachable by different *peri* groups, whereas the *bay* functional groups provide an additional fine tuning or in our case a preliminary stage for polymerizable groups [2, 4].

Functionalizing substituent groups in **2**-dye doesn't have any significant influence on the spectroscopic properties. The absorption and emission bands are equal to Perylene-dye **1** with a great Stokes-Shift of 116 nm (see Figure 4).
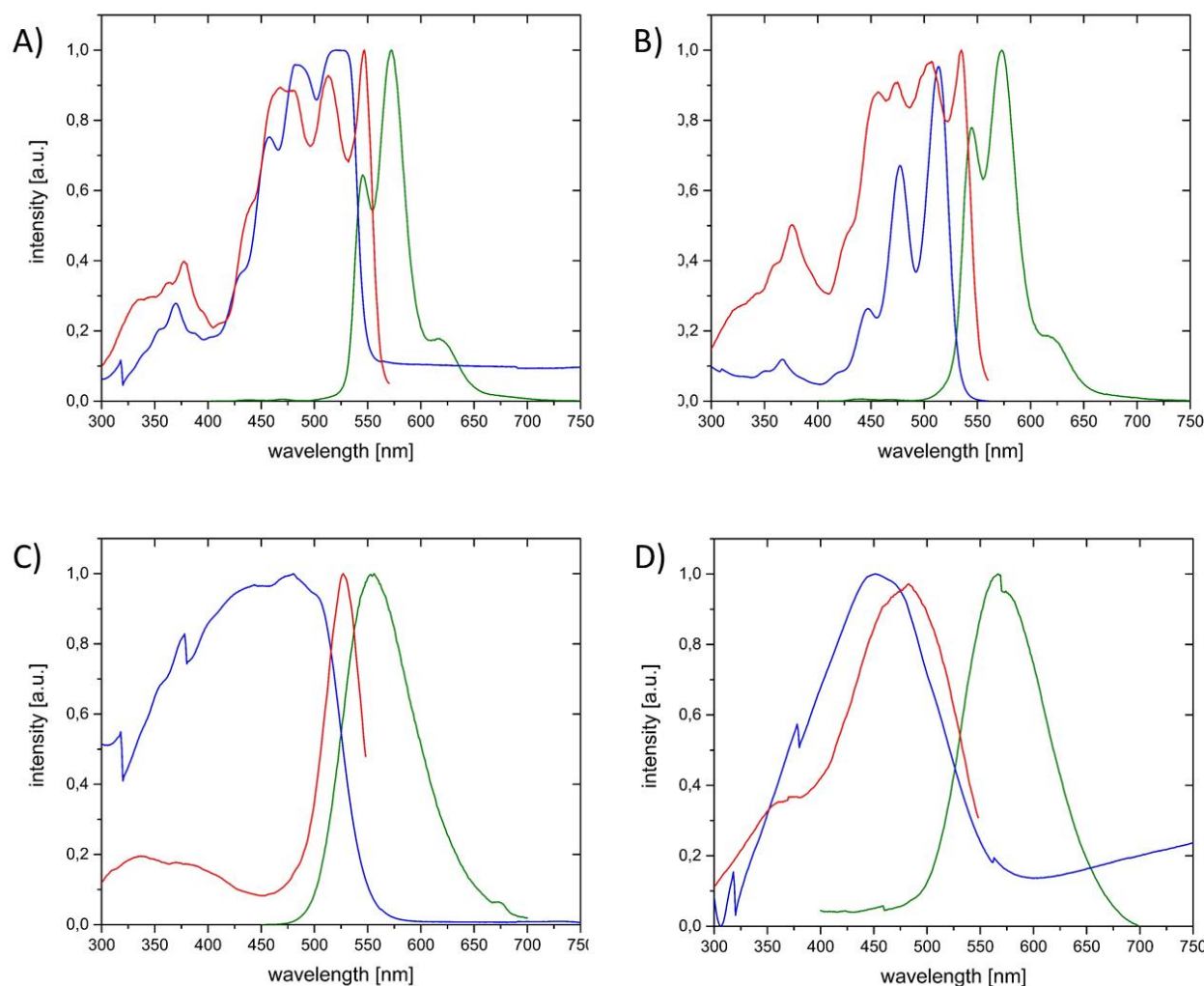
Figure 4: Normalized UV/Vis absorption in PMMA (blue), excitation (red) and emission spectra (green) in PMMA of: A) 0.0005 mol% Sigma Aldrich *N,N'*-Bis(3-pentyl)perylene-3,4,9,10-bis(dicarboximide), ex. 350 nm, em. 575 nm; B) 0.0005 mol% **2**, ex. 350 nm, em. 575 nm; C) 0.0005 mol% Radiant DCM, ex. 337 nm, em. 555 nm; D) 0.0005 mol% **4**, ex. 355 nm, em. 567 nm.

DCM has been known for several years as laser dye. It is widely used because of its broad tunability and high conversion efficiency [5]. Its spectral properties are significant considering the weak overlap between the absorption spectrum and the emission spectrum, in addition to the long lifetime under photochemical excitation [6,7].

In comparison with the spectroscopic properties of DCM the absorption and emission bands of dye-**4** are strongly shifted. The emission maximum of DCM is located at 556 nm and the absorption maximum at 480 nm. The results of the spectroscopic analysis of dye-4 shows maxima at 567 nm and 451 nm with a 40 nm larger Stokes-Shift (see Figure 4).

4. Conclusions

We have successfully synthesised the Perylene derivate **2**-dye and the DCM derivate **4**-dye, which is proven by the analysis of their spectroscopic properties. A Stokes-Shift increase from 76 nm up to 116 nm between DCM and **4**-dye was observed. Both synthesized dyes are very suitable as fluorescent dyes in POF applications because they have a large Stokes-Shift of 115 nm (**2**-dye) and 116 nm (**4**-dye), thereby reducing undesirable reabsorption effects. The integration of both dyes in a polymer was also successfully done. The obtained preform with **2**-dye was drawn to a polymer optical fibre, which can be used for various applications. Further experiments to functionalize compound **2** und **4** with polymerizable groups are planned.

5. Acknowledgements

6. References

[1] K. Kuriki und Y. Koike, Plastic optical fiber lasers and amplifiers containing lanthanide complexes, Chem. Rev. 2002, 102 (6), 2347 - 2356; DOI: 10.1021/cr010309g.

[2] S. Nakazono, Y. Imazaki, H. Yoo, J. Yang, T. Sasamori, N. Tokitoh, T. Cédric, H. Kageyama, D. Kim, H. Shinokubo, A. Osuka, Regioselective Ru-Catalyzed Direct 2,5,8,11-Alkylation of Perylene Bisimides, Chem. Eur. J. 2009, 15, 7530 - 7533; DOI: 10.1002/chem.200901318.

[3] D. Zaremba, R. Evert, L. Neumann, R. Caspary, W. Kowalsky, H. Menzel, H.-H. Johannes, Methacrylate-Based Copolymers for Polymer Optical Fibers, Polymers, 2017, 9, 34; DOI:10.3390/polym9020034
[4] E. Torres, M. N. Berberan-Santos, M. J. Brites, Synthesis, photophysical and electrochemical properties of Perylene dyes, Dyes Pigm. 2015, 112, 298 - 304; DOI: 10.1016/j.dyepig.2014.07.019.

[5] M. Meyer, J.C. Mialocq, Ground state and singlet excited state of laser dye DCM: Dipole moments and solvent induced spectral shifts. Opt. Commun. 1987, 64 (3), 264 - 268; DOI: 10.1016/0030-4018(87)90390-7.

[6] J. Bourson, D. Doizi, D. Lambert, T. Sacaze, B. Valeur, A derivate of laser dye DCM highly soluble in alkohols, Opt. Commun. 1989, 72 (6), 367 - 370; DOI: 10.1016/0030-4018(89)90441-0.

[7] E.G. Marason, Laser dye DCM: CW, synchronously pumped, cavity pumped and single-frequency performance, Opt. Commun. 1981, 37 (1), 56 - 58; DOI: 10.1016/0030-4018(81)90176-0.

Setup for the Investigation of the Influence of a Controlled Cool Down Process on the Mechanical Properties of Thermal Drawn Polymer Optical Fibers

F. Jakobs, R. Evert, D. Zaremba, J. Kielhorn, H.-H. Johannes*, W. Kowalsky

Technische Universität Braunschweig, Institut für Hochfrequenztechnik, Labor für Elektrooptik, Bienroder Weg 94, D-38106 Braunschweig, Germany.
*Corresponding author: h2.johannes@ihf.tu-bs.de

Abstract: In purpose to develop new polymer materials for POFs, the influence of the drawing process on material properties must be well known. This works focuses on a drawing tower setup, which allows to create various different cool down profiles for the drawn fiber. This is realized by using a sectional heatable glass housing in the cool down region. This allows the fiber to cool down under defined conditions all over its length. By knowing these conditions exactly, it is possible to learn more about the impact of the cool down process.

1. Introduction

PMMA-based Polymer Optical Fibers (POFs) are used in short distance data transfer. In contrast to optical fibers made from glass, POFs are much more insensitive against bending and stretching. Nevertheless, it is necessary to develop new materials improving the mechanical properties of the fibers and to make them usable in a wider range of applications.

As short polymer optical fibers drawn from small material batches are valuable for material research, it is necessary to be acquainted with the influence of the thermal drawing process on the mechanical properties of the fiber. By knowing that influence, the properties of the polymer itself can be examined. Furthermore, the mechanical stability of thermally drawn polymer optical fibers can be improved by empirical optimization of the cool down process. During the fiber drawing process, polymer chains align along the fiber axis. This effect is amplified by increasing drawing speed as well as decreasing furnace temperatures while drawing [1]. Thermal annealing causes the polymer to return to isotropic chain orientation. For highly aligned fibers this can cause a strong decrease in fiber length [1, 2]. A fast cooling of the drawn fiber, which is similar to an instant cooling of a polymer melt, leads to free volume effects [3, 4, 5]. While these topics already have been investigated, the influence of the cool down process on mechanical properties are in the focus of research here.
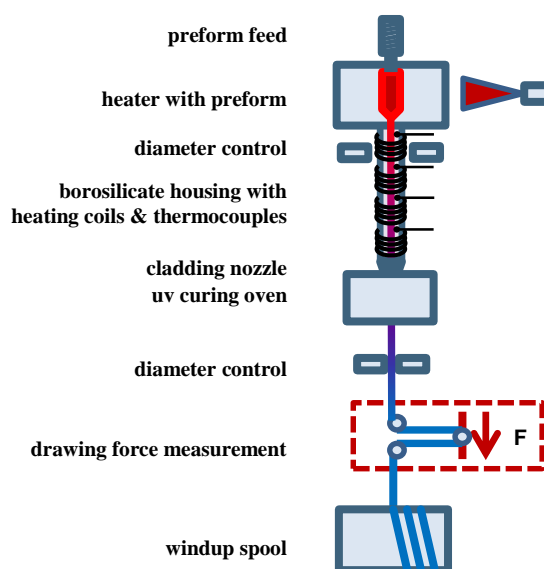

Figure 1. Drawing tower setup for polymer optical fibers.

2. Experimental

2.1 Controllable cool down section

The presented setup is an extension of the custom built fiber drawing tower shown in [7]. In Fig. 1, the schematic of the drawing tower is shown. Borosilicate tubes with an outer diameter of 28 mm and wall thickness of 1 mm are used to house the fiber path from the oven to the coating unit. With a spacing of 10 cm, holes are drilled radially into the tube as inlets for temperature sensors. For this application, calibrated type-K thermocouples were used for temperature monitoring.

The temperature gradient along the tube is generated by multiple heating coils which are powered by remote-controllable power supply which provide up to 15 A / 32 VDC. The heat coils consist of 0.6 mm Kantal (FeCrAL) wire with 30 windings per 10 cm segment. The pipe can be flushed with nitrogen from the top. The nitrogen flow smoothens the axial temperature gradient between the individual zones. The stability of the gradient along the cool down sections is dependent on the flow, the combination of the temperatures in the individual heating zones and the stability of the single temperature zones itself. PID controller are used to remote control the power supplys of the heating coils.

2.1 Mechanical characterization

The mechanical strength measurement of the drawn POF is based on the methods described in the German VDI / VDE guideline 5570 [8]. The sample fiber is fixed on both sides to fiber drums as shown in Fig. 2. Fiber ends are connected to a tungsten halogen source and the measurement receiver. The force is continuously measured while the fiber is elongated at a constant rate of extension of 100 mm/min. Tensile force, extension and transmitted optical power are measured.
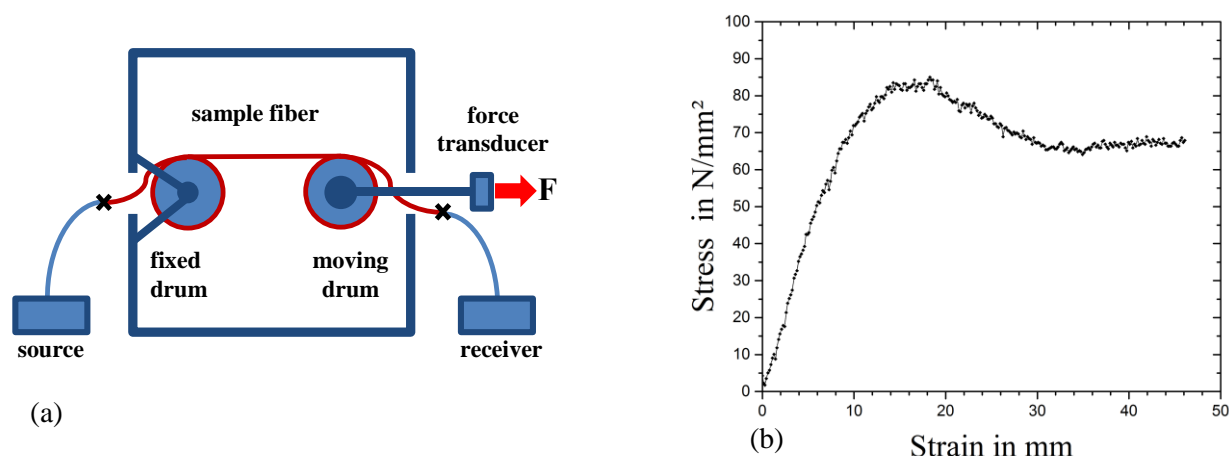

Figure 2. Schematic test setup for tensile tests (a) and measured stress-strain-curve for slowly cooled down PMMA-fiber (b).

3. First results on performance of the setup
3.1 Temperature stability

Temperature stability was measured twice over time. First, a single heating zone was used to investigate the influence of the PID controller. As shown in Fig. 4a, the temperature inside the housing - measured in the middle of the heating zone - is oscillating with a period of 30 s due to the interval of the PID controller. However, the maximum peak to peak temperature range is 3,5 °C, which appears to be appropriate when taking into consideration, that type K-thermocouples, although calibrated, haven an uncertainty of +/- 1 °C. The stability of the temperature gradient along the housing is shown in Fig. 4b. Again, all temperatures have been measured in the middle of the heating zones. Measuring spots have a spacing of 10 cm. T1 was measured below the oven and T4 was the lowest measuring spot. Measuring was started when the temperature reached be steady state inside the pipe. There was no nitrogen flow during measurement. As seen in Fig. 4b, the temperature drift is the stronger at the upper measuring points. This appears to be a result of convection flow inside the housing.
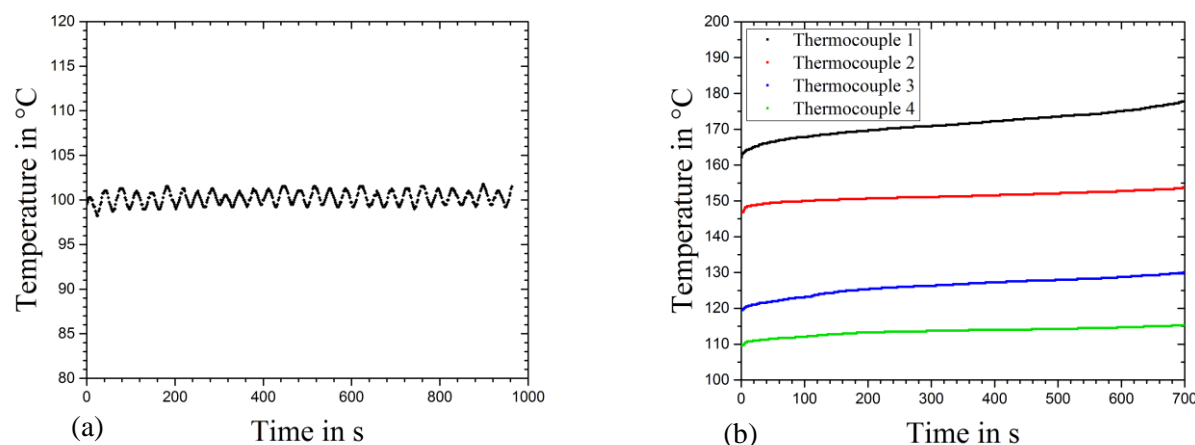
Figure 3. Temperature stability of an PID-controlled, single heating zone (a) and stability of four heating zones driven with constant current (b).

4. Conclusion

We presented an extension setup for our fiber drawing tower for investigating the influence of cool down ramp to mechanical properties. The setup and can provide a sufficient stable temperature gradient along the cool down segment. However, there is still a slight temperature drift due to convectional flow. This may be prevented by the use of an upward nitrogen flow. Using this technique also has the advantage of having the highest temperatures right on top of the housing, whereas a nitrogen downstream could cause a colder temperature zone right below the oven.

5. Outlook

As the mechanical characterization is working as well as the cool down section, we now can set up multiple measurement series with different cool down ramps. Influences on the tensile strength will be investigated as well as on shrinkage and bending losses.

3. Acknowledgements

4. References

[1]   Kuzyk, M. G. (2006). *Polymer Fiber Optics: materials, physics, and applications*. CRC press.
[2]   Jiang, C., Kuzyk, M. G., Ding, J. L., Johns, W. E., & Welker, D. J. (2002). Fabrication and mechanical behavior of dye-doped polymer optical fiber. *Journal of Applied Physics*, *92*(1), 4-12.
[3]   Fox Jr, T. G., & Flory, P. J. (1950). Second-order transition temperatures and related properties of polystyrene. I. Influence of molecular weight. *Journal of Applied Physics*, *21*(6), 581-591.
[4]   Cowie, J. M. G., & Arrighi, V. (2007). *Polymers: chemistry and physics of modern materials*. CRC press.
[5]   Tieke, B. (2014). *Makromolekulare Chemie: Eine Einführung*. John Wiley & Sons.
[6]   Koike, Y. (2014). *Fundamentals of plastic optical fibers*. John Wiley & Sons.
[7]   Caspary, R., Zaremba, D., Evert, R., Schutz, S., Mohl, S., Cichosch, A., ... & Kowalsky, W. (2014, July). Single-mode polymer optical fibers. In *Transparent Optical Networks (ICTON), 2014 16th International Conference on* (pp. 1-4). IEEE.
[8]   Daum, W., & Scholl, M. (2002). VDI/VDE-Guideline 5570-The First Comprehensive Standard on Characterization and Testing of POF.

Efficient WDM Transmission over SI-POF with a 4-channel LED Module

R. Kruglov[1*], J. Vinogradov[1], W. Huber[2], R. Engelbrecht[1], O. Ziemann[1]

1 POF-AC, Technische Hochschule Nürnberg Georg Simon Ohm, Wassertorstrasse 10, 90489 Nuremberg, Germany
2 Chips 4 Light GmbH, Nürnberger Straße 13a, 93152 Etterzhausen, Germany
*Corresponding author: roman.kruglov@pofac.th-nuernberg.de

Abstract: We report on a wavelength-division multiplexing (WDM) polymer optical fiber (POF) transmission system with a 4-channel light-emitting diode (LED) module operating at 410 nm, 440 nm, 520 nm and 660 nm. Efficient WDM coupling of all four wavelengths to a single POF is demonstrated as well as a power-efficient demultiplexer based on interference filters. A maximum aggregate bit rate of 5.3 Gb/s over 1 m and 2.4 Gb/s over 30 m of a 1-mm SI-POF at a bit-error ratio of 10^{-3} was achieved with a non-return-to-zero modulation scheme and a decision feedback equalizer, allowing error-free transmission after conventional forward error correction.

1. Introduction

Wave-division multiplexing (WDM) is a well-known technique typically used with optical fibers made of silica glass. Simultaneous data transmission at several optical carrier wavelengths over a single fiber allows to increase considerably the overall system throughput. Application of this technology might also help to improve the transmission capacity of polymer optical fibers (POF). POFs are a flexible and cost-effective solution for short-reach applications. They offer a large alignment tolerance, ease of installation and robustness against mechanical stress and electromagnetic tolerance. Using light-emitting diodes (LED) as transmitters for such systems is a preferred choice, since they meet cost and reliability advantages of the POF technology.

Previous publications [1,2] seemed to indicate that LED technology cannot provide high-speed WDM transmission with sufficient margin. However, current progress in the manufacturing of high-power and high-speed LEDs [3,4] brings now an opportunity to improve the performance of these systems. A record capacity of 11 Gb/s over 10-m link of 1-mm core-diameter step-index (SI) POF by using of three LED-based spectral channels was reported in [5]. Here, an avalanche photo-diode was required to increase the sensitivity of the receiver, but at the sacrifice of higher complexity and overall costs.

An alternative approach to increase the power margin is the optimization of the passive components, e.g. multiplexer (MUX) and demultiplexer (DEMUX). As a simple multiplexer for WDM POF links a multimode fiber coupler [6] is often used which provides generally an overall low light coupling efficiency to LED transmitters. However, the high NA and large core diameter of SI-POF allow to arrange several laser diodes (LD) or LED chips in a single butt-coupled transmission module. This eliminates a coupler from the transmission system and helps to achieve a higher power margin. In [7] the principles of WDM communication over 250 µm core-diameter graded-index POF with butt-coupled four-channel transmitter and receiver modules have already been described. In [8] 3.7 Gb/s WDM transmission with a 4-channel LED module over 1 m of a 1-mm core-diameter SI-POF using a grating-based DEMUX has been reported.

In this letter we demonstrate an improved aggregate bit rate of 5.3 Gb/s by using a 4-channel LED module for WDM POF-based applications operating at 410 nm, 440 nm, 520 nm and 660 nm combined with an interference-filter based DEMUX. Radiation and spectral parameters, as well as transmission characteristics of the LED module were measured and validated for POF transmission applications. The LED module was tested as a part of a WDM SI-POF transmission link. Two different DEMUXs based on a planar diffraction grating and interference filters are compared. The overall throughput of the transmission system was measured by employing of non-return-to-zero (NRZ) modulation scheme offering a low complexity of transceivers.

2. LED module characterization

The top view of the butt-coupled LED module is shown in Figure 1. The contour of a 1 mm core-diameter SI-POF is marked with a black dashed circle. The module includes four LEDs which are intended initially for

lighting applications. The LED chips operating at 410 nm, 440 nm, 520 nm and 660 nm are mounted on a customer-specific ceramic substrate. A protection glass is fixed with a silicone compound.
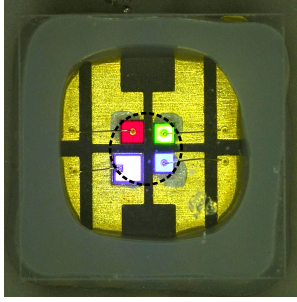

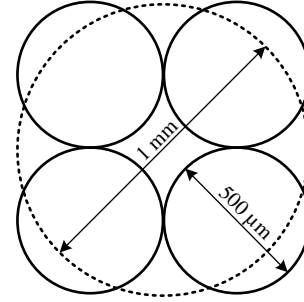Figure 1. Top view of the LED module.

Figure 2. Schematic of 4:1 coupler with 500-µm SI-POFs butt-jointed to a 1-mm diameter SI-POF.

To show an advantage of the four-channel LED module in terms of coupling losses it was compared with a typical coupler that could be used with single LEDs. The 4:1 coupler (see Figure 2) uses four 500-µm diameter input SI-POFs butt-jointed to a 1-mm diameter SI-POF with a standard FSMA coupling [9]. Due to the high numerical aperture of POF the connection losses between these two types of the fibers in the coupler do not exceed 1.7 dB. Power levels of single LEDs measured after 4:1 coupler connected with a 1-m length SI-POF are shown in the second column of the Table 1.

Table 1. Coupling efficiency of LED module to POF

Operating wavelength, nm	Fiber-coupled power at 30mA and room temperature, dBm			Gain 4:1 coupler vs. LED module, dB
	Single LED with 4:1 coupler	Single LED with 1-mm SI-POF	LED module with 1-mm SI-POF	
410	0.6	8.1	7.2	6.6
440	1.3	7.3	6.3	5.0
520	-3.1	3.0	2.2	5.3
660	-1.1	5.5	4.5	5.6

By simultaneous use of four LEDs with a single 1-mm core-diameter POF the fiber position was adjusted in a way to provide a nearly equal power reduction for all chips which results in approx. 1 dB loss (see third and fourth columns in Table 1). The overall losses for the coupler-based solution are 5-7 dB worse in contrast to the butt-coupled LED module (see fifth column in Table 1), which is due to a reduced coupling efficiency of the LEDs to a 500-µm SI-POF.

The 3-dB$_{el}$ bandwidths of 8.5 MHz, 17.5 MHz, 20 MHz and 16 MHz correspond to LEDs operating at 410 nm, 440 nm, 520 nm and 660 nm respectively [8]. These moderate values show that LEDs are not optimized for data transmission. The emitting spectra of LEDs are shown in Figure 3. FWHM spectral widths are 24 nm, 20 nm, 40 nm and 18 nm respectively.

3. Demultiplexer characterization

Recent publications show that typical insertions losses of DEMUX for WDM-POF system do not exceed 10 dB [10]. Most of these DEMUXs are based on a diffraction grating and thus provide a relatively narrow width of the spectral channels. Figure 3a shows the spectral characteristics of a DEMUX from previous work [8] which is based on a planar holographic diffraction grating (Carl Zeiss) with groove density of 1800 mm^{-1}. The DEMUX losses measured at the central wavelengths of LEDs are within the range of 7 - 10 dB. The actual insertion losses of this DEMUX for the total power of these LEDs as optical sources are within the range of 15 to 17 dB which is due to the broad spectral width of LEDs.

Figure 3b shows the spectral characteristics of a the DEMUX based on three longpass interference filters produced by CVI Melles Griot. As can been seen from the figure the spectral widths of the DEMUX channels fit much better to those of the LEDs. Thus, the difference between losses measured at the central operation wavelengths and actual values for the total power of these LEDs does not exceed 2.5 dB. Figure 4 shows a sketch of this filter-based DEMUX. The orientation angles of the dichroitic longpass interference filters (LF)

were adjusted to provide accurate splitting of the spectral channels. Additional bandpass interference filters (BF) at the DEMUX outputs provide the required crosstalk attenuation higher than 20 dB.
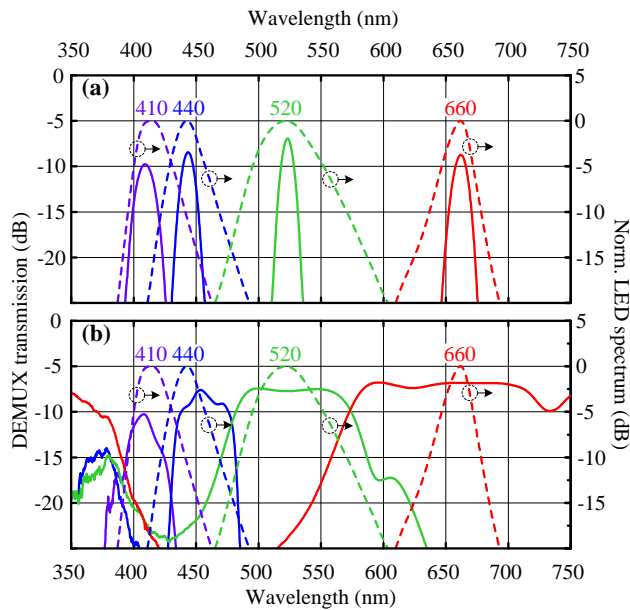

Figure 3. Transmission characteristics (solid lines) of the DEMUXs based on diffraction grating (a) and interference filters (b) and LEDs spectra (dashed lines).
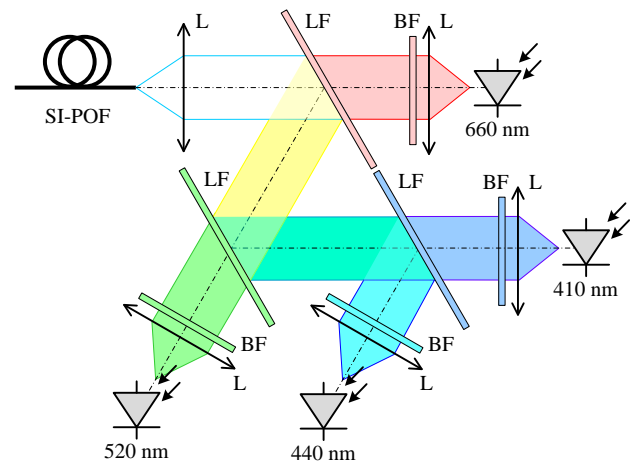

Figure 4. Schematic of four-channel demultiplexer: L – lens; LF – longpass interference filter; BF – bandpass interference filters.

4. Data transmission experiments

The WDM system consists of a 4-channel LED module, a SI-POF Mitsubishi GH 4001 with 1-mm core diameter (POF class A4a.2, according IEC 60793 2 40), an optical wavelength DEMUX based on interference filters, and optical receivers with $\varnothing$ 800 µm silicon pin photodiodes (Hamamatsu S5052) connected to trans-impedance amplifiers. The received power measured at the outputs of the DEMUX is shown in Table 2. An arbitrary waveform generator Tektronix 7102 and a real-time oscilloscope Tektronix DSA 71604 were used as digital-to-analog and analog-to-digital converters, respectively.

The four LEDs operating at a bias-current of 30 mA were modulated over a Bias-T by NRZ signals based on pseudo-random binary sequences (PRBS $2^7 - 1$). To provide a proper level of the modulation signal additional preamplifiers MERA 556+ (Mini Circuits) were used. A T/2 fractionally spaced decision feedback equalizer (DFE) with 16 feedforward and 4 feedback taps was employed for the post-processing of the received signals. The bit error ratio (BER) was then evaluated by direct error counting.

Table 2. Transmitted and received optical power after DEMUX

Channel, nm	Fiber-coupled optical power, dBm	Received power 1-m link, dBm	Received power 30-m link, dBm	Photosensitivity, A/W
410	7.2	-6.4	-12.3	0.21
440	6.3	-5.2	-8.7	0.23
520	2.2	-7.6	-9.3	0.29
660	4.5	-3.7	-10.0	0.39

The maximum throughput in spectral channels (see Figure 5) was measured for the link with 1-m length and 30-m length SI-POF at a bit-error ratio (BER) of 10^{-3} which is sufficient for implementation of a forward error correction (FEC) with 7% overhead.

The maximum bit rates achieved over 1-m link were 1 Gb/s, 1.2 Gb/s, 1 Gb/s and 2.1 Gb/s for the spectral channels operating at 410 nm, 440 nm, 520 nm and 660 nm, respectively. The maximum bit rates achieved over the 30-m link were 0.3 Gb/s, 0.7 Gb/s, 0.6 Gb/s, 0.8 Gb/s respectively. Thus, aggregate bit rates of 5.3 Gb/s and 2.4 Gb/s were achieved at a BER of 10^{-3} over 1-m and 30-m SI-POF, correspondingly.
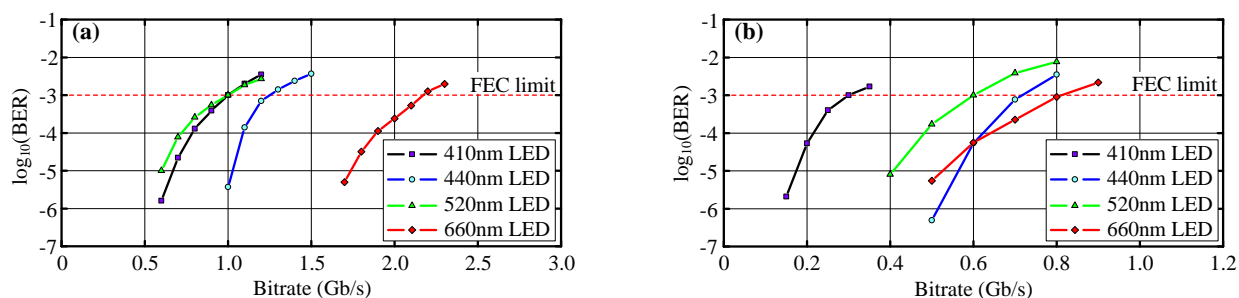
Figure 5. BER versus bit rate over 1-m link (a) and 30-m link (b).

The most considerable reduction of the system performance by increasing the fiber length occurs in the 410-nm and 660-nm spectral channel which is caused by the relatively high attenuation in PMMA SI-POF at the corresponding wavelengths.

5. Conclusion

Implementation of modern optical components like multi-channel LED modules optimized for POF data transmission allows to increase the system throughput and power budget margin which brings an opportunity to offer a competitive solution for low-cost short-reach high-speed data communication. The described optical module allows arranging four LED chips in a single butt-coupled transmission module which reduces the coupling losses. Further improvements might be resulted from employing specialized high-speed LEDs [4,5].

In comparison to the previously published work [8] the DEMUX with longpass interference filters provides a better system performance due to an accurate matching of its spectral channel widths with those of the LEDs. This results in a significant increase of SNR and power-budget as well as an increase of the maximal bit rate by 1.6 Gb/s compared to grating based WDM system [8].

6. Acknowledgements

7. References

[1] S. Junger, W. Tschekalinskij, N. Weber, "POF WDM Transmission System for Multimedia Data," in *Proc. 11th Int. Conf. on Polymer Optical Fibers*, Tokyo, 2002, pp. 69-71.

[2] V. Appelt, J. Vinogradov, O. Ziemann, "Simple FEXT Compensation in LED Based POF-WDM Systems," in *Proc. 11th Int. Conf. on Polymer Optical Fibers*, Tokyo, 2002, pp. 127-129.

[3] J. Vučić, C. Kottke, K. Habel, K.-D. Langer, "803 Mbit/s Visible Light WDM Link based on DMT Modulation of a Single RGB LED Luminary," in Proc. *OFC*, 2011, pp. 1-3, paper OWB6.

[4] J.-M. Wun, *et al.*, "GaN Based Miniaturized Cyan Light Emitting Diodes on Patterned Sapphire Substrate with Improved Fiber Coupling for Very-High-Speed Plastic Optical Fiber Communication," *IEEE Photon. J.,* vol. 4, no. 5 Oct., 2012, pp. 1520-1529.

[5] X. Li, *et al.*, "11 Gb/s WDM Transmission Over SI-POF Using Violet, Blue and Green μLEDs," in Proc. *OFC*, 2016, pp. 1-3, paper Tu2C.5.

[6] R. Kruglov, et al., "10.7 Gb/s WDM Transmission over 100-m SI-POF with Discrete Multitone," in Proc. *OFC*, 2016, pp.1-3, W4J.5.

[7] J. Mizusawa, "Advantage of POF WDM System Design," in Proc. 8th Int. Conf. on Polymer Optical Fibers, Chiba, 1999, pp. 31-35.

[8] R. Kruglov, J. Vinogradov, O. Ziemann, W. Huber, "Application of 4-channel LED Module for WDM Transmission over SI-POF," in Proc. *25th Int. Conf. Polymer Opt. Fibers*, Birmingham, 2016, pp. 1-3, paper OP9.

[9] O. Ziemann, J. Krauser, P. Zamzow, and W. Daum, *POF-Handbook: Short Range Optical Transmission Systems*, 2nd ed. Berlin, Germany: Springer-Verlag, 2008.

[10] Pinzon P, *et al.*, "Efficient Multiplexer/Demultiplexer for Visible WDM Transmission over SI-POF Technology," *J. of Lightw. Technol.* 2015, vol. 33, no. 17, 1 Sept., 2015, pp. 3711-3718.

Molecular Dynamics Simulation for the Cooling Behavior of GI-POF

D. Grothe[1], M. Beckers[1*], T. Gries[1], C.-A. Bunge[2]

1: Institut für Textiltechnik at RWTH Aachen University, Aachen, Germany
2: Hochschule für Telekommunikation Leipzig, Leipzig, Germany

*Corresponding author: markus.beckers@ita.rwth-aachen.de

Abstract: We study a novel production process for polymer optical fibers with gradient index (GI-POF) uses a specific cooling behavior of the spun fiber to create the characteristic refractive index profile. By cooling the polymer in a specific way, a density profile is created in the fiber. The density directly affects the refractive index. A molecular dynamics simulation has been developed, to analyze these effects. By simulating different cooling behaviors, its correlation between density and refractive index of the polymer is examined.

1. Introduction

For data transmission with high bandwidths and for sensing applications, polymer optical fibers with gradient index (GI-POF) often provide a reasonable alternative to glass fibers [1]. Due to their relatively large diameter, they are easier to handle than the much smaller and more delicate glass fibers. To meet the required specifications of the applications, especially high bandwidths, a characteristic gradient refractive-index profile is required. The production process of GI-POF currently consists of the spinning process and its refinement in a non-continuous way, which is expensive and complex [2]. A novel production process for GI-POF has been developed to fabricate GI-POF directly in a continuous way [3]:

Based on the conventional and low-priced melt spinning process, the spun fiber is cooled using a specific cooling behavior. The different cooling rates along the fibers cross section create a density profile because the polymer molecules in the center of the fiber have longer time to pack themselves in an energetic favorable way. There is a direct dependence between the density of the fiber and its refractive index. This leads to the desired refractive-index profile, which is characteristic to GI-POF [3]. Fig. 1 visualizes the physical principle of the novel production process of GI-POF.
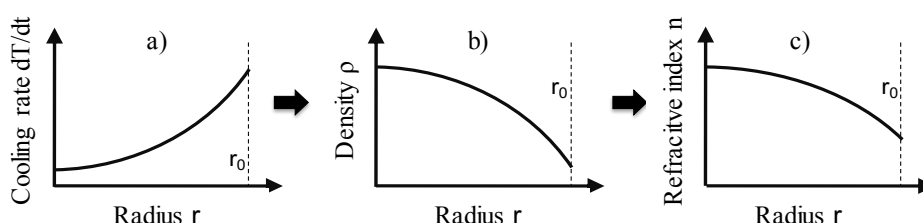

Figure 1. Principle of the novel production process for GI-POF

To demonstrate the effects, the cooling behavior has on the fiber density, a numerical model of the molecular dynamics has been developed. In a molecular-dynamics simulation, the intermolecular and intramolecular interactions between molecules in a system volume are calculated in the time domain and equations of motion are integrated for every time step. The resulting simulated system can be evaluated for its system properties such as temperature, pressure and density. Using the simulation, we can simulate the effects of different cooling behaviors on the density and the refractive index of the polymer.

2. Simulation algorithms

The basic molecular dynamics simulation consists of five steps as shown in Fig. 2.

Initial configuration

Firstly, the initial configuration is created. The simulation volume is filled with polymer molecules, which are initialized with random positions and velocities according to a Maxwell-Boltzmann distribution. Constraints are created to describe the intramolecular bonds. The constraint algorithm is explained further below.
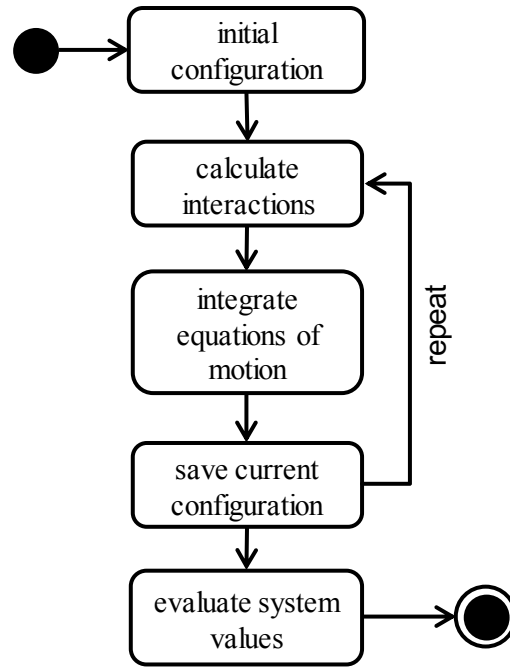
Figure 2. General flow diagram of the molecular dynamics simulation

Molecular interactions

After the initial configuration, in each time step interactions between the atoms are calculated. This is done using the Lennard-Jones potential $\mathcal{V}(r)$, which can be differentiated to obtain the force F between the atom pairs [4]:

$$F = -\frac{\partial \mathcal{V}(r)}{\partial r} \tag{1}$$

Using the calculated forces, the equations of motion can be integrated, to update the atoms' positions and velocities. The velocity Verlet algorithm provides a suitable compromise between accuracy and computing time [4]:

$$r(t + \Delta t) = r(t) + v(t) \cdot \Delta t + \frac{F(t)}{2m} \cdot \Delta t^2 \tag{2}$$

$$v(t + \Delta t) = v(t) + \frac{F(t+\Delta t) + F(t)}{2m} \cdot \Delta t \tag{3}$$

The simulation steps are then repeated. After a specified number of time steps, the system is evaluated. Thermodynamic properties such as temperature, density and pressure are calculated.

Constraints

To minimize boundary effects and to lower the number of calculated atoms, periodic boundary conditions are used. At all its boundaries, the simulation cell is mirrored. The mirrored neighbors interact with the atoms in the main cell and can move in or out of their own cell. In this way, the simulation volume appears to be infinitely large although only a small volume has to be really modelled.

To simplify calculations of intramolecular interactions, atomic bonds within molecular chains are modelled as constraints between the atoms. These constraints ensure bonding length and bonding angle between the atoms, without the computational cost of the full simulation of all interactions. A constraint for the bonding length between two atoms may look like the following:

$$\sigma_{ij} = \left[r_i(t) - r_j(t)\right]^2 - d_{ij}^2. \tag{4}$$

Here σ_{ij} represents the change of the distance between the atoms i and j. In each time step, the positions and velocities have to be adjusted to satisfy $\sigma_{ij} = 0$. This is done in an iterative way. The used algorithm is the rattle algorithm [5-6].

Typically, a molecular dynamics simulation has a constant number of elements, constant volume and no energy flow across the system boundaries. Unfortunately, this ensemble is not suitable for our simulation goals, as we want to simulate the cooling behavior of the spinning process. The cooling of the spun fiber is done at atmospheric pressure. Also, to describe the cooling behavior, we need to control the system temperature. This is done by using a Berendsen thermostat, which connects an external virtual heat bath with the system. The thermostat compares the system temperature of the current time step with the targeted temperature and accelerates each atom accordingly. Likewise, a Berendsen barostat regulates the system pressure by increasing and decreasing the system volume [7].

3. Verification

The implementation of the described algorithms has been verified by various test cases. Simulations with different configurations and in different ensembles were calculated and evaluated.

Simulations with a constant number of elements, volume and energy have been done to test the fundamental functionality of the implementation. Additional algorithms for constraints, thermostat and barostat were disabled in this step. The velocities have been evaluated after the initial configuration, as well as the root mean square deviation (RSMD) of the energy and convergence of system temperature and system pressure during the simulation. The results are shown in Fig. 3.
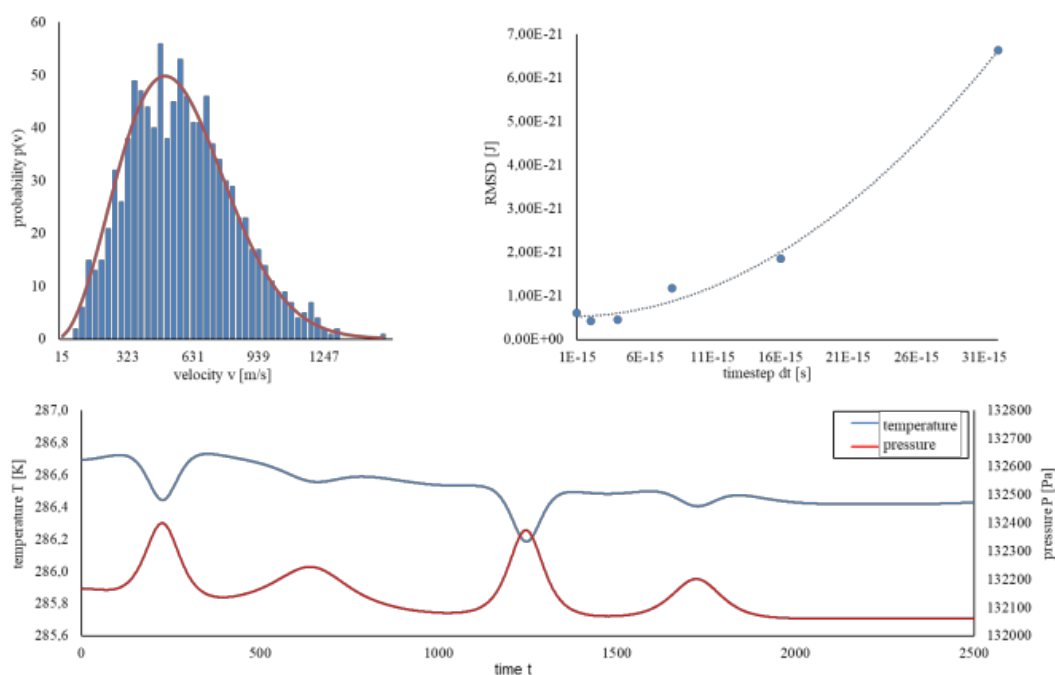

Figure 3. Velocity distribution of initial configuration (top left), RSMD of the energy dependent on the length of the time step dt (top right) and convergence of temperature and pressure during the simulation (bottom)

The generation of the initial configuration aims for Maxwell-Boltzmann distributed velocities, which represent a thermal equilibrium. As can be seen in the histogram, the velocities of the polymer chains show a Maxwellian distribution. According to [8], the RSMD of the energy increases proportionally to dt^2, which is visible in the simulation results with various values for dt. With longer simulation time, the system values converge to an equilibrium. This results in a smaller deviation of the system values for longer simulation times. The effect is shown for the system temperature and system pressure (cf. Fig. 3).

Simulations with the use of thermostat and barostat have been done to achieve constant atmospheric pressure and a constant system temperature. As seen in Fig. 4, the temperature and the pressure converge with the set values. Also, the density, which is the system value we are mainly interested in, converges accordingly.
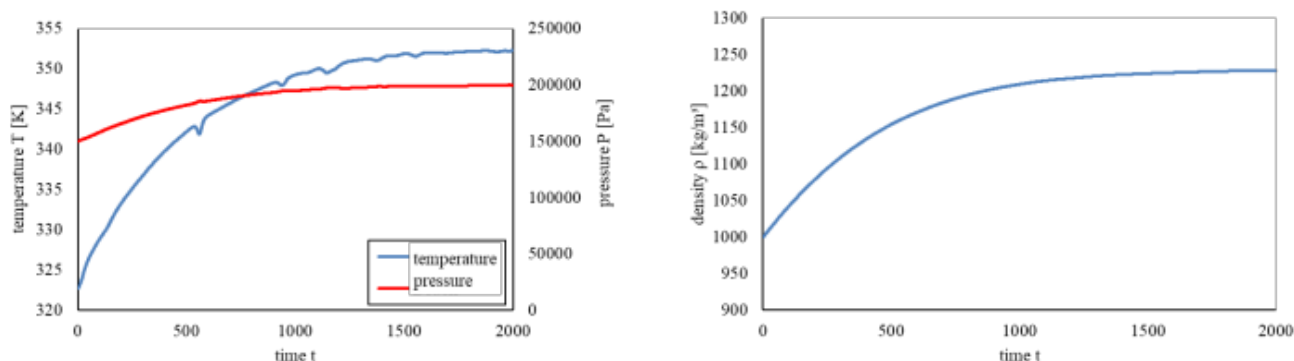
Figure 4. regulated temperature and pressure by thermostat and barostat, density during the simulation

4. Conclusion and outlook

The goal of the molecular-dynamics simulation is to simulate the cooling behavior of spun polymer fibers. By cooling the polymer melt in a specific way, the characteristic refractive-index profile should be created due to the changes in the density profile of the fiber. This relation of cooling behavior and polymer density is to be simulated.

The molecular dynamics simulation uses the Lennard-Jones-Potential to calculate interactions between the polymer chains. Intermolecular bonds are approximated by the iterative solving of constraints using the rattle algorithm. The velocity Verlet algorithm integrates the equations of motion to update positions and velocities of the polymer chains in each time step. To simulate under constant pressure and to set a specific cooling behavior, thermostat and barostat are used.

In future work, this simulation will be further expanded. The cooling behavior of PMMA is going to be simulated and the change of density evaluated. The implementation of the algorithms are going to be improved to calculate greater amounts of elements or for a longer time frame.

References

[1]: Bunge CA, Beckers M, Gries T. Polymer Optical Fibres: Fibre Types, Materials, Fabrication, Characterisation and Applications. Cambridge: Woodhead Publishing Ltd; 2016.

[2]: Ziemann O, Krauser J, Zamzow PE, Daum W. POF Handbook: Optical Short Range Transmission Systems. Berlin, Heidelberg: Springer Berlin Heidelberg; 2007.

[3]: Beckers M. Entwicklung und Analyse eines neuartigen Herstellungsverfahrens für optische Polymerfasern (POF). Dissertation. RWTH Aachen University: Shaker-Verlag; 2016.

[4]: Kotelyanskii M, Theodorou DN. Simulation Methods for Polymers. New York: Marcel Dekker; 2004.

[5]: Ryckaert JP, Ciccotti G, Berendsen HJ. Numerical integration of the cartesian equations of motion of a system with constraints: molecular dynamics of n-alkanes. J. Comput. Phys. 1977; 23:327–341.

[6]: Andersen HC. Rattle: A "velocity" version of the shake algorithm for molecular dynamics calculations. J. Comput. Phys. 1983; 52:24–34.

[7]: Berendsen HJC, Postma JPM, van Gunsteren WF, DiNola A, Haak JR. Molecular dynamics with coupling to an external bath. J. Chem. Phys. 1984; 81:3684.

[8]: Allen MP, Tildesley DJ. Computer simulation of liquids. Oxford: Clarendon Press; 1993.

Measurements with an FBG inscribed on a new type of polymer fibre

A. Theodosiou[1], O.Palchik[2], N. Tal[2], E. Shafir[3]*, G. Berkovic[3], S. Zilberman[3], and K. Kalli[1]

1 Nanophotonics Research Laboratory, Cyprus University of Technology, Limassol, Cyprus
2 Tecsolut Ltd, Gedera, Israel
3 Soreq NRC, Yavne, Israel

*Corresponding author: shafir@soreq.gov.il

Abstract: We present our latest achievements measuring the effects of temperature and pressure on a Bragg grating inscribed on a new type of non-PMMA polymer optical fibre. The fibre is produced using the Light Polymerization Spinning (LPS) process and the Bragg grating is written using a plane-by-plane femto-second laser inscription method. In particular, the 580 micron core fibre was designed to have a very low Young's modulus.

1. Introduction

Polymer optical fibres (POFs) are of interest for a number of applications, from illumination, light harvesting and sensing, to short-range data transmission in automobiles, buildings and industrial automation. A key requirement for the successful development of POFs is a variety of properties (mechanical, optical, etc...) that could be introduced into the POF material and a precisely controlled fibre production process.

Currently, the majority of POFs are made from one polymer - PMMA, and it substantially diminishes the number of possible applications for POFs, especially in the sensor field. Additionally, the POF production is inflexible requiring a number of techniques and manufacturing steps to arrive at the final product, an inflexibility that impacts the fibre's optical and mechanical properties. Unsurprisingly, the production process is long and complex and it is rarely possible to produce identical properties for two separate batch production runs, particularly when the fibre is produced with the heat-drawing process from a preform.

2. A new type of polymer fibre using Light Polymerization Spinning (LPS) process

The Tecsolut (formerly Intellisiv) company has recently presented [1] a new type of polymer optical fibre that has been developed based on an advanced, single-step, readily customizable and highly scalable Light Polymerization Spinning (LPS) process. In this process there is no polymer at the production starting point, instead formulations of commercially available monomers & other additives are used as required. A liquid formula injection process is followed by a very fast fibre UV polymerization. Thus the fibre formation and polymerization occurs simultaneously (Figure 1).
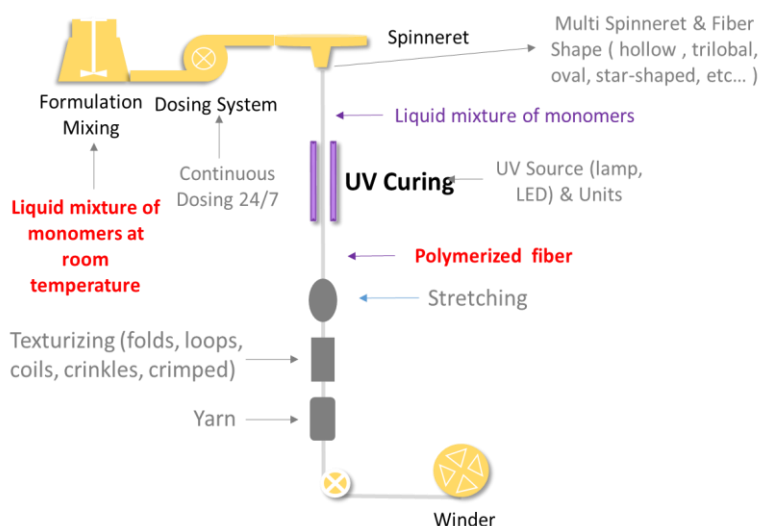

Figure 1. Light Polymerization Spinning process

Proper selection of different monomers and oligomers in the production starting point could produce POFs with vastly different mechanical or other properties (Figure 2).
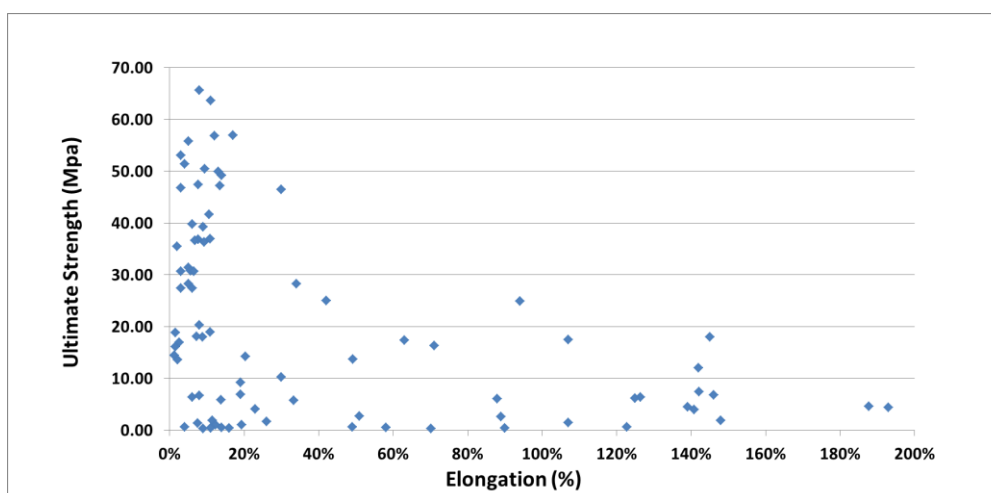
Figure 2. POFs produced by the LPS process. Each dot at this graph represents a POF with different mechanical properties (breakage strength and elongation)

Recently we have published some initial characterization results of some fibres produced by this method [2]. In addition, it was found that modified bisphenol-A fluorene diacrylates with high molecular weight could provide good optical properties and relatively very high elongation and elasticity (low Young Modulus). Here we present additional data, concentrating on one specific, very soft and flexible such fibre (580 μm core, NA=0.47), designated NTO34NTC5. This very low Young's modulus fibre demonstrates the high versatility of the aforementioned fibre production method.

3. Optical transmission of the fibres

Transmission measurements of the POFs were performed by the cut-back method [3] in which light is coupled into a given length of fibre and the transmitted power is measured as the fibre is shortened. To avoid uncertainties regarding coupling efficiency into the fibre, we successively shortened the fibre at its output end, without changing the input coupling conditions, measuring the transmitted power and calculating the loss from the changes in power transmission with fibre length.

The cut-back measurements were performed in two ways: a more accurate way using discrete wavelength (532nm) light, and a second way, more prone to experimental uncertainties, with a broadband visible source and a spectrometer, producing continuous spectral information. When the spectroscopic measurement yielded a result consistent with the laser measurement at 532nm, then the entire spectroscopic measurement was considered verified.

For the discrete measurement, our source was a 5mW 532nm laser (Global Laser Tech) coupled into a 600 μm core NA=0.39 silica fibre patch-cord, with SMA connectors (Thor Labs M21L05). The POF under test was cleaved with a razor blade, inserted into an appropriate SMA connector and butt-coupled to the silica fibre with an SMA fibre adapter. The output end of the POF was also cleaved and the power output was measured with an integrating power meter detector (Newport 818-IS-1). The fibre was cut-back three times to determine the attenuation.

The basis of the spectroscopic cut back measurement was to use as input a broadband 300-1,000 nm light source, coupled into the above mentioned 600 μm core NA=0.39 silica fibre patch-cord. A similar silica fibre patch-cord was permanently attached to the spectrometer SMA fibre input. The POF under test was butt-coupled between the two silica fibre patch-cords for the spectroscopic measurement (see Figure 3). As before, to avoid changes to the input coupling, the POF was successively cut back 3 times at its far end (i.e. the "spectrometer" end).

This set-up leaves as the only uncertainties the quality of the POF cleaves and the butt-coupling to the silica "spectrometer" fibre. As a consequence, we also expect that in this set-up insertion losses will be essentially

wavelength independent. As stated above, our validation is the compatibility of the spectroscopic 532nm result with that previously obtained with the 532nm laser.
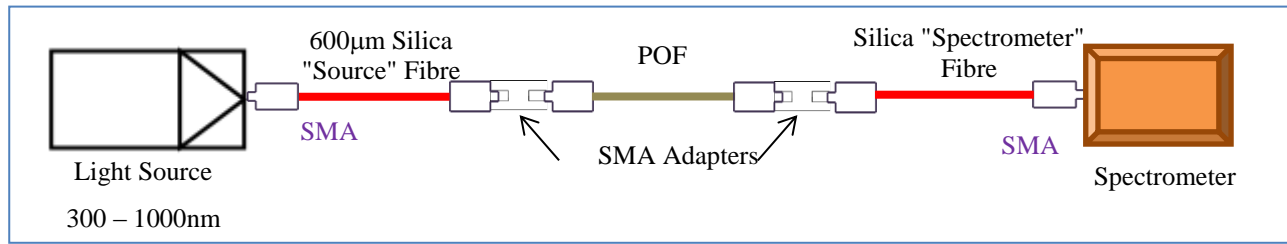

Figure 3: Set-up for spectroscopic cut-back measurements

In Figure 4 we present our results for the above mentioned fibre. The fibre loss is relatively flat over most of the visible range, with a steep increase in attenuation from 850nm.
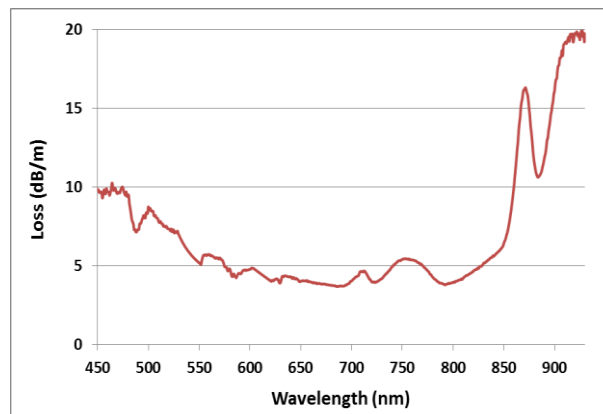

Figure 4: Spectral loss characterization of Tecsolut POF NTO34NTC5

4. Fibre Bragg Grating inscription and Characterization

The fibre sample was mounted on an air-bearing translation stage using a glass slide for a controlled motion during the inscription. The laser beam of a femtosecond laser (HighQ – femtoRegen) operating at 517 nm, with pulse duration of 220 fs and energy of ~40 nJ, was focused from the top of the fibre through a long-working-distance x50 microscope objective (Mitutoyo) mounted on a third stage. Using the Pl-by-Pl inscription method [5], we inscribed a 4th order FBG in the centre of the polymer fibre consisting of 2,000 planes of 50 μm width. The FBG period was calculated to be ~2 μm for a grating with a resonance wavelength at 1,560 nm.

Using the butt coupling method and an SMF-28 fibre circulator, we illuminated the grating with a broadband light source (Thorlabs-ASE730) and the reflection spectrum was measured using a spectrometer (Ibsen IMON) as shown in Fig. 5. After finding good alignment between the SMF and POF the fibres were glued together.
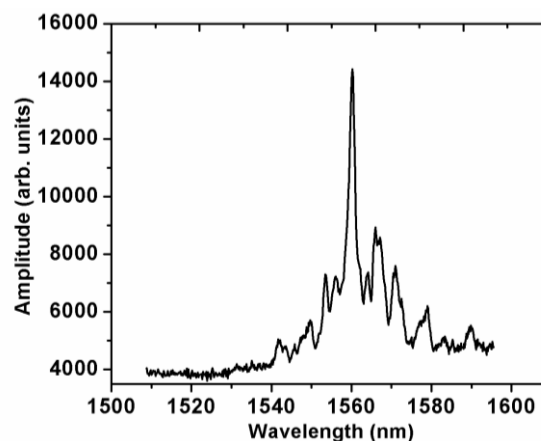

Figure 5: Spectrum of an FBG inscribed using the Pl-by-Pl inscription method on the Tecsolut POF NTO34NTC5

5. Measurements with the Fibre Bragg Grating

The sensing and measuring capabilities of the FBG inscribed with the plane-by-plane method on the Tecsolut POF were demonstrated for temperature and ambient pressure. Figure 6 (left) depicts initial results for the temperature response of the FBG peak wavelength, as measured in a climate chamber. Figure 6 (right) shows a measured response to ambient pressure, when the POF was inserted into a controlled pressure vessel.
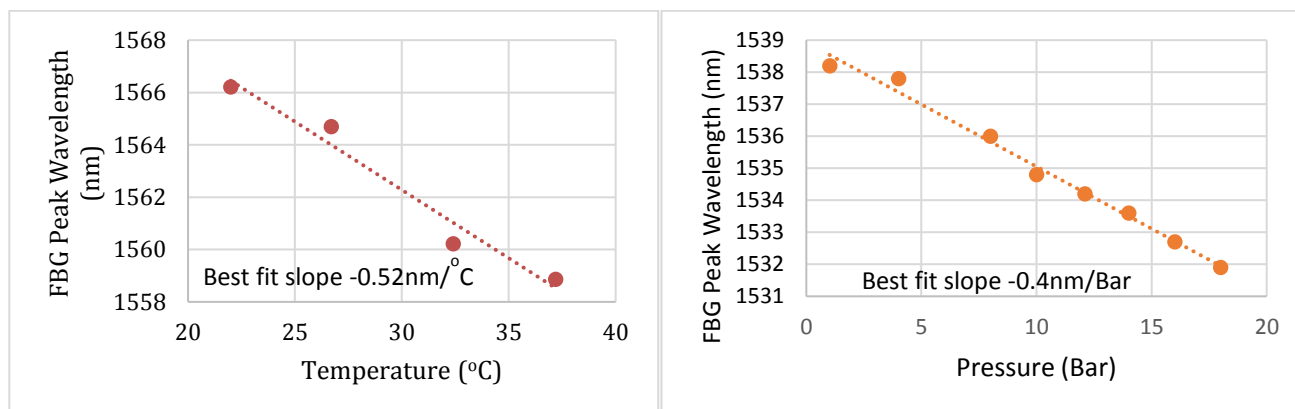

Figure 6: Wavelength response of the POF-FBG to (left) temperature and (right) ambient pressure

We would like to emphasize that the above results were not easily reproducible, and some of the experiments yielded different behaviours. We attribute this fact to hysteresis effects characterizing POFs in general as well as the highly multimode nature of the 580µm step-index POF, making reproducible and constant mode excitation of the POF very difficult. As noted these are preliminary results and additional characterization and preferably smaller core fibres are needed.

6. Conclusions

We have successfully manufactured and characterised a new type of a non-PMMA polymer optical fibre, produced by the Light Polymerization Spinning (LPS) process, which allows manufacturing of fibres with a wide range of mechanical properties. Also, using the plane-by-plane femtosecond laser inscription method, an FBG has been successfully inscribed on such fibres. For the first time, actual measurements have been performed with such a device demonstrating clear sensitivity to changes in temperature and pressure, though more work is needed in order to achieve reproducible, commercial grade results.

7. References

[1] O. Palchik, V. Palchik "Thermoset and thermoplastic fibers and preparation thereof by UV curing" US patent 20140294917.

[2] O. Palchik, N. Tal, E. Shafir, S. Zilberman, A. Theodosiou, K. Kalli "Characteristics of photo polymerized polymer optical fibres, optical properties and femtosecond laser inscription of Bragg gratings", POF-2016 – 25th International Conference on Plastic Optical Fibres, Conference Proceedings, pp. 78-81 (2017).

[3] See for example: M.G. Kuzyk, Polymer Fiber Optics: Materials, Physics, and Applications (CRC Press Boca Raton, FL.) 2007, p 146.

[5] A. Lacraz, M. Polis, A. Theodosiou, C. Koutsides, K. Kalli, "Femtosecond laser inscribed Bragg grating in low loss CYTOP polymer optical fiber", IEEE Photonics Technology Letters, 27, 7, 693-696, (2015)

POF
2017

Digitized Radio Over Plastic Optical Fiber for In-Home Network Applications

J. Heidarialamdarloo[1*], A.N. Sousa[1], E. F. J. Silva[2], R.S. Oliveira[2], R. M. Ferreira[2], A. Shahpari[2], R.N. Nogueira[2], J. C.W.A. Costa[3] and A. J. Teixeira[2]

[1] Department of Electronics, Telecommunications and Informatics, University of Aveiro and Instituto de Telecomunicações, 3810-193, Aveiro, Portugal.
[2]Federal University Western of Pará, Mendonça Furtado A., 2946, PC 68040R470, Santarém, PA, Brazil
[3] Federal University of Pará, Augusto Correa., 01, PC 66075R110, Belém, PA, Brazil.
*jamshid@ua.pt

Abstract: Radio over fiber system is the most used solution to integrate the capacity of optical fiber with the flexibility and mobility of wireless networks to support data traffic volumes on demand by end users. Graded index plastic optical fibers (GI-POFs) seem to be a very attractive alternative in home access networks when compared to the "classic" single/multimode glass optical fibers and CAT technology due to their easy installation and low prices. In this paper, we investigate and compared the transmission performance of the analog and digital radio over fiber systems over multimode GI-POF in home network scenario coexisting with 20km single mode fiber in optical access network. The performance of the two technologies is also compared by analyzing the error vector magnitude.

Keywords: plastic optical fibers, digitized radio over fiber, in-home network, EVM

1. Introduction

The rapid growth of personal smart/mobile electronic devices with new services has brought up new challenges for the next generation of both wired and wireless networks that will require unpredictable high bandwidth subscribers. Services such as ultra-high definition video streaming, online gaming, machine-to-machine communications and cloud computing are examples of applications that are fast becoming an essential part of the last mile data consumer needs, which has forced the telecommunications operators to design new solutions to improve the network infrastructure capacity, meet the user's challenging requirements while, at same time, address the growing cost pressure [1-3].

Nowadays, long-term evolution advanced (LTE-A) has been the main solution in the fourth generation of wireless (4G) access cellular technology, which can support up to 1Gbit/s data per user; with possibility of the reaching up to 10 Gbit/s in base stations (BS) with multiple sectors 4]. On the other hand, the 5th generation of mobile networks (5G), which is still undergoing through research and development, mainly focuses on, higher spectral efficiency, lower latencies, lower battery consumption scenarios [5][6]. However, from the practical point of view, conventional microwave links connecting the BS with the core of the wireless network is the main drawback due to it limited bandwidth.

In order to fulfill these challenges, the telecommunications operators are addressing solutions based on combining the optical network infrastructure and wireless broadband access to take advantage of the capacity of optical fiber with the flexibility and mobility of wireless networks. For the xhaul segment (i.e., fronthual and backhaul) the passive optical networks (PON) is a consolidated solution. However, this even-increasing demand for higher bandwidth needs to look for optical solutions for in office/home/curb/ building networks to extend the higher capacity of the PON and transport, in a transparent way, both wired and wireless signals [7][8]. In this context, the plastic optical fiber (POF), in particular; Graded-index (GI) POF provides many of 'user-friendly' benefits of the copper cables along with all the affordable performance advantages of the silica optical fiber channels and have emerged as potential solution of in home applications [9][10].

To meet this goal, Radio-over-Fiber (RoF) systems are considered a very promising solution to integrate the optical and wireless infrastructures to support data traffic volumes on demand access networks [7]. Several techniques of RoF system based on analog and digital radio signal have been proposed in the fronthaul segment. As the all transmission of the digital radio over fiber (DRoF) system is performed in digital domain it

takes a distinct advantage in compared to ARoF due to it the immunity to fiber degradations, e.g. fading due to chromatic dispersion and attenuation [11][12].

As a result, the main solution available by industry is based on DRoF concept, e.g. according to Common Public Radio Interface (CPRI). However, the main challenge of DRoF is the overall data rate that is related with a product of sampling rate and ADC bit resolution used in a digitization process, which can makes it less competitive and more cost-intense than ARoF system. Hence, we face this trade-off characterizing a DRoF with low cost in terms of bandwidth. .

In this paper, we characterized a low cost DRoF system and experimentally demonstrate a deliver digital baseband for users in a home access network, emulating 5G mobile fronthaul in C-RAN architecture. We present experimental results that address the impact of the ADC for higher and low overall data rate on the performance of the DRoF system in different scenarios, considering 50m of the GI-POF coexisting with 20 km of single mode fiber (SMF). The robustness of DRoF is compared with ARoF transmission tested in same conditions. Based on our analysis, the experiment results have confirmed that with the coexistence (i.e. SMF+GI-POF), 1.25 Gbits/s baseband signal with 16-quadrature amplitude modulation (QAM) can be accommodated in a low cost DRoF scheme.

2. Digitized Radio over GI-POFs Systems

2.1. Conceptual Diagram

DRoF transport schemes that combine both optical and electronic digitization are being studied and pointed as viable alternative solutions to ARoF systems [11]. The conceptual diagram of the proposed scenario to evaluate the implementation of the DRoF system in home access network is illustrated in Fig.1. The inbuilding network is supported by 50m of the GI-POF with attenuation of the 50dB/km at 1550 nm. The digitized signal at the output of the central office (CO), after passing 20 km of the standard SMF (SSMF) and through the building with multimode GI-POF, is propagated by the antennas to the end users. This implementation scheme can be implemented not only for more recent technologies (e.g., 4G and 5G), but also for legacy technologies existing in the network infrastructures such as 2.5G, 3G, WiFi and others.

2.2. Experimental Setup

The schematic of the experimental setup used to evaluate the radio over fiber systems in home network applications is illustrated in Figure 2. From the CO to home, the analog RoF system is constituted by an arbitrary waveform generator (AWG; M8190A, Agilent), which is responsible for generation of the 16-QAM RF signal with a 5 GHz carrier frequency, down-converted to intermediate frequency (IF) of 200 MHz by means of a local oscillator (LO) at 4.8 GHz. The signal is externally modulated by a MZM in an optical carrier sourced by an external cavity laser (ECL).
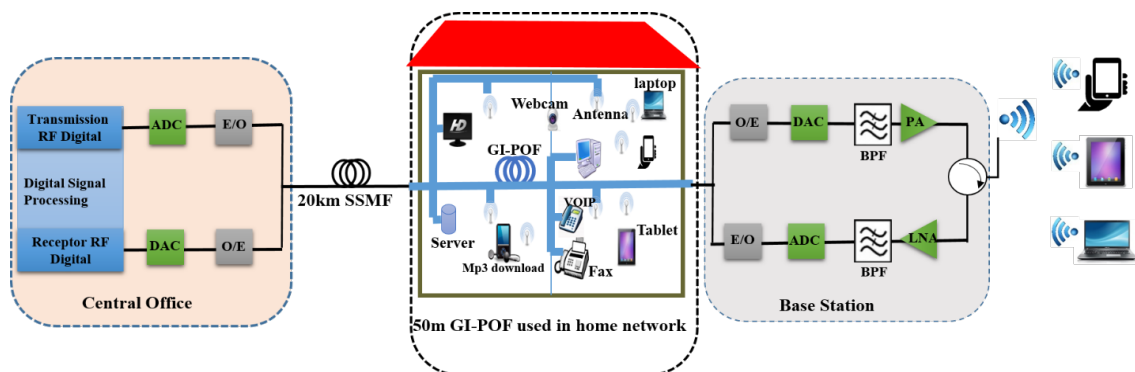

Figure 1. Diagram of the proposed digitized radio-over-fibre architecture. E/O: Electrical to Optical conversion, O/E: Optical to Electrical conversion, ADC: Analogue to Digital Conversion, DAC: Digital to Analogue Conversion, BPF: Band-Pass Filter, PA: Power Amplification, LNA: Low noise Amplifier.
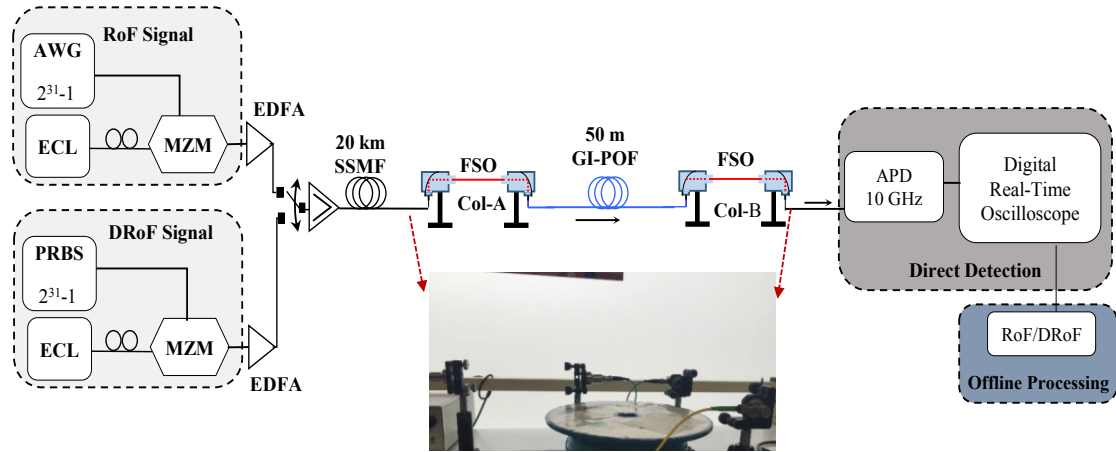
Figure 2. Experimental scenario with proposed DRoF system. AWG: Arrayed waveguide gratings, ECL: External Cavity Laser, PBRS: Pseudo Random Binary Signal, APD: Advanced Photodiode, MZM: Mach-Zehnder Modulator, FSO: Free Space Optic, EDFA: Erbium-Doped Fiber Amplifier.

The output optical signal is connected to 20 km of the standard SMF until it reaches within the building. In order to compensate fiber core diameter mismatching between two fiber cores, two collimators (Col-A, Col-B) are used. Note that, due to laboratory limitation for a proper adapter between SMF fiber and GI-POF as well as keeping bi-directional transmission for the experiment in PON, these collimators were used to minimize the loss and reflection in the two sides of GI-POF. At the receiver side, one avalanche photodiode (APD) converts the optical signal to electrical domain which is up-converted to original frequency (5 GHz) using a LO at 4.8 GHz. In the last step, the electrical output signal is read by the digital oscilloscope (Tektronix DPO 720004B), which removes a portion of the signal in time, and this sample is then analyzed offline and performance evaluation is conducted. Unlike of ARoF transmission, the DRoF signal is digitized by ADC before optical transport. Here, the IF (200 MHz) is sampled and quantized at ADC with 1.25 GHz. The stream of bits is then uploaded into the pattern generator (serial BERT Agilent N4906B). At the receiver side and after detection, DAC converts the serial digital signal to parallel. After this process, the signal is reconstructed similarly as in the ARoF technique. For both systems, the QAM mod/demod, LO and ADC/DAC operations are implemented off line in VPI@ and MATLAB.

3. Results and discussion

In this section, the results are discussed. To a fair analysis, both systems (ARoF and DRoF) were tested under same settings with MZM at PI/2, optical input power of 3 dBm. The signal IF-200 MHz with 1.25 Gbit/s modulated in 16-QAM was also considered for analog and digital transmissions. However, in DRoF system tests were performed tests with signal digitized with 4 and 8 bit resolution. Similarly to the digital system, the overall data rate is given by the product of the bit resolution and sampling rate used at ADC (e.g., 1.25 GHz). The bit rate transmitted from fiber is, respectively, 5 Gbit/s and 10 Gbit/s for 4 and 8 bits, which corresponds to the line rates 5 and 8 of CPRI specification [13]. In Table I the parameters used in this scenario are described. As the attenuation is a critical parameter in the radio over fiber transmissions, the performance of the system was measured with error vector magnitude (EVM) as function of received sensitivity. The variable optical attenuator was placed at the link before signal the receiver side to adjust the optical power received, in all the scenarios considered: b2b, b2b+GI-POF, 20 km SSMF and 20 km SSMF+50 m GI-POF.

Table 1 Parameters of experimental components DRoF assembly.

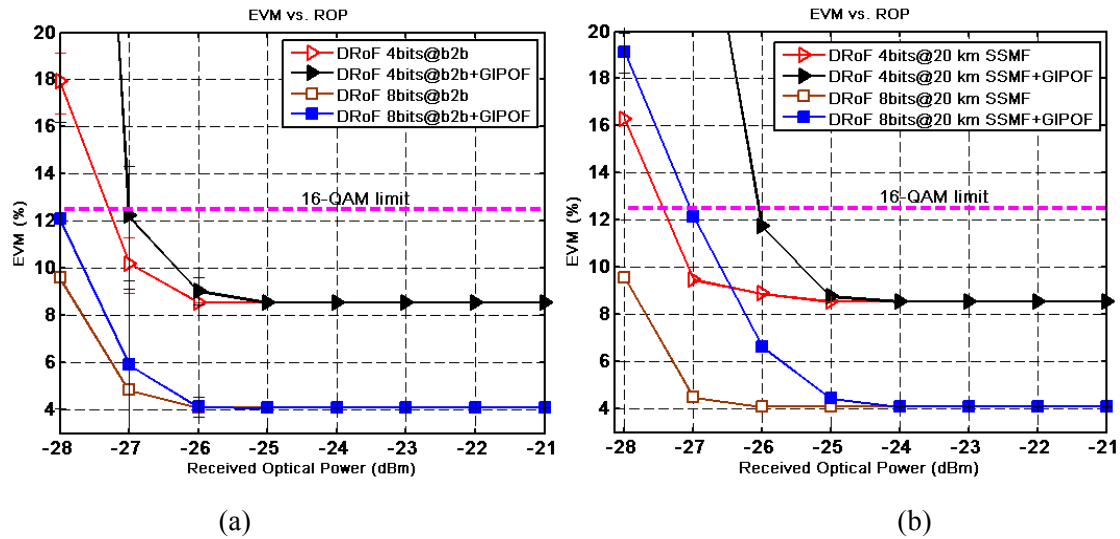| Carrier Frequency	Laser Linewidth	MZM Ext-ratio	APD responsibility	APD noise
5 GHz	10 MHz	20 dB	0.8 A/W	10^{-12} pA/Hz $^{1/2}$

(a)   (b)

Figure 3. EVM versus received optical power for (a) DRoF in an isolated scenario with b2b and b2b+GIPOF (b) DRoF in coexistence scenario with SSMF and SSMF+GIPOF.

The impact of the different ADC bit resolutions on the DRoF system as a function of the EVM, when employing 16 QAM scheme, for b2b, b2b+GI-POF (50 m) is plotted in Figure 3 (a) and (b). As it can be seen from Figure 3 (a), for tests with and without GIPOF, the EVM remains constant up to certain received power, -25 dBm for 4-bits and -26 dBm for 8-bits, and then decreases due to errors at the received side, mainly, introduced by thermal noise at APD. Then, the performance with GI-POF transmissions starts to degrade more than b2b scenario. In received optical power of -27 dBm, both transmissions are inside the 16 QAM limit [13].

However, in the coexistence scenario (Figure 3(b)) in which 20 km SSMF with 50 m GI-POF is considered, the penalties are more significant. After -25 dBm the performance of GI-POF transmission degrades severely due to modal dispersion, which induce restrictions in the received signal. It is also important to notice that the increased number of the bit resolutions means complexity and power consumption, therefore potentially increased cost in digital systems. So, in order to achieve an acceptable performance (EVM below the 12.5%), 4-bit resolution ADC is enough.

For ARoF system the analysis is similar to DRoF systems. As shown in Figure 4, comparing with DRoF, the performance of ARoF transmission decreases with increasing attenuation. In coexistence scenario, the EVM for analog transmission becomes greater than the threshold level at the received power level of -25 dBm. Nevertheless, since the transmission media are the combination of SMF and GI-POF, the penalties from modal
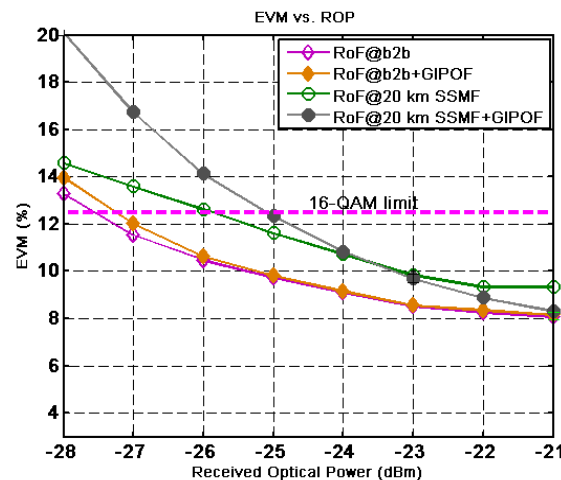

Figure 4. EVM for different scenarios in analogue ROF.

dispersion are more than those observed for DRoF system. EVM clearly shows that performance of DRoF systems remains constant up to a certain level of received power (-25 dBm), and only in -26 dBm and -27 dBm the system suffers a small penalty in coexistence scenario. This ensures that digital transmission can operate for long distances having a better sensitivity than analog RoF system.

4. Summary and outlook

In this work the transmission of RF signals in conventional DRoF systems to deliver digital baseband for end users in home access has been presented and evaluated. The viability of the DRoF system to support the standard base band transmission in home access networks is also investigated. Results show that the system has a linear behavior in terms of EVM until a certain optical power received, and a greater resolution in terms of number of bits. The experiment results show that with the coexistence of 20 km of single mode fiber (SMF) and 50 m of the GI-POF, 1.25 Gbits/s baseband signal with 16 quadrature amplitude modulation (QAM) can be accommodated in our proposed scheme. Furthermore, the proposed architecture is economically competitive for either upgrading installed systems or for new deployments.

5. Acknowledgement

6. References

[1] M. Jaber, M. A. Imran., R. Tafazolli, & A.Tukmanov, "5G backhaul challenges and emerging research directions: a survey," in IEEE Access, vol. 4, no. , pp. 1743-1766, 2016.

[2] A. Shahpari; R. M. Ferreira; R. S. Luis; Z. Vujicic; F. P. Guiomar; J. D. Reis; A. L. Teixeira, "Coherent access: a review [Invited paper]" IEEE/OSA Journal of Lightwave Tech., in Press, DOI 10.1109/JLT.2016.2623793, November 2016.

[3] Cisco Visual Networking Index: Global mobile data traffic forecast update, 2013-2018, Cisco, San Jose, CA, USA, Feb. 2013.

[4] A. Ghosh, R. Ratasuk, B. Mondal, "LTE advanced: Next generation wireless broadband technology", IEEE Transactions on Wireless Communications", vol. 17, pp. 10 – 22, 2010.

[5] METIS project,"Scenarios, requirements and KPIs for 5G mobile and wireless system", Deliverable 1.1.

[6] R. Wang, H. Hu, & X. Yang, "Potentials and challenges of C-RAN supporting multi-RATs toward 5G mobile networks," in IEEE Access, vol. 2, no. , pp. 1187-1195, 2014.

[7] Supplement 55 to ITU-T G-series Recommendations provides general information on radio-over-fibre (RoF) technologies and their applications in optical access networks.

[8] R. S. Oliveira, D. F. R Viana, M. Lima, C. R. L. Francês, A. Teixeira & João C. W. A Costa, "Digital radio over fiber system in the NG-PON2 context". Journal of Microwaves, Optoelectronics and Electromagnetic Applications (JMOe), 14, 179-193, 2015.

[9] F. Forni, Y. Shi, H. van den Boom, E. Tangdiongga and T. Koonen, "Multiband LTE-A and 4-PAM signals over large-core plastic fibers for in-home networks". IEEE Photonics Technology Letters, 28(20), 2281-2284, 2016.

[10] Y. Koike and A. Inoue, "High-Speed Graded-Index Plastic Optical Fibers and Their Simple Interconnects for 4K/8K Video Transmission," J. Lightwave Technol. 34, 1551-1555, 2016.

[11] A. Nirmalathas, A. P. Gamage, C. Lim, D. Novak & R. Waterhouse, "Digitized radio-over-fiber technologies for converged optical wireless access network", Journal of Lightwave Technology, 28, (16), pp. 2366 – 2375, 2010.

[12] A. de la Oliva, J. A. Hernandez, D. Larrabeiti and A. Azcorra, "An overview of the CPRI specification and its application to C-RAN-based LTE scenarios," in IEEE Communications Magazine, vol. 54, no. 2, pp. 152-159, February 2016.

[13] LTE, 3GPP TS 24.229 V10.6.1 (2012-01), 2013. Available: http://www.3gpp.org/specifications.

Solar Tracker Development Applied to Ambiences Illumination and Microalgae Cultivation

A.S. Allil[1*], A.O.C. Manchego[1], I.V. Rodrigues[1], R.C.S.B. Allil[1] and M.M. Werneck[1]

1 Photonics and Instrumentation Laboratory, Electrical Engineering Program, Universidade Federal do Rio de Janeiro, Brazil.

*Corresponding author: allil@poli.ufrj.br

Abstract: The Solar Lighting System is being developed at Universidade Federal do Rio de Janeiro (LIF/COPPE/UFRJ). The objectives of this project are to use solar energy in the form of light to reduce the power consumption required for lighting ambiences without windows or with low level of illumination. Another application is to provide a better microalgae culture with a brand new photobioreactor concept. The system works tracking the Sun from the sunrise till the sunset. It is composed by a Fresnel lens, which concentrates the solar beams into an optical fiber (POF) bundle placed at the lens focus.

1. Introduction

One of the countries with the highest solar irradiation index, Brazil still underuses its natural power. Data from the Eletrobras Electrical Energy Researches Center (Cepel) show that the solar irradiation on the horizontal surface at Brazilian northeast ranges from 4,4 kWh/m²/day to 5,8 kWh/m²/day. Just to take for example Germany, the worldwide leader on photovoltaic energy generation, these same indexes range from 2,9 kWh/m²/day to 3,8 kWh/m²/day [1].

Lots of engineering projects, which use renewable energy resources, are a must-have in today´s interconnected world. It is evident the growth of ideas that surrounds researches related to sunlight use as development means. Devices such as Photovoltaic Panels (PV's), High Reflective Mirror Concentrators (HR-Mirrors), and so on are some examples of energy conversion efficient ways coming directly from the Sun. Inspired by these facts, a solar tracker was developed in order to create a new lighting system with two different goals. The first one is applied to ambiences illumination aiming to attend the illuminance demand inside a specific area (such as commercial buildings, large aquaria, underground parkings and museums), and the second one is applied to microalgae culture illumination, which intends to ease the photosynthesis process inside a tank, known as photobioreactor.

The solar tracker consists of an electromechanical project, which uses rotationary machinery as motors, and optical devices, such as Fresnel lens. In addition, some sensors are employed so that important parameters – for instance, the light intensity inside an optical fiber (measured through a photodetector), the right ascension and declination angles (estimated with an accelerometer) and the area irradiation indexes (available due a pyranometer) – be analysed aiming the equipment behaviour monitoring from any location.

This system is able to track the Sun from the sunrise until the sunset due a brand new and innovator algorithm. Its function is calculate the Sun position according to the local time, season, time zone and latitude. The sensors data are stored at *LIF-Remoto*, a via web system which allows full access to the sensor readings remotely.

2. Materials and Methods

2.1 System Structure

Initially the system was developed and tested at the laboratory, shown at Figure 1, and nowadays it is located at the Universidade Federal do Rio de Janeiro (UFRJ) campus, Figure 2. The building where the structure is mounted (Biofuel, Petroleum and Derivates Center - NBPD) hosts researches related to biofuel production with microalgae use and also held a study room whose illumination is brought through this project.
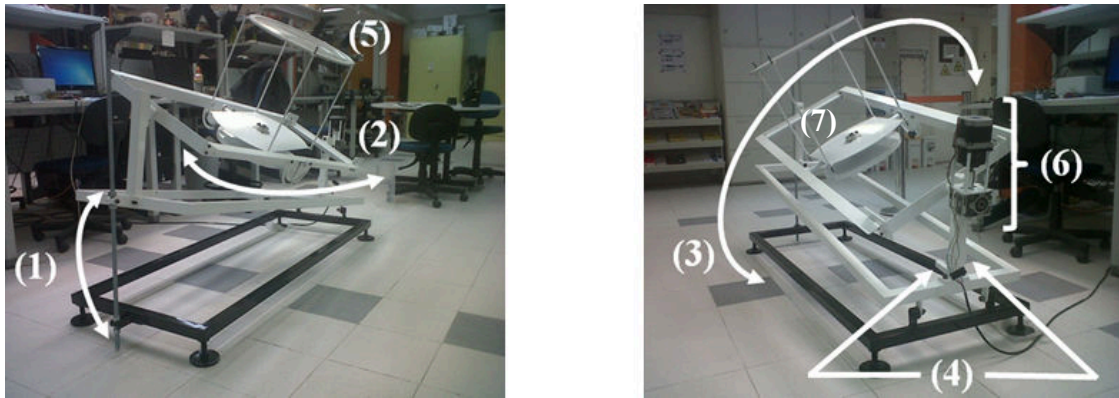
Figure 1. The prototype. 1 and 2: manually adjusted angles. 3: right ascension angle.
4: micro switches. 5: Fresnel lens. 6: stepper motor. 7: POFs bundle surface.

The left part of Figure 1 shows the structure degrees of freedom. The right part shows some sensors, micro switches and the system actuator, responsible for the tracking functionalization at any place on Earth, by simply adjusting some parameters.

Known as an equatorial mount, this tracker has latitude and declination manually adjusted (1 and 2, Figure 1). Right ascension angle is shown at (3). This axis is automatically controlled by the stepper motor and its reduction gears, presented at (6). The Fresnel lens is seen at (5) and (4) presents the end-tracking micro switches. Below and parallel to the lens plan it is possible to observe a gray surface where the optical fiber bundle is attached (7).

Figure 2. Solar tracker system installed on the roof of the Technology Center at the
Universidade Federal do Rio de Janeiro.

2.2 System Actuator Control

The stepper motor is driven by an H-Full-Bridge circuit and its control is made with hysteresis power relays technique. A microcontroller is responsible to send pulse commands that will switch the relays and consequently energize the motor stator coils, sequentially, generating a correspondent torque.

The Figure 3 shows the power and control schematics where digital pins 1 and 2 represent the microcontroller digital output.
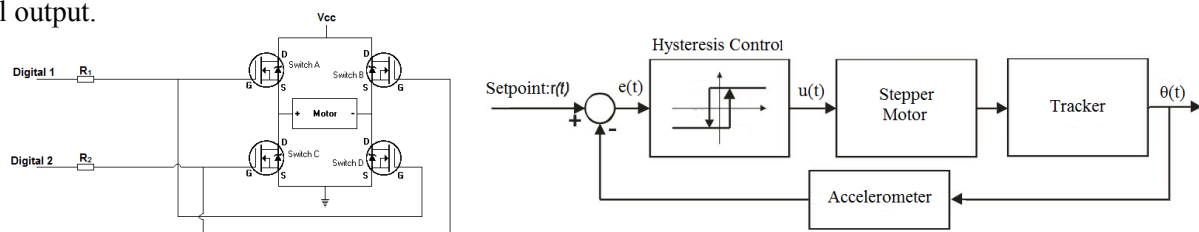

Figure 3. H-Bridge and control schematics.

2.3 Plastic Optical Fiber Bundle for ambiences illumination

For each luminaire a bundle of 120 2-mm in diameter fibers and length of 7 m is used. The output power of the system is dependent of the length of the fiber bundle. Figure 5 shows the graph of the gain (P_{out}/P_{in}) with different bundle lengths along the spectrum.

It can be noted a high attenuation on color orange/red (600-650 nm) and violet (400 nm) so, it is expected a green colored light for long bundles. With our 7 m bundle, the color is slightly green, but almost imperceptible (see Figure 6).

2.4 Plastic Optical Fiber Bundle for photobioreactor illumination

Aiming the microalgae biomass costs reduction for the biofuel production, a new concept of photobioreactor is proposed. It is expected that this project section influences the microalgae cultivation in order to increase its efficiency, and hence allow a better use and valorisation of its products and derivates.

Inspired by these facts, the cultivation at pilot plant level was performed inside a 20-liter photobioreactor. It was manufactured with a low cost material and high durability such as the PVC (Polyvinyl chloride) with internal illumination through a plastic optical fiber bundle. These POFs guide the light coming from Sun which is concentrated with the Fresnel lens. This photobioreactor is shown at Figure 4.
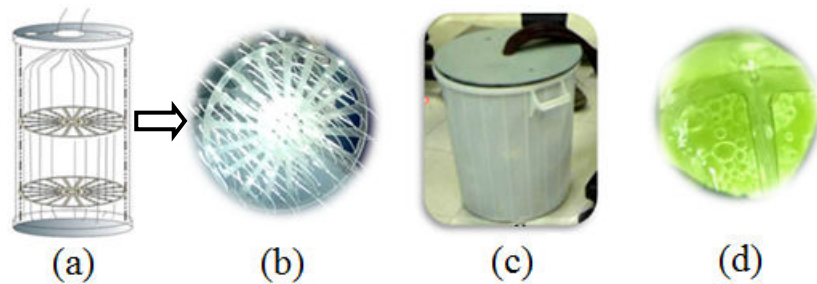
Figure 4. Microalgae photobioreactor schematics with natural illumination. (a): POFs fixation design. (b): fixation zoom in. (c): photobioreactor. (d): microalgae culture interior.

3. Results and Discussions

3.1 Light Spectrum

One of the biggest advantages of this system is the quality of the available light. While artificial sources of light have the disadvantage of wasting a lot of energy to provide a good light quality (solar spectrum), our system gives a high-quality light with very low consumption of electrical energy. Figure 5 shows that the attenuation obtained for different bundle lengths superimposed to the POF attenuation spectrum.

Figure 5. Fiber bundle gains and attenuation.

In Figure 6 we can observe the solar spectrum and the spectrum of our luminaire (green curve). At 630 nm we can realize a light attenuation as e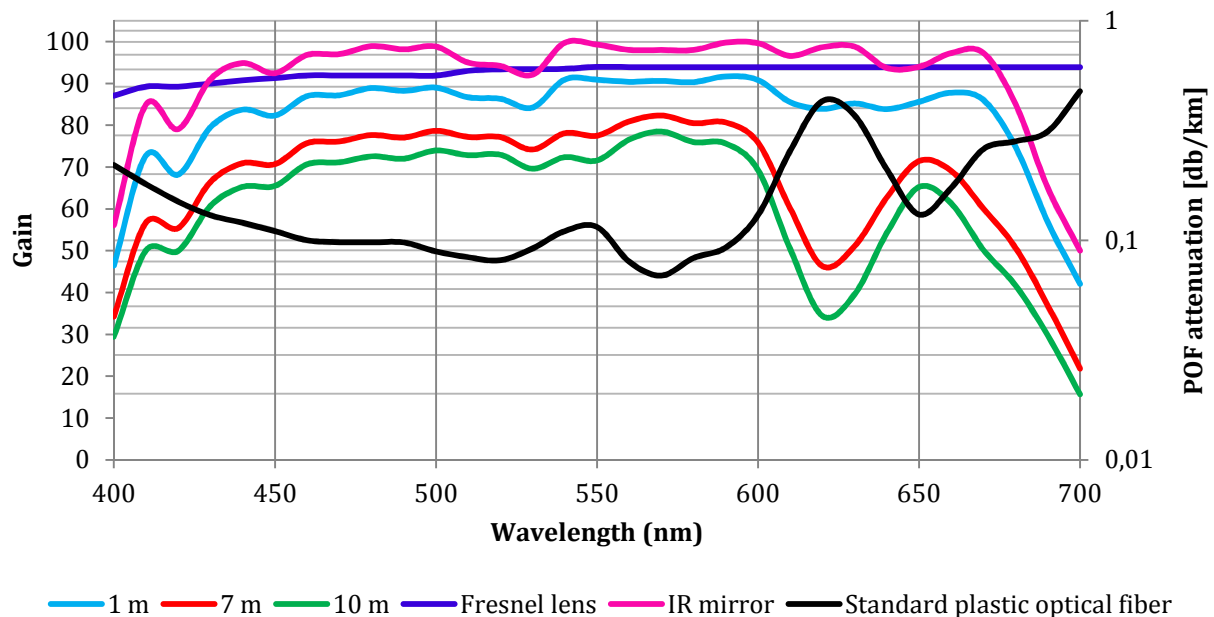xpected by Figure 5. Red curve shows the theoretical spectrum calculated according to the gains shown also at Figure 5. It is observed a considerable similar behaviour among theses curves which proves the results are in line with expectations.

The perception of light color alteration was weak for this 7 m length bundle luminaire and we can consider that the light has the visible spectrum of the Sun.
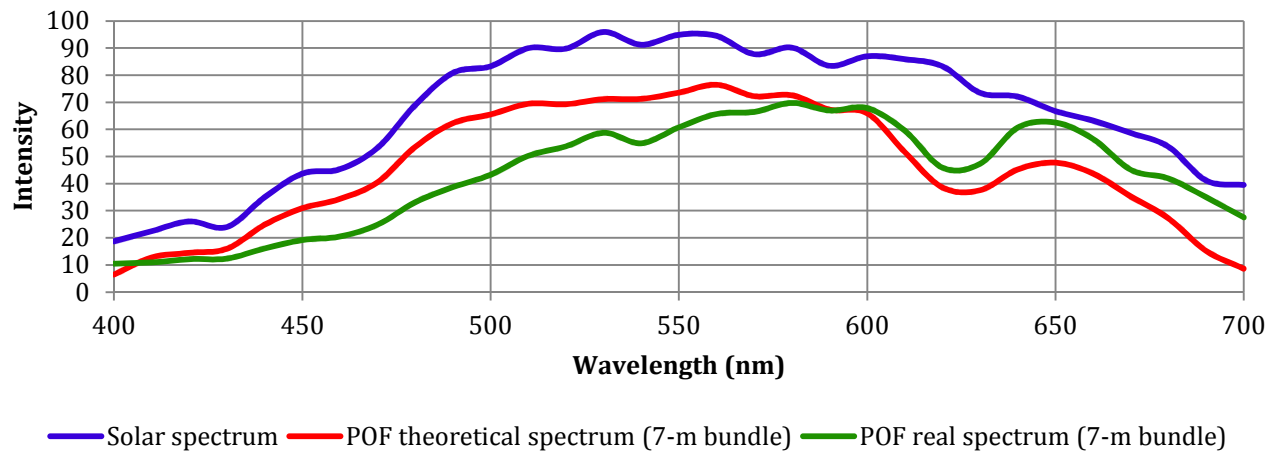

Figure 6. Solar spectrum light (blue) and project luminaire (orange).

3.2 Light Distribution

In order to test several applications, it was developed two types of luminaires. One of them (diffuse luminaire) was planned to illuminate an entire ambient and another (spot luminaire) just to illuminate a small area or object.

At the first one, the fibers are disposed lying horizontally inside the luminaire. The POFs are modified at their last 20 cm so that the light escapes through the sides of the fiber and, with the help of a reflector it illuminates the room where it is installed.

At the second one, the fibers are disposed aiming the floor (or the local where it desires to illuminate) separated by 1 cm from each other forming an illuminated area proportional to the numerical aperture of the fiber (0,5). In this case, the result is a powerful and focused spot, giving prominence to the target of illumination.

Figure 7 shows a 3D-graph of illumination in Lux of both luminaires. At the first one there is the diffuse luminaire and the applied area is 20,25 square meters. At the second one, there is the spot luminaire and the applied area is 1,6 by 1,1 m. At the moment of the data measurements below, the lens was not at its strongest possible concentration, if it were, the maximum value at the diffuse luminaire would be around 260 lux and the spot luminaire 3000 lux. It is important to notify that all measurements consider an 82-centimeter work plan height.
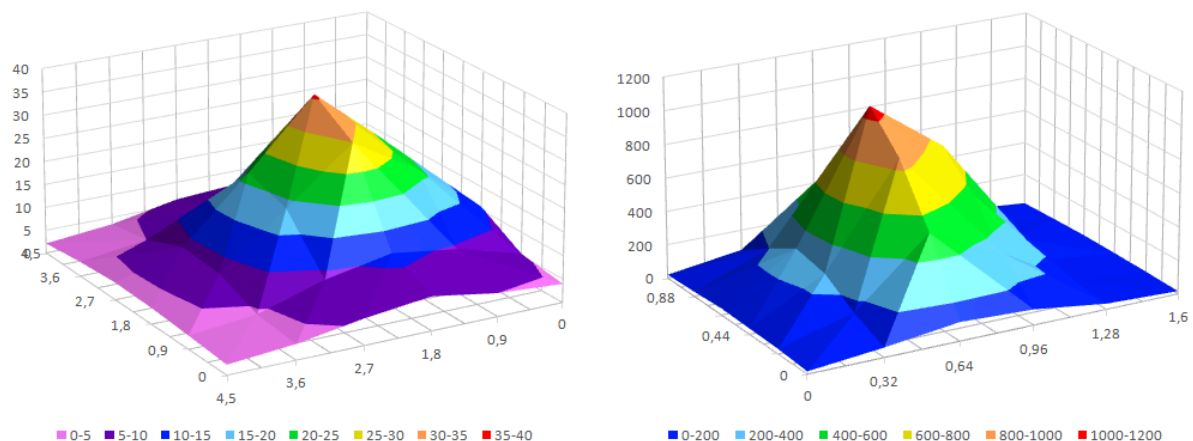
Figure 7. Diffuse luminaire (left) and spot luminaire (right) spatial distribution.

4. Conclusions

The solar tracker project and development were successfully performed. So far, the tracker is in full operation 24 hours per day and 7 days per week, without operational and control problems yet. The quality of the light is better than LED and Fluorescent bulbs. Moreover, the attenuation of the solar energy is almost insignificant.

5. Acknowledgements

6. References

[1] SALGADO, A., KIFFER, D., MOTTA, D., et al. "Sistema promete otimizar uso de energia solar na iluminação de ambientes", *FAPERJ RIO Pesquisa*, v. 1, n. 32, pp. 13 – 15, set. 2015.

Side-emitting fibers with a non-circular cross section

C.-A. Bunge[1*], B. Mohr[2], M. Beckers[2], T. Vad[2], M. Chochol[1], T. Gries[2]

1: Chair for optical communication/photonics, Hochschule für Telekommunikation Leipzig (HfTL), Gustav-Freytag-Str. 43-45, D-04277 Leipzig, Germany
2: Institut für Textiltechnik, RWTH Aachen University, Otto-Blumenthal-Str. 1, D-52074 Aachen, Germany

*Corresponding author: bunge@hft-leipzig.de

Abstract: We present a novel fiber type with a non-circular trilobal cross section. The fiber is designed for illumination purposes and features the special shape in order to form a distinct asymmetrical radiation pattern. These fibers can be used to concentrate light on particular locations in order to cure resins or polymers, but can also find its applications for illumination purposes. The polymer material is commercial optical-grade PMMA that is doped with different amounts of scatters for a controlled scattering for side emission.

1. Introduction

Side-emitting fibers are well suited for illumination purposes. They rely on different physical methods to direct the launched light to the sides [1]. While some approaches rely on photoluminescence (and thus a conversion to longer wavelengths) and optical pumping of active dopants, do most side-emitting fibers scatter the light in a controlled way. Often, the surface of the fiber is treated by sand blasting, mechanical pressure or other forms of structuring. Here, the light is coupled into radiation modes in the region near the cladding. While this approach is relatively simple to apply and can also be performed on an already installed fiber, it has the disadvantage that the surface is sensitive to touching or other environmental effects.

A more robust approach is the use of bulk scattering within the fiber material. Since all scattering is shielded from the elements it can be exposed to oil or other materials with various refractive indices without a dramatic change of the emission properties. In this contribution, we show fibers made from PMMA with additional dopants in different concentrations.

Most optical fibers are round, i.e. show a circular cross section. This usually results in a completely circularly symmetric radiation pattern around the fiber. For many illumination purposes this is desirable. But there are applications when the emitted light shall be concentrated on particular regions or shall be directed. Then, non-circular fibers can have advantages over their symmetrical counterparts. In the following, we present first results on trilobal side-emitting fibers (see Fig. 1) and investigate their radiation pattern as well as the influence of the scatterer concentration on the illumination intensity [2].
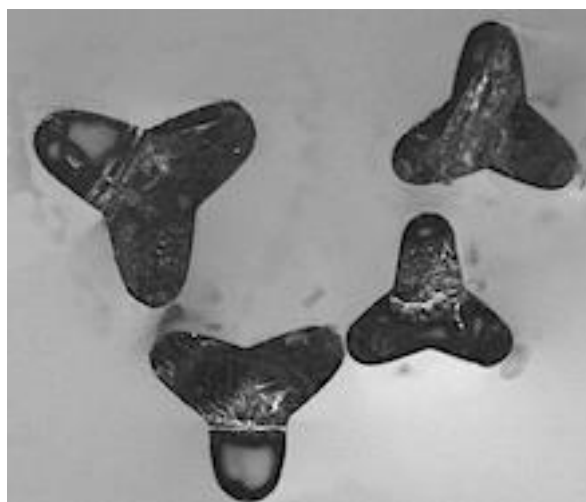

Figure 1. Cross sections of exemplary trilobal fibres.

2. Fiber design

The fibers and their cross sections are shown in Fig. 2. Their trilobal shape is easily observable. The fibers have been manufactured at the facilities of the ITA of the RWTH Aachen University with a melt-spinning processes [3]. The fibers consist of PMMA with different concentrations of a scattering polymer compound in order to control the strength of the scattering.

3. Scattering pattern

The first and most important investigation on the novel fiber type aimed at the radiation pattern of the fiber. Therefore, the far field distribution around the fiber was characterized by a goniometer setup at the HfT Leipzig laboratories. For this measurement, a HeNe laser of 633 nm and 10 mW output power launched into the fiber, which was held in an opaque tube. At the point of measurement, the tube was cut so that a 5-mm wide gap left the emitted light to the sides, where it was captured by a goniometer far-field measurement setup that took the intensity.

Fig. 2 shows the far-field distribution of one of the fibers. All fibers showed the same radiation pattern. Although only a angular range of 90° has been measured it is obvious that the pattern is not circularly symmetric. In this case, the measured power would have been constant for all angles. With a closer look and some extrapolation, one can observe that the measured main lobe shows a width of 120° between the two minima. The pattern seems to repeat itself according to the expected 120° symmetry of the cross section.
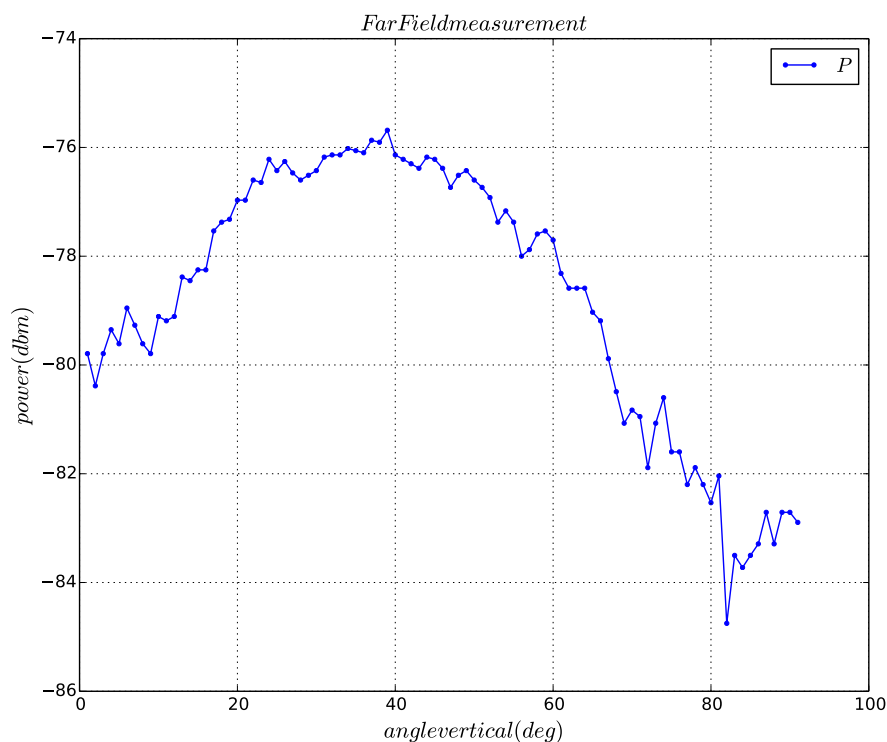
Figure 2. Far-field measurement of the trilobal fiber with a 120° symmetry.

Apart from the non-circular symmetry, the contrast between the direction of maximum intensity and its minimum can be evaluated. It lies in the range of 8 dB to 10 dB. This can be assumed in a similar way as an antenna gain in radio-frequency engineering, where the concentration of the radiated power is seen as a gain or a saving of power. There is less light lost into directions that are of no importance for the application. The trilobal shape is thus suitable to control the radiation pattern to a certain extend.

It is possible to increase the number of lobes, but the patterning effect will become smaller for larger number of lobes until the distribution approaches the case of a circularly symmetric fiber.

4. Scattering strength vs scatterer concentration

As a second property, the influence of the scatterer concentration was investigated. Fig. 3 shows the evolution of the side-emitted optical power over the fiber length for different scatterer concentrations. Therefore, the fiber was illuminated by a HeNe laser of 633 nm and 10 mW output power using a microscope objective as launching optics. The side-emitted power was collected by an Ulbricht integration sphere that was moved along the fiber, which as threaded through the sphere and the covered by an opaque tube within the sphere except for a small gap of 2 mm where the actual light emission was taken.

The side emission decreases exponentially along the fiber according to the Lambert-Beer law. Since the power is plotted logarithmically in dBm, a truly exponential decay resulted in a linear line. All four curves can be linearly fitted with negative slopes that represent their attenuation, but also correlate to the scattering strength. The red line represents the fiber with the lowest scatterer concentration of 1:4. It shows an attenuation of about 62 dB/m. The next-higher concentration (1:3) leads to an attenuation of about 68 dB/m. At a concentration of 1:2, the attenuation increases to about 84 dB/m. Finally, the highest concentration of 1:1 results in such an intense scattering that no light was observable after 20 m resulting in an approximate attenuation of 150 dB/m.
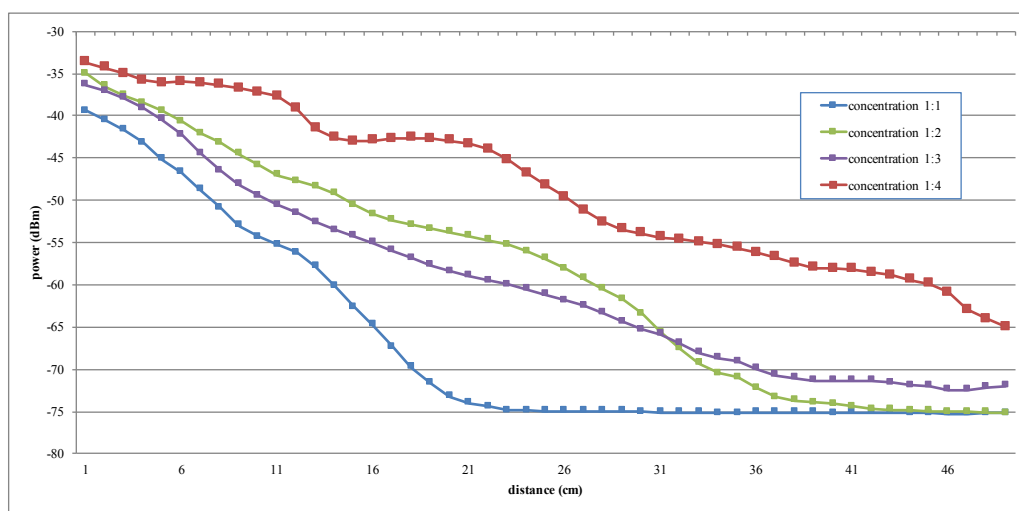
Figure 3. Evolution of the side emission over the fiber length for different scatterer concentrations.

From these values, it is observable that the scattering can be controlled by the concentration of scatterers in the bulk material. In a simple linear modelling, the scattering is proportional to the effective scattering area or diameter, which depends on the concentration of scattering centers within the material. The investigated fibers show a relative proportion of scatterers of 20%, 25%, 33% and 50%. Fig. 4 shows the attenuation (as an indication of the scattering strength) in dependence of the scatterer concentration. The is a relative good linear match.

Figure 4. Relation between attenuation and scatterer concentration.

Please note that the attenuation is not a negative property – as in conventional fibers for communication. It just shows the strength of the scattering, which is the fundamental process for the side emission. Thus, fibers with higher attenuation show a brighter side emission, but with less homogeneity.

4. Conclusion and outlook

We presented a non-circular side-emitting fiber made from PMMA. The trilobal cross section has an influence on the radiation pattern of the fiber so that it is pos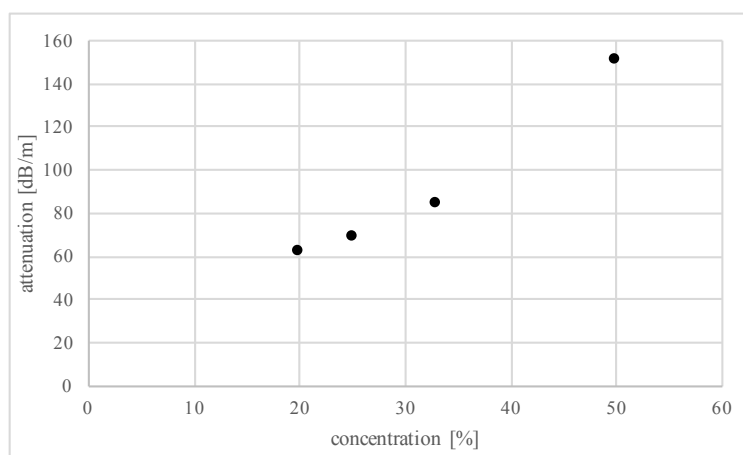sible to concentrate the emitted optical power to certain directions. The far-field pattern shows the same 120° symmetry as the fiber does. It could also be shown that the side-emission intensity can be controlled by the scatterer concentration. There seems to be a linear relation between the scattering strength and the concentration percentage of the scatterer.

Acknowledgement

References

[1]   Bunge CA, Beckers M, Gries T. Polymer Optical Fibres: Fibre Types, Materials, Fabrication, Characterisation and Applications. Cambridge: Woodhead Publishing Ltd; 2016.

[2]   J. Zubia, J. Arrue, Plastic optical fibers: An introduction to their technological processes and applications, Optical Fiber Technology, Vol. 7, pp. 101–140, 2001.

[3]   M. Beckers et. al., An overview on fabrication methods for polymer optical fibers, Polym. Int., DOI: 10.1002/pi.4805, 2014.

Simultaneous measurement of temperature and humidity using PFBG and Fabry-Perot cavity

R. Oliveira[1*], L. Bilro[1], R. Nogueira[1]

1 Instituto de Telecomunicações, Campus Santiago, 3810-193 Aveiro, Portugal
*Corresponding author: oliveiraricas@av.it.pt

Abstract: We demonstrate the capability to simultaneous measure humidity and temperature using a PFBG and a Fabry-Perot cavity formed between the silica to POF connection. To have a strong silica to POF connection, it is common practice the fusion of the fiber terminals with an optical adhesive. In this work, the same approach was used. However, careful control of the distance between the fibers is chosen in order to create a Fabry-Perot cavity. By monitoring the spectral responses to temperature and humidity of the PFBG and FPI structures, it was possible the construction of the sensitivity matrix, which allows the simultaneous measurement of these two parameters.

1. Introduction

Nowadays, sensing applications related with polymer optical fibers (POFs) have increased their number. The reason is essentially due to the opportunities that POFs can offer when compared with silica fiber optic sensors. Among them are: the negative and much larger thermo-optic coefficient [1]; the smaller Young modulus [2], allowing to withstand at high elongation regimes [3]; flexibility in bending; non-brittle nature, biological compatibility [4], ability to detect humidity [5], among others.

Fiber Bragg Gratings (FBGs) are very attractive due to the easy integration in optical components. When recorded in POFs, several advantages can be obtained when compared to their silica counterparts. Additionally, combining FBGs with other fiber optic technologies brings the opportunity to simultaneously detect different parameters. Among the different detection capabilities offered by polymer optical fiber Bragg gratings (PFBGs), the detection of temperature and humidity has been a hot topic in recent years [6]–[9]. POFs have been essentially fabricated with PMMA material, and among the different characteristics that this polymer may offer are the ability to detect temperature with higher sensitivity than silica [10], and the capability to absorb water. Despite the opportunity of measuring these two parameters, the detection of a single parameter is problematic due the cross sensitivity issues. For that reason, the research community has implemented a variety of solutions. Among them are the use of novel POF materials such as TOPAS[®] [7] and ZEONEX[®] [11], which have low water absorption capabilities, leading to the development of humidity insensitive POF devices. Other strategies report the simultaneous detection of humidity and temperature. One example of that uses a FBGs written in silica and polymer fibers [12], while another reports the use of two in-line fiber Bragg gratings recorded in a POF [13].

Another interesting fiber optic sensing device commonly employed for the detection of temperature and humidity is the Fabry-Perot interferometer (FPI). This device can be implemented in two configurations, either intrinsically, or extrinsically. Concerning the later, key advantages can be considered, such as easiness of fabrication and no need for the use of high cost equipment. Regarding the humidity detection, the common choice is based on the use of hygroscopic materials. Examples of such are Nafion [14], chitosan [15] and different photopolymerizable resins [16]–[18].

In this work the connectorization process of a silica pigtail fiber to a polymer optical fiber, will be intended to form a Fabry-Perot interferometer (FPI) based on an UV photopolymerizable resin. After that, a PFBG will be written at the POF. The reflection spectrum of the FPI and FBG will then be monitored during the temperature and humidity characterizations. At the end, the sensitivities of both fiber structures will be used in a 2 X 2 matrix that can be used for the simultaneous detection of these two parameters.

2. Principle of operation and sensor fabrication

Since most of the available fiber optic components are based on silica fibers, POFs are commonly connectorized to them in order to easily inject/collect the optical signal. It is a common practice by the scientific community the connectorization of these two dissimilar fibers through an optical adhesive that is

hardened by UV radiation. This technique is advantageous over other techniques like the connectorization of a fiber inside a ferrule [19], since it is not dependent on the diameter of the fiber neither on the concentricity of the fiber core. To connectorize the two dissimilar fibers through an adhesive, one needs to find a glue that after hardened is strong enough for the manipulation of the fibers without losing the optical signal. Nevertheless, the adhesive needs to have low influence on temperature, humidity and pressure, etc., in order to minimize the optical signal variations. Another key aspect is the refractive index of the adhesive that should be chosen in order to match the ones of the fibers employed. If the optical adhesive is not equal to one of the fibers being employed, then a displacement between the two fibers being connectorized will result on the formation of a Fabry-Perot cavity. The formation of such structure between the fibers will create a wavelength dependent intensity modulation of the input light spectrum, which is mainly caused by the optical phase difference between two reflected beams. The period of the modulation ($\Delta\lambda$), is a function of the wavelength of the radiation (λ), refractive index of the adhesive (n) and distance between the fibers (L), and it can be written as:

$$\Delta\lambda = \frac{\lambda^2}{2nL}$$

(1)

Normally, the formation of a Fabry-Perot cavity between the silica and polymer fibers is an undesired effect, since it deteriorates the signal of the structure that is being measured (i.e. FBG, LPG, MMI, etc.). To prevent the formation of such structure, the fibers are placed in contact trough their end face terminals.

2.1. *Design of the FPI sensor*

In order to create a splice between a POF and a silica pigtail fiber that works as a fiber delivering system, it was employed an optical adhesive that is harden after exposure to UV radiation. The adhesive was acquired from Norland Products, Inc. with trade name NOA86H. This adhesive has very good adhesion to plastic and glass and it has been used by the research community to connectorize silica to polymer fibers [20]. The refractive index of the adhesive at 589 nm is 1.55, it has low viscosity (200-300 cps @ 25 ºC) and it has a shore D of 75 [21], which is very attractive for high coupling strength.

The POF used in this work was a microstructured POF, doped with Rhodamine 6G. The fiber was acquired from Kiriama Pty. Ltd. and it was designed to provide few-mode behavior. Additionally, the fiber has a clad diameter of 180 μm and a core diameter of 11 μm, which are surrounded by 4 layers of air holes.

When working with PFBGs it is a standard procedure the preparation of the silica pigtail fiber termination with an FC/APC contact, which prevents Fresnel reflections at the splice joint. However, in this work, both silica and polymer fibers were prepared with an FC/PC contact, in order to have two perfect mirrors for the creation of a Fabry-Perot interferometer. The silica fiber was cleaved with a CT-30 machine and the mPOF was prepared through the cut and polish methodology described in [22].

In order to align the two fibers, a 3 axis positioner was used. Additionally two telescopic cameras were placed at each of the orthogonal axis, allowing the perfect core alignment of the fibers (see Figure 1a)). The fibers were then separated by a small distance, allowing the creation of a fringe interference (see Figure 1b)). A drop of the NOA86H is then placed between the fibers, and UV radiation from an opticure Led 200 with 2.5 w/cm^2 is then used during 10 seconds to harden the joint splice (see Figure 1c)).
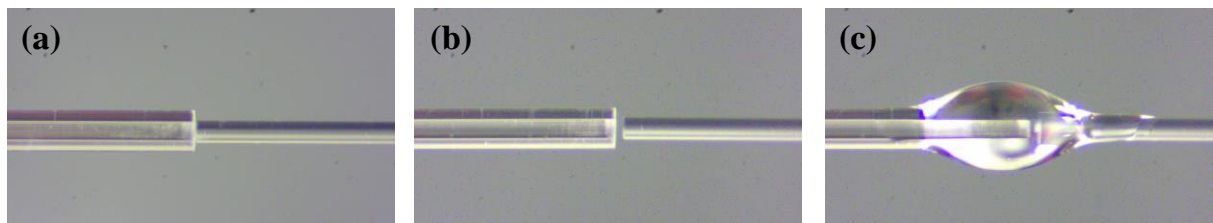

Figure 1. Process followed to create the fiber connectorization process/FPI cavity. (a) Fiber alignment; (b) longitudinal separation for the creation of the FPI cavity; (c) drop of UV glue placed between the fibers. In all images, the POF is at the left side and the silica fiber is at the right side.

2.2. *Design of the PFBG sensor*

For the production of the PFBG, it was used a 248 nm UV excimer laser (KrF Bragg Star[TM]). The inscription was based on the phase mask method and for that, the UV laser beam is guided through mirrors and it is shaped on the fiber after passing through a slit of 4.5 mm and by a phase mask suited for 248 nm UV radiation with pitch of 1033 nm. The PFBGs were written with repetition rate of 1 Hz and 3 mJ energy, giving a fluence of 33 mJ/cm^2. The complete description of the inscription setup may be found in [23].

2.3. *Temperature and humidity characterization*

For the temperature and humidity characterization an interrogator system (Micron Optics 125-500) was used to measure the reflection signal from the adhesive based FPI as well as the reflection signal from the PFBG. The temperature and humidity tests were performed in a climatic chamber (Angelantoni CH340), with resolutions of 0.25 ºC and 3 %RH in temperature and humidity, respectively. The fiber sensor was left in the vertical position, by fixing the silica pigtail fiber to a support. The complete setup can be seen in Figure 2.
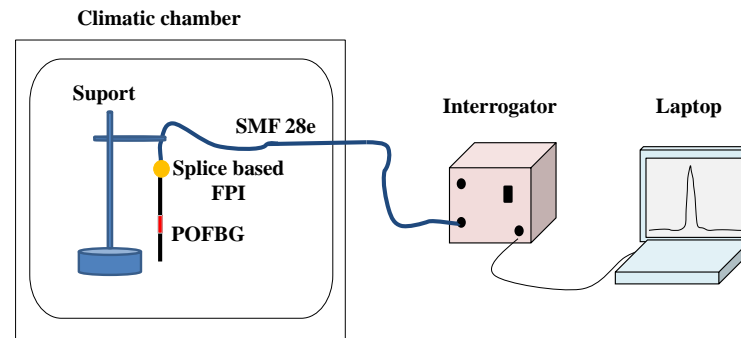

Figure 2. Setup used for the temperature and humidity characterization.

Before starting the characterizations, the fiber sensor was annealed at 70ºC during 12 hours. This procedure was done in order to full cure the adhesive, allowing an optimum adhesion to the glass fiber [21]. Additionally, the annealing process also allows the partially release of stress built-in during the POF drawing process, improving the performance of the PFBG as temperature sensor [24].

As the POF thermo-optic and thermal expansion coefficient are a function of temperature and humidity [25], [26], the characterizations were made keeping the humidity at 30 %RH and the temperature at 25ºC, respectively for the temperature and humidity tests. The temperature characterization was made by sweeping the temperature from 25 to 45 °C in 5ºC steps. On the other hand, the humidity tests were made from 30 %RH to 90 %RH in steps of 10 %RH. In both tests it was given 1 hour of stabilization before data collection, allowing enough time for the stabilization of the parameters imposed in the thermal chamber as well as the response of the PFBG and FPI.

For the humidity tests the temperature was maintained at 25 ºC. The humidity was swept from 30 % to 90 % in steps of 10 %, giving 1 hour for each step, allowing enough time for the uptake of water by the PMMA polymer, as already reported [21].

3. Results and discussion

The reflection spectra of the FPI and PFBG for the temperature and humidity characterizations may be seen in Figure 3a) and Figure 4a), respectively.

Regarding the temperature tests, the PFBG reflection spectra was linearly blue shifted with increasing temperature (see the inset in Figure 3b)), while the FPI reflection spectra was linearly red shifted (see the inset in Figure 3c)). In order to know the sensitivity of each structure, it was monitored the wavelength peak power at 3 dB. The results are shown by black dots in Figure 3b) and blue asterisks in Figure 3c) for the PFBG and FPI respectively.
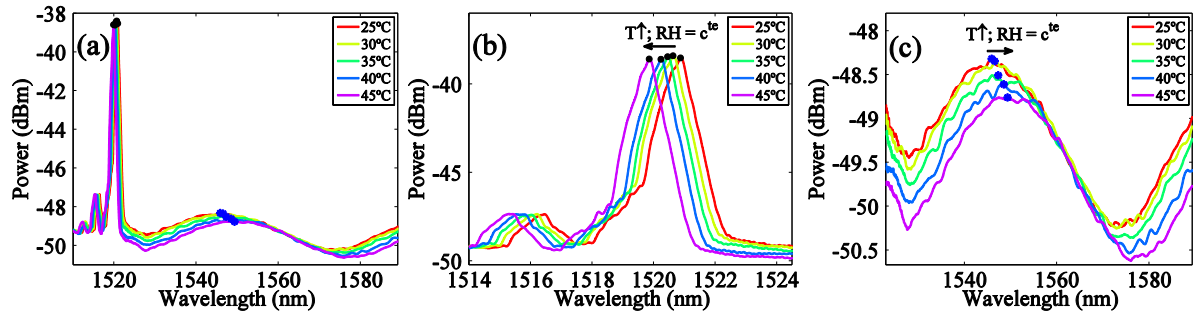
Figure 3. (a) Reflection spectra of the PFBG and FPI structures, at different temperatures and constant humidity. (b) and (c) are the insets of the PFBG and FPI spectra, respectively.

A linear regression model was adjusted to the wavelength peak power of the PFBG and FPI structures, as shown in Figure 5a), obtaining a value of -48.6 pm/°C for the PFBG and 177.5 pm/°C for the FPI. The value presented for the PFBG is quite similar to the ones reported in literature for PMMA based PFBGs written at the infrared region [27], [10], and the negative sign accounts for the net contribution of the negative thermo-optic coefficient and positive thermal expansion coefficient, which for PMMA has a higher contribution for the first, leading to have a negative net contribution. On the other hand, regarding the FPI structure, the obtained sensitivity has a positive sign. Contrary to the PMMA material, the adhesive has a positive and higher thermal expansion coefficient than the negative thermo-optic coefficient and thus, the net contribution is positive. Regarding its modulus, it was found a value of 177.5 pm/°C which is quite similar to the ones found in literature for FPI structures based on similar formulation adhesives [16], [28], [29].

For the humidity characterization, both PFBG and FPI structure where linearly red shifted with increasing relative humidity. The insets of the PFBG and FPI spectra may be seen in Figure 4b) and c), respectively. To monitor the shift of the spectra of each structure, the wavelength peak power at 3 dB was calculated. The results can be seen as black dots for the PFBG spectra and blue asterisk for the FPI spectra.
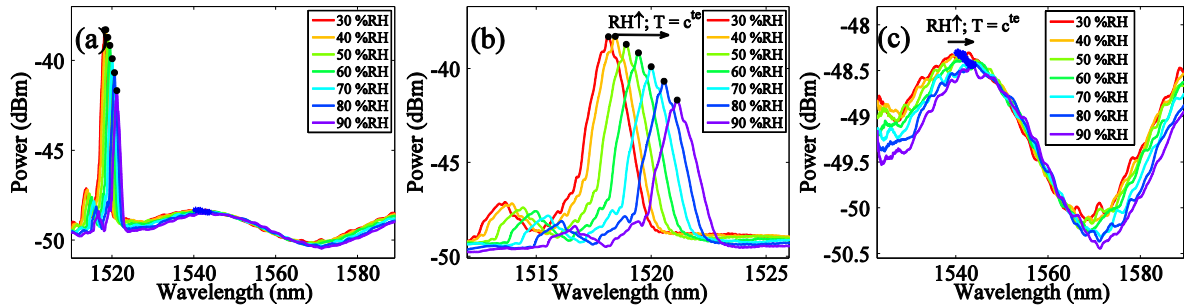

Figure 4. (a) Reflection spectra of the PFBG and FPI cavity at different humidity conditions and constant temperature. (b) and (c) are the insets of the PFBG and FPI spectra, respectively.

In order to calculate the sensitivities of the structures to humidity, a linear regression model was adjusted to the data points collected from each spectra. The results concerning the linear fits can be seen in Figure 5b). From the slope of the fits it was obtained a sensitivity of 51.1 pm/%RH for the PFBG, and a value of 55.1 pm/%RH for the FPI based adhesive structure. The positive values are the result of the net contribution of the swelling coefficient due to the humidity induced volumetric change, and the normalized refractive index change due to humidity. Additionally, the calculated sensitivity for the PFBGs is quite similar to the ones found in literature [30], [27]. Regarding the sensitivity obtained for the FPI structure it was obtained a lower value than the one found in reference [18] but similar to the one found in [16], for a similar optical adhesive.
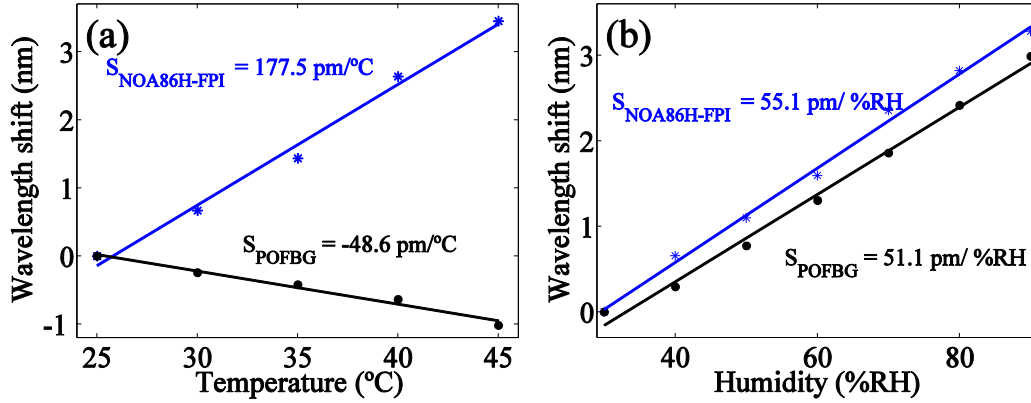
Figure 5. Linear adjustments obtained for the peak wavelength shifts collected from the temperature test at constant humidity, (a); and humidity test at constant temperature.

Considering the sensitivities obtained for both structures in the temperature and humidity characterization, it is now possible the construction of a 2 X 2 matrix which allows the simultaneous measurement of both parameters. The matrix can thus be expressed as:

$$\begin{bmatrix} RH \\ T \end{bmatrix} = \begin{bmatrix} S_{RH,PFBG} & S_{T,PFBG} \\ S_{RH,FPI} & S_{T,FPI} \end{bmatrix} \times \begin{bmatrix} \Delta\lambda_{PFBG} \\ \Delta\lambda_{FPI} \end{bmatrix} \tag{2}$$

where RH and T refers to the calculated humidity and temperature, respectively. $S_{T,PFBG}$ and $S_{RH,PFBG}$ are the PFBG temperature and humidity sensitivities, respectively, while, $S_{T,FPI}$ and $S_{RH,FPI}$ are the FPI sensitivities to temperature and humidity, respectively. Finally, $\Delta\lambda_{PFBG}$ and $\Delta\lambda_{FPI}$ are the measured wavelength shift of the PFBG and FPI structure, respectively.

3.   Conclusions

In this work it was demonstrated the capability to simultaneous measure humidity and temperature using an FBG written in a POF and the conventional adhesive splice procedure used to splice the silica pigtail fiber to the POF, which in the present case was set to have a gap between the fibers in order to create a Fabry-Perot cavity. Results have shown linear tendencies for both structures for the two parameters under test. Based on that, it was possible to create a 2 X 2 sensitivity matrix, which allows the simultaneous measurement of temperature and humidity.

References

[1]   K. Minami, *Handbook of Plastic Optics*, 2nd ed. Weinheim, Germany: Wiley-VCH Verlag GmbH & Co. KGaA, 2010.

[2]   A. Cusano, A. Cutolo, and J. Albert, *Fiber Bragg grating sensors: Recent advancements, industrial applications and market exploitation*, 1st ed. Sharjah : Bentham Science Publishers, 2011.

[3]   Z. Xiong, G. D. Peng, B. Wu, and P. L. Chu, "Highly tunable Bragg gratings in single-mode polymer optical fibers," *IEEE Photonics Technol. Lett.*, vol. 11, no. 3, pp. 352–354, 1999.

[4]   G. Emiliyanov, J. B. Jensen, O. Bang, P. E. Hoiby, L. H. Pedersen, E. M. Kjær, and L. Lindvold, "Localized biosensing with Topas microstructured polymer optical fiber," *Opt. Lett.*, vol. 32, no. 5, pp. 460–462, 2007.

[5]   W. Zhang, D. J. Webb, and G.-D. Peng, "Investigation Into Time Response of Polymer Fiber Bragg Grating Based Humidity Sensors," *J. Light. Technol.*, vol. 30, no. 8, pp. 1090–1096, 2012.

[6]   A. Fasano, G. Woyessa, P. Stajanca, C. Markos, K. Nielsen, H. K. Rasmussen, K. Krebber, and O. Bang, "Fabrication and characterization of polycarbonate microstructured polymer optical fibers for high-temperature-resistant fiber Bragg grating strain sensors," *Opt. Mater. Express*, vol. 6, no. 2, pp. 649–659, 2016.

[7]   C. Markos, A. Stefani, K. Nielsen, H. K. Rasmussen, W. Yuan, and O. Bang, "High-Tg TOPAS microstructured polymer optical fiber for fiber Bragg grating strain sensing at 110 degrees," *Opt. Express*, vol. 21, no. 4, pp. 4758–4765, Feb. 2013.

[8]   R. Oliveira, T. H. R. Marques, L. Bilro, R. Nogueira, and C. M. B. Cordeiro, "Multiparameter POF Sensing based on Multimode Interference and Fiber Bragg Grating," *J. Light. Technol.*, vol. 35, no. 1, pp. 3–9, 2016.

[9]   X. Chen, W. Zhang, C. Liu, Y. Hong, and D. J. Webb, "Enhancing the humidity response time of polymer optical fiber Bragg grating by using laser micromachining," *Opt. Express*, vol. 23, no. 20, pp. 25942–25949, 2015.

[10]   W. Yuan, A. Stefani, and O. Bang, "Tunable Polymer Fiber Bragg Grating (FBG) Inscription: Fabrication of Dual-FBG Temperature Compensated Polymer Optical Fiber Strain Sensors," *IEEE Photonics Technol. Lett.*, vol. 24, no. 5, pp. 401–3, Mar. 2012.

[11]   G. Woyessa, A. Fasano, C. Markos, A. Stefani, H. K. Rasmussen, and O. Bang, "Zeonex microstructured polymer optical fiber: fabrication friendly fibers for high temperature and humidity insensitive Bragg grating sensing," *Opt. Mater. Express*, vol. 7, no. 1, p. 286, Jan. 2017.

[12]   C. Zhang, W. Zhang, D. J. Webb, and G.-D. Peng, "Optical fibre temperature and humidity sensor," *Electron. Lett.*, vol. 46, no. 9, p. 643, 2010.

[13]   G. Woyessa, J. K. M. Pedersen, A. Fasano, K. Nielsen, H. K. Markos, Christos Rasmussen, and O. Bang, "Simultaneous measurement of temperature and humidity with microstructured polymer optical fiber Bragg gratings Simultaneous measurement of temperature and humidity with microstructured polymer optical fiber Bragg gratings," in *25th International Conference on Optical Fiber Sensors*, 2017, vol. 10323, p. 103234.

[14]   J. S. Santos, I. M. Raimundo, C. M. B. Cordeiro, C. R. Biazoli, C. A. J. Gouveia, and P. A. S. Jorge, "Characterisation of a Nafion film by optical fibre Fabry-Perot interferometry for humidity sensing," *Sensors Actuators, B Chem.*, vol. 196, pp. 99–105, 2014.

[15]   T. Fu, Y. Yang, J. Lin, T. Yeh, and P. Han, "A Polymer-Coated Hollow Core Fiber Fabry- Pérot Interferometer for Sensing Liquid Level," vol. 3, no. 1, pp. 16–18.

[16]   C. Lee, Y. You, J. Dai, J. Hsu, and J. Horng, "Chemical Hygroscopic polymer microcavity fiber Fizeau interferometer incorporating a fiber Bragg grating for simultaneously sensing humidity and temperature," *Sensors Actuators B*, vol. 222, pp. 339–346, 2016.

[17]   Y. Yang and C. Lee, "Airgap Fiber Fabry – Pérot Interferometer Using a Hollow Core Fiber Coated with a Layer of Photopolymer for Measurement of Relative Humidity and Temperature," in *5th International Symposium on Next-Generation Electronics (ISNE)*, 2016.

[18]   Y.-W. You, J.-H. Dai, and C.-L. Lee, "Highly hygroscopic polymer microcavity fiber Fizeau interferometer for humidity sensing," *Prog. Electromagn. Res. Symp. PIERS 2014*, pp. 831–834, 2014.

[19]   A. Abang and D. J. Webb, "Demountable connection for polymer optical fiber grating sensors," *Opt. Eng.*, vol. 51, no. 8, p. 80503, Aug. 2012.

[20]   X. Hu, P. Mégret, and C. Caucheteur, "Surface plasmon excitation at near-infrared wavelengths in polymer optical fibers," *Opt. Lett.*, vol. 40, no. 17, pp. 3998–4001, Sep. 2015.

[21]   Norland Products, "Norland Optical Adhesive 86H." 2016.

[22]   R. Oliveira, L. Bilro, and R. Nogueira, "Smooth end face termination of microstructured, graded-index, and step-index polymer optical fibers," *Appl. Opt.*, vol. 54, no. 18, pp. 5629–5633, Jun. 2015.

[23]   R. Oliveira, L. Bilro, and R. Nogueira, "Bragg gratings in a few mode microstructured polymer optical fiber in less than 30 seconds," *Opt. Express*, vol. 23, no. 8, pp. 10181–10187, 2015.

[24]   K. E. Carroll, C. Zhang, D. J. Webb, K. Kalli, A. Argyros, and M. C. Large, "Thermal response of Bragg gratings in PMMA microstructured optical fibers," *Opt. Express*, vol. 15, no. 14, pp. 8844–8850, Jul. 2007.

[25]   T. Watanabe, N. Ooba, Y. Hida, and M. Hikita, "Influence of humidity on refractive index of polymers for optical waveguide and its temperature dependence," *Appl. Phys. Lett.*, vol. 72, no. 13, p. 1533, 1998.

[26]   R. M. Waxler, D. Horowitz, and A. Feldman, "Optical and physical parameters of Plexiglas 55 and Lexan," *Appl. Opt.*, vol. 18, no. 1, p. 101, 1979.

[27]   R. Oliveira, L. Bilro, J. Heidarialamdarloo, and R. Nogueira, "Fabrication and characterization of polymer fiber Bragg gratings inscribed with KrF UV laser," in *The 24th International Conference on Plastic Optical Fibres*, 2015, pp. 371–375.

[28]   X. L. Tan, Y. F. Geng, X. J. Li, Y. L. Deng, Z. Yin, and R. Gao, "UV-Curable Polymer Microhemisphere-Based Fiber-Optic Fabry-Perot Interferometer for Simultaneous Measurement of Refractive Index and Temperature," *IEEE Photonics J.*, vol. 6, no. 4, 2014.

[29]   B. Sun, Y. Wang, J. Qu, C. Liao, G. Yin, J. He, J. Zhou, J. Tang, S. Liu, Z. Li, and Y. Liu, "Simultaneous measurement of pressure and temperature by employing Fabry-Perot interferometer based on pendant polymer droplet," *Opt. Express*, vol. 23, no. 3, p. 1906, 2015.

[30]   W. Zhang and D. J. Webb, "Humidity responsivity of poly(methyl methacrylate)-based optical fiber Bragg grating sensors," *Opt. Lett.*, vol. 39, no. 10, pp. 3026–3029, May 2014.

■

Advances in POF Bragg grating sensors inscription using only one laser pulse for photonic applications

Carlos A. F. Marques[1,*], Andreas Pospori[2], Luis Pereira[3], Paulo Antunes[1], Maria F. Domingues[1], Ole Bang[4], David J. Webb[2,*], Paulo André[5]

[1]Instituto de Telecomunicações, Physics Department & I3N, Universidade de Aveiro, Campus Universitário de Santiago, 3810-193 Aveiro, Portugal
[2]Aston Institute of Photonic Technologies, Aston University, Aston Triangle, B4 7ET Birmingham, UK
[3]Physics Department & I3N, Universidade de Aveiro, 3810-193 Aveiro, Portugal
[4]Department of Photonics Engineering, Technical University of Denmark, DK-2800 Kgs. Lyngby, Denmark
[5]Instituto de Telecomunicações and Department of Electrical and Computer Engineering, Instituto Superior Técnico, Technical University of Lisbon, 1049-001 Lisbon, Portugal
*Corresponding authors: cmarques@av.it.pt / d.j.webb@aston.ac.uk

Abstract: We report the first high-quality POFBG (uniform and phase shifted-POFBGs) sensors inscribed with only one KrF laser pulse at 850 nm region. The devices have been inscribed in a PMMA fibre, with a core doped with BDK for photosensitivity enhancement. The produced Bragg structure rejects more than 16 dB transmitted power, providing ~98% reflectivity, which is well suited for sensing/optical communication applications. The ability to inscribe these high-quality sensors effectively can significantly reduce their production cost in industry. Importantly, the inscription process reported here could be used during the POF drawing process, for simultaneous fabrication of the fibre and POFBG devices.

1. Introduction

In recent years, the technology of fabrication of FBGs in polymer optical fibres (POFBGs) has been intensively developed using uniform FBGs, tilted FBGs, chirped FBGs, or FBG-based Fabry–Perot interferometer [1,2]. Specific material properties, such as low Young's modulus (about 3 GPa compared to 72 GPa for glass), a wider range of strain that the POFs can withstand as well as biological compatibility open a variety of new applications unattainable for silica fibre [1-4]. In the last few years, there is an increase in the research of POFBG technology in the hot topics such as human life safety applications [1-6]. In order to reduce their production costs in industry there are some valid options to reduce the inscription times of POFBGs such as using dopants or different laser inscription systems and even different POF materials [5].

On the order hand, recently, it was showed the scope and potential that POF offers for endoscopic implementation [6]. This works showed that the acoustic sensitivity for POF is thirteen times higher than for silica fibre. However, in order to mitigate the problems encountered related with sensitivity level, a potential transition from uniform FBGs to Fabry-Perot cavities or phase-shifted POFBGs (PS-POFBGs) can be the solution [6]. The goal with that is to deliver a narrower spectral profile, which it can potential used to achieve higher sensitivities. Until now, the literature only provides a single report on a PS-FBG in POFs with quality, which was for use at THz frequencies by using a point-by-point FBG fabrication method [7] presenting some issues to produce with relative low cost.

For the first time, we report high-quality POFBGs (uniform and PS-POFBG) inscribed with only one krypton fluoride (KrF) laser pulse at 850 nm region with high-quality. The devices have been inscribed in a single-mode poly (methyl methacrylate) optical fibre, with a core doped with benzyl dimethyl ketal (BDK) for photosensitivity enhancement. A 10 mm long uniform phase mask customized for 248 nm chosen for 850 nm grating inscriptions was used. One laser pulse with a duration of 15 ns and energy 6.3 mJ is adequate to introduce a refractive index change of $\sim0.7\times10^{-4}$ in the fibre core. The high-quality produced Bragg grating structure rejects more than 16 dB transmitted power, thus providing around 98% reflectivity. Moreover, the ability to inscribe these high-quality sensors effectively can significantly reduce their production cost in industry.

2. Experimental setup and results

A KrF excimer laser system operating at 248 nm wavelength has been used for the POFBGs inscription. The laser pulse duration is 15 ns and the pulse energy can be pre-set; in this study, the energy more suitable for this grating

type is 6.3 mJ. Since the fibre core is doped with BDK for photosensitivity enhancement, where the absorption coefficient of BDK is much higher at wavelengths shorter than 325 nm, shorter laser inscription wavelengths enhance its effects [8]. The fibre is 3-ring microstructured with a hole diameter 1.74 µm and average pitch 3.7 µm. Its core size is 8 µm and its external diameter 130 µm. A cross-section image of the POF used in this work is shown in Fig. 1 (a). Before the inscription, POF pieces of length between 15 cm and 35 cm were glued into demountable FC/PC connectors to facilitate the POFBG interrogation (see Fig. 1 (b)). The average loss per connector is less than 1 dB. The laser beam is focused in the fibre core utilizing a plano-convex cylindrical lens with effective focal length of 200 mm. The effective spot size of the beam on the fibre surface is 20 mm in width and 32.4 µm in height. For the Bragg structures inscription, we used the typical uniform phase mask technique with 10 mm in width with a period of Λ_{PM} =567.8 nm and it can produce gratings with Bragg wavelengths approximately at λ_B = 844 nm. The experimental setup to inscribe Bragg structures is depicted in Fig. 1 (c).
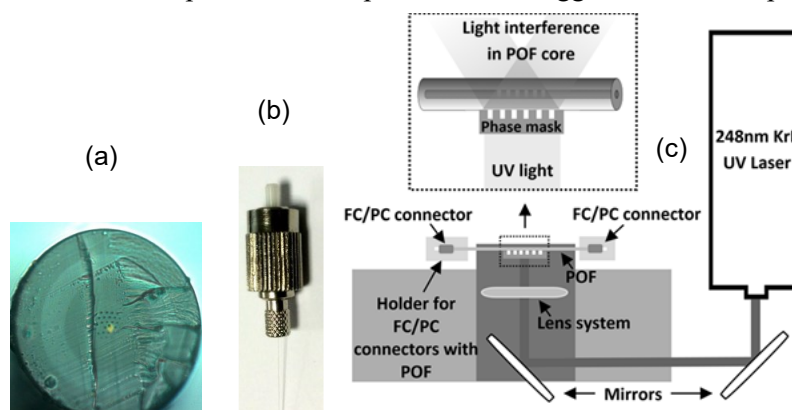

Figure 1.   (a) Fibre cross-section. (b) Demountable FC/PC connector. (c) Inscription setup.

2.1 Uniform Bragg grating with one pulse

After the exposure of a single pulse, the reflectivity of the grating increases for a few minutes following a second order exponential saturation. Fig. 2 (a) shows the growth of the reflected power, which follows a second order exponential saturation for approximately 4 minutes. Similar growth behaviour has been previously reported when Bragg gratings were produced in dye-doped PMMA optical fibre using a Nd:YAG laser system with operational wavelength at 325 nm [9]. In that work, the laser pulse energy was 4.5 mJ, the pulse duration was 5 ns, the repetition rate 10 Hz, and the total exposure time was 88 minutes. When the authors stopped the irradiation, the reflectivity of the Bragg grating was close to zero. Then, the authors noticed its growth after the exposure. The reflectivity had a similar growth dynamic as in our case. However, in their case the growth rate was slower, with the saturation level being reached after 8 hours, while in our work the saturation came in 4 minutes.
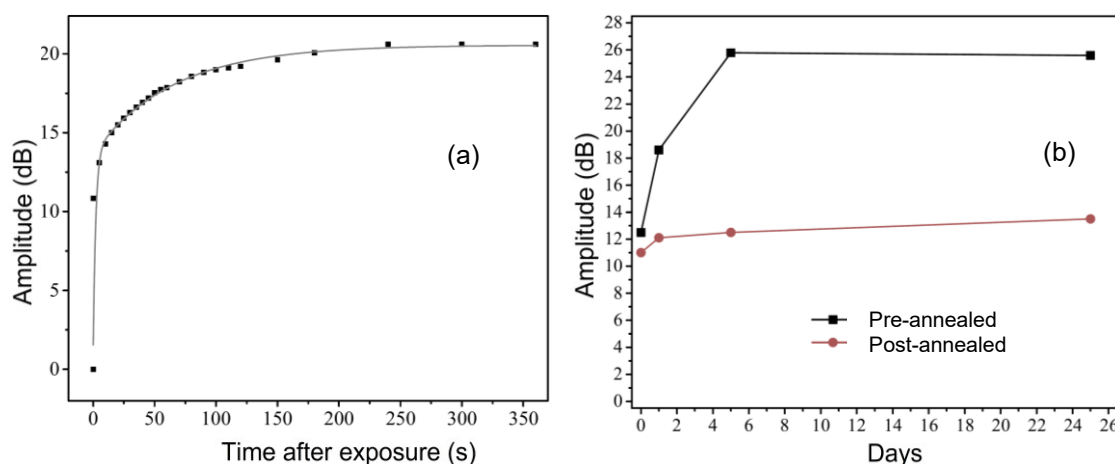

Figure 2.   (a) Reflection growth rate over time after one laser pulse with energy of 6.3 mJ. (b) Thermal annealing effects on pre-annealed and post-annealed POFBGs.

To further investigate this phenomenon, another POF was pre-annealed for 10 minutes in a container filled with water heated at 55±1 °C, and then a POFBG was inscribed with one laser pulse of 6.3 mJ. Furthermore, another POFBG was inscribed in a non-annealed POF with three laser pulses of 6.3 mJ, and then it was post-annealed at 55±1 °C for 2 minutes. Fig. 2 (b) shows the positive effects of both pre and post-annealing on the reflection of POFBGs over time. Considering the above results, we can conclude that a single laser pulse in a pre-annealed POF is adequate for a POFBG inscription.

Figs. 3 (a) and (b) show the reflection and transmission spectra of the POFBG, respectively, which have been taken 7 days after the inscription. The reflection spectrum can be different on each fibre side, which can be strongly influenced from the insertion loss (introduced during the custom-made fibre connectorization). The reflected power at one fibre end was 27.3 dB and at the other end was 31.5 dB from noise level as shown in Fig. 3 (a). Note that the Bragg wavelength has been shifted from 844.4 nm to 841.2 nm, because the fibre was placed with some tension on the inscription setup in order to avoid being bent. Therefore, when the POF was removed from the setup, the POF returned to its original length and the grating period became shorter. Fig. 3 (b) shows that the POFBG has a 17.9 dB transmission rejection. Therefore, the POFBG obtained R = 98.4% reflectivity after the KrF laser pulse.
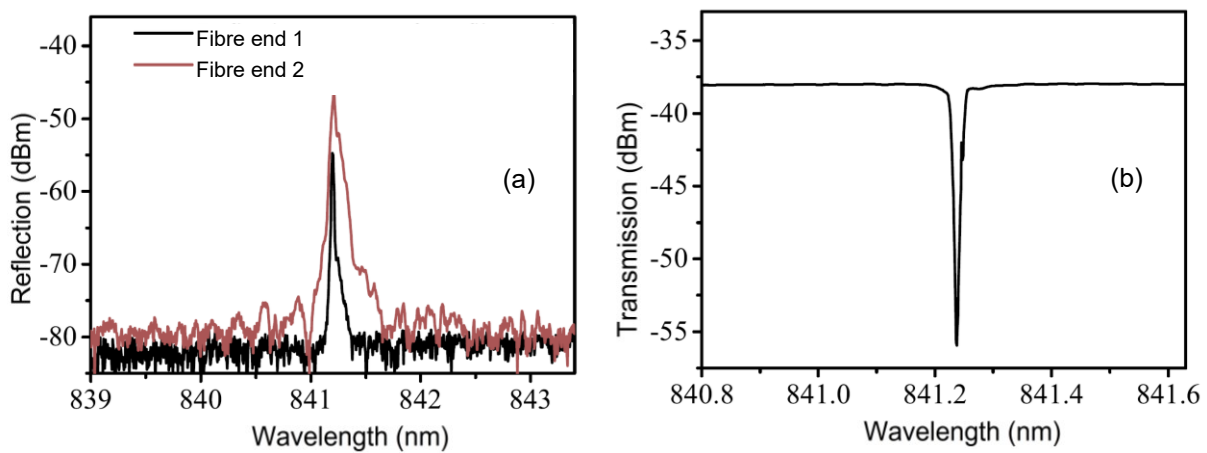

Figure 3.   (a) Reflection and (b) transmission spectra of the POFBG inscribed with one laser pulse.

2.2 Phase-shifted Bragg grating with one pulse

To inscribe PS-POFBGs, the phase shift defects were created directly during the grating inscription process by placing on the phase mask very narrow blocking apertures (a metal wire with 40 μm diameter) in the center of the UV beam, as it is schematically illustrated in Figs. 4 (a) and (b). The phase shift occurs because, where the UV beam is blocked, the mean fibre index is less than in the rest of the grating. It resulted in the inscription of two FBGs separated by a very small gap in a single fabrication process, producing a phase shift on the structure. Fig. 4 (b) shows the case where two narrow blocking apertures are inserted to achieve two phase shifts on the structure. Fig. 4 (c) gives the reflection spectra of inscribed uniform and PS-POFBG after an UV pulse. The uniform POFBG presents a reflectivity around 30 dB and a bandwidth of 0.13 nm at 3dB. We can see that there are two main bands in the PS-POFBG successfully inscribed. The refractive index modulation produced by narrow wire acts as a phase shift of the grating during the inscription process. The channel space of these two reflection bands is about 60 pm, and the transmission notch depth is about 10 dB. Comparing these PS-POFBG spectra with uniform POFBG ones, the slopes of the PS-POFBG compared with normal POFBG in the linear regions are enhanced (see Fig. 4 (c), which will result in the same input signal yielding detected signals with amplitudes that differ by a higher factor [10]. We can fabricate the PS-POFBGs in transmission with very sharp notches of 3 dB width (~15 pm) as shown in the inset of Fig. 4 (d) depending the total grating length (in this case 10 mm length). Figs. 4 (e) and (f) also show a comparison of simulated and experimental results showing a good agreement between them when is used one and two narrow blocking apertures in different position, respectively (see Figs. 1 (a) and (b)). The simulation of the PS-POFBG spectrum can be accomplished using the transfer matrix method [11]. The success rate of the PS-POFBG photo-inscription is quite high – more than 98% – give us a high repeatability of fabrication.
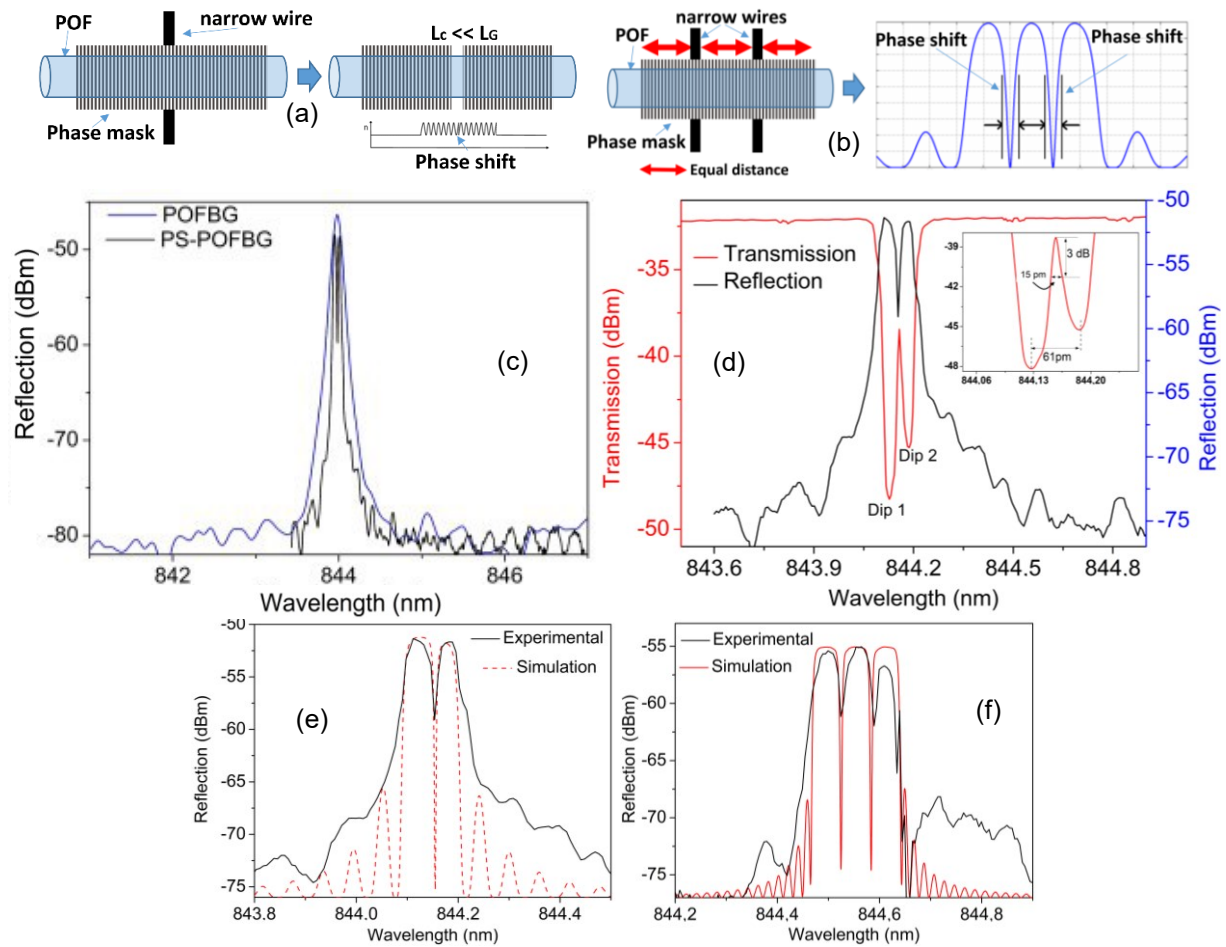
Figure 4. Schematic configurations of the PS-POFBG fabricated with very narrow metal wires positioned: (a) in the centre of the UV beam, (b) in different positions. (c) Reflection spectra of inscribed uniform POFBG and PS-POFBG after an UV pulse UV beam. (d) Reflection/transmission spectra of a PS-POFBG. Simulated and experimental spectra for (e) one phase-shift and (f) two phase-shifted inserted.

3. Conclusions

A fast and accurate inscription with only one KrF laser pulse of good quality Bragg structures (uniform and PS-POFBGs) in a doped PMMA mPOF is reported for the first time. The gratings were created through the phase mask technique, using 248 nm UV light. The POFBGs were created at 850 nm region and produced Bragg grating structure rejects more than16 dB transmitted power, which is well suited for photonic applications. Furthurmore, the inscription process reported here could be used during the POF drawing process, for simultaneous fabrication of the fibre and POFBG devices, which could be a strong progress for POF technology.

References

[1] C. A. F. Marques, et al, "Polymer optical fiber sensors in human life safety", Optical Fiber Technology 36, 144 (2017).
[2] D. J. Webb, "Fiber Bragg grating sensors in polymer optical fibers", Meas. Sci. Technol. 26, 092004 (2015).
[3] C.A.F. Marques, et al, "Chirped Bragg gratings in PMMA step-index polymer optical fiber," IEEE PTL 29, 500 (2017).
[4] C. A. F. Marques, et al, "Highly sensitive liquid level monitoring system utilizing polymer fiber Bragg gratings," Opt. Express 23, 6058 (2015).
[5] Y. Luo, et al, "Fabrication of Polymer Optical Fibre (POF) Gratings", Sensors 17, 511 (2017).
[6] C. Broadway, et al, "A compact polymer optical fiber ultrasound detector", Proc. SPIE. 9708, 970813 (2016).
[7] S. F. Zhou, et al, "Phase-Shifted Fiber Bragg Gratings for Terahertz Range", IEEE PTL 24, 1875, (2012).
[8] A. Pospori, et al, "Polymer optical fiber Bragg grating inscription with a single UV laser pulse", Opt. Express 25, 9028 (2017).
[9] H. B. Liu, et al, "Novel growth behaviors of fiber Bragg gratings in POF under UV irradiation with low power," IEEE PTL 16, 159 (2004).
[10] Q. Wu and Y. Okabe, "High-sensitivity ultrasonic phase-shifted fiber Bragg grating balanced sensing system," Opt. Express 20, 28353 (2012).
[11] T. Erdogan, "Fiber grating spectrum", IEEE/OSA JLT 15, 1277 (1997).

Stable Fibre Bragg Gratings inscribed in doped microstructured polymer optical fibre based on PMMA

R. Min[1], B. Ortega[1*], K. Nielsen [2]and O. Bang[2]

1 Instituto de Telecomunicaciones y Aplicaciones Multimedia, Universitat Politècnica de València, C/Camino de Vera, s/n, 46022 Valencia, Spain)
 2 DTU Fotonik, Department of Photonics Engineering, DK-2800 Kgs. Lyngby, Denmark

*Corresponding author: bortega@dcom.upv.es

Abstract: In this paper we demonstrate stable gratings inscribed in BDK doped PMMA fibres. Resonance wavelength and reflectivity was monitored for 50 days. The results are explained in terms of the physical underlying mechanisms in BDK doped fibres during UV photo inscription.

1. Introduction

Polymer optical fibre (POF) is a growing technology, especially in the fields of sensors and telecommunications [1, 2]. Despite of the fact related to the higher losses or lower bandwidth with respect to silica optical fibres (SOF), POFs show several advantages respect to silica fibres, such as their low stiffness, potential low cost, easy handling and installation, biocompatibility and low weight.

Among their current applications, POF sensors apply to a large variety of areas, such as deformation and pressure [3], humidity [4], biological [5] sensors, etc. In the field of telecommunications, POF is used for short distance connections such as in-vehicle networks (cars, trains or air planes), local area networks (offices, homes or buildings) and interconnection (on-board or intra-board) [6].

However, POF gratings are still under research; high quality gratings fabrication require photosensitive fibres; so far great advances have been done to this concern both in undoped [7] and doped [8,9] fibres. Regarding the former ones, the required refractive index changes for optical fibre gratings fabrication cannot be obtained in PMMA under 325 nm UV radiations unless photosensitivity of fibres is increased by straining them during irradiation. The photosensitive mechanism of 1% strained PMMA fibres at 325 nm have been confirmed as a competitive process between photo degradation and photo-polymerization [7]. When the PMMA fibre is irradiated under stress, the former creates monomers and radicals which form newly rearranged polymer chains. However, fibre relaxation after fabrication due to the material viscoelastic properties leads to unstable gratings [10] and annealing techniques must be addressed in order to avoid any loss in the grating strength and shift in the resonance wavelength.

The stability of polymer gratings is a critical issue mentioned by a few papers [10, 14, 15-17]. The use of non annealed PMMA fibers for grating fabrication under strain with 325nm UV laser lead to a decrease of reflectivities once the strain is released, followed by a later increase [10] to finally reach an approximate stable reflectivity after 50 days but the resonant wavelength did not reach a stable value. Pre-annealed POFs allow to fabricate more stable short term performance gratings at both larger strain and higher temperature [17]. However, both non-annealed and annealed trans-4-stilbenemethanol-doped polymer optical fibers were studied in terms of FBG stability and post-inscription thermal annealing process was necessary to produce stable gratings [14]. The mechanisms underlying the gratings inscription depend on the chemical composition of the PMMA and the dopant concentration but the energy of the UV irradiation is likely to determine the prevailing processes [15], which are linked to the molecular characteristics of the inscribed fiber, and therefore, strongly related to temporal stability of the gratings. As a recent result, long-term stable chirped FBGs have been demonstrated by using pure PMMA pre-annealed fibers at 70 ℃ for 6 hours and employing a 248-nm UV KrF excimer laser for grating inscription [16].

In this paper, we demonstrate stable gratings inscribed in BDK doped PMMA fibres and the results are explained in terms of the physical underlying mechanisms in BDK doped fibres during UV photo inscription.

2. Gratings Fabrication in doped fibre

High refractive index change was achieved under UV irradiation by using a step index POF which core was doped by a photo initiator called benzyl dimethyl ketal (BDK) [8] and the fabrication of a highly photosensitive microstructured polymer optical fibre using BDK as a dopant led to strong fibre gratings without using extra dopants to compensate the index reduction produced by the photosensitizer in the core [9].

Such photosensitive BDK doped fibres are activated by a transition within the molecular orbital of the $>C = O$ group followed by an α-splitting to produce free radicals when illuminated by UV light. A series of reactions can happen, as shown in Fig.1 [11], i.e. photo polymerization and also, the coupling of the benzoyl radicals, depending on the BDK concentration [12].

In this work, a benzyl dimethyl ketal (BDK) doped mPOF was fabricated at DTU, as detailed in [9]. A 325nm CW He-Cd laser (Kimmon IK3301R-G) emitting an output power of 32mW was employed for grating inscription in a setup where the fibre was mounted horizontally in a v-groove and the beam was focused onto the fibre using a cylindrical lens. In this case, the fibre was 0.1% strained during the inscription, in order to minimize any photosensitivity effect due to the strain [9] and keep prevailing the effect of the dopant. The UV light was passed through a phase mask and scanned at 3m/s speed along the fibre for the grating fabrication up to the total grating length of 0.35cm. A phase mask with a grating pitch of 570nm was employed.
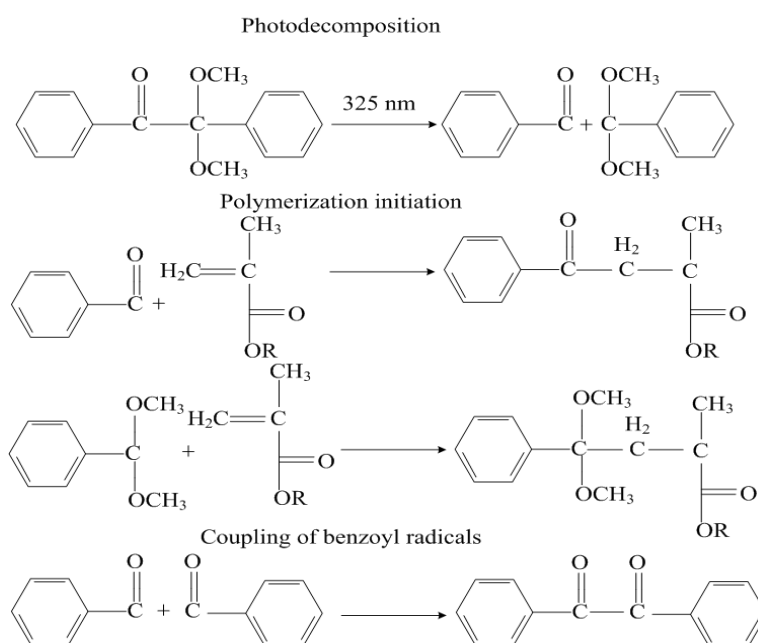

Figure 1. Possible photochemical reactions of BDK in POF [11].

In order to monitor the transmission spectra during the grating growth, the output signal from a Superlum broadband source (SLD-MS-351) centred at 847 nm was launched into the POF fibre and the other end of mPOF was connected to an OSA (ANDO AQ6317C). Both ends of the mPOF were mounted inside a connector ferule and cleaved with a portable cleaver [13].

Fig.2 shows the transmission experimental measurements obtained with 0.1 nm resolution bandwidth and a Bragg wavelength shift towards longer wavelengths can be observed along the growth process which corresponds to a positive refractive index change, as expected [9]. At the end of the inscription, the grating is centred at 846.1nm and shows a 98.4% reflectivity at such wavelength. Assuming the fundamental mode is completely confined within the core, the obtained refractive index change in the 0.35cm long grating can be estimated as $2.12 \cdot 10^{-4}$, similar to that obtained in [14].
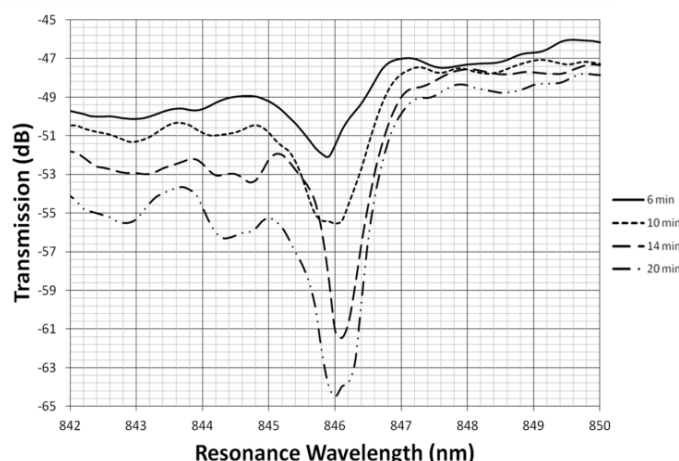
Figure 2.Transmission spectra of a FBG inscribed in doped fibre during the inscription.

3. Stability measurements and discussion

After finishing the inscription, the strain of the fibre was released and the evolution of the resonance wavelength and reflectivity was monitored for 50 days, as shown in Fig.3. As can be observed, both wavelength resonance and reflectivity keep almost constant after the first six days during the period under test.

Fibre material relaxation after gratings inscription process includes, at least, two components, one is due to molecules rearrangement and the second is due to viscoelastic effect due to strain release [11]. As explained above, photo degradation and polymerization contribute to the total UV induced refractive index change in a competitive process, and as a result, molecules change their lengths, as was demonstrated in [7]. Material relaxation from internal UV induced changes will be affected by the size of the newly created molecules, which can be in the spatial resolution limit, and therefore, will depend on the chemical composition and the dopant concentration [15].
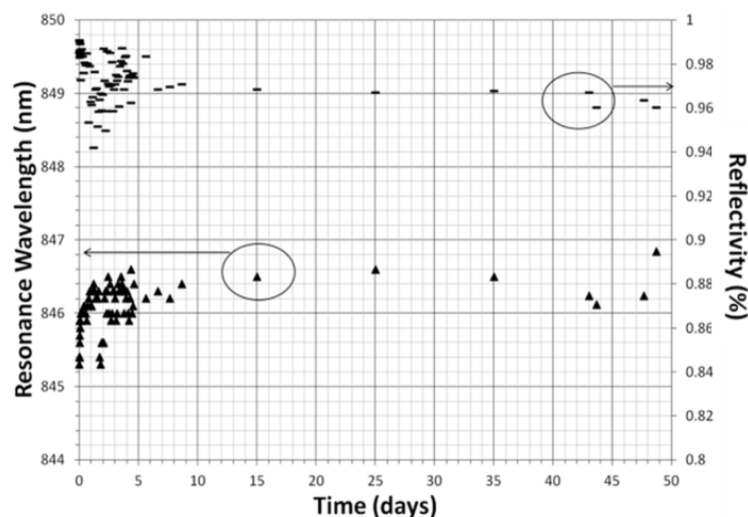

Figure 3. Resonance wavelength and reflectivity evolution over time of gratings fabricated in BDK doped fibre.

Other previously published results [15] show the need of thermal pre- and post-annealing to increase the stability of the FBG in BDK doped fibre, which confirm the complexity of the stable behaviour of gratings inscribed in polymer fibers and their dependences on both the material and the inscription conditions.

In any case, we found that strain release after fabrication in the case of strained fibre during fabrication, especially when the level of strain is about 1% [10] during inscription requires fibre annealing techniques to achieve stable gratings.

4. Conclusion

Long term stable FBG has been fabricated in BDK-doped PMMA optical fibre in doped mPOF and a discussion on the UV underlying inscription mechanisms has been addressed to understand the stability of gratings fabricated in different polymer fibres although further studies are required in order to identify the prevailing processes and molecular structure of the fibres under the concrete fabrication conditions.

5. Acknowledgements

6. References

1. K. Peters, 'Polymer optical fiber sensors: A review', Smart Mater. Struct., 20, 013002 (2011).

2. C. Lethien, C. Loyez , J. P. Vilcot, N. Rolland , P. A.& Rolland, 'Exploit the bandwidth capacities of the perfluorinated graded index polymer optical fiber for multi-services distribution', Polymers, 2011, 3, pp. 1006-1028 (2011).

3. I. P. Johnson, D. J.Webb , K. Kalli, :'Hydrostatic pressure sensing using a polymer optical fibre Bragg gratings', Proc. SPIE 8351, Third Asia Pacific Optical Sensors Conference, 835106 (January 31, 2012).

4. S. Höll，Haupt M, Fischer UH, 'Design and development of an injection-molded demultiplexer for optical communication systems in the visible range', App. Opt., 52, pp. 4103-4110 (2013).

5. C. Zhang, W. Zhang , D. J. Webb, , G. D. Peng, 'Optical fibre temperature and humidity sensor', Electron. Lett., 46, pp. 643-644 (2010).

6. G. Emiliyanov, P. E. Høiby, L. H. Pedersen, O. Bang, 'Selective serial multi-antibody biosensing TOPAS with microstructure polymer optical fibers', Sensors, 13, pp. 3242-3251 (2013).

7. D. Sáez-Rodríguez, K. Nielsen, O. Bang, D. J. Webb, 'Photosensitivity mechanism of undoped poly(methyl methacrylate) under UV radiation at 325 nm and its spatial resolution limit', Opt. Lett., 39, pp. 3421-3424 (2014).

8. Y. Luo, Q. Zhang, H. Liu, G. D. Peng, 'Gratings fabrication in benzyl dimethyl ketal doped photosensitive polymer optical fibers using 355 nm nanosecond pulsed laser', Opt. Lett., 35, pp.751-753 (2010).

9. D.Sáez-Rodríguez, K. Nielsen, H. K. Rasmussen, O. Bang, D.J. Webb, 'Highly photosensitive polymethyl methacrylate microstructured polymer optical fiber with doped core', Opt. Lett., 38, pp. 3769-3772 (2013).

10. D.Sáez-Rodríguez , K.Nielsen, , O. Bang, , D. J. Webb, 'Time-dependent variation of fiber Bragg grating reflectivity in PMMA-based polymer optical fibers', Opt. Lett., 40, pp. 1476-1479 (2015).

11. W.Wu, Y.Luo, X.Cheng, X.Tian, W.Qiu , B. Zhu, G-D.Peng, Q.Zhang, 'Design and fabrication of single mode polymer optical fibre gratings', J Optoelectron Adv M., 12, pp. 1652-1659 (2010).

12. H. Franke, 'Optical recording of refractive-index patterns in doped poly-(methyl methacrylate) films', App. Opt., 23, pp. 2729-2733 (1984).

13. D.Sáez-Rodríguez, R. Min, B. Ortega, K. Nielsen, D. J. Webb, 'Passive and Portable Polymer Optical Fiber Cleaver ' , IEEE Photo. Technol. Lett., 28, pp. 2834-2837 (2016).

14. X. Hu, D. Kinet, P.Mégret, C. Caucheteur, 'Control over photo-inscription and thermal annealing to obtain high-quality Bragg gratings in doped PMMA optical fibers', Opt. Lett., 41, pp. 2930-2933 (2016).

15. A.Pospori, C.A.F.Marques, O. Bang, D. J.Webb, P. André, 'Polymer optical fiber Bragg grating inscription with a single UV laser pulse', Opt. Express, 25, pp. 9028-9038 (2017).

16. C.A.F. Marques, P. Antunes, P. Mergo, D.J. Webb, P. André, 'Chirped Bragg gratings in PMMA step-index polymer optical fiber' IEEE Photo. Technol. Lett, 29, pp.500-503 (2017).

17. Y. Wu, A. Stefani, M. Bache, T. Jacobsen, B. Rose, N. Herholdt-Rasmussen, F. K. Nielsen, S.Andresen, O. B. Sorensen, K.S. Hansen, O. Bang, 'Improved thermal and strain performance of annealed polymer optical fiber Bragg gratings' Opt. Commun, 284, pp.176-182 (2011).

Near-field scanning optical microscopy using plastic optical fibers

A. Smirnov[1*], E. Rostova[1], G. Dietler[1], S. K. Sekatskii[1]

1 LPMV, IPHYS, Ecole Polytechnique Fédérale de Lausanne, Lausanne 1015, Switzerland
*Corresponding author: anton.smirnov@epfl.ch

Abstract:

Nowadays, sharpened glass fiber – made probes attached to a quartz tuning fork and exploiting the shear force – based feedback is by far the most popular in the field of Scanning Near-field Optical Microscopy (SNOM). These probes are expensive, very fragile and their fabrication is difficult, hard to control and in many cases a hazardous process.

We're presenting SNOM probes made from plastic optical fibers with a thin core (850 nm). The sharp tips were prepared by chemical etching of the fibers via organic solvent, and the probes were prepared by proper gluing of sharpened fibers onto the quartz tuning fork (TF). An excellent "durability" on par with the good topographical resolution of these probes was reported.

1. Introduction

The resolution of optical microscopes is limited by Abbe diffraction limit and typically it is approximately 200-300 nm. To better resolve an object, another technique should be used. Near-field Scanning Optical Microscope (SNOM) breaks the resolution limit exploiting the properties of the evanescent waves. Resolution of such image is limited by the size of the aperture and it is approximately 30-100 nm. The main advantage of SNOM in comparison with classical optical microscopes is the linking of topographic information with the optical image. By far the most popular SNOM probe is a metal-coated tapered optical glass fiber on which apex an aperture for the light transmission, whose diameter is between 50 and 200 nm, is formed. A common problem of this approach is the fragility of the tip. We propose the way to solve this problem – using the plastic optical fibers (POF), that are much less fragile in comparison to glass fibers. Furthermore, preparation of POF-made SNOM tips doesn't require using of hazardous HF treating, which remains the most popular approach to prepare SNOM probes from the glass fibers [1–4]. Results of the experiments in this way are presented below.

2. Results and Discussion

The polymethylmethacrylate optical fibers (POF) used in our previous work [5] were purchased from A.R.T. Photonics GmbH, Germany. It is step index type fibers with a diameter of 250 µm made of high purity PMMA core and a fluorinated PMMA cladding. Since these fibers were relatively heavy and had large core diameter (~100 µm), we decided to change them into polystyrene 125 µm diameter fibers (specially ordered and prepared for us by Paradigm Optics Company, USA) with the acrylic core (diameter is 0.85 µm).

Looking back on the way of the preparing of the glass fiber probes (detailed procedure described in [6]) we elaborated similar protocol for POF. To protect the fiber from acid vapour double-layer solution was used. It was a mixture 9:1 of dichloromethane (DCM) and ethyl acetate (EA, Aldrich) with water. Using pure solvent (DCM or EA or something else) results into inappropriate shape of the tip due to different the dissolution rate of the core and the cladding. The mixture of DCM and EA allows to avoid this problem. Moreover, using of such an etchant results into most significant weight loss of POF in it. The etching of the POF is a quick (tens of seconds) and self-terminating process which results in the formation of the sharp conical tip with the radius of curvature equal to 30 – 150 nm (Figure 1).
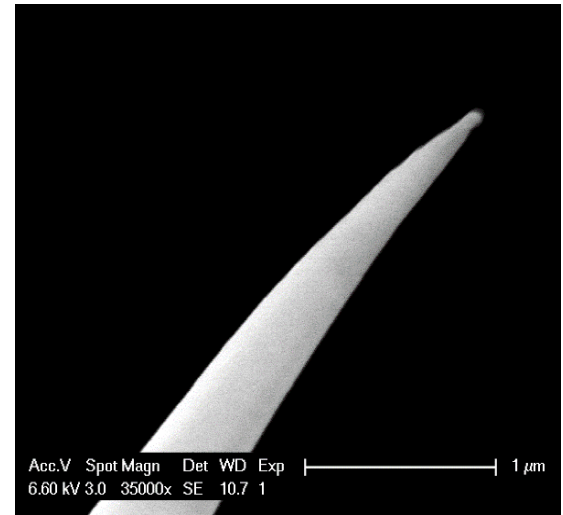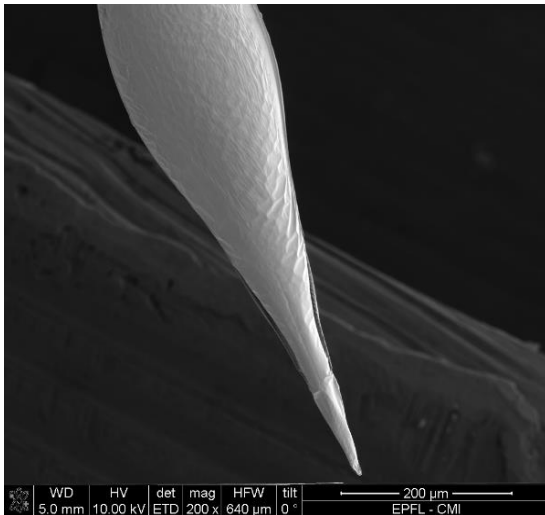
Figure 1. SEM images of the etched POF tip

The sharpened POF SNOM probes were glued onto the quartz TF in the double resonant conditions following the procedure outlined in [7]. Since such montage requires the matching of the frequencies, it is essential to glue carefully both the fiber onto the metal case of the TF (to create the "hinging point") and 40 micron-diameter glass driving rod connecting the fiber and one of the TF's prongs (see Figure 2), as well as precisely control the length of a free-standing part of the fiber beam. It was found that this distance should be equal to 3.0±0.1 mm, in the case of the use of 125 μm POF tip. The driving rod connecting the probe with one of the TF's prongs should be glued at ~1.55 mm distance from the fiber hinging point. Such a method of attaching of fiber to the tuning fork results in quite large quality factor: initial value of Q lying in the range of 10 000 – 12 000, which is characteristic for a free unloaded tuning fork in air, drops down to the values ranging 3000–6000 after proper gluing of a glass fiber probe onto it.
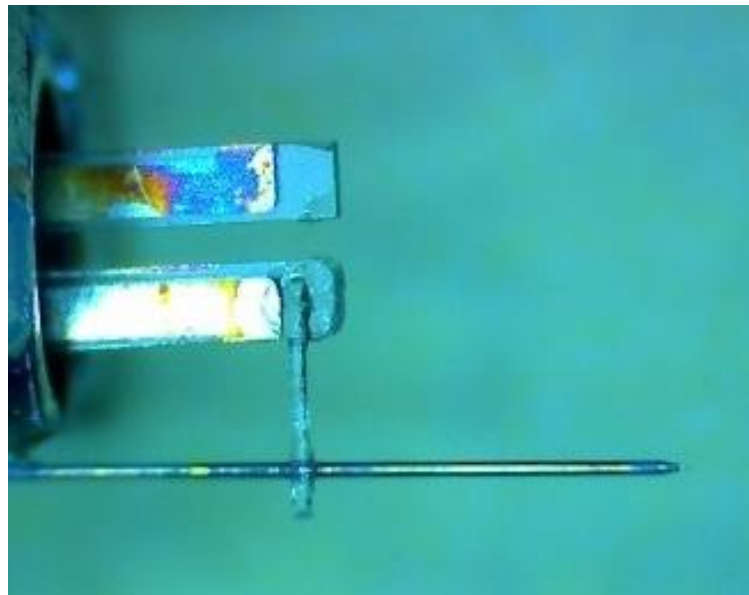

Figure 2. The double resonant emplacement of a fiber probe onto a tuning fork;

The performance of the aperture POF SNOM probes has been assessed exploiting them as probes of the slightly modernized customarily made Scanning Near-Field Optical Microscope, which main features were discussed earlier [7, 8]. In Figure 3, we present the Shear force topographical image of TGZ01 calibrating grating routinely used to calibrate Atomic Force Microscope.
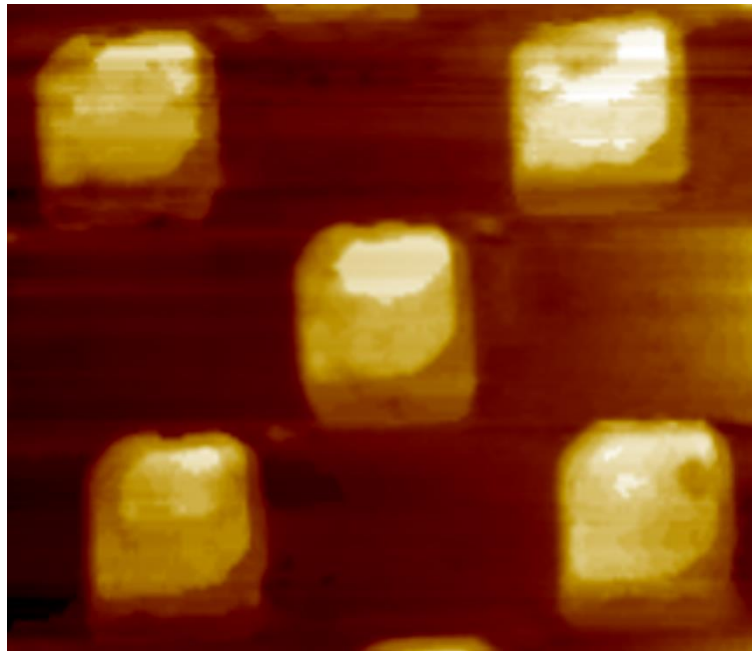

Figure 1 Shear force topographical image of TGZ01 calibrating grating. Constant Q-factor mode of the proprietary SNOM controller was used as a feedback source. Scan size: 3x3µm

As an example biological application, mica samples containing amino-fibrils deposited onto the surface, were used, see Figure 4 left.
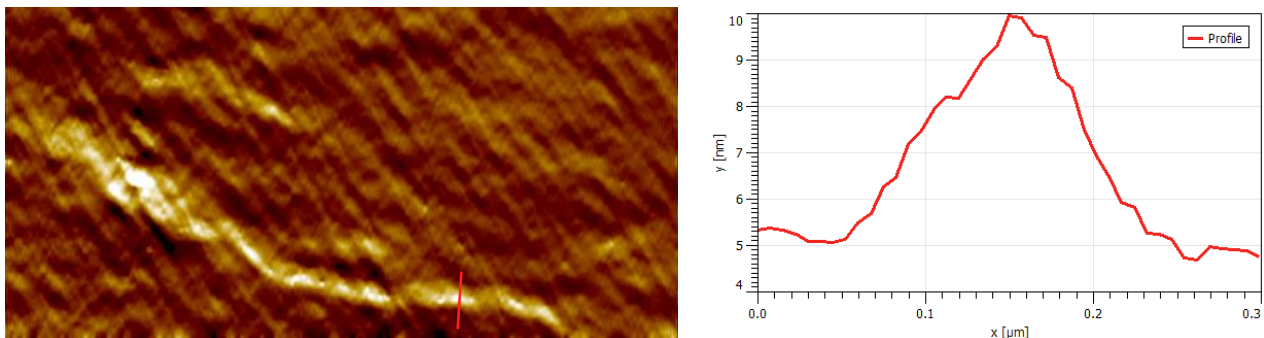

Figure 2 Left: Shear Force topographical image of the amino-fibrils deposited on the mica surface. Constant Q-factor mode of the proprietary SNOM controller was used as a feedback source. Scan size: 4x2µm. Right: Profile of the amino-fibrils from the left image along the red line.

3. Conclusion

We reported the first use Of course, presented images are not the best example of POF probes topographical performance. Furthermore, these images were obtained via probe which already touched the surface few times. And this is a direct proof of "durability" of POF-made SNOM tips. At the current stage, elaboration of the metal coating procedure for these probes which is essential for optical SNOM imaging   is in process.

4. Acknowledgements

5. References

[1] M.A. Paesler, P.J. Moyer Near Field Optics: Theory Instrumentations, and Applications, Wiley, New York, 1996.

[2] D. Courjon, in: Near-Field Microscopy and Near-Field Optics, Imperial College Press, London, 2003.

[3] H. Taha, A. Strinkovski, A. Manevitch, A. Khatchatouriants, R. Dekhter, E. Ammann, A. Lewis, Nature Biotechnology 21 (2003) 1378.

[4] A.V. Zayats, D. Richards (Eds.), Nano-optics and Near-field Optical Microscopy, Artech House, 2008.

[5] H. Chibani, K. Dukenbayev, M. Mensi, S. K. Sekatskii and G. Dietler, Ultramicroscopy 110, 211-215 (2010)

[6] Haber, L. H., Schaller, R. D., Johnson, J. C. and Saykally, R. J. (2004), Shape control of near-field probes using dynamic meniscus etching. Journal of Microscopy, 214: 27–35.

[7] Cherkun, A. P., Serebryakov, D. V., Sekatskii, S. K., Morozov, I. V., & Letokhov, V. S. (2006). Double-resonance probe for near-field scanning optical microscopy. *Review of scientific instruments*, *77*(3), 033703.

[8] D. V. Serebryakov, S. K. Sekatskii, A. P. Cherkun et al., J. Microsc. 229, Pt. 2, 287 (2008).

Portable, in-line and low cost refractive index sensor for liquids

D. P. Duarte[1,2*], R. N. Nogueira[1], L. B. Bilro[1]

1 Instituto de Telecomunicações - Pólo de Aveiro, 3810-193 Aveiro, Portugal
2 Physics Department, Aveiro University, 3810-193 Aveiro, Portugal

*Corresponding author: DDuarte@av.it.pt

Abstract: A portable in-line and low cost refractive index sensor for liquids was developed based on the Fresnel reflection, where the critical angle of the totally reflected light between the interface of two media is detected. A LED is used as light source and a POF, with a well-established numeric aperture, will guide the light to the prism surface. The reflected light is detected by a CCD array. Both LED as the CCD are controlled with an electronic board with remote sensing by wireless. A resolution of 1.2 x 10^{-4} RIU was obtained with a potential cost lower than 100 €.

1. Introduction

Refractive index is represented as a dimensionless number that describes how light propagates through a medium and thus it is an important parameter of characterization of that material. The refractive index can be seen as the factor by which the speed of radiation with a certain wavelength are reduced with respect to their vacuum values. This reduction of velocities will have an effect on the refraction or bent and on reflection of light between material interfaces, depending on the angle of light incidence. In complex fluids, such as drinks, the refractive index (RI) is normally measured for assessment of dissolved or submicronic materials like the sugar concentration. In other industries, it is also an important propriety to measure oil/water ratios, glycol/water ratios like in antifreeze, and inaccessible liquids such as the electrolyte of rechargeable cells [1].

The first refractometer developed and sold commercially in 1881 was developed by Ernst Abbe with a design that is still in use today, known as Abbe refractometer. This refractometer uses two prisms where the sample is putted between. Light from a polychromatic source enters the illuminating prism until it reaches the sample where refraction and total reflection will occur at critical angle. The light will then exit the other prim to a scaled telescope that rotates to search for a dark/illuminated boundary area that will be observed in a position that depends on the sample refractive index [2]. Resolution in the order of magnitude of 10^{-4} RIU are common in this design. For high resolution measurements, with precision in the order of magnitude of 10^{-4} to 10^{-5} RIU, laboratory digital refractometers are usually used as the preferred commercial application. The principle of operation of this type of refractometers are based on the determination of the critical angle of where total reflection of light occurs in the interface of two mediums. These two mediums are composed by the liquid of which RI we wanted to determinate and a prism that will act as sample holder. A light source, usually a long-life LED, is focused onto a prism surface via a lens system. Depending on its refractive index, the incoming light below the critical angle of total reflection is partly transmitted into the sample, whereas for higher angles the light is totally reflected. This light reflectivity's are RI dependent and detected by a high-resolution CCD sensor array [1], [3]. These commercial RI sensors are not in-line and real monitoring prepared for applications where this type of monitorization is required.

Other high resolution RI sensors were also developed in academia. This includes optical fiber intrinsic sensing mechanisms as macrobending [4], D-shape [5], tapers [6] and U-shaped clad removed tapers [7]. The use of fiber gratings, Bragg (FBG), tilted (TFBG) and long (LPG) is also a common subject of development in interferometric based sensors. Examples include Etched FBG Fabry-Pérot [8], LPG Fabry-Pérot taper [9], TFBG [10]. Other type of interferometric RI sensors that do not use gratings but instead other fiber elements are Fabry-Pérot Photonic-Crystal Fiber (PCF) [11], Sagnac loop PCF [12], Michelson taper interferometer [13], core offset Mach Zehnder [14]. Surface plasmon resonance (SPR) based sensor are also a very common research subject for RI sensor using both prism [15] and fiber based interrogation mechanisms. The latter includes uncladded fiber metal films [16], uncladded fiber metal nanoparticles [17], D-shaped fiber metal films [18] and tapers [19], and also using tilted gratings to promote SPR interaction [20]. All the resolutions and RI range of this sensor can be seen summarized in Table 1.

Table 1. State of art of the most common commercial and academia sensing mechanism.

Commercial prism based sensors			
	Range (RIU)	**Resolution (RIU)**	**Ref.**
Abbe Refractometer	1.3 – 1.7	10^{-4}	[2]
Lab. Digital Refractometer	1.3 – 1.6	$10^{-5} – 10^{-4}$	[3]
Intrinsic Intensity based sensors			
	Range (RIU)	**Resolution (RIU)**	**Ref.**
Macrobending (POF)	1.3 – 1.59	5×10^{-3}	[4]
D-shape (POF)	1.33 – 1.44	6.48×10^{-3}	[5]
Taper	1.37 – 1.40	5×10^{-4}	[6]
U-shaped clad removed Taper (POF)	1.33 – 1.45	5×10^{-4}	[7]
Gratings and grating based interferometric sensors			
	Range (RIU)	**Resolution (RIU)**	**Ref.**
Etched FBG Fabry-Pérot	1.33 – 1.4	1.4×10^{-5} (a)	[8]
LPG Fabry-Pérot Taper	1.333 – 1.362	5.8×10^{-6} (a)	[9]
TFBG	1.415 – 1.455	3×10^{-5} (a)	[10]
Non-grating interferometric based sensors			
	Range (RIU)	**Resolution (RIU)**	**Ref.**
Fabry-Pérot PCF based	1.33 – 1.45	1.2×10^{-5}	[11]
Sagnac loop PCF	≈ 1.333	4×10^{-6} (a)	[12]
Taper Michelson interferometer	1.33 – 1.36	5.1×10^{-4} (a)	[13]
Core offset Mach Zehnder	1 – 1.0022	6.2×10^{-6} (a)	[14]
SPR based sensing			
	Range (RIU)	**Resolution (RIU)**	**Ref.**
Wavelength Interrogation Prism	---	10^{-6} (a)	[15]
Uncladded Fiber Silver Film	1.33 – 1.39	1.5×10^{-6} (b)	[16]
Uncladded Fiber Gold Nanoparticles	1.33 – 1.41	2×10^{-5} (b)	[17]
Fiber D-shaped Gold Film	1.33 – 1.39	6.3×10^{-6} (b)	[18]
Fiber Taper Gold Film	1.435 – 1.445	4×10^{-7} (b)	[19]
TFBG gold Film	1.33 – 1.38	1×10^{-5} (b)	[20]

[a]1 pm spectral analyzer resolution; [b]10 pm spectral analyzer resolution

It is important to notice that although the interferometric and SPR sensors present high resolution and can be easily applied for in-line and real time monitoring, a spectral interrogation system is mandatory for sensing, which increases substantially the costs for a commercial application.

In this work the development of a low-cost RI sensor design is presented. This sensor was developed based on the following premises: it can be implemented as in-line and real time sensing; presents low cost in its development and implementation to be commercial competitive; present low complexity and high reproducibility in its development and implementation and have the highest possible resolution by cost rate. Having these criteria in consideration, a prism based refractometer, adapted for in-line measurements, presents the best solution that meets all the requirements stated.

1.1 Sensor design

The developed RI sensor was established for in-line liquid measurement and is based on the Fresnel reflection of light principle, more specifically the particular case of Snell's law. The operation of this refractometer was designed to acquire the critical angle where light is totally reflected between the interface of two media. The interaction of light with this interface is stated by Snell's law as:

$$n_1 \sin(\theta_1) = n_2 \sin(\theta_2) \qquad (1)$$

Where n_1 and n_2 is the refractive indices of the first and second medium, and θ_1 and θ_2 are the angles on incidence and refraction of light to and from the interface respectively. These two media are composed by the liquid, of which we want to determinate the refractive index, and a prism (with $n_1 = 1.46$) that will act as a mandatory higher index medium and where the light will propagate. A long-life LED (IF-E93) is used as light source and a plastic optical fiber (POF), with a well-established numeric aperture (NA = 0.5), will guide the light to the prism surface. Here the POF will have a fundamental role of guiding and limiting the spread of light (light cone) that will reach the interface. This prevents the use of a converging lens to focus the light, which simplifies the sensing system in comparison with a traditional refractometer. When light reaches the interface

with incident angle θ_1, below the critical angle of total reflection, this is, when $\theta_2 = 90°$, it is partly transmitted into the liquid, whereas for higher angles the light is totally reflected, creating a dark/light region on the other face of the prism. This region is detected by a high-resolution CCD sensor array (tcd1304dg) with a pixel resolution of 8 μm. A temperature sensor is also present for future measurement compensation. All these components are protected in a waterproof box that is submerged for measurements. Both LED source as the CCD sensor array are controlled with an electronic board with a microcontroller (Raspberry Pi A+) and wireless connector for remote sensing (Figure 1).
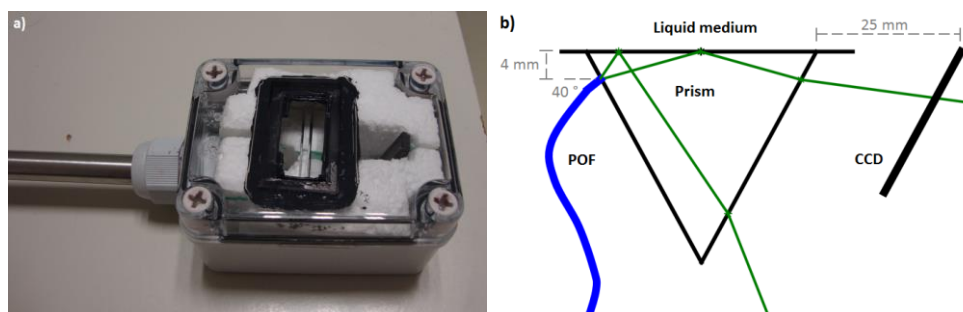

Figure 1. a) RI sensor with the components cased in a waterproof box. Only the prism is in contact with the external medium b) Scheme of the sensor physical principle when the liquid of the external medium is in contact with the prism.

2. Experimental results

Several tests to the sensor were performed to assess its behavior with the increase of the external liquid medium when submersed. An example of the signal behavior coming from the CCD array is observed in Figure 2 a).
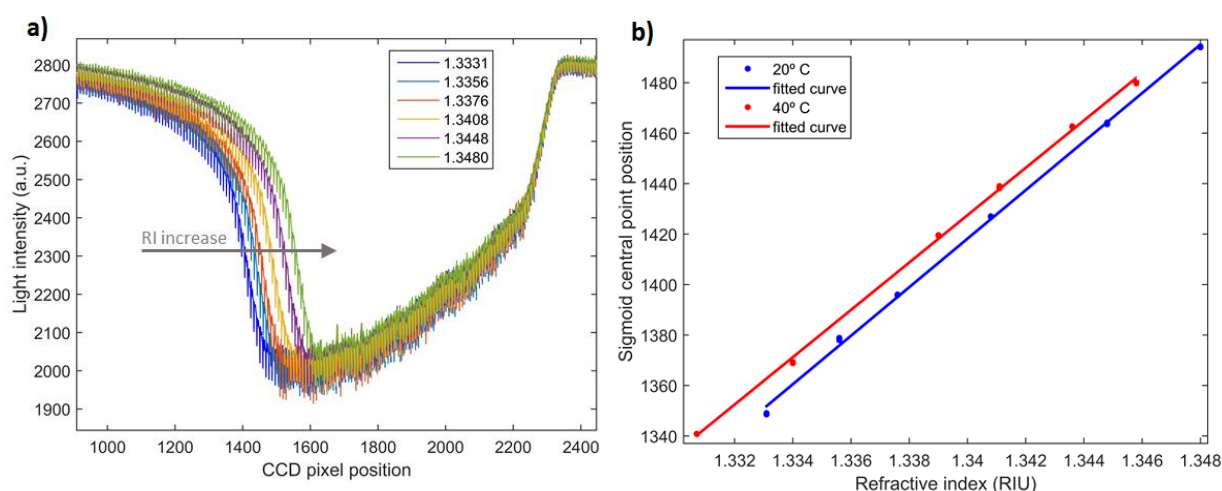

Figure 2. a) CCD light detection variation with the increase of the external medium refractive index. b) Evolution of the central sigmoid point value with the increase of the external medium refractive index for 20° C and 40° C.

The raw data coming from the CCD array is treated firstly with a Savitzky–Golay smoothing processing technique followed by a sigmoid curve fitting by least squares technique. The fitting will give the necessary curve parameters which the most important one will be the sigmoid central point position that will change with the increase of the external medium RI. For each RI value, 3 individual measurements were performed. Depending on the liquid temperature, the position of the central sigmoid point will also be affected (Figure 2 b). Considering the CCD resolution of 8 μm and the variation observed with the sensor, a refractive index resolution of 1.2×10^{-4} RIU was obtained which is comparable to the most used bench refractometers.

A test with colored and turbid liquids with increasing RI were also performed to assess its influence in a measurement (Figure 3). For the colored liquid, a red dye was used which has absorption for the used green light LED. For turbidity, corn starch was added to the solution until reaches 3725 nephelometric formazine units (NTU).
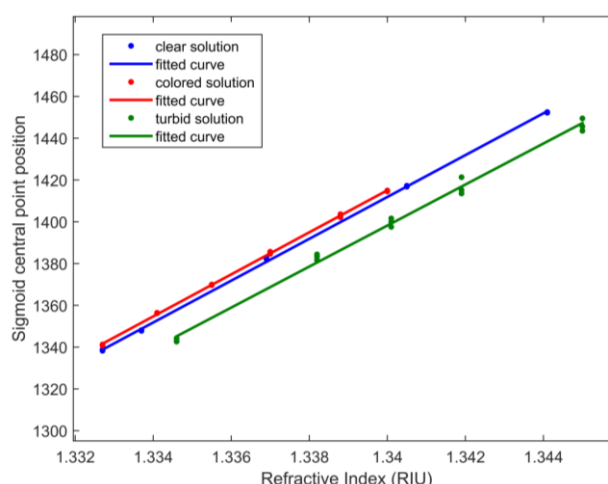
Figure 3. Colored and turbid solution influence in the refractive index assessment.

The results showed that for colored liquids, the change to the RI variation calibration is almost negligible, with a measured error of 2 x 10^{-4} RIU in respect of what is expected to the clear liquid. The turbid liquid, in other hand, introduces a higher measurement error of about 2 x 10^{-3} RIU which indicates that this sensor is not appropriate for high resolution measurements of turbid liquids, but it is still useful if high resolution is not needed.

3. Expected costs

A cost analysis of this sensor was performed for a 3-meter-deep liquid reservoir and which is summarized in Table 2. Overall it is proven that a high resolution in-line and real-time RI sensor can be developed for lower than 100 €, compared to the 5000 € solutions observed in market.

Table 2. Sensor cost assessment for 3-meter-deep reservoir.

Sensor Component	Price (€)	Sensor Component	Price (€)
Box and structure	35	Raspberry Pi A+	25
LED	8	Prism	3
3 m fiber	3.2	Temperature sensor	3
CCD	22	**TOTAL**	**99,2**

4. Conclusion

The developed sensor has accomplished the objective of being an in-line and real time monitoring solution, showing also to be simple and easy to build. The obtained resolution of 1.2 x 10^{-4} RIU is comparable to the mostly used commercial beach refractometers but with potential cost lower than 100 €. When in presence of turbid liquids, a measurement resolution of 2 x 10^{-3} RIU is obtained. This sensor will be ideal for monitoring in real time industrial application as wine fermentation, drink industry, and oil industry.

5. Acknowledgements

6. References

[1] G. H. Meeten, "Refractive Index Measurement," in *Measurement, Instrumentation, and Sensors Handbook, Second Edition: Electromagnetic, Optical, Radiation, Chemical, and Biomedical Measurement*, Second., J. G. Webster and H. Eren, Eds. CRC Press, 2014, pp. 50-1-50–11.
[2] A. W. S. Tarrant, "Optical Measurements," in *Instrumentation reference book*, 4th ed., W. Boyes, Ed. Butterworth-Heinemann/Elsevier, 2010, pp. 499–519.
[3] Anton Paar, "The Universal Refractometer." 2016.
[4] J. Zubia, G. Garitaonaindía, and J. Arrúe, "Passive device based on plastic optical fibers to determine the indices of refraction of liquids," *Appl. Opt.*, vol. 39, no. 6, p. 941, Feb. 2000.
[5] F. Sequeira *et al.*, "Refractive Index Sensing with D-Shaped Plastic Optical Fibers for Chemical and Biochemical Applications," *Sensors*, vol. 16, no. 12, p. 2119, Dec. 2016.
[6] P. Polynkin, A. Polynkin, N. Peyghambarian, and M. Mansuripur, "Evanescent field-based optical fiber sensing device for measuring the refractive

index of liquids in microfluidic channels," *Opt. Lett.*, vol. 30, no. 11, p. 1273, Jun. 2005.

[7] C. Teng, N. Jing, F. Yu, and J. Zheng, "Investigation of a Macro-Bending Tapered Plastic Optical Fiber for Refractive Index Sensing," *IEEE Sens. J.*, vol. 16, no. 20, pp. 7521–7525, Oct. 2016.

[8] W. Liang, Y. Huang, Y. Xu, R. K. Lee, and A. Yariv, "Highly sensitive fiber Bragg grating refractive index sensors," *Appl. Phys. Lett.*, vol. 86, no. 15, p. 151122, Apr. 2005.

[9] Jin-Fei Ding, A. P. Zhang, Li-Yang Shao, Jin-Hua Yan, and Sailing He, "Fiber-taper seeded long-period grating pair as a highly sensitive refractive-index sensor," *IEEE Photonics Technol. Lett.*, vol. 17, no. 6, pp. 1247–1249, Jun. 2005.

[10] N. J. Alberto, C. A. Marques, J. L. Pinto, and R. N. Nogueira, "Simultaneous strain and refractive index sensor based on a TFBG," in *Proc European Workshop on Optical Fibre Sensors*, 2010, vol. 7653, p. 765324.

[11] T. Wang and M. Wang, "Fabry–Pérot Fiber Sensor for Simultaneous Measurement of Refractive Index and Temperature Based on an In-Fiber Ellipsoidal Cavity," *IEEE Photonics Technol. Lett.*, vol. 24, no. 19, pp. 1733–1736, Oct. 2012.

[12] C. Wu *et al.*, "In-line microfluidic integration of photonic crystal fibres as a highly sensitive refractometer," *Analyst*, vol. 139, no. 21, pp. 5422–5429, Jul. 2014.

[13] Z. Tian, S. S. Yam, and H. Loock, "Refractive index sensor based on an abrupt taper Michelson interferometer in a single-mode fiber," *Opt. Lett.*, vol. 33, no. 10, p. 1105, May 2008.

[14] D.-W. Duan, Y.-J. Rao, L.-C. Xu, T. Zhu, D. Wu, and J. Yao, "In-fiber Mach–Zehnder interferometer formed by large lateral offset fusion splicing for gases refractive index measurement with high sensitivity," *Sensors Actuators B Chem.*, vol. 160, no. 1, pp. 1198–1202, Dec. 2011.

[15] J. Homola, S. S. Yee, and G. Gauglitz, "Surface plasmon resonance sensors: review," *Sensors Actuators B Chem.*, vol. 54, no. 1–2, pp. 3–15, Jan. 1999.

[16] R. C. Jorgenson and S. S. Yee, "A fiber-optic chemical sensor based on surface plasmon resonance," *Sensors Actuators B Chem.*, vol. 12, no. 3, pp. 213–220, Apr. 1993.

[17] Y. Shao, S. Xu, X. Zheng, Y. Wang, and W. Xu, "Optical Fiber LSPR Biosensor Prepared by Gold Nanoparticle Assembly on Polyelectrolyte Multilayer," *Sensors*, vol. 10, no. 4, pp. 3585–3596, Apr. 2010.

[18] Y.-C. Lin, "Characteristics of optical fiber refractive index sensor based on surface plasmon resonance," *Microw. Opt. Technol. Lett.*, vol. 55, no. 3, pp. 574–576, Mar. 2013.

[19] D. Monzón-Hernández, J. Villatoro, D. Talavera, and D. Luna-Moreno, "Optical-fiber surface-plasmon resonance sensor with multiple resonance peaks," *Appl. Opt.*, vol. 43, no. 6, p. 1216, Feb. 2004.

[20] C. Caucheteur, Y. Shevchenko, L.-Y. Shao, M. Wuilpart, and J. Albert, "High resolution interrogation of tilted fiber grating SPR sensors from polarization properties measurement.," *Opt. Express*, vol. 19, no. 2, pp. 1656–1664, 2011.

POF
2017

WDM Transmission over Graded-Index Plastic Optical Fiber

T. Almeida[1*], R. Oliveira[1] A. M. Rocha[1,2], L. Bilro[1] and R. Nogueira[1]

1 Instituto de Telecomunicações, Campus Universitário de Santiago, 3810-193, Aveiro, Portugal
2 I3N, Campus Universitário de Santiago, 3810-193, Aveiro, Portugal

*Corresponding author: telmopelicano@av.it.pt

Abstract: In this work, we demonstrate the transmission of 50 Gb/s over 50 m of multimode graded-index polymer optical fiber. The transmission has been achieved employing wavelength division multiplexing technology with four channels in the C Band 12.5 Gb/s each. The results presented here will improve the current state of the art in short distance applications employing POF, paving the way for a more intense use of this fiber in the near future.

1. Introduction

Nowadays, the possibility of the fiber to the home (FTTH), for simultaneous transmission of different services such as internet, telephone, digital television is real. However, to meet the more demanding expectations of the end user, it is necessary to improve the physical infrastructure of the existing communication networks in order to obtain the best ratio between quality of service and price of implementation. So the demand for optical devices that process information at a reduced cost and easy to install is a reality. Polymer optical fibers (POFs) are being pointed as a lower-cost and a viable alternative to silica fiber in short-distance applications. The use of this type of fiber has several advantages such as simpler and less expensive components, easier to manipulate and connectorize, greater flexibility and resilience to bending, shock, and vibration.

Recently, perfluorinated graded index plastic optical fiber (GI-POF) has emerged as a contending technology for short reach telecom applications such as data centre interconnection [1], [2] and FTTH applications [3]. Moreover, wavelength division multiplexing (WDM) has already been proposed as a solution to expand the capacity using SI-POFs at the visible region [5]–[7].

This fiber has special characteristics, such as, small bending radius (~5 mm), low dispersion and high bandwidth [4]. GI-POF has a fiber loss lower than 60 dB/km at the near infrared region. On the other hand, at the telecom region, were most of the fiber components are already developed for silica based fiber, this POF presents losses higher than 160 dB/km However, using the C-Band has the associated advantage of operating in the standard optical telecommunications window, where integration with the standard single mode fiber (SMF) optical fiber networks could be simplified.

In this paper we report for the first time a transmission experiment with four channels operating at 12.5 Gb/s each over 50 m of GI-POF in the C-Band. This is an example of a WDM transmission system operating at 50 Gb/s.
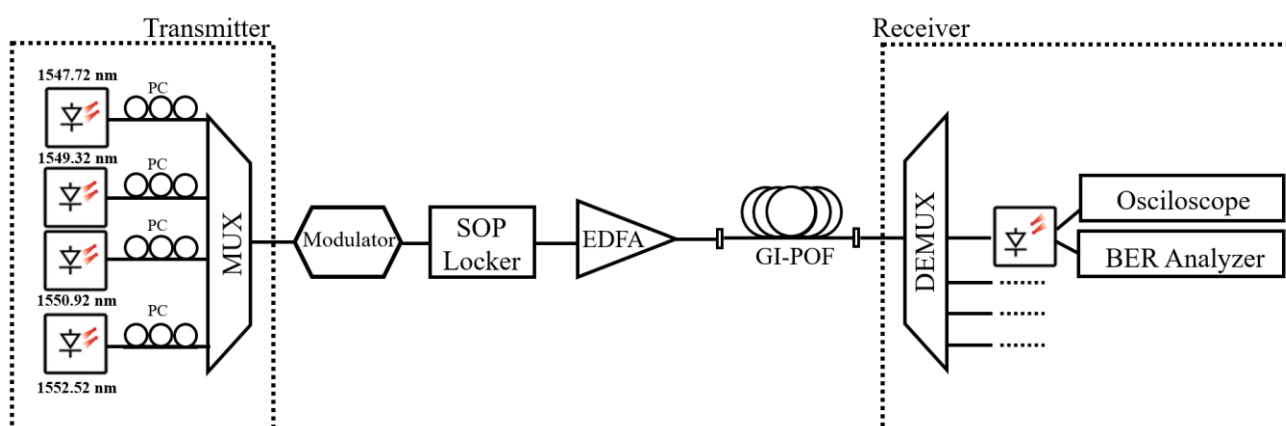
2. Experimental Setup

Figure 1. Experimental setup diagram.

Figure 1 shows the diagram of the transmission setup used. The setup is composed of four DFB lasers (EXFO IQS 2403) that are launched into individual polarization controllers and then combined in a multiplexer. The four wavelengths are 1547.72 nm, 1549.32 nm, 1550.92 nm and 1552.52 nm. The optical signal is modulated with NRZ format with a $2^{15}-1$ pseudo random sequence through a Rohde & Schwarz SMR50 signal generator and the SHF bit pattern generator module. The state of polarization (SOP) locker (Thorlabs PL100S) is used to fix and optimize the polarization state of the optical signal. An EDFA (IPG EAD-500-C3-W) is used to boost the signal before being launched into the 50 m GI-POF from Chromis Fiberoptics, Inc.. The fiber is from Chromis Fiberoptics, Inc. The fiber is terminated with FC/PC contacts and it was connected to the 9 um core silica patch cords in both transmitter and receiver side by direct fiber end-to-end connection using FC/PC fiber adaptors. We stress out that the connection from the multimode GI-POF to the single mode silica fiber at the receiver side is one of the biggest problems in this type of configuration, since more than 99 % of the signal will be lost. The four WDM channels were separated using a demultiplexer. An APD photo detector (Oclaro AT10XGC) was used. Optical eye diagrams and bit error ratio (BER) measurements were studied using an oscilloscope (HP 54610B) and the SHF error analyser module.

3. Results and Discussion

In order to analyse the spectrum of the four WDM system, before and after transmission, it was used a multimode optical spectrum analyser (Yokogawa AQ6375). Before the GIPOF, the EDFA was not used and the spectra were measured after the SOP locker, either with one laser on and with the four lasers where on. After the transmission, the EDFA was used to boost the signal from 2.30 dBm to 20 dBm, and the spectra were collected at the output of the GI-POF, either when only one laser was on and when all the lasers were on. The results obtained for the different scenarios can be seen in Figure 2.
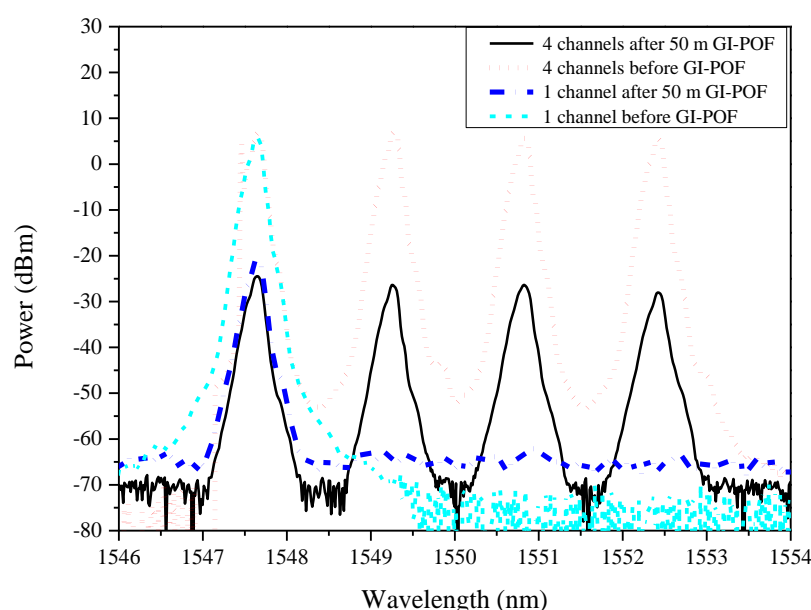

Figure 2. Channel spectra collected before and after propagation in the GI-POF

As can be seen from Figure 2, the peak power obtained after the transmission is lowered when compared with the one obtained for the direct configuration. This result is expected, due the high fiber attenuation at the C-Band and the simplified coupling. Therefore, the EDFA is not enough to amplify the signal to the same amount as it was in the launching conditions. Another observation is that the spectra shape is preserved after transmission for both configurations (with four channels and with only one channel). From these results it becomes clear the possibility to demodulate each of the four signals.

In order to check the performance of the four WDM system at 12.5 Gb/s, the 1547.72 nm wavelength channel was selected for the BER analysis. The result is shown in Figure 3 for a maximum received power of -22 dBm.
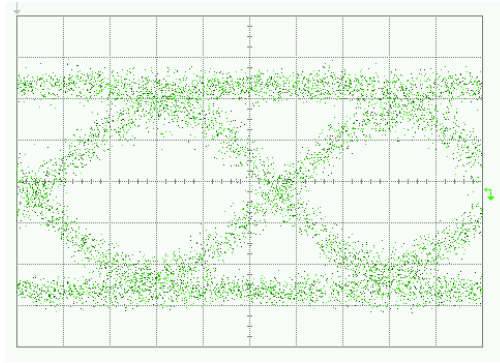
Figure 3. Eye diagram obtained for the 1547.72 nm channel, after transmission and considering the system operating with four channels.

As can be seen from Figure 3, the eye is clearly opened and measurements of the BER revealed error free operation.

In order analyse the performance of the four WDM system at 12.5 Gb/s, it was measured the BER for two distinct channels (i.e. 1547.72 nm and 1549.32 nm), either when all the channels are used and in single-channel operation. These results are also compared with back to back performance and can be seen in Figure 4.
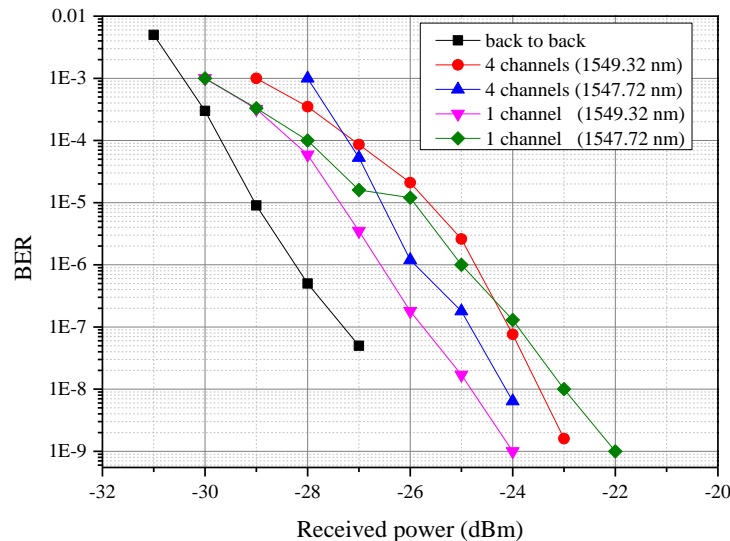

Figure 4. BER vs. received power for four channels launched into the fiber and just one channel. The measured channels were 1549.32 nm and 1547.72 nm.

The results show similar performance for either a four channel or a single channel scenario, being the channel at 1549.32 nm, the one that presents the best performance. This shows that inter-channel crosstalk does not significantly affect the performance. The high attenuation of the fiber at this wavelength region and the high coupling loss from the multimode GI-POF to the single mode silica fiber are the major performance impairments. Despite these issues, when compared to back-to-back performance, the penalty in received power has a maximum of 4 dB for the WDM operation in 1549.32 nm for a BER of $1e^{-7}$.

4. Conclusion

This paper, to the best of our knowledge, successfully demonstrates for the first time WDM transmission at the C-band over GI-POF. We proposed a four channel WDM system that achieves 50 Gb/s transmission over 50 m of GI-POF with a BER penalty of 4 dB. In the future, a more efficient multimode to single mode coupling techniques would provide an ampler optical power budget, which would enable an increment in both fiber length and channel number.

References

[1] Y. Shao, R. Cao, Y.-K. Huang, P. N. Ji, and S. Zhang, "112-Gb/s Transmission over 100 m of Graded-Index Plastic Optical Fiber for Optical Data Center Applications," in *Optical Fiber Communication Conference*, 2012, p. OW3J.5.

[2] H. Yang, S. C. Lee, E. Tangdiongga, F. Breyer, S. Randel, and T. Koonen, "40-Gb/s Transmission over 100m Graded-Index Plastic Optical Fiber Based on Discrete Multitone Modulation," in *Optical Fiber Communication Conference*, 2009, p. PDPD8.

[3] H.-C. Peng, H.-H. Lu, C.-Y. Li, H.-S. Su, and C.-T. Hsu, "Integration of FTTH and GI-POF in-house networks based on injection locking and direct-detection techniques.," *Opt. Express*, vol. 19, no. 7, pp. 6749–6755, 2011.

[4] Y. Koike and K. Koike, "Progress in low-loss and high-bandwidth plastic optical fibers," *J. Polym. Sci. Part B Polym. Phys.*, vol. 49, no. 1, pp. 2–17, Jan. 2011.

[5] P. J. Pinzón, I. Pérez, and C. Vázquez, "Visible WDM System for Real-Time Multi-Gb/s Bidirectional Transmission over 50-m SI-POF," *IEEE Photonics Technol. Lett.*, vol. 28, no. 15, pp. 1696–1699, 2016.

[6] X. Li, N. Bamiedakis, J. J. D. McKendry, E. Xie, R. Ferreira, E. Gu, M. D. Dawson, R. V. Penty, and I. H. White, "11 Gb/s WDM Transmission Over SI-POF Using Violet, Blue and Green μLEDs," in *Optical Fiber Communication Conference*, 2016, p. Tu2C.5.

[7] R. Kruglov, S. Loquai, J. Vinogradov, O. Ziemann, C.-A. Bunge, G. Bruederl, and U. Strauss, "10.7 Gb/s WDM Transmission over 100 m SI-POF with Discrete Multitone," in *Optical Fiber Communication Conference*, 2016, p. W4J.5.

Sensitivity optimization of POF sensors based on an intensity low-cost configuration targeting chemical and biochemical sensing

F. Sequeira[1,2*], R. Nogueira[1], A. Rudnitskaya[2,3], N. Cennamo[4], L. Zeni[4], L. Bilro[1,5]

1 Instituto de Telecomunicações, Aveiro, Portugal
2 CESAM, University of Aveiro, Aveiro, Portugal
3 Department of Chemistry, University of Aveiro, Aveiro, Portugal
4 Department of Industrial & Information Engineering, University of Campania Luigi Vanvitelli, Aversa, Italy
5 I3N/FSCOSD, Department of Physics, University of Aveiro, Aveiro, Portugal
*Corresponding author: fsequeira@av.it.pt

Abstract: We report the development of RI POF sensors for water quality assessment using simple, fast and low-cost methods. The modification of the surface roughness of the POF's sensing region allowed to increase the sensor's sensitivity. The optical monitoring was performed through an intensity-based low-cost system comprising a LED, an optical coupler and two photodetectors. These sensors can be used for liquid refractive index sensing with 10^{-4} RIU resolution and future developments aim chemical and biochemical sensing using selective layers.

1. Introduction

Water quality assessment using low-cost POF sensors and remote monitoring systems are the aim of this research group. Monitoring of surface water status is of fundamental importance since its chemical pollution presents a threat to human health and to the aquatic environment. However, the monitoring of relevant parameters is constrained by the availability and cost of commercial sensors. Bilro et al. presented a review of POF sensor technology with a special focus on intensity variation schemes and low-cost solutions [1].

Numerous studies related to refractive index (RI) POF sensors can be found in the literature. Bilro et al. reported theoretical modelling of D-shaped POFs at different macrobending conditions and external RI, which was validated by experimental results [2]. Recently this group reported the development of a POF sensor for RI sensing with 6.48×10^{-3} RIU resolution with simple and low-cost methods, through the optimization of the sensing region length in D-shaped POFs [3].

Aiming chemical and biochemical sensing, the selectivity to the analytes of interest can be imparted to the optical fibre by using appropriate recognition layers or sensing membranes. Cennamo et al. have reported several biological and chemical sensors based on SPR (surface plasmon resonance) in a D-shaped POF [4], [5], [6] with typical optical resolution of around 6×10^{-4} RIU [7].

In this paper we report the development of a low cost, fast and reusable POF RI sensor for aqueous medium with less than 4×10^{-4} RIU resolution, which allows future developments for chemical and biochemical sensing.

2. Materials and methods

2.1 POF preparation and modification

Commercially available step-index plastic optical fibres (POFs) from Asahi Kasei, DB-1000, were selected with 1 mm diameter and 0.5 numerical aperture (NA). The core, 980 µm, is made of polymethyl methacrylate (PMMA) with 1.49 refractive index and the cladding consists in a fluorinated polymer.

Three sensors were prepared – Sensor A, B and C. First, the optical fibres were cut to the desired length, around 60 cm, using a POF cutter. The tips of the fibres were polished using sandpaper with different grain sizes (5, 3, 1 and 0.3 µm). In a selected portion of the fibre, with 5 cm length, the perfluorinated polymer cladding was removed using solutions of acetone and distilled water. In this process the fibre needs to be handled carefully to prevent from breaking. After cladding removal, the fibres were washed with distilled water several times and the thickness of this region was measured with a *Mitutoyo* Micrometer. Sensors B and C were subjected to a gentle polish with fiber optic polishing film of 12 µm, washed with distilled water several times and the thickness of the sensing region was measured using the same procedure. This polishing process aimed to increase the roughness of the sensing region without significantly changing the thickness of this region.

2.2 Optical monitoring - refractive index sensing

The sensors were characterized to RI using sucrose solutions with increasing refractive index varying from around 1.33 (only water) to 1.41. Sucrose solutions were prepared with distilled water and the refractive index (*nD*) at 25ºC was measured with the *Refractometer Abbemat 200* from *Anton Paar*, with 1×10^{-4} resolution.

The fiber was placed in a reactor and characterized in transmission using a LED (660 nm), an optical coupler (90:10) and two photodetectors. The signal output was monitored in real time with *LabView* software. The signal is self-referenced, avoiding source fluctuation and external variations (*k*). The response was first recorded in distilled water (k_{water}), with constant stirring. After 15 min the distilled water was removed with a syringe and the next solution was added and removed in order to clean the reactor, after which was added again and the signal recorded ($k_{solution}$). At the end, a washing step with distilled water was repeated several times (remove solution and add water). The tests were recorded in continuum and the average value of 5 min was used for data analysis. The signal output was the normalized transmitted signal to water (k_{norm}):

$$k_{norm} = \frac{k_{solution}}{k_{water}} .$$

$$(1)$$

When the solutions were removed from the reactor, their refractive index was measured using the *Refractometer Abbemat 200* from Anton Paar, with 1×10^{-4} resolution.

3. Results and discussion

All sensors were inspected with *LEICA DM750M* microscope, Figure 1. The obtained images allow to confirm the increase of the sensing region roughness through the polishing procedure.
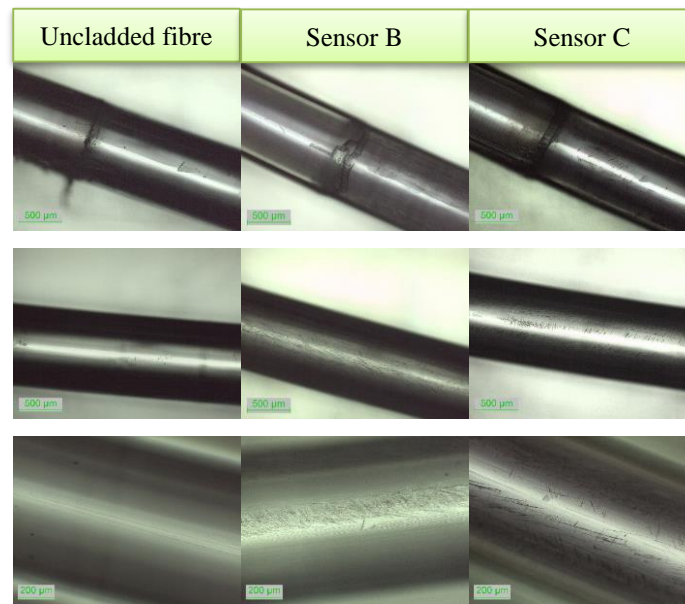

Figure 1. Microscope images: view of the transition and central zones of the sensing region.

The thickness of the fibres was measured using a *Mitutoyo* Micrometer, 30 times along the sensing region, and the mean value and standard deviation were calculated. The results are presented in Table 1. Results show that there is no relevant difference in the obtained thickness after the polishing procedure applied to Sensors B and C.

Table 1. Thickness of the sensing region for all the preparation steps.

Sensor		Thickness (mm)
A	Original POF	1.012 ± 0.003
	Uncladded – Sensor A	0.990 ± 0.002
B	Original POF	0.999 ± 0.005
	Uncladded	0.973 ± 0.004
	After polishing – Sensor B	0.972 ± 0.005
C	Original POF	0.998 ± 0.001
	Uncladded	0.973 ± 0.001
	After polishing – Sensor C	0.972 ± 0.001

For each sensor three tests were performed in order to verify repeatability. The average value of the three tests (k_{avg}) was calculated and plotted against the average of the real RI value measured in the refractometer, Figure 2a. For the uncladded POF is clearly seen that, in this range of refractive index, there is no variation of the transmitted signal except for RI of 1.41 (sensor A). When the sensing region was softly polished with 12 μm polishing film (sensors B and C) an increase of the transmitted signal with increase of external RI was observed. The response of sensors B and C is not exactly the same, which indicates that this is not a repeatable manufacturer process, although the responses are very similar. For both polished sensors, it was observed a recover with water, Figure 2b shows the results obtained for Sensor B.
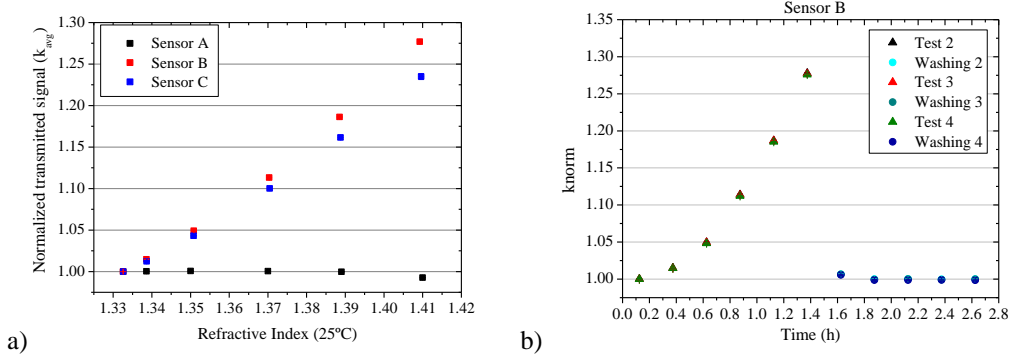

a)   b)

Figure 2. Normalized transmitted signal: (a) Sensors A,B,C - average value of three tests performed (k_{avg}) with refractive index variation; (b) Sensor B - RI test and washing (k_{norm}) with time, for the three tests performed.

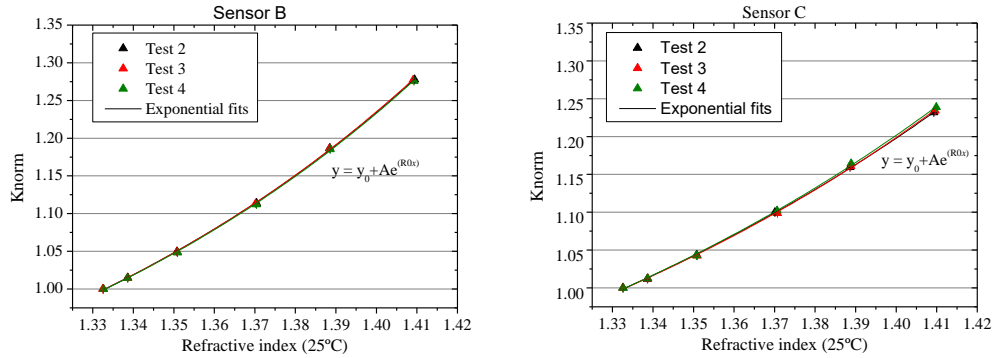For each RI test performed an exponential fitting was applied to the obtained results, Figure 3.

Figure 3. RI tests and exponential fitting: Sensor B and Sensor C.

The sensitivity (S) and resolution (Δn) of the sensors are defined by:

$$S = \left|\frac{\partial k_{norm}}{\partial n_{ext}}\right| = R_0 A e^{(R_0 n_{ext})} \text{ and } \Delta n = \frac{1}{S} . \delta k_{normmax}, \qquad (2)$$

where $\delta k_{normmax}$ is the maximum value of standard deviation obtained for the test considered. Sensitivity and resolution were calculated and depicted in Figure 4.
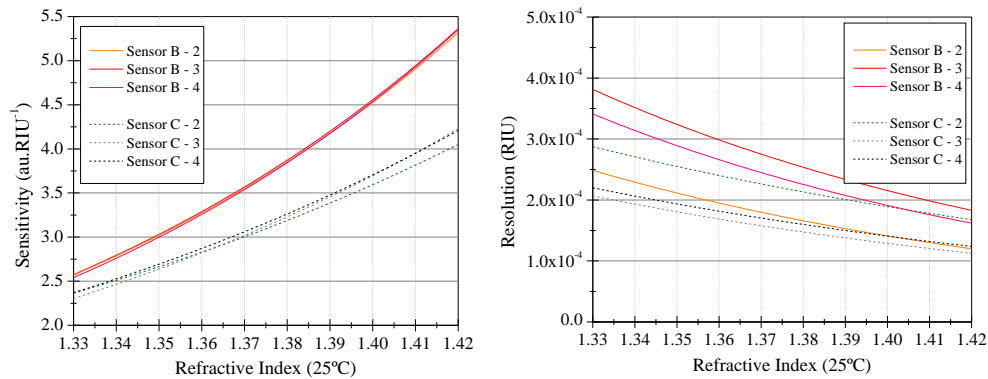

Figure 4. Sensitivity and resolution: Sensor B and Sensor C.

The obtained sensitivity and resolution are dependent on the refractive index of the external medium. This work aims the development of POF sensors for chemical and biochemical sensing, therefore, the external refractive index will be dependent of the selective layer that is deposited / grown in the surface of the sensing region. Nevertheless, in the studied range (1.33 – 1.41) the obtained resolution is inferior to 4.0×10^{-4} RIU, which allows future developments for chemical/biochemical sensing and also the use of these sensors for liquid refractive index sensing.

4. Conclusion

Refractive Index POF sensors were successfully developed using simple, fast and low-cost procedures. The soft polishing process allowed to increase the roughness of the sensing region of POFs without significant change in the obtained thickness. These sensors have a resolution inferior to 4.0×10^{-4} RIU, which allows future developments for chemical and biochemical sensing through the use of selective layers and also its use as a refractive index sensor for liquids. Very promising results were obtained: repeatable response with RI variation; very good resolution; complete and fast recover with washing; similar response obtained for different sensors. Future work aims to continue this study in order to better understand the influence of the surface roughness in RI sensing with uncladded POFs and the development of chemical and biochemical sensors for water quality assessment through simple, fast, low-cost and environmental friendly procedures.

5. Acknowledgements

6. References

[1]   L. Bilro, N. Alberto, J. L. Pinto, and R. Nogueira, "Optical sensors based on plastic fibers.," *Sensors (Basel).*, vol. 12, no. 9, pp. 12184–207, Jan. 2012.

[2]   L. Bilro, N. J. Alberto, L. M. Sá, J. D. L. Pinto, and R. Nogueira, "Analytical Analysis of Side-Polished Plastic Optical Fiber as Curvature and Refractive Index Sensor," vol. 29, no. 6, pp. 864–870, 2011.

[3]   F. Sequeira *et al.*, "Refractive Index Sensing with D-Shaped Plastic Optical Fibers for Chemical and Biochemical Applications," *Sensors*, vol. 16, no. 12, p. 2119, 2016.

[4]   N. Cennamo *et al.*, "An innovative plastic optical fiber-based biosensor for new bio/applications. The case of celiac disease," *Sensors Actuators B Chem.*, vol. 176, pp. 1008–1014, Jan. 2013.

[5]   N. Cennamo, G. D'Agostino, M. Pesavento, and L. Zeni, "High selectivity and sensitivity sensor based on MIP and SPR in tapered plastic optical fibers for the detection of L-nicotine," *Sensors Actuators B Chem.*, vol. 191, pp. 529–536, Feb. 2014.

[6]   N. Cennamo *et al.*, "An easy way to realize SPR aptasensor: A multimode plastic optical fiber platform for cancer biomarkers detection," *Talanta*, vol. 140, pp. 88–95, 2015.

[7]   N. Cennamo, D. Massarotti, L. Conte, and L. Zeni, "Low cost sensors based on SPR in a plastic optical fiber for biosensor implementation.," *Sensors (Basel).*, vol. 11, no. 12, pp. 11752–60, 2011.

INSTALLATION 4.0 WITH PLASTIC OPTICAL FIBRE

J.Faller [1*]

1: homefibre digital network gmbh, Fratresstrasse 20, 9800 Spittal a.d.Drau Austria

Abstract:

Plastic Optical Fibre for home network is marketed since years. The Gigabit Ethernet transmission and IEEE standard brought a strong momentum for product development and acceptance of POF systems in the market. The big breakthrough in the market is still pending, although an increasing number of industrial companies are observing technology and markets and some of them are entering the market with new products. Several concepts to deploy this technology have been introduced and approved successfully. The learnings form the market show an enormous potential and some hurdles to apply and to install POF in home networks. We have learned from the market that, on one side, today and future digital homes will need a reliable and efficient broadband infrastructure, while on the other side, the building industry is under cost pressure to decrease building and installation cost. This is the big chance for POF. There is a gap between the demand of more and better connectivity and less installation cost. Today this gap must be filled up and paid by the end-user for the price of energy inefficient network products and systems and a lot of related disadvantages of "No New Wire" technologies, to get acceptable connectivity in their home. Thus, POF is in fact the most promising technology to cover the demand on comprehensive and flexible connectivity, for builder, end-user, service provider and installer.

To use this opportunity, we propose to consider that digitalization, IP broadband technology and new services have a strong impact and correlation with electrical installation, related smart home- and IoT concepts. Beside an almost confusing number of proprietary IoT systems, an integrated IP-based approach opens a wide field of opportunities and perspectives for consumer friendly and demand oriented systems. The basic therefore is always a reliable infrastructure and sufficient connectivity which allows flexible integration of components and applications.

In this Tutorial, we like to discuss the well-known pros and cons of POF technology with focus on the impact to and the combination with the electrical installation. We like to show a concept how electrical installation and POF broadband network can be merged to a high efficient installation concept, called INSTALLATION 4.0. This concept leads to a home infrastructure which

1. covers the complete broadband traffic, from internet to UHD TV streaming, and
2. offers the backbone for the IP-based smart home and IoT applications and gateways
3. and allows the end user to adapt his home according his personal requirement, either with conventional electrical installation or as a real smart home.

The aim of our activities is to create and deploy a new electrical broadband installation standard. It will be an electrical installation in a star-wired architecture combined with plastic optical fibre, available everywhere in the home. This concept allows builder to install an entire broadband infrastructure with a minimum of investment and offers a maximum of connectivity and flexibility for installer and end-user. It is the basic of the digital home.

This tutorial will give an overview about the practical experiences we have made with POF and IP-Home Networks until today and show challenges, opportunities, perspectives and concrete ways to the future.

Requirement to a Modern Home Network
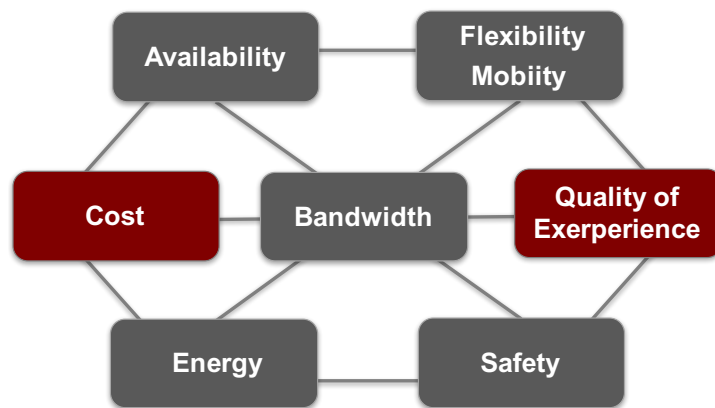
Picture 1: Requirement to a modern home network

Picture 2: The gap between connectivity demand an investment

Key words: Connected Home, connected TV, Home Network, Infrastructure, Smart Home, Electrical Installation, IoT, Smart Home